

# EVALUATION OF NONLINEAR CONSTITUTIVE PROPERTIES OF CONCRETE

by

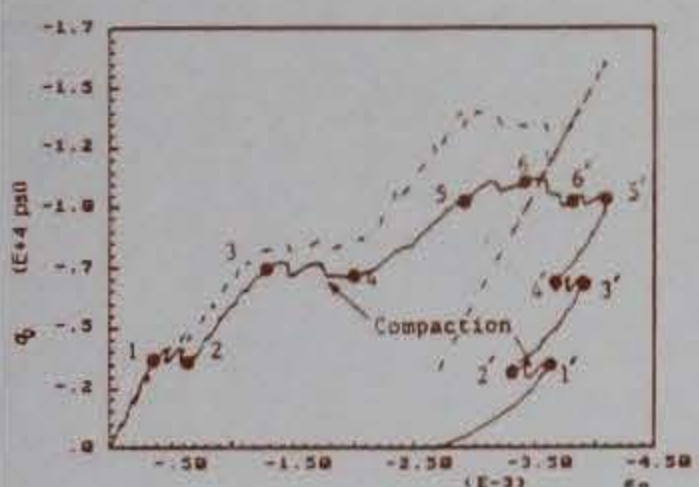
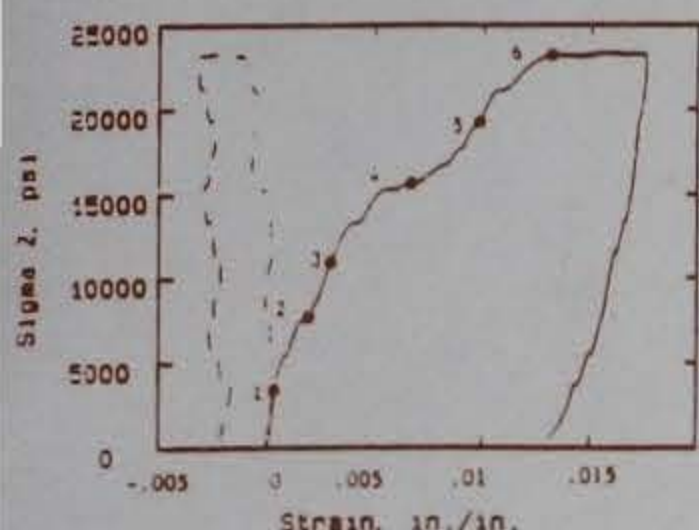
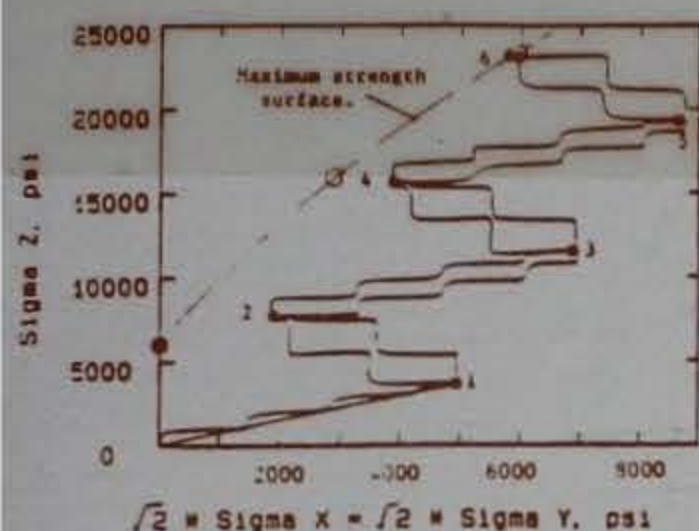
Charles Dean Norman

Structures Laboratory

DEPARTMENT OF THE ARMY

Waterways Experiment Station, Corps of Engineers  
3909 Halls Ferry Road, Vicksburg, Mississippi 39180-6199

US-CE-C Property of the  
United States Government



February 1990

Final Report

Approved For Public Release; Distribution Unlimited

RESEARCH LIBRARY  
US ARMY ENGINEER WATERWAYS  
EXPERIMENT STATION  
VICKSBURG, MISSISSIPPI

Prepared for Ballistic Missile Office  
Norton Air Force Base, California 92409-6468

and

Defense Nuclear Agency  
Washington, DC 20305-1000





21144813

TAY  
W34  
no. SL-90-1

Unclassified

SECURITY CLASSIFICATION OF THIS PAGE

REPORT DOCUMENTATION PAGE				Form Approved OMB No. 0704-0188	
1a. REPORT SECURITY CLASSIFICATION Unclassified			1b. RESTRICTIVE MARKINGS		
2a. SECURITY CLASSIFICATION AUTHORITY			3. DISTRIBUTION/AVAILABILITY OF REPORT		
2b. DECLASSIFICATION/DOWNGRADING SCHEDULE			Approved for public release; distribution unlimited.		
4. PERFORMING ORGANIZATION REPORT NUMBER(S) Technical Report SL-90-1 (CTIAC Report No. )			5. MONITORING ORGANIZATION REPORT NUMBER(S)		
6a. NAME OF PERFORMING ORGANIZATION USAEWES Structures Laboratory		6b. OFFICE SYMBOL (If applicable) CEWES-SC-R		7a. NAME OF MONITORING ORGANIZATION	
6c. ADDRESS (City, State, and ZIP Code) 3909 Halls Ferry Road Vicksburg, MS 39180-6199			7b. ADDRESS (City, State, and ZIP Code)		
8a. NAME OF FUNDING/SPONSORING ORGANIZATION Ballistic Missile Office		8b. OFFICE SYMBOL (If applicable)		9. PROCUREMENT INSTRUMENT IDENTIFICATION NUMBER	
8c. ADDRESS (City, State, and ZIP Code) Norton Air Force Base CA 92409-6468			10. SOURCE OF FUNDING NUMBERS		
			PROGRAM ELEMENT NO.	PROJECT NO.	TASK NO.
			WORK UNIT ACCESSION NO.		
11. TITLE (Include Security Classification)  Evaluation of Nonlinear Constitutive Properties of Concrete					
12. PERSONAL AUTHOR(S) Norman, C. Dean					
13a. TYPE OF REPORT Final Report		13b. TIME COVERED FROM Oct 1987 to May 1989		14. DATE OF REPORT (Year, Month, Day) February 1990	
15. PAGE COUNT 216					
16. SUPPLEMENTARY NOTATION Available from National Technical Information Service, 5285 Port Royal Road, Springfield, VA 22161.					
17. COSATI CODES			18. SUBJECT TERMS (Continue on reverse if necessary and identify by block number)		
FIELD	GROUP	SUB-GROUP	Computer models      Material properties		
			Concrete      Plasticity		
			Constitutive models		
19. ABSTRACT (Continue on reverse if necessary and identify by block number)  This report describes the development of a methodology that allows for the objective evaluation of the predictive capabilities of concrete constitutive models.  The structural analysis and design of concrete structures is often based on large-scale finite element computations. A key component of the finite element method is the constitutive model that is usually selected and calibrated based on a few simple tests. The primary reason for this is the lack of understanding of the complex response features of concrete and numerical difficulties encountered when attempting to model these features. Also, the error in response predictions due to an inappropriate constitutive model is difficult to define in a complex large-scale structural analysis problem.  (Continued)					
20. DISTRIBUTION/AVAILABILITY OF ABSTRACT <input type="checkbox"/> UNCLASSIFIED/UNLIMITED <input checked="" type="checkbox"/> SAME AS PT. <input type="checkbox"/> DTIC USERS			21. ABSTRACT SECURITY CLASSIFICATION Unclassified		
22a. NAME OF RESPONSIBLE INDIVIDUAL			22b. TELEPHONE (Include Area Code)		22c. OFFICE SYMBOL



## 19. ABSTRACT (Continued).

The method of evaluation, as developed herein, consists of the following steps:

1. The design and execution of a series of material properties tests which provide data sufficient for the calibration of the constitutive model under consideration.
2. Calibration of the model using the data developed in Step 1.
3. Design and execution of the series of verification tests which provide data sufficient for defining key complex material response features that are to be modeled.
4. Direct comparison of model predicted response with experimental measurements through the use of a constitutive driver.

The constitutive models were evaluated, the Fracture Energy Based Model (FEBM) and the Endo-chronic Concrete Plasticity Model (ECPM).

While there are very many constitutive models for concrete currently available in the literature, it was not possible within the scope of this research project to evaluate all of them, although the methodology presented should be equally applicable to all. The selection of the FEBM and the ECPM is not intended to endorse these models as the better ones. The results show that, although they are able to predict qualitatively some key response features observed in the verification tests, they fail to predict accurately other response features. These models were selected because they are two of the more recent and comprehensive ones and also the theoretical development of the two is significantly different.



## PREFACE

The research reported herein was conducted at the US Army Engineer Waterways Experiment Station (USAEWES), Structures Laboratory (SL), under the sponsorship of the Ballistic Missile Office (BMO) of the US Air Force, Norton Air Force, Base, CA. The general concept and financial support for this study were further promoted by the Defense Nuclear Agency (DNA). Funds for the publication of the report were provided from those made available for operation of the Concrete Technology Information Analysis Center (CTIAC) at WES, SL. This is CTIAC Report No. 86.

The BMO project officer was LT Rob Michael and the technical director was Dr. Mike Katona, TRW Systems, Norton Air Force Base. LTC Don Gage and CPT John Higgins, US Air Force, and Dr. Kent Goering, DNA, were involved in this project through their agencies.

Dr. C. Dean Norman, Concrete Technology Division (CTD), SL, WES, prepared this report in partial fulfillment of the Ph.D. requirements from the University of Texas at Austin. The University's supervisory committee included Drs. Jose Roesset, Eric Becker, John Tassoulas, Phillip Johnson, and James Jirsa. The late Dr. Nathan M. Newmark accepted membership on the committee but was unable to serve.

The work was accomplished during the period October 1987 through May 1989 at WES under the general supervision of Mr. Bryant Mather, Chief, SL, and Mr. Ken Saucier, Chief, CTD. Messrs. Michael I. Hammons and Donald M. Smith, CTD, conducted tests, data reduction, general review, and discussions of test results. Ms. Sharon Garner, CTD, was directly responsible for modifying and developing effective software in the WES Constitutive Driver used in the evaluation of constitutive models for this study. Dr. John Peters, Geotechnical Laboratory, provided many helpful discussions, and Messrs. Dan Wilson and James Shirley, CTD, SL, performed outstanding work through the test program designed and directed by Dr. Norman. The technical report was published by the Information Technology Laboratory, WES.

COL Larry B. Fulton, EN, is the Commander and Director of WES. Dr. Robert W. Whalin is the WES Technical Director.



## Table of Contents

	<u>Page</u>
Preface .....	i
Conversion Factors, Non-SI to SI (Metric) Units of Measurement.....	iii
1. Introduction.....	1
1.1 Background.....	1
1.2 Objectives.....	5
1.3 Scope.....	6
1.4 Outline.....	6
2. Stress Strain Response of Concrete.....	11
2.1 General.....	11
2.2 Loaders, Test Devices, and Instrumentation.....	15
2.3 Unconfined Compression Tests.....	21
2.4 Hydrostatic Compression Test.....	26
2.5 Uniaxial Strain Test.....	27
2.6 Triaxial Compression Test.....	30
2.7 Verification Tests.....	38
3. Constitutive Equations.....	56
3.1 General.....	56
3.2 Linear Elasticity.....	57
3.3 Conventional Plasticity.....	64
3.4 Material Stability Postulates, Uniqueness.....	76
3.5 Examples of Hardening and Softening Formulations.....	81
3.6 Fracture Energy Based Model.....	89
3.7 Endochronic Plasticity Model.....	104
4. Comparison of Model Predictions Versus Test Results.....	128
4.1 General.....	128
4.2 WES-Constitutive Driver.....	128
4.3 Comparison of Model Predictions with WES Tests.....	133
4.4 FEBM and ECPM - VT4-1, VT4-2, VT4-3.....	190
4.5 FEBM and ECPM - VT5-1, VT5-2, VT5-3.....	196
5. Conclusions/Recommendations.....	200
5.1 Summary.....	200
5.2 Conclusions.....	201
5.3 Recommendations.....	205
6. Bibliography.....	208



# CONVERSION FACTORS, NON-SI TO SI (METRIC)

## UNITS OF MEASUREMENT

Non-Si units of measurement can be converted to SI (metric) units as follows:

<u>Multiply</u>	<u>By</u>	<u>To Obtain</u>
inches	25.4	millimetres
feet per second	0.3048	metres per second
kips (1,000-lb mass)	453.59237	kilograms
kips (force) per square inch	6.894757	megapascals
pounds (force)	4.448222	newtons
pounds (force) per square inch	0.006894757	megapascals



# Evaluation of Non-linear Constitutive

## Properties of Concrete

### Chapter 1: Introduction

#### 1.1 Background.

The complex stress-strain response features of concrete have been studied and discussed considerably in the technical literature with summaries of these results presented in many textbooks (e.g., Neville<sup>(1)\*</sup>, Chen<sup>(2)</sup>, etc.). Some of the key response features which can have a significant impact on the development of constitutive models include:

- a. The dependence of yield or maximum strength surfaces on confining stress.
- b. The occurrence of plastic volume change and in particular plastic volume change due to pure shear loading.
- c. Strain softening under displacement controlled loading conditions.

The general effects of these features on stress strain response are presented in Figures 1.1 through 1.3. Figure 1.1 shows the effects of increasing confining stress on the stiffness and strength of a concrete specimen under increasing axial stress. Figure 1.2 shows the increase in plastic volume change (compaction) due to pure shear loading, while Figure 1.3 presents test results indicating strain softening at low confining stress levels. From a qualitative standpoint, these response features can be partially explained by considering the internal structure of concrete at the three-phase level (aggregate, cement matrix, air voids). Such a description is presented graphically in Figure 1.4a, which represents a specimen from a well proportioned concrete mixture which has been properly consolidated and cured. Furthermore, it is assumed that the nominal maximum size of the aggregate is small compared to the minimum dimension of

\*Numbers in parenthesis indicate references presented at the end of the dissertation.



the specimen so that on any plane cut through the specimen, the normal and shear stress distributions can be effectively represented as a constant average value (made up of the contributions from the aggregates, cement paste, and voids). In this unloaded specimen, some cracks will be observed, primarily at the aggregate-cement matrix interface. These cracks develop during the curing process and are primarily due to differences in aggregate and cement paste stiffnesses, shrinkage, and thermal properties. When compressive axial stresses alone are applied in the vertical direction (Figure 1.4b) and monotonically increased, microcracks will begin to propagate through the cement matrix which results in a net decrease in the stiffness of the specimen. These cracks will be oriented primarily vertically on the exposed outer surface due to the tensile strains developed in the circumferential direction. Cracks will coalesce into longer vertical cracks as the stress is increased up to some maximum value where failure will occur. Actually, if the load is applied in displacement control, the load will, from this maximum value, decrease as the axial strain continues to increase, however, significant specimen cracking and damage, will be very apparent). On the other hand, if hydrostatic stresses are applied to the test specimen (Figure 1.4c), the initial cracks (Figure 1.4a) will begin to close so that shear stresses can be transferred more effectively across the aggregate-cement paste interfaces. As the hydrostatic stress increases, the normal component of stress on a typical aggregate surface element will increase, and therefore the frictional shear strength at this point will increase. In general, this confining stress effect is to increase the effective moduli of the specimen as well as the maximum strength and yield surfaces.

As the hydrostatic stresses increase, the volume decreases (compaction), and part of this volume change is irrecoverable (plastic) as shown in Figure 1.2. This, of course, is unlike the response of most metals where essentially no plastic volume change occurs as all plastic strains are associated with shear due to slip between grain



boundaries. This difference in response between polycrystalline metals and concrete is primarily due to the more heterogeneous internal structure of concrete. As voids and microcracks close under increasing hydrostatic stress, the volume decreases. However, the volume at a particular level of hydrostatic stress is not necessarily a minimum for that level of stress due to the fact that microcracks and voids can still exist due to the complicated microstress distribution in the specimen which can cause bridging around local discontinuities. As a pure shear stress is applied (at constant hydrostatic stress), a further decrease in volume occurs (Figure 1.2). This feature can be explained by approximating concrete, at a particular level of hydrostatic stress, as a loosely packed system of incompressible spheres. If any pure shear distortion is applied to the system, the volume must decrease. Also, one should consider the shearing effect of concrete along a rough crack where each application of shear tends to smooth the crack and therefore decrease the volume of the specimen containing the crack.

The third response feature listed above (strain softening) has received considerable discussion in the past and continues to be vigorously debated. The main issue is: "Should strain softening be considered a property of the material or a result of the structural geometry and loading conditions on the test specimen?" The later argument is generally based on: (a) the frequent observation of barreling of test specimens which indicates that unwanted shear stresses are being applied at the specimen boundaries and that the stress and strain state in the specimen are not homogeneous; (b) significant cracking of the test specimen, which again implies an inhomogeneous stress state in the material; (c) local inhomogeneities are observed within the test specimen and are usually associated with shear banding, etc. The central question concerning softening is localization, which implies that the assumption of a homogeneous continuum is not valid. If, on the other hand, test results are interpreted so that strain softening is to be considered a material property: (d) the



applied stresses at the specimen boundaries should be uniform, and the current specimen geometry must be given as a constant times the initial geometry; (e) the internal damage or response mechanisms (i.e., fracture, void closure, etc.) should be uniformly distributed over the specimen volume and not localized in bands of specific regions. Figure 1.4d presents conceptually what might occur in a test specimen during a softening test. The main point here is that fractures in aggregates, void closures etc. are uniformly distributed throughout the specimen volume.

The complex response features discussed here present special problems for constitutive models. The pressure sensitivity of the yield surface simply means that yield and maximum strength surfaces must be defined in terms of the confining stress level. The plastic volume change problem is usually addressed, with varying degrees of success, by defining yield surfaces which close on the hydrostatic axis or by the use of cap models. When the former method, to account for volume change, is used, constitutive models tend to overpredict lateral strains on many stress paths. To correct this problem, a nonassociated flow rule can be used which in effect changes the direction of the plastic strain vector and can therefore reduce the lateral strain component.

When strain softening is modeled as a material property, the approach used generally is to degrade or damage the maximum strength surface according to some rule which relates decrease in strength (or, say, cohesion) to a softening parameter (e.g. plastic strains) as total strains continue to increase under decreasing load.

Once constitutive models are developed which reasonably predict these complex response features, other problems are encountered when these models are implemented and used in dynamic finite-element codes. The nonassociated flow rule results in a nonsymmetric material stiffness matrix which can cause a significant increase in computational time. Also, realistic load paths can be defined along which the nonassociated model will become unstable according to



certain material stability postulates. Strain softening models also violate material stability postulates which can result in problems of numerical instability and nonunique solutions. Generally, softening and non-associated flow models tend to be undesirably sensitive to small variations in prescribed initial conditions for dynamics problems.

If a particular response feature is to be effectively modeled, then the basis for the development of the model should be sound repeatable material properties test data completely defining that response feature. On the other hand, material stability postulates should be considered when appropriate but should not be the driving force in the development of the model. More specifically, the complex material response features of concrete to be used in a particular structure should be evaluated through a carefully planned laboratory material properties test program, designed to subject the material to stress and strain histories similar to those which will occur at critical regions in the structure under the design loads. Furthermore, generic tests (e.g., uniaxial strain, unconfined compression, etc.) should be conducted to determine basic material response characteristics, validity of homogeneity and isotropy assumptions, and values for parameters used to calibrate constitutive models of interest. Finally, the concrete material should be subjected to complex load path tests, which can be used to evaluate the consistency and predictive capability of potential concrete constitutive models.

## 1.2 Objectives

The objectives of this research are:

- a. The development of a methodology for evaluating constitutive models for plain concrete.
- b. The application of this methodology in the evaluation of two advanced constitutive models.



### 1.3 Scope

The method of evaluation, as developed herein, consists of the following steps:

1. The design and execution of a series of material properties tests which provide data sufficient for the calibration of the constitutive model under consideration.
2. Calibration of the model using the data developed in step 1.
3. Design and execution of a series of verification tests which provide data sufficient for defining key complex material response features that are to be modeled.
4. Direct comparison of model predicted response with experimental measurements through the use of a constitutive driver.

The two constitutive models to be evaluated are the Fracture Energy Based Model (FEBM) (3) and the Endochronic Concrete Plasticity Model (ECPM) (4).

While there are very many constitutive models for concrete, currently available in the literature, it was not possible within the scope of this research project to evaluate all of them, although the methodology presented should be equally applicable to all. The selection of the FEBM and the ECPM is not intended to endorse these models as the better ones. The results show that although they are able to predict qualitatively some key response features observed in the verification tests they fail to predict accurately other response features. These models were selected because they are two of the more recent and comprehensive ones and also the theoretical development of the two is significantly different.

### 1.4 Outline

In Chapter 2, general stress-strain response features of concrete will be discussed along with some of the implications of strain softening. Loaders and test devices that were used in generating test results for this research project along with instrumentation used are then discussed. Finally calibration and verification test results are presented and discussed. Basic concepts of elasticity



and plasticity are presented in Chapter 3 with emphasis on generalizing the results observed in simple material-properties tests. Also, in Chapter 3, a detailed derivation of the equations for the FEBM and the ECPM are presented and the calibration of model parameters is discussed. In Chapter 4, the two models are calibrated, exercised against the verification tests results, and comparisons of tests results versus model predictions are made. Conclusions and recommendations for future research are presented in Chapter 5.

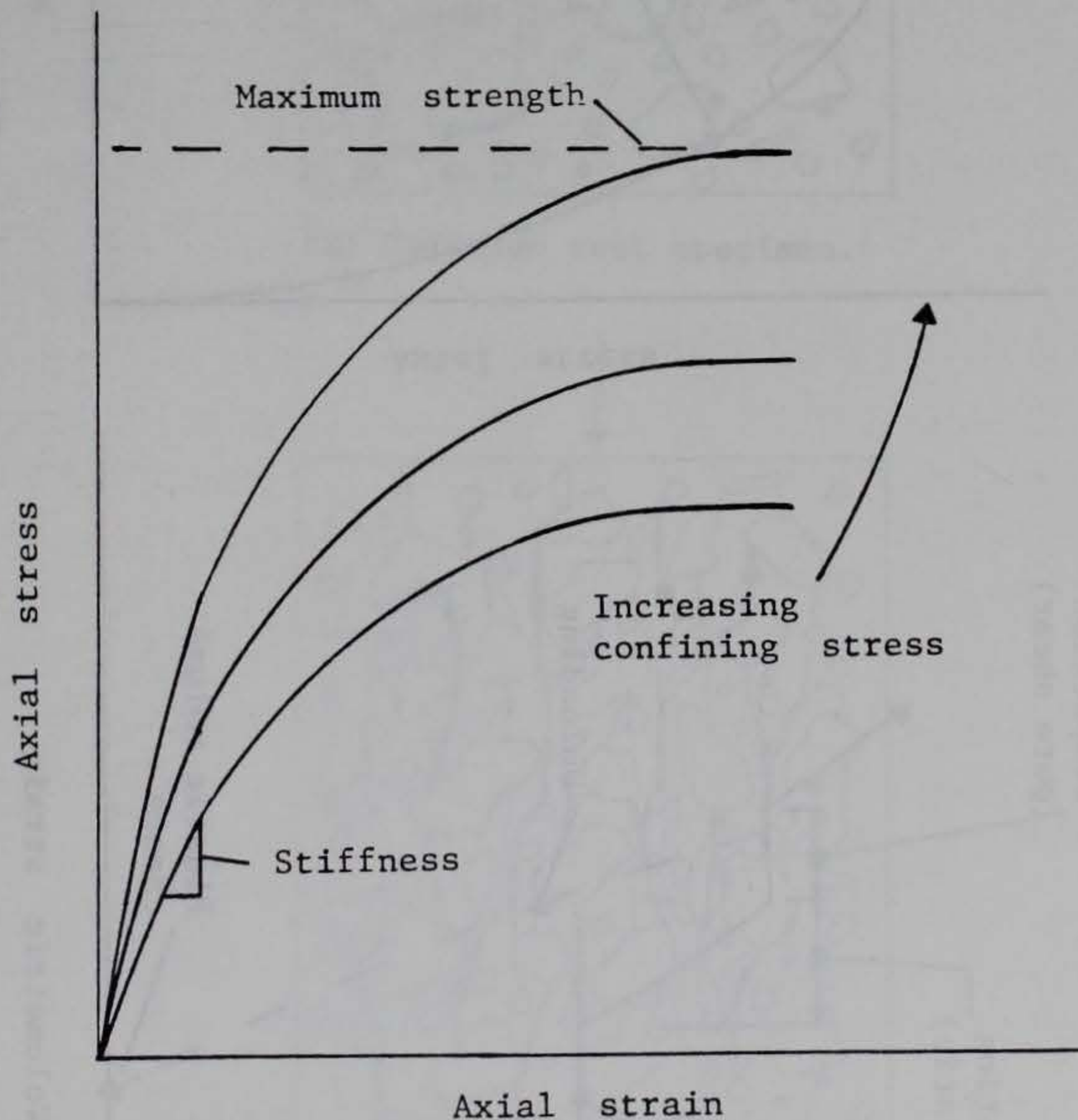


Figure 1.1. Effects of confining stress on maximum strength and stiffness.



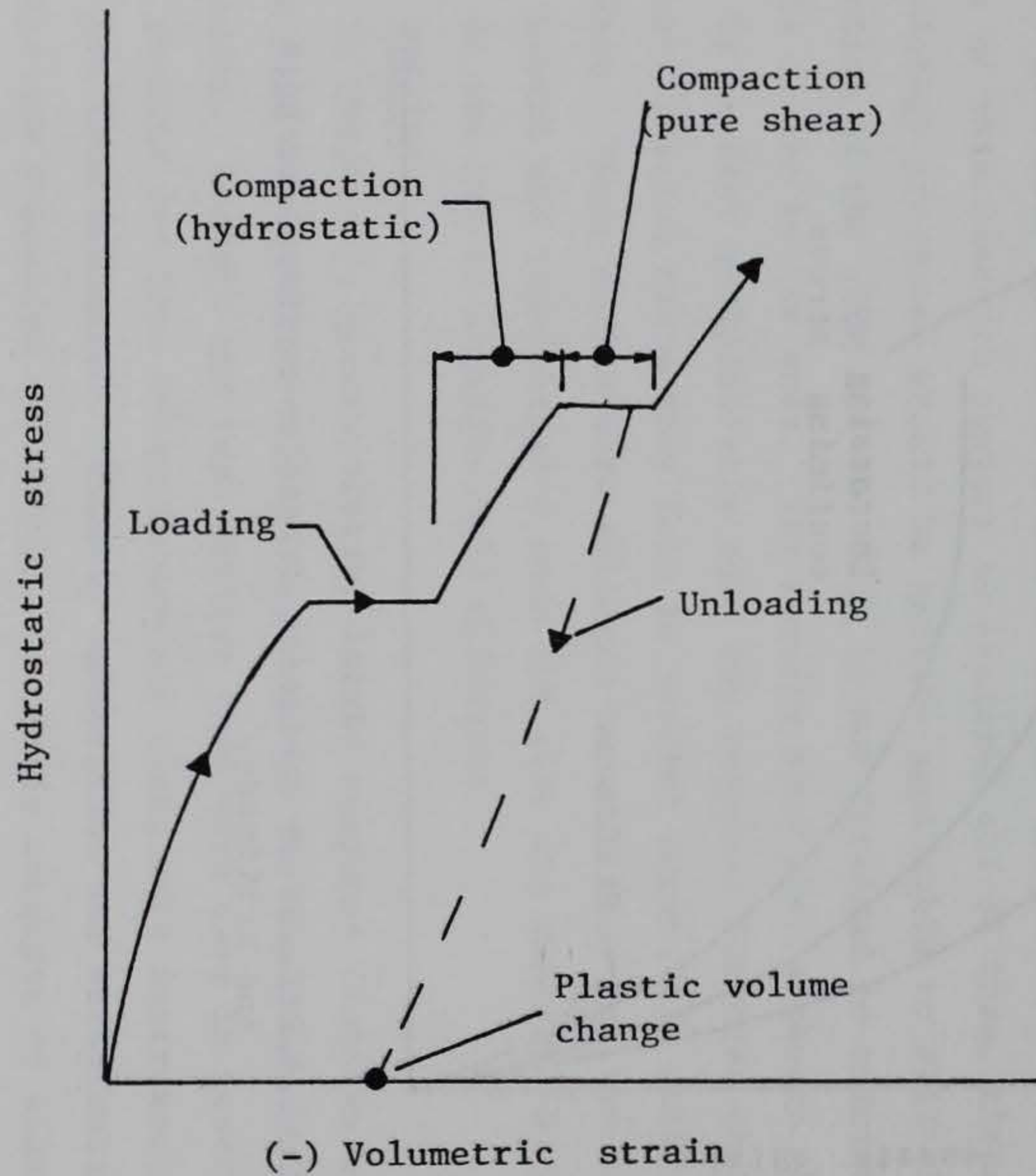


Figure 1.2. Decrease in volume (compaction) under hydrostatic and pure shear loading.

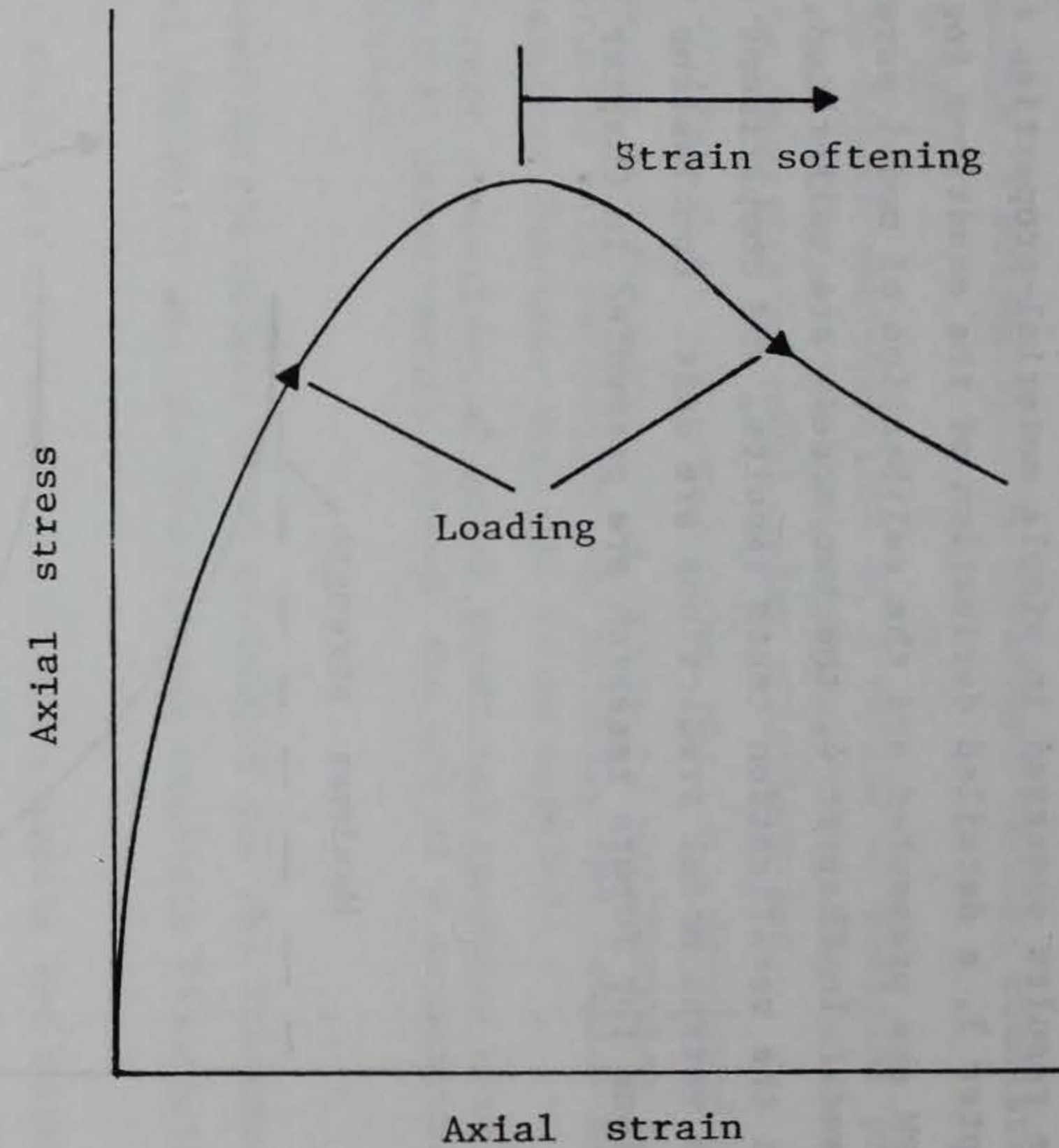
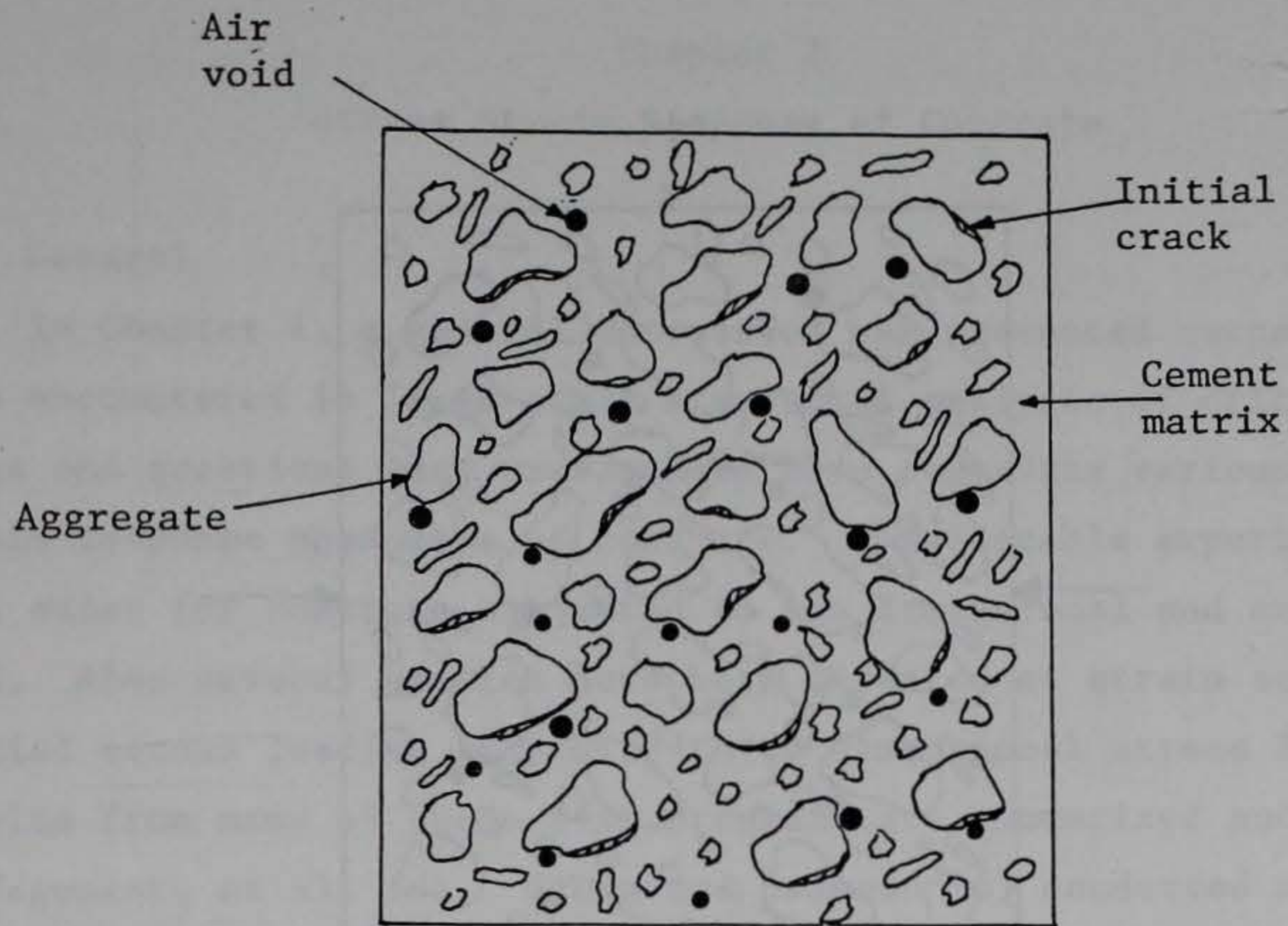
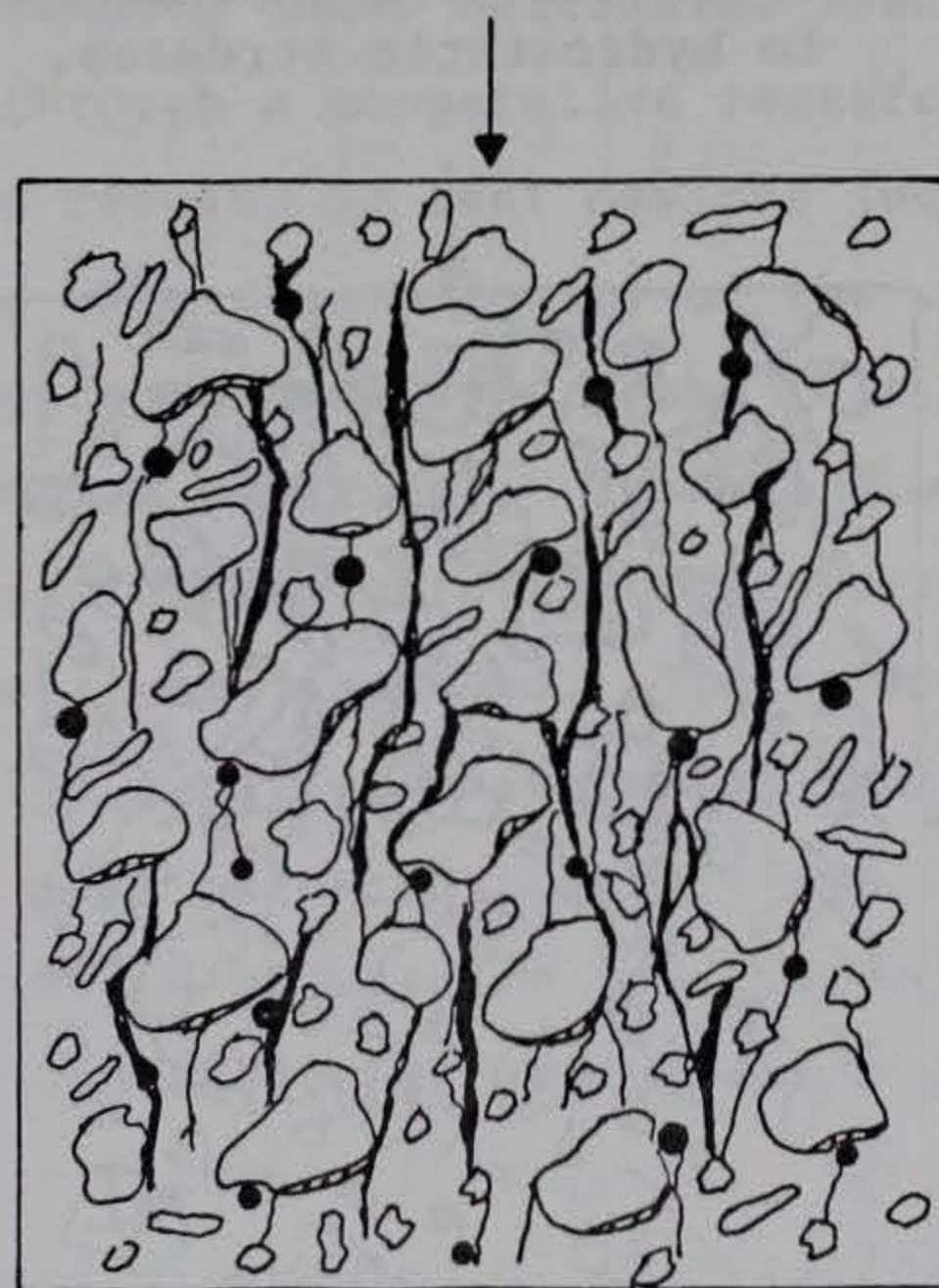


Figure 1.3. Strain softening.





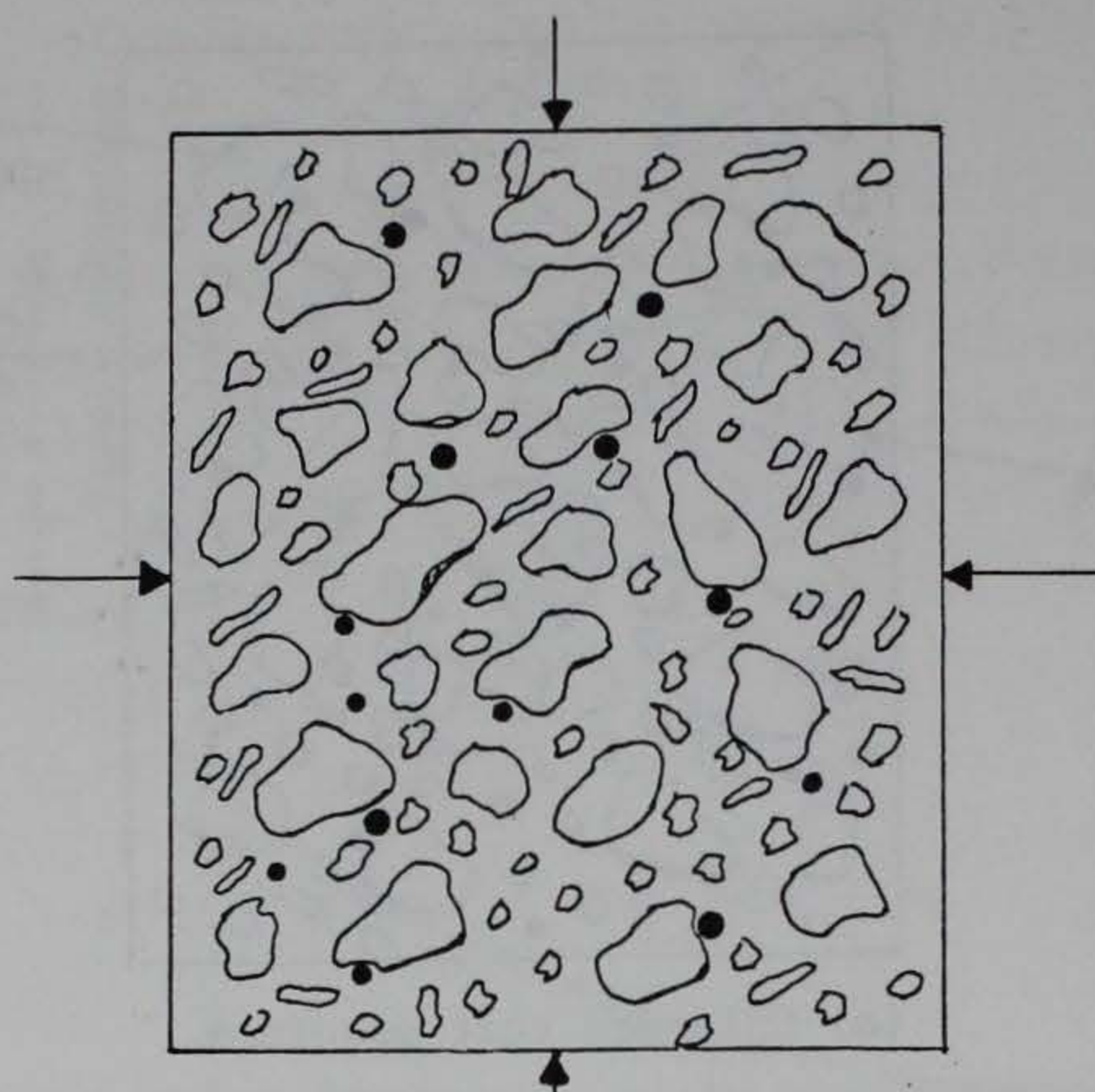
(a) Unloaded test specimen.



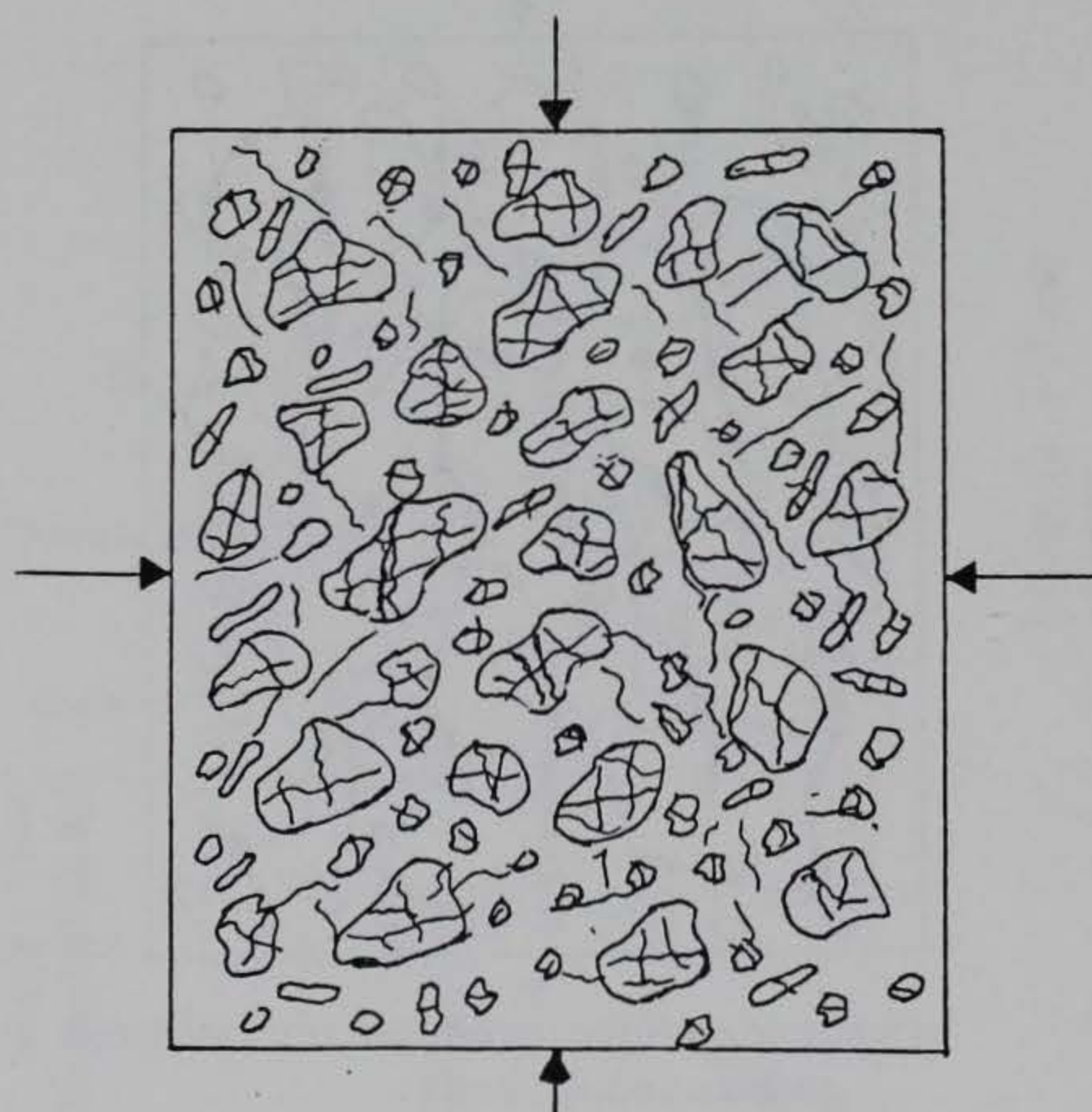
(b) Cracks observed in unconfined compression test.

Figure 1.4. Internal characteristics of concrete (sheet 1 of 2).





(c) Crack and void closure due to hydrostatic stresses.



(d) Aggregate fracture, softening concept.

Figure 1.4. Internal characteristics of concrete (sheet 2 of 2).



## Chapter 2

### Stress Strain Response of Concrete

#### 2.1 General

In Chapter 1, a general discussion was presented concerning problems encountered in large scale structural analysis of critical structures and questions many researchers have regarding various stress strain response phenomena of concrete. Considerable experimental data exist for concrete subjected to one dimensional and axisymmetric load. Also several studies have been directed at strain softening, biaxial stress loading and fully three dimensional stress loading. Results from many of these test programs are summarized and discussed by Hegemier, et al. (5). Green and Swanson (6) conducted an extensive study of the general constitutive properties of concrete at intermediate pressure levels (i.e. 10 - 12 ksi) while Van Mier (7) addressed strain softening under multiaxial loading conditions. Gerstle et al. (8) through a cooperative research effort showed the sensitivity of tests results to test devices (boundary conditions) and test procedures. The vast majority of the existing test data is based on simple or proportional load paths (i.e. the ratio of the applied stresses remains constant). In this Chapter, specific stress-strain response characteristics of concrete for simple and complex load paths will be discussed. Furthermore, an attempt is made to show that high quality, repeatable, and consistent test data can be obtained for well prepared concrete specimen and furthermore these data can and should be used in calibrating constitutive models. Nominal unconfined compressive strengths for concretes tested in this study range from  $f'_c = 2$  ksi to  $f'_c = 7$  ksi. It is not intended to present herein a broad discussion of the many different complex response characteristics of concrete, but rather to discuss those features which are of primary importance in constitutive modeling in general and specifically for the fracture energy based model and the endochronic model. Essentially two types of tests will be discussed,



calibration tests and verification tests. Calibration tests are conducted to determine values for parameters or coefficients used in the mathematical formulation of a particular model. Verification tests are designed to evaluate specific predictive capabilities of a constitutive model. Obviously a calibration test for one model might serve as a verification test for another model.

Before discussing test results it is important to keep in mind that in a test we are measuring quantities such as force, (F), pressure (P), and displacement (U), then dividing these (i.e. force and displacement) by initial areas  $A_0$  and lengths  $L_0$  to obtain stress and strain. The equations we use are of course

$$\text{STRESS} = F / A_0 \quad (1)$$

$$\text{STRESS} = U / L_0$$

The validity of using these equations to interpret or infer material constitutive properties should be determined based on the following conditions (Pariseau (9)):

1. Test specimen must be homogeneous
2. A homogeneous state of stress must exist in the specimen at all times.
3. No significant changes in specimen geometry can occur during a test.

When these conditions are met one can reasonably assume constitutive properties derived from equation (1) are real material properties. Furthermore, if an appropriate number of tests are conducted along load paths which capture the key response features of the material one can construct rational constitutive models which effectively represent the material response under a wide range of load histories. If on the other hand these conditions are not met, one must be careful in inferring material properties from equation (1) and in using constitutive models constructed from such tests. The degree to which the above conditions are met has special significance in interpreting



strain softening as a material response phenomenon or a structural response feature. When concrete is modeled as a homogeneous, isotropic material the assumption is made that the aggregates and pores are randomly distributed throughout the cement paste matrix and that the microcrack surface and width is relatively small when considering a representative volume of the material. This representative volume in general must be large enough so that the effects of stress concentrations, and any other discontinuities in the material can be smeared over the volume so that an equivalent homogeneous stress and strain state can be determined which effectively characterizes all the important features of material response. The reason for conducting material properties tests is precisely to measure these stress and strain states along load paths which are critical considering the application. At high stresses and especially in the softening region the validity of assumptions of homogeneity become more and more questionable. Many researchers have pointed out that at ultimate strength and in the softening region there are localizations of damage (eg. shear banding) and that test specimens exhibiting these effects must be considered structural elements and not as materials subjected to states of homogeneous stress and strain.

Bazant (10) found that strain softening can be observed only when local inhomogeneities exist in a material. The question is, how significant are the inhomogeneities in terms of the effects they have on stress-strain response features of interest. Once this question is answered one can determine what conditions (e.g. inhomogeneities) must be considered in constructing a rational constitutive model for a particular problem. Local inhomogeneities lead to strain softening which can be identified as a material instability according to Drucker's postulates (see Chapter 3). Drucker (17) points out "Philosophically, perhaps, all macroscopic systems are stable in the sense that if all conditions are or could be taken into account the complete behavior of the system could be followed in detail...

Instability as normally understood may arise when some but not all of



the attributes of a system are considered." For strain softening in concrete the instability is due to the assumptions that the stress strain response is rate independent and homogeneous.

In this chapter, loaders, test devices, and instrumentation commonly used in conducting material property tests will be discussed (Section 2.2). The location of the loaders and test devices and the laboratories where different tests were conducted is identified in section titles (i.e. Waterways Experiment Station (WES); the University of Eindhoven, Netherlands (UEN); and the University of Colorado, Boulder (UCB)). Calibration tests are discussed in Sections 2.3 through 2.6 and verification tests are discussed in 2.7.



## 2.2 Loaders, Test Devices, and Instrumentation

### 2.2.1 100-kip Servo-Controlled Hydraulic Loader (WES)

The 100-kip servo-hydraulic loader is capable of applying tensile or compressive loads up to a maximum level of 100,000 lb. The loader can be manually or computer controlled to produce a desired load or displacement rate. The input to the servo-control unit is produced by an arbitrary digital function generator which can be programmed to produce an infinite number of load or displacement histories. The applied force is measured by a load cell while the displacement of the loader head is measured by an internal linear variable displacement transducer (LVDT). Strains are usually measured by epoxy-backed constantan resistance strain gages bonded to the specimen with high-strength strain-gage adhesive. Unconfined compression tests, tension tests, and some low confinement triaxial tests can be conducted in this loader.

### 2.2.2 440-kip Universal Testing Machine (WES)

The 440-kip loader can apply tensile or compressive loads up to a maximum of 440,000 lb. The machine is displacement controlled by manually adjusting hydraulic valves to achieve the desired displacement rate. The axial load is measured by an internal load cell while displacements are measured by an external LVDT across the loading heads. Strains are usually measured by strain gages bonded to the specimen. This machine is used to conduct unconfined compression tests and cylindrical triaxial compression tests.

### 2.2.3 2400-kip Loader (WES)

The 2400-kip servo-hydraulic loader can apply tensile or compressive loads up to a maximum of 2,400,000 lb. The load or displacement rate are controlled by an analog function generator capable of ramp, sine, or triangular functions. The load is measured by an internal load cell while the displacements are measured by an



external LVDT. This device is used to conduct unconfined compression tests, cylindrical triaxial tests, and multiaxial compression tests.

#### 2.2.4 40-ksi Cylindrical Triaxial Chamber (WES)

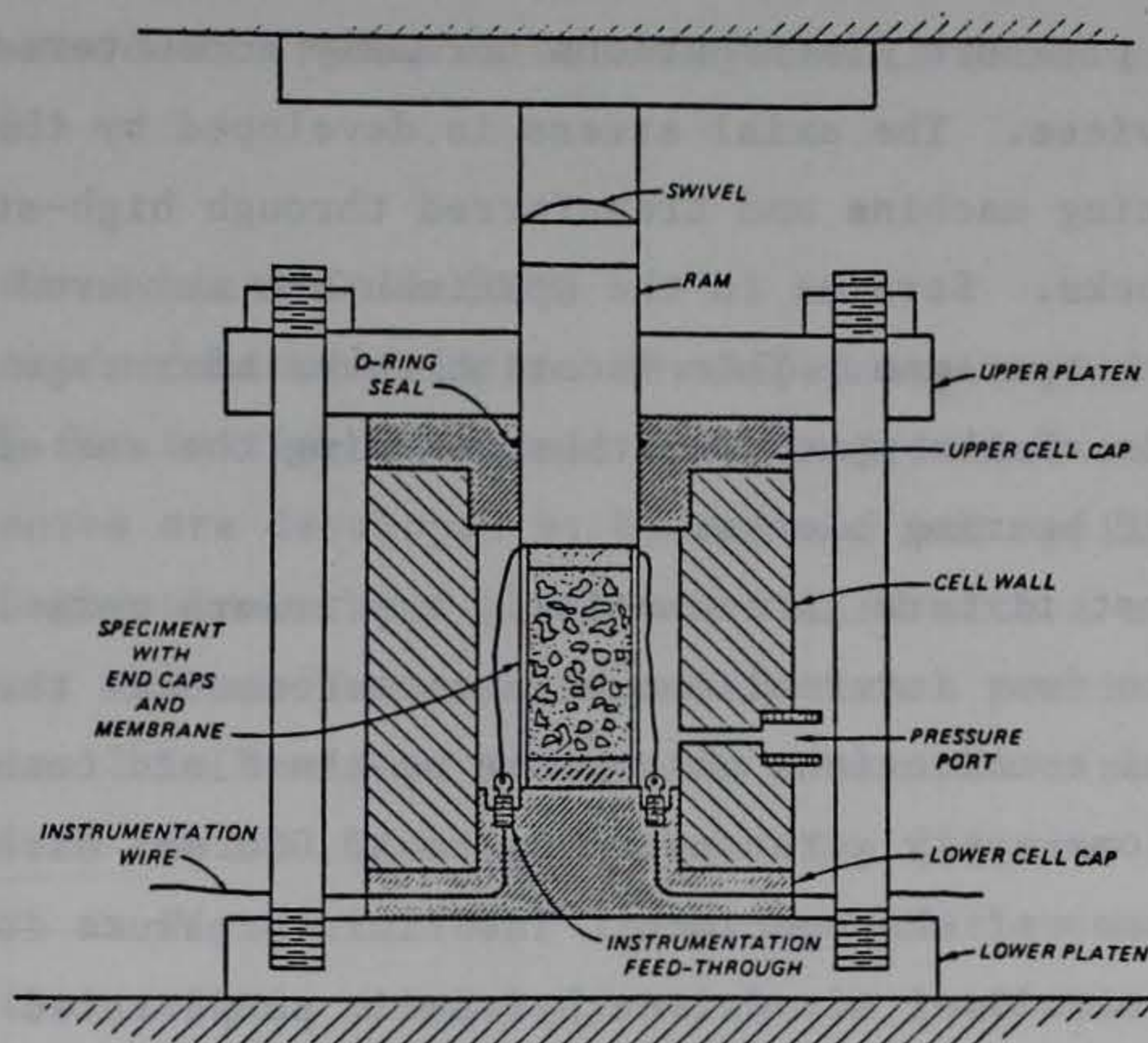
The 40-ksi cylindrical triaxial test device is capable of conducting multiaxial tests on nominal 2.125-inch diameter by 3.5-inch long cylindrical specimens at confining stresses up to 40,000 psi and axial stresses up to 125,000 psi. Figure 2.1(a) shows a cross-section of the device. The confining pressure is developed by a manually controlled, air-driven hydraulic pump rated at 75,000 psi. The fluid used in the device is a low-viscosity white mineral oil. Eight 7/8-inch diameter bolts clamp the upper and lower platens together and carry the loads produced by the fluid pressure against the upper and lower cell caps. The device has the capability to exit up to four channels of instrumentation through Fusite-type fittings in the base.

In preparing for a test, hardened steel end caps were placed on each end of a specimen. The specimen was subsequently encased in an impermeable 60 durometer neoprene membrane. Hose clamps were used to secure the membrane at each end of the specimen. The jacketed specimen was placed in the device, and the device was completely assembled. This assembly was then moved as a unit and placed in the 440-kip universal testing machine. A swivel was placed on the top of the ram to compensate for any eccentricities in the device or the testing machine.

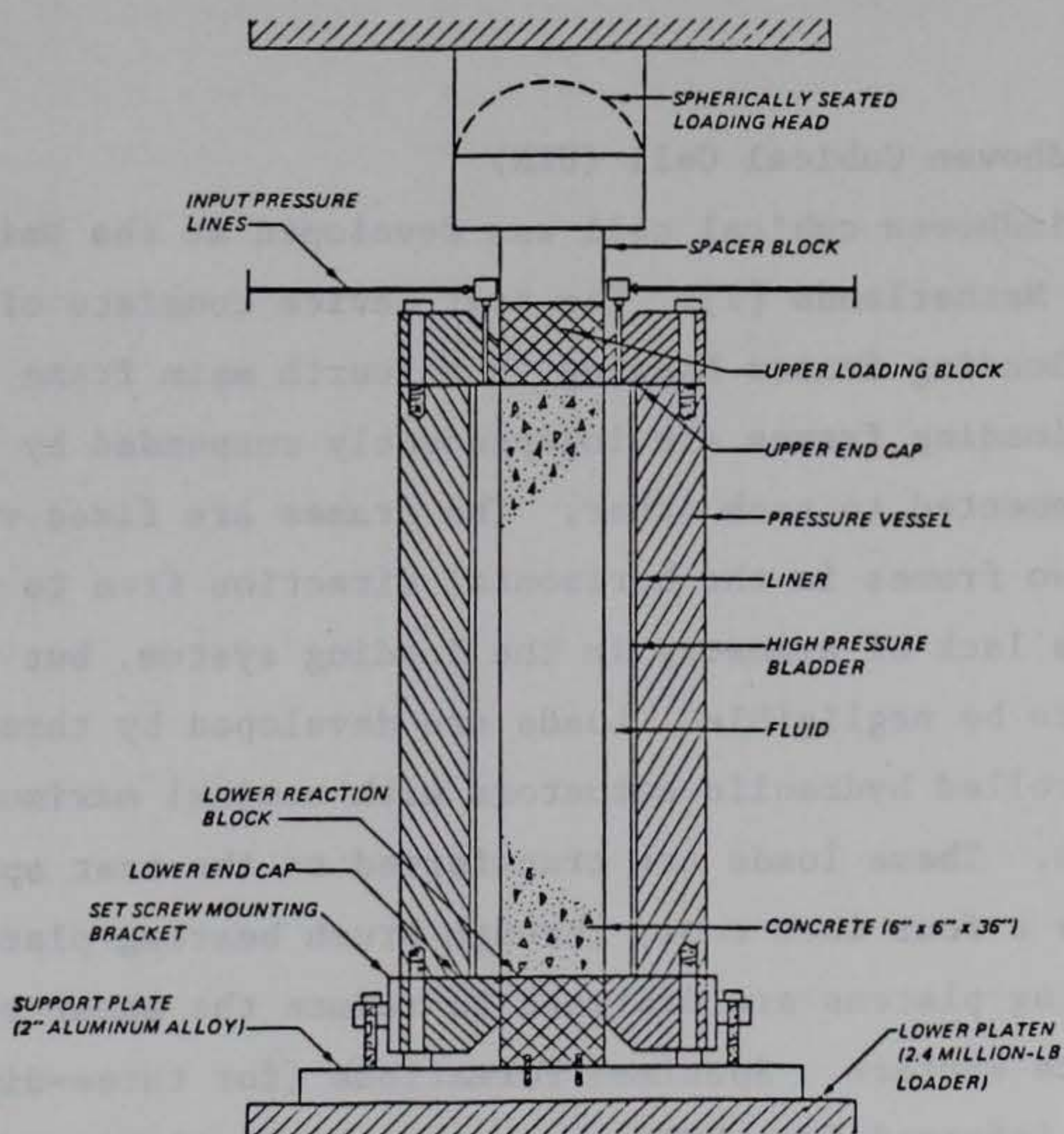
#### 2.2.5 30-ksi Multiaxial Test Device (WES)

The 30-ksi multiaxial test device is used in conjunction with the 2400-kip universal testing machine to test 6-inch by 6-inch by 36-inch rectangular prismatic specimens under a wide range of three-dimensional compressive stress states. A vertical cross-section of the device is shown in Figure 2.1(b). The test device incorporates fluid cushion technology to minimize surface shear friction and





(a) 40 ksi cylindrical triaxial chamber



(b) 30 ksi multiaxial test device

Figure 2.1 WES test devices



nonuniform pressure distributions normally encountered in other types of test devices. The axial stress is developed by the 2400-kip universal testing machine and transferred through high-strength steel bearing blocks. Strains in the specimen are measured in the central third of the specimen. This location takes advantage of the 6:1 aspect ratio of the specimen, thus reducing the end effects induced by the rigid bearing blocks.

The test fixture is essentially a pressure vessel which is divided into four internal chambers to accommodate the individual bladder/seal combinations which make up the fluid cushions. The fluid cushions apply stresses of up to 30,000 psi directly to the vertical faces of the specimen. The fluid pressure is developed by manually controlled, air-driven hydraulic pumps rated at 75,000 psi. A low-viscosity white mineral oil is used as the pressurizing fluid. Strains are measured using internal embedded integral lead strain gages.

#### 2.2.6 Eindhoven Cubical Cell (UEN)

The Eindhoven cubical cell was developed at the University of Eindhoven, Netherlands [7]. The test device consists of three identical loading frames hanging in a fourth main frame structure. The three loading frames are independently suspended by steel cables and not connected to each other. The frames are fixed vertically with the two frames in the horizontal direction free to move. This causes some lack of symmetry in the loading system, but this effect was found to be negligible. Loads are developed by three independent servo-controlled hydraulic actuators with nominal maximum capacities of 450 kips. These loads are transferred to the test specimen, which is normally a four inch cube, through brush bearing platens. The brush bearing platens are designed to reduce the shear restraint at the concrete surface. Specimen formations (for three-dimensional tests) are inferred from LVDT measurements of relative displacement between the steel blocks upon which the brush rods are clamped. A

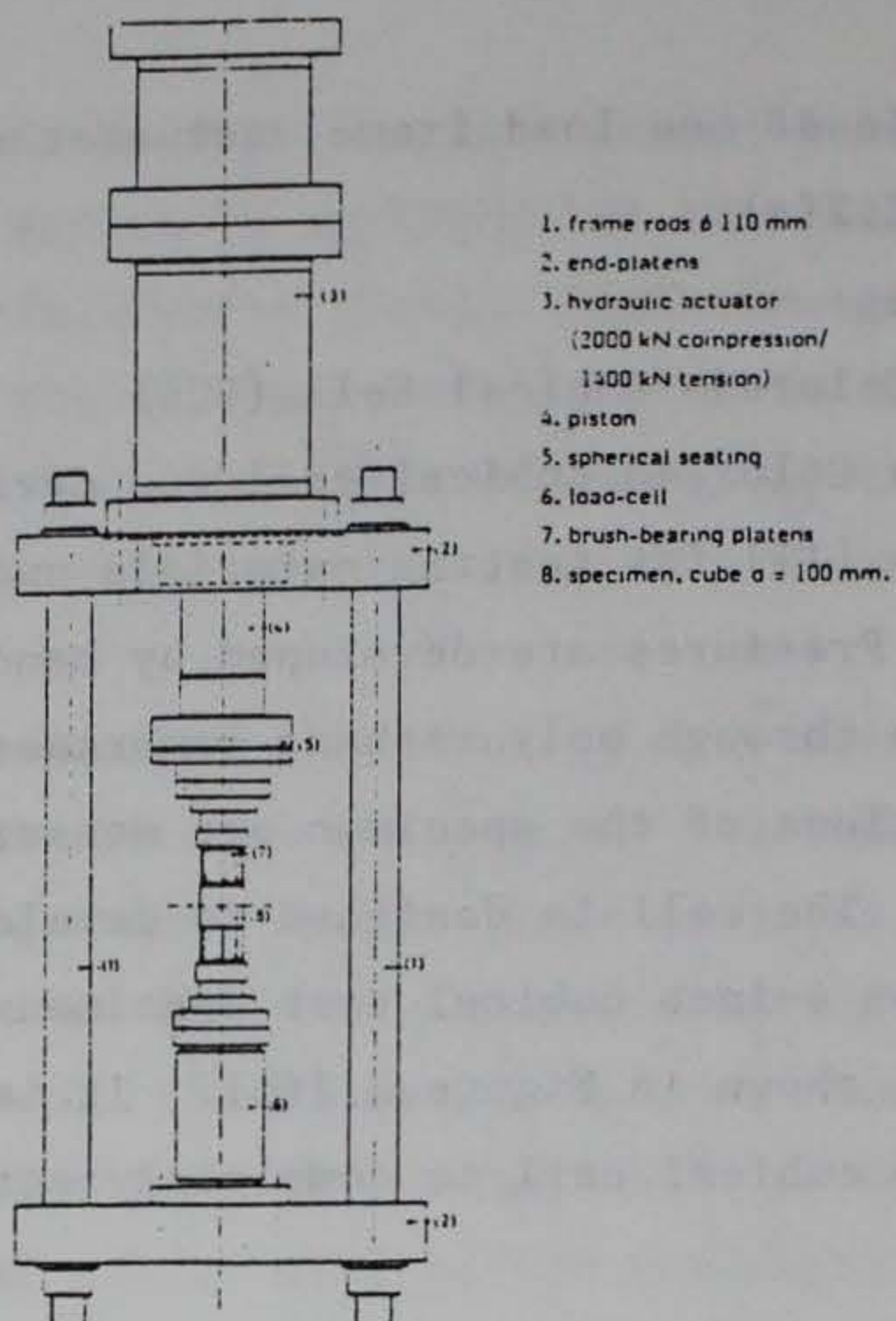


schematic of one load frame, actuator system is shown in Figure 2.2(a).

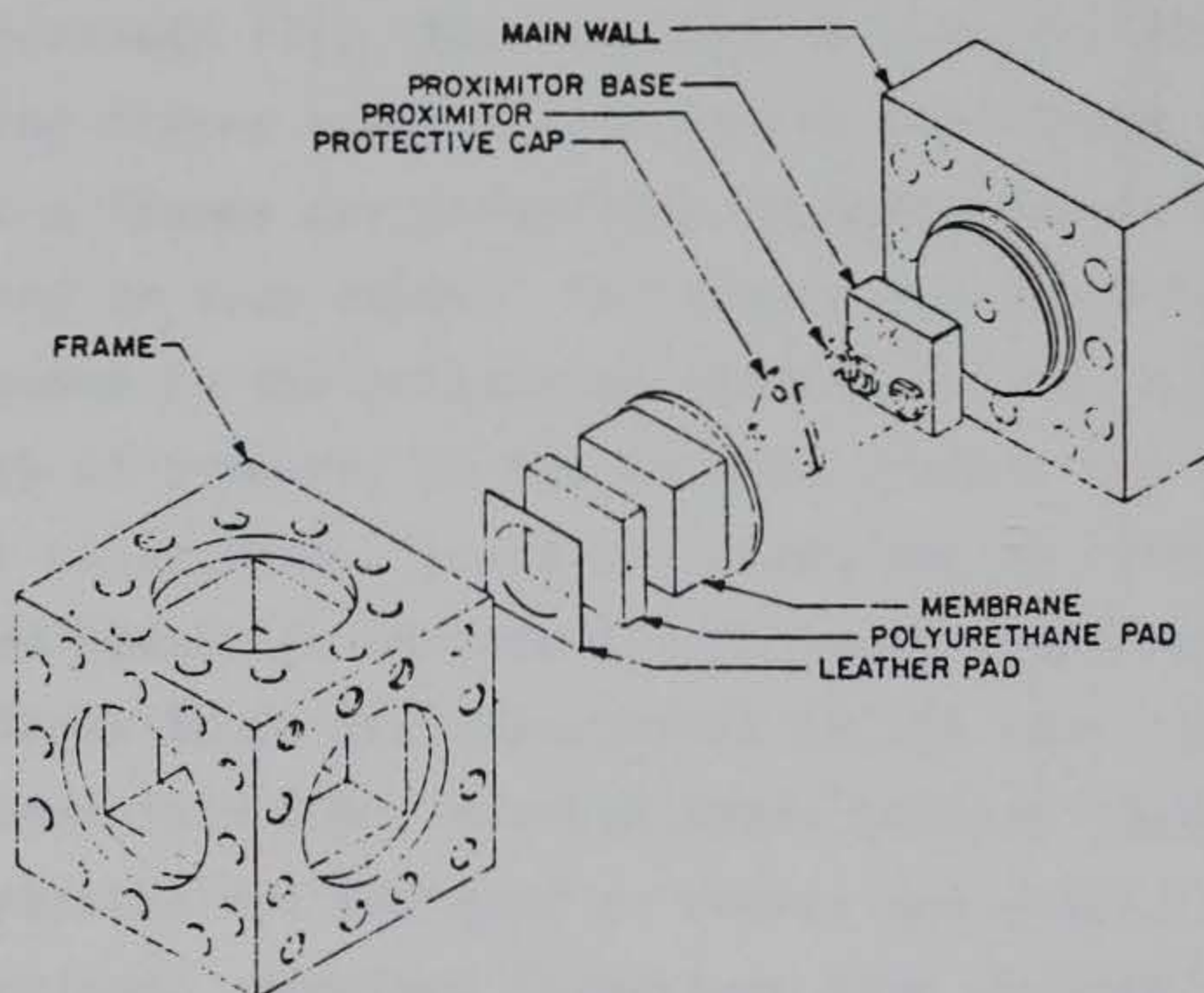
#### 2.2.7 Colorado Cubical Cell (UCB)

The Colorado cubical cell was developed at the University of Colorado [11] for testing materials under multiaxial compressive loads. Pressures are developed by hand pumps and applied to the specimen through polyurethane membranes filled with a silicone fluid. Deformations of the specimen are measured with a proximeter probe system. The cell is designed to develop a maximum stress of 12 to 15 ksi on 4-inch cubical test specimens. Key features of the cubical cell are shown in Figure 2.2(b). It is important to note that the Colorado cubical cell is completely stress or load controlled.





(a) Eindhoven cubical cell (from (18))



(b) Colorado cubical cell

Figure 2.2 Eindhoven and Colorado test devices



### 2.3 Unconfined Compression Tests

To the naked eye concrete appears mainly as a two phase composite material consisting of different size aggregates embedded in a cement paste matrix. One can usually observe some small pores also, but these can be kept to a minimum if proper care is taken in mixture proportioning, specimen casting, and consolidation. Through a microscope one can observe microcracks primarily located at the coarse aggregate-mortar interface. As the magnification of the microscope increases one observes that the number of phases in the concrete composite increases. For the purposes of this study the two phase approximation is useful in explaining the stress strain response features of concrete. However, the constitutive models addressed herein assume homogeneous isotropic materials. The appropriateness of these assumptions depends on defects (eg. microcrack, pores, etc.) being spatially distributed in a random manner and relatively small in number compared to the specific material volume of interest as discussed in Section 2.1.

Figure 2.3 presents the results of an unconfined compression test of concrete conducted in displacement or stroke control. The region OA might be considered the elastic region, with point A defining the proportional limit, while AB is the hardening region and BC and larger strains could be considered the softening region. It is generally observed that the microcracks which exist at zero load, at aggregate-mortar interfaces, increase in surface area and number as the stress is increased from point 0 to A. At some point near A microcracks begin to propagate through the mortar and continue to propagate and coalesce in a stable manner up to some point below B in the region AB. At this point the cracks begin to propagate in an unstable manner and failure will be observed at about point B in a load control test device. Considerable discussion is given to the points described above by Kotsovos and Newman [12]. If at any point in the program of loading for Figure 2.3 unloading occurs followed by reloading the load will return to essentially the same point where



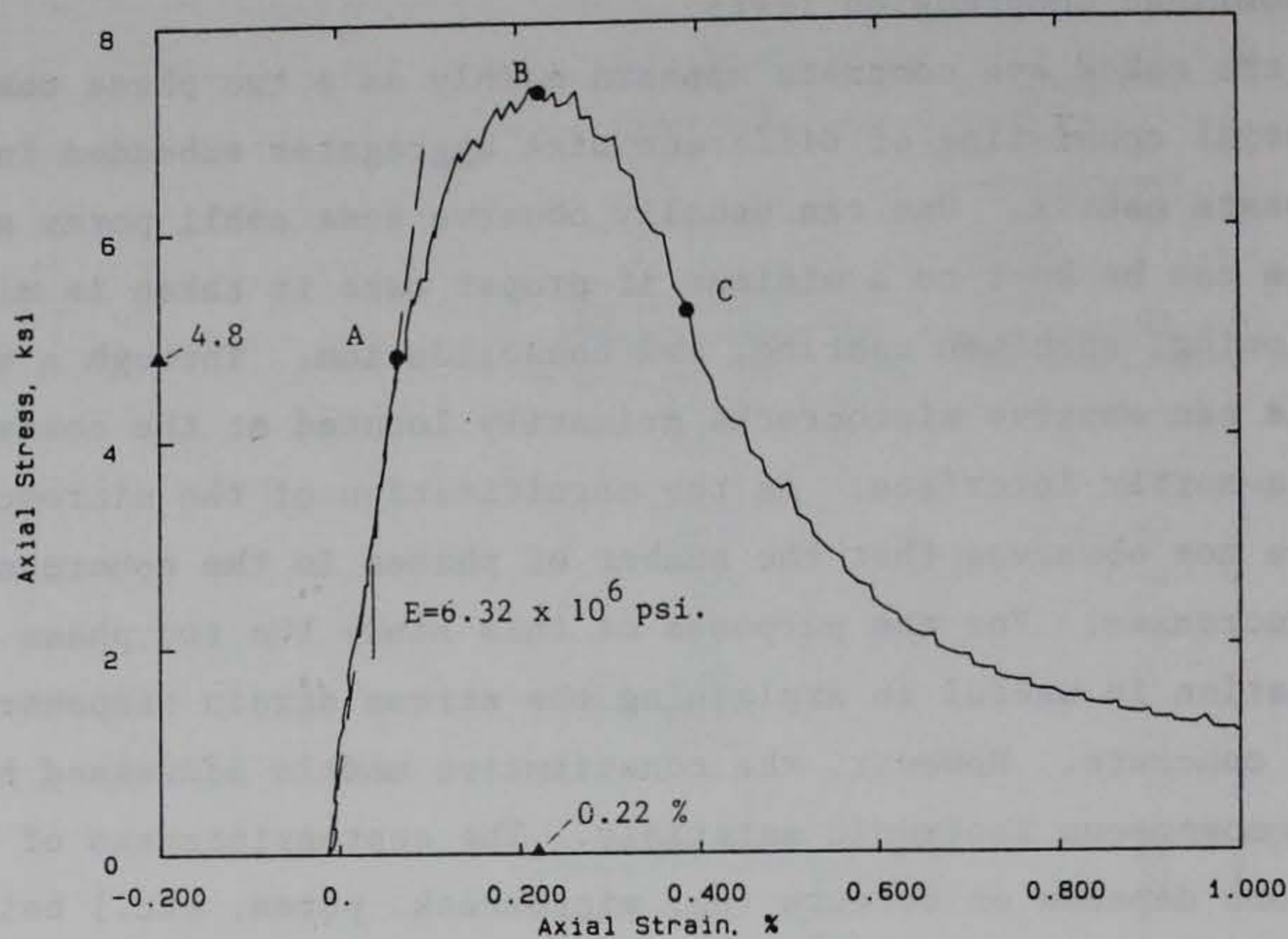


Figure 2.3 Stress-strain response, for unconfined compressive test (stroke control)

unloading occurred and then the stress strain response as shown in Figure 2.3 will continue under monotonic loading. Unloading reloading moduli will be somewhat less than the initial value and some hysteresis will be observed. At higher and higher strains the loading unloading moduli become softer and softer with more and more hysteresis. At strains greater than those associated with point B in Figure 2.3 visual cracks will be detected on the outside surface of the specimen. These cracks will essentially be vertical and definitely indicate that the specimen is no longer an intact continuum. This observation provides the basis for most arguments that softening is a structural phenomenon as opposed to a material property. However, it should be kept in mind that these observations are for the unconfined test.

Some other quantitative observations can be made concerning the material response features for the  $f'_c = 6.5$  ksi concrete as shown in Figure 2.3. For this concrete specimen the diameter is 2.065 in. and



length is 4.25 in. The coarse aggregate is limestone with maximum size of 3/8 inch, the water-cement ratio for the mixture is 0.46, and the test specimen is approximately one year old. Stress is force per unit original area and strains are measured by 3/4 and 1-inch foil strain gages glued to the specimen and by an LVDT measuring loader head movement corrected for the compliance of the loader system.

Figure 2.3 represents a continuous loading of a specimen to very large strains. In order to further explore the response characteristics of concrete, especially in the linear elastic region a series of tests were conducted to assess the linear elastic features of the material at stresses below the "yield point." For a companion specimen to the one used in the test of Figure 2.3, a series of loading, unloading, and reloading tests were conducted to determine accumulations of plastic strains, softening of unloading-reloading moduli and indications of damage. The test procedure was to load up to a specified level of axial stress then unload to zero stress. The test specimen was then removed from the loader tested dynamically to determine its compressional wave velocity, (which is a measure of dynamic modulus), measured with a micrometer to determine permanent strains, and then placed back in the loader and the test procedure repeated to a higher level of axial stress. Since the ultimate strength of the concrete of Figure 2.3 is  $f'_c = 7.5$  ksi (which is the result of one year of aging on the nominal 6.5 ksi concrete), these load-unload tests were conducted at  $0.3 f'_c$ ,  $0.5 f'_c$ ,  $0.75 f'_c$ ,  $0.9 f'_c$ , and on the final loading program the specimen was loaded to an axial strain of  $\epsilon = 1.5\%$ . The results of this test program are presented in Figure 2.4. The relatively small effect of load-unload cycles on  $E$  and wave velocity indicates the linear elastic response characteristics of the  $f'_c = 6.5$  ksi concrete for stresses below  $A$ . Figure 2.5 presents a composite plot of the  $f'_c = 6.5$  ksi and the  $f'_c = 2$  ksi stress strain curves, which represent upper and lower bounds of concrete strengths studied in this report.



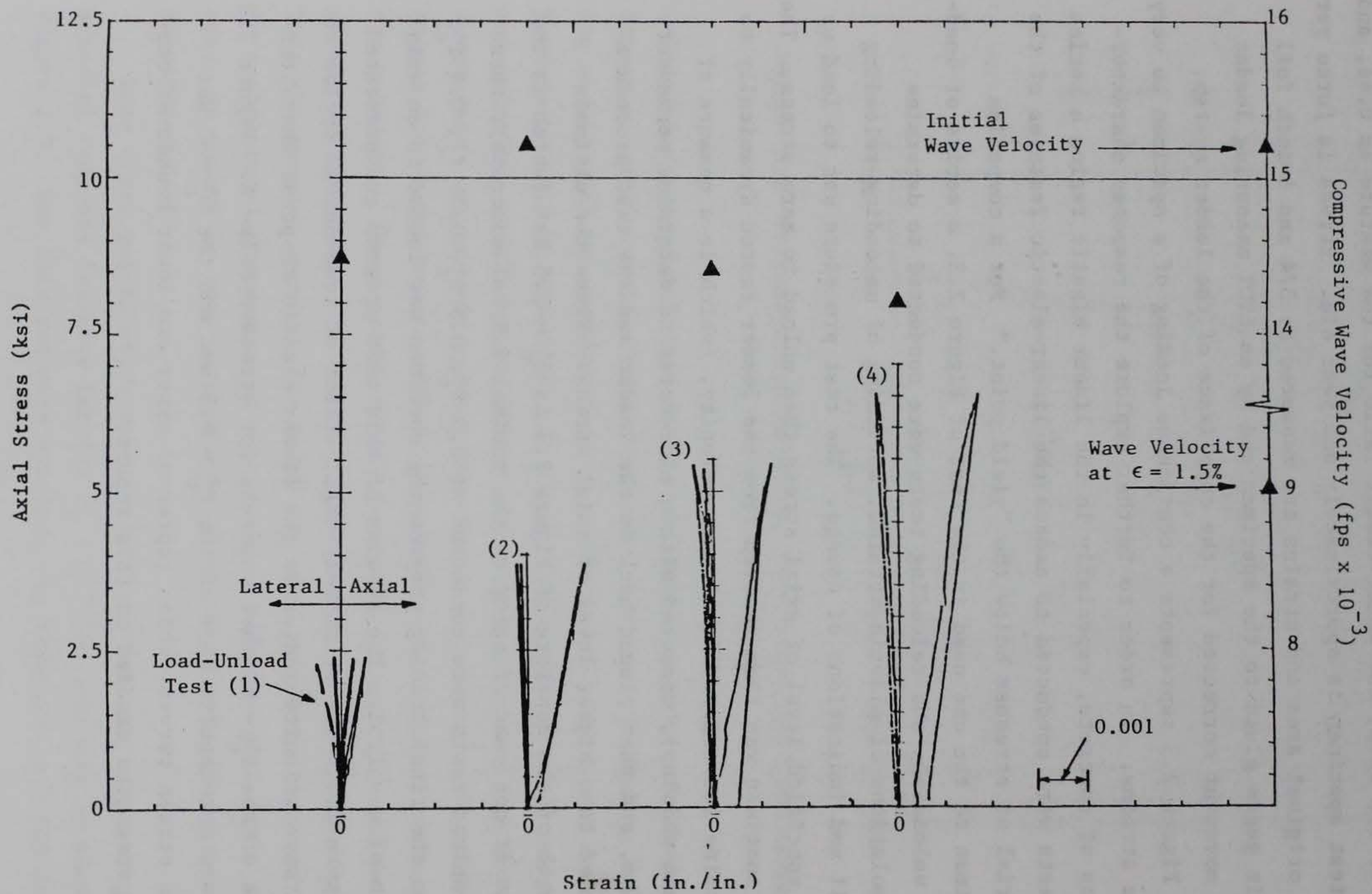
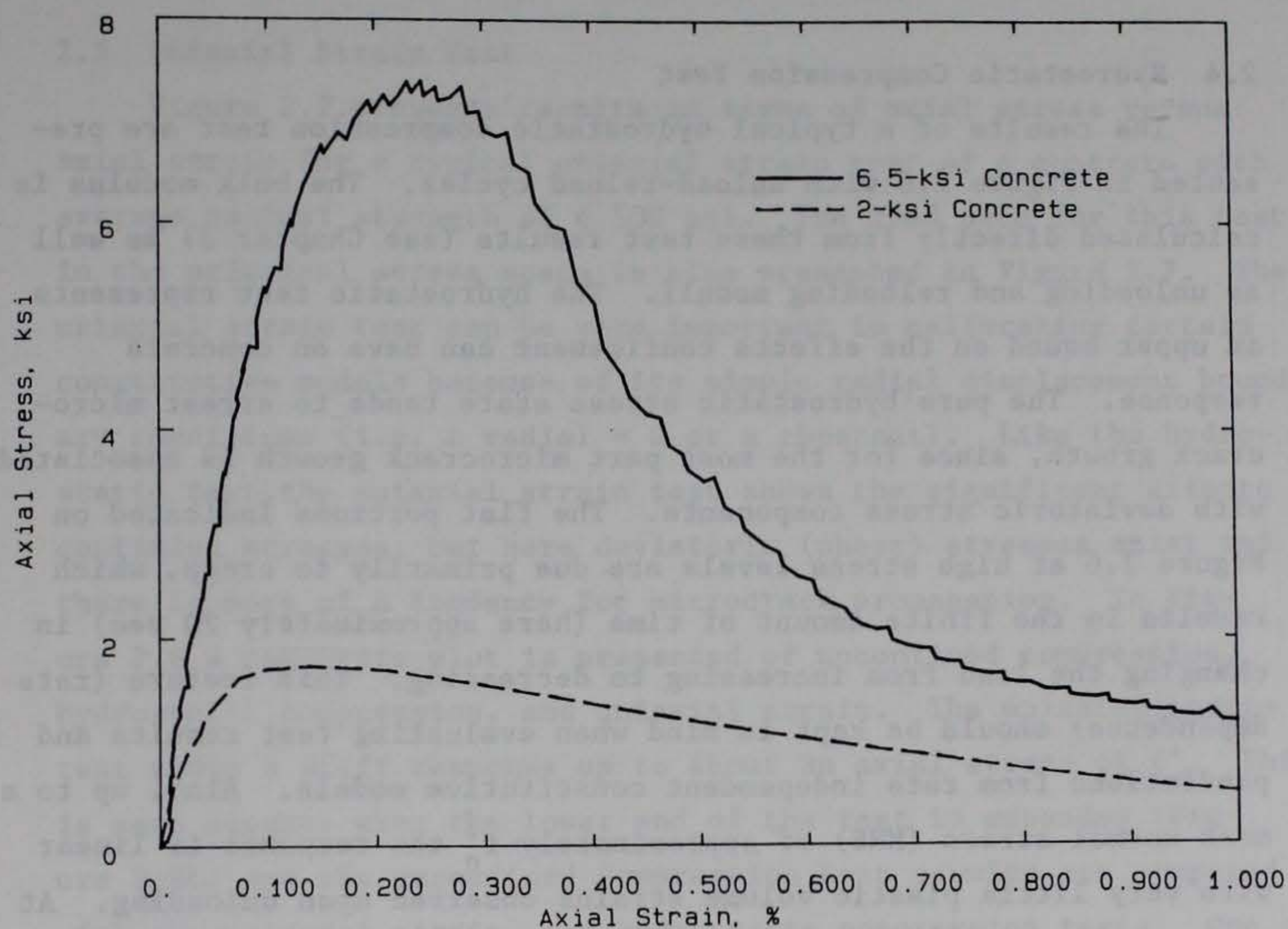


Figure 2.4 The effects of load unload cycles on modulus and wave speeds





**Figure 2.5 Unconfined compression tests, low and high strength concretes**



## 2.4 Hydrostatic Compression Test

The results of a typical hydrostatic compression test are presented in Figure 2.6 with unload-reload cycles. The bulk modulus is calculated directly from these test results (see Chapter 3) as well as unloading and reloading moduli. The hydrostatic test represents an upper bound on the effects confinement can have on concrete response. The pure hydrostatic stress state tends to arrest microcrack growth, since for the most part microcrack growth is associated with deviatoric stress components. The flat portions indicated on Figure 2.6 at high stress levels are due primarily to creep, which results in the finite amount of time (here approximately 20 sec) in changing the load from increasing to decreasing. This feature (rate dependence) should be kept in mind when evaluating test results and predictions from rate independent constitutive models. Also, up to a mean normal stress (MNS) of approximately  $f'_c$  the response is linear with very little plastic volume strains observed upon unloading. At MNS = 10 ksi the bulk modulus begins to soften and approaches a near constant value at approximately, MNS = 18 ksi.

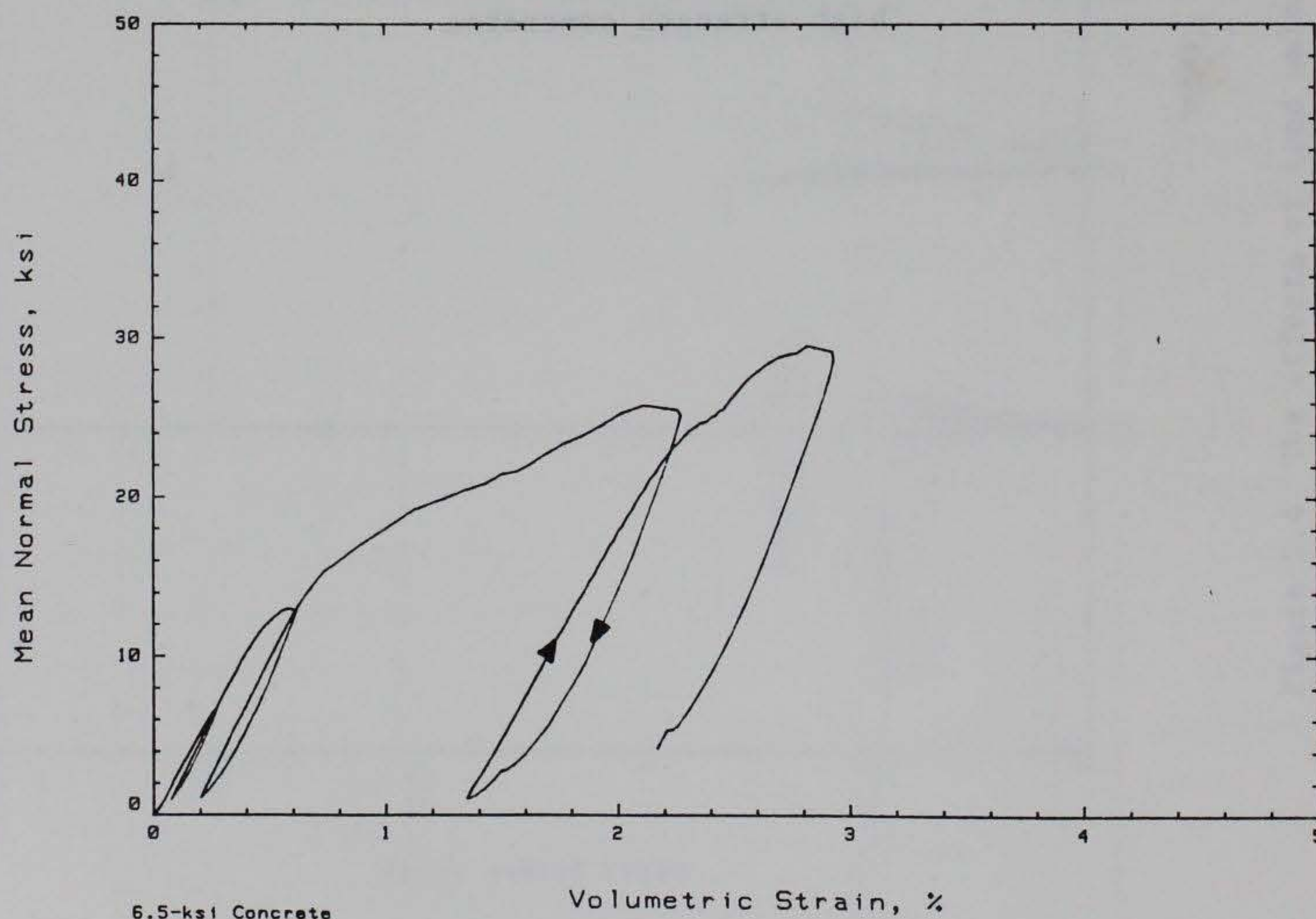


Figure 2.6 Hydrostatic test with unload-reload cycles



## 2.5 Uniaxial Strain Test

Figure 2.7 presents results in terms of axial stress versus axial strain for a typical uniaxial strain test of a concrete with average nominal strength of 6,500 psi. The load path for this test in the principal stress space is also presented in Figure 2.7. The uniaxial strain test can be very important in calibrating certain constitutive models because of its simple radial displacement boundary conditions (i.e.  $\epsilon_{\text{radial}} = 0$  or a constant). Like the hydrostatic test the uniaxial strain test shows the significant effects of confining stresses, but here deviatoric (shear) stresses exist and there is more of a tendency for microcrack propagation. In Figure 2.8 a composite plot is presented of unconfined compression, hydrostatic compression, and uniaxial strain. The uniaxial strain test shows a stiff response up to about an axial stress of  $f'_c$ . This is seen clearer when the lower end of the test is expanded (Figure 2.8b) and the unconfined compression test results are compared with the uniaxial strain, and hydrostatic compression tests. One can reasonably assume that elastic response is occurring in all three tests up to a level of axial stress of 75% to 80% of  $f'_c$  for this concrete. From Figure 2.8b, it can be seen that all three tests start out with equivalent moduli in terms of ratios of axial stress to axial strain that are essentially linear and continue up to an axial stress of approximately 5 ksi. (Note we defined yield in the unconfined compression test at 4.8 ksi). At stresses above this value each curve begins to strain harden, with the hydrostatic test hardening being the largest, the unconfined test indicating apparent softening, and the uniaxial strain test in between.



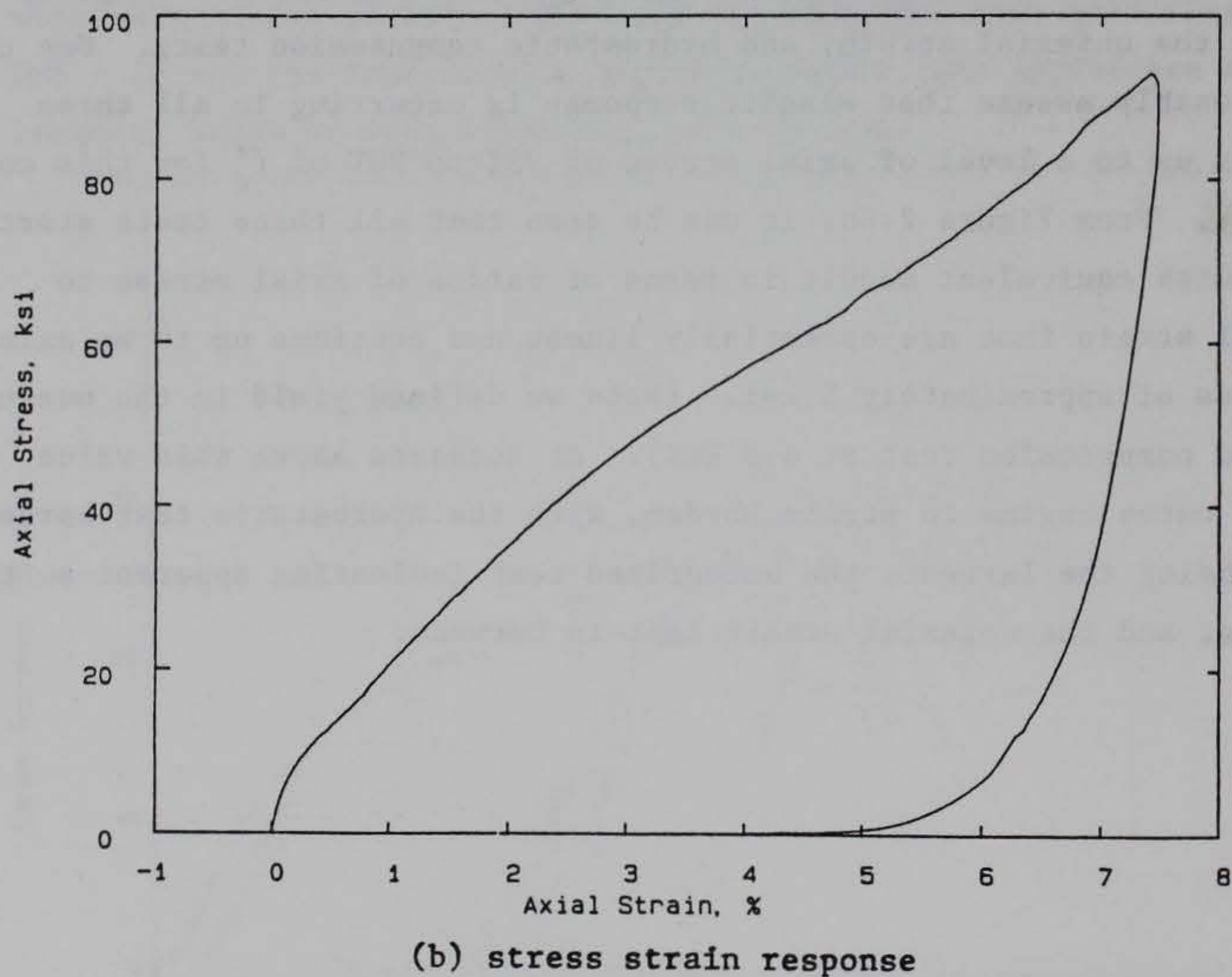
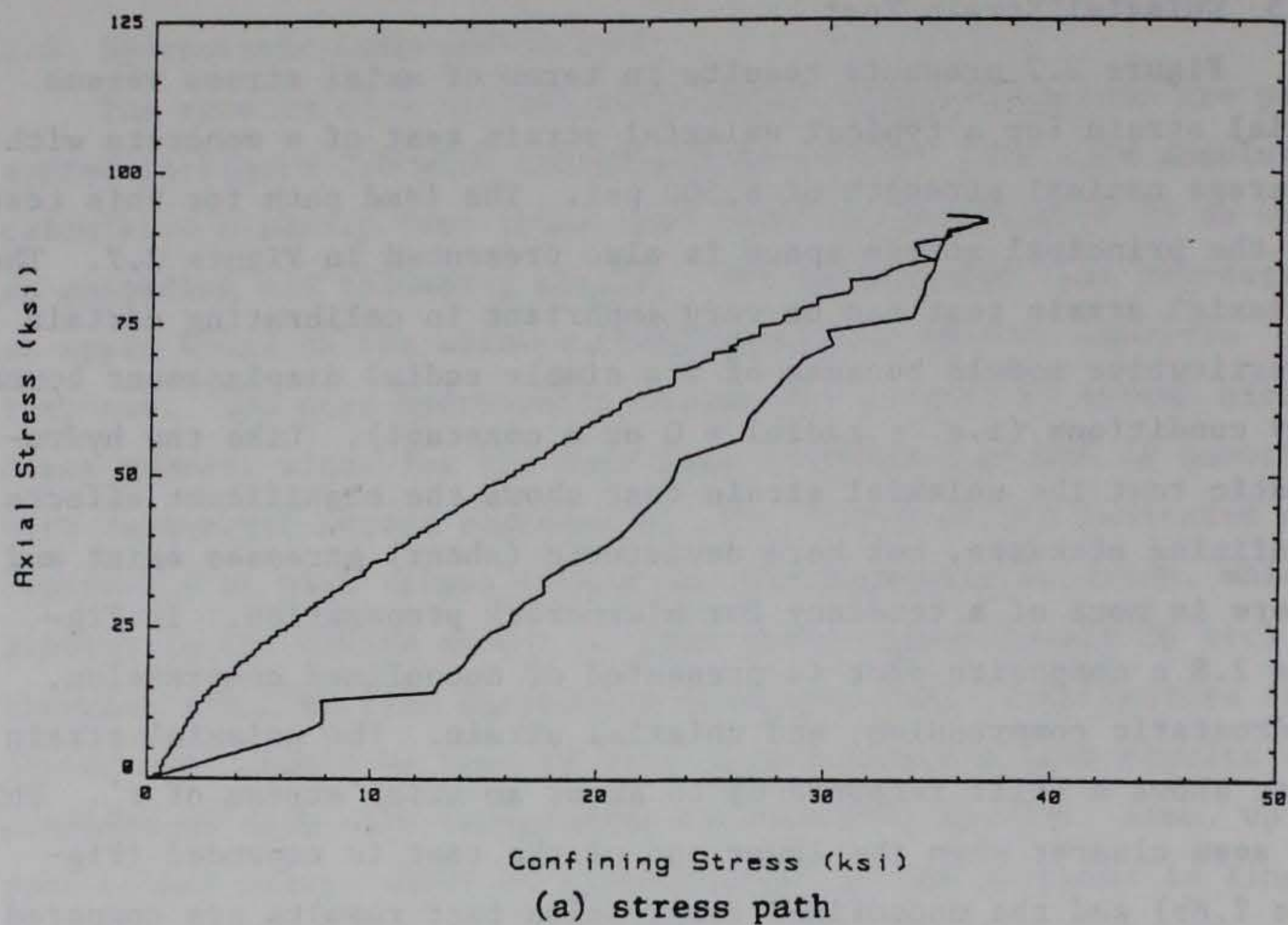


Figure 2.7 Uniaxial strain test results



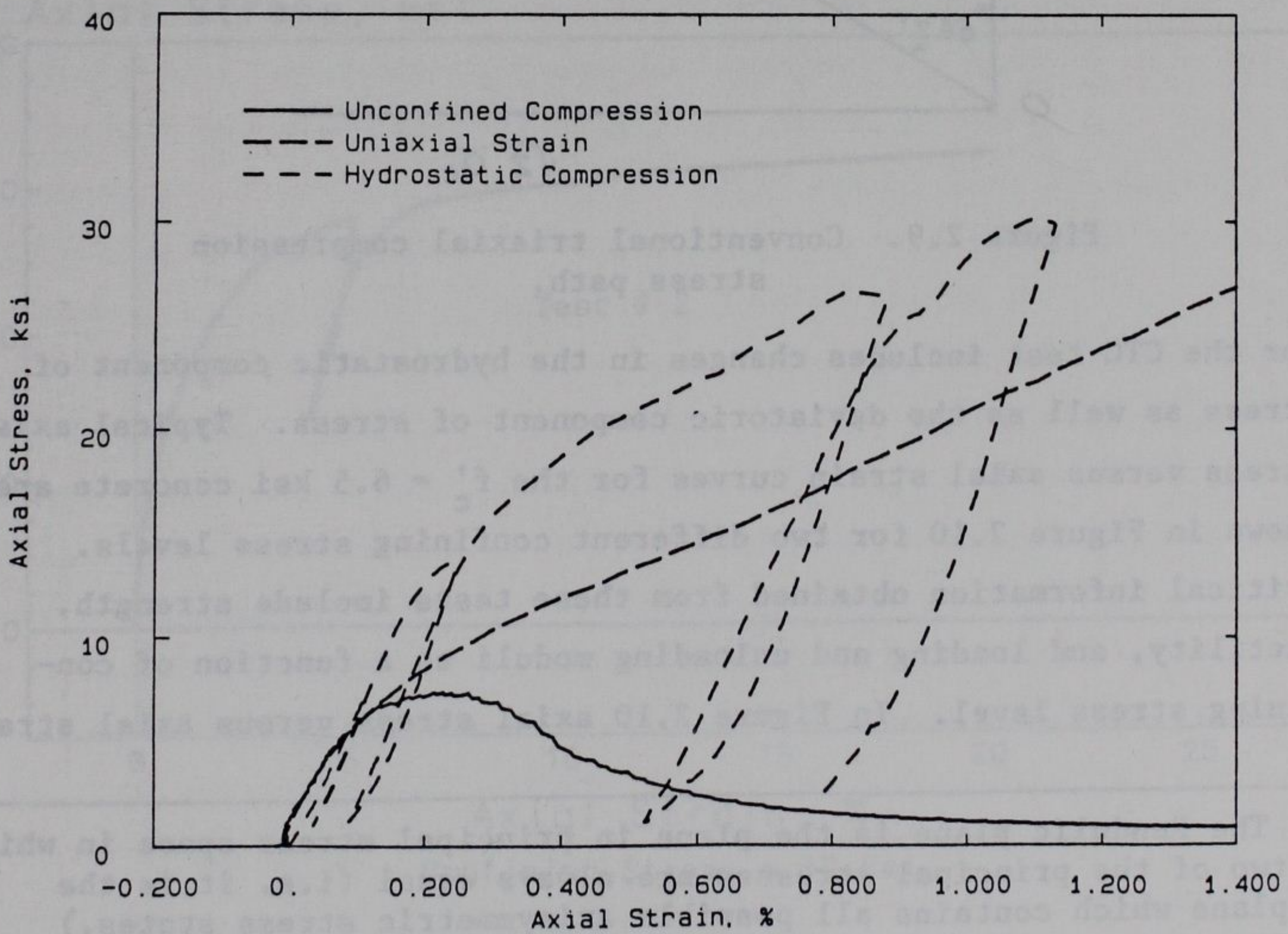
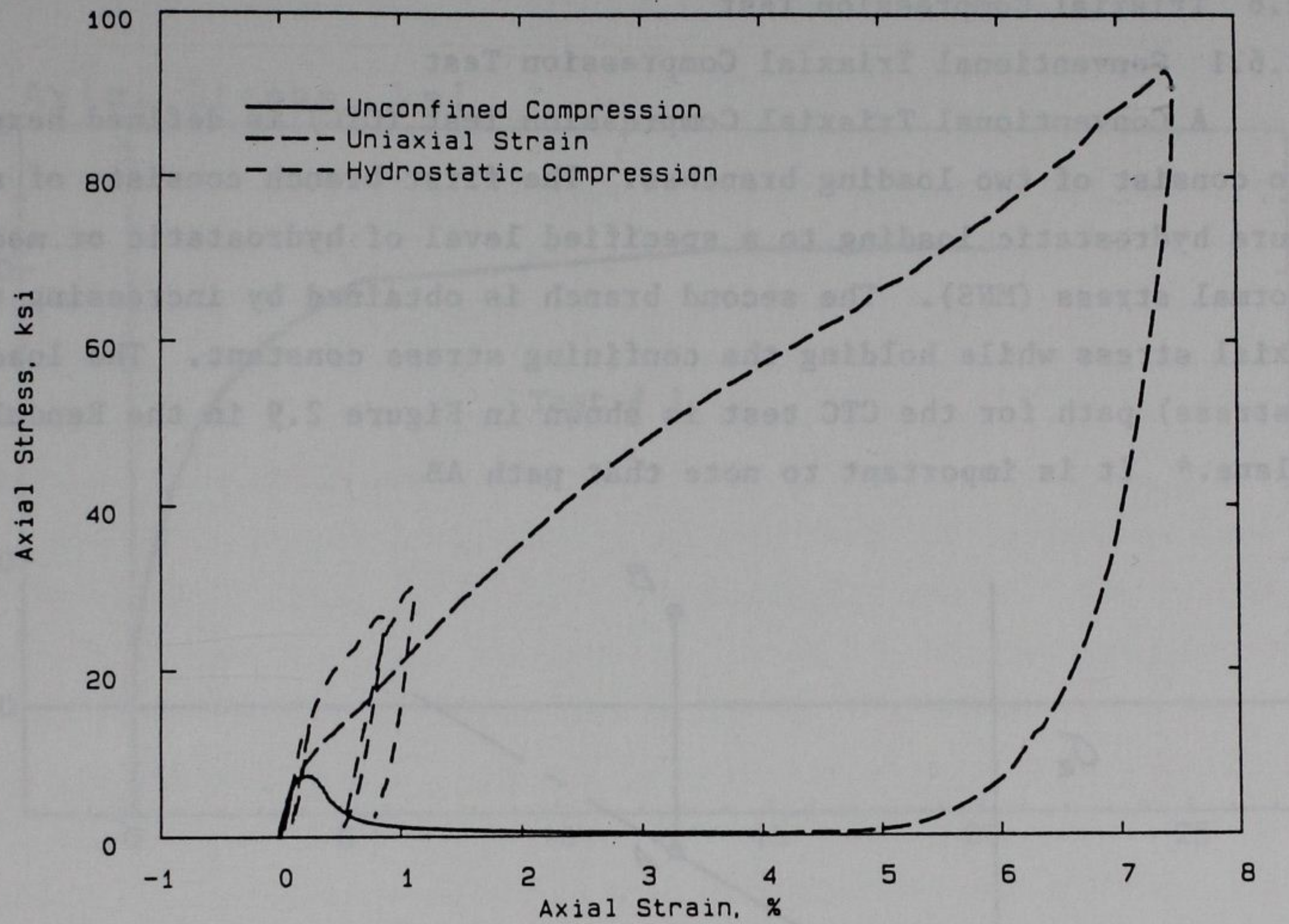


Figure 2.8 Composite plots, unconfined, uniax. strain, hydrostatic



## 2.6 Triaxial Compression Test

### 2.6.1 Conventional Triaxial Compression Test

A Conventional Triaxial Compression Test (CTC) is defined herein to consist of two loading branches. The first branch consists of a pure hydrostatic loading to a specified level of hydrostatic or mean normal stress (MNS). The second branch is obtained by increasing the axial stress while holding the confining stress constant. The load (stress) path for the CTC test is shown in Figure 2.9 in the Rendulic plane.\* It is important to note that path AB

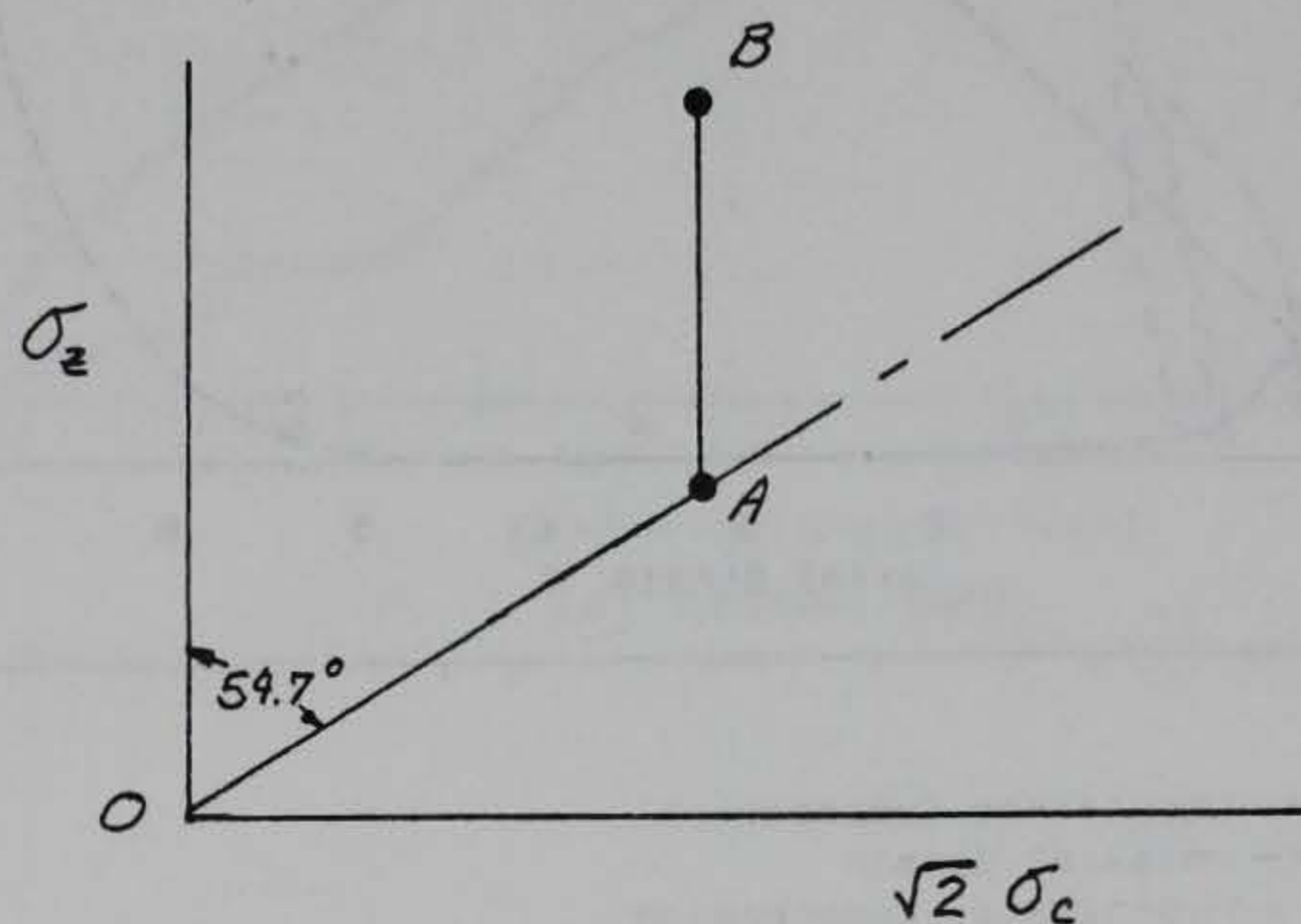


Figure 2.9. Conventional triaxial compression stress path.

for the CTC test includes changes in the hydrostatic component of stress as well as the deviatoric component of stress. Typical axial stress versus axial strain curves for the  $f'_c = 6.5$  ksi concrete are shown in Figure 2.10 for two different confining stress levels. Critical information obtained from these tests include strength, ductility, and loading and unloading moduli as a function of confining stress level. In Figure 2.10 axial stress versus axial strain

---

\* The Rendulic plane is the plane in principal stress space in which two of the principal stresses are always equal (i.e. it is the plane which contains all possible axisymmetric stress states.)



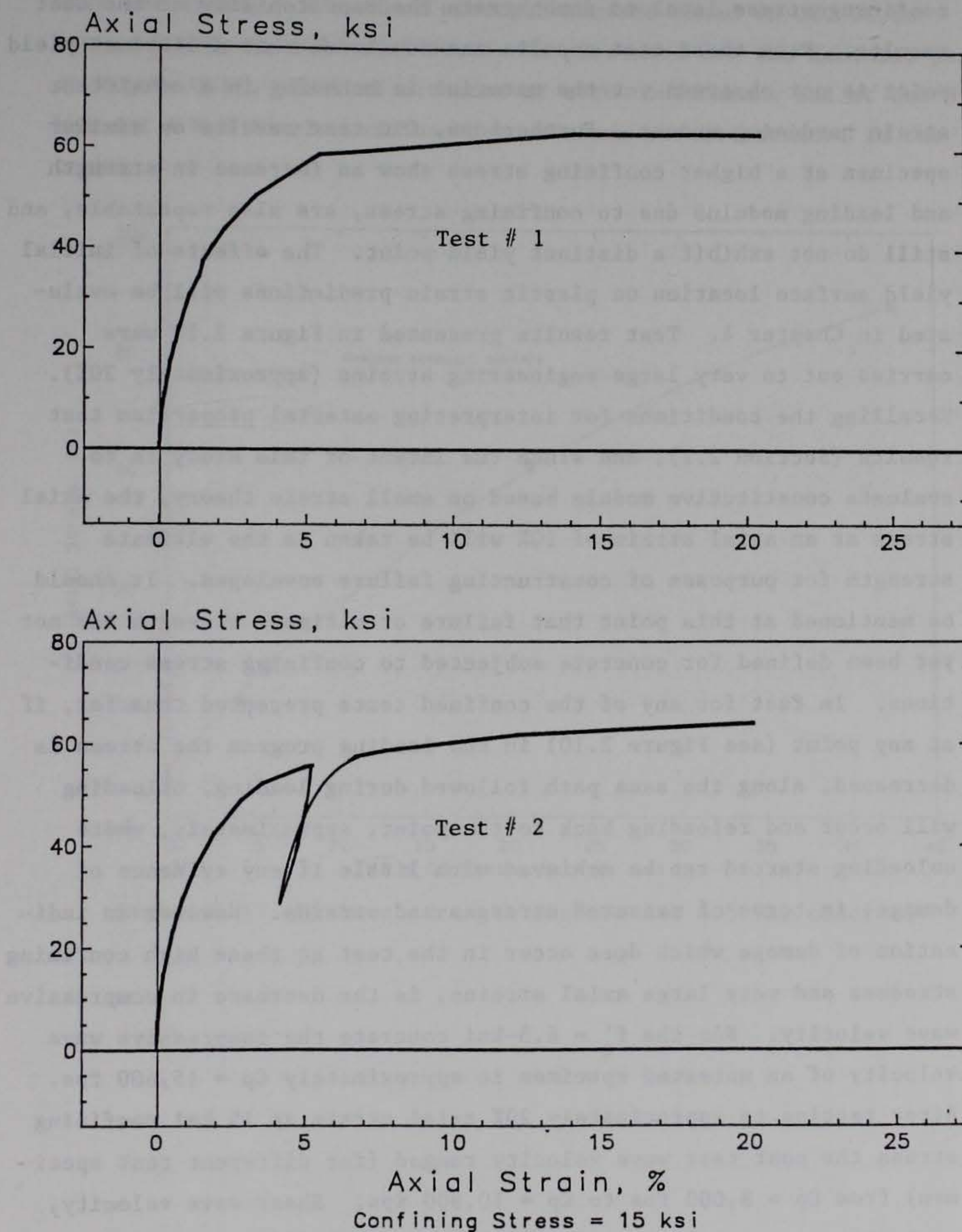


Figure 2.10 Conventional triaxial compression tests, with unload-reload cycle



are presented for CTC tests on two similar test specimens at each confining stress level to demonstrate the repeatability of the test results. From these test results one concludes that a distinct yield point is not observed yet the material is behaving in a consistent strain hardening manner. Furthermore, CTC test results on similar specimen at a higher confining stress show an increase in strength and loading modulus due to confining stress, are also repeatable, and still do not exhibit a distinct yield point. The effects of initial yield surface location on plastic strain predictions will be evaluated in Chapter 4. Test results presented in Figure 2.10 were carried out to very large engineering strains (approximately 20%). Recalling the conditions for interpreting material properties test results (Section 2.1), and since the intent of this study is to evaluate constitutive models based on small strain theory, the axial stress at an axial strain of 10% will be taken as the ultimate strength for purposes of constructing failure envelopes. It should be mentioned at this point that failure or ultimate strength has not yet been defined for concrete subjected to confining stress conditions. In fact for any of the confined tests presented thus far, if at any point (see Figure 2.10) in the loading program the stress is decreased, along the same path followed during loading, unloading will occur and reloading back to the point, approximately, where unloading started can be achieved with little if any evidence of damage, in terms of measured stresses and strains. However an indication of damage which does occur in the test at these high confining stresses and very large axial strains, is the decrease in compressive wave velocity. For the  $f'_c = 6.5$ -ksi concrete the compressive wave velocity of an untested specimen is approximately  $C_p = 15,600$  fps. After testing to approximately 20% axial strain at 15 ksi confining stress the post test wave velocity ranged (for different test specimen) from  $C_p = 8,000$  fps to  $C_p = 10,800$  fps. Shear wave velocity, pretest, was measured at approximately  $C_s = 9,300$  fps while post test values ranged from  $C_s = 5,700$  fps to  $C_s = 6,340$  fps. These



measurements indicate similar degradation in compressive and shear wave velocities. A maximum strength surface based on CTC tests stress levels at 10% axial strain is presented for the Rendulic plane in Figure 2.11. Failure stresses at zero confinement and at the 3 ksi and 4 ksi levels were based on maximum stress attained in the tests.

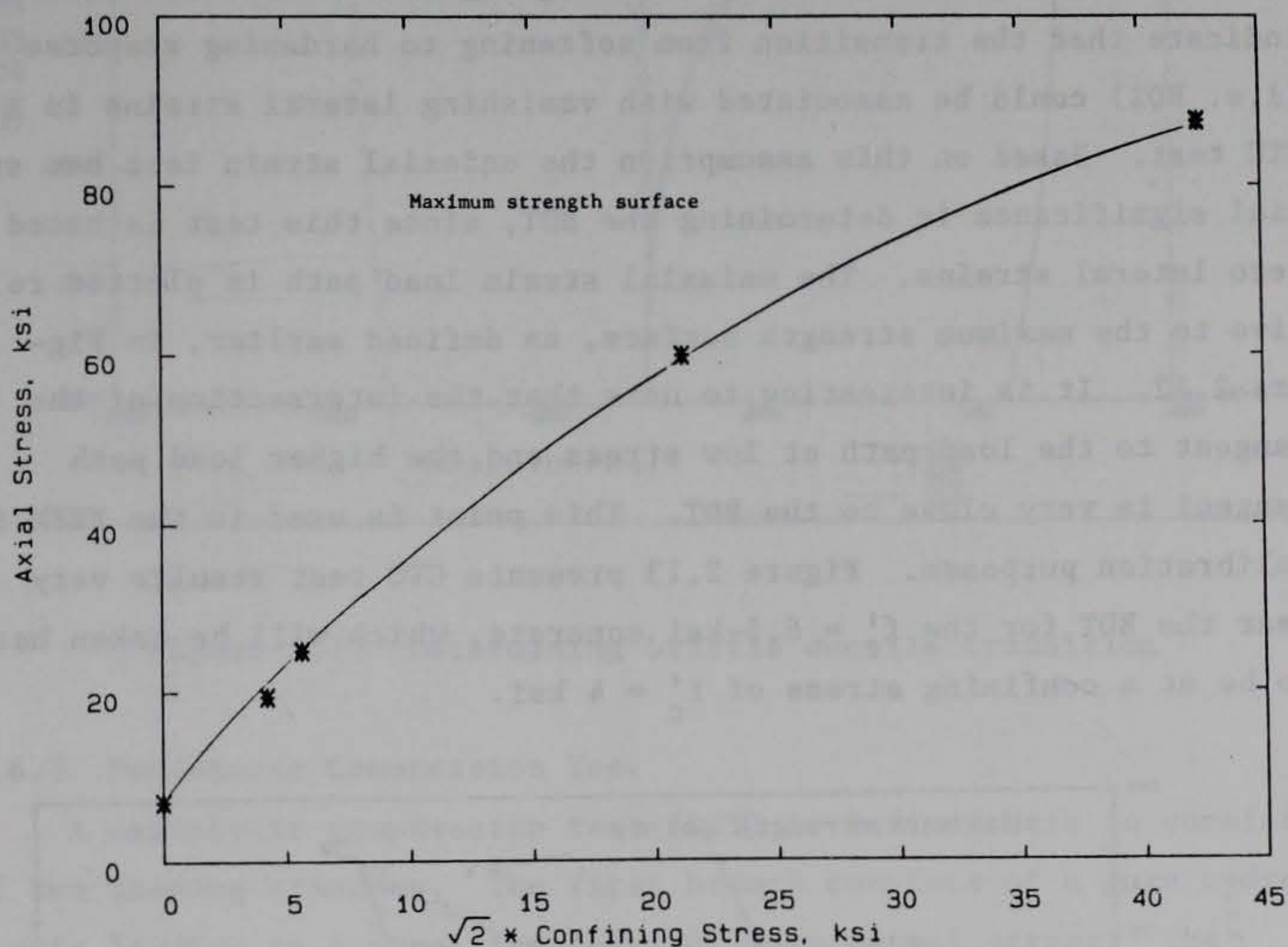


Figure 2.11 Maximum strength surface for 6.5-ksi concrete



### 2.6.2 Brittle Ductile Transition

The brittle ductile transition (BDT) is defined here as the confining stress which separates the apparent softening response region and the strain hardening response region in stress space. Lateral strains in low confinement tests are predominantly tensile in the softening region, while predominantly compressive lateral strains occur in the high confinement hardening region. This would seem to indicate that the transition from softening to hardening response (i.e. BDT) could be associated with vanishing lateral strains in a CTC test. Based on this assumption the uniaxial strain test has special significance in determining the BDT, since this test is based on zero lateral strains. The uniaxial strain load path is plotted relative to the maximum strength surface, as defined earlier, in Figure 2.12. It is interesting to note that the intersection of the tangent to the load path at low stress and the higher load path tangent is very close to the BDT. This point is used in the FEBM for calibration purposes. Figure 2.13 presents CTC test results very near the BDT for the  $f'_c = 6.5$ -ksi concrete, which will be taken here to be at a confining stress of  $f'_c = 4$  ksi.

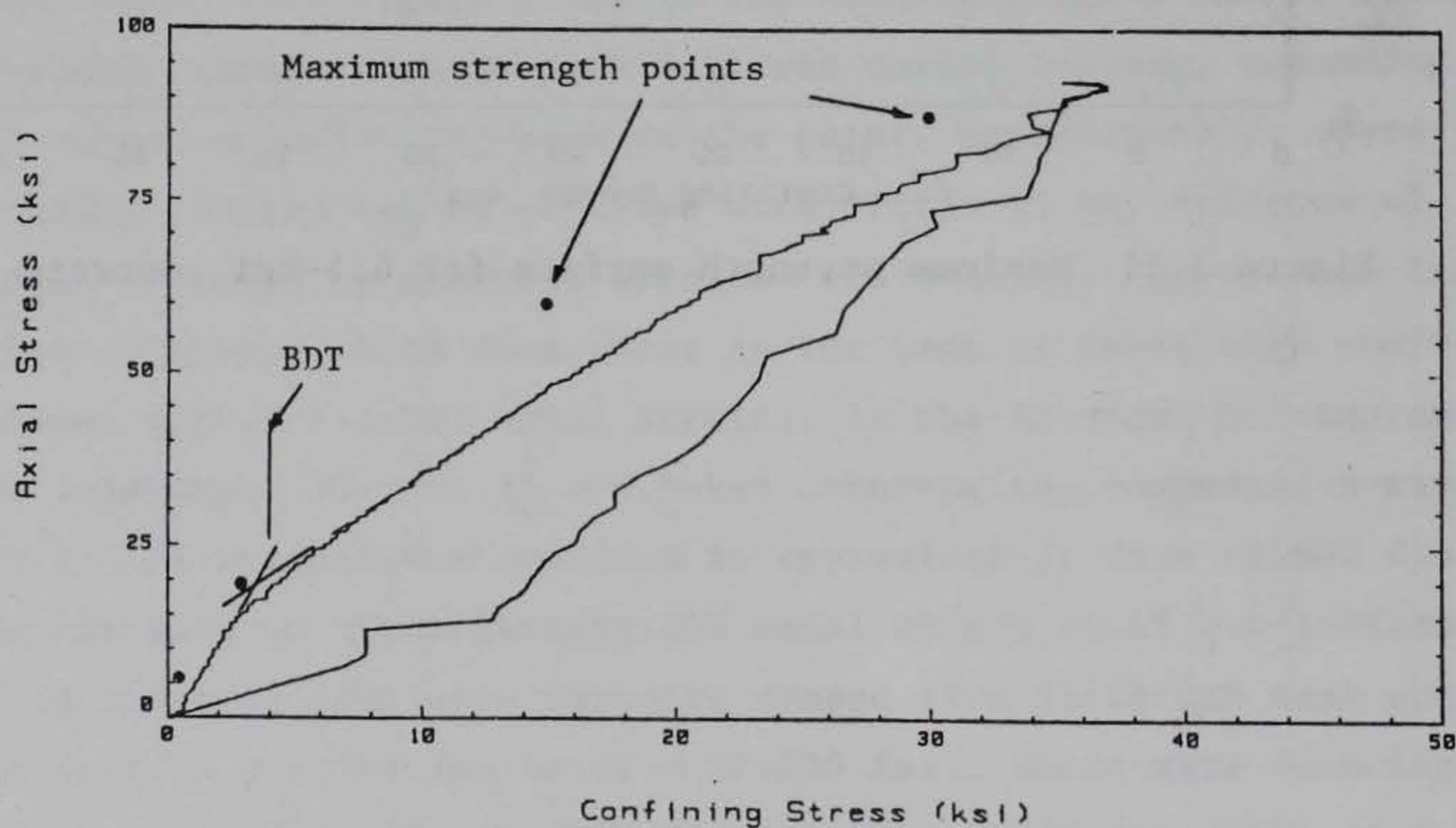


Figure 2.12 Brittle ductile transition relative to uniax. strain test



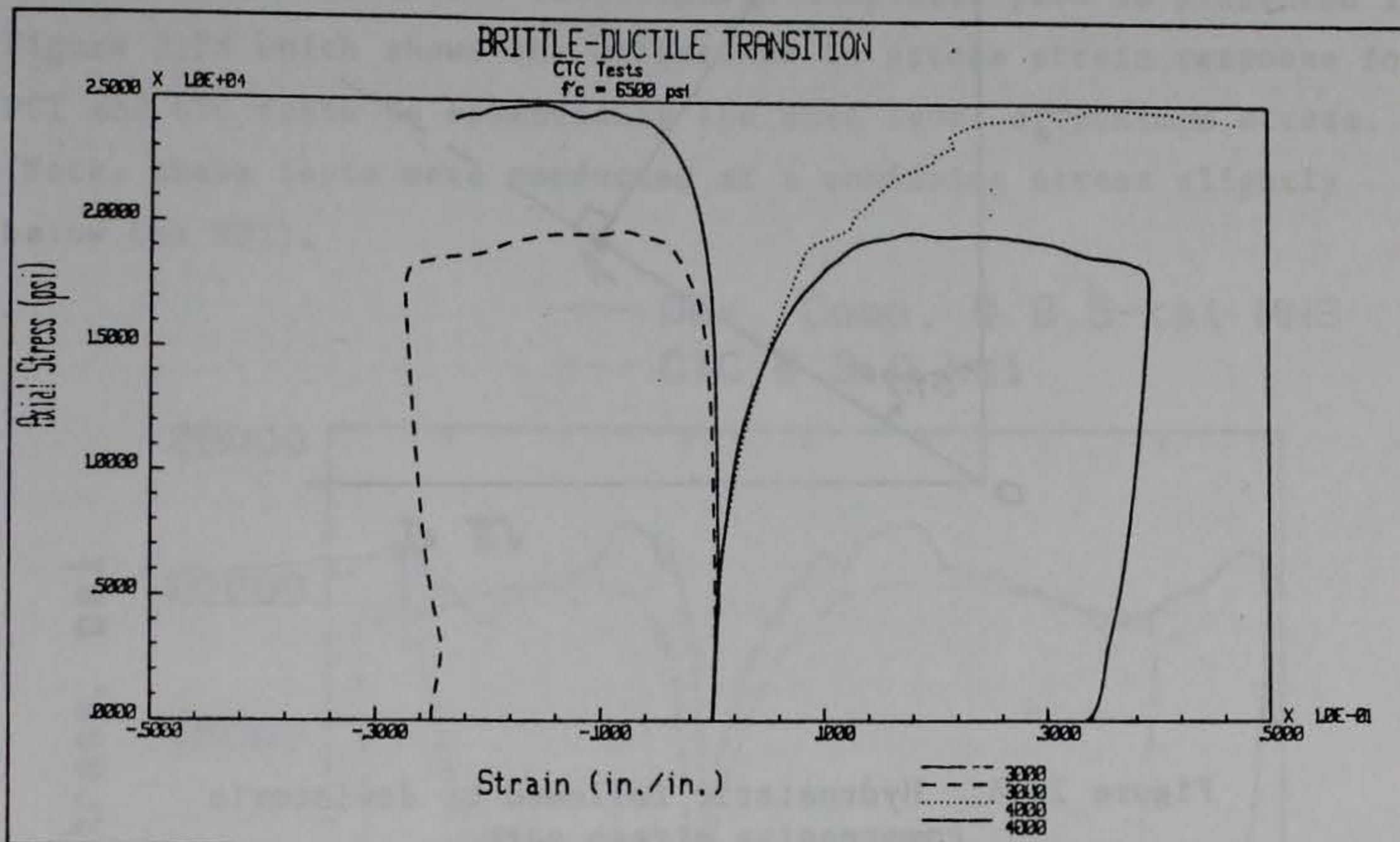


Figure 2.13 Determining brittle ductile transition

### 2.6.3 Deviatoric Compression Test

A deviatoric compression test (DCT) is defined here to consist of two loading branches. The first branch consists of a pure hydrostatic loading to a specified level of mean normal stress. The second branch is a pure deviatoric branch along a stress path, which in the Rendulic plane can be defined as  $\Delta\sigma_z = -2\Delta\sigma_c$ . A typical ideal DCT load path is shown in Figure 2.14. Figure 2.15 presents axial stress versus axial and lateral strains for DCT conducted on  $f'_c = 6.5$ -ksi concrete at two different mean normal stress (MNS) levels. The primary significance of the deviatoric compression test is that the MNS remains constant while increments in deviatoric stress occur. Therefore the effects of hydrostatic and deviatoric stresses on hardening can be studied by conducting CTC test and DCT to the same point on the failure surface. Also, the change in



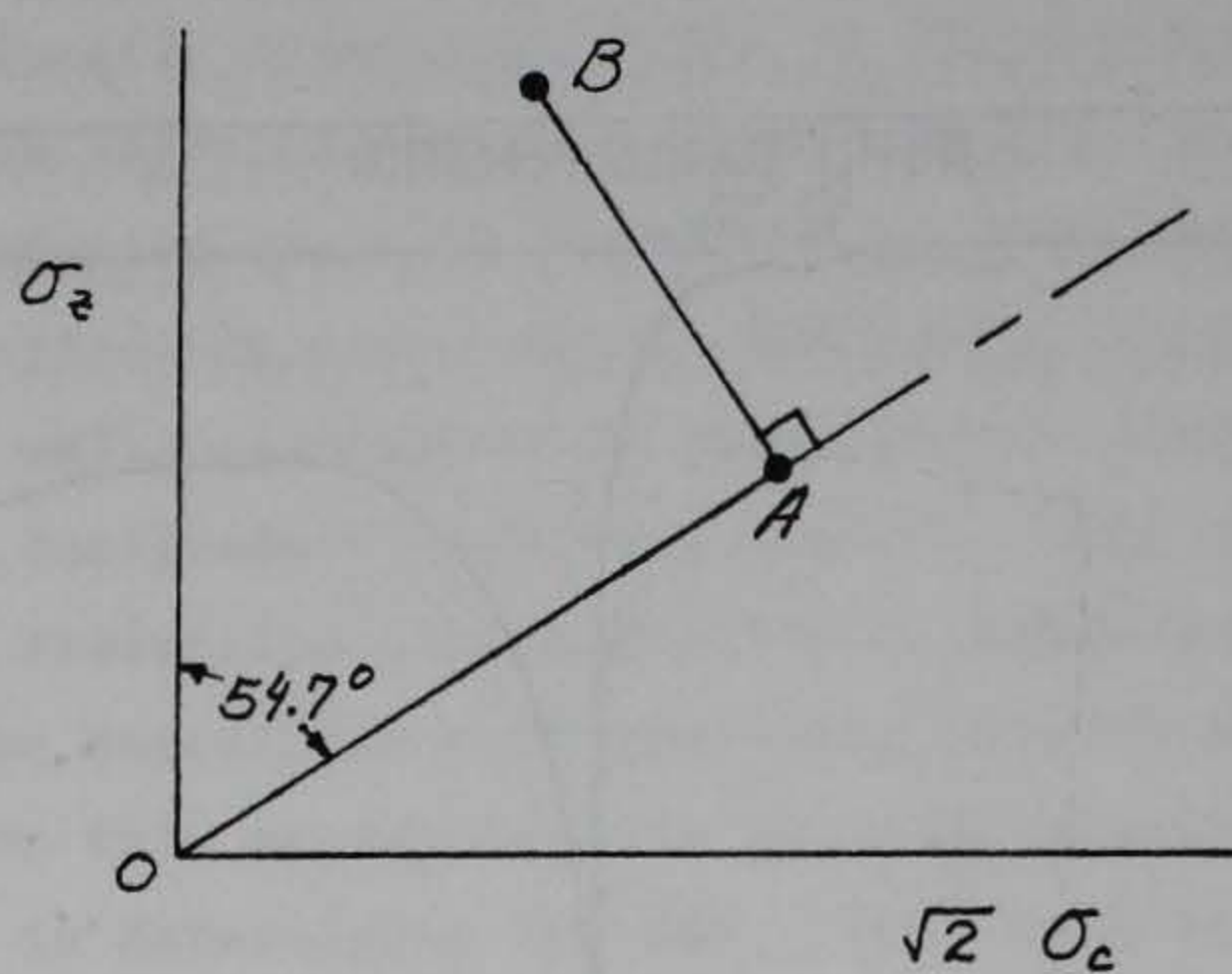


Figure 2.14. Hydrostatic followed by deviatoric compressive stress path.

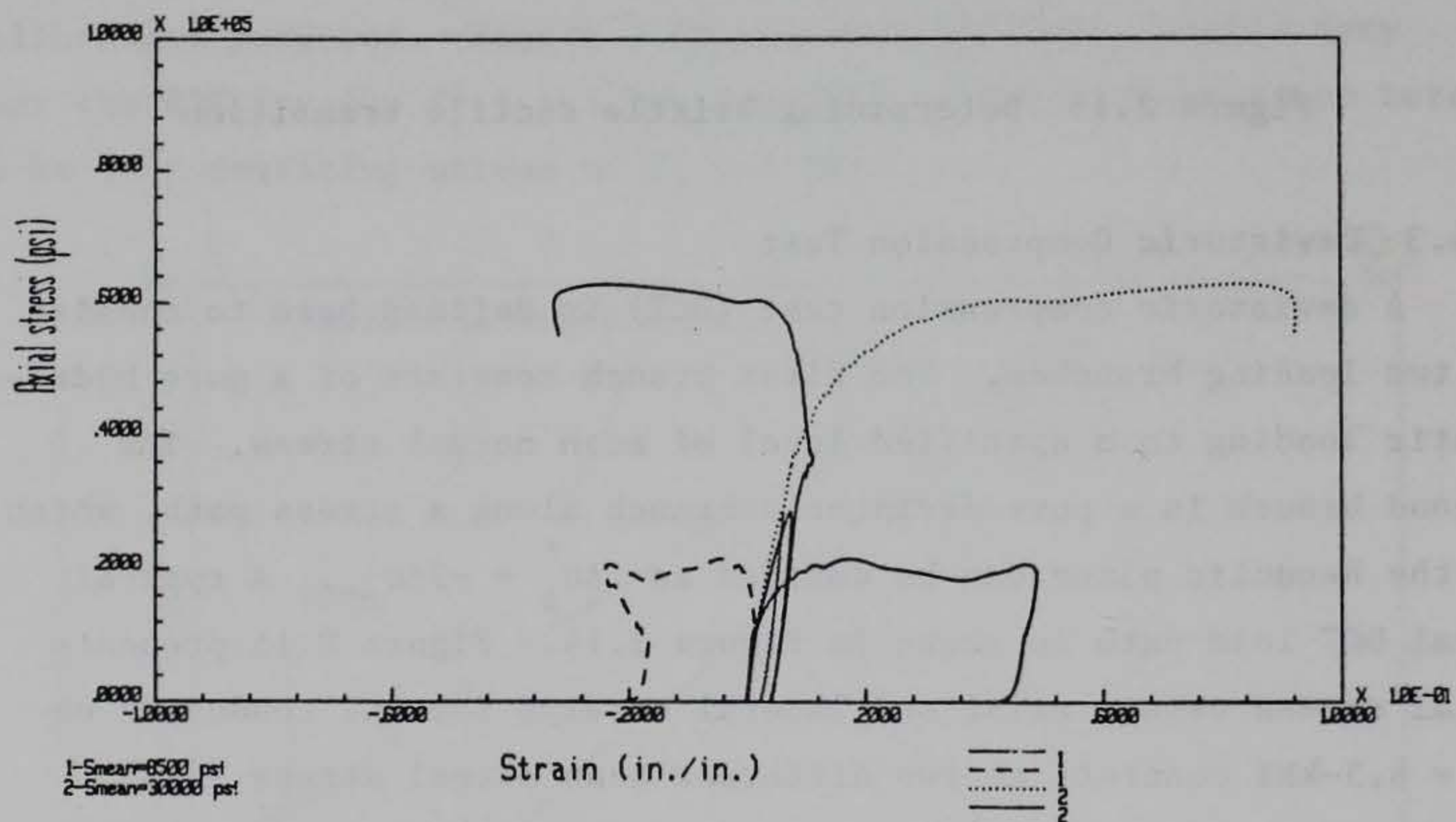


Figure 2.15. Deviatoric compression tests at low and high confining stress.



plastic volumetric strain during the pure deviatoric branch is a measure of shear-volumetric coupling. A composite plot is presented in Figure 2.16 which shows the difference in stress strain response for DCT and CTC tests to essentially the same level of maximum stress. (Note, these tests were conducted at a confining stress slightly below the BDT).

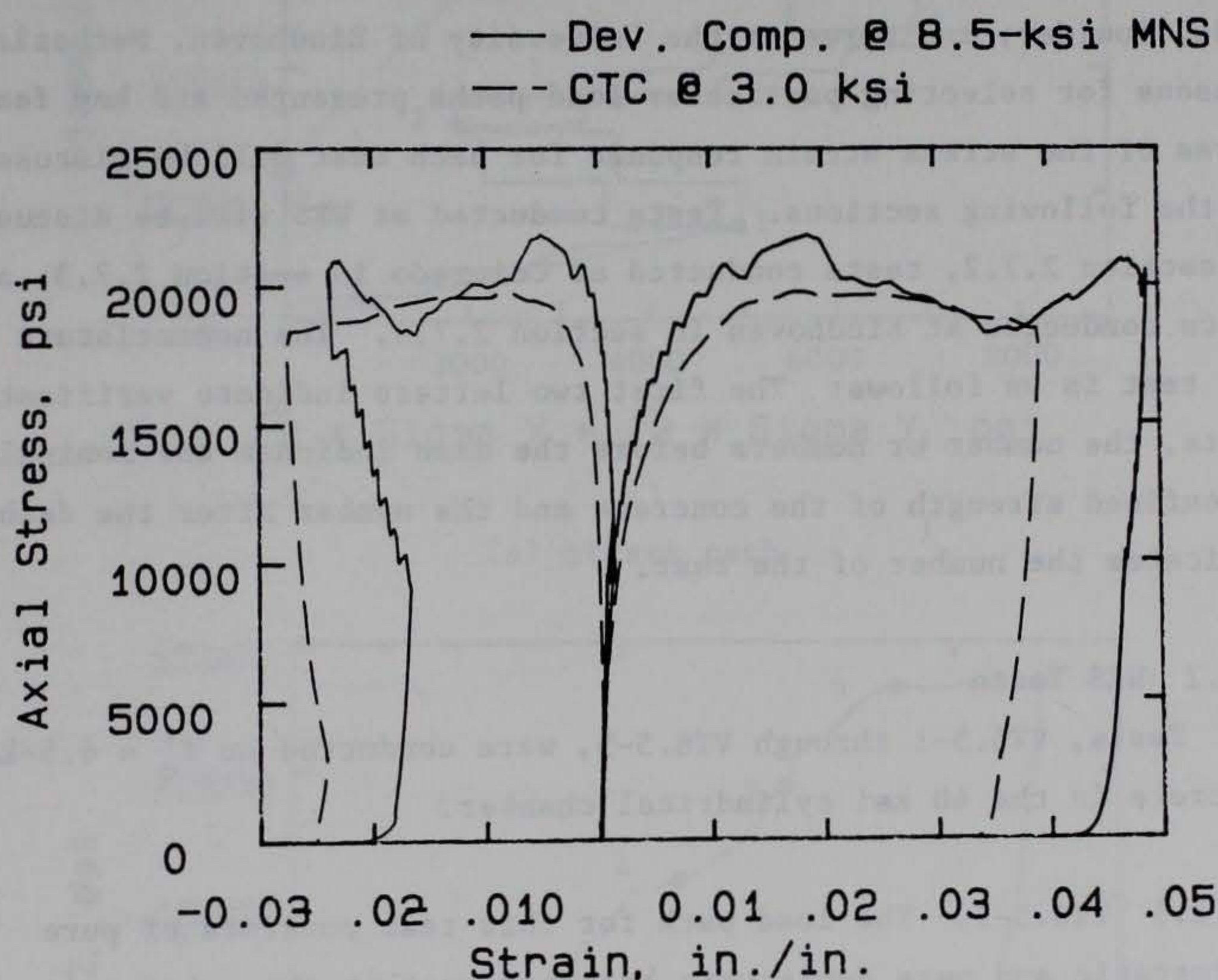


Figure 2.16 Composite plot, to same maximum stress level



## 2.7 Verification Tests

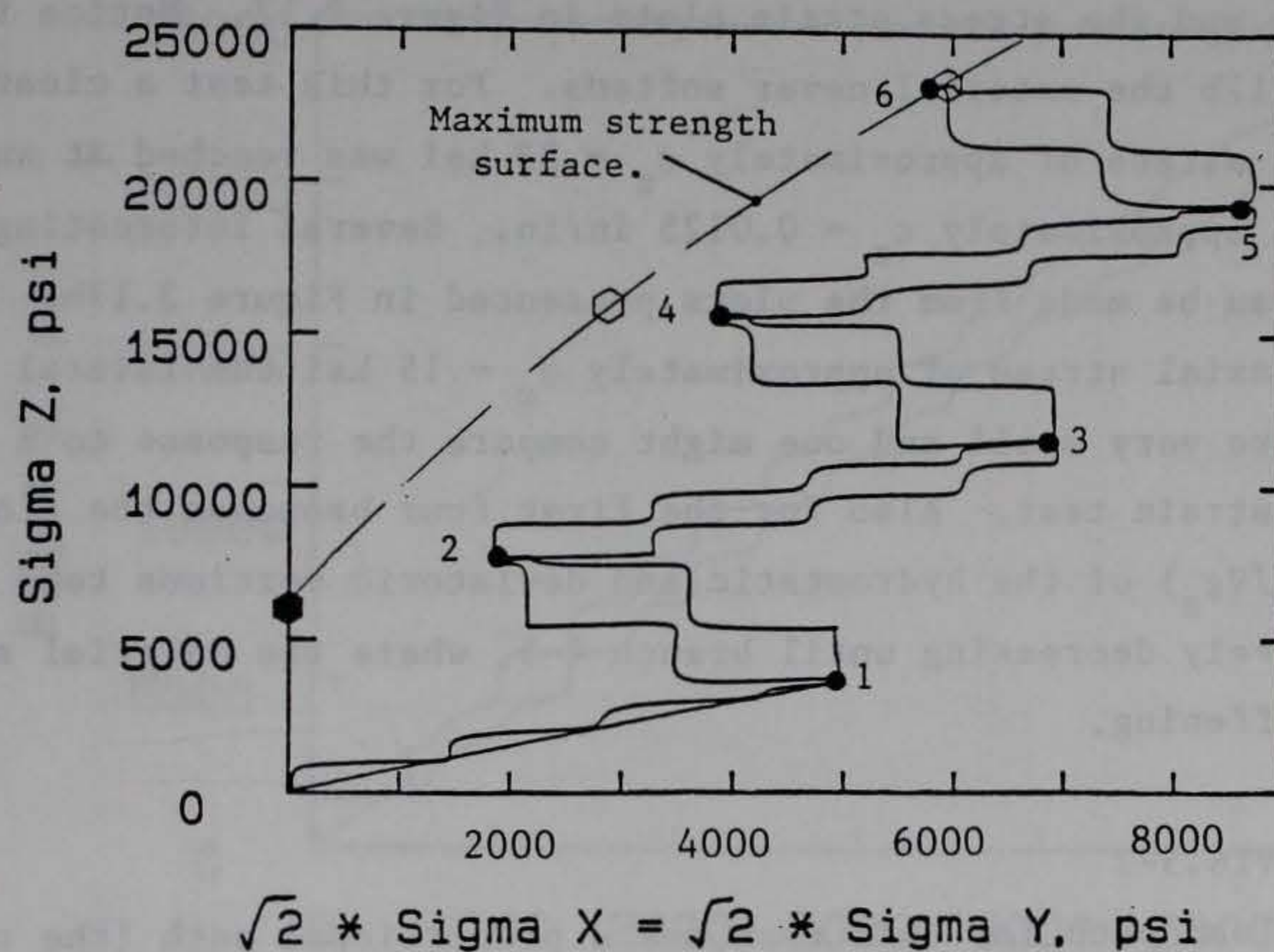
2.7.1 General. A series of 12 complex load path tests (verification tests) were conducted on concretes of different strengths ranging from nominally 2 ksi to 7 ksi. Six tests were conducted at the Waterways Experiment Station (WES), three at the University of Colorado, Boulder, and three at the University of Eindhoven, Netherlands. Reasons for selecting particular load paths presented and key features of the stress strain response for each test will be discussed in the following sections. Tests conducted at WES will be discussed in section 2.7.2, tests conducted at Colorado in section 2.7.3, and tests conducted at Eindhoven in section 2.7.4. The nomenclature for the test is as follows: The first two letters indicate verification tests, the number or numbers before the dash indicate the nominal unconfined strength of the concrete and the number after the dash indicates the number of the test.

### 2.7.2 WES Tests

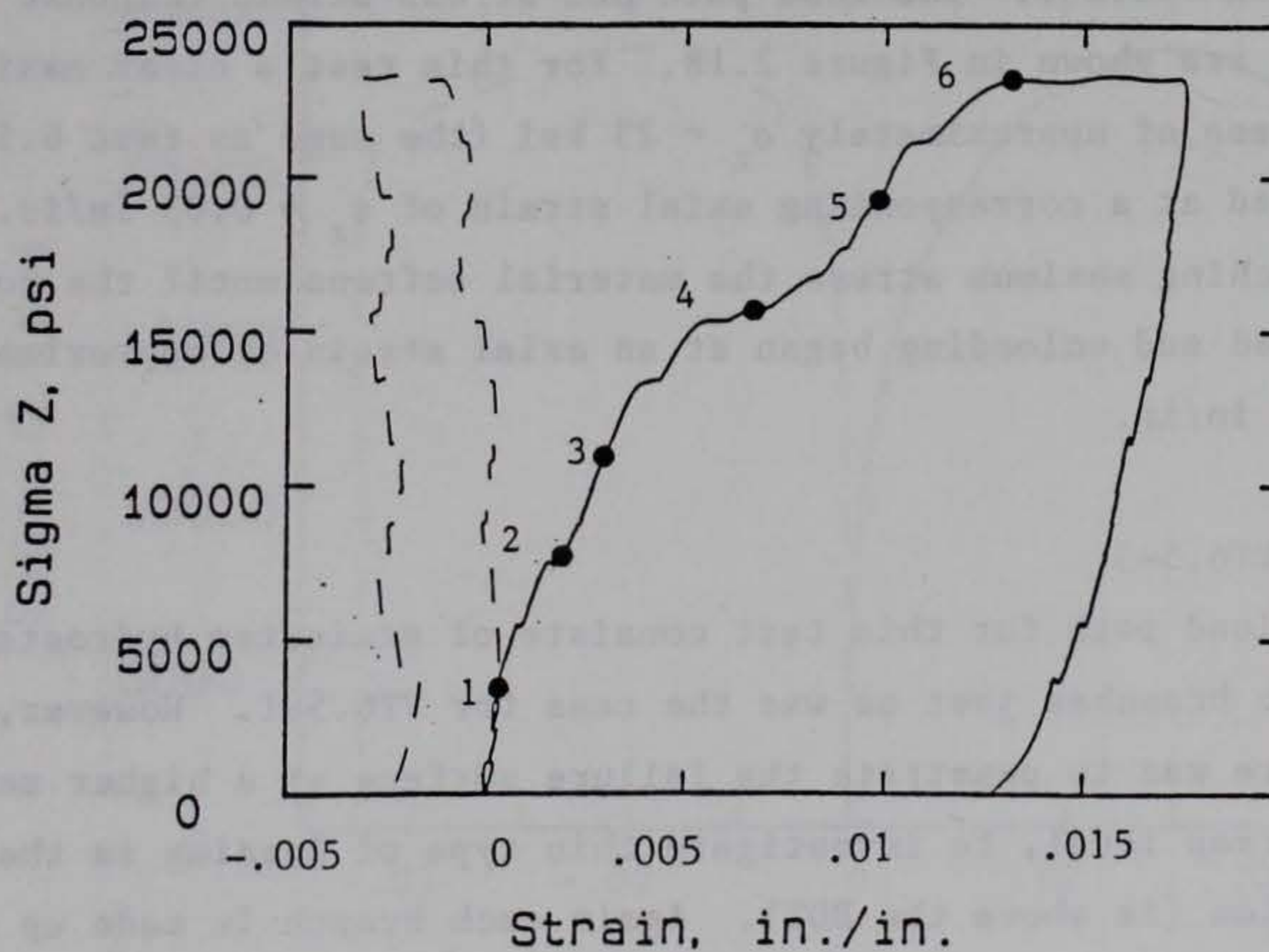
Tests, VT6.5-1 through VT6.5-5, were conducted on  $f'_c = 6.5$ -ksi concrete in the 40 ksi cylindrical chamber.

2.7.2.1 VT6.5-1. The load path for this test consists of pure hydrostatic and pure deviatoric branches so that the volumetric deviatoric coupling can be evaluated. The load path (Figure 2.17a) was designed to penetrate the failure surface near the BDT (i.e. confining stress 4 ksi). The arrows on the load path indicate the loading and unloading portions of the test. The first branch (0-1) represents pure hydrostatic compression. However, as shown in Figure 2.17a for this test the axial and radial increments are large enough so that the hydrostatic and deviatoric branches are themselves made up of stairstep axial and radial stress increments. The significance of this increment size will be discussed in Chapter 4. Points of transition from one branch to the other are marked on the





(a) stress path



(b) Axial stress versus axial and lateral strains

Figure 2.17 WES test, VT6.5-1, hydrostatic deviatoric load path at low confining stress region, with stress strain response



load path and the stress strain plots in Figure 2.17. Notice from Figure 2.17b the material never softens. For this test a clear maximum axial stress of approximately  $\sigma_z = 23$  ksi was reached at an axial strain of approximately  $\epsilon_z = 0.0125$  in/in. Several interesting observations can be made from the plots presented in Figure 2.17b. First, up to an axial stress of approximately  $\sigma_z = 15$  ksi the lateral strains are very small and one might compare the response to a uniaxial strain test. Also for the first four branches the slope (i.e.  $\Delta\sigma_z / \nabla\epsilon_z$ ) of the hydrostatic and deviatoric portions tend to be progressively decreasing until branch 4-5, where the material seems to be stiffening.

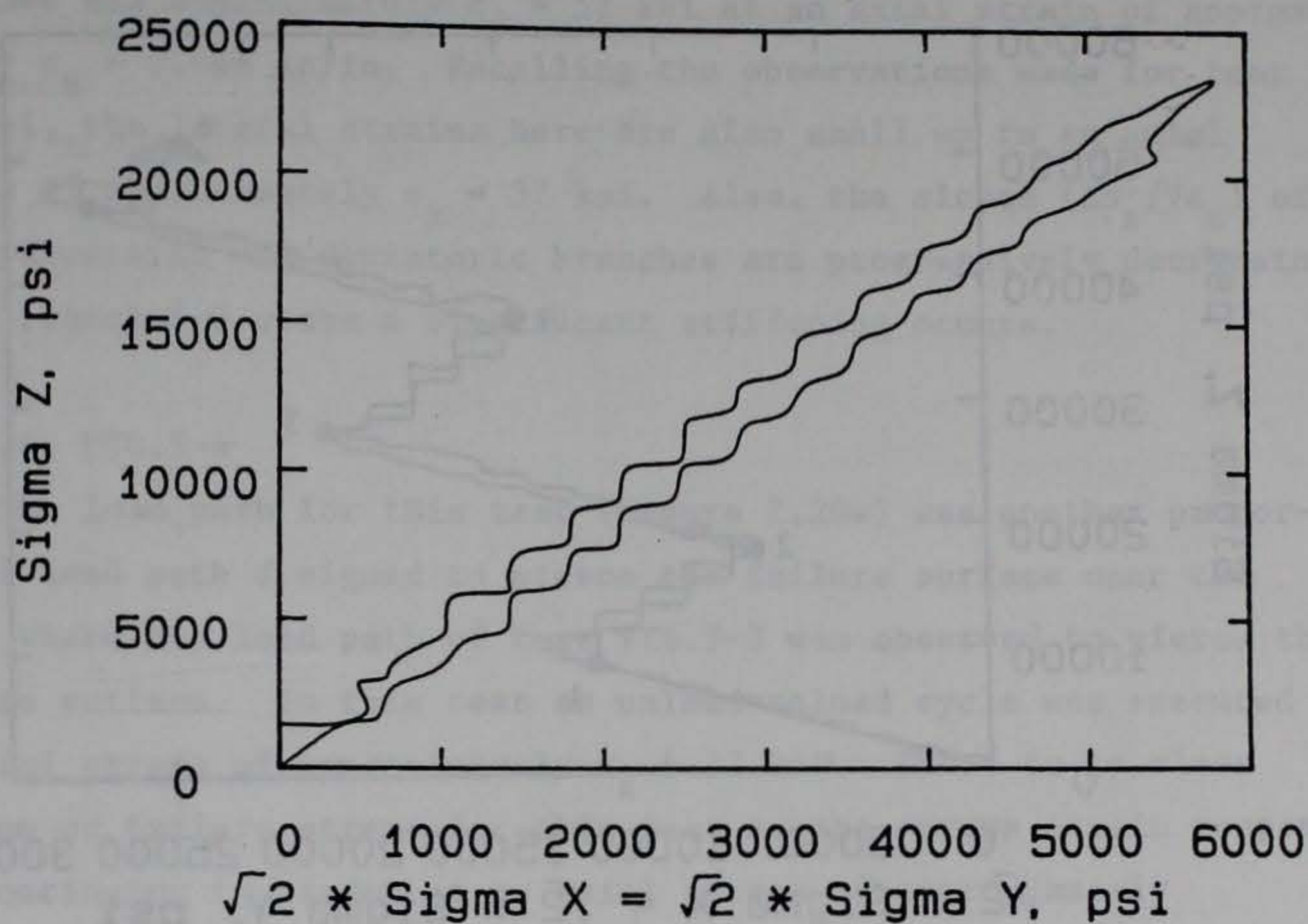
#### 2.7.2.2 VT6.5-2

The load path for this test was a proportional path (the ratio of lateral to axial stresses are kept constant throughout the test) designed to pierce the maximum strength surface near the BDT as was the case in VT6.5-1. The load path and stress strain response for this test are shown in Figure 2.18. For this test a clear maximum axial stress of approximately  $\sigma_z = 23$  ksi (the same as test 6.5-1) was reached at a corresponding axial strain of  $\epsilon_z = 0.03$  in/in. After reaching maximum stress the material softens until the loading was stopped and unloading began at an axial strain of approximately  $\epsilon_z = 0.05$  in/in.

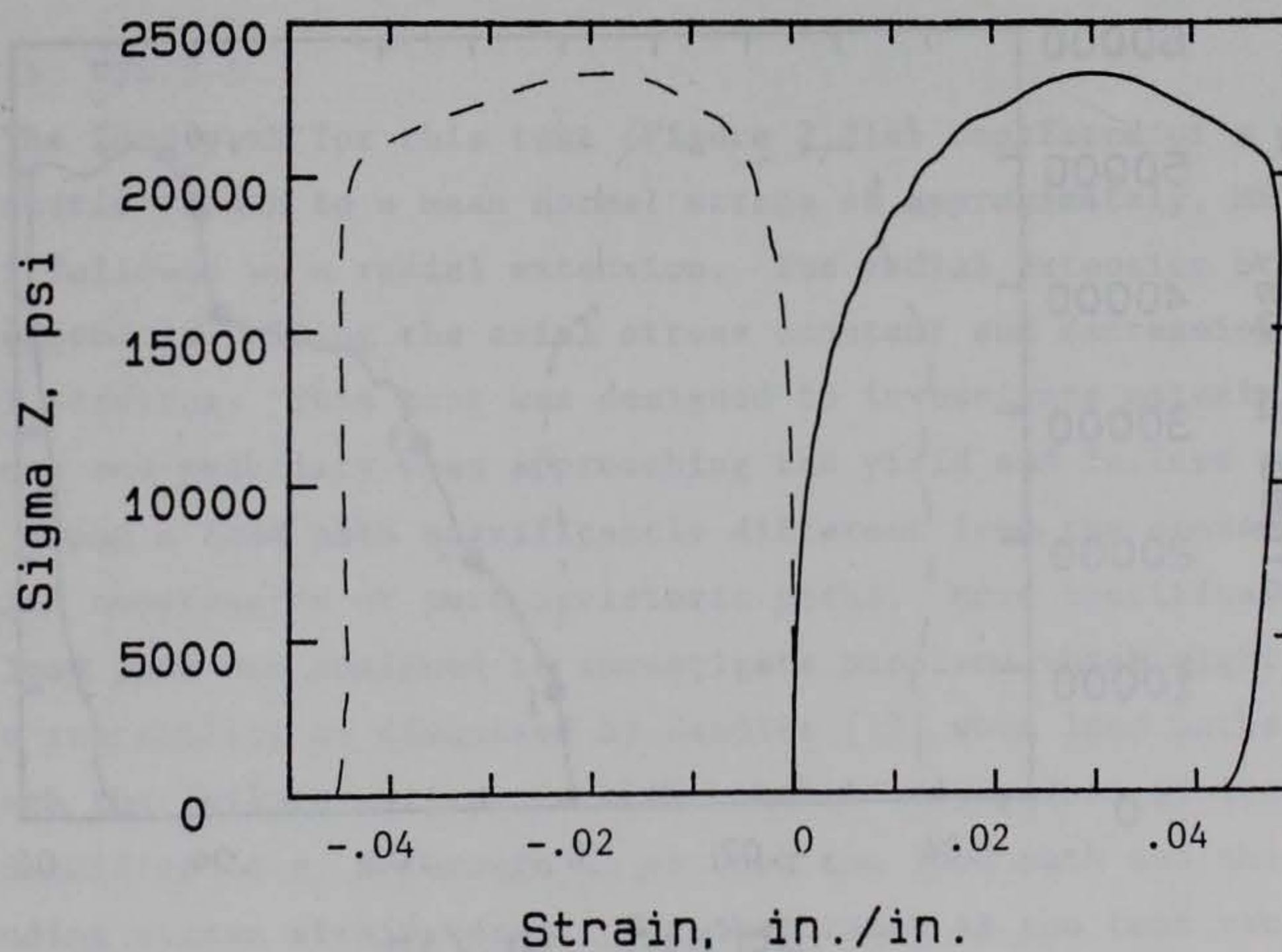
#### 2.7.2.3 VT6.5-3

The load path for this test consists of staircase hydrostatic deviatoric branches just as was the case for VT6.5-1. However, the intent here was to penetrate the failure surface at a higher mean normal stress level, to investigate this type of loading in the hardening region (ie above the BDT). Again each branch is made up of independent increments of axial and radial stress. Corresponding points of transition from hydrostatic to deviatoric branches are shown in Figure 2.19a and Figure 2.19b. The maximum axial stress





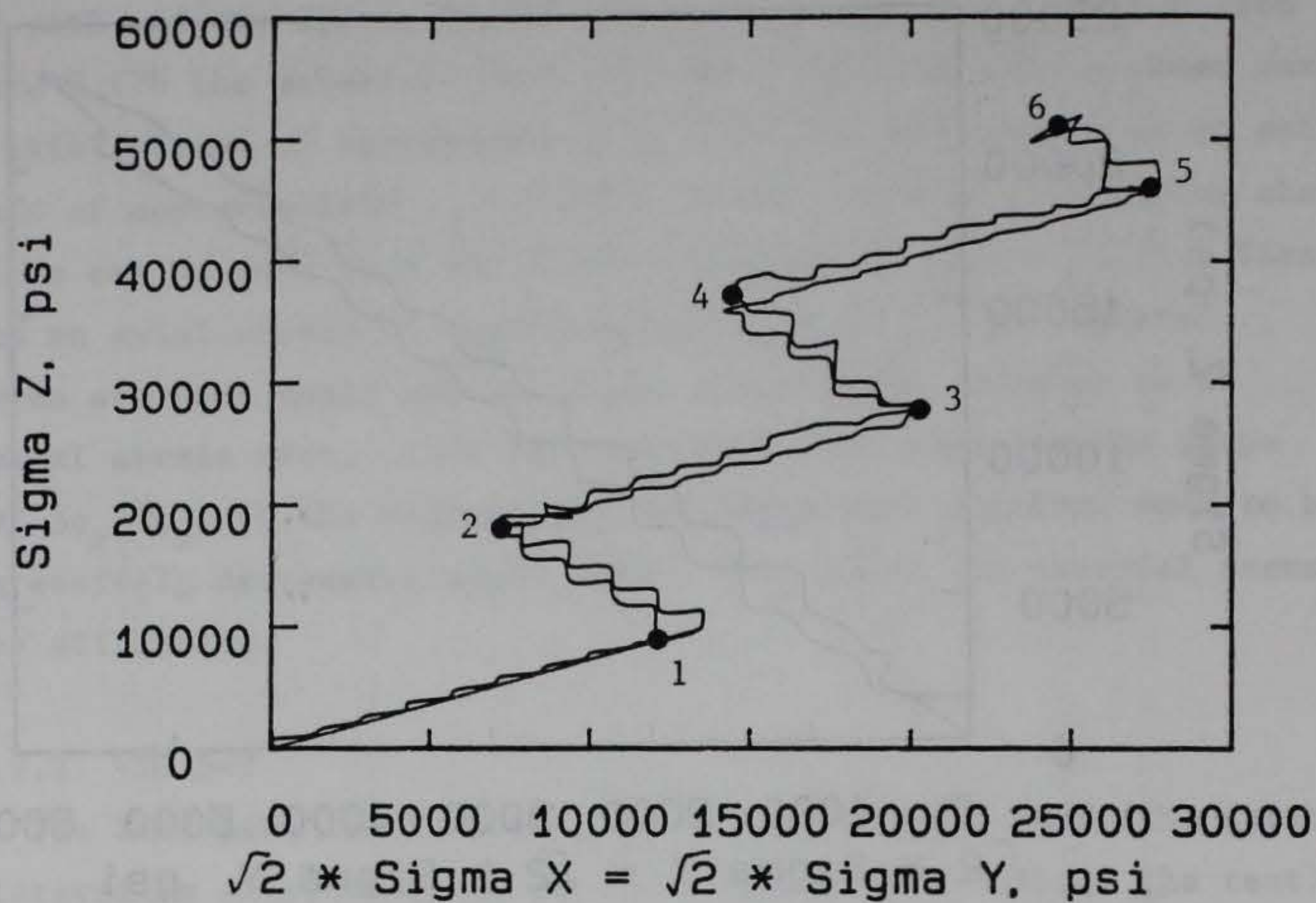
(a) stress path



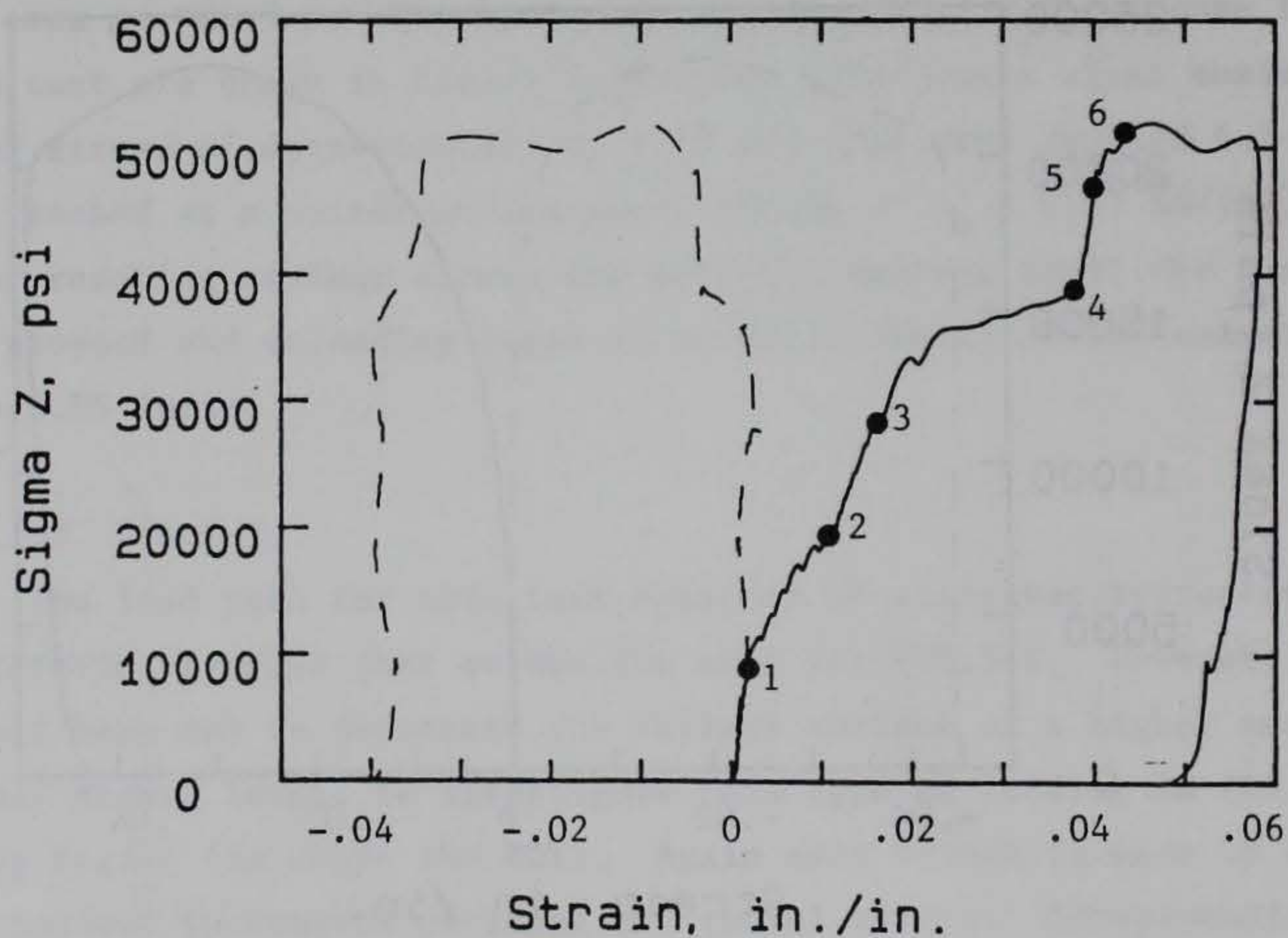
(b) Axial stress versus axial and lateral strains

Figure 2.18 WES Test, VT6.5-2, proportional load path in the softening region, with stress strain response





(a) stress path



(b) axial stress versus axial and lateral strains

Figure 2.19 WES test, VT6.5-3, hydrostatic deviatoric load path at high confining stress region, with stress strain response



attained was approximately  $\epsilon_z = 52$  ksi at an axial strain of approximately  $\sigma_z = 0.046$  in/in. Recalling the observations made for test VT6.5-1, the lateral strains here are also small up to an axial stress of approximately  $\sigma_z = 37$  ksi. Also, the slopes ( $\Delta\sigma_z/\nabla\epsilon_z$ ) of the hydrostatic and deviatoric branches are progressively decreasing up to branch 4-5 where a significant stiffening occurs.

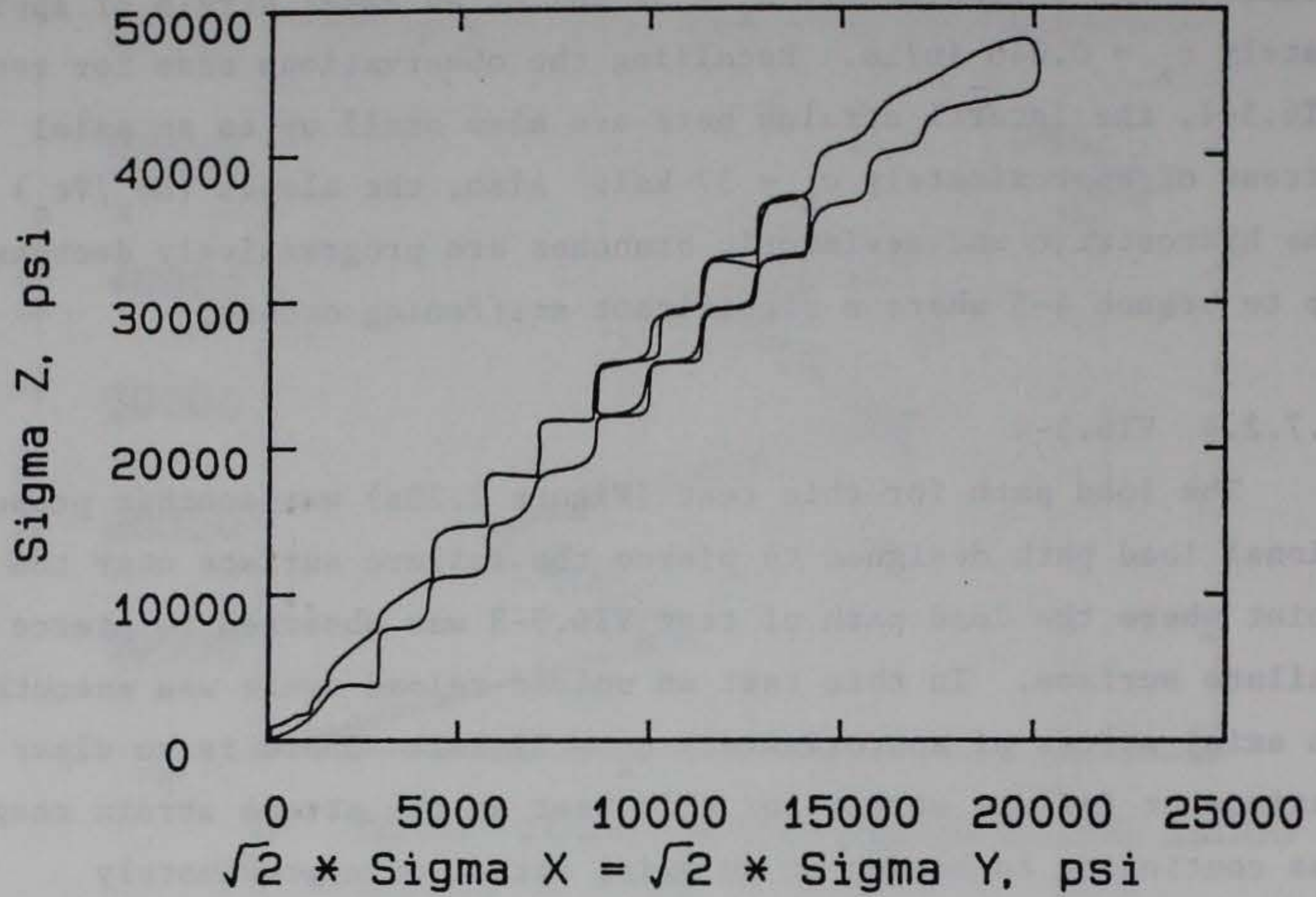
#### 2.7.2.4 VT6.5-4

The load path for this test (Figure 2.20a) was another proportional load path designed to pierce the failure surface near the point where the load path of test VT6.5-3 was observed to pierce the failure surface. In this test an unload-reload cycle was executed at an axial stress of approximately  $\sigma_z = 37$  ksi. There is no clear maximum or failure stress for this test as the stress strain response was continuing to harden at an axial stress of approximately  $\sigma_z = 48$  ksi and corresponding axial strain of  $\epsilon_z = 0.059$  in/in.

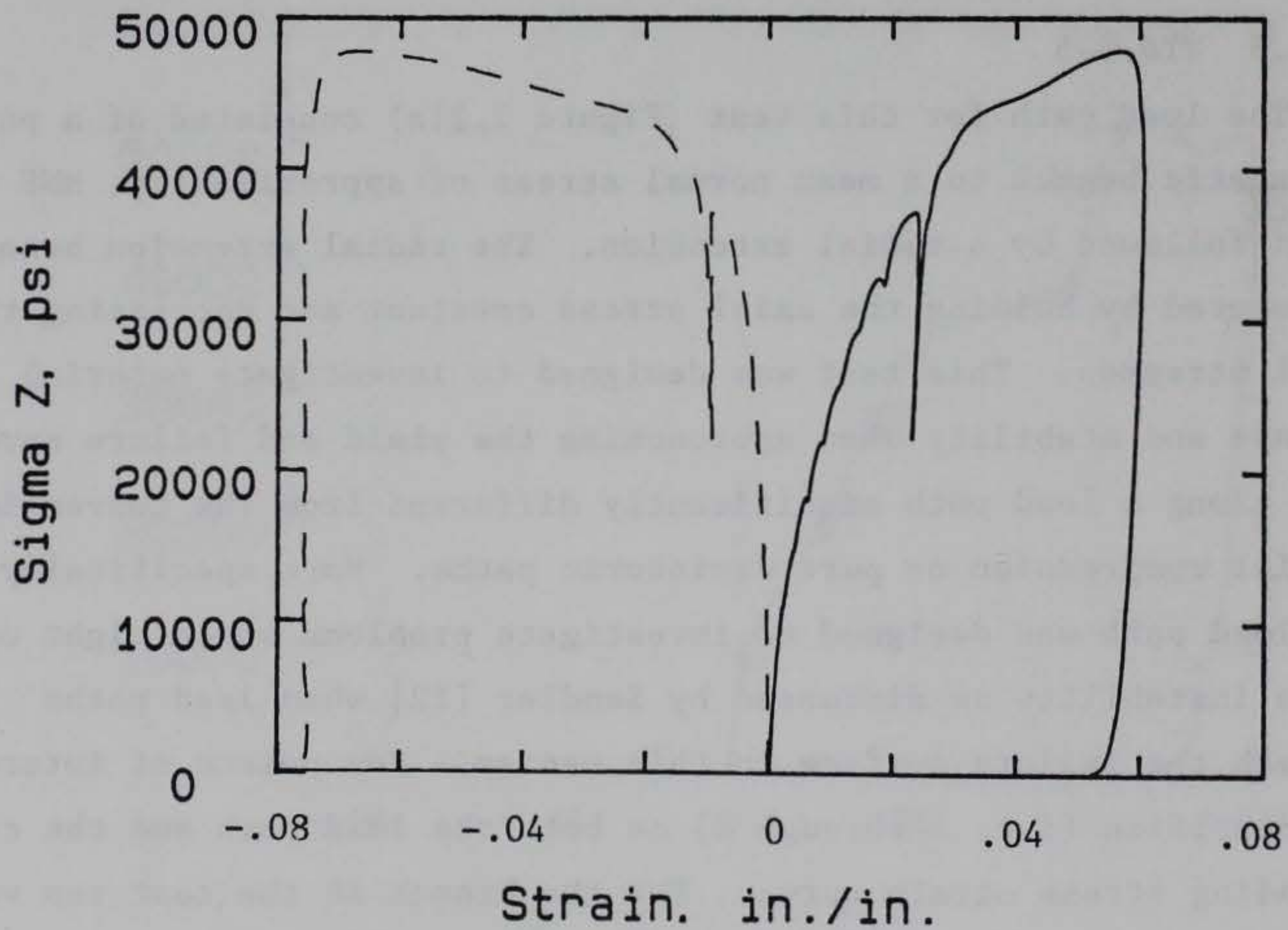
#### 2.7.2.5 VT6.5-5

The load path for this test (Figure 2.21a) consisted of a pure hydrostatic branch to a mean normal stress of approximately, MNS = 26 ksi followed by a radial extension. The radial extension branch is executed by holding the axial stress constant and decreasing the radial stresses. This test was designed to investigate material response and stability when approaching the yield and failure envelopes along a load path significantly different from the conventional triaxial compression or pure deviatoric paths. More specifically this load path was designed to investigate problems which might occur due to instability as discussed by Sandler [12] when load paths approach the failure surface in this manner. Key points of interests are identified (i.e. A through G) on both the load path and the corresponding stress strain curve. For the branch AB the test ran very smoothly as the axial load was easily held constant while the radial load was decreased. However, at point B to F (which is in the





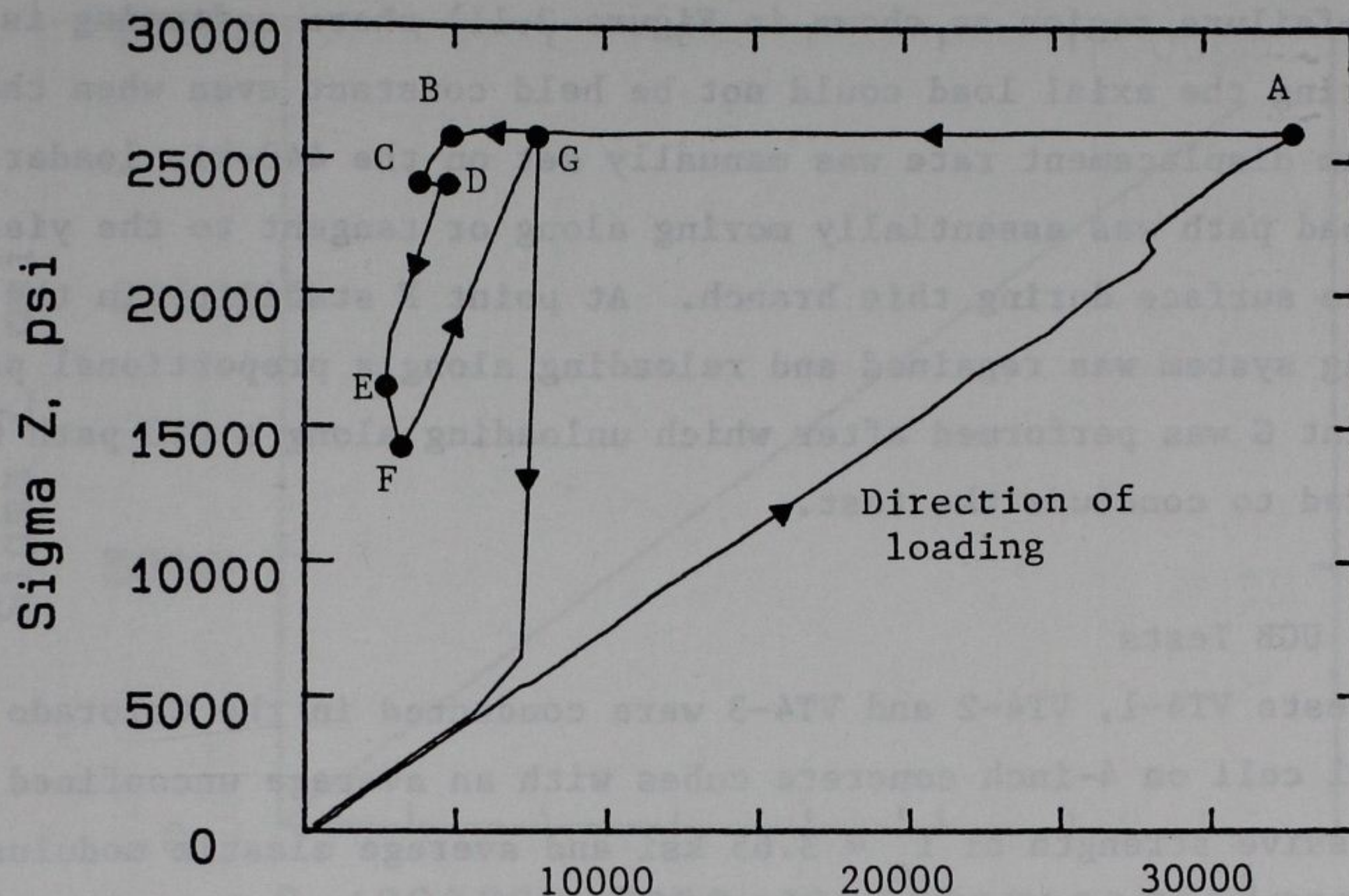
(a) stress path



(b) axial stress versus axial and lateral strains

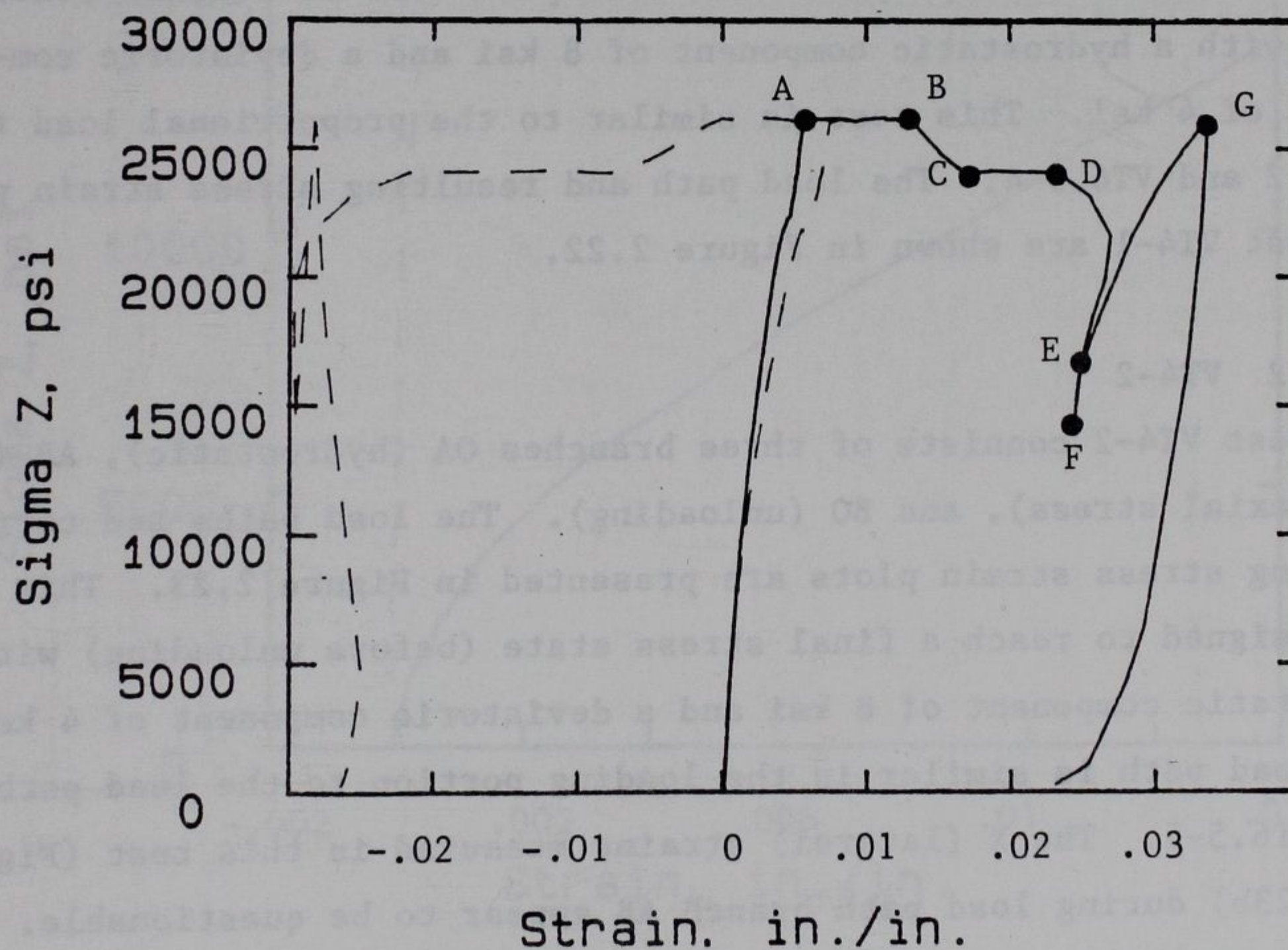
Figure 2.20 WEST test, VT6.5-4, proportional load path in the hardening region, with stress strain response





$$\sqrt{2} * \Sigma X = \sqrt{2} * \Sigma Y, \text{ psi}$$

(a) stress path



(b) axial stress versus axial and lateral strains

Figure 2.21 WES test, VT6.5-5, hydrostatic load path then radial expansion, with stress strain response



yield-failure region as shown in Figure 2.11) where softening is occurring the axial load could not be held constant even when the maximum displacement rate was manually set on the 440-kip loader. The load path was essentially moving along or tangent to the yield or failure surface during this branch. At point F stability in the loading system was regained and reloading along a proportional path to point G was performed after which unloading along a CTC path was executed to conclude the test.

### 2.7.3 UCB Tests

Tests VT4-1, VT4-2 and VT4-3 were conducted in the Colorado cubical cell on 4-inch concrete cubes with an average unconfined compressive strength of  $f'_c = 3.65$  ksi and average elastic modulus of  $E = 3 \times 10^6$  psi.

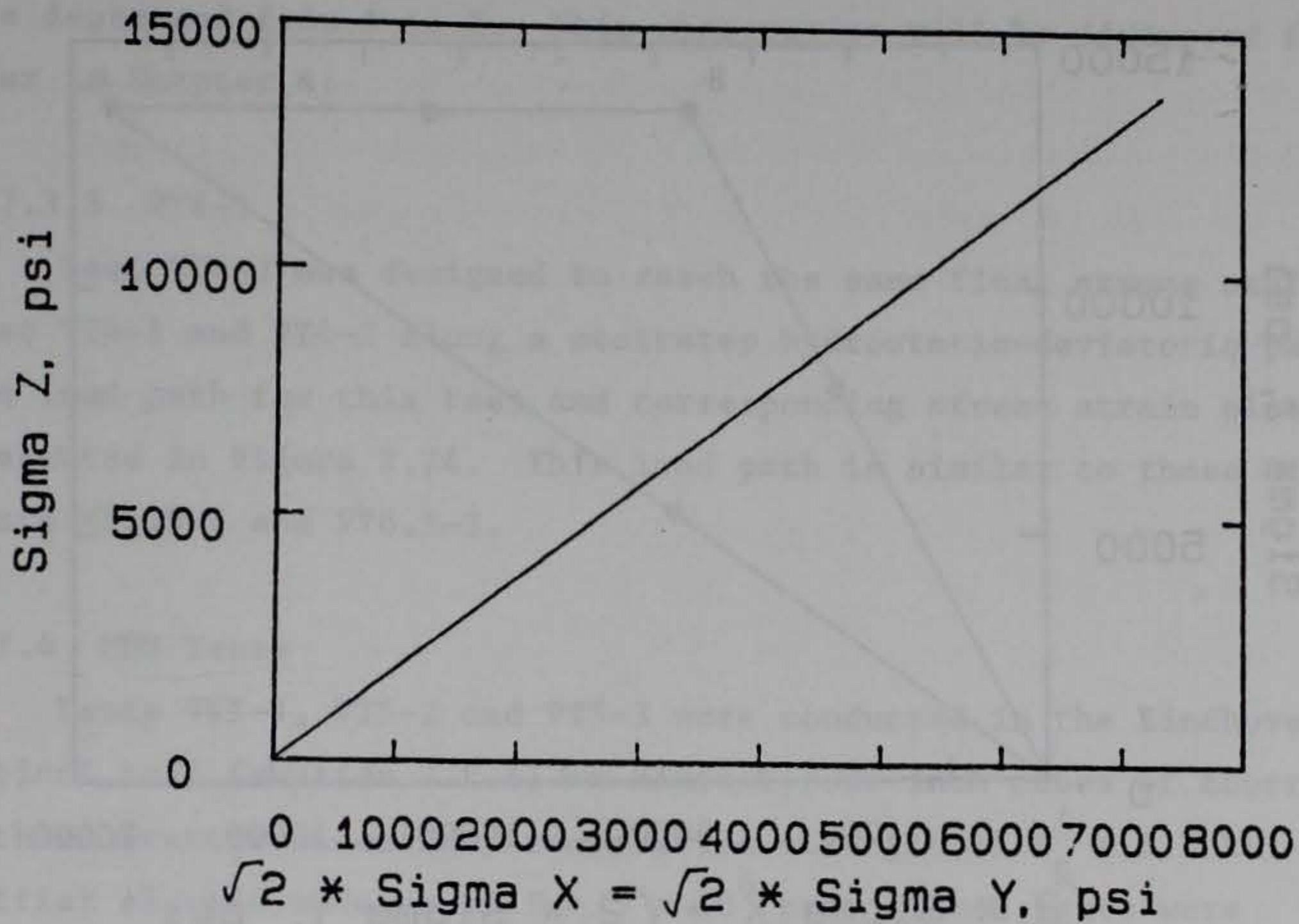
#### 2.7.3.1 VT4-1

Test VT4-1 is a proportional load path test to a final stress state with a hydrostatic component of 8 ksi and a deviatoric component of 4 ksi. This test is similar to the proportional load tests VT6.5-2 and VT6.5-4. The load path and resulting stress strain plots for test VT4-1 are shown in Figure 2.22.

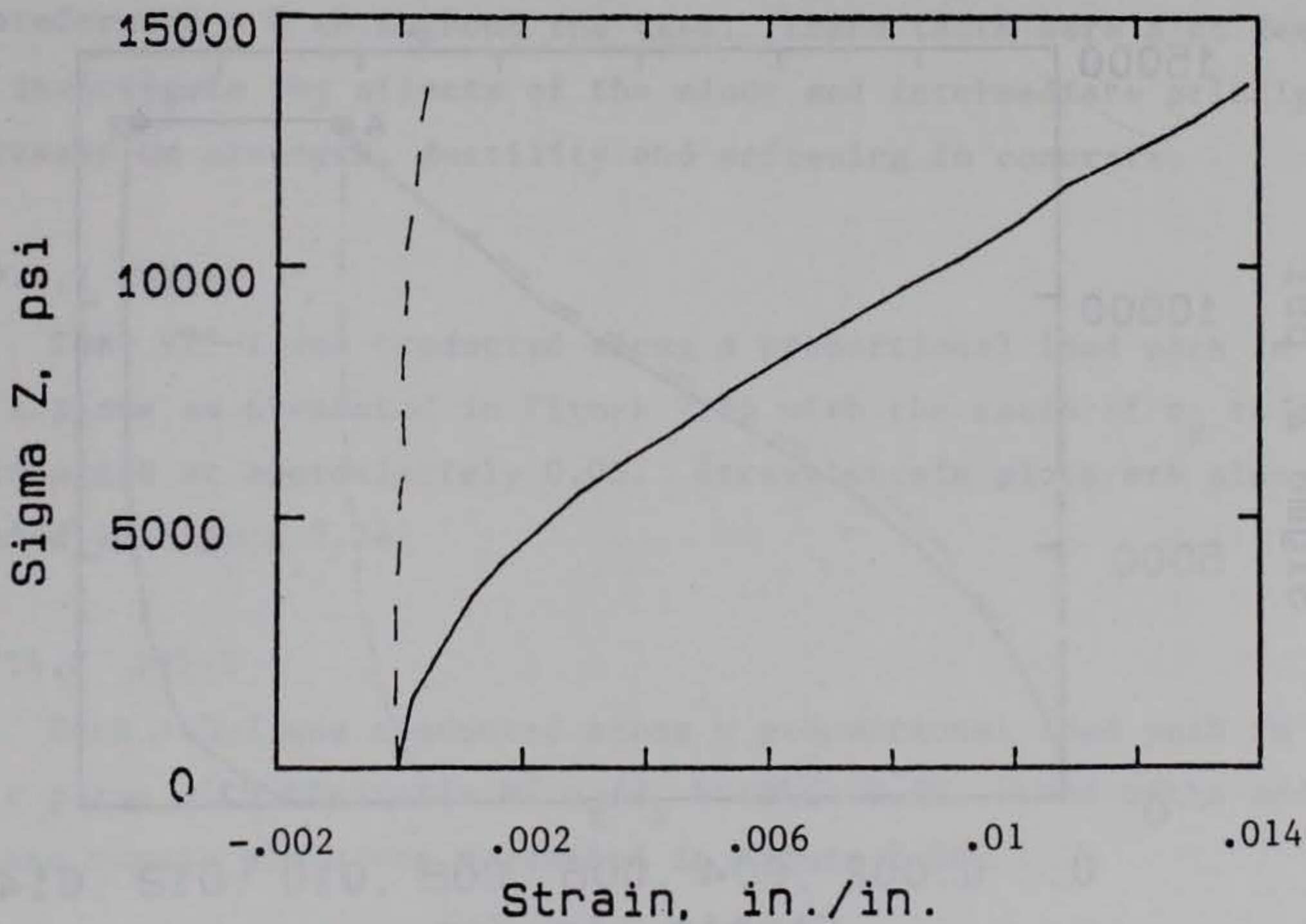
#### 2.7.3.2 VT4-2

Test VT4-2 consists of three branches OA (hydrostatic), AB (constant axial stress), and BO (unloading). The load paths and corresponding stress strain plots are presented in Figure 2.23. This test was designed to reach a final stress state (before unloading) with a hydrostatic component of 8 ksi and a deviatoric component of 4 ksi. This load path is similar in the loading portion to the load path of test VT6.5-5. The X (lateral) strains measured in this test (Figure 2.23b) during load path branch AB appear to be questionable. One would expect the lateral strains to decrease as the lateral stresses





(a) stress path



(b) axial stress versus axial and lateral strains

Figure 2.22 UCB test, VT4-1, proportional load path in the hardening region, with stress strain response



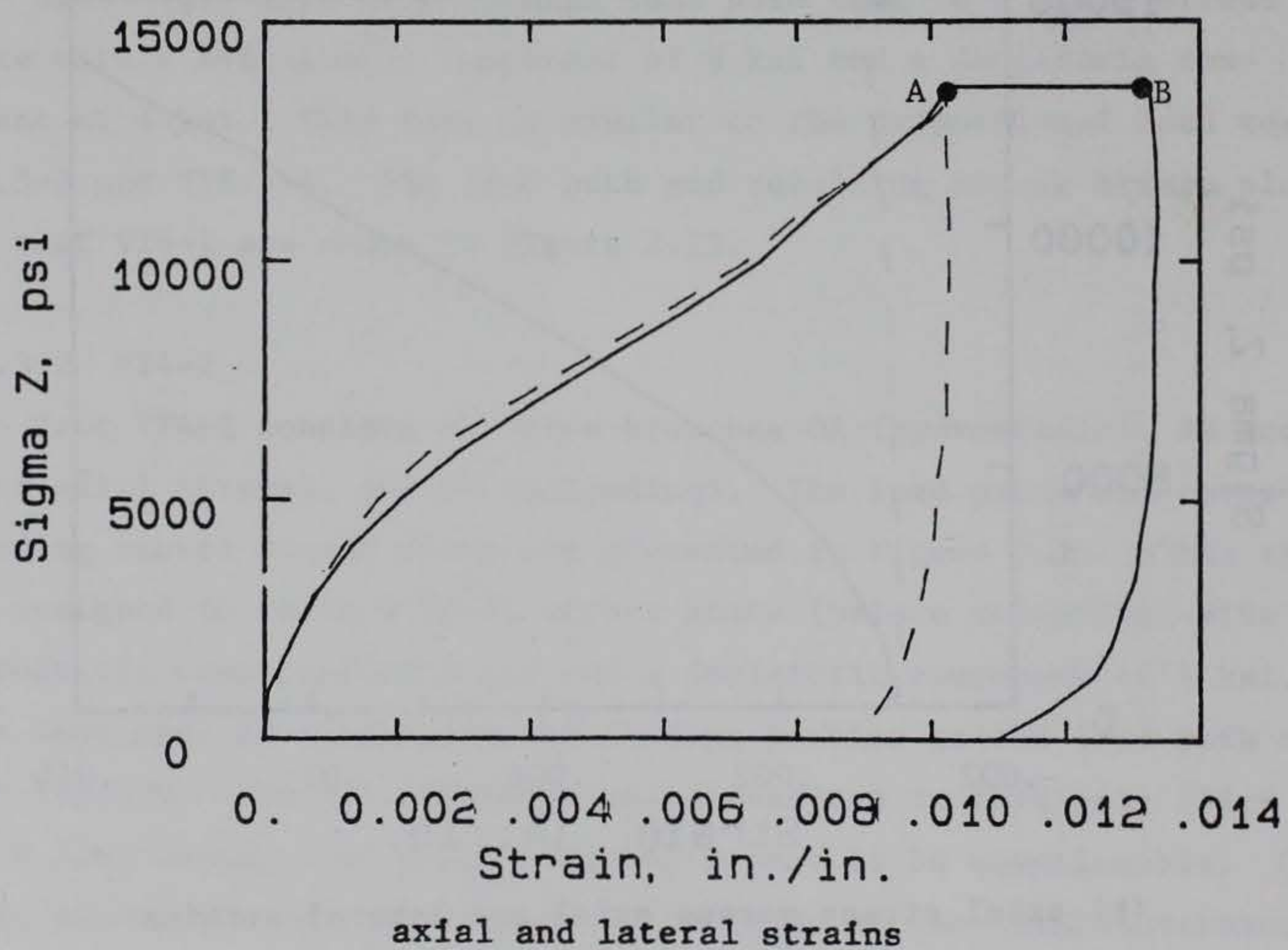
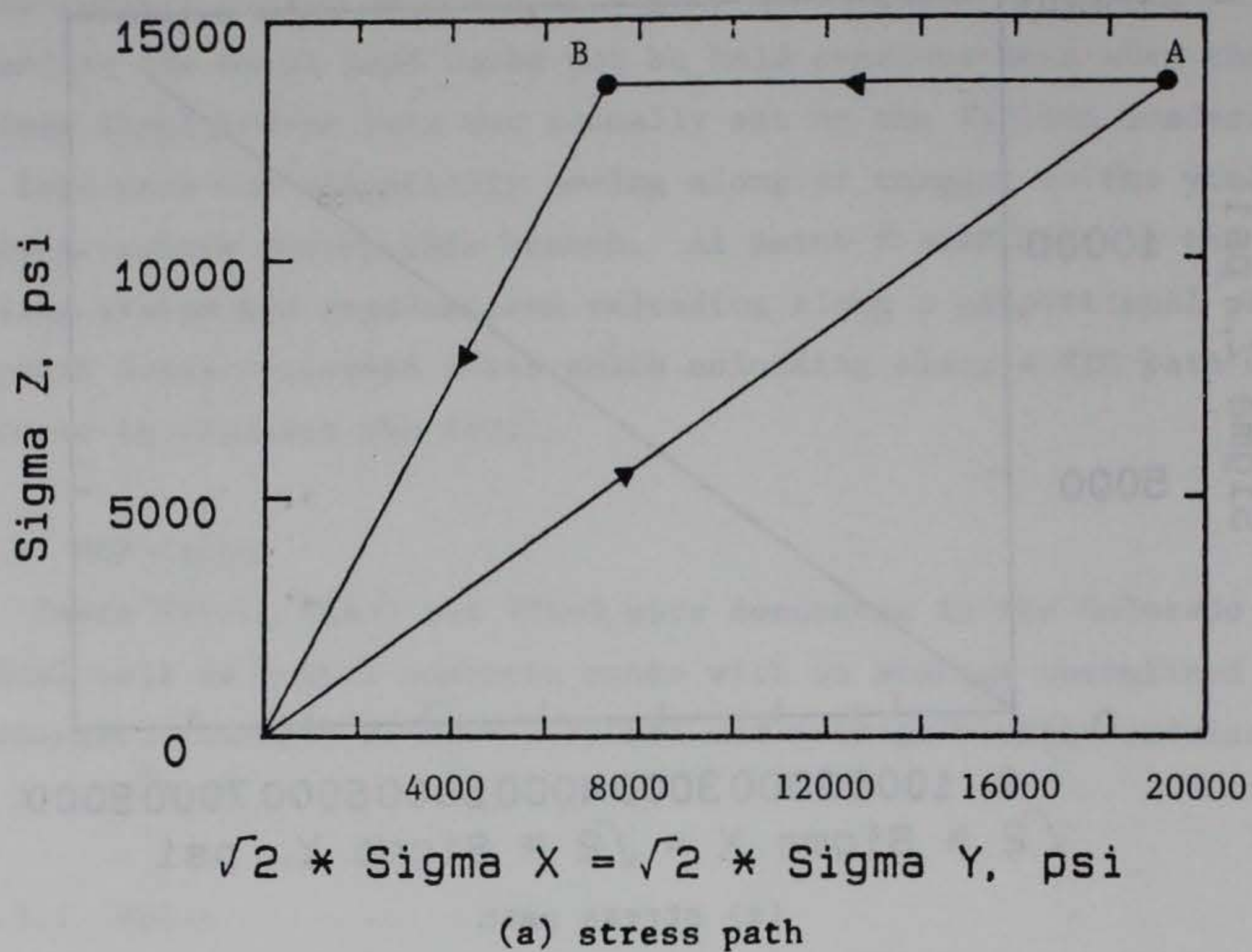


Figure 2.23 UCB test, VT4-2, hydrostatic load path then radial expansion, with stress strain response



are decreased from A to B. This observation will be discussed further in Chapter 4.

#### 2.7.3.3 VT4-3

Test VT4-3 was designed to reach the same final stress state of test VT4-1 and VT4-2 along a stairstep hydrostatic-deviatoric path. The load path for this test and corresponding stress strain plots are presented in Figure 2.24. This load path is similar to those of tests VT6.5-1 and VT6.5-3.

#### 2.7.4 UEN Tests

Tests VT5-1, VT5-2 and VT5-3 were conducted in the Eindhoven cubical cell (section 2.2.6) on nominal four inch cubes of concrete with an average unconfined compressive strength of  $f'_c = 5.2$  ksi and initial elastic modulus of  $E = 5 \times 10^6$  psi. These tests were designed to simulate plane strain conditions in the x, z plane, therefore  $\epsilon_y = 0$  throughout the test. These tests were also designed to investigate the effects of the minor and intermediate principal stresses on strength, ductility and softening in concrete.

##### 2.7.4.1 VT5-1

Test VT5-1 was conducted along a proportional load path in the x, z plane as presented in Figure 2.25 with the ratio of  $\sigma_x$  to  $\sigma_z$  maintained at approximately 0.05. Stress strain plots are also presented in Figure 2.24.

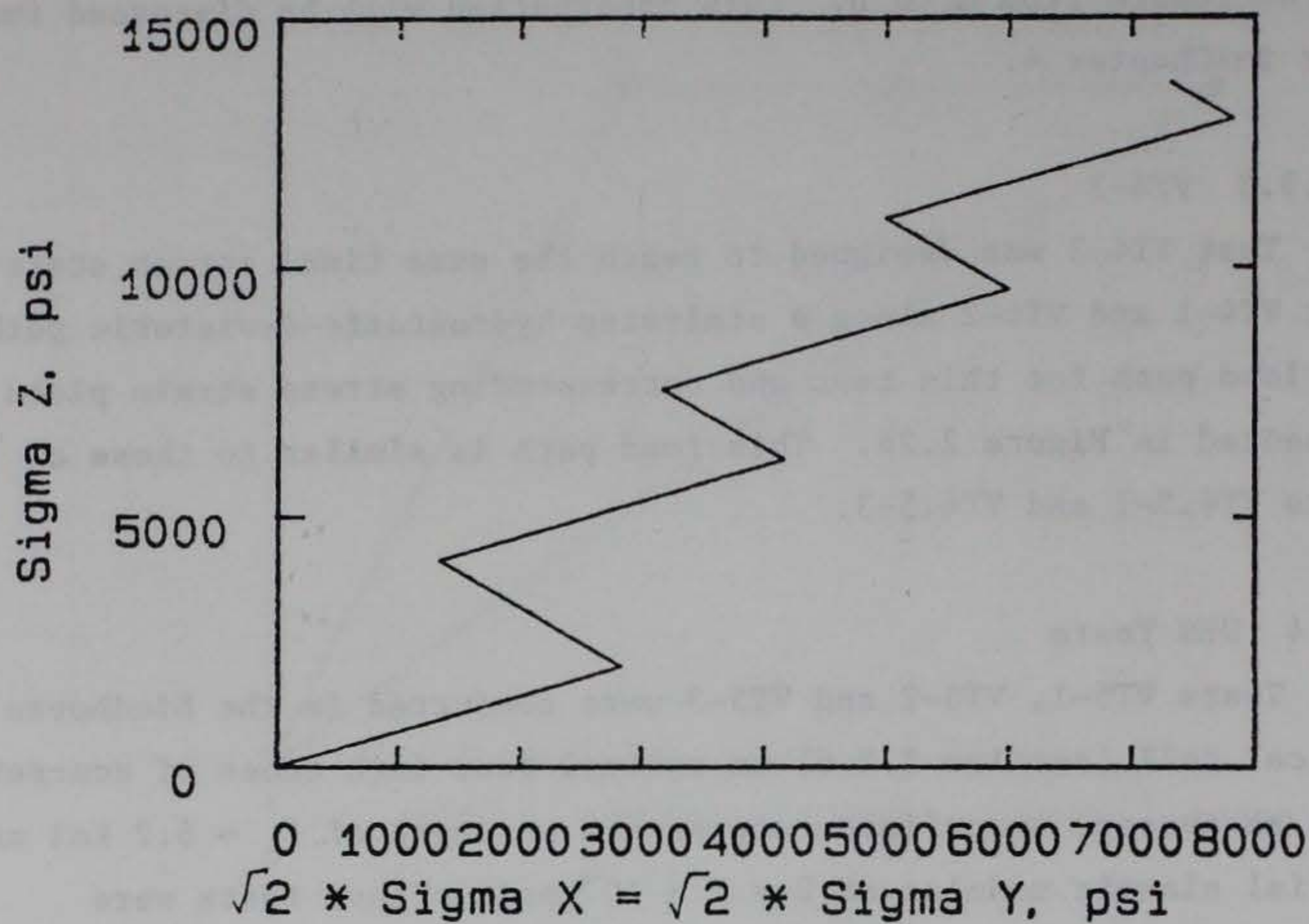
##### 2.7.4.2 VT5-2

Test VT5-2 was conducted along a proportional load path in the x, z plane with the ratio of  $\sigma_x/\sigma_z$  held at 0.10. Load paths and stress strain plots are presented in Figure 2.26.

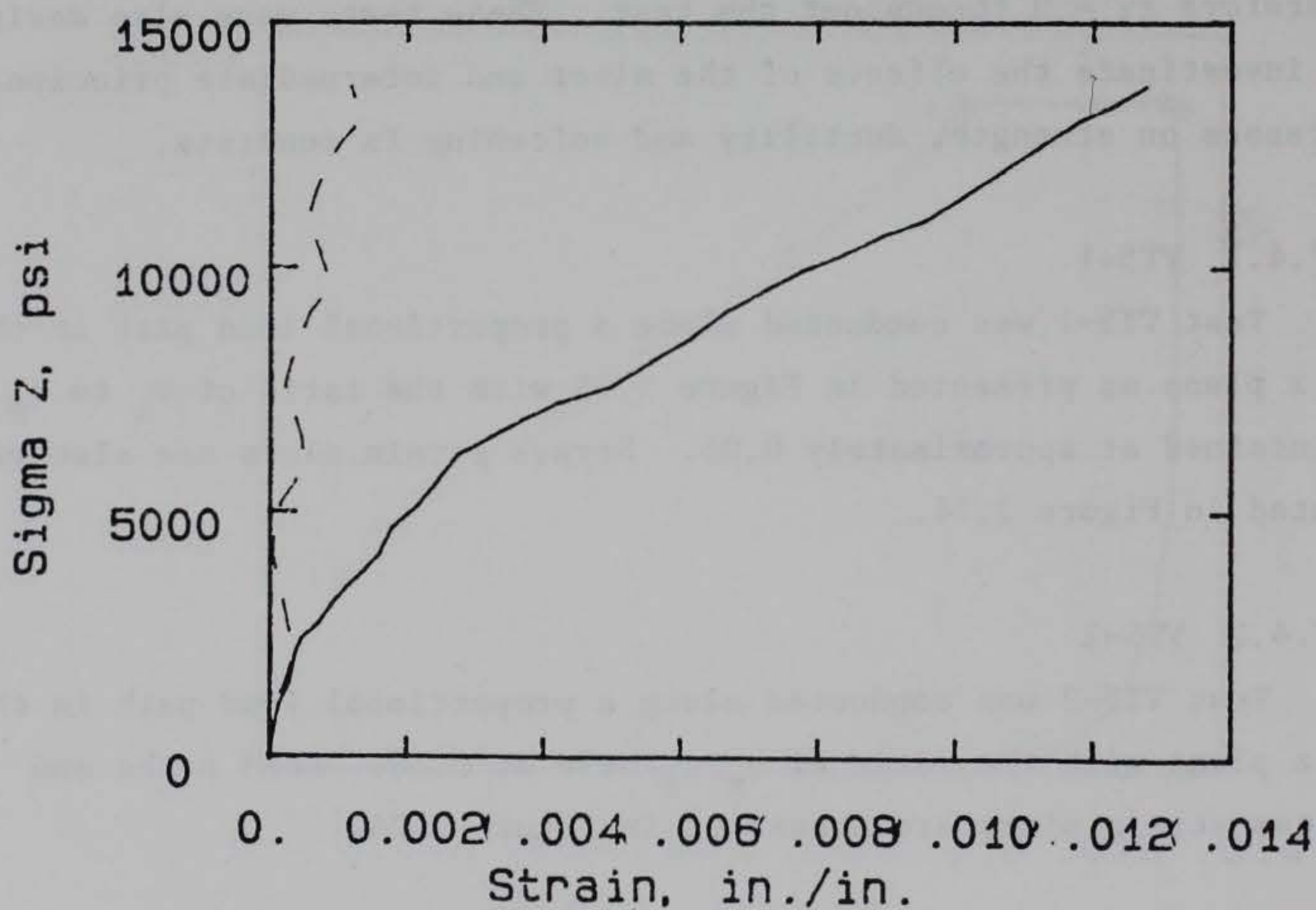
##### 2.7.4.3 VT5-3

Test VT5-3 was conducted with  $\sigma_x = 0$  while still maintaining





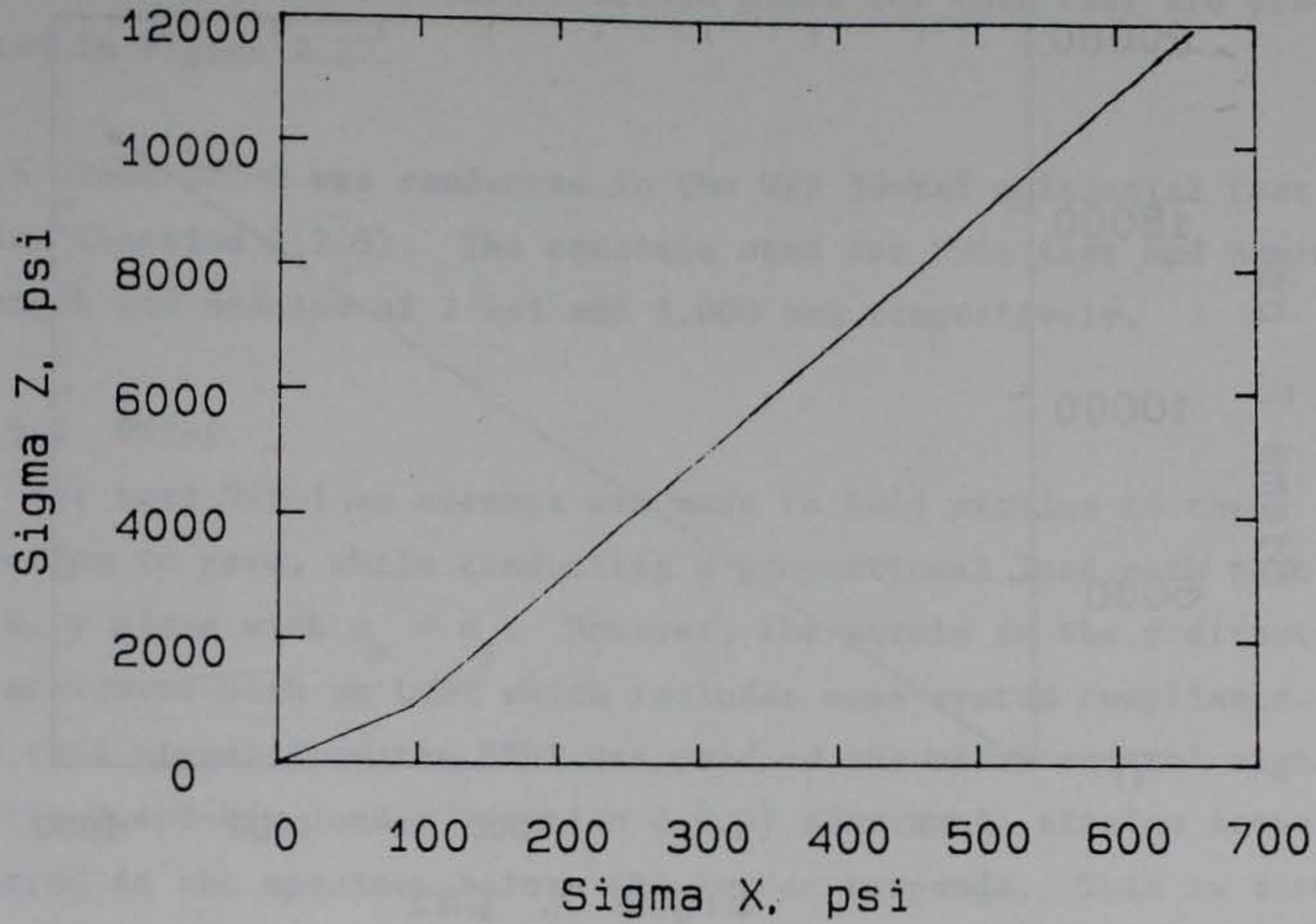
(a) stress path



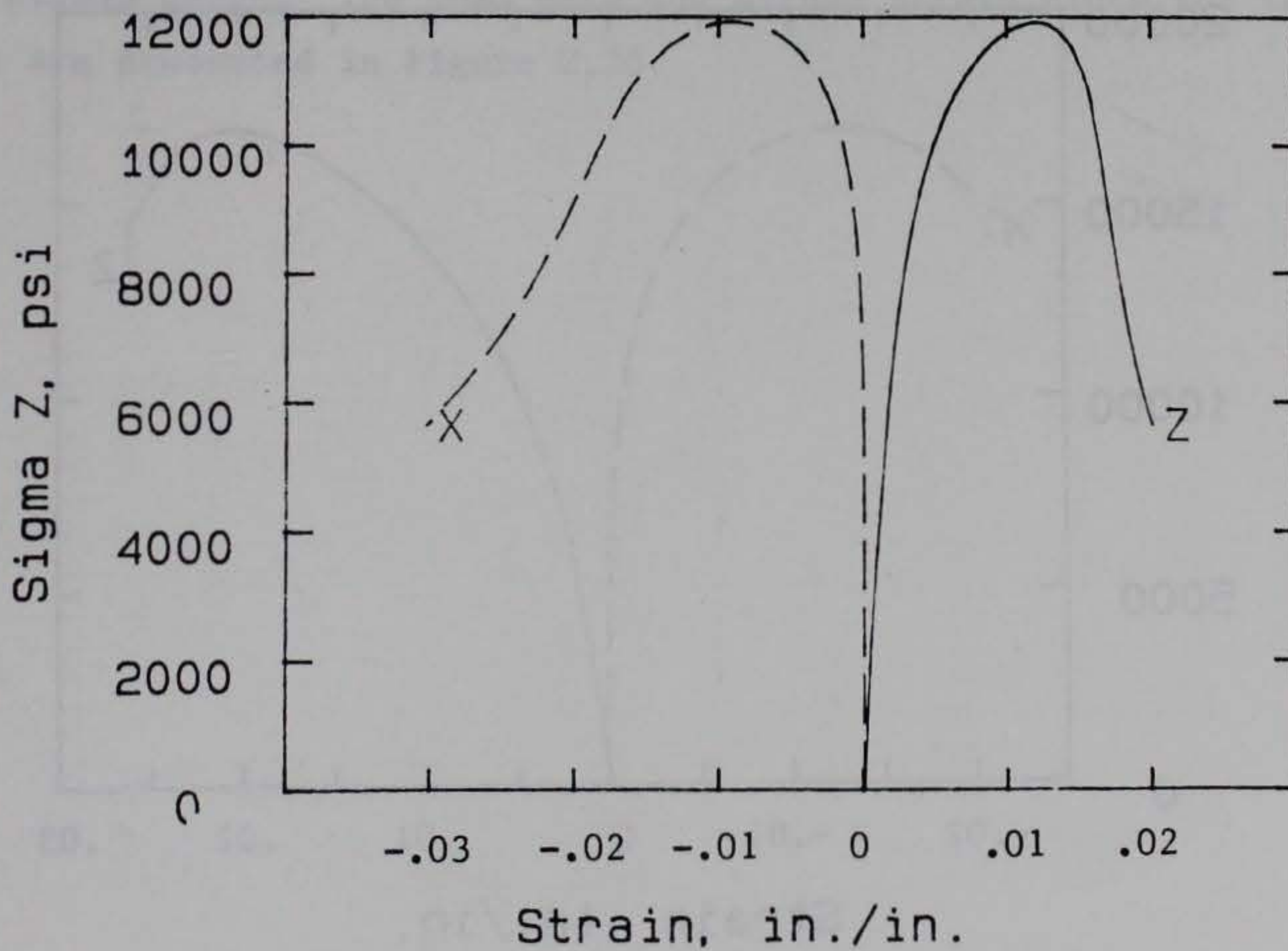
(b) Axial stress versus axial and lateral strains

Figure 2.24 UCB test, VT4-3, hydrostatic deviatoric load path with stress strain response





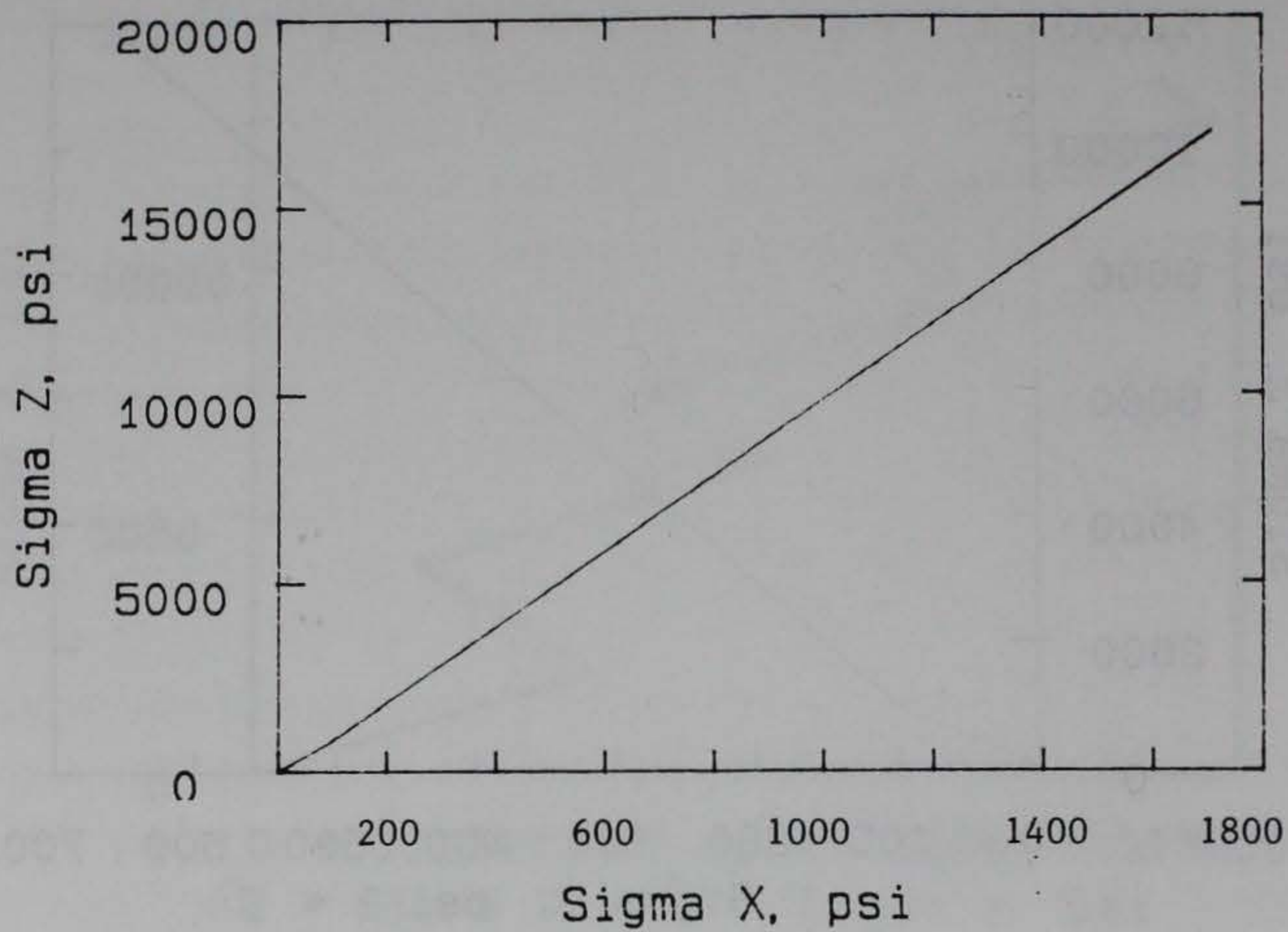
(a) stress path



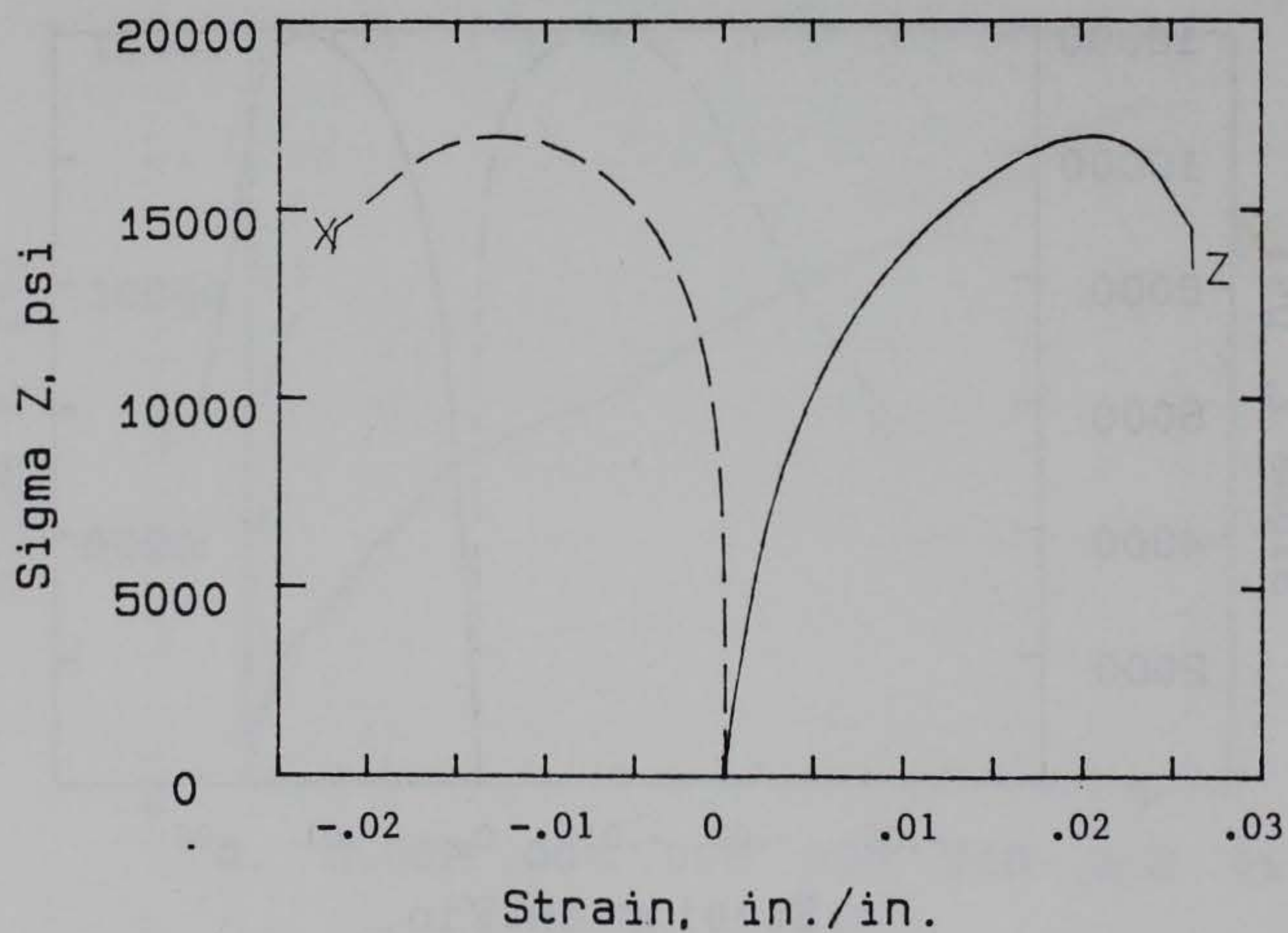
(b) stress in z direction versus strains in z and x directions

Figure 2.25 UEN test, VT5-1, plane strain in x, z plane  
proportional load path, with stress strain response





(a) stress path



(b) stress in z direction versus strains in z and x directions

Figure 2.26. UEN test, VT5-2, plane strain in x, z plane proportional load path, with stress strain response.



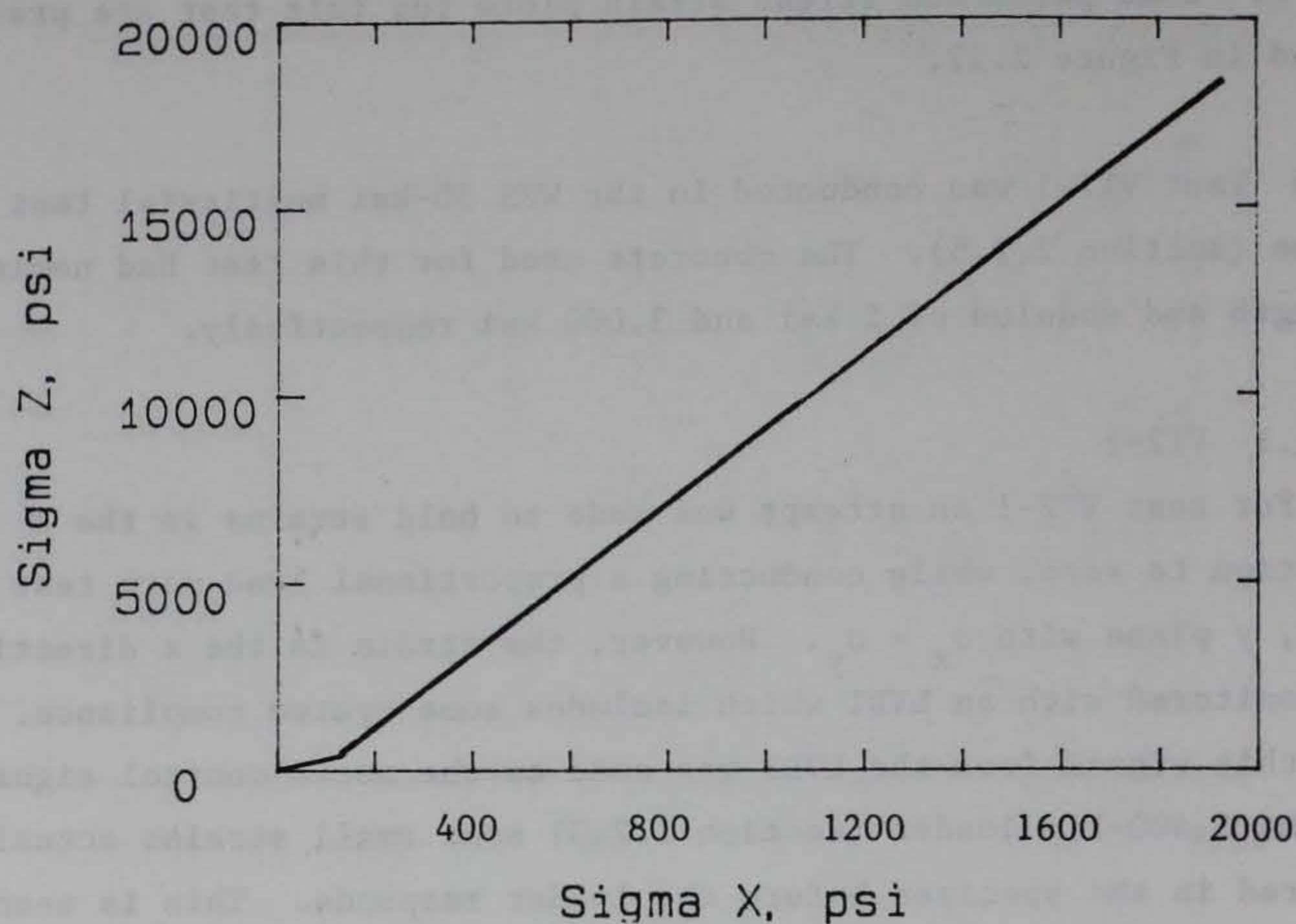
$\epsilon_y = 0$ . Load paths and stress strain plots for this test are presented in Figure 2.27.

2.7.5 Test VT2-1 was conducted in the WES 30-ksi multiaxial test device (section 2.2.5). The concrete used for this test had nominal strength and modulus of 2 ksi and 3,000 ksi respectively.

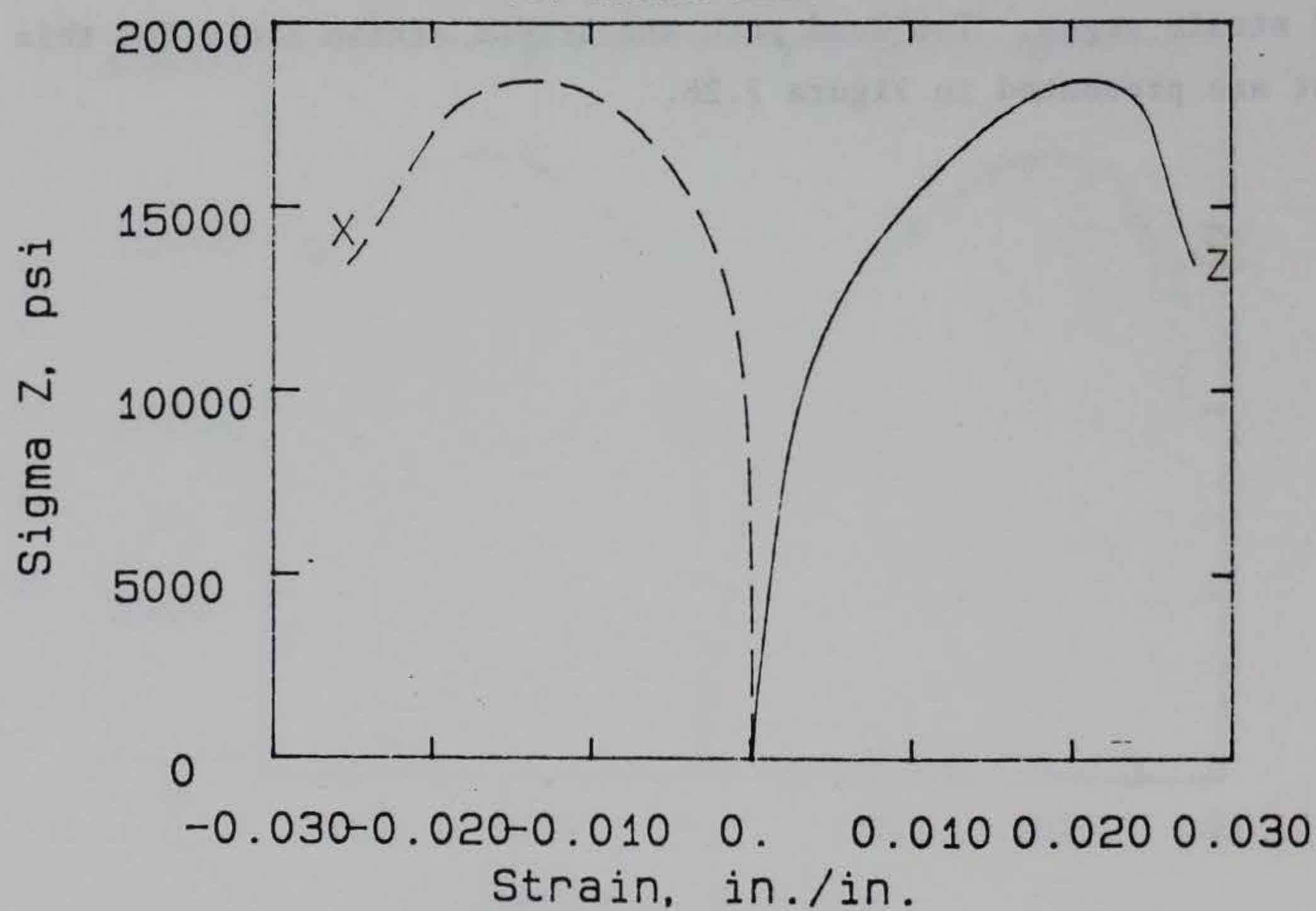
#### 2.7.5.1 VT2-1

For test VT2-1 an attempt was made to hold strains in the  $z$  direction to zero, while conducting a proportional load path test in the  $x, y$  plane with  $\sigma_x = \sigma_y$ . However, the strain in the  $z$  direction was monitored with an LVDT which includes some system compliance. When this signal from the LVDT was used as the servo control signal for the 2,400-kip loader (section 2.2.3) some small strains actually occurred in the specimen before the loader responds. This is seen in Figure 2.28 which presents plots of strain as measured by the embedded strain gages. The load path and stress strain plots for this test are presented in Figure 2.28.





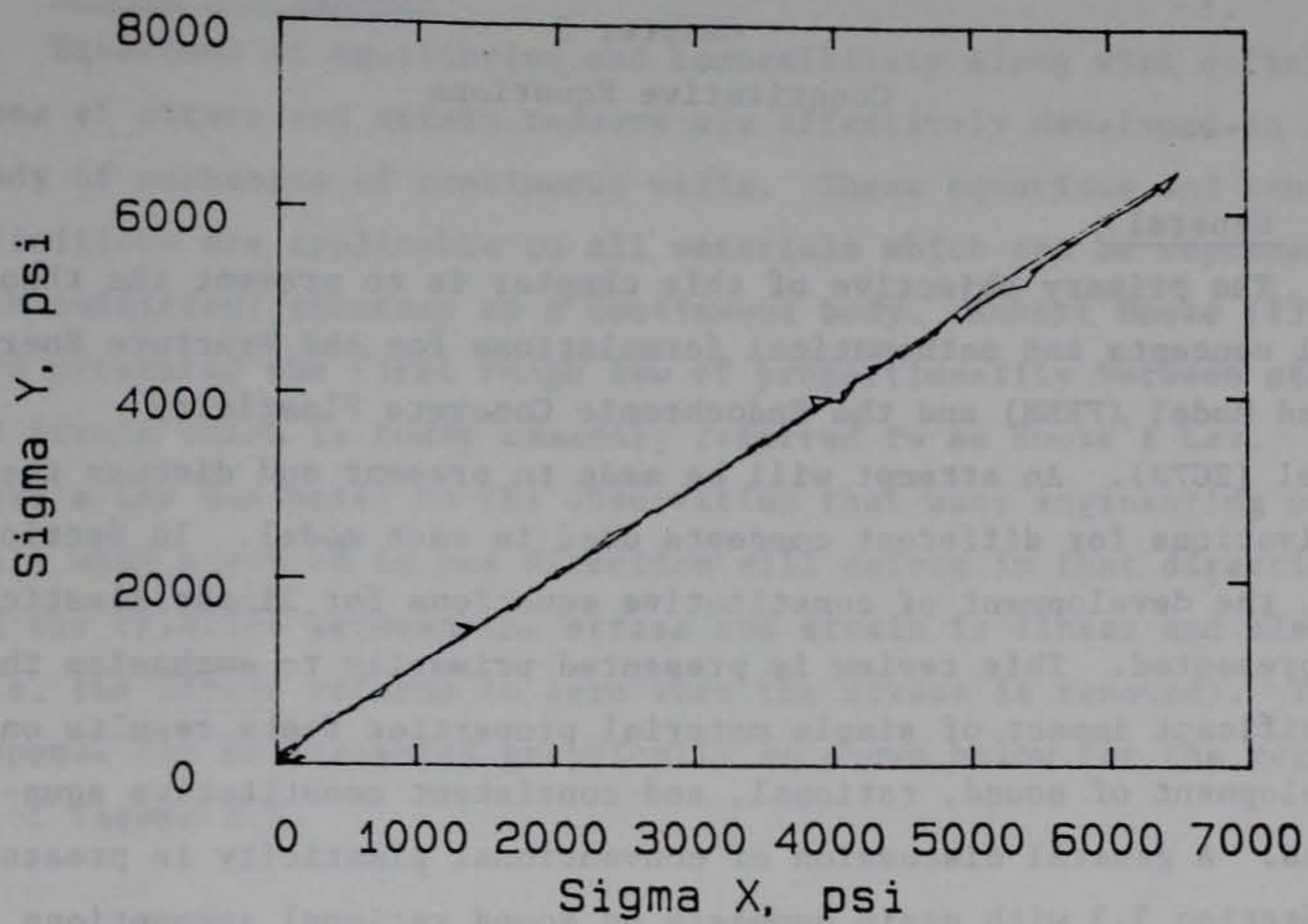
(a) stress path



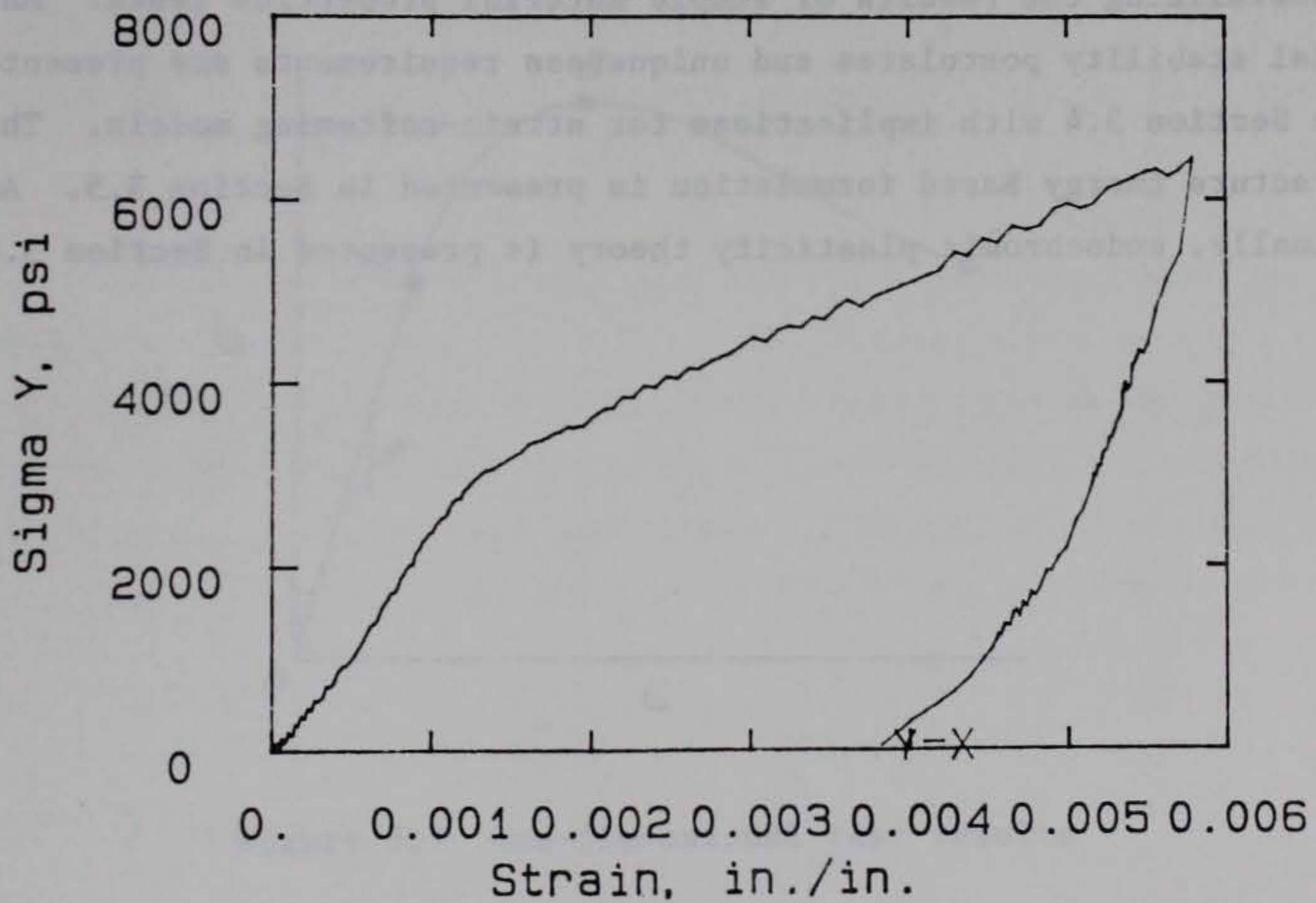
(b) stress in z direction versus strains in z and x directions

Figure 2.27 UEN test, VT5-3, plane strain in x, z plane proportional load path, with stress strain response





(a) stress path



(b) stress in y direction versus strain in y = strain in x direction

Figure 2.28 WES test, VT2-1, plane strain test in the x, y plane proportional load path, with stress strain response



## Chapter 3

### Constitutive Equations

#### 3.1 General.

The primary objective of this chapter is to present the theoretical concepts and mathematical formulations for the Fracture Energy Based Model (FEBM) and the Endochronic Concrete Plasticity Model (ECPM). An attempt will be made to present and discuss the motivations for different concepts used in each model. In Section 3.2, the development of constitutive equations for linear elasticity is presented. This review is presented primarily to emphasize the significant impact of simple material properties tests results on the development of sound, rational, and consistent constitutive equations. A general discussion of conventional plasticity is presented in Section 3.3 with again emphasis on sound rational assumptions in generalizing the results of simple material properties tests. Material stability postulates and uniqueness requirements are presented in Section 3.4 with implications for strain-softening models. The Fracture Energy Based formulation is presented in Section 3.5. And finally, endochronic plasticity theory is presented in Section 3.6



### 3.2 Linear Elasticity.

Equations of equilibrium and compatibility along with definitions of stress and strain tensors are effectively developed in the study of mechanics of continuous media. These equations and tensor definitions are applicable to all materials which can be represented with sufficient accuracy as a continuous body. Robert Hooke [13] in 1676 presented the first rough law of proportionality between stress and strain which is today commonly referred to as Hooke's Law.

Hooke's Law was based on the observation that many engineering materials when stressed in one direction will deform in that direction and the relation between the stress and strain is linear and elastic (i.e. the strain returns to zero when the stress is removed). This response can be presented graphically as shown below for the region OA of Figure 3.1.

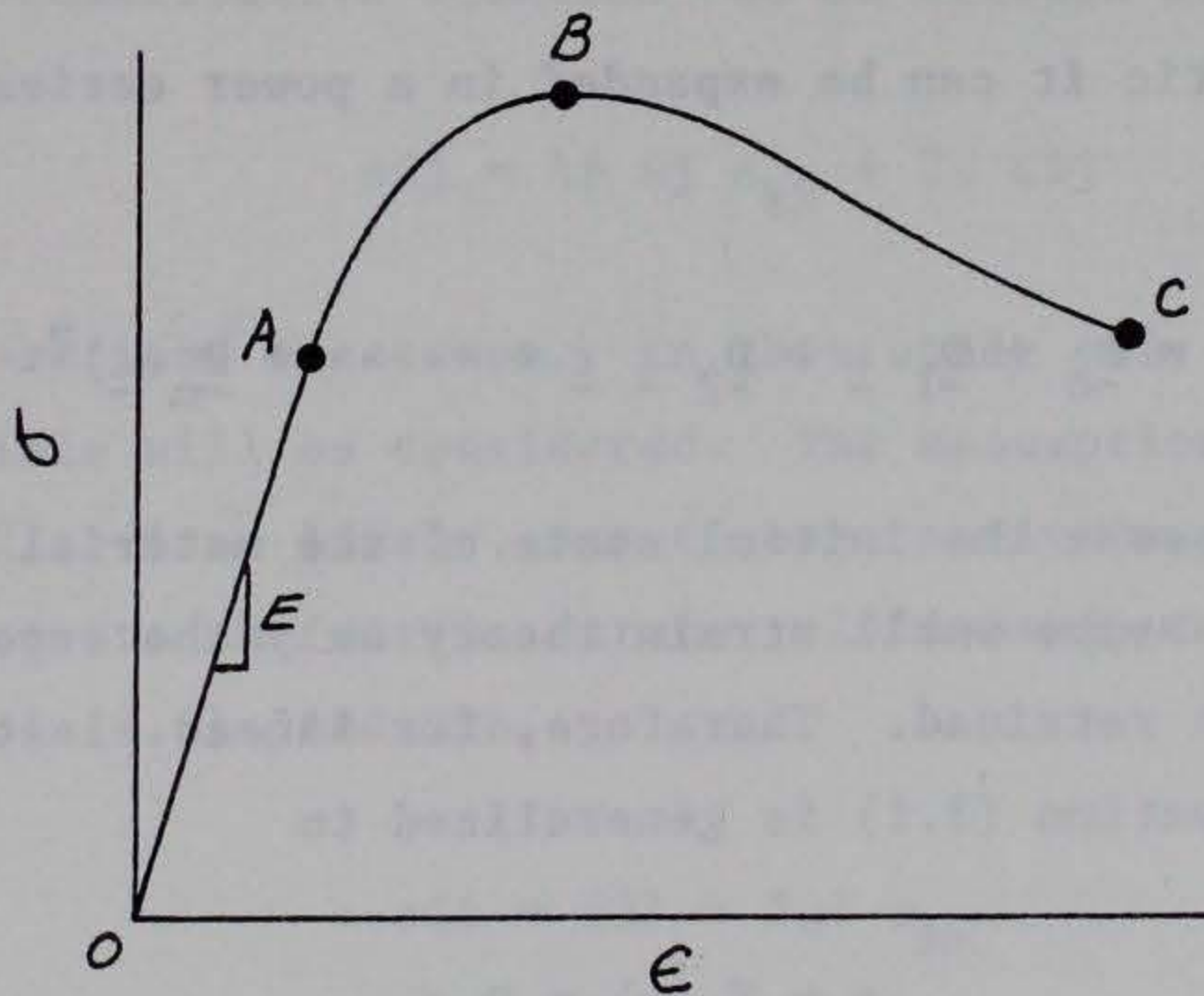


Figure 3.1 One-dimensional test results

This curve is typical for many materials subjected to a homogeneous stress state in one dimension. Mathematically the linear



relationship between stress and strain in the region OA can be written

$$\sigma = E \epsilon \quad 3.1$$

Where  $\sigma$  is axial stress,  $\epsilon$  the corresponding axial strain,  $E$  is Young's modulus, and the point A is referred to as the proportional limit of the material. The region ABC in the figure will be discussed in later sections. Since the state of stress and strain is completely determined by the stress tensor  $\underline{\sigma}$  and strain tensor  $\underline{\epsilon}$  and since the one dimensional relationship between stress and strain is linear and elastic up to the proportional limit, a natural generalization of Hooke's Law is obtained by assuming a one to one analytic relationship between  $\underline{\sigma}$  and  $\underline{\epsilon}$ ,

$$\underline{\sigma} = \underline{F}(\underline{\epsilon}) \quad 3.2$$

Since  $\underline{F}$  is analytic it can be expanded in a power series in terms of  $\underline{\epsilon}$  as

$$\underline{F} = \underline{D}_0 + \underline{D}_1 \underline{\epsilon} + \underline{D}_2 \underline{\epsilon} \underline{\epsilon} + \dots + \underline{D}_n (\underline{\epsilon})^n \quad 3.3$$

Further, if we assume the initial state of the material is stress and strain free and assume small strain theory only the second term in (3.3) needs to be retained. Therefore, for linear elastic small strain theory equation (3.1) is generalized to

$$\underline{\sigma} = \underline{F}(\underline{\epsilon}) = \underline{D} \underline{\epsilon} \quad 3.4$$

in index notation this is expressed as

$$\sigma_{ij} = D_{ijkl} \epsilon_{kl} \quad (i, j, k, l = 1, 2, 3) \quad 3.5$$



It was Cauchy who first made this generalization of Hooke's Law. If the material is homogeneous the coefficients  $D_{ijkl}$  will be independent of the location of the point and it is easily shown that

$$D_{ijkl} = D_{jikl}$$

and

$$D_{ijkl} = D_{ijlk}$$

due to the symmetry of  $\sigma_{ij}$  and the symmetric and skew symmetric decomposition of  $D_{ijkl}$  (See Sokolnikoff [14]). This reduces the number of independent constants in  $D_{ijkl}$  to 36. The existence of the strain energy density function, which is based on thermodynamic arguments, reduces the number of independent constants to 21 for the most general case of an anisotropic elastic material. If the elastic properties of the material are equal in all directions it is said to be isotropic and the number of independent elastic constants reduces to 2 and the constitutive equation can be written as

$$\sigma_{ij} = \lambda \delta_{ij} \epsilon_{kk} + 2\mu \epsilon_{ij} \quad 3.6$$

where  $\lambda, \mu$  are Lamé constants. In this study only assumed isotropic materials will be considered. The assumptions made for  $\underline{F}$  in equation (3.2), (i.e. linear, one to one, analytic, and power series expansion) require the stress strain relationship to be reversible. Contraction of (3.6) leads to

$$\sigma_{ii} = (3\lambda + 2\mu) \epsilon_{kk}$$

which when substituted in (3.6) leads to

$$\epsilon_{ij} = \frac{1}{2\mu} \sigma_{ij} - \frac{\lambda \delta_{ij}}{2\mu} \frac{\sigma_{kk}}{(3\lambda + 2\mu)} \quad 3.7$$



The Lamé constants in Equations (3.6) and (3.7) can be determined from simple test results as follows:

1. Simple tension (or compression): all stresses except  $\sigma_{11}$  are zero, from (3.7)

$$\epsilon_{11} = \frac{1}{2\mu} \sigma_{11} - \frac{\lambda}{2\mu} \frac{\sigma_{11}}{(3\lambda + 2\mu)}$$

$$\epsilon_{11} = \frac{(\lambda + \mu)}{\mu(3\lambda + 2\mu)} \sigma_{11} \quad 3.8$$

and

$$\epsilon_{22} = \epsilon_{33} = - \frac{\lambda}{2\mu(3\lambda + 2\mu)} \sigma_{11}$$

recalling from Hooke's law the ratio of stress to strain is defined as Young's modulus. The coefficient of  $\sigma_{11}$  in (3.8) can be set equal to  $1/E$  such that

$$E = \frac{\mu(3\lambda + 2\mu)}{(\lambda + \mu)} .$$

Poisson's ratio is defined as  $\nu = \frac{\epsilon_{22}}{\epsilon_{11}} = \frac{\epsilon_{33}}{\epsilon_{11}}$

$$\nu = \frac{\lambda}{2(\lambda + \mu)}$$

The Lamé constants are often expressed in terms of  $E$  and  $\nu$  as

$$\lambda = \frac{E\nu}{(1 + \nu)(1 - 2\nu)}$$

$$\mu = \frac{E}{2(1 + \nu)} .$$



2. Pure hydrostatic compression:  $\sigma_{11} = \sigma_{22} = \sigma_{33} = \frac{\sigma_{kk}}{3} = \sigma_m$  with all other  $\sigma_{ij} = 0$ . From this test the bulk modulus (K) can be determined as mean stress per unit volume change

$$\sigma_m = K \epsilon_{kk}$$

$$K = \lambda + \frac{2}{3} \mu .$$

3. Pure shear,  $\sigma_{12} = \sigma_{21}$ , with all other  $\sigma_{ij} = 0$ . From this test the shear modulus (G) can be determined as shear stress per unit change in shear strain.

$$\sigma_{12} = G \gamma_{12}$$

$$G = \mu$$

4. Uniaxial strain,  $\sigma_{11}$  is continuously increased while holding the lateral strains at 0, i.e.  $\epsilon_{22} = \epsilon_{33} = 0$ . From this test the constrained modulus (M) is determined as the ratio of  $\sigma_{11}$  to  $\epsilon_{11}$

$$\sigma_{11} = M \epsilon_{11}$$

$$M = (\lambda + 2\mu) .$$

Quite often in the development and evaluation of constitutive models it is useful to consider the shear (deviatoric) components of the stress and strain tensors independent from the hydrostatic (volumetric) components. For an isotropic linear elastic material this can be done by defining the deviatoric stress tensor  $S_{ij}$  and deviatoric strain tensor  $e_{ij}$ , as



$$S_{ij} = \sigma_{ij} - \delta_{ij} \sigma_m$$

and

$$e_{ij} = \epsilon_{ij} - \delta_{ij} \epsilon_m$$

where  $\epsilon_m = \epsilon_{kk}/3$ .

As previously shown contraction of (3.6) leads to

$$3\sigma_m = (3\lambda + 2G) \epsilon_{kk}$$

$$= 3K \epsilon_{kk}$$

$$\sigma_m = K \epsilon_{kk} \quad 3.9(a)$$

which is the hydrostatic or volumetric component of (3.6). By substituting equation (3.6) into the deviatoric stress expression along with the above equation for  $\sigma_m$  the deviatoric or shear component of the constitutive equation can be expressed as

$$S_{ij} = 2G e_{ij} \quad 3.9(b)$$

Either equations 3.6 or 3.9 can be used to solve constitutive problems for linear elastic isotropic materials. Given the strain tensor the stress tensor is uniquely defined or conversely given the stresses the strains are uniquely defined. Also, for finite element applications, the same solutions can be obtained in rate or incremental form as

$$\dot{\underline{\underline{\sigma}}} = \underline{\underline{D}} \dot{\underline{\underline{\epsilon}}}$$

or

$$\dot{\underline{\underline{\epsilon}}} = \underline{\underline{D}}^{-1} \dot{\underline{\underline{\sigma}}}$$



The discussion presented in this section and derivations of equations can be found in many texts on elasticity such as Sokolnikoff [14], Chen and Saleeb [15], etc. The main reason the derivation is presented here, is to point out that in developing the governing three-dimensional constitutive equations of elasticity, a simple one dimensional test was evaluated (Hooke's Law), the mathematical description of the test was generalized based on sound mathematical assumptions, and the number of independent material constants required was determined based on arguments of thermodynamics and material symmetry. Also, four material properties tests were described which provide results that can be used to determine key response features of the material. It is not unreasonable to expect that more tests will need to be defined and conducted to determine key response features of materials in nonlinear and plastic regions.

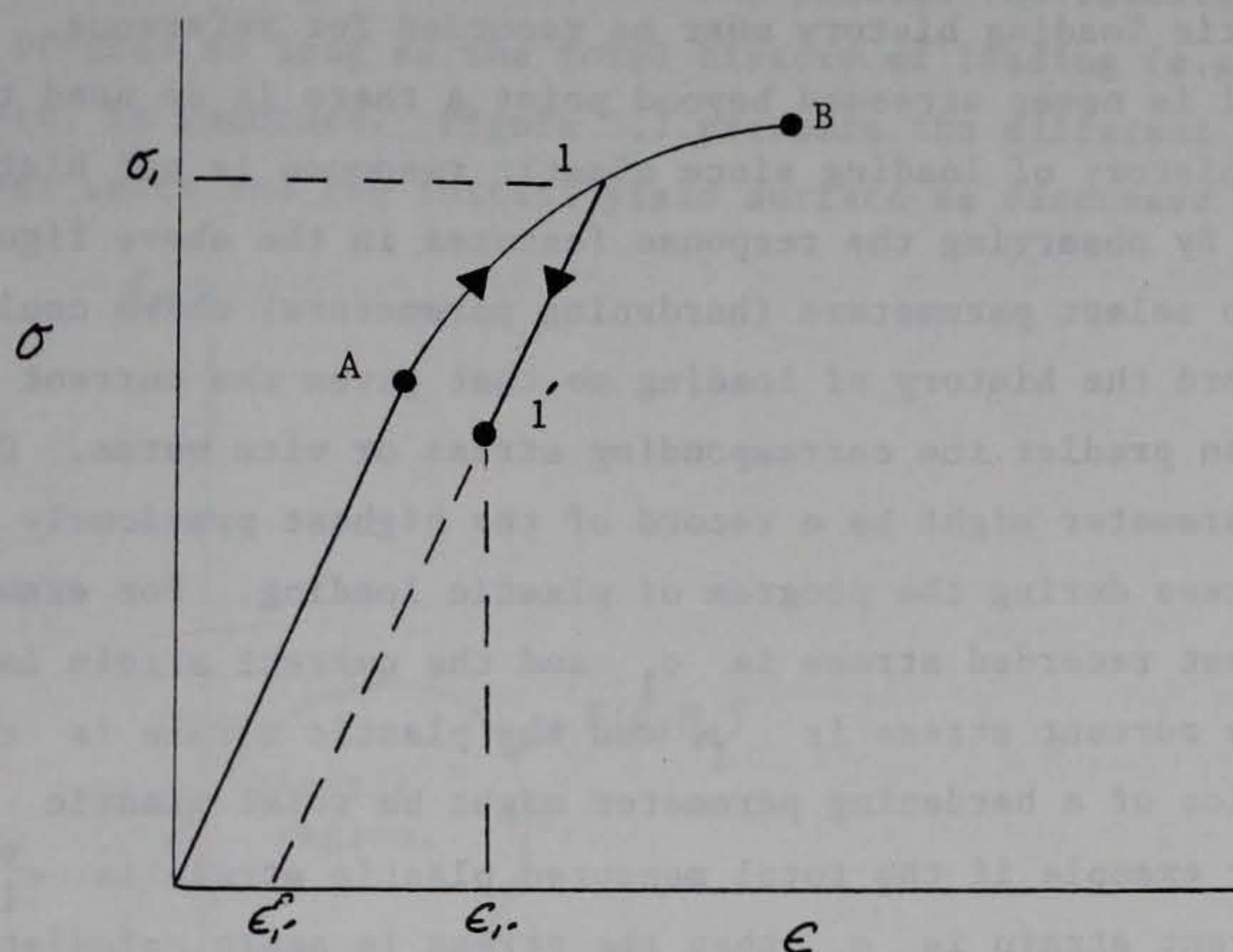


### 3.3 Conventional Plasticity

In the previous section a brief review of the derivation of linear elastic constitutive equations was presented for materials which can be reasonably approximated as homogeneous and isotropic. This derivation was based on the results of a simple one dimensional material properties test, sound mathematical assumptions, and rational application of material symmetry restrictions. In this section a derivation of the equations of conventional plasticity will be presented. In general the same approach will be used here as was used for the linear elastic case in terms of generalizing the results of a simple test based on rational and, consistent assumptions of mathematics and mechanics. However, as is well known, the derivation is not quite so simple and direct as for the linear elastic case, due in part to the need to postulate a specific yield surface, define a direction for plastic strain, and determine loading and unloading criteria.

The development of equations in this section essentially follows that presented in Martin [16] and it is assumed that the reader is generally familiar with plasticity theory. Only material nonlinearity is considered so that strains and rotations are small. Furthermore, emphasis is placed on rate independent hardening plasticity where there is no flow (i.e. increasing strain at constant stress). Returning to the simple one dimensional test shown in Figure 3.1, when a program of loading causes the stress to reach point A (yield point or proportional limit) initial yielding of the material occurs. Up to this point (A) if the loading program causes the stress to decrease, unloading will occur along the original linear elastic path at constant modulus  $E$  and no plastic strains are accumulated. If on the other hand the loading program continues to cause the stress (or strain) to increase, hardening occurs, and plastic (irrecoverable) strains begin to accumulate. The definition of plastic loading is taken here to mean that plastic strains increase during plastic loading. If in the hardening region (AB in Figure 3.1) the loading





Loading-unloading response of a hardening material

program begins to cause the stress (strain) to decrease, unloading occurs along a linear elastic path with modulus  $E$  as shown in the figure above. The material represented by the figure above is referred to as a hardening material because when unloading occurs (say at point 1) followed by reloading a linear elastic response is observed back up to point 1 where the stress  $\sigma_1$  is greater than  $\sigma_A$ , the initial yield stress. Therefore we might say that the plastic loading program from A to 1 hardened (or pushed up) the yield point of the material from  $\sigma_A$  to  $\sigma_1$ . An important feature of the stress strain response presented is that once the material is stressed beyond point A, a knowledge of the loading history is required in order to predict the stress corresponding to a particular



strain, or to predict the strain corresponding to a particular stress. The material is said to be history dependent and a portion of its plastic loading history must be recorded for reference. If the material is never stressed beyond point A there is no need to record the history of loading since elastic response is not history dependent. By observing the response features in the above figure we might try to select parameters (hardening parameters) which could be used to record the history of loading so that given the current strain we can predict the corresponding stress or vice versa. One hardening parameter might be a record of the highest previously attained stress during the program of plastic loading. For example if the highest recorded stress is  $\sigma_1$  and the current strain is  $\epsilon_A$  then the current stress is  $\sigma_1$ , and the plastic strain is  $\epsilon_1^P$ . Another choice of a hardening parameter might be total plastic strain. For example if the total measured plastic strain is  $\epsilon_1^P$  and the current strain is  $\epsilon_A$  then the stress is again calculated as  $\sigma_1$ .

The concept of yield point (i.e. proportional limit) in the one-dimensional test can be generalized directly to a yield hyper-surface in stress space. The region bounded by this surface is the elastic region and when the stress path, corresponding to a loading program, lies inside this region there is no accumulation of plastic strain. The hardening concept is generalized by making the yield surface a function of stress  $\sigma$  and parameters  $H_\alpha$  ( $\alpha = 1, 2, \dots, n$ ) which represent a portion of the loading history (recorded history) contributing to the position of the yield surface and plastic strain. The initial yield surface is therefore defined as:

$$F = F(\sigma, H_\alpha)$$

Recalling the one-dimensional test, the recorded history parameters could be components of plastic strain, measures of work, or some



internal variables, because one could derive a simple mathematical model for this test and successfully predict the results of any loading program as long as the total history of loading (e.g. plastic strain) is recorded. Figure 3.2 presents the different regions of stress space and the initial yield surface as discussed above.

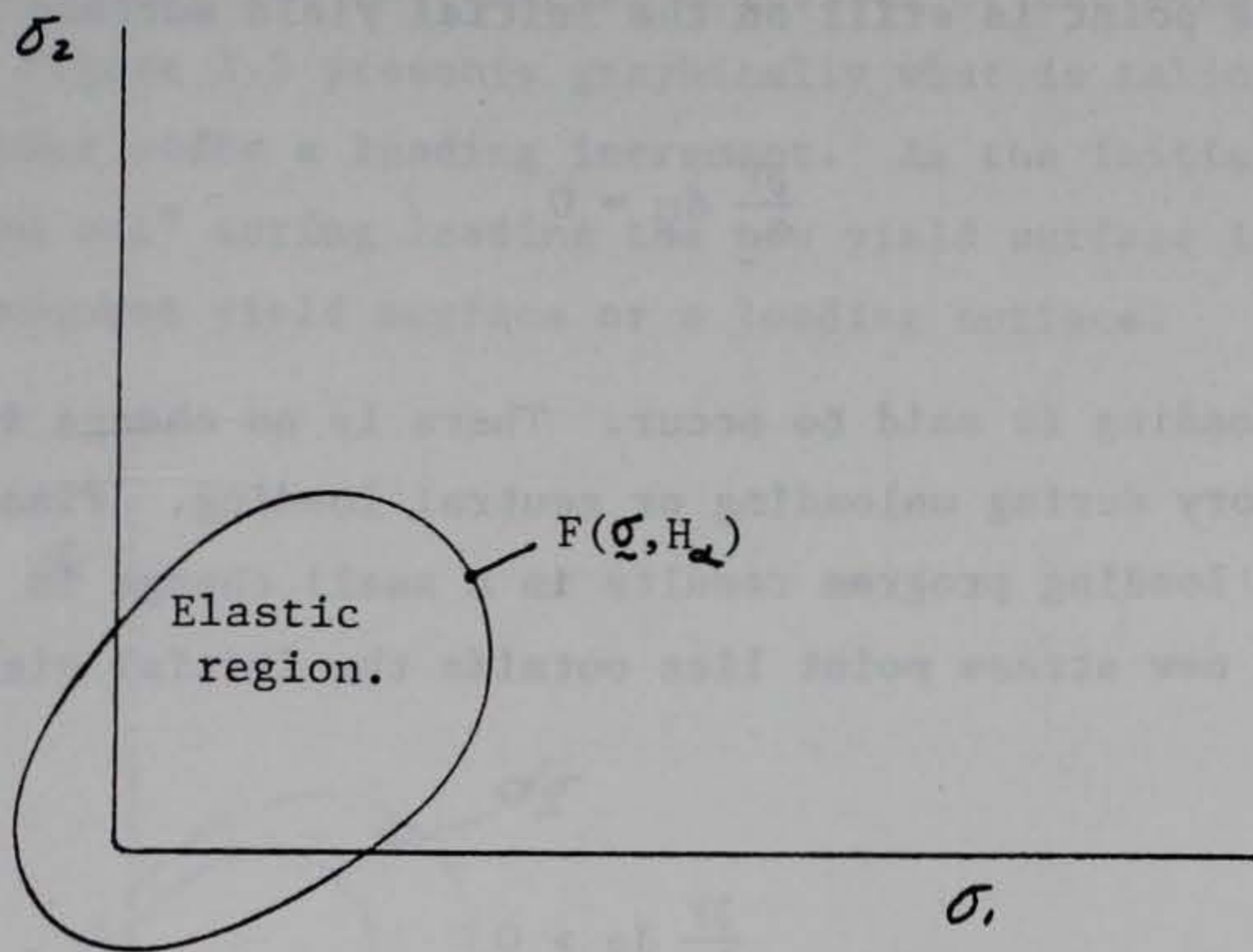


Figure 3.2 Yield surface and elastic region in stress space

It is clear that for points inside the yield surface  $F < 0$ , while for points on the yield surface  $F = 0$ , and for points outside the yield surface  $F > 0$ . Due to the incremental nature of plasticity we are interested in small changes in stress and strain. If a program of loading has resulted in the stress point being on the initial yield surface then

$$F(\sigma, H_\alpha) \Big|_{H_\alpha} = 0$$

If the loading program continues and results in a small change in stress  $d\sigma$  such that the new stress point falls inside the initial yield surface then



$$dF \Big|_{H_\alpha} = \frac{\partial F}{\partial \underline{\sigma}} d\underline{\sigma} < 0$$

and unloading is said to occur. If on the other hand the loading program continues and results in a change in stress  $d\underline{\sigma}$  such that the new stress point is still on the initial yield surface then

$$\frac{\partial F}{\partial \underline{\sigma}} d\underline{\sigma} = 0$$

and neutral loading is said to occur. There is no change in the recorded history during unloading or neutral loading. Finally, if the continued loading program results in a small change in stress  $d\underline{\sigma}$  such that the new stress point lies outside the initial yield surface then

$$\frac{\partial F}{\partial \underline{\sigma}} d\underline{\sigma} > 0$$

and loading is said to occur. It is important to note that we have defined criteria for unloading, neutral loading, and loading based on gradients of the yield surface while  $H_\alpha$  remains constant. Also, we observe that stress states outside the yield surface cannot be obtained unless there is a change in the recorded history  $H_\alpha$ . Therefore when loading occurs,  $H_\alpha$  must change and we could write the following

$$F(\underline{\sigma}, H_\alpha) = 0 \quad 3.10$$

and

$$F(\underline{\sigma} + d\underline{\sigma}, H_\alpha + dH_\alpha) = 0$$

Equations (3.10) imply

$$dF = \frac{\partial F}{\partial \underline{\sigma}} d\underline{\sigma} + \frac{\partial F}{\partial H_\alpha} dH_\alpha = 0 \quad 3.11$$



Equation (3.11) is often referred to as the consistency condition, and as will be shown later provides for a smooth transition between loading and unloading conditions. Equations 3.10 and 3.11 play a very important role in the development of plastic constitutive equations. Note these equations are differential in form and this must be kept in mind when incremental solutions of the equations are sought. Figure 3.3 presents graphically what is taking place in stress space under a loading increment. As the initial yield surface is "pushed out" during loading the new yield surface is referred to as a subsequent yield surface or a loading surface.

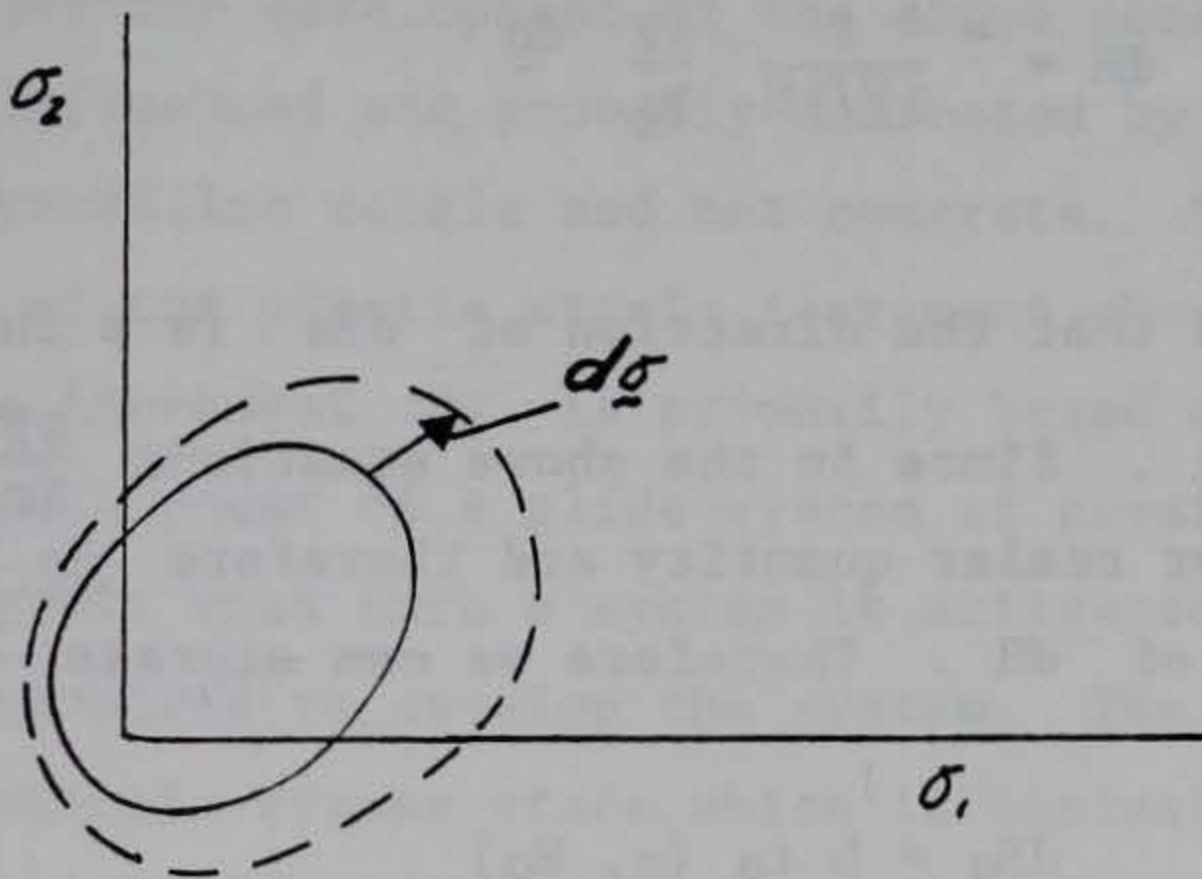


Figure 3.3 Subsequent yield or loading surfaces

In order to complete the development of a general plasticity theory we must determine the functional relationship between the increment of plastic strain and stress, hardening parameters, and increments of stress. Since we require that plastic strains do not increase unless the recorded history increases, it is reasonable to assume that changes in the recorded history  $dH_\alpha$  are the result of a stress increment  $d\sigma$  and can depend on the current stress  $\sigma$  and recorded history  $H_\alpha$ . Therefore, we can write (in index notation)

$$d\epsilon_i^P = h_{i\alpha} (d\sigma, H_\alpha) dH_\alpha \quad 3.12$$



This general representation satisfies the requirement that plastic strains do not accumulate unless the recorded history changes. Also since we are concerned here with hardening behavior only (i.e. no flow) no terms can appear in (3.12) which are independent of  $d\sigma$  and furthermore since we consider infinitesimal  $d\sigma$ , terms of second and higher order in  $d\sigma$  can be neglected. Therefore we can assume that  $d\epsilon_i^p$  is homogeneous and degree one in components of  $d\sigma$ . Recalling the one dimensional test, it is reasonable to assume that  $d\sigma$  controls the magnitude of  $dH_\alpha$ , which can be argued by considering equation (3.11) with only 1 recorded history parameter.

$$dH = - \frac{1}{\partial F / \partial H} \frac{\partial F}{\partial \sigma} d\sigma$$

Also it can be assumed that the direction of  $dH_\alpha$  is a function of  $\sigma$ ,  $H_\alpha$ , and not  $d\sigma$ . Since in the above equations  $\frac{\partial F}{\partial \sigma} d\sigma$  is in effect a dot product or scalar quantity and therefore  $d\sigma$  contributes only to the magnitude of  $dH$ . Therefore we can express  $dH_\alpha$  as

$$dH_\alpha = b \, t_\alpha(\sigma, H_\alpha) \quad 3.13$$

where  $b$  can be evaluated by substituting (3.13) into the consistency condition. When this result is substituted back in (3.12) we have

$$d\epsilon_i^p = - \frac{h_{i\alpha} \, t_\alpha}{t_\beta \frac{\partial F}{\partial H_\beta}} \frac{\partial F}{\partial \sigma_k} d\sigma_k \quad 3.14$$

Since we have assumed  $h_{i\alpha}$ ,  $t_\alpha$  and  $\partial F / \partial H_\alpha$  each depend only on the state variables  $\sigma$ ,  $H_\alpha$  equation (3.14) can be written

$$d\epsilon_i^p = f_i(\sigma, H_\alpha) \frac{\partial F}{\partial \sigma_k} d\sigma_k$$



since  $f_i(\underline{\sigma}, H\alpha)$  is a vector valued function of  $\underline{\sigma}$ ,  $H\alpha$  we can express this vector as

$$f_i(\underline{\sigma}, H\alpha) = G(\underline{\sigma}, H\alpha) \frac{\partial g(\underline{\sigma}, H\alpha)}{\partial \sigma_i} \quad 3.15$$

here  $G(\underline{\sigma}, H\alpha)$  can be considered a scalar hardening coefficient and  $g(\underline{\sigma}, H\alpha)$  can be considered the plastic potential function.

In summary we have generalized the one-dimensional constitutive equation to predict the hardening plasticity behavior of suitable materials loaded in three dimensions. At this point it is important to note that the development of the above constitutive equations was strongly influenced and probably dominated by observations from tests on polycrystalline metals and not concrete. The assumption that the direction of the plastic strain increment should be independent of the stress increment  $d\underline{\sigma}$  is primarily based on conditions required for the development of a glide-system of crystal grains. Plastic strains result when such a system is activated, and a certain stress state is required to develop the system. The required stress state is a macroscopic stress state which is equivalent to some statistical average of individual grain shears along critical slip directions. Once the stress state for the glide system is developed, along with a preferred direction for plastic strain, the stress increment  $d\underline{\sigma}$  only contributes to the magnitude of the plastic strain. Based on the above arguments and the observations that very little plastic volume change is observed during plastic loading the plastic strain increment direction is assumed independent of  $d\underline{\sigma}$  and the plastic potential is assumed independent of hydrostatic stress. The assumption of no plastic volume strain is not appropriate for concrete and the role of the stress increment in affecting plastic strain direction will be discussed in Chapter 4. Finally, the basic equations are, in incremental form using index notation:



strain decomposition

$$d\epsilon_i = d\epsilon_i^e + d\epsilon_i^p$$

linear elasticity

$$d\epsilon_i^e = C_{ij} \sigma_j$$

where  $C_{ij}$ , is the compliance matrix reduced to the isotropic, linear elastic form with constant coefficients.

yield surface

$$F \leq 0$$

where the inequality sign is used since we are considering all accessible states of stress. Finally, the plastic strain increment  $d\epsilon_i^p$  is determined from the following conditions

$$\begin{array}{llll} d\epsilon_i^p = 0 & \text{for } F(\underline{\sigma}, H\alpha) < 0 & \text{elastic region} \\ & \text{for } F(\underline{\sigma}, H\alpha) = 0 & \text{unloading} \\ d\epsilon_i^p = 0 & \text{and } \frac{\partial F}{\partial \underline{\sigma}} d\underline{\sigma} \leq 0 & \text{or neutral loading} \\ & \text{for } F(\underline{\sigma}, H\alpha) = 0 & \text{loading} \\ d\epsilon_i^p = G \frac{\partial g}{\partial \sigma_i} \frac{\partial F}{\partial \sigma_k} d\sigma_k & \text{and } \frac{\partial F}{\partial \underline{\sigma}} d\underline{\sigma} \geq 0 & \text{or neutral loading} \end{array}$$

The inequalities are included for both unloading and loading conditions due to the consistency condition, which as previously pointed out provides for a smooth transition between the behavior in loading and unloading. Change in recorded history



$$dH_\alpha = - \frac{t_\alpha}{t_\beta \frac{\partial F}{\partial H_\beta}} \frac{\partial F}{\partial \sigma_k} d\sigma_k$$

where  $t_\alpha = t_\alpha(\underline{\sigma}, H_\alpha)$

For the case of plastic flow we must allow change in plastic strains while the stress remains constant. However, this is in conflict with our previous assumption that plastic strains cannot occur as long as the yield surface remains fixed which implies no change in recorded history parameters  $H_\alpha$ . This problem can be resolved by recognizing that  $H_\alpha$  are only part of the total internal parameters which affect plastic strains. These additional internal parameters are defined here as  $J_\beta$  ( $\beta = 1, \dots, m$ ) such that

$$d\varepsilon_j^P = h_{j\alpha} dH_\alpha + \bar{h}_{j\beta} dJ_\beta$$

where  $\bar{h}_{j\beta} = \bar{h}_{j\beta}(\sigma_j, H_\alpha, J_\beta)$

From a computational standpoint flow can be allowed by defining a maximum strength surface which bounds all loading surfaces. When the stress point tries to move outside this surface it is forced back by some return procedure to a new stress point which is still on the surface and the associated plastic strains are calculated.

Quite often the plastic strain increment is written as

$$d\varepsilon^P = \dot{\lambda} \frac{\partial g}{\partial \underline{\sigma}}$$

where  $\dot{\lambda}$  is a scalar hardening parameter defined as

$$\dot{\lambda} = G(\underline{\sigma}, H_\alpha) \frac{\partial F}{\partial \underline{\sigma}} d\underline{\sigma}$$



Recalling the consistency condition (Equation 3.11),

$$dF = \frac{\partial F}{\partial \underline{\sigma}} d\underline{\sigma} + \frac{\partial F}{\partial H} dH = 0$$

here it is assumed that  $H$  is a scalar function of the plastic strain vector  $\underline{\epsilon}^P$ , we can solve for the scalar hardening parameter. Substituting the expressions

$$d\underline{\sigma} = \underline{E} d\underline{\epsilon}^e$$

$$dH = \frac{\partial H}{\partial \underline{\epsilon}^P} d\underline{\epsilon}^P$$

in the consistency condition results in

$$\frac{\partial F}{\partial \underline{\sigma}} \underline{E} (d\underline{\epsilon} - d\underline{\epsilon}^P) + \frac{\partial F}{\partial H} \frac{\partial H}{\partial \underline{\epsilon}^P} d\underline{\epsilon}^P = 0$$

and since

$$d\underline{\epsilon}^P = \dot{\lambda} \frac{\partial g}{\partial \underline{\sigma}}$$

an expression for the scalar hardening parameter can be obtained as

$$\dot{\lambda} = \frac{\frac{\partial F}{\partial \underline{\sigma}} \underline{E} d\underline{\epsilon}}{\frac{\partial F}{\partial H} \frac{\partial H}{\partial \underline{\epsilon}^P} \frac{\partial g}{\partial \underline{\sigma}} - \frac{\partial F}{\partial \underline{\sigma}} \underline{E} \frac{\partial g}{\partial \underline{\sigma}}}$$

Recalling

$$d\underline{\sigma} = \underline{E} d\underline{\epsilon}^e = \underline{E} (d\underline{\epsilon} - d\underline{\epsilon}^P)$$



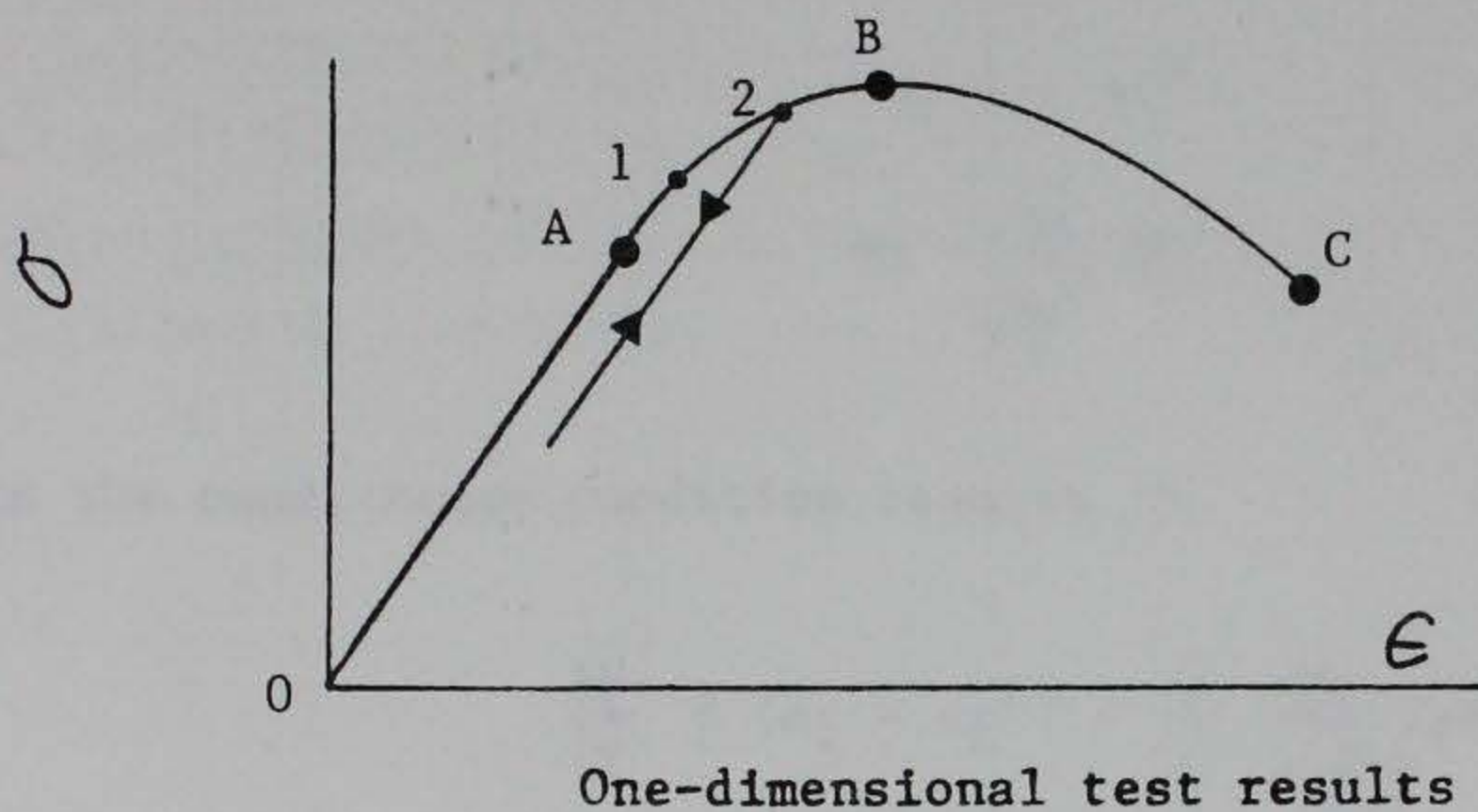
the incremental constitutive equation can be expressed as

$$d_{\underline{g}} = \left[ \begin{array}{c} \underline{E} - \frac{\frac{\partial F}{\partial \underline{g}}}{\frac{\partial F}{\partial H}} \frac{\underline{E}}{\frac{\partial H}{\partial \epsilon^p}} \frac{\frac{\partial g}{\partial \underline{g}}}{\frac{\partial g}{\partial \underline{g}}} - \frac{\frac{\partial F}{\partial \underline{g}}}{\frac{\partial F}{\partial \underline{g}}} \underline{E} \frac{\frac{\partial g}{\partial \underline{g}}}{\frac{\partial g}{\partial \underline{g}}} \end{array} \right] d_{\underline{g}}$$



### 3.4 Material Stability Postulates, Uniqueness.

The stability postulates discussed in this chapter are not presented as thermodynamic or physical requirements of real materials. These postulates are often used as a basis for developing constitutive equations for certain classes of materials. Returning to the one dimensional test as shown below, we observe that a monotonic increase in stress produces a monotonic increase in strain in the region 0 A B.



This can be expressed mathematically as

$$(\sigma^2 - \sigma^1) (\epsilon^2 - \epsilon^1) \geq 0 \quad 3.16$$

and this inequality can be taken as the meaning of work hardening in the one dimensional case. The equal sign is provided to allow for infinite or 0 slope. Equation 3.16 is simply based on the observation that the assumed homogeneous, isotropic material when subjected to a one dimensional monotonic increment of stress responds with a monotonic increment in strain. Inequality (3.16) can be generalized to represent multi-dimensional states of stress and strain in the following way. A monotonic change in a single stress component results in a straight line path in stress space, and we require the product of this change in stress with the associated change in strain to be non-negative, therefore



$$(\sigma_i^2 - \sigma_i^1) \cdot (\epsilon_i^2 - \epsilon_i^1) \geq 0 \quad 3.17$$

Since an infinitesimal stress increment is applied monotonically and results in an infinitesimal strain increment inequality (3.17) can be expressed as

$$d\sigma \, d\epsilon \geq 0 \quad 3.18$$

Another feature of the one dimensional test is that the unloading slope in the region AB is elastic and this slope is greater than the slope in the hardening plastic loading region. This feature can be preserved if it is required that the complementary work around a closed cycle in stress be non-positive, therefore

$$\oint \epsilon \, d\sigma \leq 0 \quad 3.19$$

The equal sign holds for stress cycles in the elastic region. If the stress cycle produces a change in plastic strain  $\Delta\epsilon^P$  which is infinitesimal or small, inequality (3.19) is referred to as the second postulate in the weak form. If no restrictions are placed on the size of  $\Delta\epsilon^P$  inequality (3.19) is referred to as the second postulate in the strong form. Drucker [17] also identifies work hardening for the one dimensional tests with monotonic increments in stress producing monotonic increments in strain. However, in generalizing this feature Drucker considers the work done by an external agency which slowly applies load then slowly removes the load. The external agency is completely independent of the loading program which produces the existing state of stress and strain in the material. Drucker then states that for all sets of added stresses (due to the external agency) work hardening implies that the material will remain in equilibrium and:



1. The external agency does positive work during the application of load

$$d\sigma \, d\varepsilon > 0$$

2. The net work performed by the external agency during a cycle (application and removal of the load) is non-negative.

$$d\sigma \, (d\varepsilon - d\varepsilon^e) = d\sigma \, d\varepsilon^p \geq 0$$

As previously mentioned, these postulates are not intended to be physical or thermodynamic requirements for the behavior of real materials but can be used to develop rational and consistent constitutive relations for broad classes of engineering materials. These stability postulates prohibit the types of stress strain responses shown in Figure 3.4.

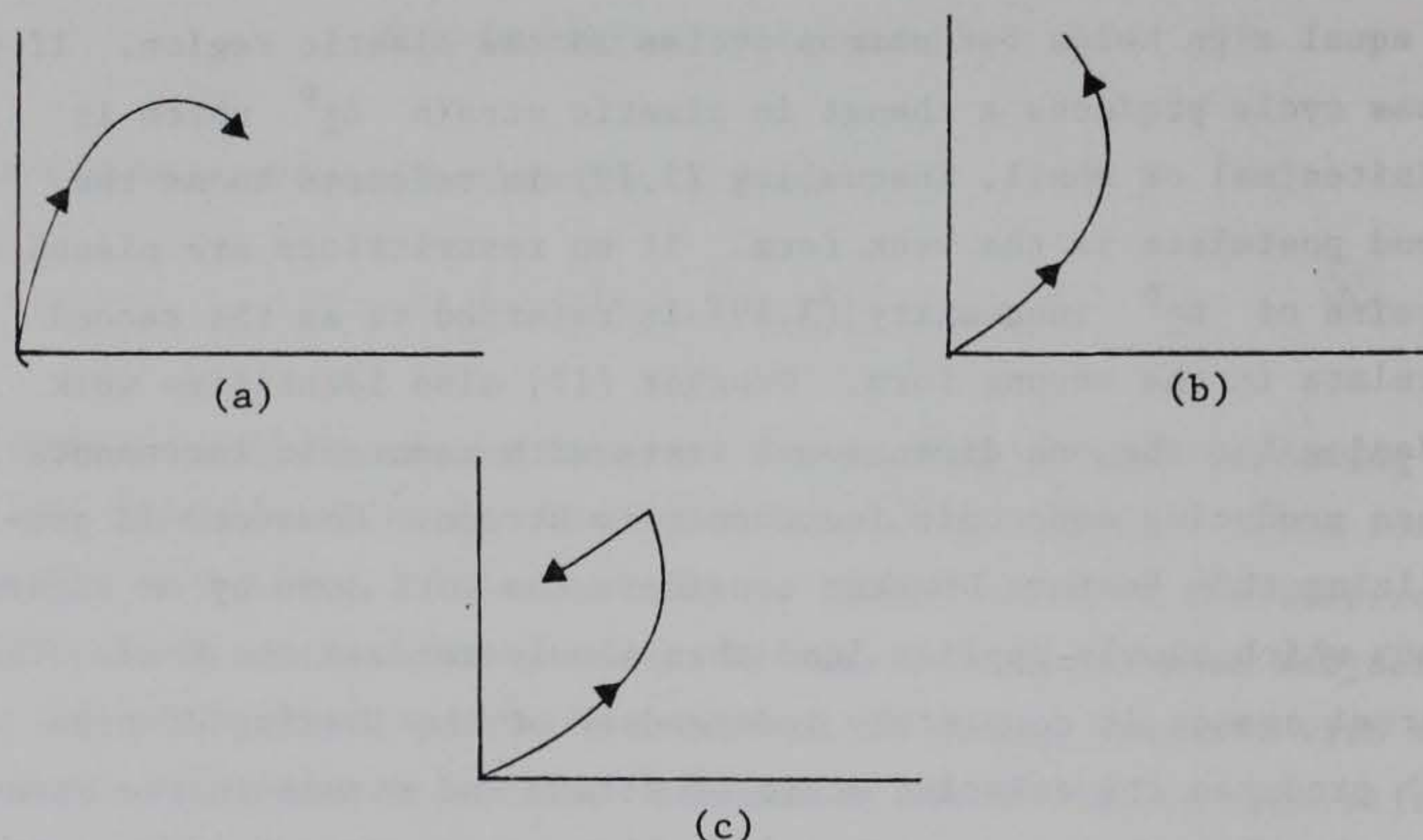


Figure 3.4 Examples of response features which violates stability postulates

Figure 3.4(a) of course is the response feature referred to as strain softening and is often observed as shown previously in unconfined and



low confinement compression tests on concrete and other materials. It was reasoned by Bažant [10] that strain softening can only be observed on material test specimen with micro-inhomogeneities. Often we construct a constitutive model based on a softening stress-strain curve (actually developed from a force displacement curve) which assumes homogeneity of stress and strain when significant inhomogeneities actually occur (eg. cracking, shear bonding, etc.). Constitutive models developed in this way should not be expected to effectively reproduce material response over a wide range of complex loading conditions. Therefore, it is expected that some models may provide good results for specific load cases and be totally inappropriate and possibly unstable for other load cases.

The stability postulates presented above are considered as mathematical restrictions on constitutive relations in plasticity theory. These restrictions result in the requirement that the yield surface be convex. At a singular point (corner, vertex) on a yield surface or at the intersection of two or more surfaces the plastic strain increment must be within the fan or hypercone bounded by the normals to the respective surfaces at the singular point. Furthermore, for hardening, satisfying the stability postulates leads to a sufficient condition for uniqueness of solution in the incremental sense, where equilibrium equations and kinematic relations are linear. Since yielding and other nonlinear response features of concrete are strongly dependent on the confining stress level, different forms of loading and failure surfaces are often used for different stress regions. When these surfaces are combined in a constitutive model, intersecting corners can occur. If the loading stress path intersects these surfaces at a corner point, obviously there exist more than one surface normal at this point and the direction of plastic strain is not uniquely defined. If the plastic strain increment at such a singular point, which is the intersection of say  $m$  continuous yield surfaces, is taken as the linear combination of the  $m$  plastic strain increments for the reactive surfaces, then the



solution is unique and the stability postulates are satisfied. Here reactive implies those surfaces which are to be used for computing plastic strain increments. Proofs of uniqueness can be found in Martin [16] Pages 109-114.



### 3.5. Examples of Hardening and Softening Formulations.

Consider a homogeneous isotropic material subjected to loading under plane stress conditions such that  $\sigma_3 = 0$ . Furthermore, assume the material behaves the same under tension and compression and that the Von Mises yield condition is appropriate for describing the initial yield and subsequent (loading) yield surfaces for the material. Also, let the one-dimensional response of the material to axial stress be as shown in Figure 3.5.

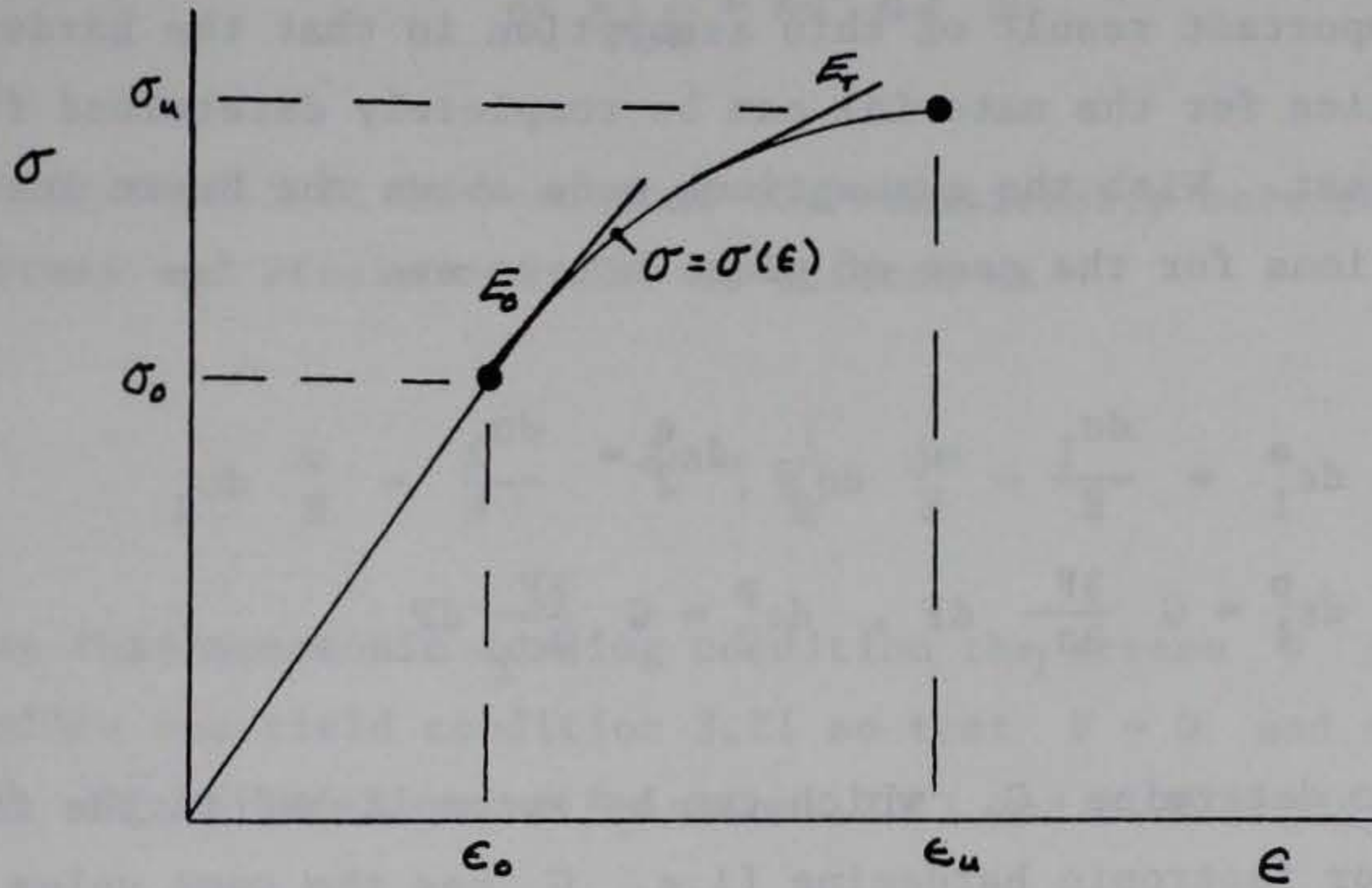


Figure 3.5. One dimensional response of example hardening material

For the Von Mises surface initial yielding will occur when the state of stress satisfies the condition

$$\sigma_1^2 + \sigma_2^2 - \sigma_1\sigma_2 = \sigma_0^2 \quad 3.20$$

and for any subsequent yield or loading surface the stress state will satisfy the condition

$$F = \sigma_1^2 + \sigma_2^2 - \sigma_1\sigma_2 - \bar{\sigma}^2 = 0 \quad 3.21$$



where  $\bar{\sigma}^2 = \frac{1}{2}(\sigma_1^2 + \sigma_2^2) + \sigma_1\sigma_2$ , assuming  $\bar{\sigma} \geq \sigma_0$ .

Finally, it is assumed that an associative flow rule is appropriate so that it only remains to determine  $G(\sigma_{ij}, H\alpha)$ , the scalar hardening parameter, before stress strain response problems can be solved. To this end we assume that the hardening is isotropic which means that  $G$  is constant on any particular yield or loading surface. An important result of this assumption is that the hardening characteristics for the material can be completely determined from one simple test. With the assumptions made above the basic incremental equations for the case of plane stress are

$$\begin{aligned} d\epsilon_1^e &= \frac{d\sigma_1}{E} - \frac{\nu}{E} d\sigma_2, \quad d\epsilon_2^e = \frac{d\sigma_2}{E} - \frac{\nu}{E} d\sigma_1 \\ d\epsilon_1^p &= G \frac{\partial F}{\partial \sigma_1} dF, \quad d\epsilon_2^p = G \frac{\partial F}{\partial \sigma_2} dF \end{aligned} \quad 3.22$$

It remains to determine  $G$ , which can be accomplished in the following way for isotropic hardening (i.e.  $G$  has the same value at all points on any one subsequent yield or loading surface). Assume that a monotonic one dimensional compression test is conducted on the material discussed above such that the stress strain response is as presented in Figure 3.5. Since the basic equations must apply to this test and since the loading is monotonic, we can write

$$d\epsilon = \frac{d\sigma}{E} \quad 0 \leq \sigma \leq \sigma_0$$

and

$$d\epsilon = d\epsilon^e + d\epsilon^p \quad \sigma > \sigma_0$$



Therefore from equations (3.22) for  $d\epsilon_1$ ,

$$d\epsilon_1 = \frac{d\sigma_1}{E} + G \frac{\partial F}{\partial \sigma_1} \left( \frac{\partial F}{\partial \sigma_1} d\sigma_1 \right)$$

where here  $\sigma_1 = \sigma$ , and  $\sigma_2 = 0$  such that

$$d\epsilon = \left[ \frac{1}{E} + 4\sigma^2 G \right] d\sigma \quad 3.23$$

From Figure 3.5 it is seen that the relationship between increments of stress and strain can also be written as

$$d\epsilon = \frac{1}{E_T} d\sigma \quad 3.24$$

During this monotonic loading condition the stress  $\sigma$  continuously satisfies the yield condition 3.21 so that  $F = 0$  and consequently  $\sigma = \bar{\sigma}$ . With this in mind Equations 3.23 and 3.24 imply.

$$G = \frac{1}{4\bar{\sigma}^2} \left[ \frac{1}{E_T} - \frac{1}{E} \right] \quad 3.25$$

For this example we are treating compression as positive and only concerned with the positive quadrant of  $\sigma_1, \sigma_2$  space. From 3.25

$G(\underline{\sigma}, H\alpha)$  is a function, of the current stress state (through  $\bar{\sigma}$ ) and could also be expressed as a function of plastic strain  $\epsilon^P$ . Therefore, given Equations 3.22 and 3.25 we can solve hardening plasticity problems under monotonic loading given a particular stress path in plane stress space  $(\sigma_1, \sigma_2)$ . From Figure 3.5 we can write  $E_t(\bar{\sigma})$  so that the integration of Equations 3.22 could be performed with relative ease. For a particular continuous proportional loading path (say  $\sigma_1 = 2\sigma_2$ ) the effect on the loading surfaces is uniform



expansion as shown in Figure 3.6. The reason for this is that as loading progresses  $\bar{\sigma}$  increases and  $G$  is always positive since  $E_t < E$ .

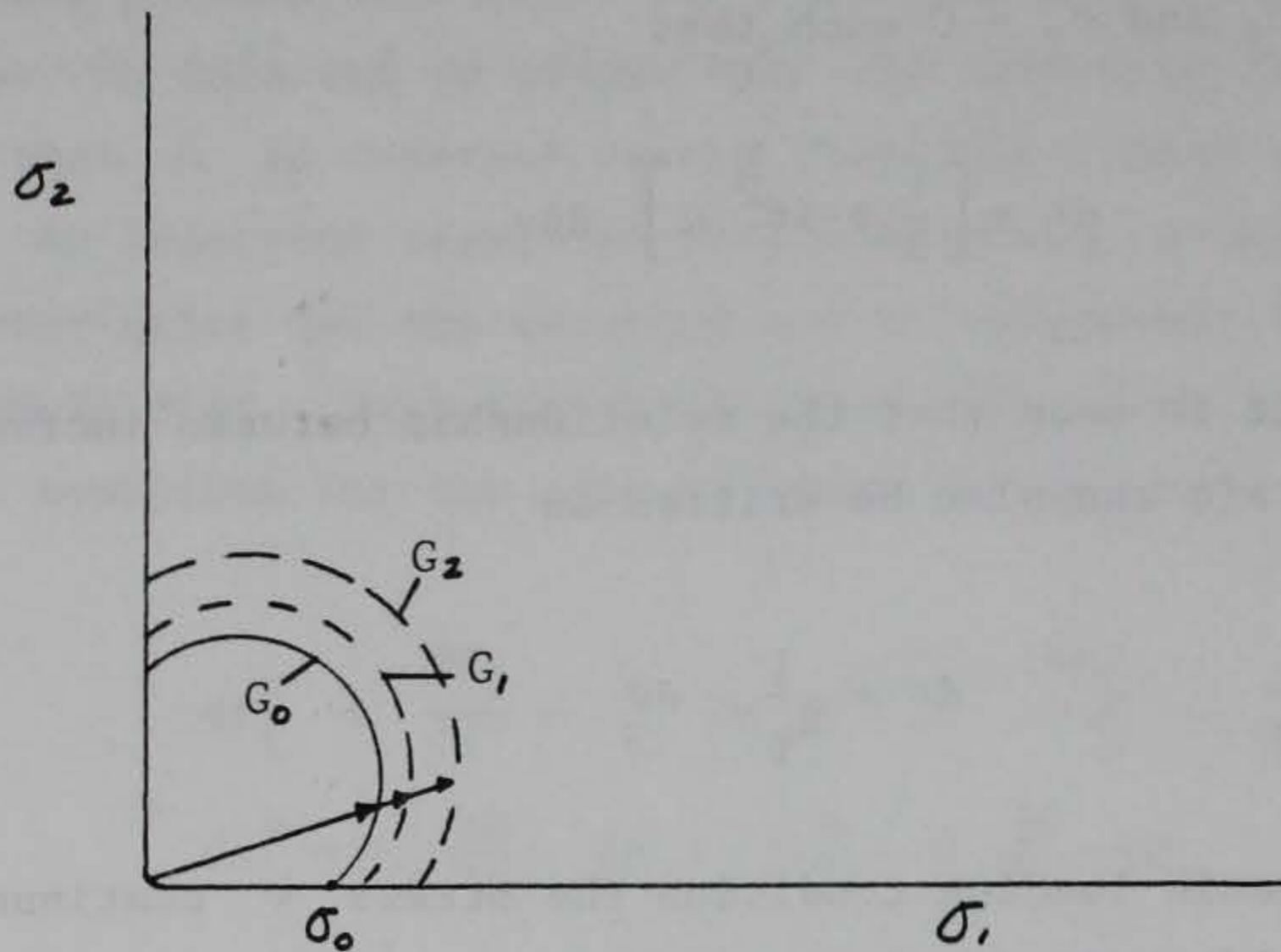


Figure 3.6 Isotropic hardening of yield surfaces

Based on the above assumptions the exact solution to the problem of continuous proportional loading ( $d\sigma_1 = 2d\sigma_2$ ) to a final stress state  $\sigma_1 = 2\sigma_0$  can be obtained. For this example we take the case where  $E_t = \text{constant}$ .

At the end of the elastic region (ie;  $\sigma_1 = \frac{2\sqrt{3}}{3} \sigma_0$ ,  $\sigma_2 = \frac{\sqrt{3}}{3} \sigma_0$ ) the elastic strains are calculated from (3.22) as

$$\epsilon_1^e = \frac{\sqrt{3} \sigma_0}{3E} (2-\nu)$$

$$\epsilon_2^e = \frac{\sqrt{3} \sigma_0}{3E} (1-2\nu)$$

For the remainder of the stress path, the total strains can be determined by integration as



$$\epsilon_1 = \frac{\sigma_0}{E} (2-\nu) + \frac{.63450}{E} \frac{E - E_T}{E_T}$$

$$\epsilon_2 = \frac{\sigma_0}{2E} (1-2\nu)$$

The main point to be made here is that for hardening plasticity the solution to this simple problem can be obtained in closed form.

If on the other hand, the one-dimensional response to axial loading is observed to be that presented in Figure 3.7 several different problems arise in obtaining the solution of the plane-stress problem.

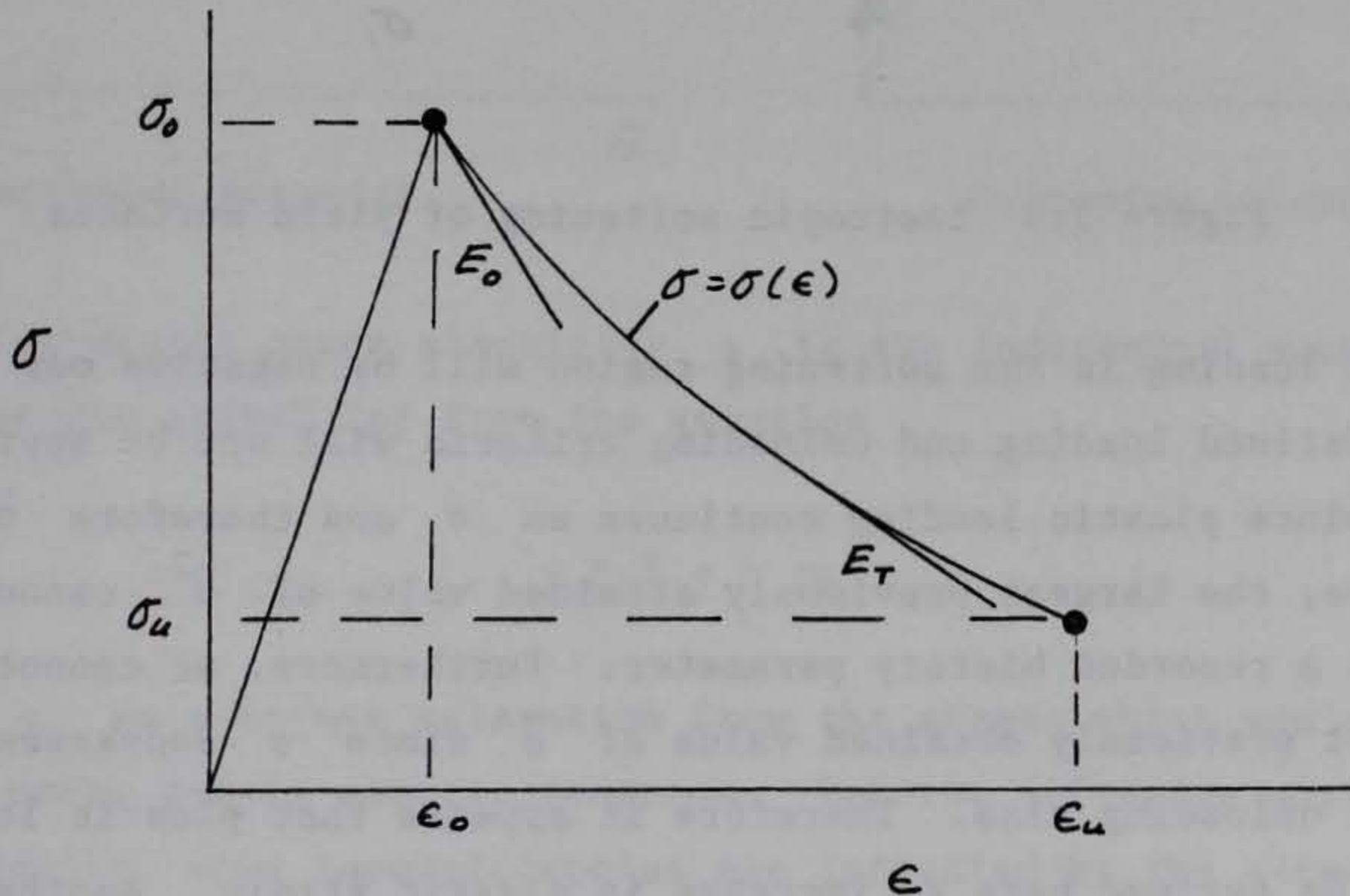


Figure 3.7. One dimensional response of example softening material

Here it is assumed that the softening behavior observed in the one dimensional test (Figure 3.7) is generalized to an isotropic softening in plane-stress space. The qualitative effect of the softening on subsequent yield surfaces is shown in Figure 3.8. Since the increment in stress  $d\sigma$  for



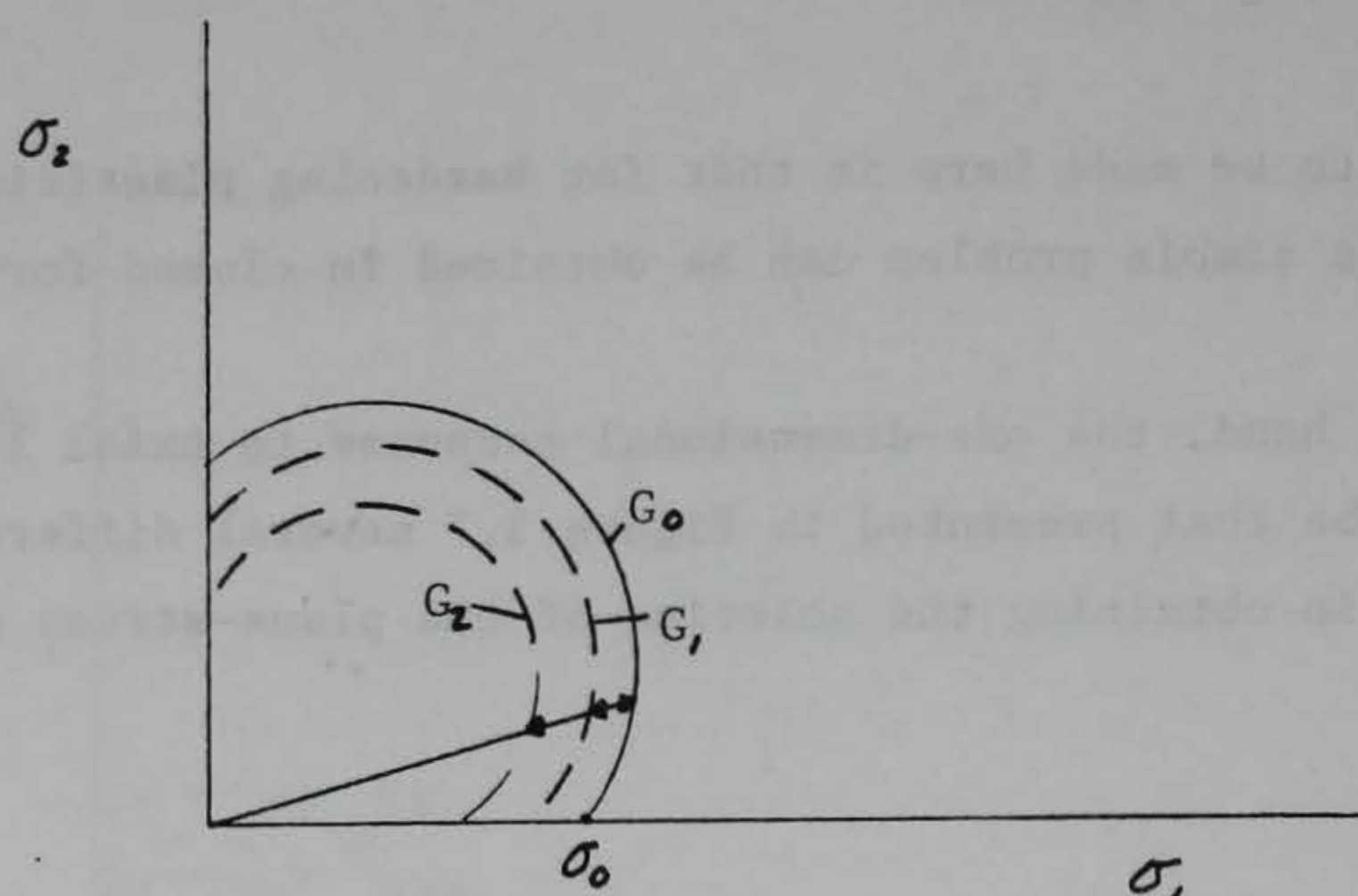


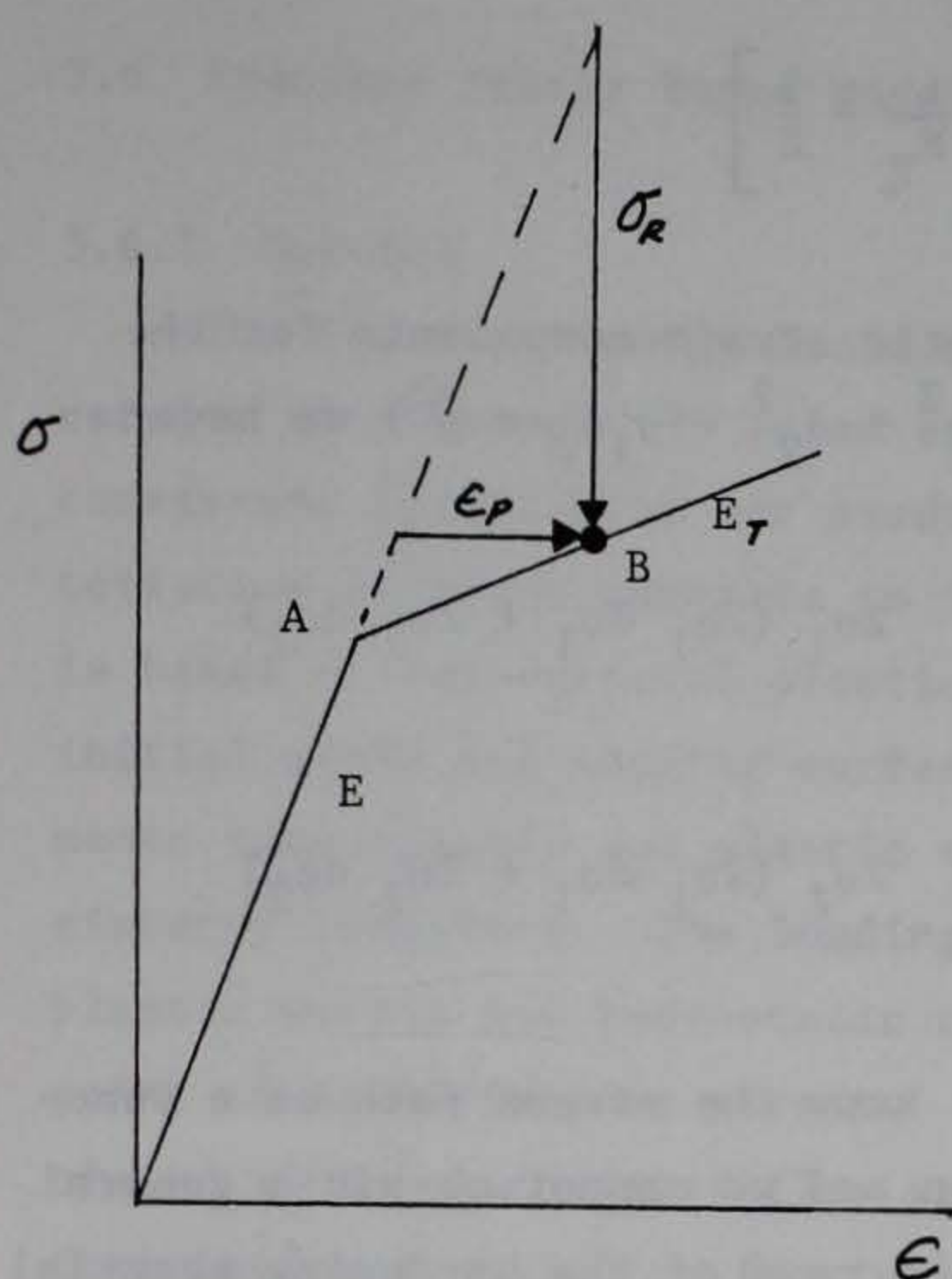
Figure 3.8 Isotropic softening of yield surfaces

plastic loading in the softening region will be negative our previously defined loading and unloading criteria will not be appropriate. Also, since plastic loading continues as  $\sigma$  and therefore  $\bar{\sigma}$  decrease, the largest previously attained value of  $\bar{\sigma}^2$  cannot be used as a recorded history parameter. Furthermore, we cannot use the smallest previously obtained value of  $\bar{\sigma}$  since  $\sigma$  decreases under elastic unloading also. Therefore it appears that plastic loading should be defined here as increase in plastic strain. Another problem encountered in softening materials is demonstrated in the figure on the following page.

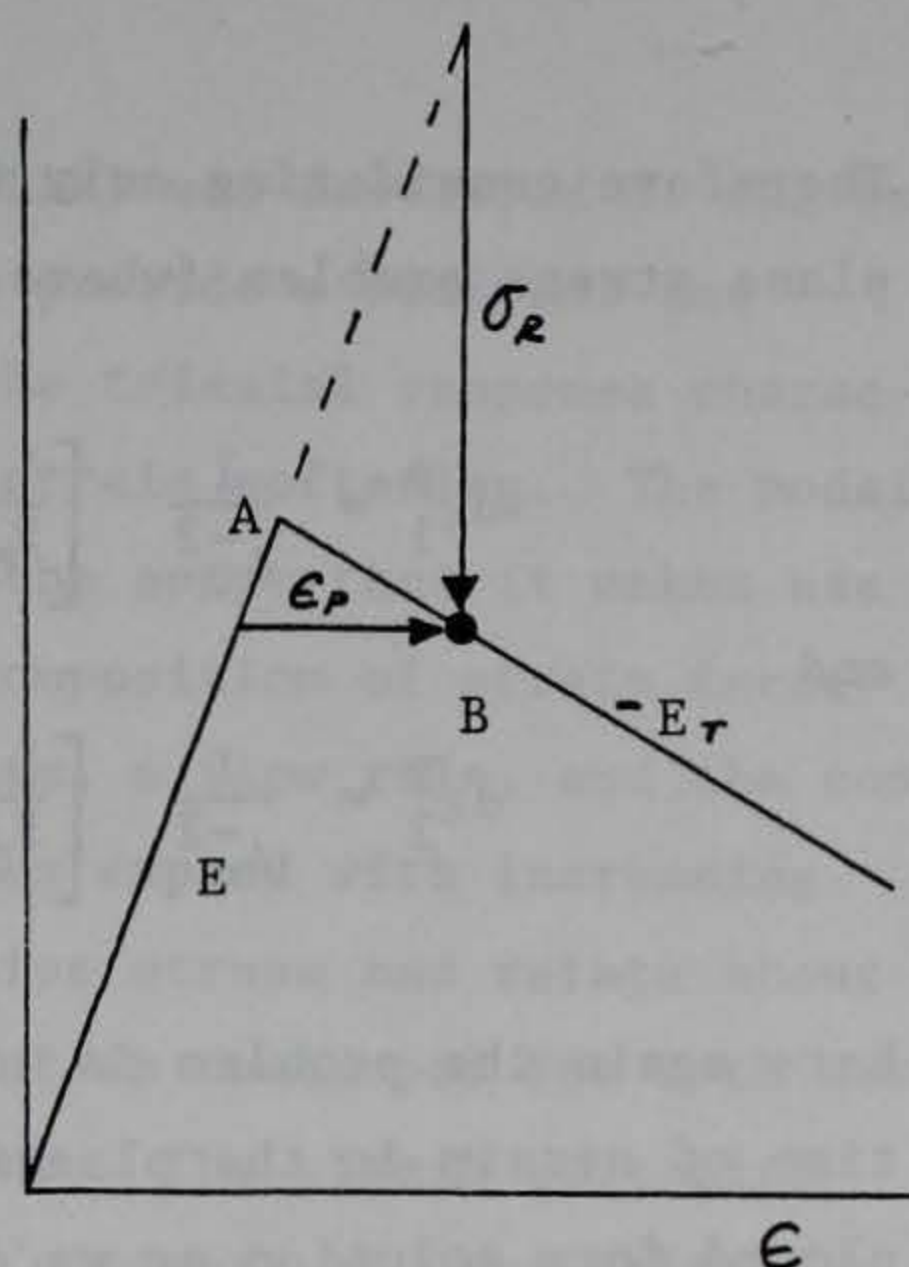
For stress space plasticity,  $\sigma$  is the independent variable and strains are solved for from the equation

$$\epsilon = \frac{\sigma}{E} + \epsilon^p$$





Hardening material.



Softening material.

while for strain space plasticity  $\epsilon$  is the independent variable and stresses are solved for from the equation

$$\sigma = E \epsilon - \sigma_R$$

where  $\sigma_R$  is a stress relaxation from the stress which would be predicted under purely elastic response. For the softening problem, conceptually, some inconsistencies are indicated by the stress space formulation. First the end point  $(\epsilon_B, \sigma_B)$  cannot be reached by following a monotonic load path and since the strain must be specified in this test we do not know a priori what the final stress  $\sigma_B$  will be. The stress space formulation could be used for the isotropic softening problem by developing a softening function  $G$  in the following way. Specializing Equations 3.22 to the softening material shown above following the same procedures used for the hardening material results in



$$G = \frac{1}{4\sigma^2} \left[ \frac{1}{E_T} + \frac{1}{E} \right]$$

Therefore considering only the plastic strain components for the plane stress problem (where  $F = \sigma_1^2 + \sigma_2^2 - \sigma_1\sigma_2 = \bar{\sigma}^2$ ) we have

$$d\epsilon_1^P = \frac{1}{4\sigma^2} \left[ \frac{1}{E_T} + \frac{1}{E} \right] 2\sigma_1 (2\sigma_1 d\sigma_1 + 2\sigma_2 d\sigma_2)$$

and

$$d\epsilon_2^P = \frac{1}{4\sigma^2} \left[ \frac{1}{E_T} + \frac{1}{E} \right] 2\sigma_2 (2\sigma_1 d\sigma_1 + 2\sigma_2 d\sigma_2)$$

Here again the problem is we do not know the stress path as a function of strain in the plastic region and we cannot obtain a general closed form solution as we did in the case of the hardening material using a stress space formulation. For the special case of an isotropic material and a symmetric-monotonic plastic loading path (ie  $\epsilon_1 = \epsilon_2$ ) to a final plastic strain state of  $\epsilon_1^P = \epsilon_2^P = \epsilon_o$  a solution for the softening material problem can be obtained. For this case  $\sigma_1 = \sigma_2$ , and  $-d\sigma_1 = -d\sigma_2$  due to symmetry. Therefore from the above equations

$$\int_0^{\epsilon_1^P} d\epsilon_1^P = \epsilon_o \quad d\epsilon_1^P = -2 \left( \frac{1}{E_T} + \frac{1}{E} \right) \int_{\sigma_1^P}^{\sigma_1^O} d\sigma_1$$

and

$$\epsilon_1^P = \epsilon_o = 2 \left( \frac{1}{E_T} + \frac{1}{E} \right) (\sigma_1^A - \sigma_1^O)$$

from which the final stress  $\sigma_1^O$  can be solved for. The point to be made here is that an additional assumption (symmetry) had to be made before this simple problem could be solved.



### 3.6 Fracture Energy Based Model

#### 3.6.1 General

The Fracture Energy Based Model (FEBM) was developed at the University of Colorado (3) in an effort to provide a rational and consistent formulation for predicting the triaxial response characteristics of plain concrete to include strain softening. The model is based on conventional plasticity in the sense that it makes use of initial yield and loading surfaces, decomposition of strain increments into elastic and plastic components, a flow rule, and the consistency condition. The loading surfaces expand with increasing plastic strain and hydrostatic compressive stress and rotate about a point of equal tension stress. The model is developed for both associated and nonassociated flow assumptions. The strain softening formulation is based on fracture energy concepts and the criterion that strain softening occurs when the loading stress state reaches the failure surface at a confining stress less than the confining stress which defines the brittle-ductile transition.

#### 3.6.2 Failure Surface

The failure surface used in the FEBM was developed by Leon (18), and is based on forcing continuity between the Mohr-Coulomb friction law and the tension cut off condition of Rankine. Mathematically the two parameter surface is represented as

$$F = \left[ \frac{\sigma_1 - \sigma_3}{f'_c} \right]^2 + Mo \frac{\sigma_1}{f'_c} - C_o = 0 \quad 3.28$$

where  $\sigma_1$  = Major principal stress  
 $\sigma_3$  = Minor principal stress  
 $Mo$  = friction parameter  
 $C_o$  = cohesive parameter.  
 $f'_c$  = Unconfined Compressive Strength



When  $\sigma_1 = 0$  equation 3.28 yields

$$\frac{\sigma_3^2}{f_c'^2} = C_0$$

so that taking  $\sigma_3 = f_c'$  for this case results in  $C_0 = 1$ . This is the same result found for the Mohr-Coulomb surface where  $C_0$  would be defined as the normalized cohesion of the material while the friction parameter  $M_0$  is not exactly the same as the coefficient of internal friction, which is defined in the Mohr-Coulomb model, it is a measure of the slope of the failure surface (and loading surfaces to be discussed in the next section).

The failure surface defined by Equation (3.28) and shown in Figure 3.9 represents the maximum strength of the material when the normalized cohesive

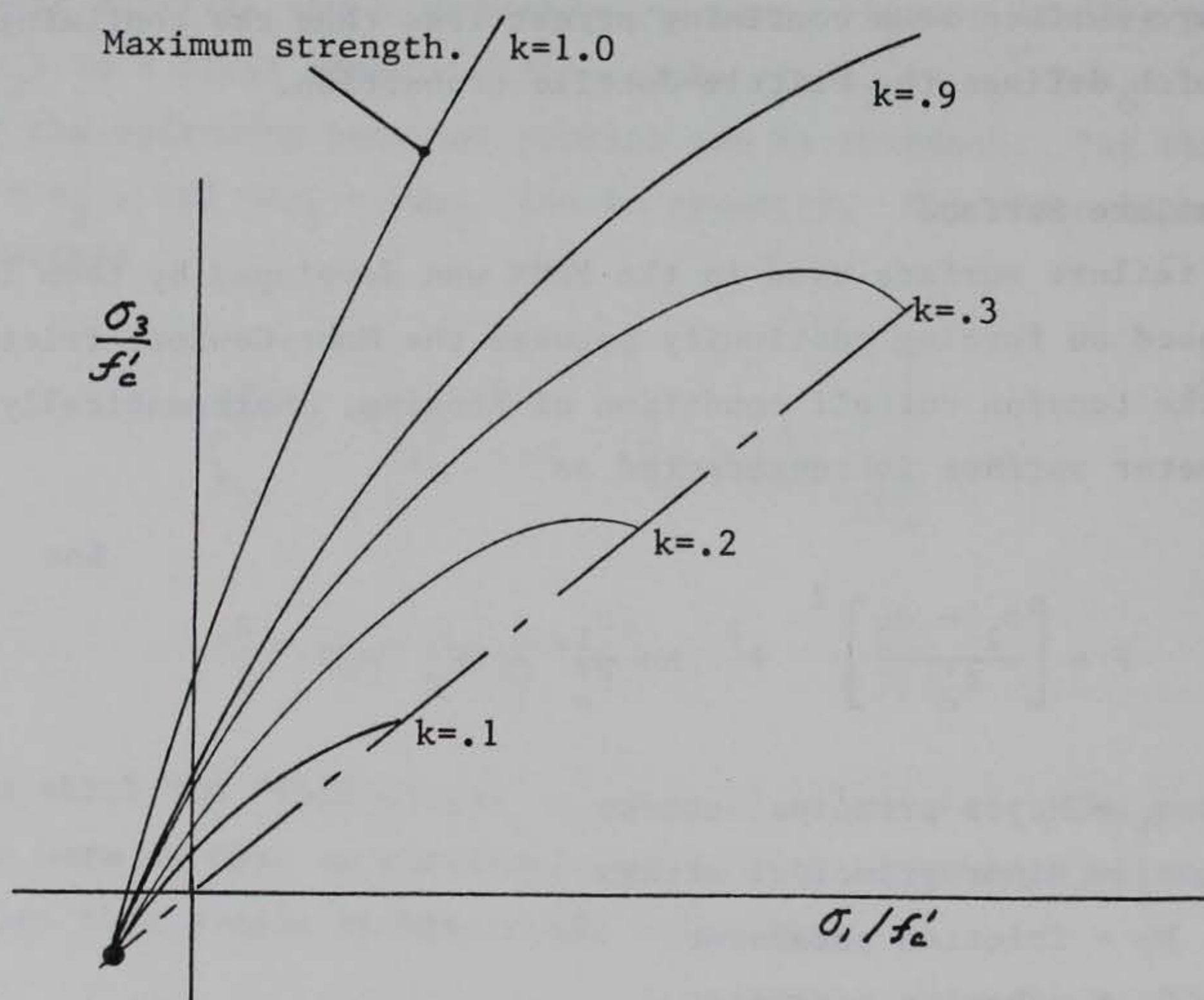


Figure 3.9 Hardening and maximum strength surfaces for the FEBM



parameter  $C_o = 1$ .  $M_o$  can be determined by setting  $\sigma_3 = 0$  and defining the value of  $\sigma_1$  for this condition as  $\sigma_1 = f'_t$  which leads to

$$M_o = \frac{f'_c{}^2 - f'_t{}^2}{f'_c f'_t} \quad 3.29$$

where  $f'_t$  = unconfined tensile strength

### 3.6.3 Loading Surfaces (Hardening)

The loading surfaces for the FEBM during hardening can be expressed as

$$F(\sigma_1, \sigma_3, k) = \left[ (1 - k) \frac{\sigma_1^2}{f'_c{}^2} + \frac{\sigma_1 - \sigma_3}{f'_c} \right]^2 + k^2 M_o \frac{\sigma_1}{f'_c} - k_o^2 \quad 3.30$$

$C_o = 0$

where  $k(\epsilon_p)$  = hardening parameter,  $k_o \leq k \leq 1$   
 $k_o$  = value of  $k$  defining the initial yield surface

Loading surfaces for different values of  $k$  are presented in Figure 3.9. Three important observations can be made regarding the loading surfaces.

1. When  $k = 1$  the loading surface corresponds to the failure surface  $F$ .
2. The hardening behavior is not purely isotropic, since the loading surfaces essentially rotate about a common point in the tension region.
3. The loading surfaces intersect the hydrostat at angles other than  $90^\circ$  and other corners exists at  $60^\circ$  intervals in deviatoric sections.

In order to simulate the pressure sensitive behavior of concrete the hardening parameter is expressed as a function of plastic strain and



confining stress. The development of the expression for  $k$  was motivated by the fact that increasing the confining stress ( $\sigma_1 = \sigma_2$ ) increases the maximum strength ( $\sigma_3$ ) and the strain ( $\epsilon_3$ ) at which maximum strength is reached. Therefore, one could conduct tests at low, medium, and high confining stresses then normalize the ordinate (i.e.  $\sigma_3(\epsilon^P)/\sigma_{3\max} = k$ ) and plot  $k$  versus plastic strain ( $\epsilon^P$ ) up to strains where maximum strength is attained. The general characteristics of these curves are shown in Figure 3.10. To simulate this variation of  $k$  with  $\epsilon^P$ , a monotonically increasing elliptic function of  $\epsilon^P$  was selected.

$$k(\epsilon^P, \chi^P) = k_0 + \frac{1 - k_0}{\epsilon^P} \sqrt{2\epsilon^P \chi^P - (\epsilon^P)^2} \quad 3.31$$

where  $\chi^P$  = ductility parameter, the plastic strain when maximum strength is attained for a given confining stress.

$$\dot{\epsilon}^P = \sqrt{\dot{\epsilon}_1^P \cdot \dot{\epsilon}_2^P} = \text{equivalent plastic strain rate.}$$

An empirical expression was developed for  $\chi^P$  which is also calibrated from low, medium, and high confining stress test results. This expression is

$$\chi^P = A_H \left( \frac{\sigma_1}{f'_c} \right)^2 + B_H \left( \frac{\sigma_1}{f'_c} \right) + C_H \quad 3.32$$

Ideally for a given concrete three triaxial compression tests can be conducted (eg. low, medium, high confining stress ( $\sigma_1$ )) and three values of  $\chi^P$ , measured. Then knowing  $f'_c$  and  $\sigma_1$  these equations in the unknowns  $A_H$ ,  $B_H$ , and  $C_H$  can be determined, and solved.



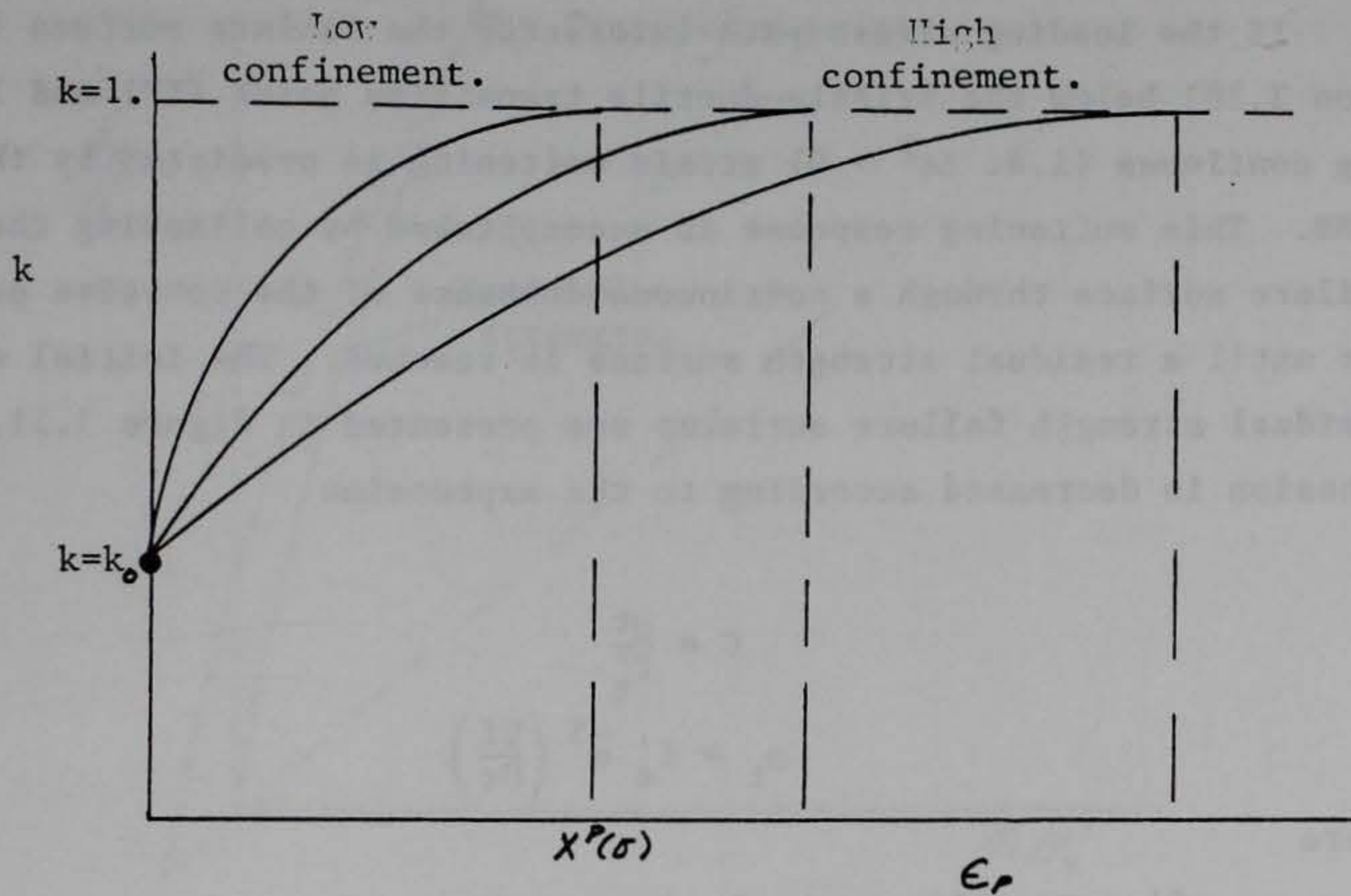


Figure 3.10 Effects of confining stress on hardening parameter  $k$



### 3.6.4 Loading Surfaces (Softening)

If the loading stress path intersects the failure surface (Equation 3.28) below the brittle-ductile transition point (TP) and loading continues (i.e.  $\Delta\epsilon^P > 0$ ) strain softening is predicted by the FEBM. This softening response is accomplished by collapsing the failure surface through a continuous decrease of the cohesive parameter until a residual strength surface is reached. The initial and residual strength failure surfaces are presented in Figure 3.11. The cohesion is decreased according to the expression

$$C = \frac{\sigma_t}{f'_t}$$

$$\sigma_t = f'_t e^{-5 \left( \frac{U_f}{U_r} \right)} \quad 3.33$$

where

$f'_t$  = tensile strength of concrete

$\sigma_t$  = degrading tensile strength

$U_f$  = crack opening displacement measured in a direct tension test

$U_r$  = residual crack opening displacement, crack opening at fracture.

As shown in Figure 3.11 the decrease in cohesion is accompanied by an increase in  $M$  (the frictional parameter) or say a frictional hardening. In effect the softening surfaces rotate about the point TP in stress space. The relation between  $M$  and  $C$  is assumed as

$$M = M_r - (M_r - M_o) C \quad 3.34$$

Where  $M_r$  is the value of the frictional parameter at residual strength. The cohesion parameter  $C$  can therefore be thought of as the softening parameter and can be determined from a simple uniaxial tension test (which is conducted in stroke control). The results



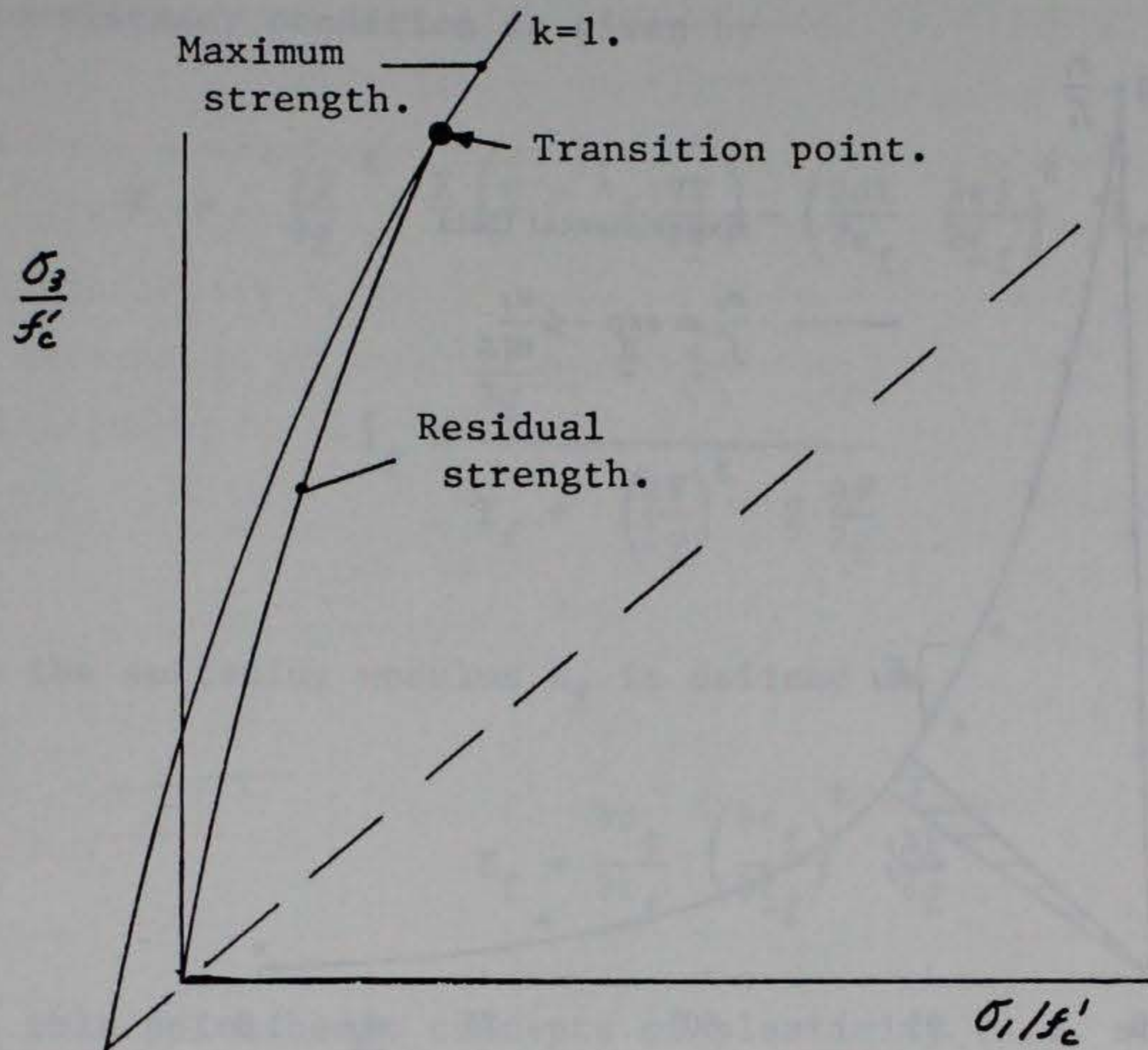


Figure 3.11 Rotation of softening surfaces about TP

from a direct tension test along with predictions from equation 3.33 are presented in Figure 3.12, (from Reference 3). The motivation for using the direct tension test for defining softening in compressive stress states, was based on the idea that the strain softening phenomenon is dominated by microcrack growth which is associated with dilation (expansion) in compressive tests. Considering the case of direct tension a strain softening plasticity formulation can be developed in the same manner as for hardening plasticity. Assuming the initial yield and loading surfaces can be defined by the maximum tension strength surface



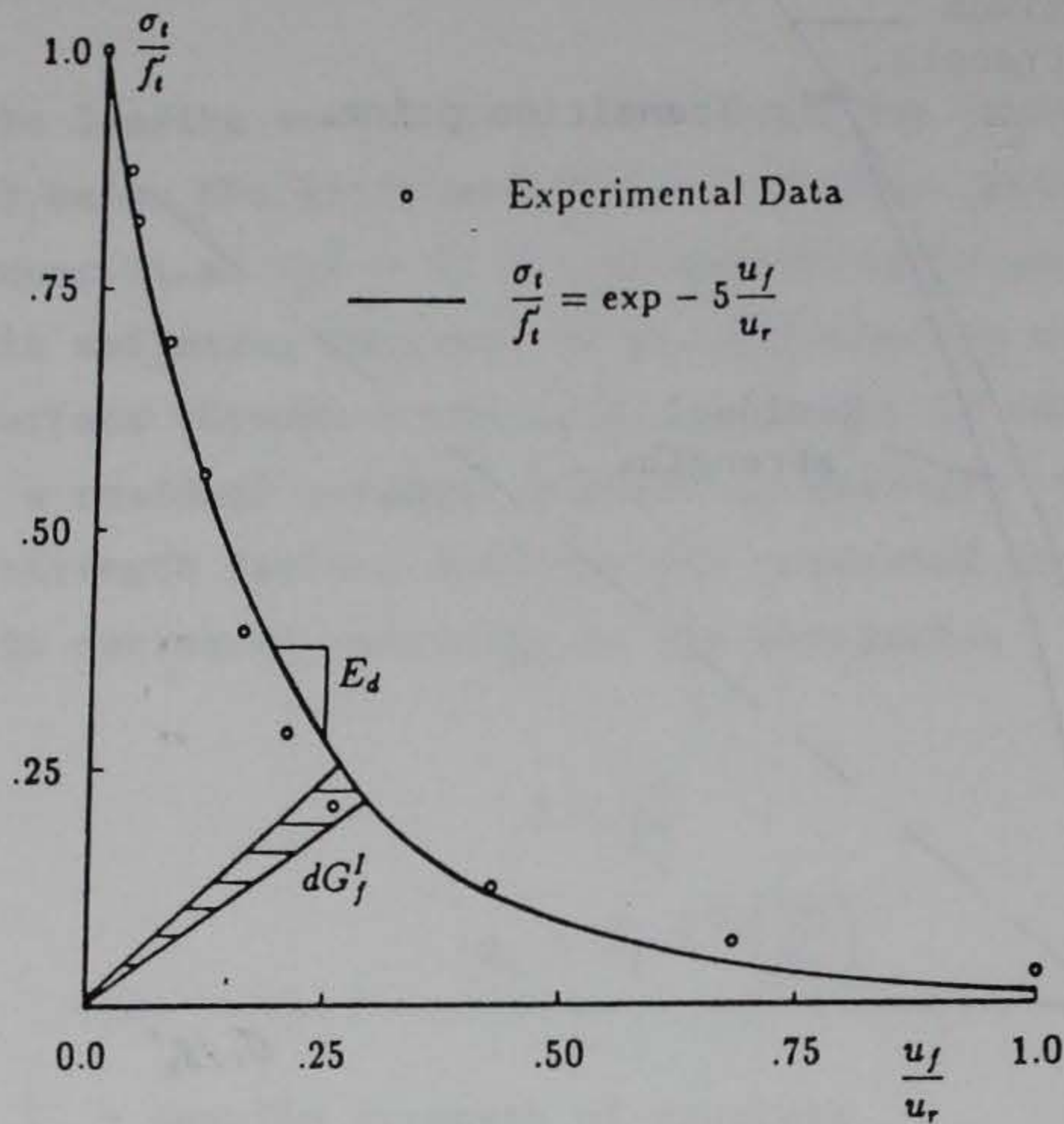


Figure 3.12 Softening in a direct tension test

$$F(\sigma_l, \sigma_t) = \sigma_l - \sigma_t = 0$$

where  $\sigma_t = \sigma_t(\epsilon_f)$   
 $\epsilon_f = \text{fracture strain}$

and that the plastic (fracture) strain in tension is defined in rate form as

$$\dot{\epsilon}_f = \dot{\lambda}_f \frac{\partial F}{\partial \sigma}$$

where

$$\dot{\lambda}_f = G \frac{\partial F}{\partial \sigma} d\sigma$$



the consistency condition is given by

$$\begin{aligned} \dot{\bar{F}} &= \frac{\partial \bar{F}}{\partial \bar{\sigma}}^t E \left( \dot{\bar{\epsilon}} - \dot{\lambda}_f \frac{\partial \bar{F}}{\partial \bar{\sigma}} \right) - \left( \frac{\partial \sigma_t}{\partial \epsilon_f} \frac{\partial \epsilon_f}{\partial \bar{\epsilon}_f} \right)^t \dot{\lambda}_f \frac{\partial \bar{F}}{\partial \bar{\sigma}} = 0 \\ \dot{\lambda}_f &= \frac{\frac{\partial \bar{F}}{\partial \bar{\sigma}}^t E \dot{\bar{\epsilon}}}{E_f + \left( \frac{\partial \bar{F}}{\partial \bar{\sigma}} \right)^t E \frac{\partial \bar{F}}{\partial \bar{\sigma}}} \end{aligned} \quad 3.35$$

where the softening modulus  $E_f$  is defined as

$$E_f = \frac{\partial \sigma_t}{\partial \epsilon_f} \left( \frac{\partial \epsilon_f}{\partial \bar{\epsilon}_f} \right)^t \frac{\partial \bar{F}}{\partial \bar{\sigma}} \quad 3.36$$

Up to this point basic concepts of plasticity (i.e. strain rate decomposition, normality, consistency) have been applied to a strain softening material. However, when attempting to compute  $E_f$  from Equation (3.36) a problem arises due to the fact that  $\sigma_t$  is defined as a function of  $U_f$  not  $\epsilon_f$  (Equation 3.33, Figure 3.12). The reason for this is that in a direct tension test (in displacement control) at peak stress the microcracks coalesce into a localized band and the response of the specimen is better or more appropriately defined in terms of stress versus displacement (crack opening displacement) as shown in Figure 3.13 (from Reference 3). In the FEBM this problem is addressed by using the chain rule such that

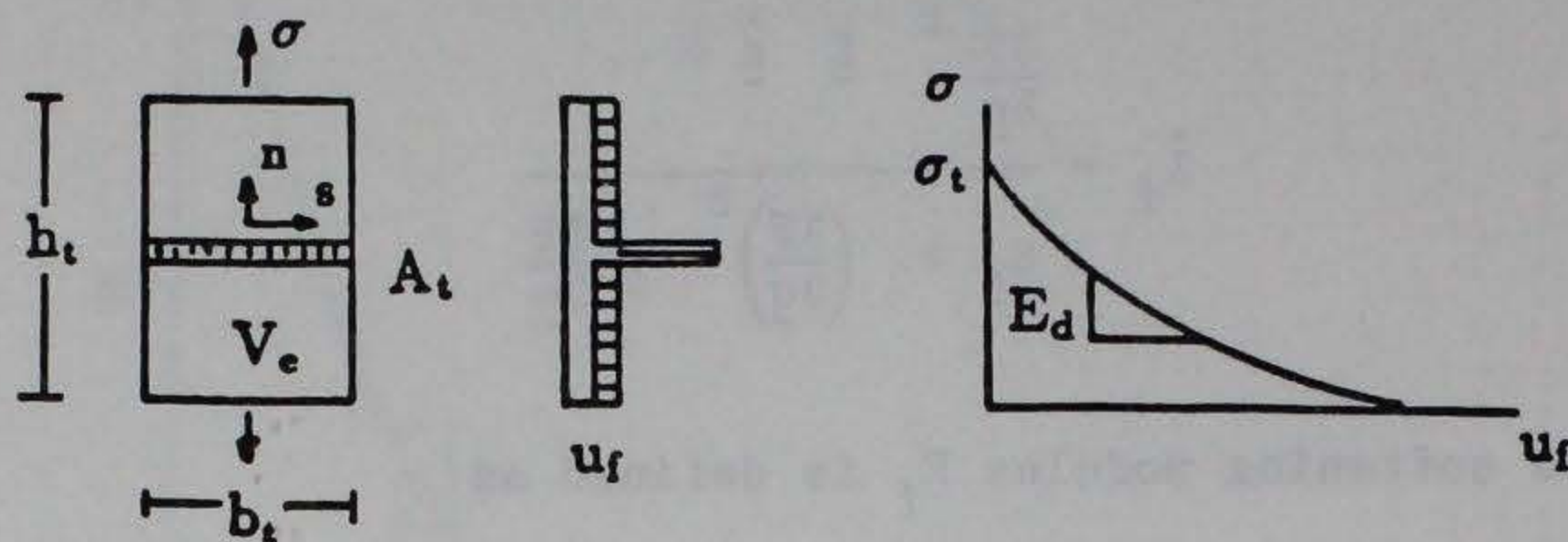
$$\frac{\partial \sigma_t}{\partial \epsilon_f} = \frac{\partial \sigma_t}{\partial U_f} \frac{\partial U_f}{\partial \epsilon_f}$$

Therefore, the softening modulus can be expressed as

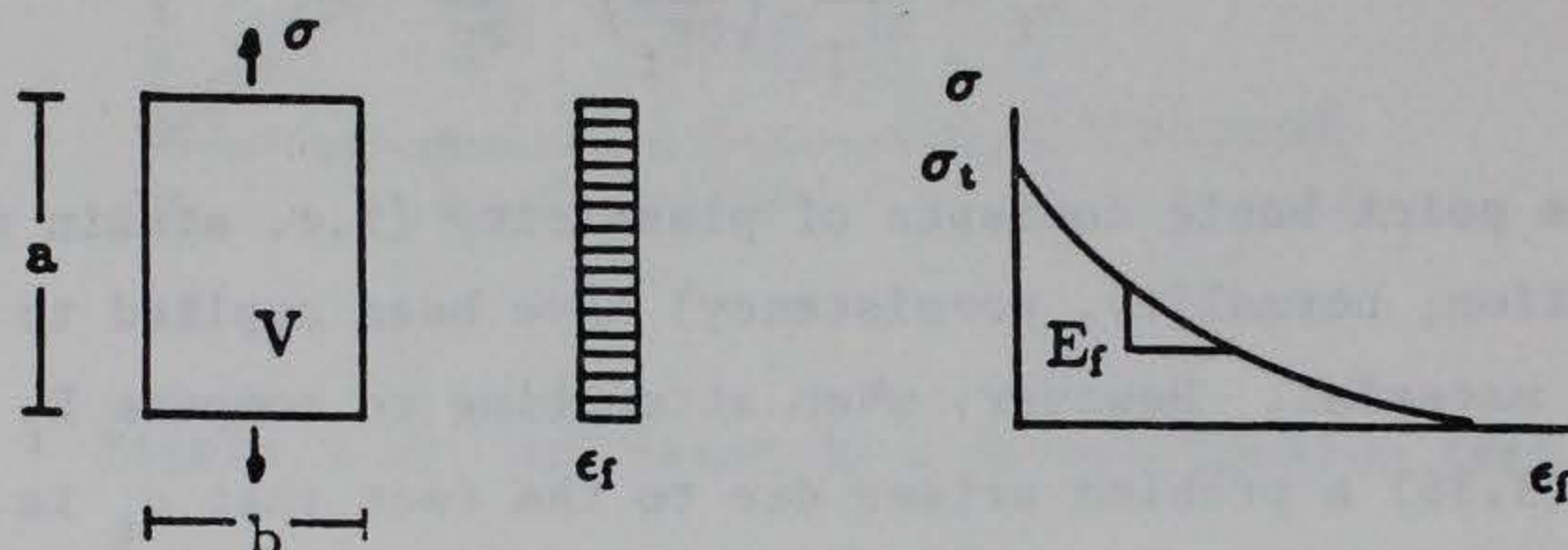
$$E_f = \frac{\partial \sigma_t}{\partial \epsilon_f} \frac{\partial u_f}{\partial \epsilon_f} \frac{\partial \epsilon_f}{\partial \bar{\epsilon}_f} \frac{\partial \bar{F}}{\partial \bar{\sigma}} \quad 3.37$$



and the only term which cannot be directly computed is  $\partial U_f / \partial \epsilon_f$ . It is here where an assumption is made which will allow for the extension of the strain



Composite Crack Band Element



Equivalent Continuum

Figure 3.13 Localization versus continuum ideas, from (3)

softening theory to compressive stress states but also results in a theory which when implemented in a finite element analysis procedure will exhibit mesh sensitivity. Essentially this assumption is to smear the effect of the localized crack band over the volume of the test specimen. This is accomplished by expressing the softening modulus (for the direct tension test) as

$$E_f = E_d h_t$$



where  $E_d = \partial \sigma_t / \partial U_f$

$h_t = \partial U_f / \partial \epsilon_f$ , height of test specimen.

$$\left( \frac{\partial \epsilon_f}{\partial \epsilon_{\sim f}} \right)^t \frac{\partial F}{\partial \sigma} = 1$$

For the direct tension test  $h_t$  can also be expressed as the elementary volume of the test specimen divided by the cracked surface area.

$$h_t = \frac{V}{A_t}$$

The theory is extended to compressive stress states directly by using the failure surface in the post peak region

$$F_p = \left( \frac{\sigma_1 - \sigma_3}{f'_c} \right)^2 + M \frac{\sigma_1}{f'_c} - C = 0$$

where  $C$  and  $M$  are defined by Equations (3.33) and (3.34), respectively. Also, in the softening region the equivalent plastic (fracture) strain increment is determined from

$$\dot{\epsilon}_f = \left\langle \dot{\epsilon}_{\sim f}^t \cdot \dot{\epsilon}_f \right\rangle^{\frac{1}{2}}$$

where the McCauley brackets  $\langle \rangle$  extract only the positive components (tension) of the inelastic fracture strain rate tensor  $\dot{\epsilon}_f$ . The only question remaining for the compressive formulation is how to determine  $\partial U_f / \partial \epsilon_f$  for compressive stress states. Here, a similar argument as used previously for the case of direct tension is presented. The assumption is made that under compressive states an equivalent characteristic length can be defined such that



$$\frac{\partial U_f}{\partial \epsilon_f} = \frac{V}{Ac} = hc$$

One might think of the volume fraction  $Ac/V$  as microcrack density in compression. While it was quite clear how to determine  $A_t$  in the tension test it is not so obvious how  $Ac$  (the fracture surface area) should be determined for low confinement compression tests. Under unconfined and very low confinement compression tests, vertical (splitting tensile) cracks form which are the result of mode I type fracture (ie fracture due to tension only) in the circumferential direction. If the area of these vertical cracks, which are the result of splitting compression, is defined as  $Ac$  then the fracture energy associated with this fracture can be expressed as

$$\Omega_{cs} = G_f^I \Delta Ac$$

When results of compressive splitting tests are compared to direct tension tests (see Figure 3.14) it is seen that the fracture energy release rates in tension and splitting compression are quite similar. As the confining stress is increased the tensile cracks tend to coalesce into a single shear band which is inclined to the vertical axis of the specimen. The area of this shear fracture surface  $\Delta A_s$  is of the same order of magnitude as  $\Delta A_t$  and this type fracture is essentially mode II (ie fracture due to shear). The energy associated with this fracture can be expressed as

$$\Omega_{cv} = G_f^{II} \Delta A_s \approx G_f^{II} \Delta A_t$$

By equating the energy in compressive splitting tests to that in compressive shear an approximate expression can be determined for  $\Delta Ac$

$$\Delta Ac = \frac{G_f^{II}}{G_f^I} \Delta A_t$$



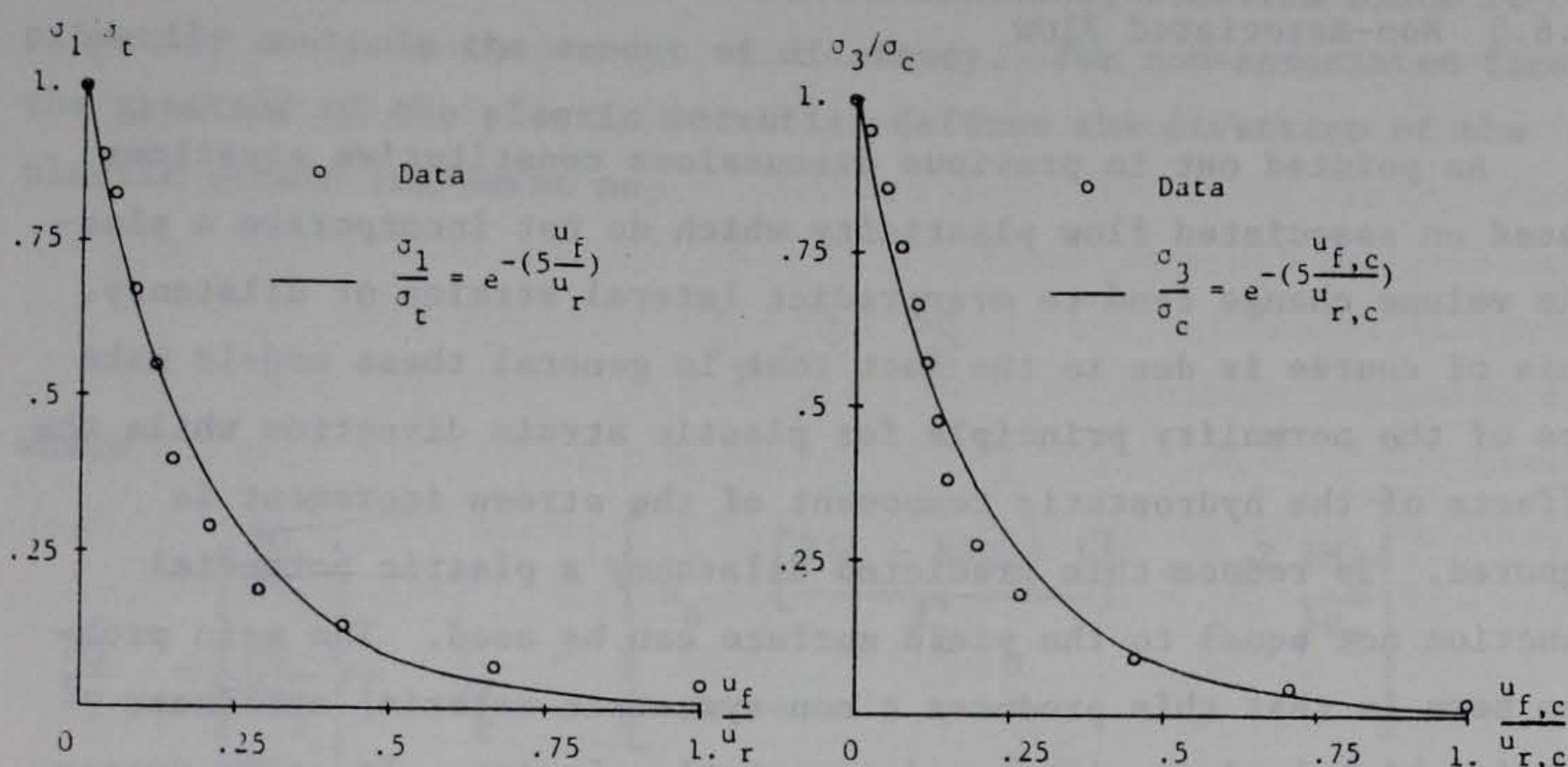


Figure 3.14 Comparison of softening in tension and compression

and therefore

$$h_c = \frac{G_f^I}{G_f^{II}} h_t$$

where  $h_t$  here is the height of the test specimen. From test results it was determined that the ratio  $G_f^{II}/G_f^I$  increases rapidly with confining stress and the following empirical formula was developed.

$$\frac{G_f^{II}}{G_f^I} = A_s \left( \frac{\sigma_l}{f'_c} - \frac{f'_t}{f'_c} \right)^4 + B_s \left( \frac{\sigma_l}{f'_c} - \frac{f'_t}{f'_c} \right)^2 + 1$$



where  $A_s$  and  $B_s$  are determined (in a manner similar to that discussed for the hardening coefficients  $A_h$ ,  $B_h$  and  $C_h$ ) based on low and high confining stress tests.

### 3.6.5 Non-Associated Flow

As pointed out in previous discussions constitutive equations based on associated flow plasticity which do not incorporate a plastic volume change tend to overpredict lateral strains or dilatancy. This of course is due to the fact that in general these models make use of the normality principle for plastic strain direction while the effects of the hydrostatic component of the stress increment is ignored. To reduce this predicted dilatancy a plastic potential function not equal to the yield surface can be used. The main problem here is that this produces a non-symmetric material stiffness matrix which leads to increased computational time. It seems reasonable to assume a plastic potential function that is similar in form to experimentally verified yield and loading surfaces and also is consistent, in terms of predicted lateral strains, with test results.

For the FEBM non-associated flow is characterized by a plastic potential function ( $Q$ ) which is not equal to the loading surface  $F$ . The plastic potential for non-associated flow hardening response is defined as.

$$Q(\sigma_1, \sigma_3, k, M_Q) = \left[ (1-k) \frac{\sigma_1^2}{f_c'^2} + \frac{(\sigma_1 - \sigma_3)^2}{f_c'^2} \right]^2 + k^2 \frac{MQ}{f_c'} - k^2 C = 0 \quad 3.38$$

and for softening response

$$Q(\sigma_1, \sigma_3, k, M_Q) = \left( \frac{\sigma_1 - \sigma_3}{f_c'} \right)^2 + \frac{MQ}{f_c'} - C = 0 \quad 3.39$$



From equations (3.38) and (3.39) it can be seen that the only differences in the plastic potential and the loading surfaces (i.e. equation (3.30)) is in the modification of the friction parameter  $M \rightarrow MQ$ . The parameter  $MQ$  is referred to as the dilatancy function since it primarily controls the amount of dilatancy. For non-associated flow the gradient of the plastic potential defines the direction of the plastic strain increment as

$$\dot{\epsilon}_p = \dot{\lambda} \frac{\partial Q}{\partial \sigma}$$

where

$$\frac{\partial Q}{\partial \sigma} = \begin{Bmatrix} \frac{\partial Q}{\partial \sigma_1} \\ \frac{\partial Q}{\partial \sigma_2} \\ \frac{\partial Q}{\partial \sigma_3} \end{Bmatrix} = \frac{1}{f'_c} \begin{bmatrix} S_h \left[ \frac{2(1-k)\sigma_1 + 1}{f'_c} \right] + k^2 \frac{\partial MQ}{\partial \sigma_1} \\ 0 \\ -S_h \end{bmatrix}$$

where

$$S_h = 2 \left[ (1-k) \frac{\sigma_1^2}{f'_c} \right] + \frac{\sigma_1 - \sigma_3}{f'_c}$$

From the above it can be seen that  $\frac{\partial MQ}{\partial \sigma_1}$  is a measure of the lateral component of the plastic strain vector and can be determined from triaxial compression tests at different confining stress levels. Essentially  $MQ$  is determined from three tests, unconfined tension, low confined compression and moderate confined compression. An iterative procedure was used to select  $MQ$  to best fit the experimental data. It was found that an empirical relation for  $MQ$  as a function of  $\sigma_1$  could be determined as

$$M_Q = D \left( \frac{10}{f'_c} \right)^{1/2} \left( \sigma_1 - f'_t \right)^{3/2} - E \left( \frac{10}{f'_c} \right)^{1/4} \left( \sigma_1 - f'_t \right)^{5/4} + F \sigma_1$$



### 3.7 Endochronic Plasticity Model

#### 3.7.1 Background

The first endochronic plasticity theory was proposed by Valanis (19) in 1971 and was based on the principle that the history of deformation of a material could be defined in terms of a "time scale" which is not real time but is a property of the material. The time scale is assumed to be a monotonically increasing function of the total deformation of the material and is essentially a metric of the deformation path in strain space. Also, the theory does not depend on the notion of a yield surface and definitions of loading, unloading, or reloading criteria as is the case of conventional plasticity. The first theory attracted considerable review, and discussion in the engineering community. Probably the most prominent criticisms of the theory were presented by Sandler (20) and Rivlin (21). Sandler's criticism was based on the fact that the theory fails to predict closed hysteresis loops during unloading and reloading of a simple endochronic material. Sandler then showed where this problem could lead to numerical instability and non-uniqueness of solution. Rivlin carefully analyzed the feasibility and plausibility of using the endochronic theory to model materials in general. Rivlin was also critical of the thermodynamic arguments used in the development of the theory. The problem of hysteresis loop closure was addressed by Valanis (22) and formed the basis of the new endochronic theory for concrete which is discussed in Section 3.6.3. A key feature of the new endochronic theory is that the time scale (intrinsic time) is assumed to be a monotonically increasing function of the plastic strain increment. A detailed discussion of the derivation of the new endochronic theory is presented by Valanis and Read (4).



### 3.7.2 The First Endochronic Theory (Simple Model)

Consider a one-dimensional test of a material which is linear in stress versus strain and whose deformation is also a function of time. When an axial stress, which is a function of time, is applied to the material, the strain is a function of the total history of loading up to the present time. If the program of loading, here  $\sigma(t)$ , is continuous and differentiable then in a small interval of time  $d\tau$  the stress changes by  $\frac{d\sigma}{d\tau} d\tau$  this change in stress results in a change in strain  $d\epsilon$  and the relationship between these changes in stress and strain during this short interval in time is

$$d\epsilon(t) = C(t-\tau) \frac{d\sigma(\tau)}{d\tau} d\tau \quad 3.40$$

The total strain at time  $(t)$  is then

$$\epsilon(t) = \int_0^t C(t-\tau) \frac{d\sigma(\tau)}{d\tau} d\tau \quad 3.41$$

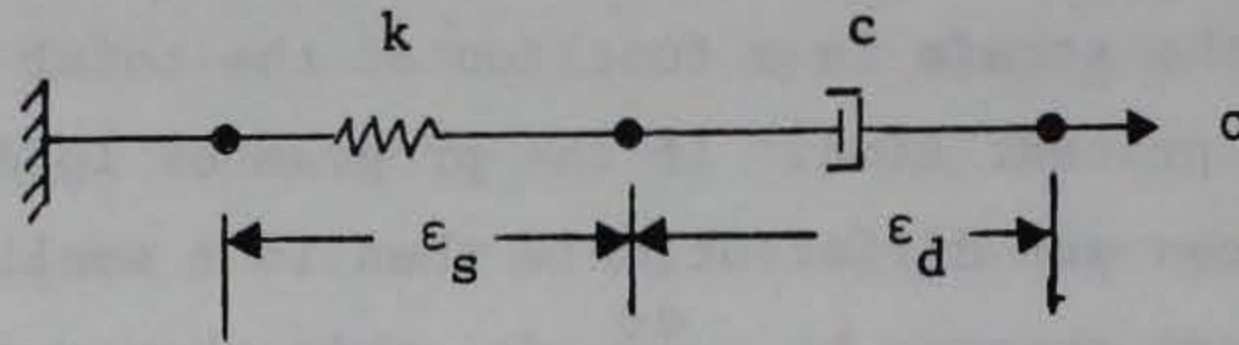
A material whose response can be reasonably approximated by (3.41) can be referred to as a linear hereditary material. If in reverse we consider a program of straining which results in a change in stress we obtain a relationship

$$\sigma(t) = \int_0^t k(t-\tau) \frac{d\epsilon(\tau)}{d\tau} d\tau \quad 3.42$$

The functions  $c(t)$  and  $k(t)$  are referred to as the creep function and relaxation function respectively and are properties of the material.  $C(t)$  can be thought of as the strain produced by a suddenly applied constant stress of unit magnitude, while  $k(t)$  represents the stress required to produce and maintain a constant strain of unit



magnitude. Linear hereditary material behavior can be approximated using a Maxwell model which is presented in the Figure below.



Maxwell Model

The change in strain for a differential change in time for the model is

$$d\epsilon = d\epsilon_s + d\epsilon_d$$

and since

$$\sigma = E \epsilon_s = C \dot{\epsilon}_d$$

Therefore

$$\dot{\epsilon}_s = \frac{\dot{\sigma}}{E} + \frac{\sigma}{C} \quad 3.43$$

When a Maxwell model is subjected to a suddenly applied constant strain  $\epsilon_0$ , and the corresponding value of stress is  $\sigma_0$  equation (3.43) can be integrated subject to these initial conditions to obtain

$$\sigma(t) = \sigma_0 e^{-Et/c} = E \epsilon_0 e^{-Et/c} \quad 3.44$$



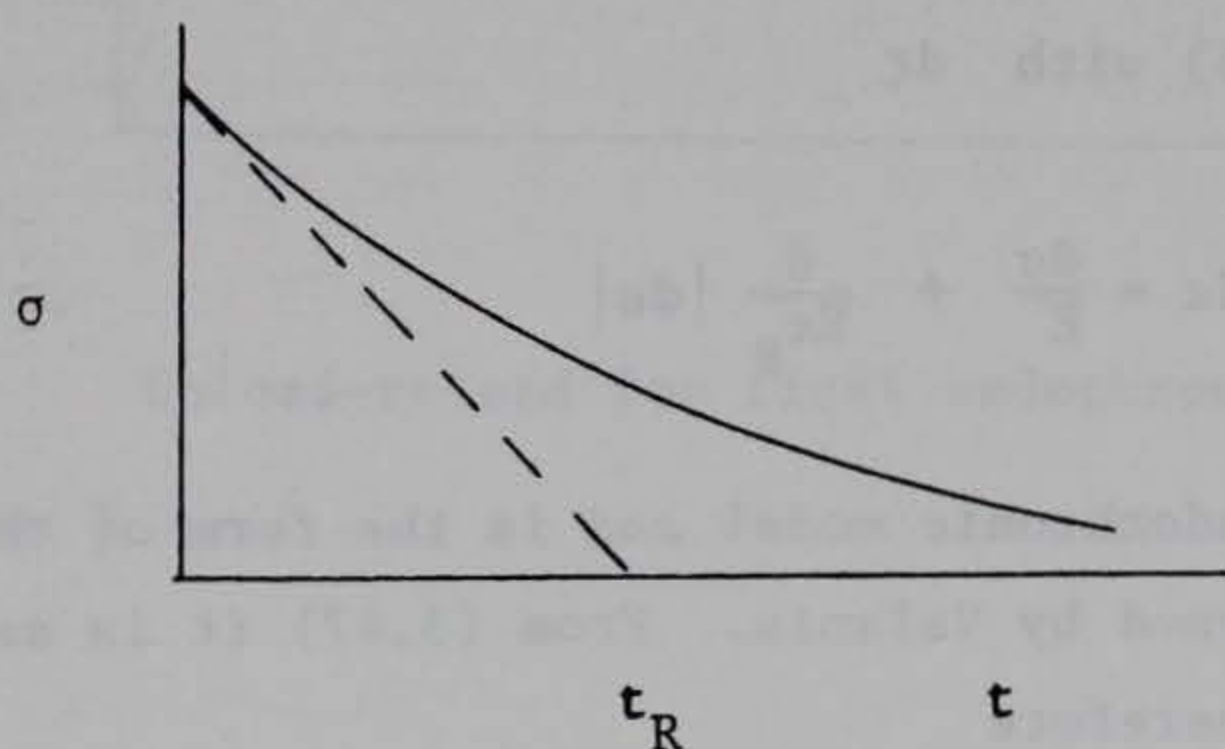
This defines the relaxation function for a Maxwell model. The rate of stress change is

$$\dot{\sigma}(t) = - \left( \frac{E\sigma_0}{C} \right) e^{-Et/c}$$

so that the initial rate (i.e. at  $t = 0^+$ ) is

$$\dot{\sigma}(0^+) = - \frac{E\sigma_0}{C}$$

The relaxation time is defined as the time for the stress to relax to zero if the relaxation rate continued at  $(\dot{\sigma}(t = 0^+))$ . Under these conditions the equation for stress relaxation is easily determined from the figure below



Stress relaxation in Maxwell Model

Therefore  $t_R$  is determined as

$$t_R = \frac{C}{E}$$



and is a property of the material. Equation (3.43) can be rewritten as

$$\frac{d\epsilon}{dt} = \frac{d\sigma}{E dt} + \frac{\sigma}{E t_R} \quad 3.45$$

or

$$d\epsilon = \frac{d\sigma}{E} + \frac{\sigma}{E t_R} dt \quad 3.46$$

If now we wish to use equation (3.46) to model static loading of a rate independent material, the time scale is unimportant and we could define another measure of time, (i.e. intrinsic time)  $\zeta$  such that the differential of intrinsic time could be written

$$d\zeta = |d\epsilon|$$

Replacing  $dt$  in (3.46) with  $d\zeta$

$$d\epsilon = \frac{d\sigma}{E} + \frac{\sigma}{E t_R} |d\epsilon| \quad 3.47$$

This is the simplest endochronic model and is the form of the first endochronic model proposed by Valanis. From (3.47) it is seen that for loading  $d\epsilon > 0$  therefore

$$\left. \frac{d\sigma}{d\epsilon} \right|_{d\epsilon > 0} = E \left( 1 - \sigma/E t_R \right) = E_L$$

while for unloading  $d\epsilon < 0$  and

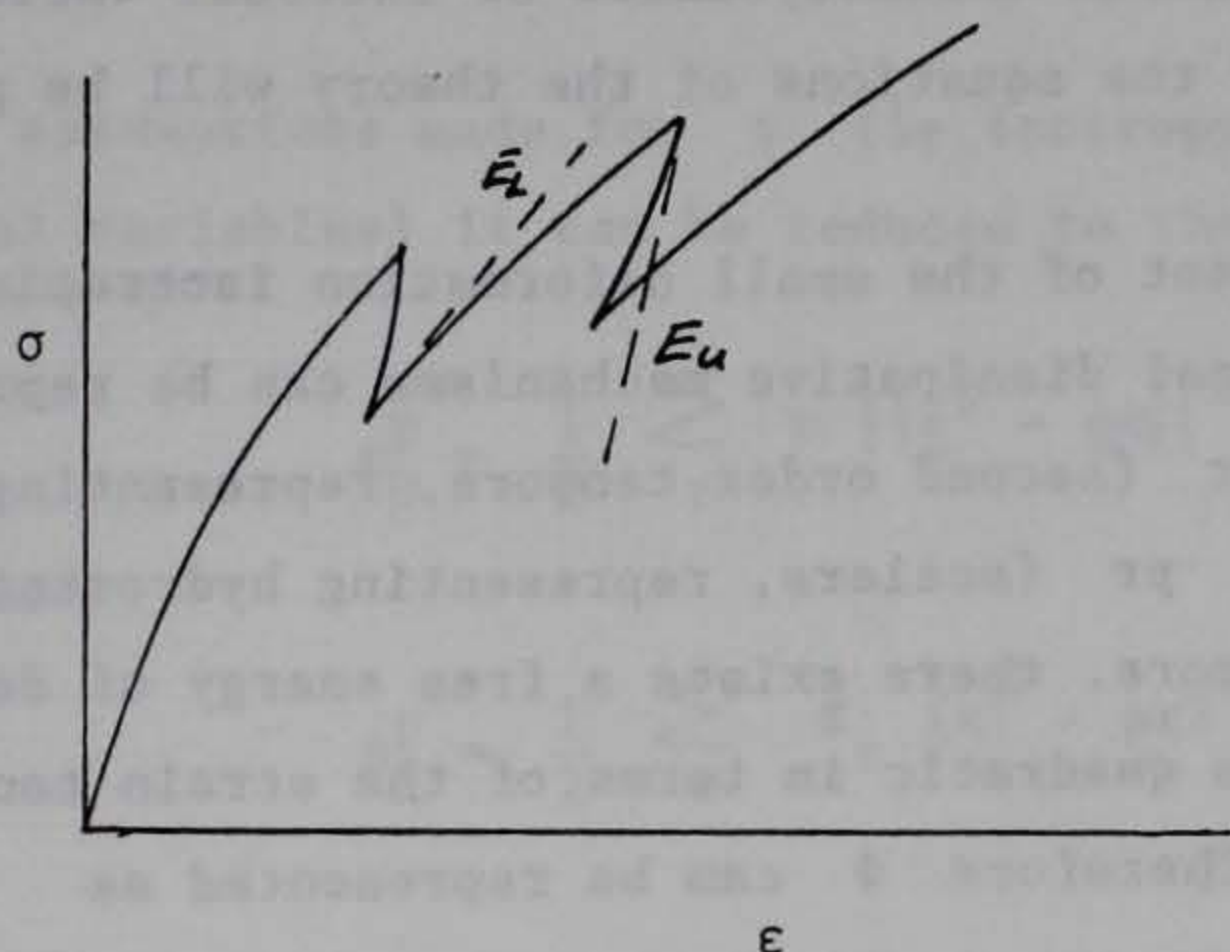
$$\left. \frac{d\sigma}{d\epsilon} \right|_{d\epsilon < 0} = E \left( 1 + \sigma/E t_R \right) = E_u$$



so that for  $\sigma > 0$  and large enough  $E_{t_R}$

$$0 < E_L < E_u$$

This formulation leads to a response as shown below and clearly violates Drucker's stability postulate for an unload reload cycle of stress. This problem was alleviated by Valanis [22] by introducing a new intrinsic time measure which will be discussed in Section 3.6.3.



Unload-reload for first endochronic model



### 3.7.3 The New Endochronic Theory

#### 3.7.3.1 Basic Equations

As mentioned previously the endochronic theory is based on the hypothesis that the current state of stress in a material is a linear functional of the entire history of deformation where the history is defined with respect to an intrinsic time which is a function of the plastic strain increment. The foundation of the theory is based on the theory of irreversible thermodynamics of internal variables, the derivation of some of the equations of the theory will be presented in this section.

For the development of the small deformation isotropic theory it is assumed that internal dissipative mechanisms can be represented by internal variables  $gr$  (second order tensors, representing deviatoric mechanisms) and  $pr$  (scalars, representing hydrostatic mechanisms). Furthermore, there exists a free energy of deformation function  $\psi$  which is quadratic in terms of the strain tensor and internal variables. Therefore  $\psi$  can be represented as

$$\psi = \psi_D + \psi_H$$

where

$$\psi_D = \psi_D(\underline{\epsilon}, gr)$$

$$\psi_H = \psi_H(\epsilon, pr)$$

The function  $\psi$  can be further decomposed into elastic  $\psi^e$  and plastic  $\psi^p$  parts such that

$$\psi_D^p = \psi_D^p(\underline{\epsilon}^p, gr)$$

$$\psi_H^p = \psi_H^p(\epsilon^p, pr)$$



The thermodynamic relations for the plastic parts of the constitutive equations are.

$$\underline{s} = \frac{\partial \psi_D^P}{\partial \underline{e}^P}$$

$$\sigma = \frac{\partial \psi_H^P}{\partial \epsilon^P}$$

Due to the assumptions made for  $\psi$  (ie isotropy, quadratic in strain and internal variables) it can be reduced to the canonical forms

$$\psi_D^P = \frac{1}{2} \sum_r \mu ||\underline{e}^P - g_r||^2$$

and

3.48

$$\psi_H^P = \frac{1}{2} \sum_r K_r (\epsilon^P - p_r)^2$$

A simple one dimensional model of an endochronic material is presented on the following page.

The force in each spring is

$$Q_r = \mu_r (\underline{e}^P - q_r)$$

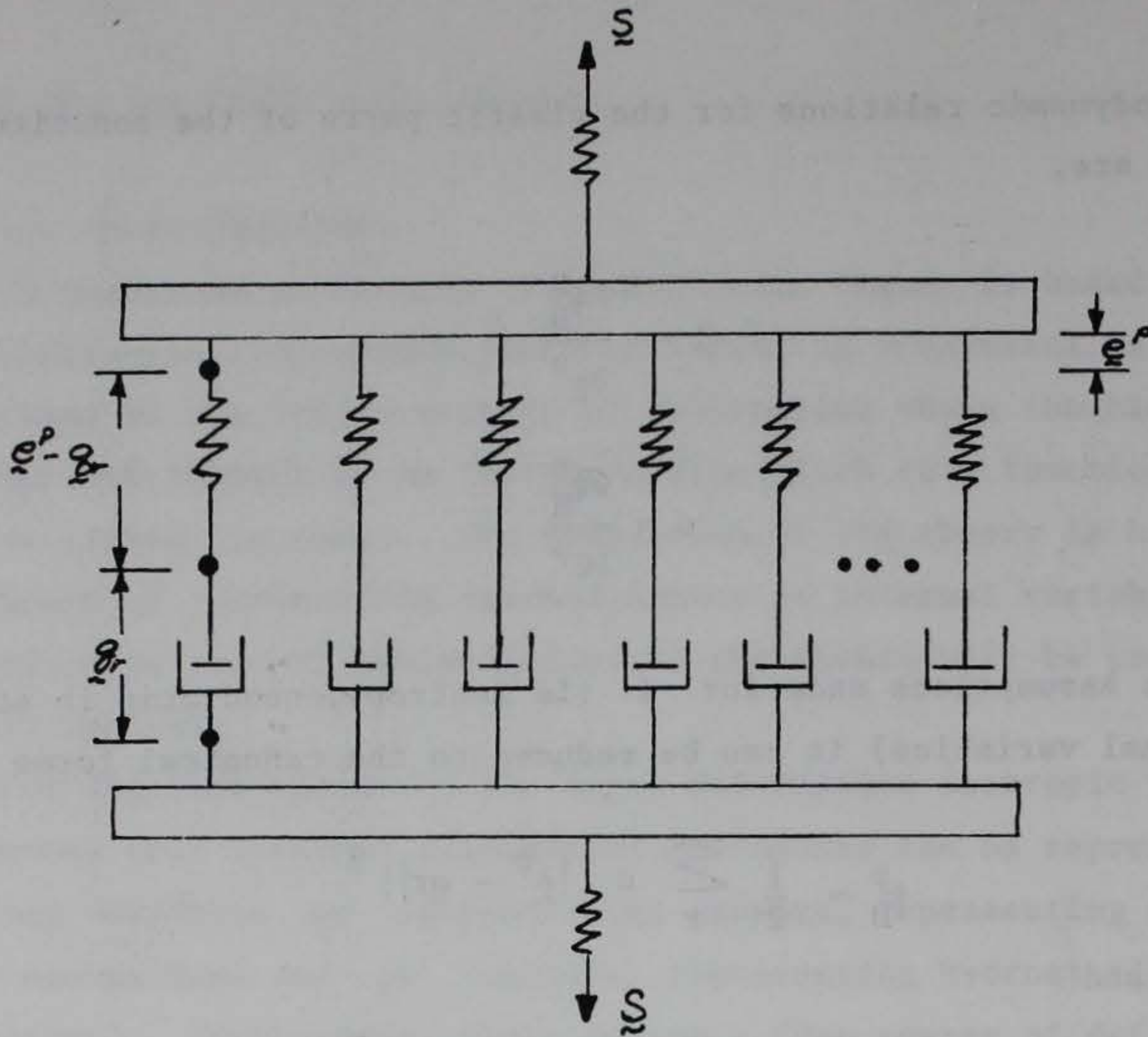
and the contribution to the free energy of endochronic element  $r$  is

$$\psi^r = \frac{1}{2} \mu_r (\underline{e}^P - g_r)^2$$

and therefore

$$\psi = \sum_r \psi^r$$





One-dimensional model with several endochronic elements

also

$$\frac{\partial \psi}{\partial \underline{e}^p} = \sum_r \mu_r (\underline{e}^p - \underline{q}_r) = \sum_r Q_r = \underline{S}$$

and

$$-\frac{\partial \psi}{\partial \underline{q}_r} = \mu_r (\underline{e}^p - \underline{q}_r) = Q_r$$

Similar equations can be written for the hydrostatic part.  $Q_r$  and  $P_r$  are internal stress type quantities and  $\underline{q}_r$  and  $\underline{p}_r$  internal strain type quantities with the characteristics that they cannot be measured as we normally measure stress or strain. Since the entropy for the system must be increasing



$$-\frac{\partial \psi_D^P}{\partial \underline{q}_r} d\underline{q}_r > 0 \quad ||d\underline{q}_r|| > 0$$

$$-\frac{\partial \psi_H^P}{\partial p_r} dp_r > 0 \quad |dp_r| > 0$$

and therefore expressing  $d\underline{q}_r$  , and  $dp_r$  , in rate forms we have.

$$-\dot{\underline{Q}}_r \cdot \dot{\underline{q}}_r > 0$$

$$-P_r \cdot \dot{p}_r > 0$$

For irreversible thermodynamics it is usually assumed that constitutive equations give the forces (stresses) as functions of the fluxes (strains) or vice versa. This assumption can be expressed as

$$\underline{Q}_r = b_r^{(1)} \dot{\underline{q}}_r$$

No sum on  $r$

$$P_r = b_r^{(2)} \dot{p}_r$$

In these expressions  $b_r^{(1)}$  and  $b_r^{(2)}$  play the same role that the scalar shear and bulk moduli play in relating elastic deviatoric stresses to deviatoric strains and hydrostatic stresses to volumetric strains.

From the previous expressions for  $\underline{Q}_r$  and  $P_r$  the "evolution" equations are developed as

$$\frac{\partial \psi_D^P}{\partial \underline{q}_r} + b_r^{(1)} \dot{\underline{q}}_r = 0$$

$$\frac{\partial \psi_H^P}{\partial p_r} + b_r^{(2)} \dot{p}_r = 0$$



Finally, recalling Equation 3.48.

$$\mu_r q_r + b_r^{(1)} \dot{q}_r = \mu_r \dot{\epsilon}^P$$

and

$$k_r p_r + b_r^{(2)} \dot{p}_r = k_r \dot{\epsilon}^P$$

or

$$\frac{\mu_r}{b_r^{(1)}} q_r + \frac{dq_r}{dt} = \mu_r \frac{d\epsilon^P}{dt}$$

and

$$\frac{k_r}{b_r^{(2)}} p_r + \frac{dp_r}{dt} = k_r \frac{d\epsilon^P}{dt}$$

For a rate independent material the independent variable in the above equation does not have to be real time, but must only be a monotonically increasing parameter which effectively records the history of loading of the material.

For the endochronic theory a parameter is chosen and defined as intrinsic time (Z) which is a function of plastic strain.

Replacing dt with dz the evolution equations become

$$\frac{\mu_r}{b_r^{(1)}} q_r + \frac{dq_r}{dz_s} = \mu_r \frac{d\epsilon^P}{dz_s}$$

and

$$\frac{k_r}{b_r^{(2)}} p_r + \frac{dp_r}{dz_H} = k_r \frac{d\epsilon^P}{dz_H}$$

These equations can be solved using Laplace Transform techniques with Z as the independent variable. This procedure for the deviatoric



evolution equation is presented here. First the Laplace transform of each term is taken.

$$L \left\{ \frac{\mu_r}{b_r(1)} \right\} Q_r + L \left\{ \frac{dQ_r}{dz_s} \right\} = L \left\{ \frac{\mu_r d\tilde{e}^P}{dz_s} \right\}$$

Therefore defining  $\alpha_r = \frac{\mu_r}{b_r(1)}$

$$\alpha_r Q_r(s) + s Q_r(s) - Q_r(0) = \mu_r s \tilde{e}^P(s) - \mu_r \tilde{e}^P(0)$$

and

$$\tilde{e}^P(0) = 0$$

Which can be rearranged to express  $Q_r(s)$  in terms of  $\tilde{e}^P(s)$

$$Q_r(s) = \frac{Q_r(0)}{(\alpha + s)} + \mu_r \frac{1}{(\alpha + s)} s \tilde{e}^P(s)$$

Taking the inverse transform of this equation, and observing that the second term is the product of two transforms and therefore its inverse is a convolution integral

$$Q_r = Q_r(0) \exp^{-\alpha_r z_s} + \mu_r \int_0^{z_s} \exp^{-\alpha_r (z_s - z'_s)} \frac{d\tilde{e}^P}{dz'_s} dz'_s$$

and similarly for the hydrostatic part.

$$P_r = P_r(0) e^{-\lambda_r z_H} + K_r \int_0^{z_H} e^{-\lambda_r (z_H - z')} \frac{d\epsilon^P}{dz'} dz'$$

$$\text{where } \lambda_r = \frac{K_r}{b_r(2)}$$



Finally since

$$\underline{s} = \sum_r Q_r \text{ and } \sigma = \sum_r P_r$$

$$\underline{s} = \sum_r Q_r(o) e^{-\alpha_r z_s} + \int_0^{z_s} \rho(z_s - z') \frac{d\underline{\epsilon}^P}{dz'} dz' \quad 3.48a$$

and

$$\sigma = \sum_r P_r(o) e^{-\lambda_r z_H} + \int_0^{z_H} \phi(z_H - z') \frac{d\epsilon^P}{dz'} dz'$$

where

$$\rho = \sum_r \mu_r e^{-\alpha_r z_s}$$

$$\phi = \sum_r \lambda_r e^{-\lambda_r z_H}$$

Equations (3.48a) are the general constitutive equations for the endochronic theory. It is important to note here that the development of the endochronic constitutive equations follows accepted conventional procedures and the concept of intrinsic time or pseudo time is not new (e.g. viscoelasticity applications). Furthermore, the exponential forms in 3.48a result from direct application of applied mathematics principles and not from arbitrary assumptions or curve fits of experimental data. The basic equations of the new endochronic plasticity theory can be expressed as

$$\underline{s} = \int_0^{z_s} \rho(z_s - z') \frac{d\underline{\epsilon}^P}{dz'} dz' \quad 3.49$$

$$\sigma = \int_0^{z_H} \phi(z_H - z') \frac{d\epsilon^P}{dz'} dz' \quad 3.50$$

$$d\underline{\epsilon}^P = d\underline{\epsilon} - \frac{d\underline{s}}{2\mu} \quad 3.51$$

$$d\epsilon^P = d\epsilon - \frac{d\sigma}{k} \quad 3.52$$



$$dz^2 = ||d\tilde{\epsilon}^P||^2 + k^2 |d\epsilon^P|^2 \quad 3.53$$

$$dz_s = \frac{dz}{F_s}, \quad dz_H = \frac{dz}{kF_H} \quad 3.56$$

where

$\tilde{S}$  = Deviatoric stress tensor.

$\sigma$  = Hydrostatic stress.

$( )^P$  = Denotes plastic components.

$\mu$  = Elastic shear modulus.

$K$  = Elastic bulk modulus.

$F_s$  = Shear hardening parameter.

$F_H$  = Hydrostatic hardening parameter.

$Z$  = Intrinsic time scale.

$Z_s$  = Intrinsic time for shear response.

$Z_H$  = Intrinsic time for hydrostatic response.

$k$  = A constant which determines the magnitude of shear volumetric coupling

$\rho(z), \phi(z)$  = Weakly singular kernel functions such that

$$\rho(0) = \phi(0) = \infty$$

but  $\rho(z)$  and  $\phi(z)$  are integrable

in the domain  $0 \leq Z < \infty$

Intrinsic time is analogous to recorded history parameters used in conventional plasticity. The form of  $dz$  in Equation (3.53) was developed based on the idea that the intrinsic time increment is given by the increment of the plastic strain path in plastic strain space and therefore could be written in general as

$$dz^2 = P_{ijkl} d\epsilon_{ij}^P d\epsilon_{kl}^P \quad 3.57$$

where the metric  $P$  is a fourth order, isotropic tensor with the general representation

$$P_{ijkl} = k_1^2 \delta_{ij} \delta_{kl} + K_2^2 \delta_{ik} \delta_{jl} \quad 3.58$$



Combining 3.57 and 3.58

$$dz^2 = k_1^2 d\epsilon_{ii}^p d\epsilon_{kk}^p + k_2^2 d\epsilon_{kj}^p d\epsilon_{kj}^p$$

or

$$dz^2 = k_1^2 |d\epsilon^p|^2 + k_2^2 ||d\tilde{\epsilon}^p||^2 \quad 3.59$$

which is equivalent to Equation (3.53) to within an immaterial multiplicative constant. The requirement that  $\rho(z)$  and  $\phi(z)$  in Equations 3.49 and 3.50 be weakly singular kernels, essentially comes from the need for the new model to predict closed hysteresis loops under unloading - reloading cycles (this was a major problem with the first model). This idea is demonstrated in the following example. Consider a typical plot of simple shear stress  $S$  versus shear strain  $\gamma$  as shown in Figure 3.15. It is assumed in this figure that a yield point exists but that the slope of the stress strain curve is continuous throughout. If we wish to plot shear stress versus plastic shear strain  $\gamma_p$ , as shown in Figure 3.15, the  $S, \gamma$  axes can be rotated as shown and the slope of the curve at  $\gamma_p = 0$  will be infinite.

The endochronic theory for this case will yield

$$s = \int_0^{z_r} \rho(z_s - z') \frac{d\gamma}{dz'} dz'$$

Therefore

$$\left. \frac{ds}{d\gamma^p} \right|_{\gamma^p = 0} = \rho(z_s - z') = \infty$$

which requires  $\rho(0) = \infty$ .



The series expansion for  $\rho$

$$\rho = \sum_r \mu_r e^{-\alpha_r z_s}$$

satisfies the requirement  $\rho(0) = \infty$ .

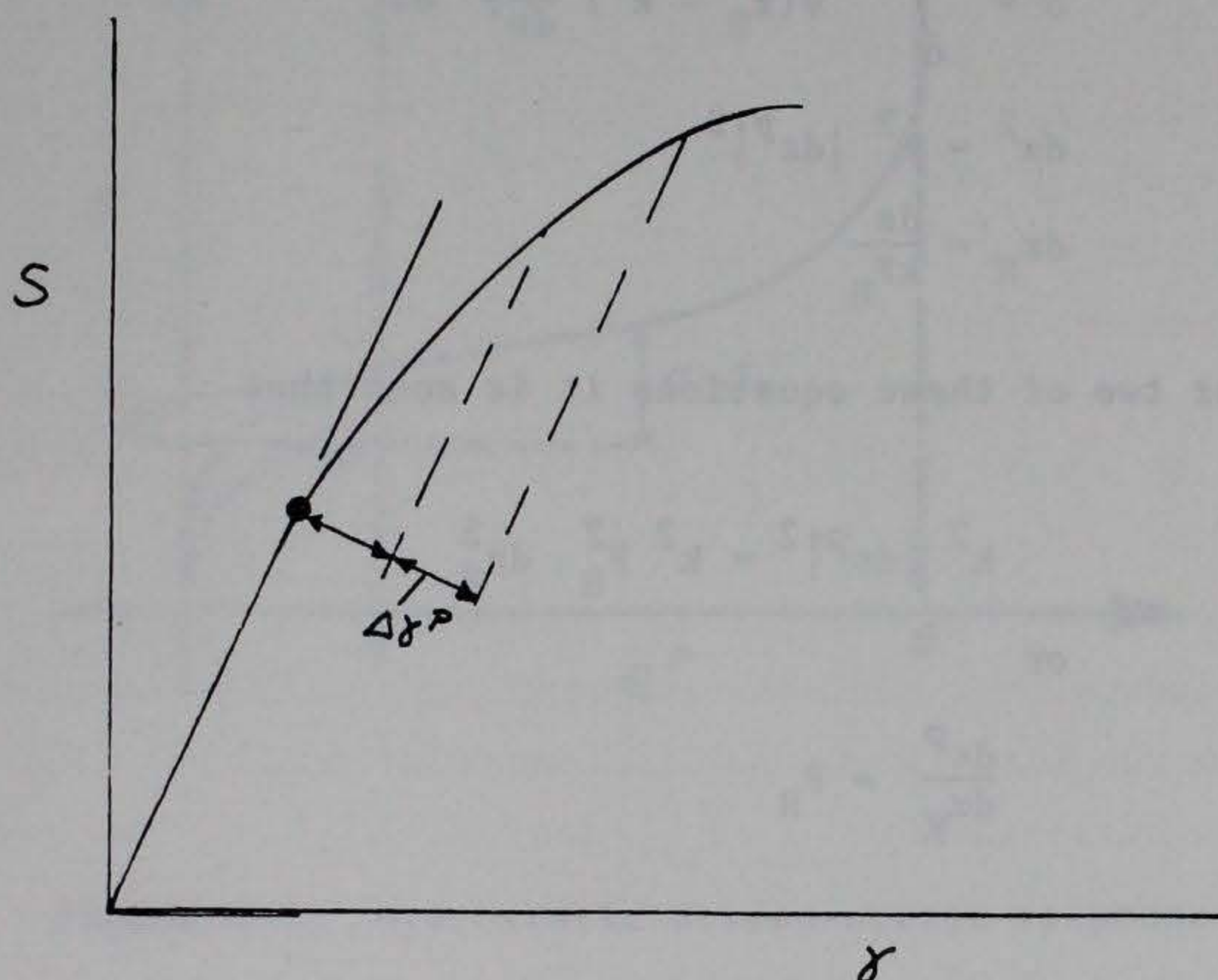


Figure 3.15 Simple shear stress-strain response features

The parameters which must be calibrated in the theory can be divided into three groups: parameters which describe pure hydrostatic response, parameters which describe the shear volumetric coupling, and those parameters which describe the deviatoric (shear) response. The calibration of these parameters will be discussed in the following sections.

### 3.7.3.2 Hydrostatic Response

Typical response features of concrete to pure hydrostatic stress were discussed in Chapter 2. The endochronic functions  $\phi(Z_H)$  and  $F_H$  must be defined and calibrated to capture these key hydrostatic



stress-volumetric strain features of the concrete in the stress range of interest for a particular problem. Assuming that the reference state is the natural state then under monotonic pure hydrostatic loading conditions the following basic equations apply:

$$\sigma = \int_0^{z_H} \phi(z_H - z') \frac{d\epsilon^P}{dz'} dz$$

$$dz^2 = k^2 |d\epsilon^P|^2$$

$$dz_H = \frac{dz}{kF_H}$$

From the latter two of these equations it is seen that

$$k^2 |d\epsilon^P|^2 = k^2 F_H^2 dz_H^2$$

or

$$\frac{d\epsilon^P}{dz_H} = F_H$$

therefore

$$\sigma = \int_0^{z_H} \phi(z_H - z') F_H (\epsilon^P) \Big|_{z'} dz' \quad 3.60$$

Equation 3.60 provides the functional form to be used for calibrating  $\phi$  and  $F_H$  to predict general hydrostatic response features. A typical hydrostatic stress strain curve is presented in Figure 3.16. The effect of the hardening function  $F_H$  is best seen in this figure where a hardening function  $F_H = 1$  leads to plastic flow at a stress  $\sigma_0$ . It is assumed that the general form of  $F_H$  should be

$$F_H = e^{\beta \epsilon^P}$$



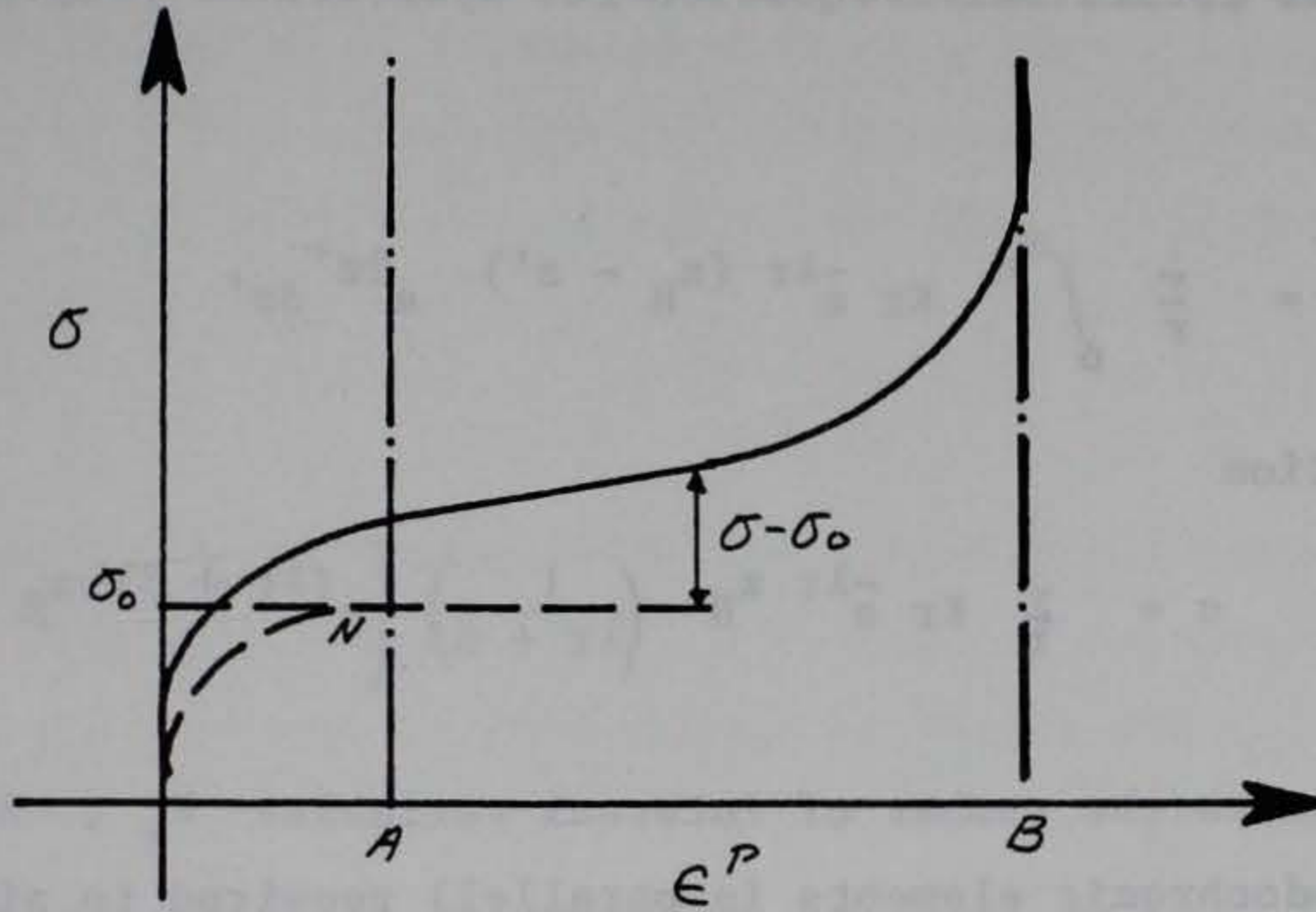


Figure 3.16 Hydrostatic stress-strain response feature

then expressing  $e^{\beta\epsilon^P}$  in a power series expansion and only retaining linear terms we have

$$F_H = 1 + \beta\epsilon^P$$

From Equations 3.53 and 3.56 it is easily shown that (since for hydrostatic response  $d\epsilon^P = dz_s = 0$ ) .

$$dz_H = \frac{d\epsilon^P}{F_H} = \frac{d\epsilon^P}{1 + \beta\epsilon^P}$$

which upon integration leaves

$$z_H = \frac{1}{\beta} \ln (1 + \beta\epsilon^P)$$



therefore

$$e^{\beta z_H} = 1 + \beta \epsilon^P = F_H$$

Also it is noticed that pure hydrostatic response is independent of  $k$ . Therefore the constitutive equation for hydrostatic response becomes

$$\sigma = \sum_r \int_0^{z_H} K_r e^{-\lambda_r (z_H - z')} e^{\beta z'} dz'$$

or upon integration

$$\sigma = \sum_r K_r e^{-\lambda_r z_H} \left( \frac{1}{\lambda_r + \beta} \right) \left[ e^{(\lambda_r + \beta) z_H} - 1 \right]$$

Where  $r$  represents the number of internal variables  $K_r$ ,  $\lambda_r$  (or the number of endochronic elements in parallel) required to simulate the hydrostatic response to the desired level of accuracy. Therefore there are three parameters  $K_r$ ,  $\lambda_r$ , and  $\beta$  which must be determined based on pure hydrostatic test results.

The calibration of the parameters  $K_r$ ,  $\lambda_r$ , and  $\beta$  is accomplished by first defining a stress  $\sigma^*$  such that

$$\sigma^* = \frac{\sigma}{F_H} = \frac{\sigma}{1 + \beta \epsilon^P}$$

and since for the hydrostatic test  $\beta \epsilon^P = \beta z_H$  and if we assume  $1 + \beta \epsilon = e^{\beta \epsilon^P}$  we have

$$\sigma^* = \sum_r \frac{K_r}{(\beta + \lambda_r)} \left[ 1 - e^{-(\beta + \lambda_r) z_H} \right]$$

so the two curves of Figure 3.16 can now be used.  $\beta$  is determined from the straight line portion of the second branch of the hydrostat from the requirement that



$$\sigma = \sigma_o (1 + \beta \epsilon^P)$$

Next a plot is made of  $(\sigma_o - \sigma^*)$  versus  $Z_H$  (here  $Z_H = \frac{1}{\beta} \ln (1 + \beta \epsilon^P)$ ) based on hydrostatic data (note  $\beta$  is known) and values of  $K_r$  and  $\lambda_r$  are selected which give the desired fit to this curve.



### 3.7.3.3 Shear Response.

The shear response is defined by Equations 3.49, 3.53, and 3.56 which require determination of the response functions  $\rho(Z_s)$  and  $F_s$  along with the coupling constant  $k$ . As discussed in Chapter 2 the hardening characteristics of concrete in shear are very sensitive to the confining stress level, also this hardening is dependent on the direction of loading in the deviatoric plane which can be defined by the similarity angle  $\theta$ . Therefore it is assumed that

$$F_s = F_s(\sigma, \theta)$$

and  $F_s$  can be determined from a series of hydrostatic pure deviatoric tests as discussed in Chapter 2. The simplest and most direct way to determine the shear parameters is from a triaxial test in the  $\pi$  plane (ie shear under zero hydrostatic stress). However, there were no tests performed like this for the concretes reported herein and therefore hydrostatic pure deviatoric test results must be used. Changes in hydrostatic plastic strain  $\epsilon^P$  due to increments of shear stress result due to change in  $Z$  as defined in Equation (3.53) and the corresponding change in  $Z_H$  from Equation 3.56. If the kernel  $\phi(Z_H)$  in Equation 3.50 is approximated with a Dirac  $\delta$  function

$$\phi(Z_H) = K_o \delta(Z_H)$$

Equation 3.50 results in

$$\sigma = K_o \cdot \frac{d\epsilon^P}{dz_H} \quad 3.61$$

and for pure hydrostatic loading

$$\sigma = K_o (1 + \beta \epsilon^P) \quad 3.62$$

Therefore Equation (3.62) is essentially a linear hardening model. Equation 3.62 seems reasonable especially for the initial portion of



the hydrostat (ie prior to signs of locking up) and if  $\sigma_1$  is the mean stress during a pure deviatoric load increment we can write

$$d\epsilon^P = \frac{\sigma_1}{K_0} dz_H \quad 3.63$$

Therefore as  $dz_H$  increases due to application of pure shear increments, due to equations 3.53 and 3.56,  $d\epsilon^P$  will increase as defined by Equation 3.63. Defining the intrinsic time  $dZ$  in terms of a parameter  $d\zeta$  such that

$$d\zeta_s = ||d\epsilon^P||, \quad d\zeta_H = |d\epsilon^P|$$

a differential relationship between  $d\zeta_s$  and  $dy$  can be derived, where  $dy$  is the change in the intrinsic time in addition to the change caused by pure hydrostatic loading. This expression is

$$\frac{d\zeta_s}{dy} = \left[ \frac{2ay}{1 + 2ay} \right]^{\frac{1}{2}} \quad 3.64$$

where

$$a = \frac{k_o \beta}{k\sigma_1}$$

and

$y = Z - Z^1$ ,  $Z^1$  is the value of  $Z$  at the completion of the pure hydrostatic branch of loading.

Equation 3.64 can be integrated to give

$$\zeta_s = \frac{1}{2a} \left[ x \sqrt{x^2 - 1} - \log \left( x + \sqrt{x^2 - 1} \right) \right] \quad 3.65$$



where  $X = 1 + \frac{K_o \beta}{\sigma_1} \zeta_H^s$ ,  $\zeta_H^s$  is the hydrostatic strain caused by shear loading at constant pressure.

Finally if  $W$  is defined as the increase in  $Z_s$  after the hydrostatic loading such that.

$$W = Z_s - Z_s^1$$

a differential relation between  $d\zeta_s$  and  $dW$  can be determined as

$$\frac{d\zeta_s}{dW} = F_s \left[ \frac{2aF_s W}{1 + 2aF_s W} \right]^{\frac{1}{2}} \quad 3.66$$

which governs  $d\zeta_s$  during loading in a deviatoric section after hydrostatic loading. Since

$$F_s = F_s(\sigma, \theta)$$

$F_s$  will remain constant during loading in a deviatoric section at constant  $\theta$ . Finally for this type of loading Equation (3.49) can be written for a pure shear path as

$$\tau = \int_0^W \rho(W - W^1) \frac{d\gamma^p}{dW^1} dW^1$$

and

$$\tau = \frac{FS}{\sqrt{2}} \int_0^W \rho(W - W^1) \left[ \frac{2aF_s W}{1 + 2aF_s W} \right]^{\frac{1}{2}} dW^1 \quad 3.67$$



Valanis (20, in an appendix) shows that

$$\lim_{z \rightarrow \infty} \int_0^z \rho(z - z') \left[ \frac{2aF_s z'}{1 + 2aF_s z'} \right]^{\frac{1}{2}} dz' = M_{\infty}$$

where

$$M(\sqrt{2}\gamma^P) = \int_0^{\sqrt{2}\gamma^P} \rho(z') dz'$$

and

$$M_{\infty} = M(\infty) < \infty$$

therefore the shear stress behaves asymptotically to values  $\tau^{\infty}$  at different levels of mean stress and can be written

$$\tau^{\infty} = \frac{F_s}{\sqrt{2}} M_{\infty}$$

and the form of  $F_s$  can be determined by comparing  $\tau^{\infty}$  at different mean stress levels.

$$\frac{\tau^{\infty}(\sigma_a)}{\tau^{\infty}(\sigma_b)} = F_s$$

The functional form of  $\rho$  is determined by solving Equation (3.67) numerically knowing  $\tau$  and  $a$  (from experiments).



## Chapter 4

### Comparison of Model Predictions Versus Test Results

#### 4.1 General

The Fracture Energy Based Model (FEBM) and the Endochronic Concrete Plasticity Model (ECPM) are calibrated for the concrete materials used in the verification tests, and stress strain response predictions are discussed and compared with test results in this chapter. The concept and operational details of the WES Constitutive Driver (WCD), which is used in this study, is discussed in Section 4.2. Calibration of the constitutive models and an analysis of predicted and measured results are presented in section 4.3 WES Tests, 4.4 Colorado Tests and 4.5 Eindhoven Tests. Most emphasis is placed on comparisons for the WES Tests, because a more extensive calibration test program was conducted at WES for the  $f'_c = 6.5$  ksi concrete. In essence a calibration parameter sensitivity study is presented in this chapter. The objective of this sensitivity study is not to optimize the values of calibration parameters but rather to discuss the consistency between parameter values determined from a calibration tests and those values of the parameters required for better model predictions.

#### 4.2 WES-Constitutive Driver

The original concept for the WES Constitutive Driver (WESCD) was based on the need to develop a consistent method to better evaluate predictions from large scale dynamic finite-element codes. As discussed in section 1.1, the effectiveness and efficiency of the constitutive model was obscured by the overall size and complexity of these large scale problems. Therefore, the concept was to develop and implement a few rational and consistent constitutive models in an easy to use modular software package, with graphics, and a significant experimental data base. This would allow the objective evaluation of different models and also provide an assessment method which



could be used to improve the predictive capabilities of specific models. The WESCD consists of the following modules:

1. User defined loading histories for driving constitutive models in principal stress, or strain space or under mixed control.
2. Constitutive models.
3. Solution models for numerical integration of the constitutive equations.
4. Experimental data base.

The WESCD is written in Fortran 77 with graphic components based on Hewlett Packard-Advanced Graphics Package. The user interface for the WESCD is described in the following 4 "pages".

#### Page 1: Selection of Concrete Model

The first page, shown in Figure 4.1 allows the user to choose the constitutive model of interest.

<p>WES - VICKSBURG, MS</p> <p><b>CONSTITUTIVE DRIVER</b></p> <p>Version 002 - 1988</p>			
<p>CONSTITUTIVE MODELS</p>			
Leon Assoc. Flow	<input type="checkbox"/>	<input type="checkbox"/>	Endochronic
Leon Nonassoc. Flow	<input type="checkbox"/>	<input type="checkbox"/>	Weidlinger
Ottosen	<input type="checkbox"/>	<input type="checkbox"/>	Chen & Han
Klisinski	<input type="checkbox"/>		
			<div style="border: 1px solid black; display: inline-block; padding: 2px 5px;">REPEAT</div> <div style="border: 1px solid black; display: inline-block; padding: 2px 5px;">NEXT</div> <div style="border: 1px solid black; display: inline-block; padding: 2px 5px;">EXIT</div>

Figure 4.1 Constitutive model selection



### Page 2: Selection of Material Parameters

The second page, shown in Figure 4.2, displays some of the characteristic features of the constitutive model of interest. In Figure 4.2 deviatoric and meridian sections of the loading and failure

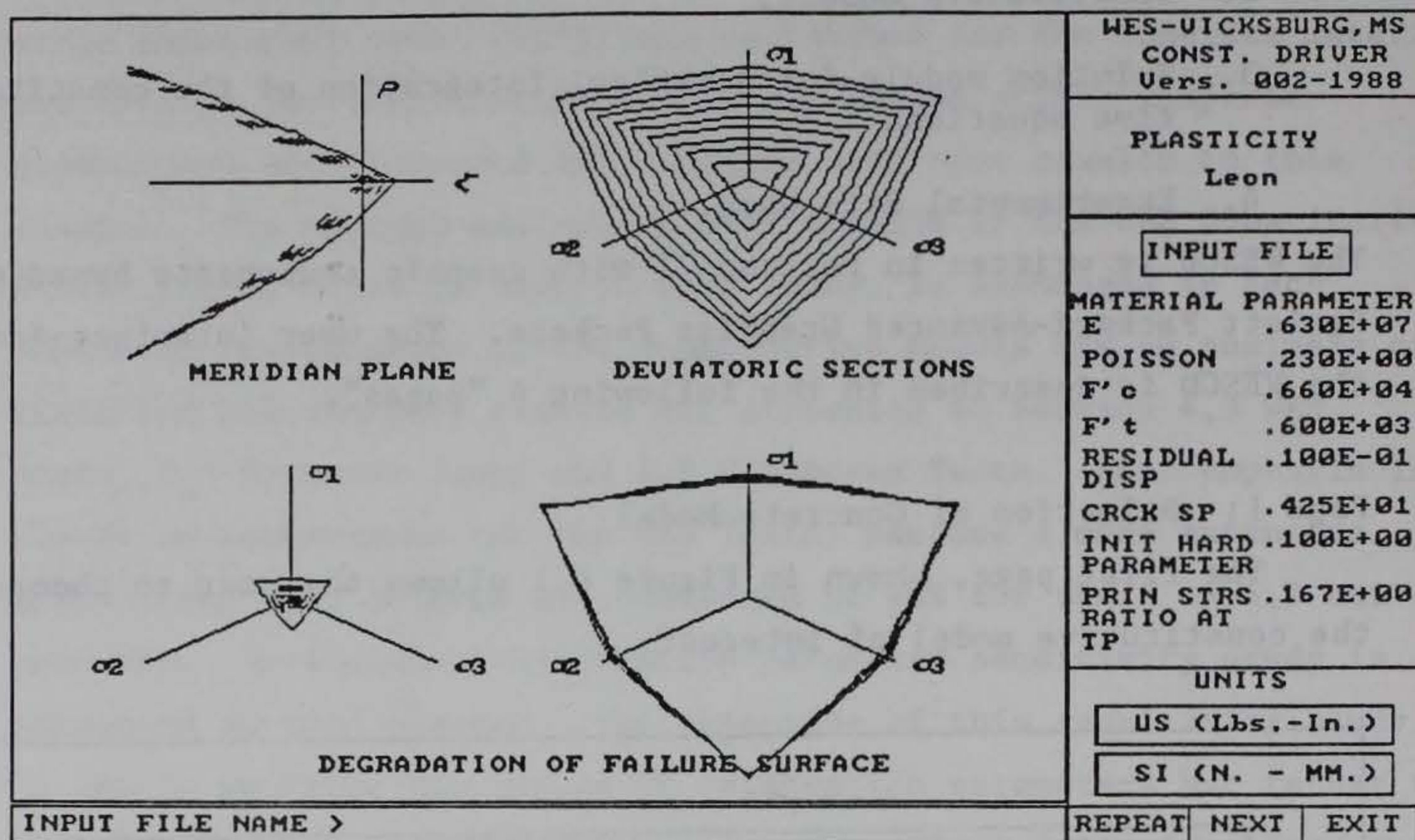


Figure 4.2 Constitutive model parameters

surfaces for the FEBM are presented with indications where the surfaces degrade during softening. Also on this page the user is prompted to specify certain material parameters for the concrete. To specify or vary the internal parameters (e.g. hardening parameters for the FEBM) the user must make changes within the constitutive model module.

### Page 3: Selection of Load History

This page, as shown in Figure 4.3, prompts the user to select either stress, strain, or mixed control. The primary reason for the



development of a mixed control formulation was for simulation of tests such as uniaxial strain.

<div style="text-align: center;"> <div>STRESS CONTROL</div> <div>MIXED CONTROL</div> <div>STRAIN CONTROL</div> </div> <p>NOTE: ONLY STRAIN CONTROL AVAILABLE FOR ENDOCHRONIC &amp; WEIDLINGER MODELS</p>	<b>WES-VICKSBURG, MS</b> <b>CONST. DRIVER</b> <b>Vers. 002-1988</b>									
	<b>PLASTICITY</b> <b>Leon</b>									
	<b>LOAD HISTORY</b> <input type="checkbox"/> DATA BASE <input type="checkbox"/> NOT AVAILABLE									
	<div style="text-align: center;"><b>ECHO</b></div> <table border="1" style="width: 100%;"> <tr> <td><math>\sigma_z - \sigma_{xy}</math></td> <td><math>\epsilon_z - \epsilon_{xy}</math></td> </tr> <tr> <td><math>\tau_o - \sigma_o</math></td> <td><math>\lambda_o - \epsilon_o</math></td> </tr> <tr> <td><math>\tau_o - \theta_s</math></td> <td><math>\lambda_o - \theta_e</math></td> </tr> <tr> <td><math>\sigma_z - \epsilon_{zxy}</math></td> <td><math>\tau_o - \lambda_o</math></td> </tr> <tr> <td><math>\sigma_o - \epsilon_o</math></td> <td><math>\theta_s - \theta_e</math></td> </tr> </table>	$\sigma_z - \sigma_{xy}$	$\epsilon_z - \epsilon_{xy}$	$\tau_o - \sigma_o$	$\lambda_o - \epsilon_o$	$\tau_o - \theta_s$	$\lambda_o - \theta_e$	$\sigma_z - \epsilon_{zxy}$	$\tau_o - \lambda_o$	$\sigma_o - \epsilon_o$
$\sigma_z - \sigma_{xy}$	$\epsilon_z - \epsilon_{xy}$									
$\tau_o - \sigma_o$	$\lambda_o - \epsilon_o$									
$\tau_o - \theta_s$	$\lambda_o - \theta_e$									
$\sigma_z - \epsilon_{zxy}$	$\tau_o - \lambda_o$									
$\sigma_o - \epsilon_o$	$\theta_s - \theta_e$									
<div style="display: flex; justify-content: space-between;"> <span>REPEAT</span> <span>NEXT</span> <span>EXIT</span> </div>										

Figure 4.3 Control mode

User input histories can be defined or a history in the Experimental Data Base Module can be selected. A variety of plotting options are available for presenting experimental and predicted results.

#### Page 4: Solution of Response History Analysis

This page Figure 4.4 presents the results of the analysis for the particular plotting option selected. For the example presented in Figure 4.4, axial stress versus axial and circumferential strain are presented for the FEBM compared to experimental results. A rescaling option is available to force identical scales on different plots for comparison purposes.



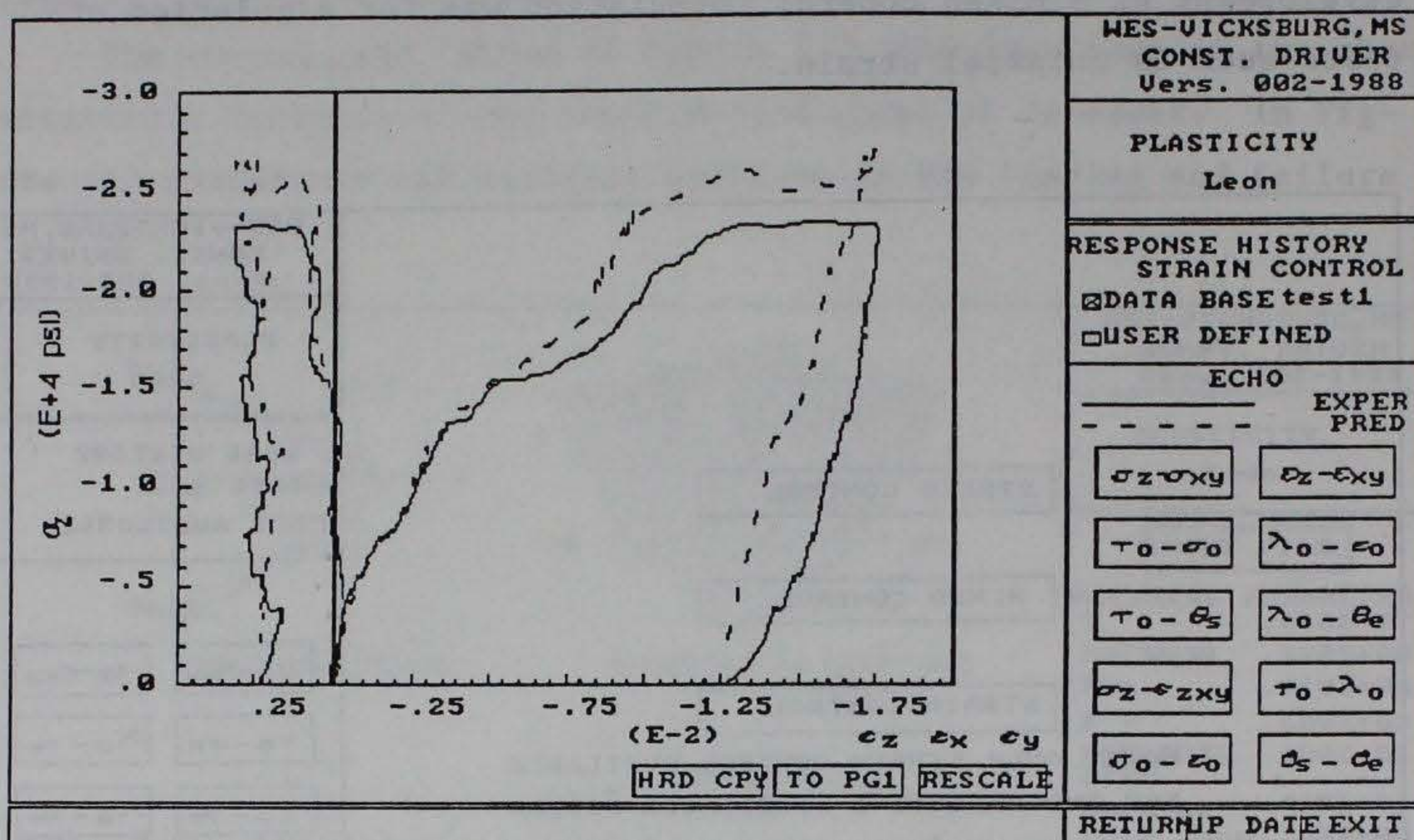


Figure 4.4 Model prediction versus test results



### 4.3 Comparison of Model Predictions with WES Tests

#### 4.3.1 General

Verification tests conducted at WES include: VT6.5-1 through VT6.5-5 and VT2-1. These tests were briefly discussed in Section 2.7 and will be discussed in more detail here along with comparisons with predicted results from the FEBM and the ECPM.

#### 4.3.2 The FEBM Test VT6.5-1

Test VT6.5-1 provided excellent data for model verification, as all four strain gages were effective throughout the entire test. The as measured axial stress versus axial and circumferential strains are presented in Figure 4.5. From pretest and posttest micrometer measurements the permanent axial strain was 0.0133 in/in. and the permanent circumferential strain was 0.0067 in/in. Based on these observations the axial and circumferential strain gages indicated in Figure 4.5 were selected for use in model comparisons. The difference in measured strains in Figure 4.5 is due to normal variation in electrical measurements, slight differences in bonding for the different gages, and probably most due to the fact that the different 1/2-in. gages are bonded to different percentages of aggregate and cement paste at the different locations. The effect of confining stresses up to approximately 40 ksi on the response of these gages has been evaluated through calibration tests on steel cylinders and found to be negligible.

Based on the calibration tests for the  $f'_c = 6.5$  ksi concrete the model parameters for the FEBM were determined as:

Elastic Modulus	$E_o = 6,300$ ksi
Poisson's ratio	$\nu = 0.23$
Compressive Strength	$f'_c = 6.6$ ksi
Tensile Strength	$f'_t = 0.6$ ksi
Rupture Displacement	$U_r = 0.01$ in.



Crack Spacing

 $h_t = 4.25 \text{ in.}$ 

Initial Hardening Parameter

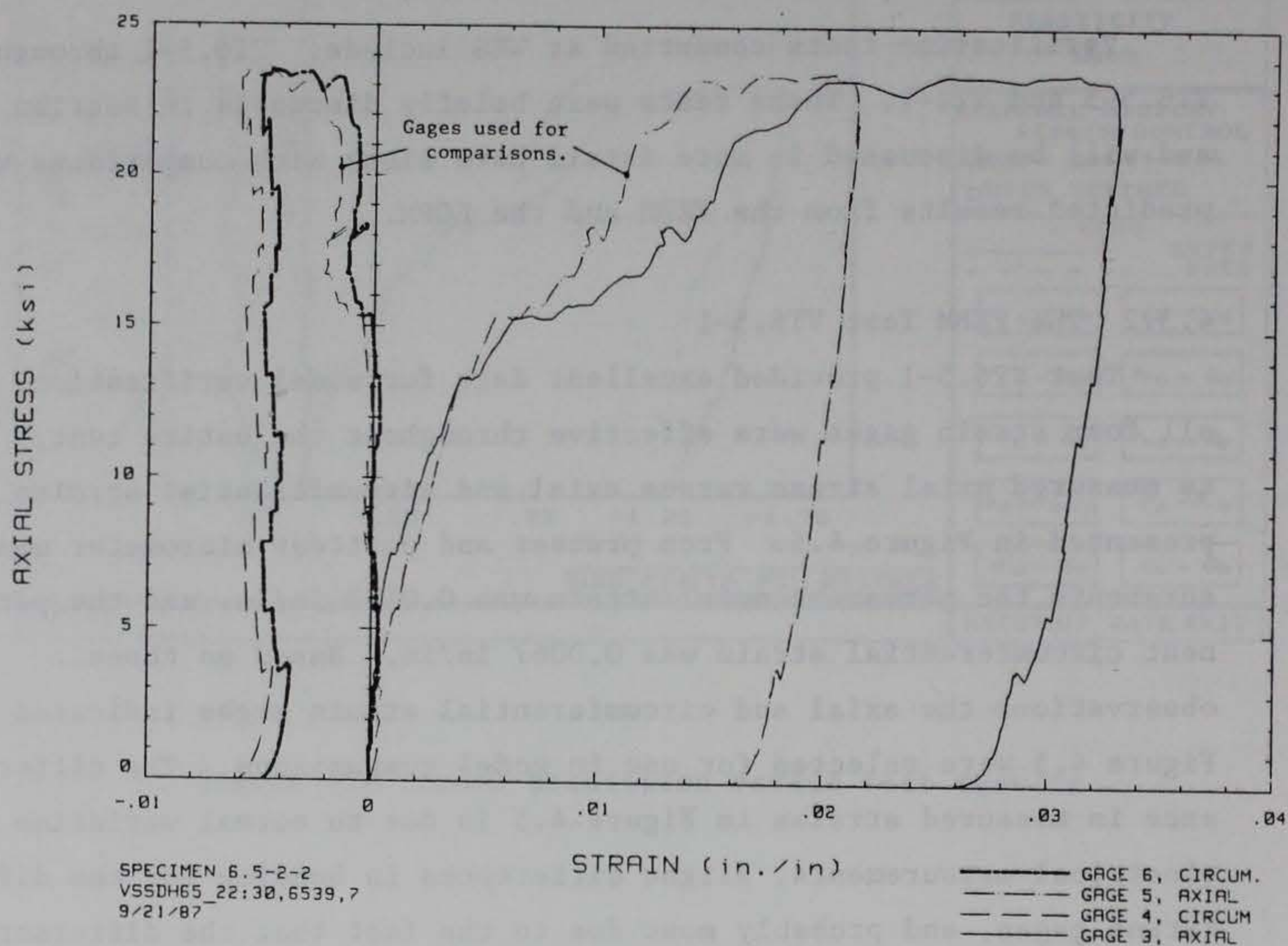
 $k_o = 0.1$ 

Figure 4.5 Actual test data for VT6.5-1

Hardening coefficients for calculation of ductility

parameter  $\chi_p$ 

$$A_H = 5.9$$

$$B_H = 13.0$$

$$C_H = -0.6$$

Coefficients for calculation of friction parameter ( $M_q$ ) for non-associated flow.

$$D = 12.0$$



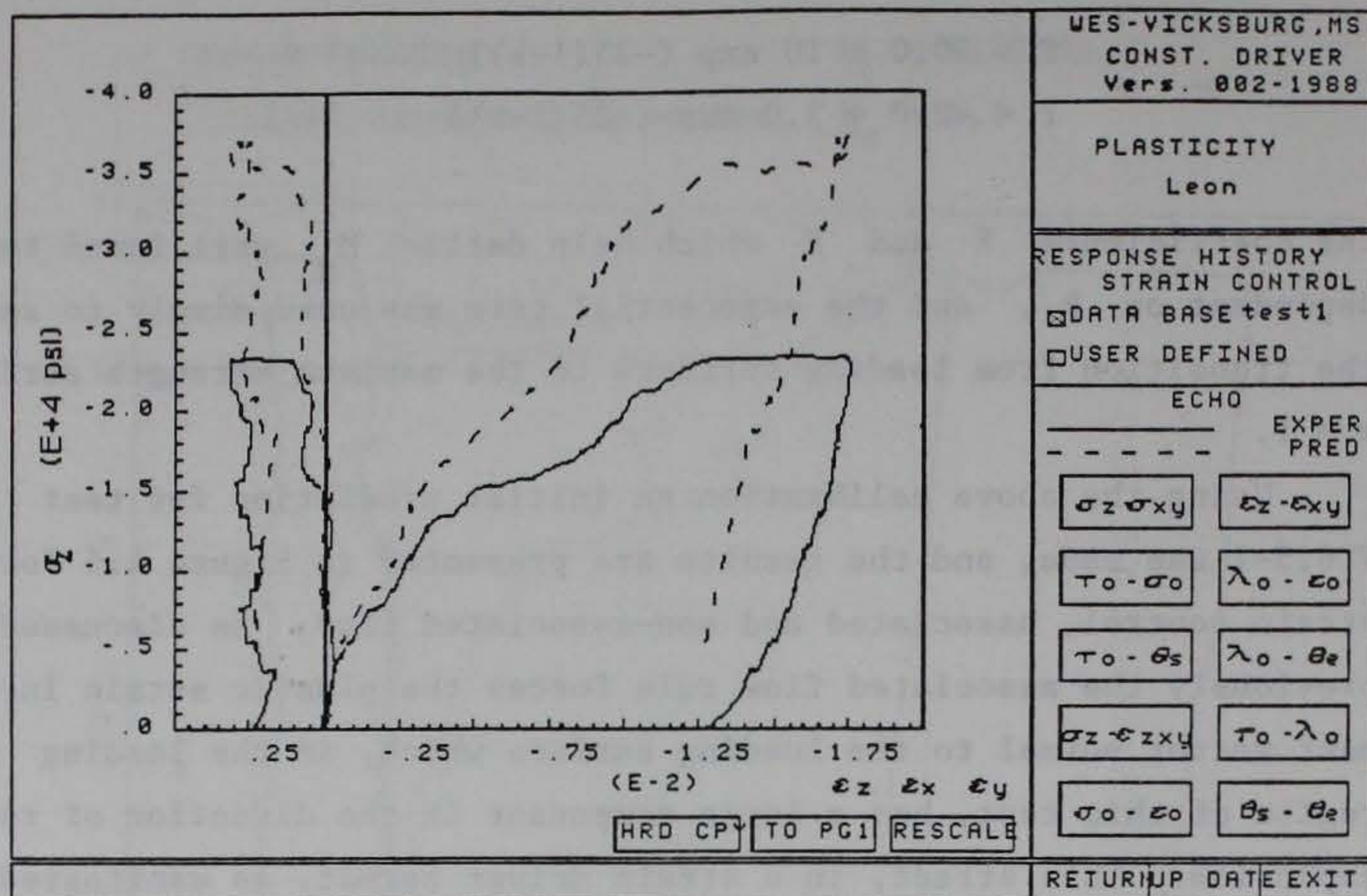
$$E = 20.0 + 10 \exp (-25(1-k))$$

$$F = -2.0 + 3.0 \exp (-25(1-k))$$

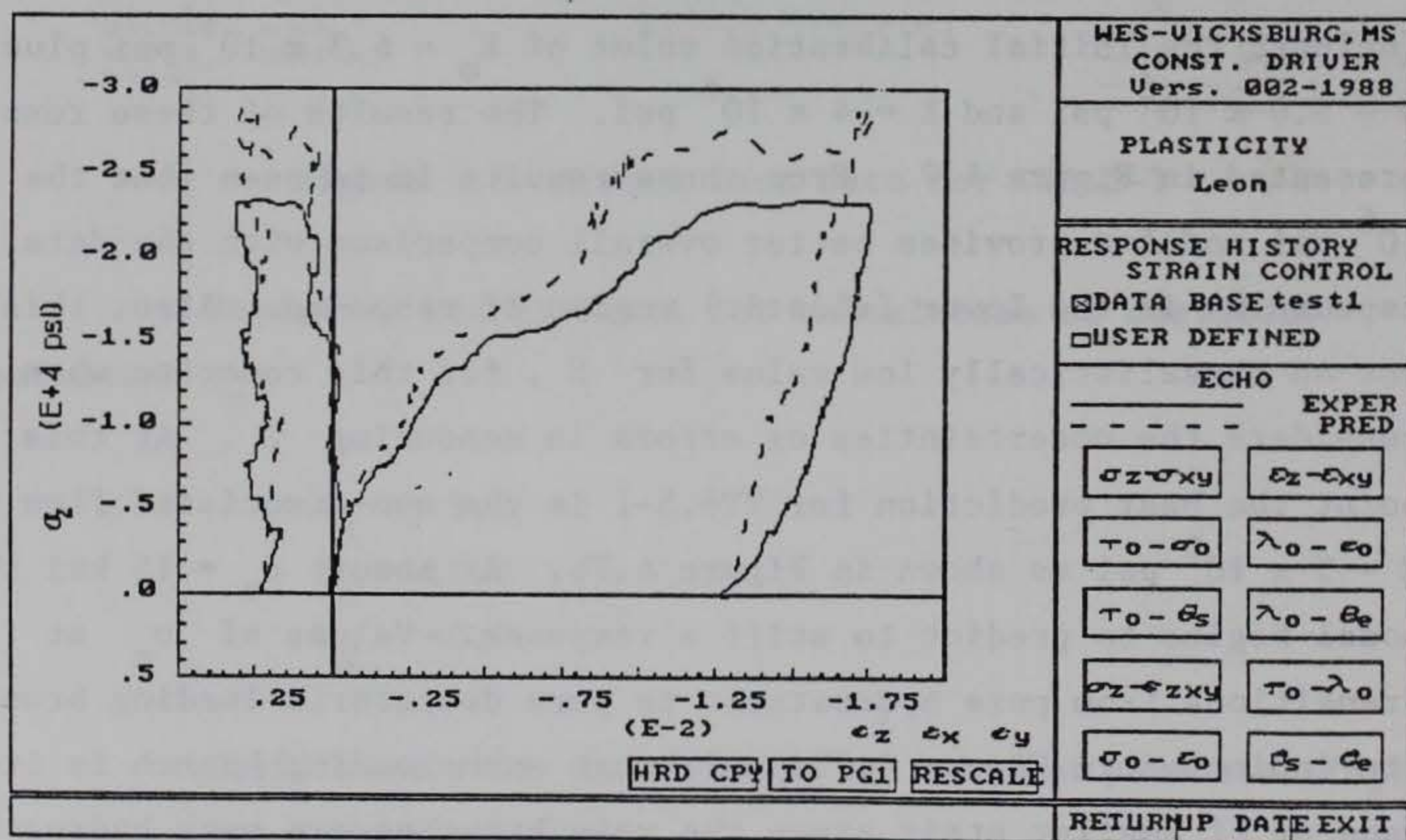
The coefficients  $E$  and  $F$  which help define  $M_q$  were found to be dependent on  $k$ , and the exponential term was used simply to smooth the transition from loading surfaces to the maximum strength surface  $k = 1$ .

Using the above calibration an initial prediction for test VT6.5-1 was made, and the results are presented in Figure 4.6 for strain control, associated and non-associated flow. As discussed previously the associated flow rule forces the plastic strain increment vector normal to the loading surface which, in the loading region of this test, has a large component in the direction of radial expansion. This effect, in a strain driven format, is manifested by overpredicting the confining stress. The non-associated flow prediction compares much better with test data as shown in Figure 4.6b and this version will be used in the following. Three values of elastic modulus were used to determine prediction sensitivity. These values included the initial calibration value of  $E_o = 6.3 \times 10^6$  psi plus  $E = 5.0 \times 10^6$  psi and  $E = 4 \times 10^6$  psi. The results of these runs are presented in Figure 4.7. From these results it is seen that the  $5 \times 10^6$  psi modulus provides better overall comparison with the data, especially in the lower (elastic) region of response. Also, this is not an unrealistically low value for  $E$ , for this concrete when one considers the uncertainties or errors in measuring  $E$ . At this point the best prediction for VT6.5-1 is the non-associated flow with  $E = 5 \times 10^6$  psi as shown in Figure 4.7b. At about  $\sigma_z = 15$  ksi the model begins to predict to stiff a response. Values of  $\sigma_z$  at transitions from pure hydrostatic to pure deviatoric loading branches are indicated in Figure 4.7b. Although each loading branch is itself made up of smaller stair steps the main branches are pure hydrostatic (0-1, 2-3, 4-5), which primarily compact and stiffen the material, and pure deviatoric (1-2, 3-4, 5-6) which shear the material and also





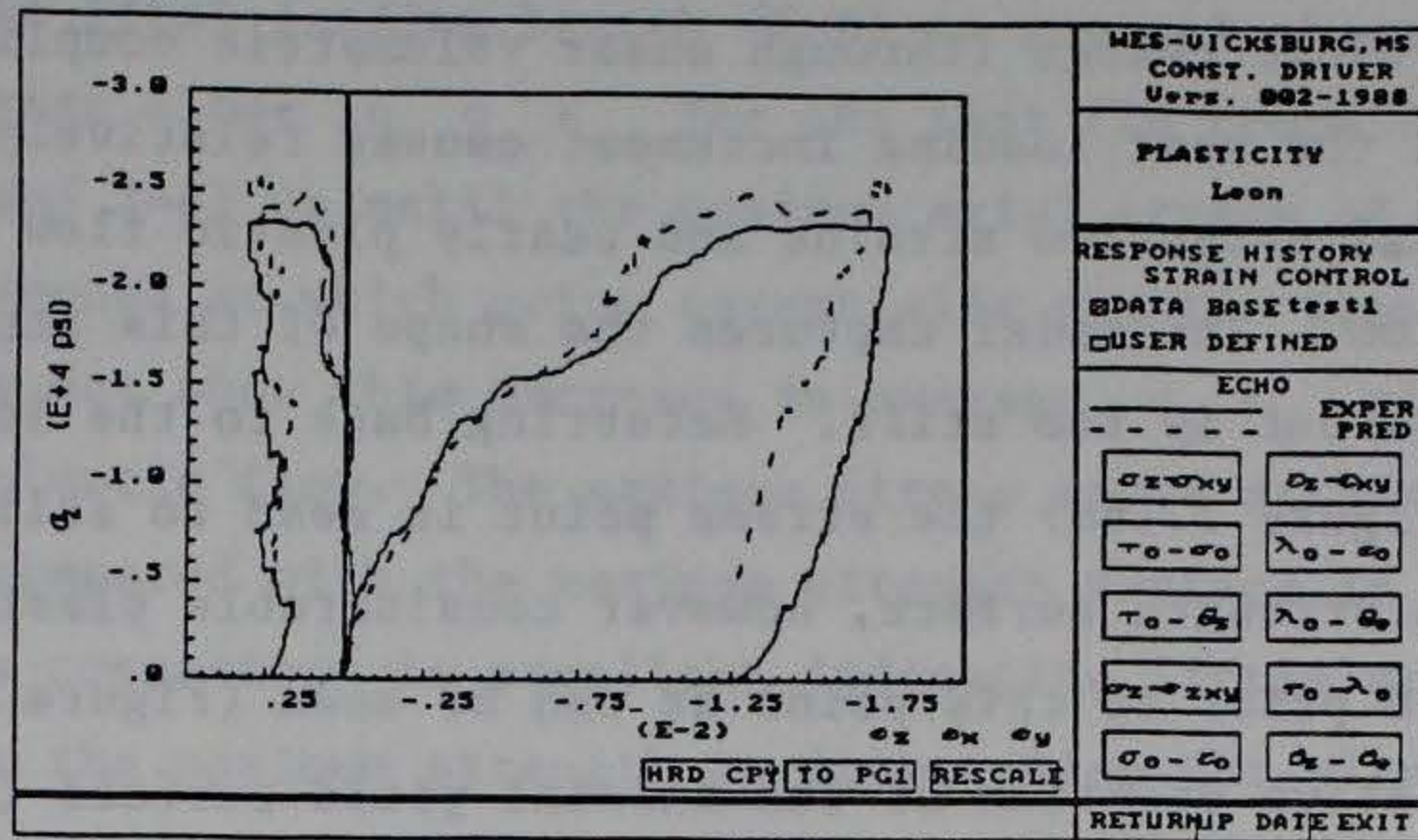
(a) associated flow



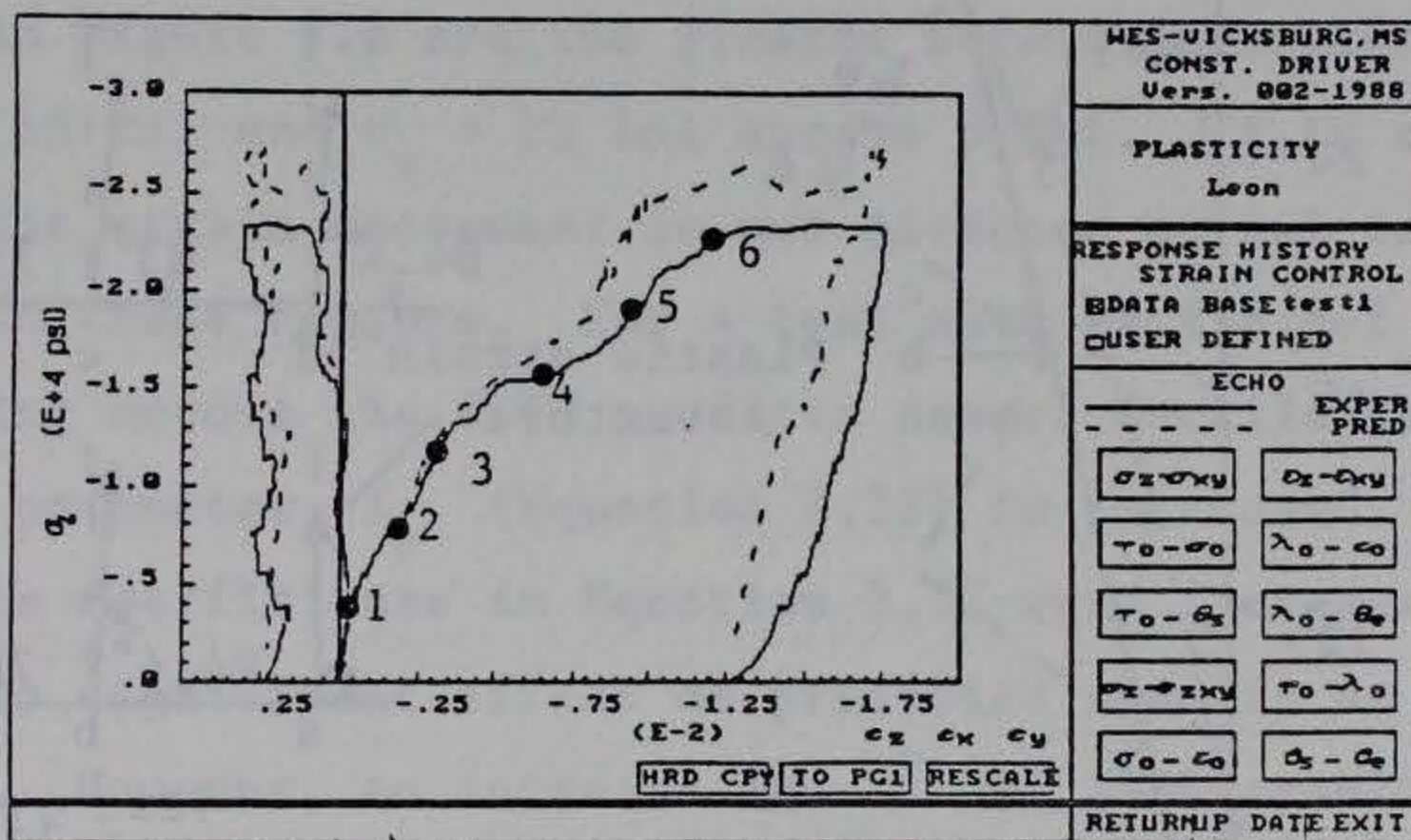
(b) non-associated flow

Figure 4.6 FEBM-VT6.5-1, initial calibration

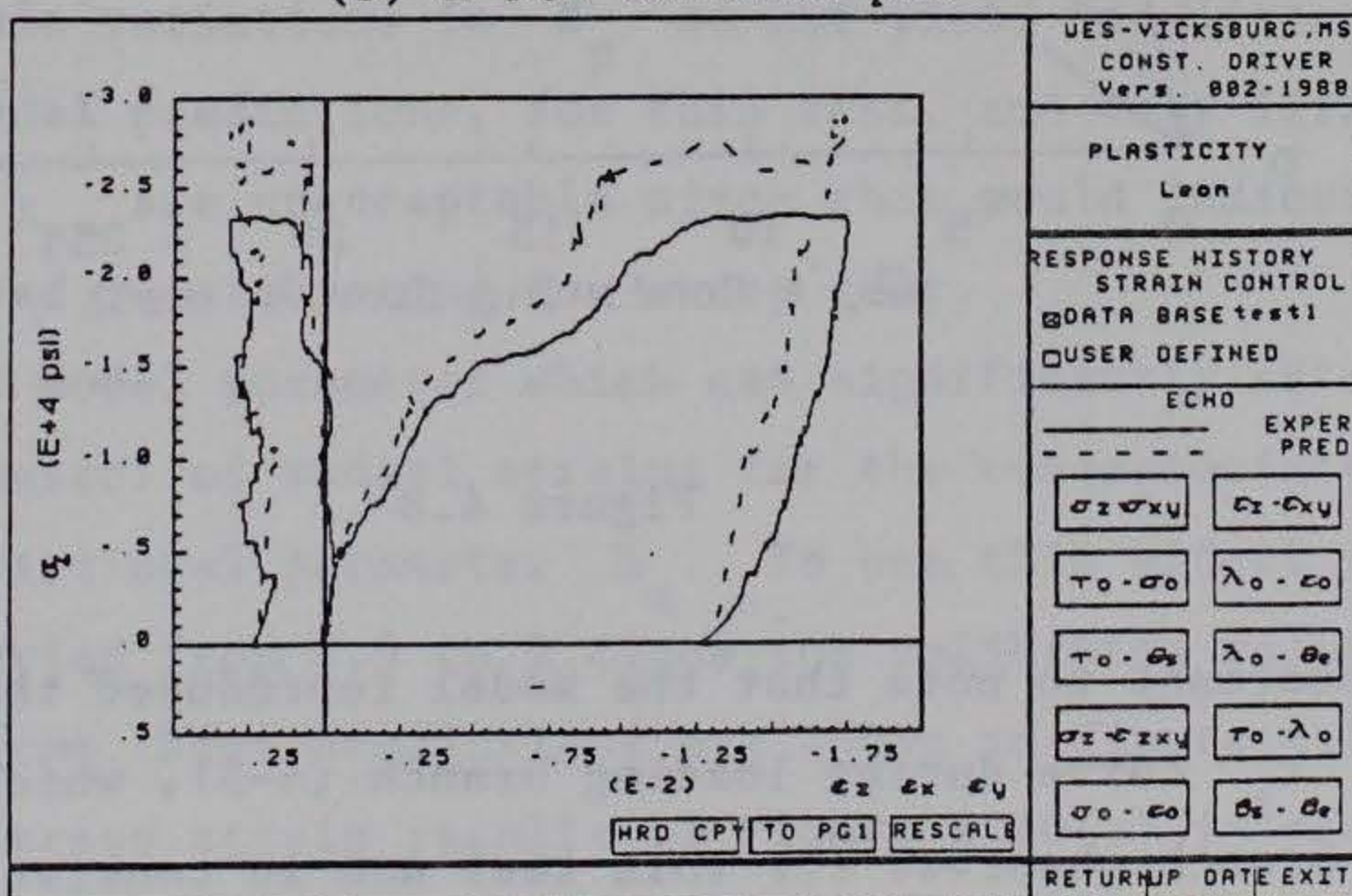




(a) E=4.0 million psi



(b) E=5.0 million psi



(c) E=6.3 million psi

Figure 4.7 FEBM-VT6.5-1, varying E



cause volume change (through shear volumetric coupling). At  $\sigma_z \approx 15$  ksi, the next loading increment causes relatively large increments of radial extension strains and nearly plastic flow in the axial direction. The model captures the shape of this stress strain response but is too stiff. Referring back to the load path for this test (Figure 2.16a) the stress point is seen to still be inside the maximum strength surface, however considerable plastic loading has occurred prior to this point as can be seen (Figure 4.8) referring to the relative position of the initial yield surface ( $k = k_0$ ).

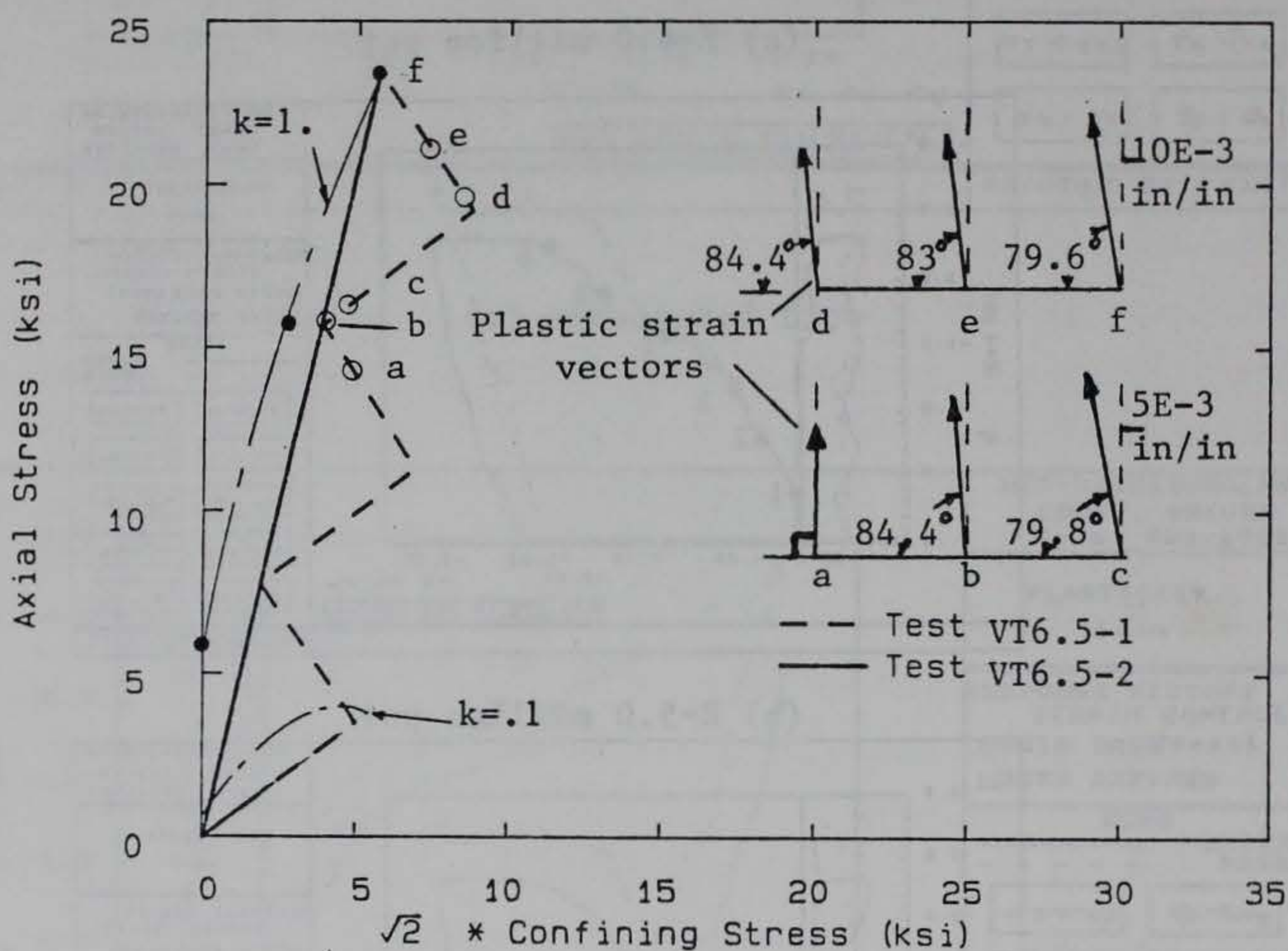


Figure 4.8

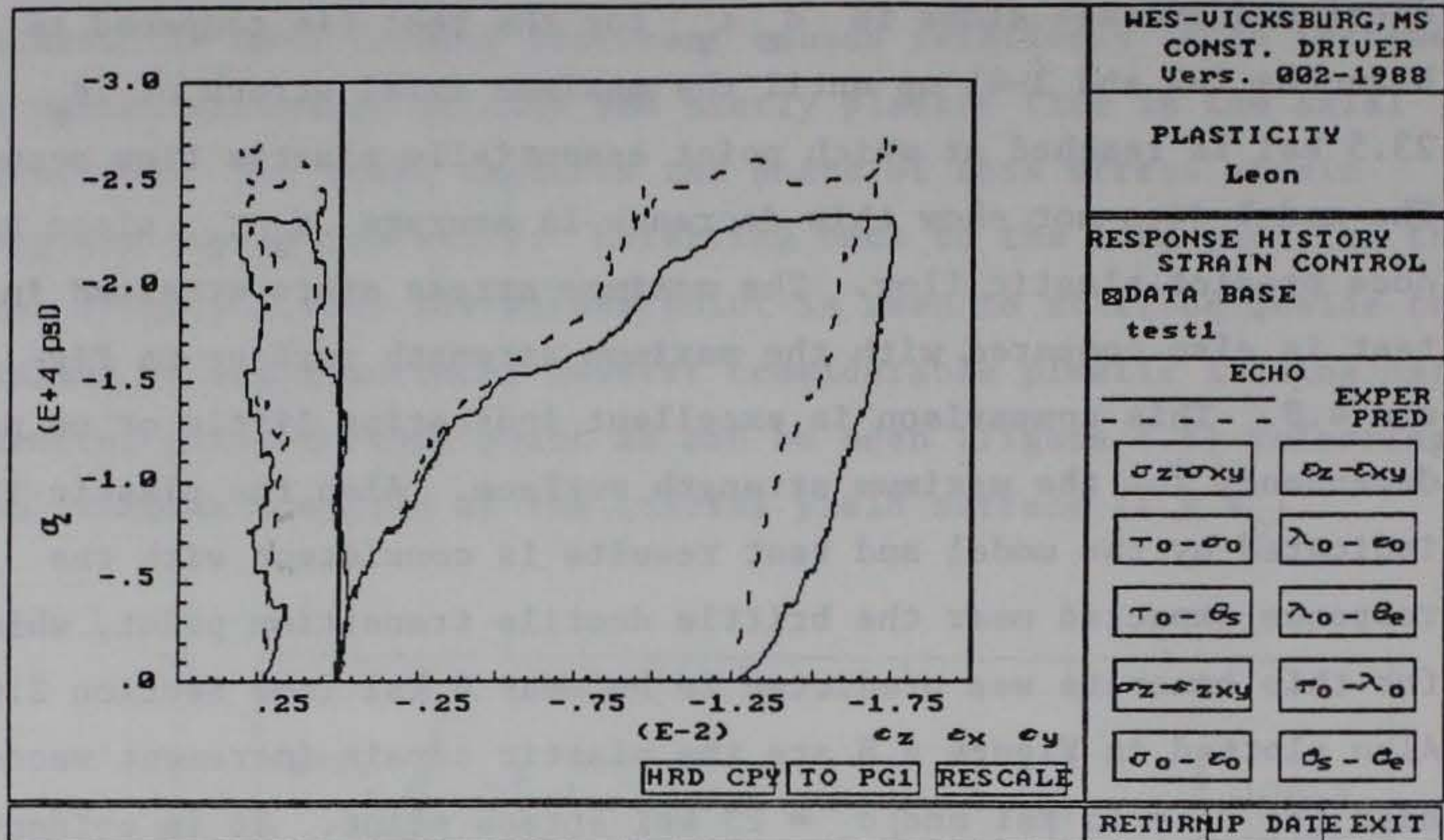
It is important to note that the model reproduced the concave form of the  $\sigma_z - \epsilon_z$  curve during loading branch (4-5), which is the only concave branch observed for this test and is consistent with the expected hydrostatic response in this region as discussed in



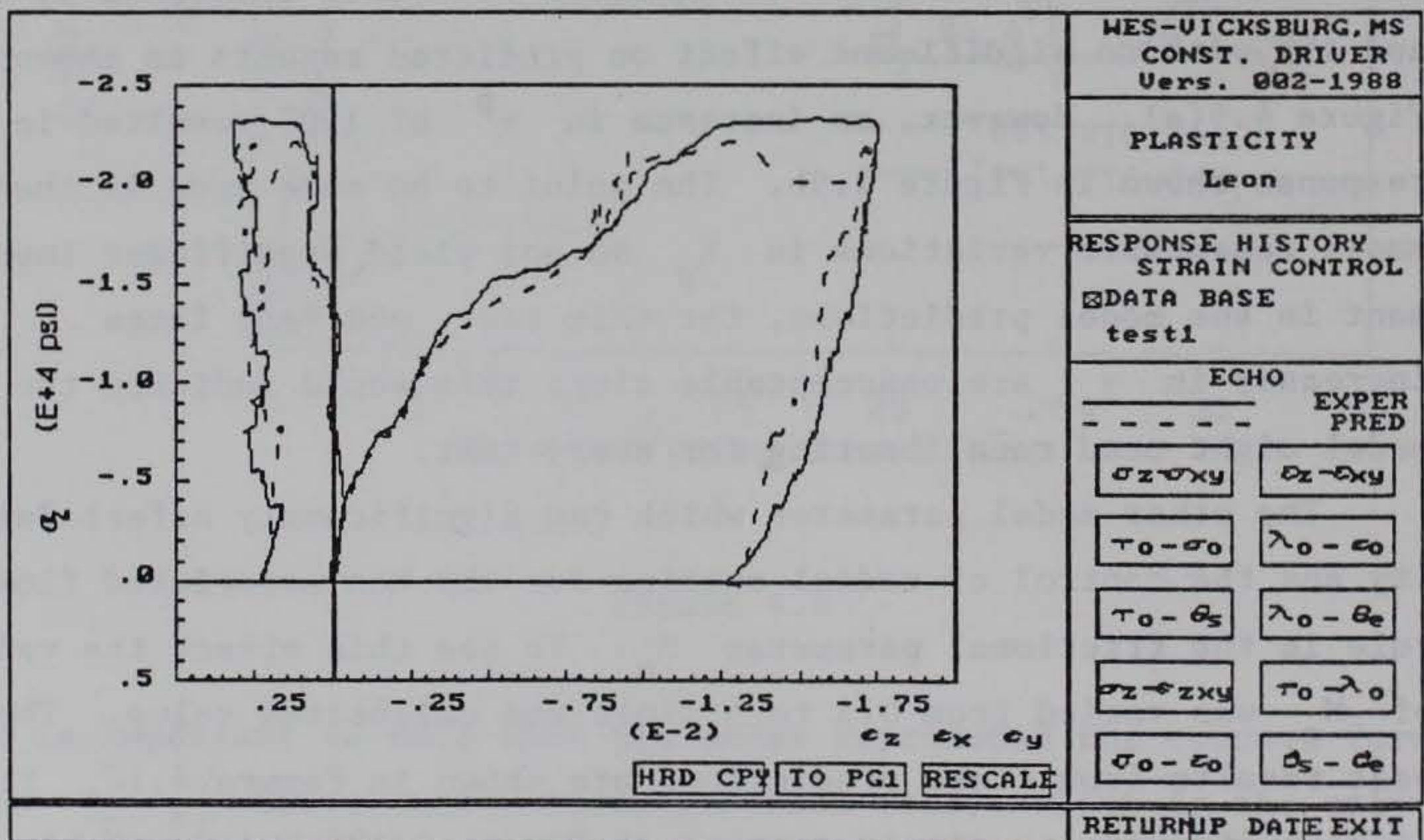
Chapter 2. The final loading branch (5-6) in general shows a decreased average slope in  $\sigma_z \epsilon_z$  for the test (ie compared to branches 1-2 and 3-4) up until the maximum axial stress of  $\sigma_z$  23.5 ksi is reached at which point essentially plastic flow occurs. The model does not show this decrease in average  $\sigma_z \epsilon_z$  slope but does predict plastic flow. The maximum stress state attained in the test is also compared with the maximum strength surface in Figure 4.8. This comparison is excellent indicating little or no path dependency for the maximum strength surface. Also the plastic flow indicated by the model and test results is consistent with the response expected near the brittle ductile transition point, which for this concrete was predicted to be near 4 ksi (see Section 2.6.2). Also plotted in Figure 4.8 are the plastic strain increment vectors near the  $\sigma_z = 15$  ksi and  $\sigma_z = 23$  ksi stress point. It is evident that the plastic strain increment is not directed normal to the loading surfaces in these regions. For a test such as VT6.5-1 where no strain softening occurs the FEBM predicts a more ductile response if the ductility parameter  $X_p$  (Equation 3.32) is increased. To see this effect the coefficients in Equation 3.32 were increased by 10% and 15% with no significant effect on predicted results as shown in Figure 4.9(a). However, an increase in  $\chi^p$  of 150% resulted in the response shown in Figure 4.9b. The point to be made here is that small reasonable variations in  $X_p$  do not yield significant improvement in the model predictions, for this test, and very large increases in  $\chi_p$  are unacceptable since this would indicate the model might need recalibrating for every test.

The other model parameter which can significantly affect ductility and the control of radial strains for the non-associated flow rule is the frictional parameter  $M_q$ . To see this effect the value of  $M_q$  was varied from 0.5 to 5 times the calibrated value. The best results from these predictions are shown in Figure 4.10. The spike in the stress strain results of Figure 4.10(a) is probably due to some relative scatter in experimental data. Also, this point is





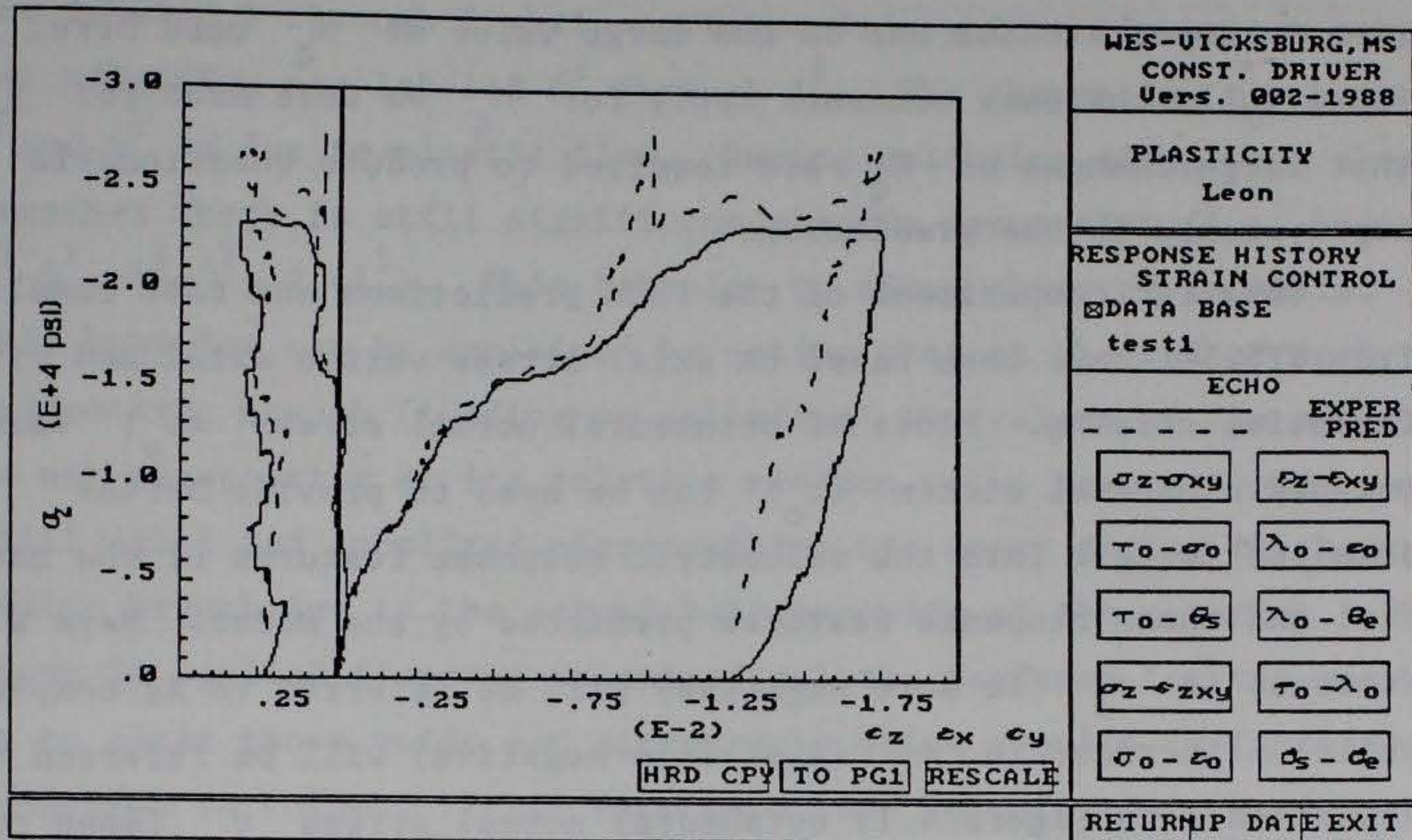
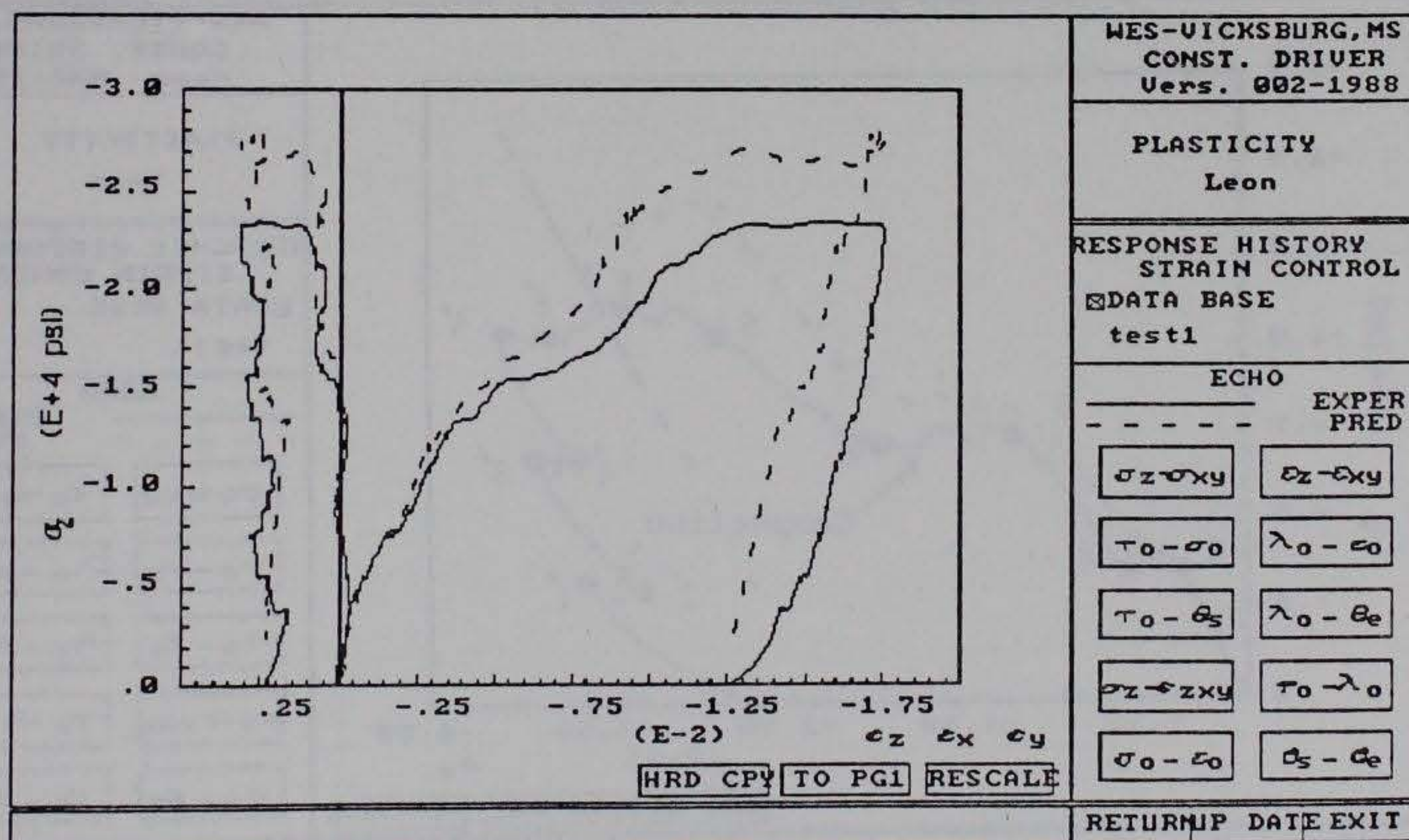
(a)  $X_p = X_p(\text{initial}) \cdot 1.15$



(b)  $X_p = X_p(\text{initial}) \cdot 1.5$

Figure 4.9 Increasing ductility parameter  $X_p$ .



(a)  $M_q = M_q (\text{initial}) \cdot 5$ (b)  $M_q = M_q (\text{initial}) \cdot 0.5$ Figure 4.10 Variation of frictional parameter  $M_q$ .



near the BDT point and the model may be more sensitive to perturbation in input strains due to the large value of  $M_q$  used here. Essentially the same comments apply for  $M_q$  as were made for  $\chi_p$  in that large changes of  $M_q$  are required to produce questionable improvements in the predictions.

Thus far comparisons of the FEBM predictions and test results from VT6.5-1 have been based on axial stress versus axial and circumferential strains. Plots of octahedral normal stress ( $\sigma_o$ ) versus octahedral normal strain ( $\epsilon_o$ ) can be used to provide better detailed insight into the volumetric response features of the material and those response features predicted by the model. Here a decrease in  $\epsilon_o$  (ie more negative) will be referred to as compaction while an increase in  $\epsilon_o$  (i.e. less negative) will be referred to as expansion. In Figure 4.11 octahedral normal stress  $\sigma_o$  (mean normal stress) is plotted against octahedral normal strain  $\epsilon_o$  (average strain) for the model, initial calibration versus test results.

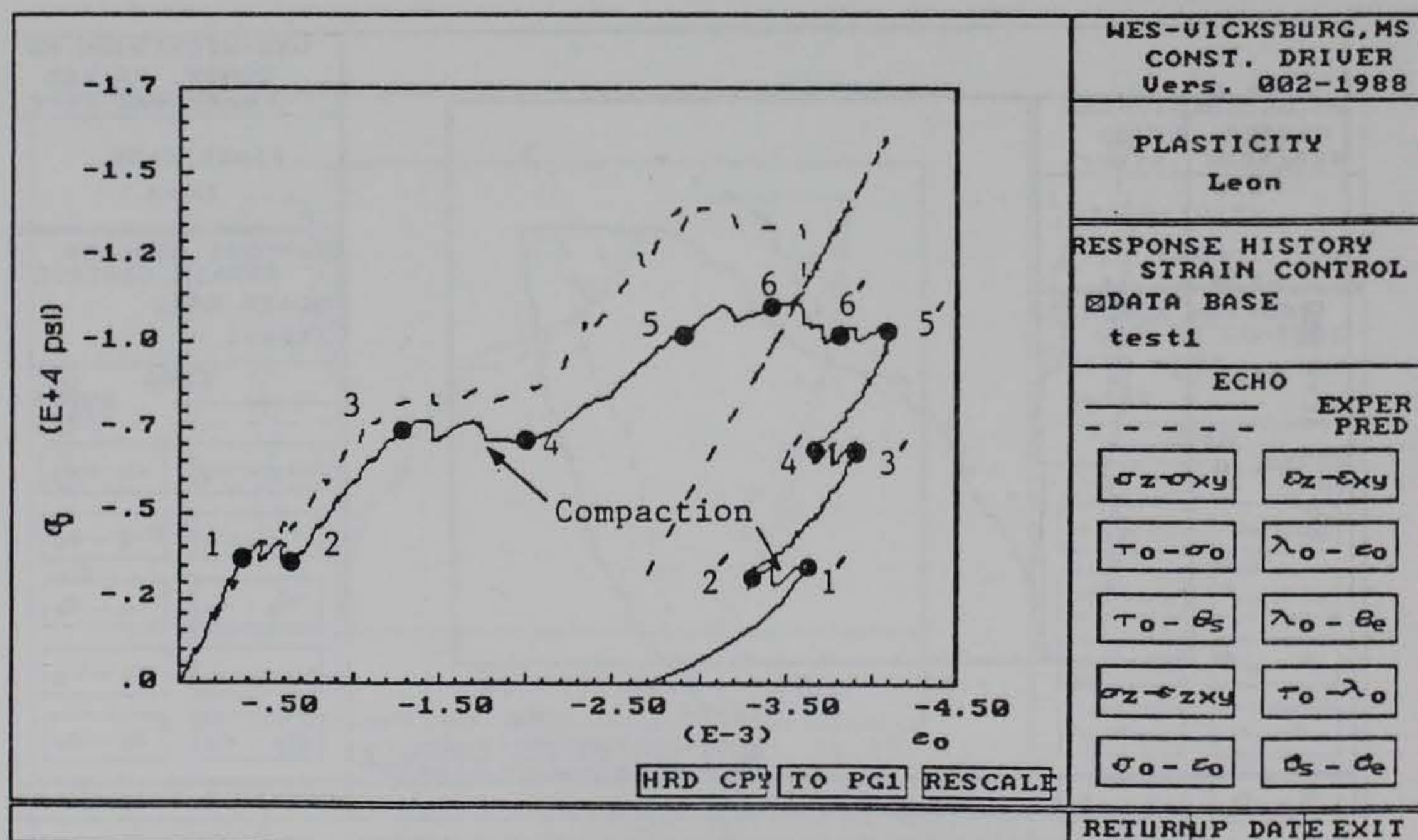


Figure 4.11 FEBM-VT6.5-1, comparison of predicted and measured octahedral stresses and strains



Points of transition from pure hydrostatic to pure deviatoric loading are labeled 1 through 6 while corresponding points (in stress space) for unloading are labeled  $6^1$  through  $1^1$ . The change in  $\epsilon_0$  between 6 and  $6^1$  is due to plastic flow. During unloading along pure shear branches there is still significant plastic compaction (i.e. branches  $6^1-5^1$ ,  $4^1-3^1$ ,  $2^1-1^1$ ). This behavior is often observed in soils. This behavior can be explained by noting that at the end of each hydrostatic branch (loading or unloading) the volume of the material is not necessarily at its relative minimum value because voids can still exist and localized microcracking can occur during the hydrostatic branch due to the actual heterogeneity of the material. When shear is applied (loading or unloading) the tendency for the material is to close those voids and microcracks which results in further reduction in volume. It is very important to note that the isotropic hardening model fails to capture this response. This key response feature points out the need for some type of kinematic hardening (ie where loading surfaces can translate as a rigid body) or other model response feature to capture this unloading behavior.



### 4.3.3 ECPM Versus Test V76.5-1

The ECPM was calibrated for the  $f'_c = 6.5$  ksi concrete based on the general procedures for model calibration as discussed in section 3.6.3. The ECPM developed here could be considered an elementary or simple model since only one endochronic element is used (i.e. one kernel function for shear and one for hydrostatic response). These kernels are represented here as

$$\rho(Z_s) = A_1 e^{-\alpha_1 Z_s}$$

$$\phi(Z_H) = B_1 e^{-\beta_1 Z_H}$$

Furthermore the model includes a coupling term so that the hydrostatic response is given by

$$\sigma = \int_0^{Z_H} \phi(Z_H - Z') \frac{d\epsilon^p}{dz'} dz' + \int_0^{Z_H} \Gamma(Z_H - Z') \underline{s} \cdot \frac{d\epsilon^p}{dz'} dz'$$

and the kernel  $\Gamma$  is approximated as

$$\Gamma(Z_H) = \Gamma e^{-Co} \epsilon^p \phi(Z_H)$$

The coefficients in these kernel functions were determined for the  $f'_c = 6.5$  ksi concrete as.

$$A_1 = 5,279 \text{ ksi}$$

$$\alpha_1 = 140$$

$$B_1 = 13,010 \text{ ksi}$$

$$\beta_1 = 1,301$$



$$\Gamma_0 = 0.176 \text{ ksi}$$

$$C_0 = 19.9$$

Values of the shear modulus ( $G$ ) and initial bulk modulus were determined to be.

$$G = 2,561 \text{ ksi}$$

$$K_0 = 3,000 \text{ ksi}$$

The bulk modulus was assumed to vary linearly with the hydrostatic stress as

$$K = K_0 + K_1 \sigma$$

$$\text{where } K_1 = 25$$

The shear hardening parameter  $F_s$  and the hydrostatic hardening parameter  $F_H$  are approximated as

$$F_s = \tau_s + \beta_s \sigma$$

and

$$F_H = e^{\beta_H \epsilon^p}$$

$$\text{where } \tau_s = 1.63 \text{ ksi}$$

$$\beta_s = 0.689$$

$$\beta_H = 70$$

$F_s$  is continuously evaluated in the model during the loading and unloading process according to the equation



$$F_s = \frac{\tau_s + \beta_s \sigma}{\tau_s + Pr\beta_s}$$

where  $\sigma$  = current hydrostatic stress

$Pr$  = maximum hydrostatic stress expected for a particular problem (here  $Pr = 30$  ksi)

And finally the shear-volumetric coupling parameter  $k$  (Equation 3.53) is expressed as

$$k = K_o e^{-\beta_k \epsilon^p}$$

where  $K_o = 0.405$

$\beta_k = 45$

Using the above parameters an initial prediction of VT6.5-1 was made. The results of this prediction are presented in Figure 4.12 in terms of axial stress versus axial and lateral strains. The comparison is quite good especially considering that this is a simple endochronic model. A more important observation is made when comparing the invariants  $\sigma_o$  and  $\epsilon_o$  for the model and test results, which is presented in Figure 4.13. The ECPM simulates (at least qualitatively) the unloading phase of the test, and in fact predicts compaction during pure deviatoric unloading branches. The significance of this feature is seen by comparing the results presented in Figure 4.13 with similar predictions by the FEBM as presented in Figure 4.11. It is obvious that failure to capture the unloading response characteristics in a structural dynamics problem which might involve many unload-reload cycles could result in an accumulation of error that is unacceptable in structural analysis and design. The effects of altering one of the hardening parameters ( $F_H$ ) is shown in Figures 4.14 and 4.15 where  $\beta_H$  is varied from 40 to 100. Using the lower value of  $\beta_H$  is seen to result in a softening behavior while



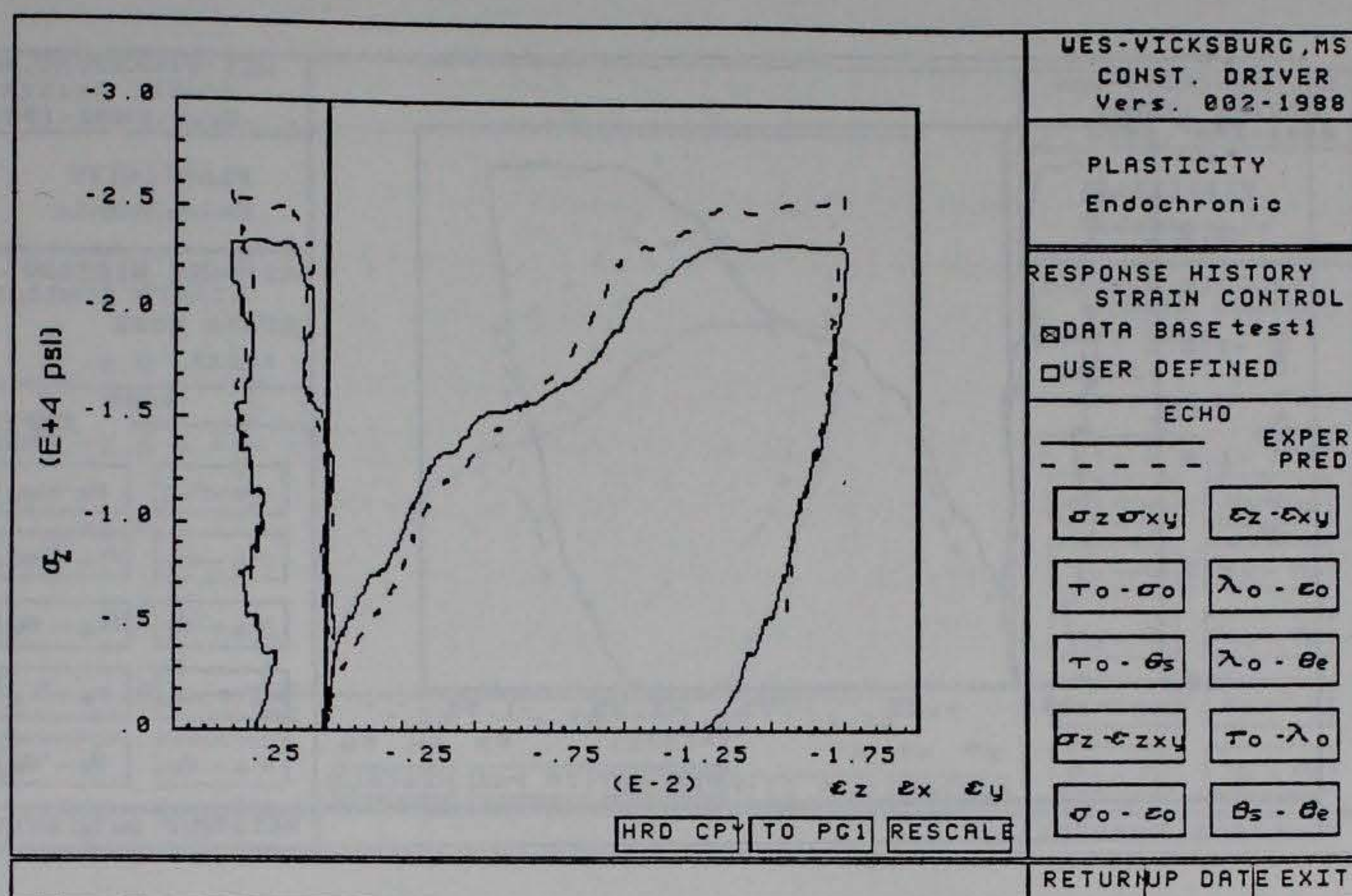


Figure 4.12 ECPM-VT6.5-1, initial calibration

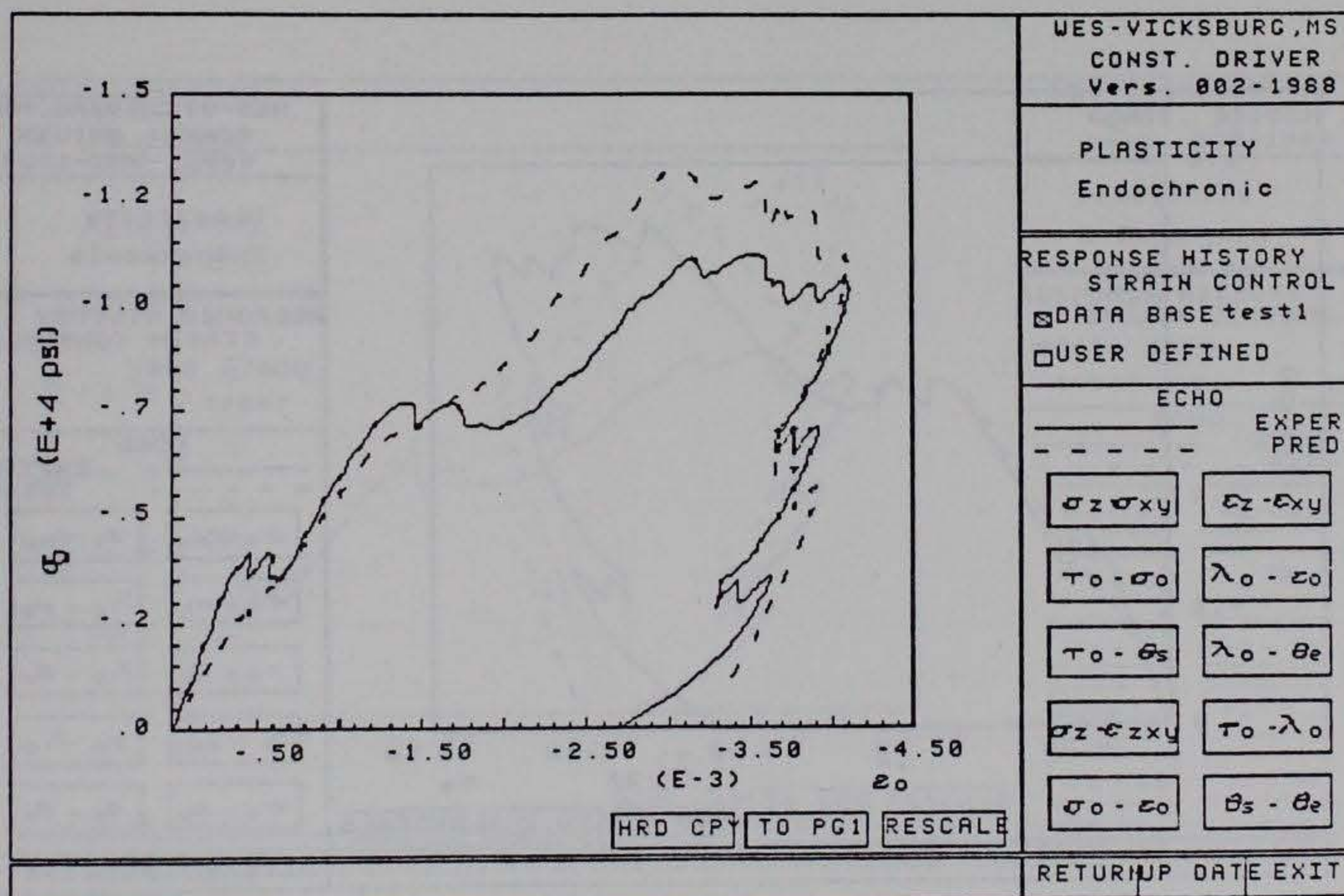
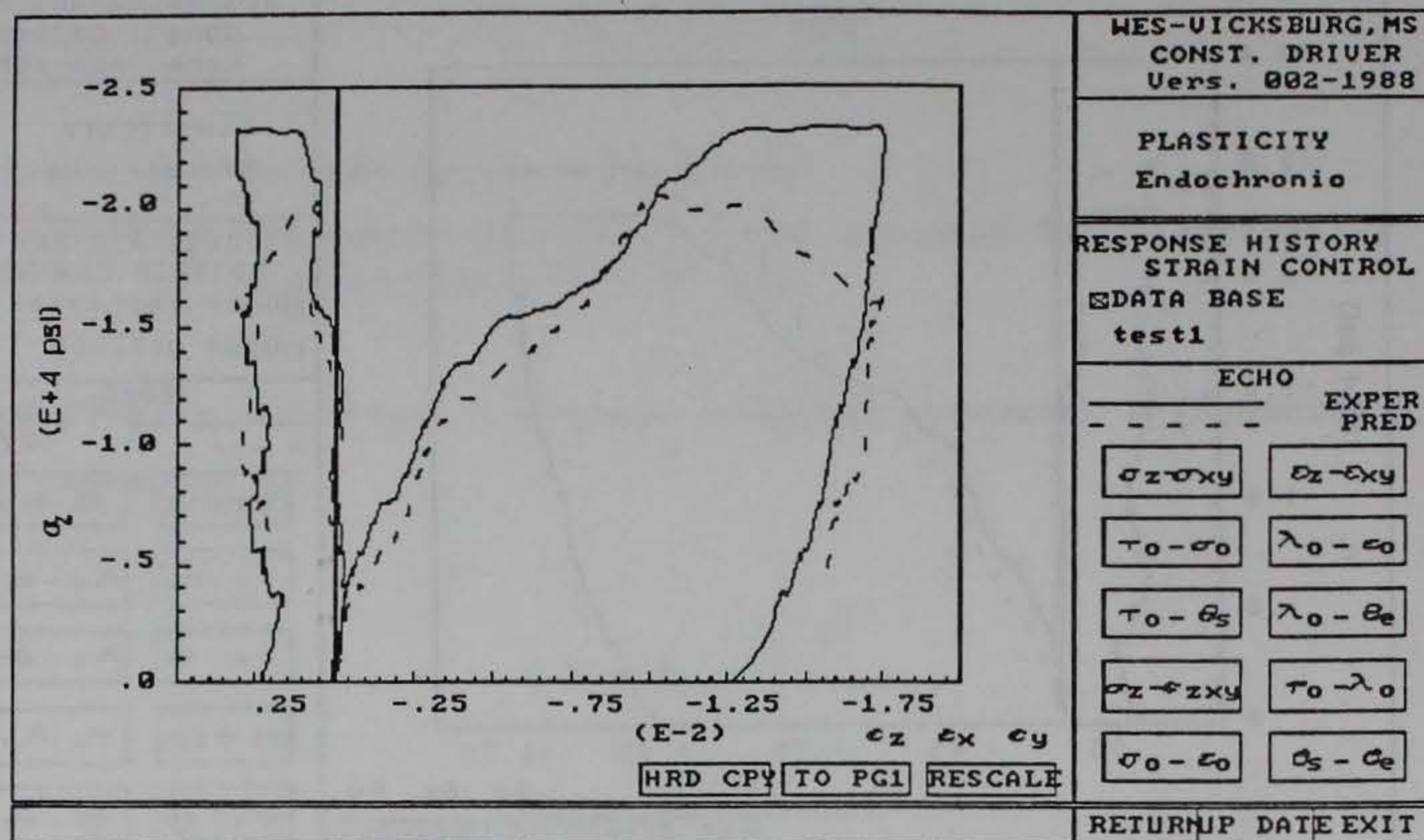
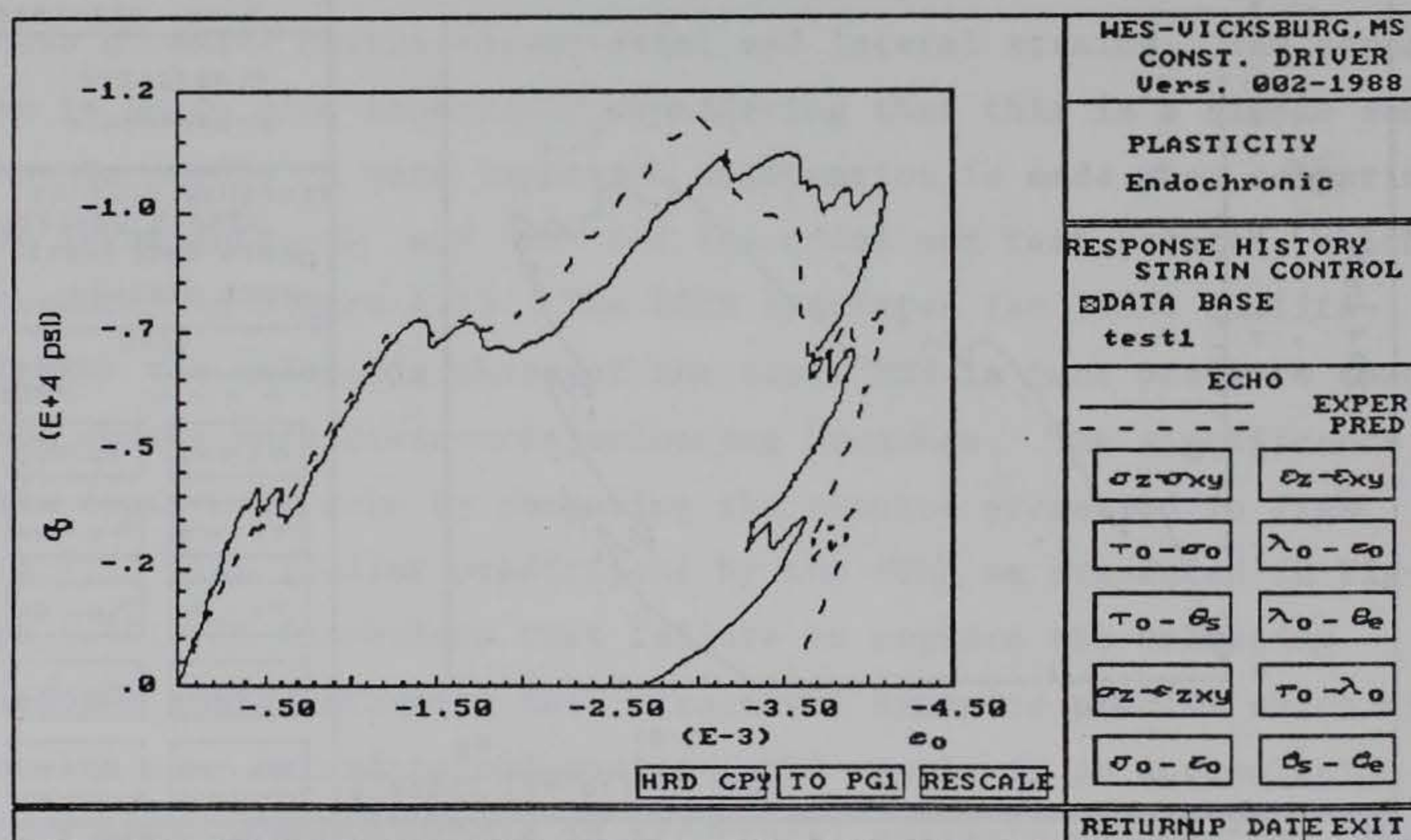


Figure 4.13 ECPM-VT6.5-1, comparison of predicted and measured octahedral stresses and strains





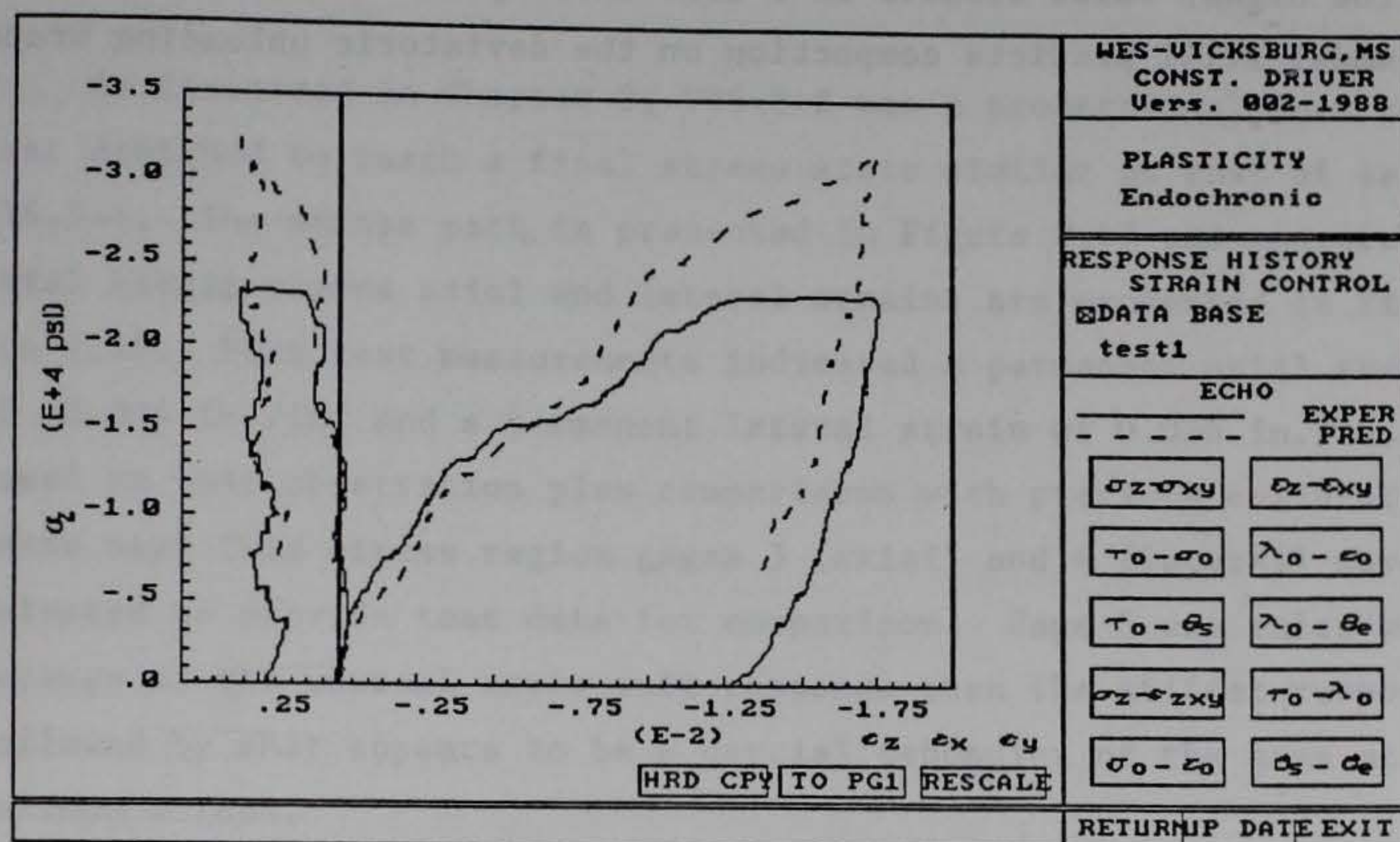
(a) normal stresses and strains



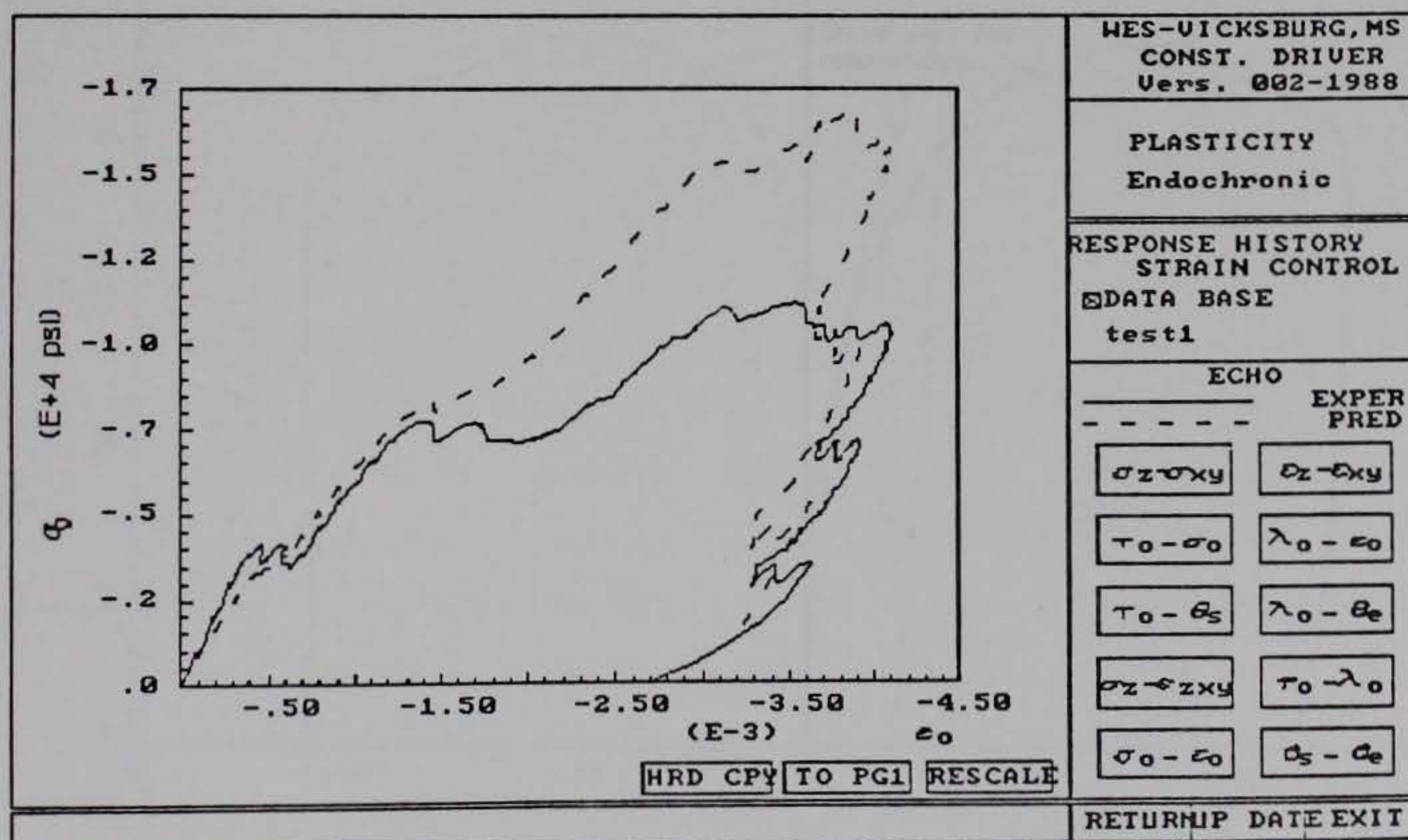
(b) octahedral stress versus strain

Figure 4.14 ECPM-VT6.5-1,  $\beta_H = 40$





(a) normal stresses and strains



(b) octahedral stress versus strain

Figure 4.15 ECPM-VT6.5-1,  $\beta_H = 100$



the higher value results in a stiffer response. In either case, the model still predicts compaction on the deviatoric unloading branches.

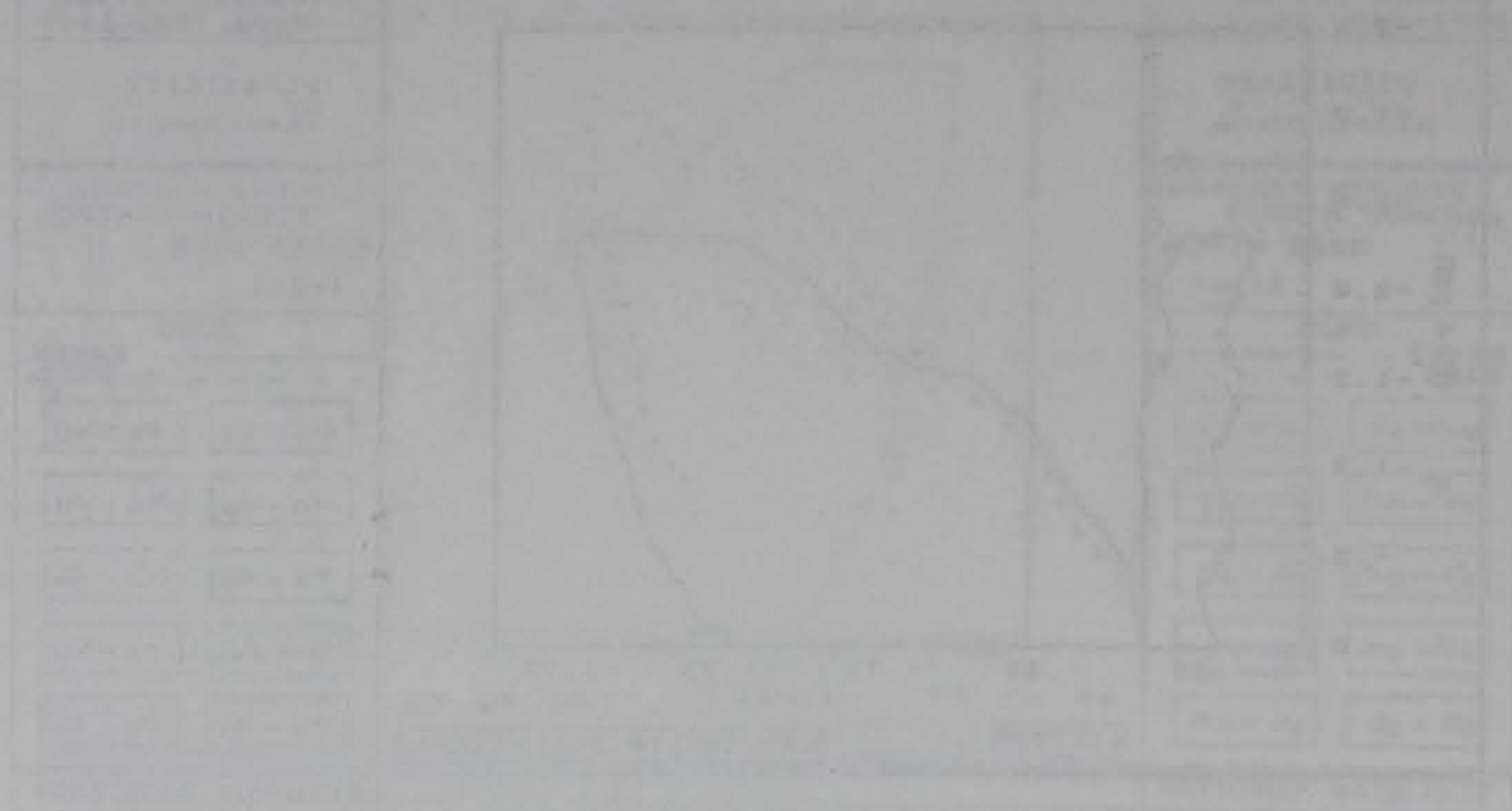


Figure 1. Loading and unloading curves for the model.



Figure 2. Loading and unloading curves for the model with multiple cycles.



#### 4.3.4 FEBM Versus Test VT6.5-2

As discussed in Chapter 2, VT6.5-2 was a proportional load path test designed to reach a final stress state similar to that of test VT6.5-1. The stress path is presented in Figure 2.17 and measured axial stress versus axial and lateral strains are presented in Figure 4.16. Post test measurements indicated a permanent axial strain of  $-0.034$  in./in. and a permanent lateral strain of  $0.036$  in./in. Based on this observation plus comparisons with previous calibration tests near this stress region gages 3 (axial) and 4 (lateral) were selected to provide test data for comparison. Gage 5 was ruled out because of the unusual early soft response then the stiffer response followed by what appears to be a partial debonding of the gage at maximum stress.

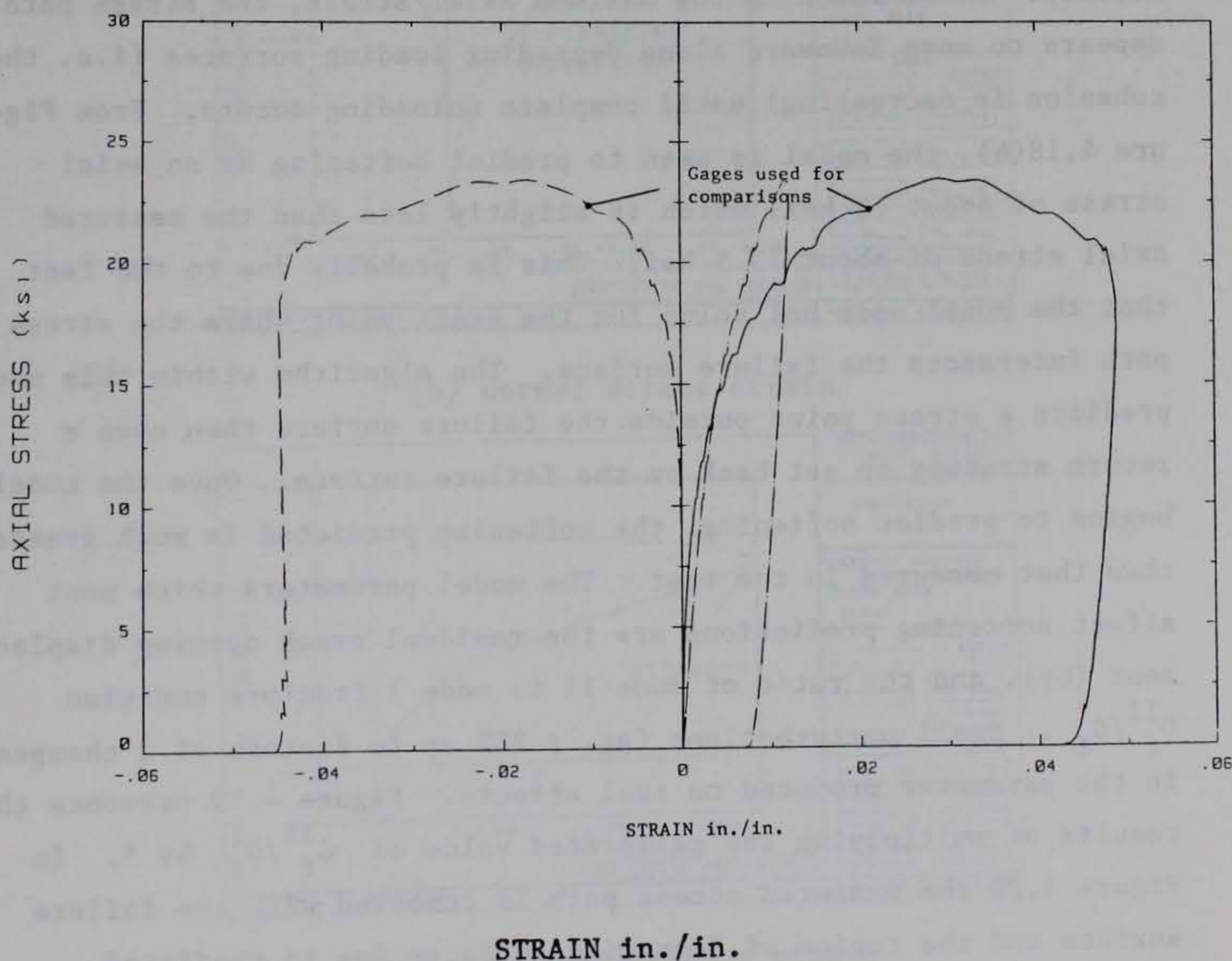
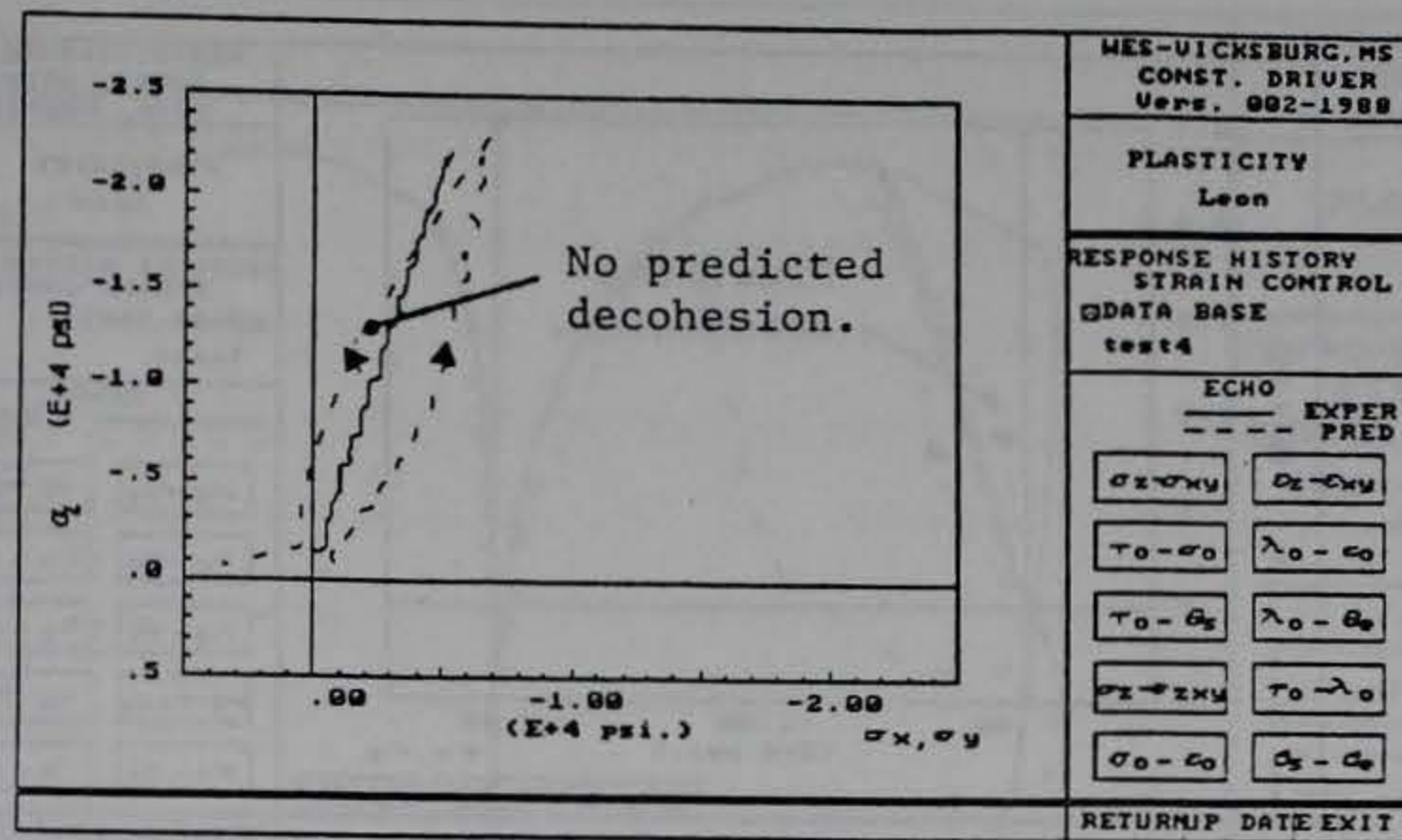


Figure 4.16 Actual test data for test VT6.5-2

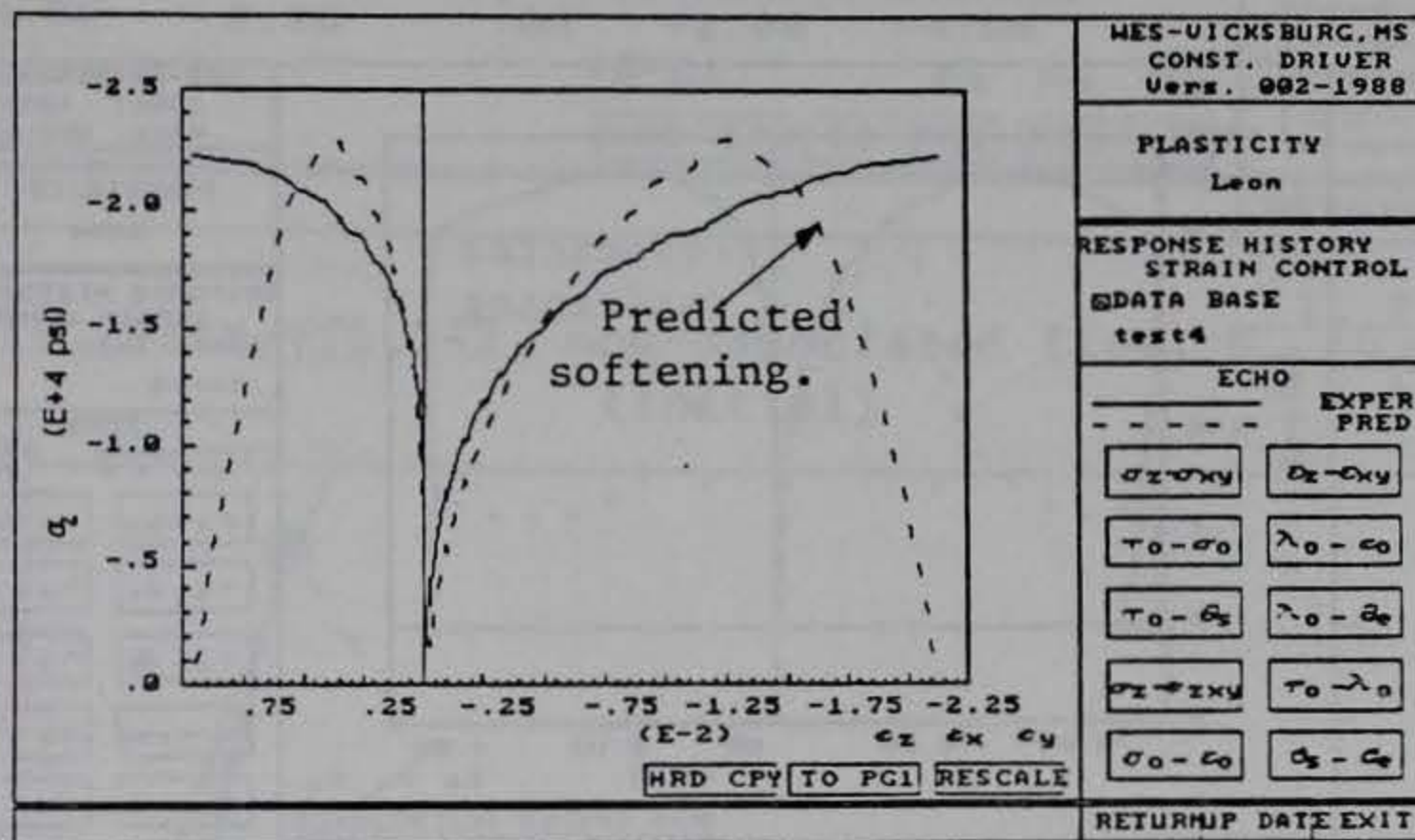


Predicted stresses using the FEBM (associated flow) are presented in Figure 4.17. Notice here that the model predicts loading up to the failure surface (Figure 4.17a) then softening is predicted in terms of stress-strain response (Figure 4.17(b)) while the stress path moves down the failure surface. This response is presented in terms of  $\sigma_0$  versus  $\epsilon_0$  in Figure 4.17(c). This is inconsistent with the theory of the model, in that there is no predicted decohesion of the failure surface as softening is occurring. The significant affect, on response, of initial dilation is seen in Figure 4.17(c). Results from the non-associated flow version of the FEBM are presented in Figure 4.18. Here the predicted stress path (Figure 4.18(a)) tends toward the test stress path at a confining stress of about -4 ksi then continues to load up to an axial stress of about -21 ksi (which is close to the maximum measured axial stress). After reaching the maximum axial stress, the stress path appears to move downward along degrading loading surfaces (i.e. the cohesion is decreasing) until complete unloading occurs. From Figure 4.18(b), the model is seen to predict softening at an axial stress of about 22 ksi, which is slightly less than the measured axial stress of about 23.5 ksi. This is probably due to the fact that the model does not solve for the exact point where the stress path intersects the failure surface. The algorithm within this model predicts a stress point outside the failure surface then uses a return strategy to get back on the failure surface. Once the model begins to predict softening, the softening predicted is much greater than that measured in the test. The model parameters which most affect softening predictions are the residual crack opening displacement ( $U_r$ ), and the ratio of mode II to mode I fracture energies  $G_f^{II}/G_f^I$ . Small perturbations (eg.  $\pm 20\%$  up to factors of 2 changes) in the parameter produced no real effects. Figure 4.19 presents the results of multiplying the calibrated value of  $G_f^{II}/G_f^I$  by 5. In Figure 4.20 the measured stress path is compared with the failure surface and the region of degrading surfaces due to predicted

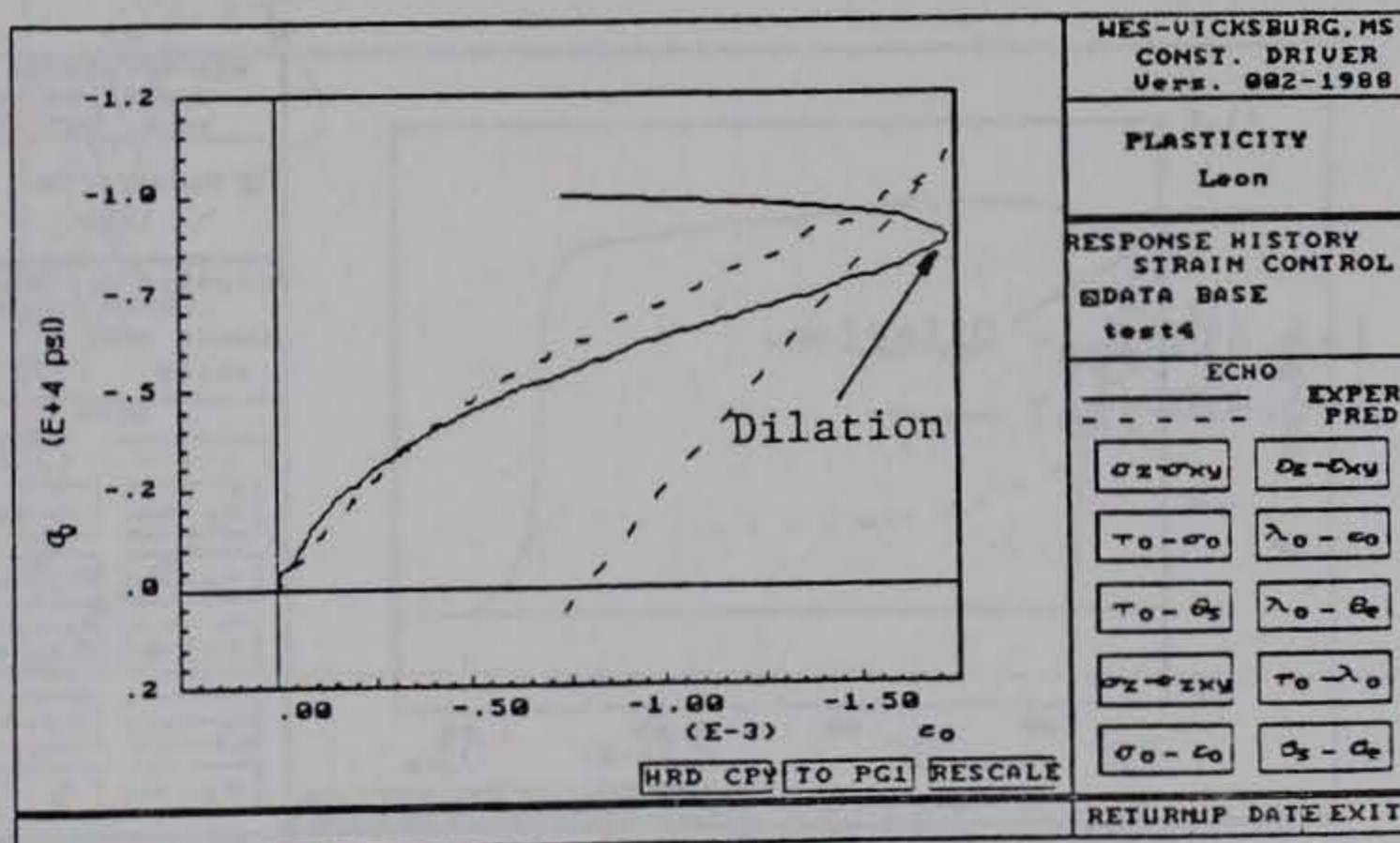




(a) stress path



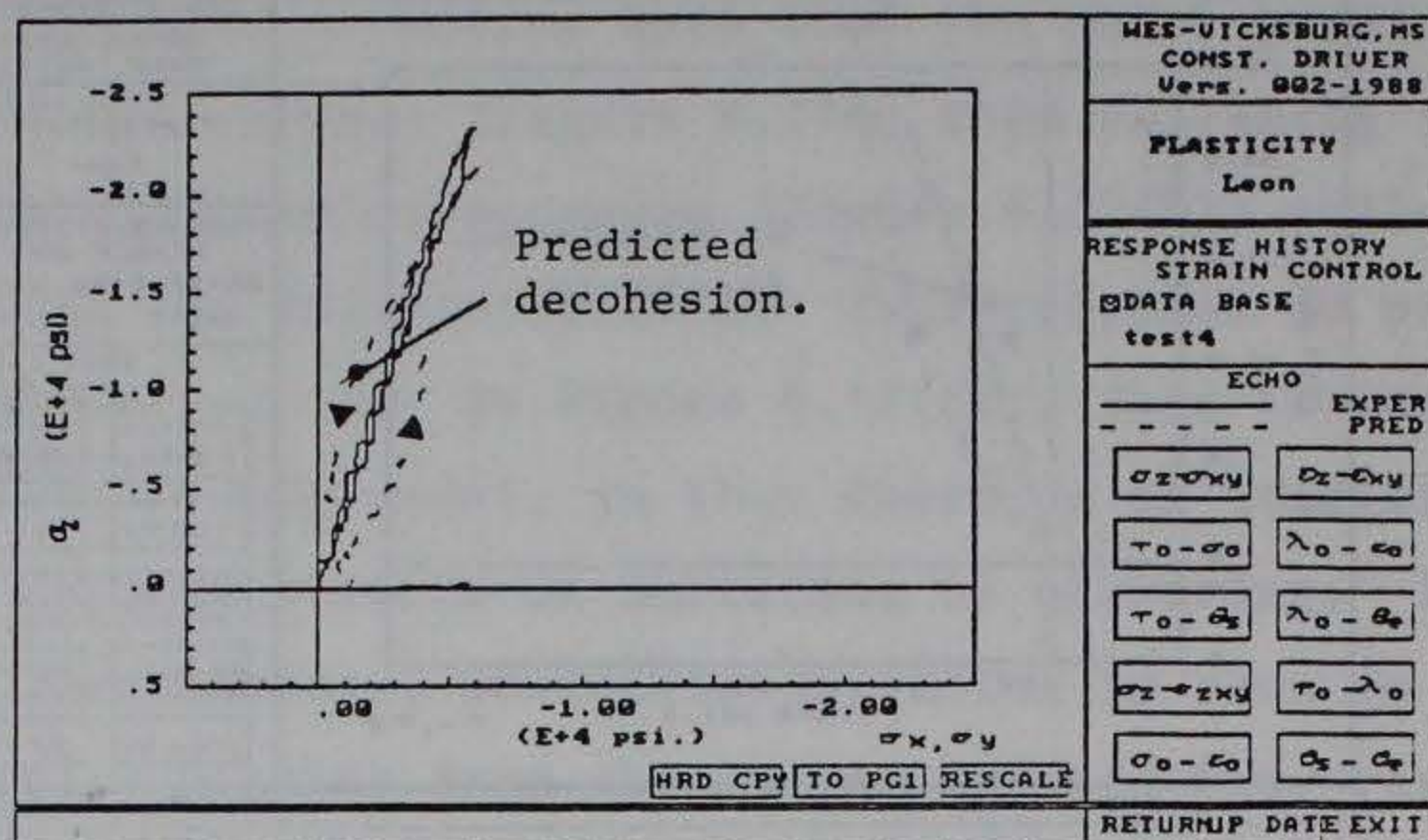
(b) normal stress strain



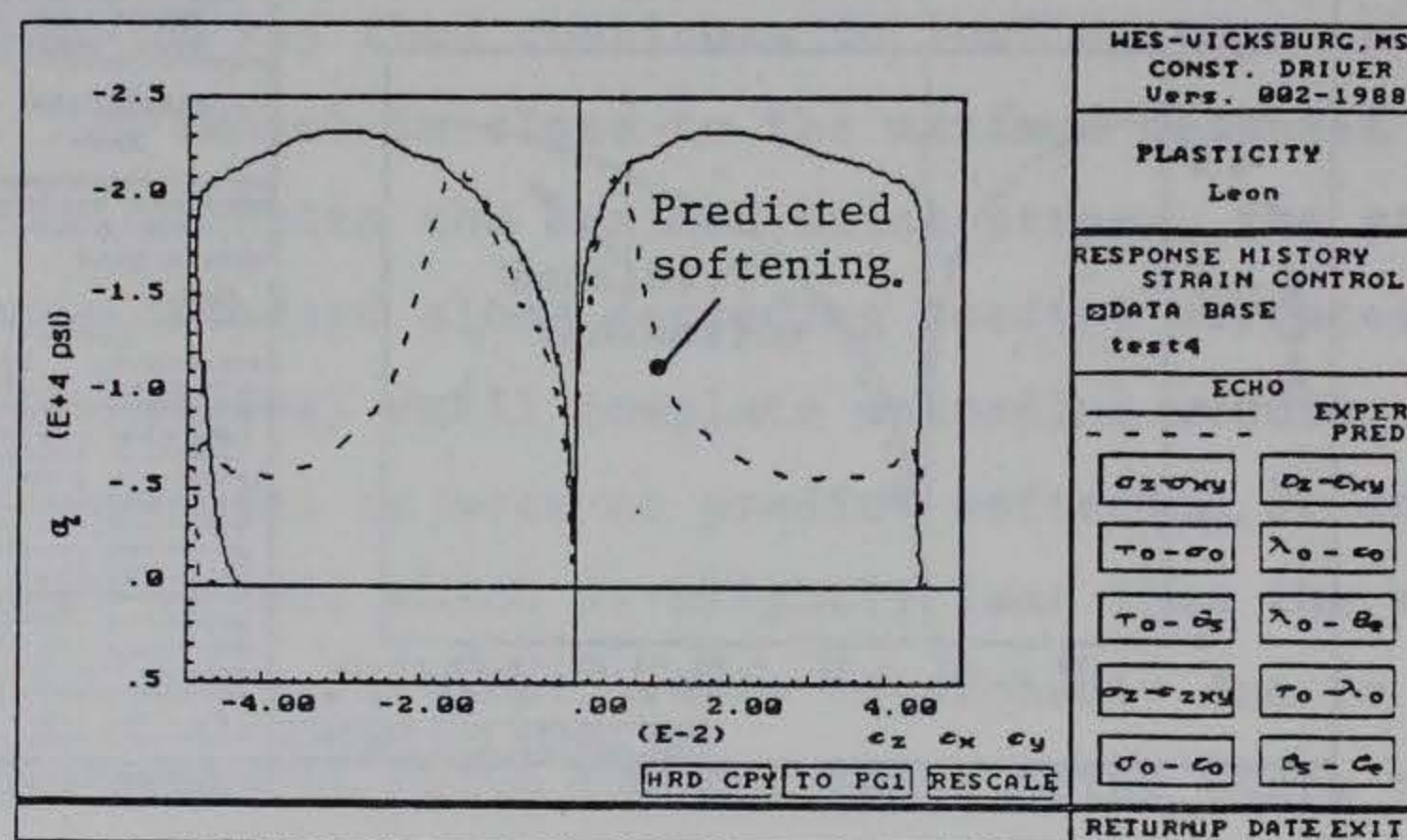
(c) octahedral stress strain

Figure 4.17 FEBM-VT6.5-2, associated flow, initial calibration

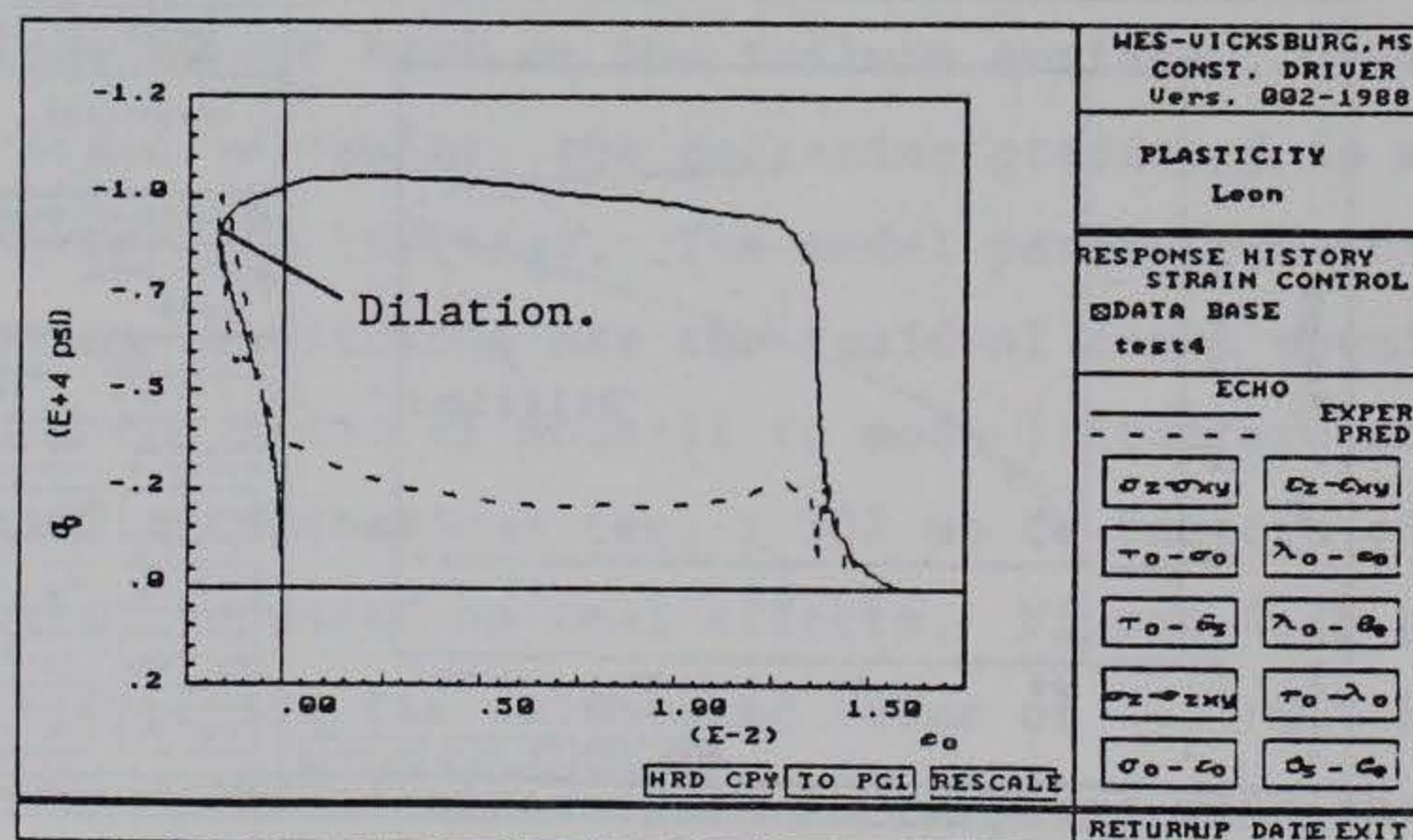




(a) stress path



(b) normal stress strain



(c) octahedral stress strain

Figure 4.18 FEBM-VT6.5-2, non-associated flow, initial calibration



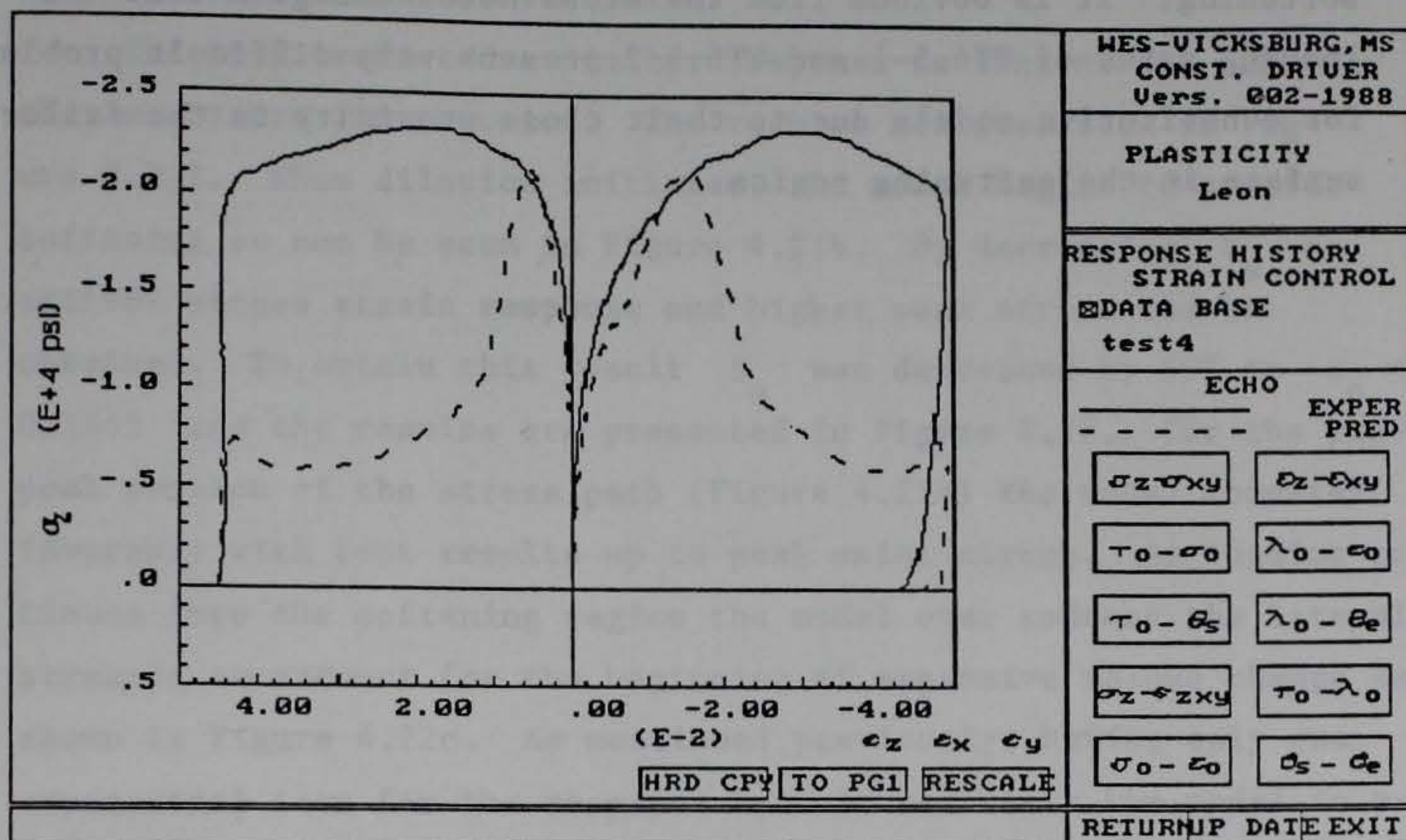


Figure 4.19 FEBM-VT6.5-2, non-associated flow,  $G_f^{II}/G_f^I = 5 \cdot G_f^{II}/G_f^I$  (initial)

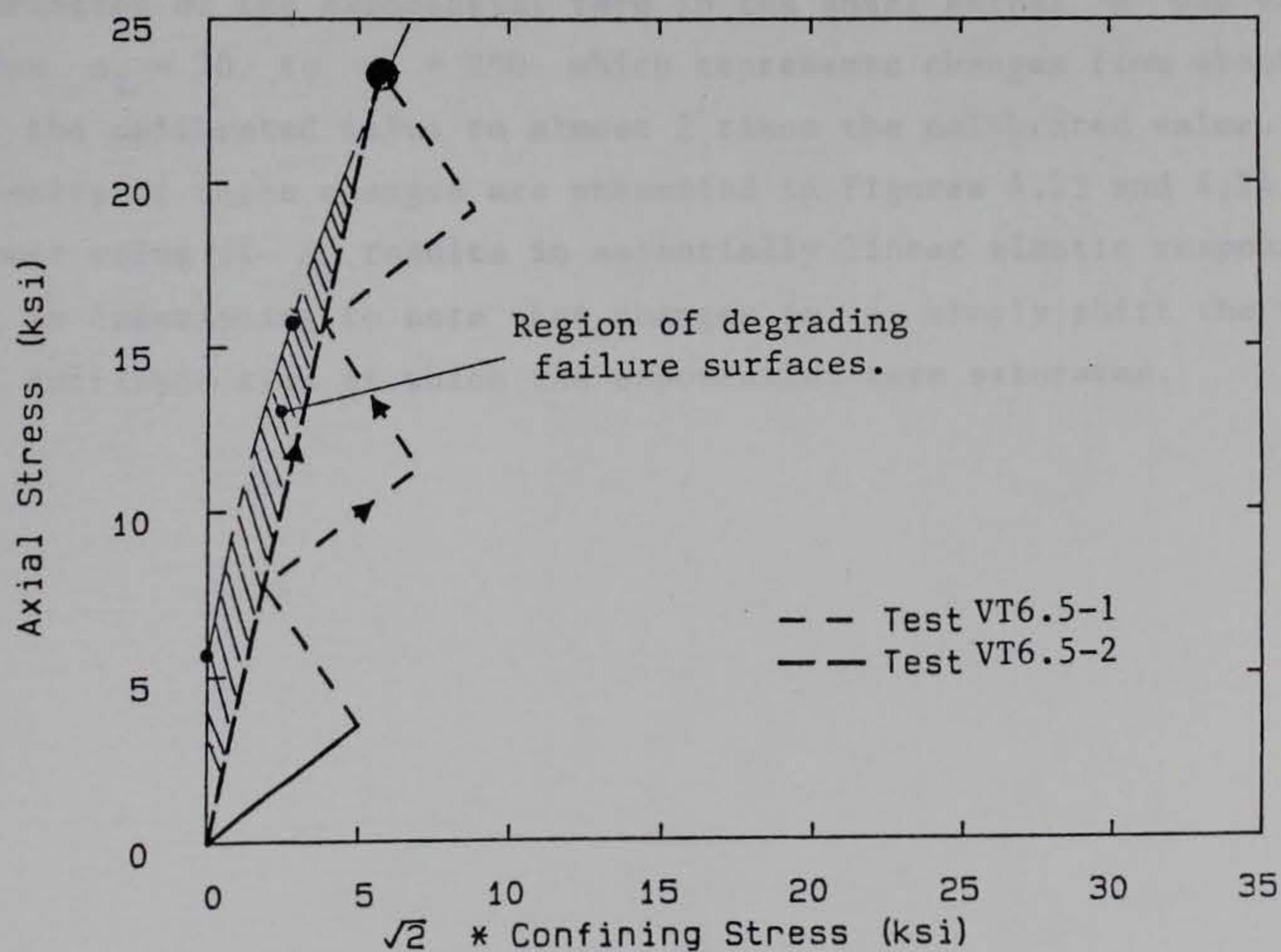


Figure 4.20 Region of degrading failure surfaces



softening. It is obvious from the cross hatched region that the loading paths of VT6.5-1 and VT6.5-2 present very difficult problems for constitutive models due to their close proximity to the failure surface in the softening region.

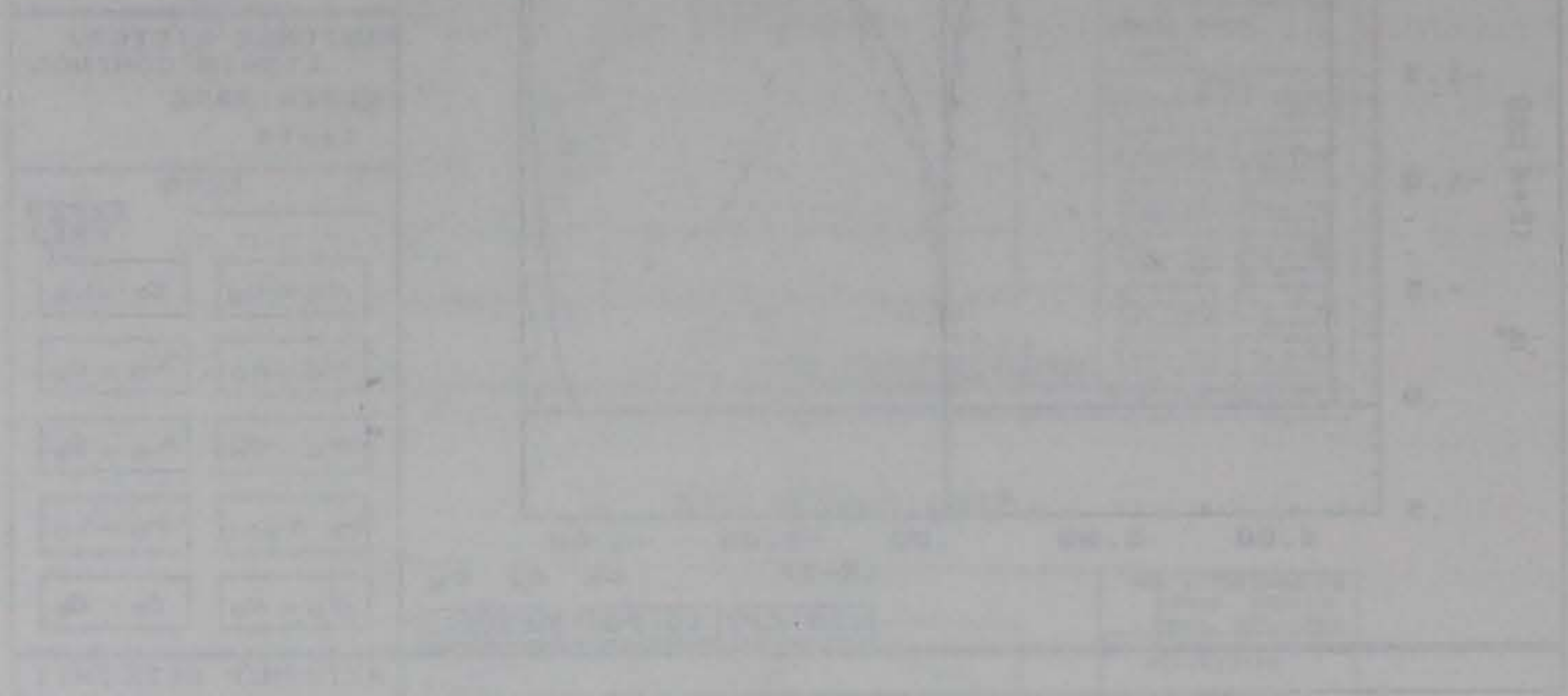


Figure 4.17. Loading paths, VT6.5-1, VT6.5-2, normalized stress,  $\sigma/\sigma_0$  vs. normalized strain,  $\epsilon/\epsilon_0$ .



Figure 4.18. Loading paths, VT6.5-1, VT6.5-2, normalized stress,  $\sigma/\sigma_0$  vs. normalized strain,  $\epsilon/\epsilon_0$ .

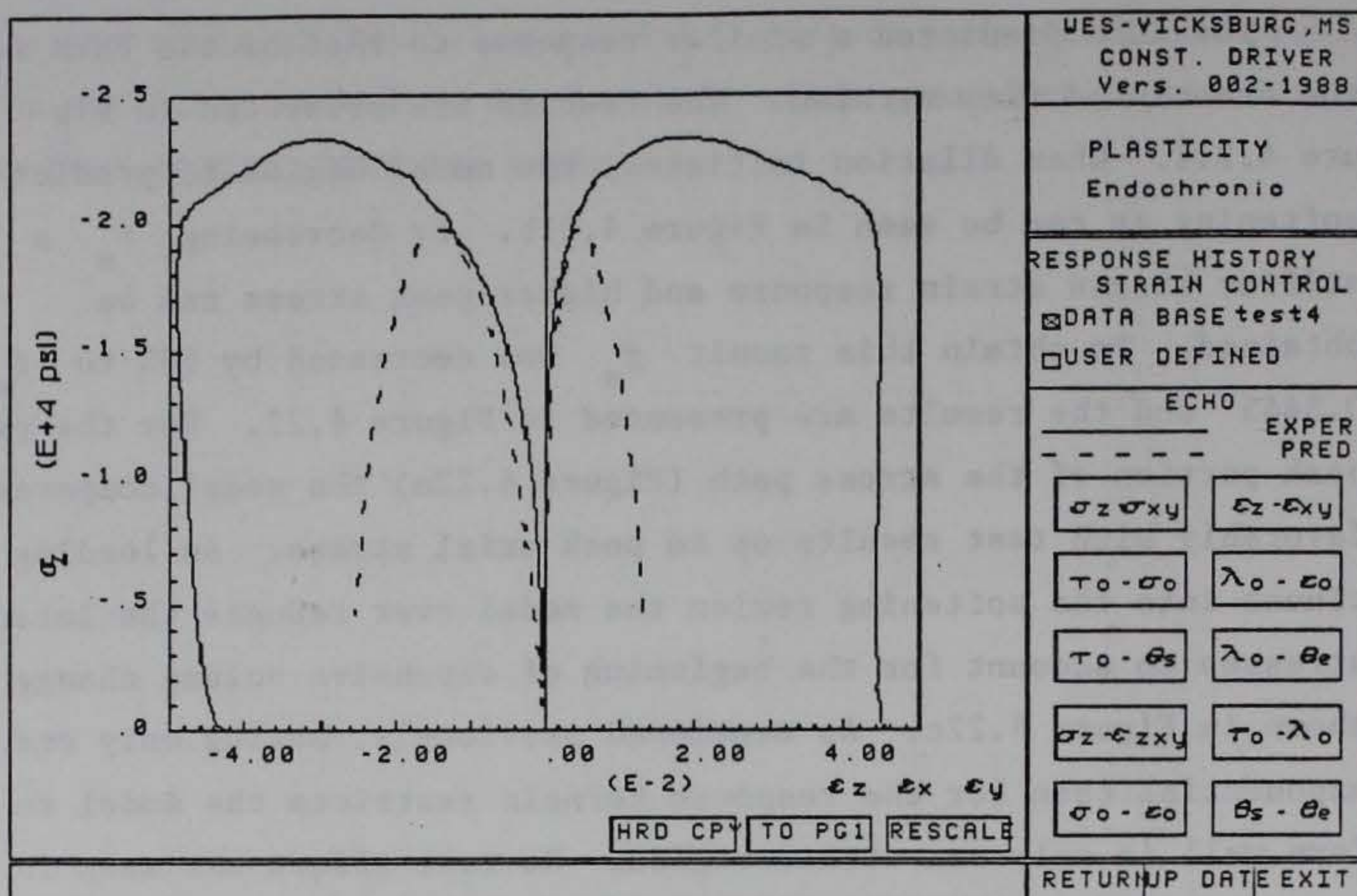
Figure 4.19. Loading paths, VT6.5-1, VT6.5-2, normalized stress,  $\sigma/\sigma_0$  vs. normalized strain,  $\epsilon/\epsilon_0$ .



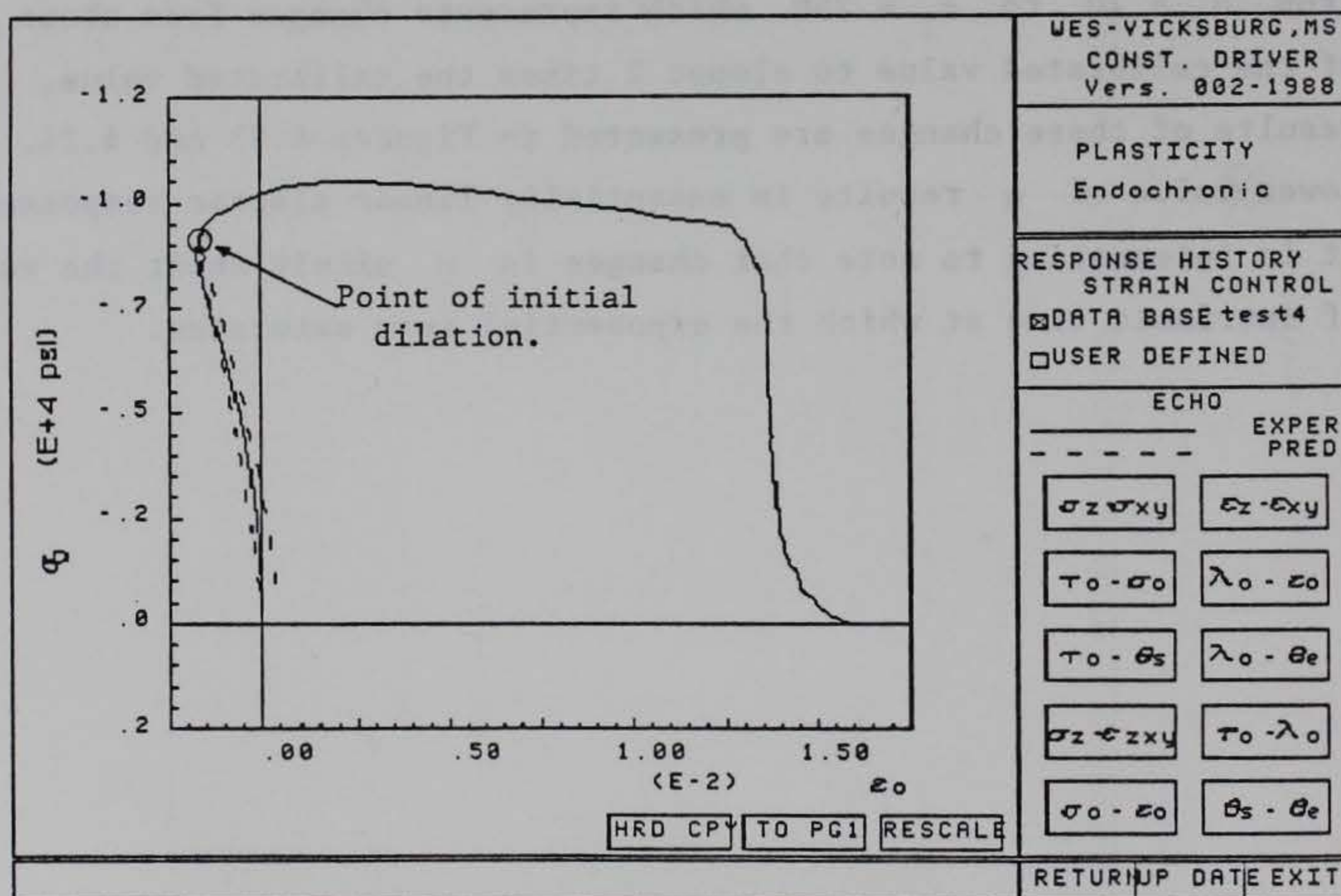
#### 4.3.5 ECPM Versus Test VT6.5-2

The ECPM predicted a similar response to that of the FEBM for the associated flow version. The results are presented in Figure 4.2.1. When dilation initiates, the model begins to predict softening as can be seen in Figure 4.21b. By decreasing  $F_s$  a stiffer stress strain response and higher peak stress can be obtained. To obtain this result  $\beta_s$  was decreased by 50% to  $\beta_s = 0.3445$  and the results are presented in Figure 4.22. For the pre-peak portion of the stress path (Figure 4.22a) the model compares favorably with test results up to peak axial stress. As loading continues into the softening region the model over reduces the lateral stresses to account for the beginning of expansive volume change as shown in Figure 4.22c. As mentioned previously, having only one exponential term for the response kernels restricts the model to perform well in only one stress region. No real effect was seen in reasonable variations of other parameters. To look at the affect of variation of the exponential term in the shear kernel  $\alpha$  was varied from  $\alpha_1 = 70$  to  $\alpha_1 = 250$  which represents changes from about 50% of the calibrated value to almost 2 times the calibrated value. The results of these changes are presented in Figures 4.23 and 4.24. The lower value of  $\alpha$  results in essentially linear elastic response. It is interesting to note that changes in  $\alpha$  simply shift the value of intrinsic time at which the exponential term saturates.





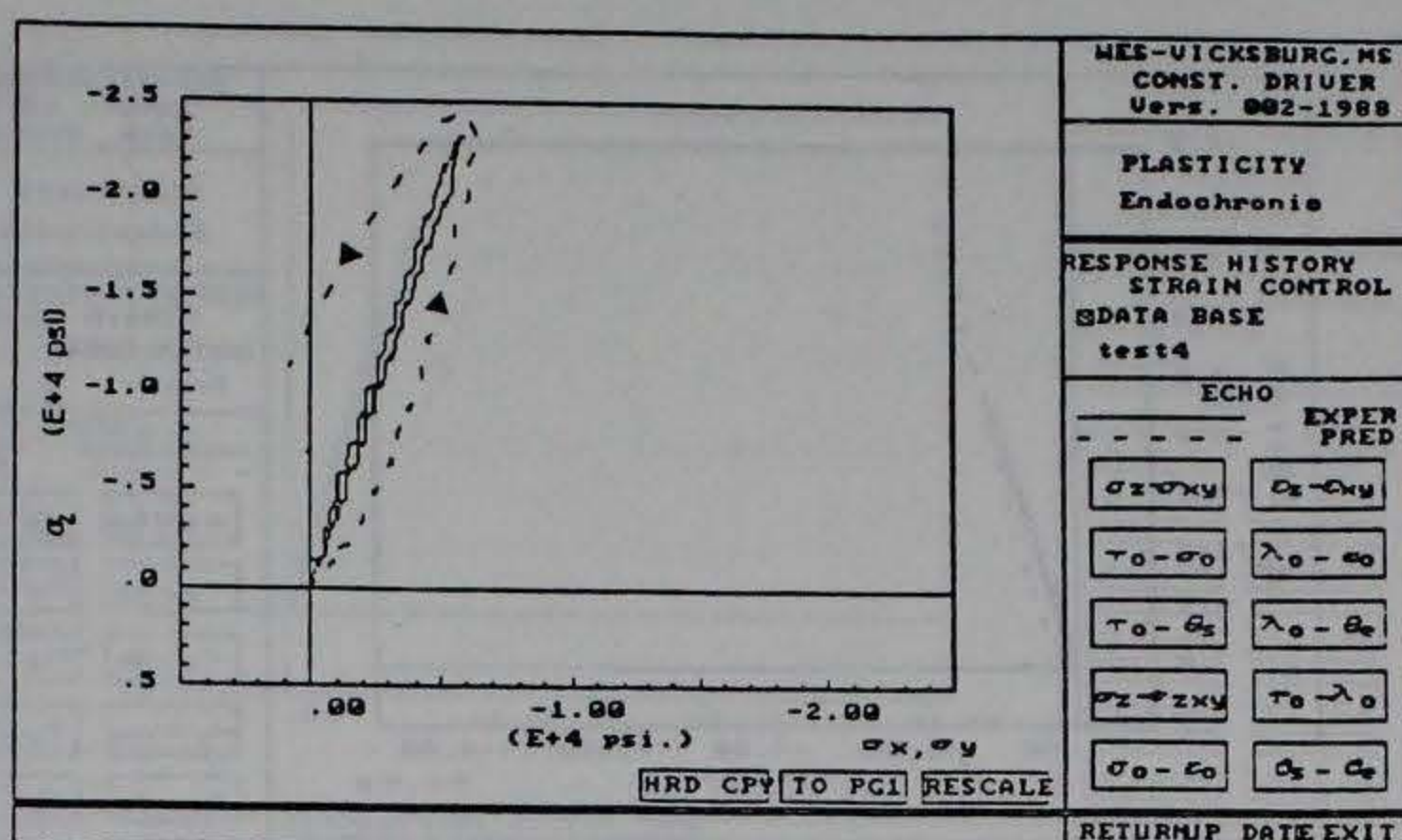
(a) normal stress strain



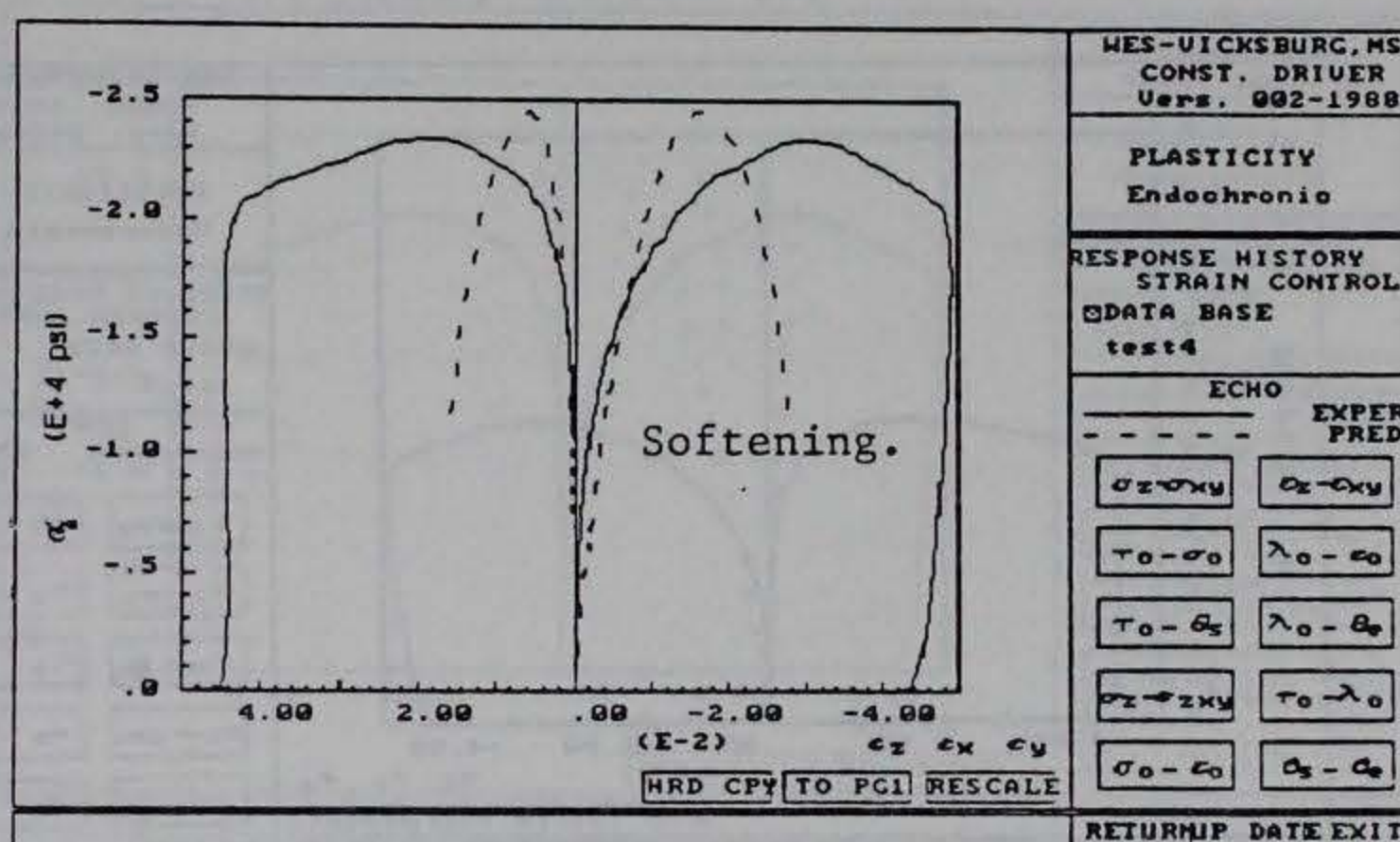
(b) octahedral stress strain

Figure 4.21 ECPM-VT6.5-2, initial calibration

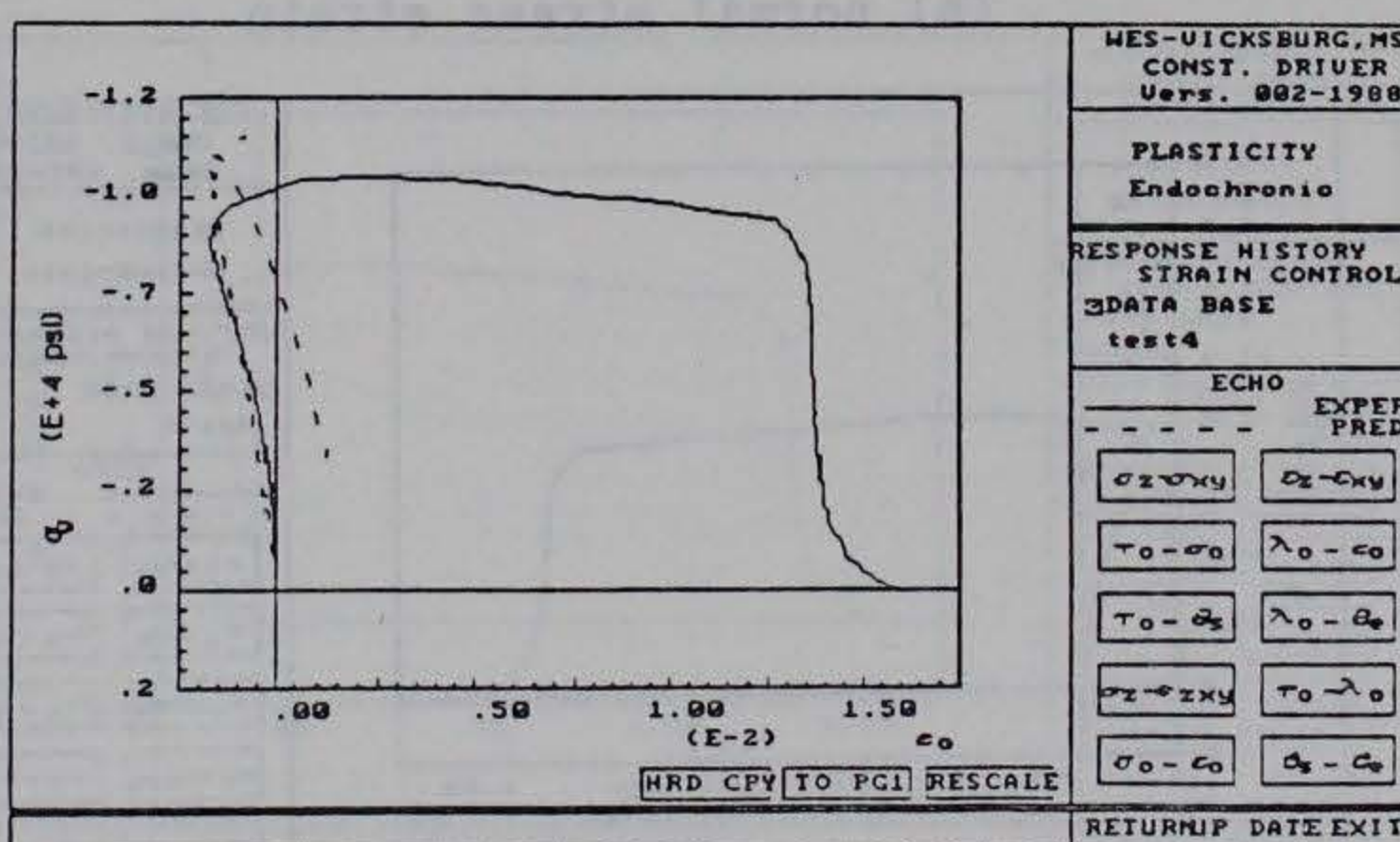




(a) stress path



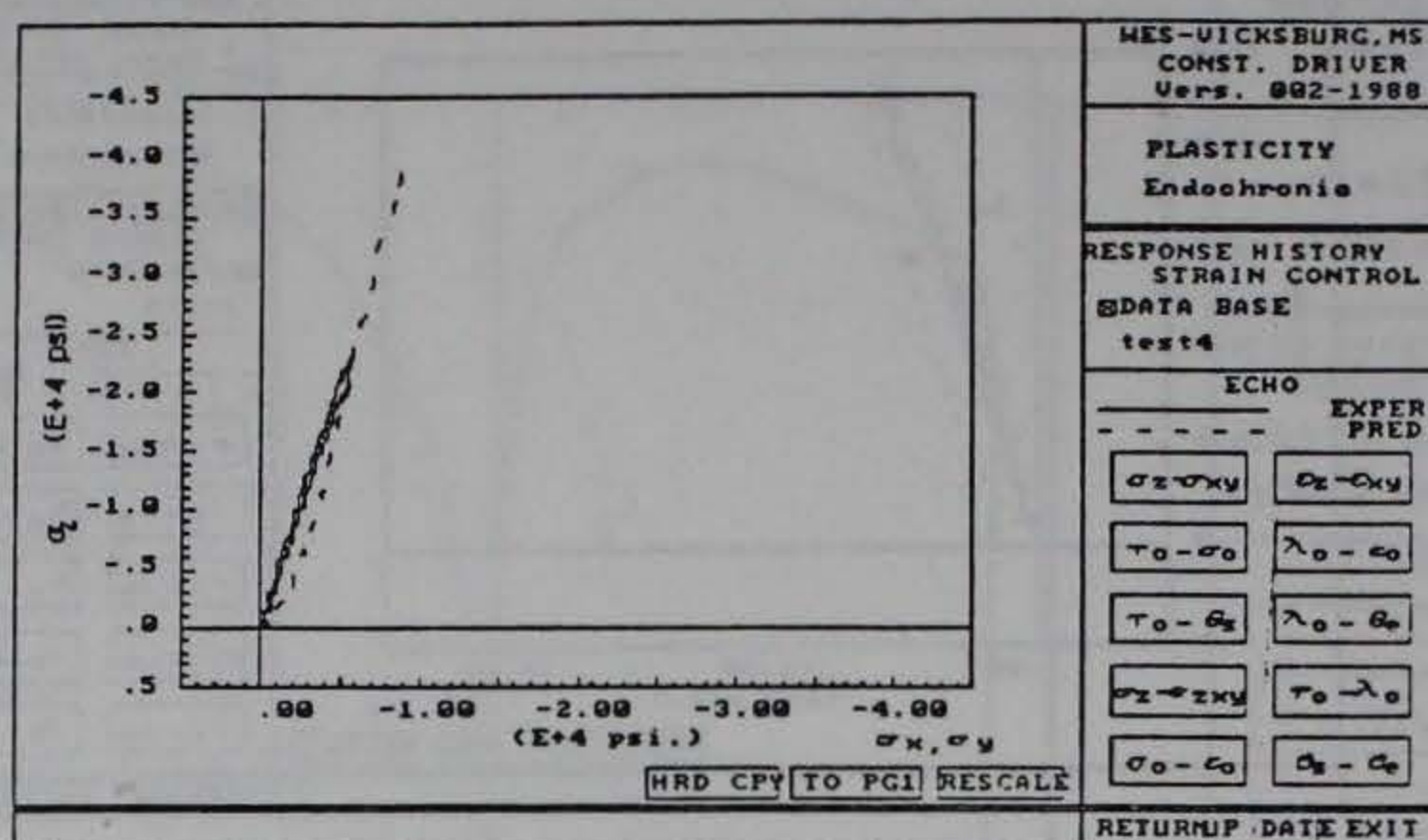
(b) normal stress strain



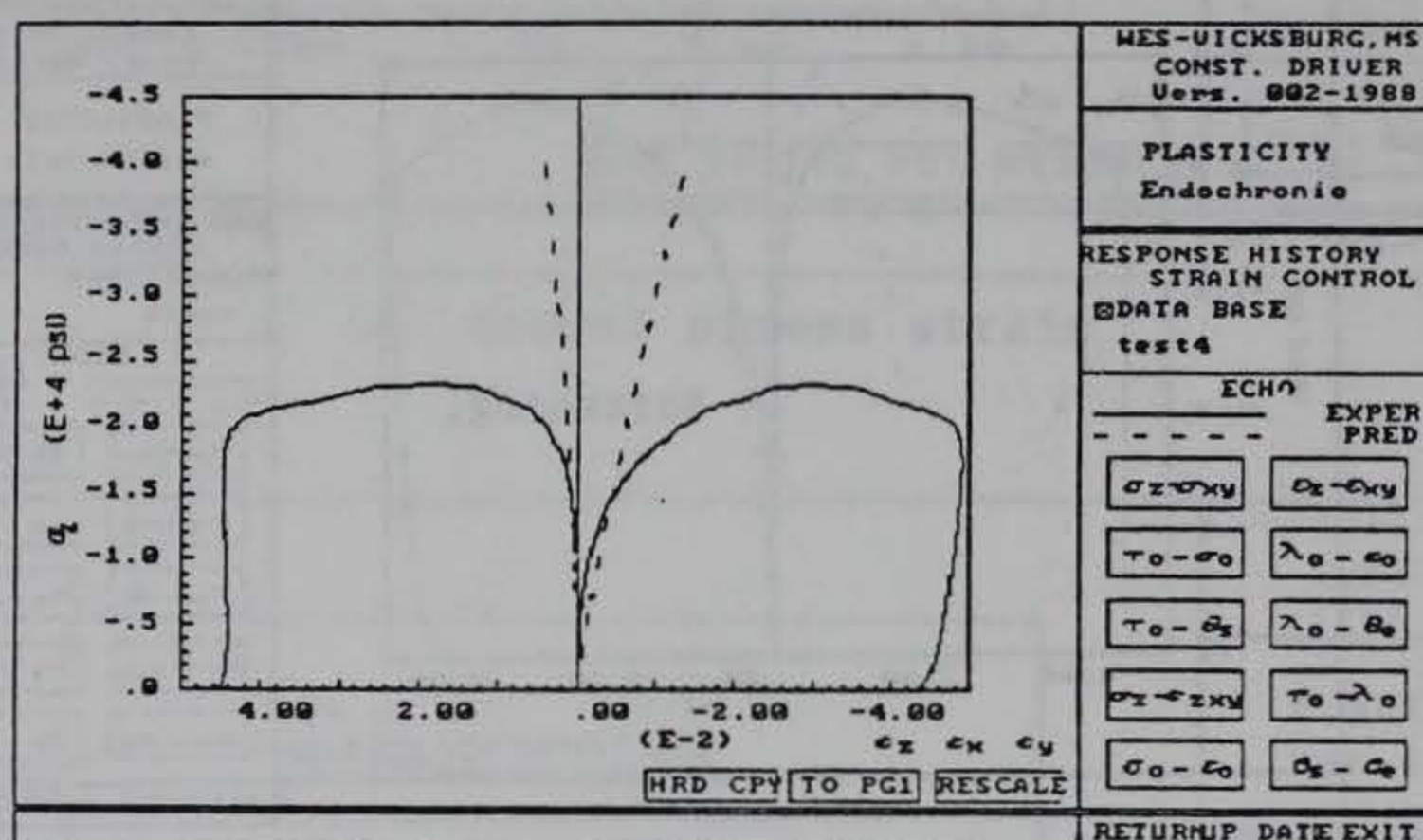
(c) octahedral stress strain

Figure 4.22 ECPM-VT6.5-2,  $\beta_s = 0.5 \cdot \beta_s$  (initial)

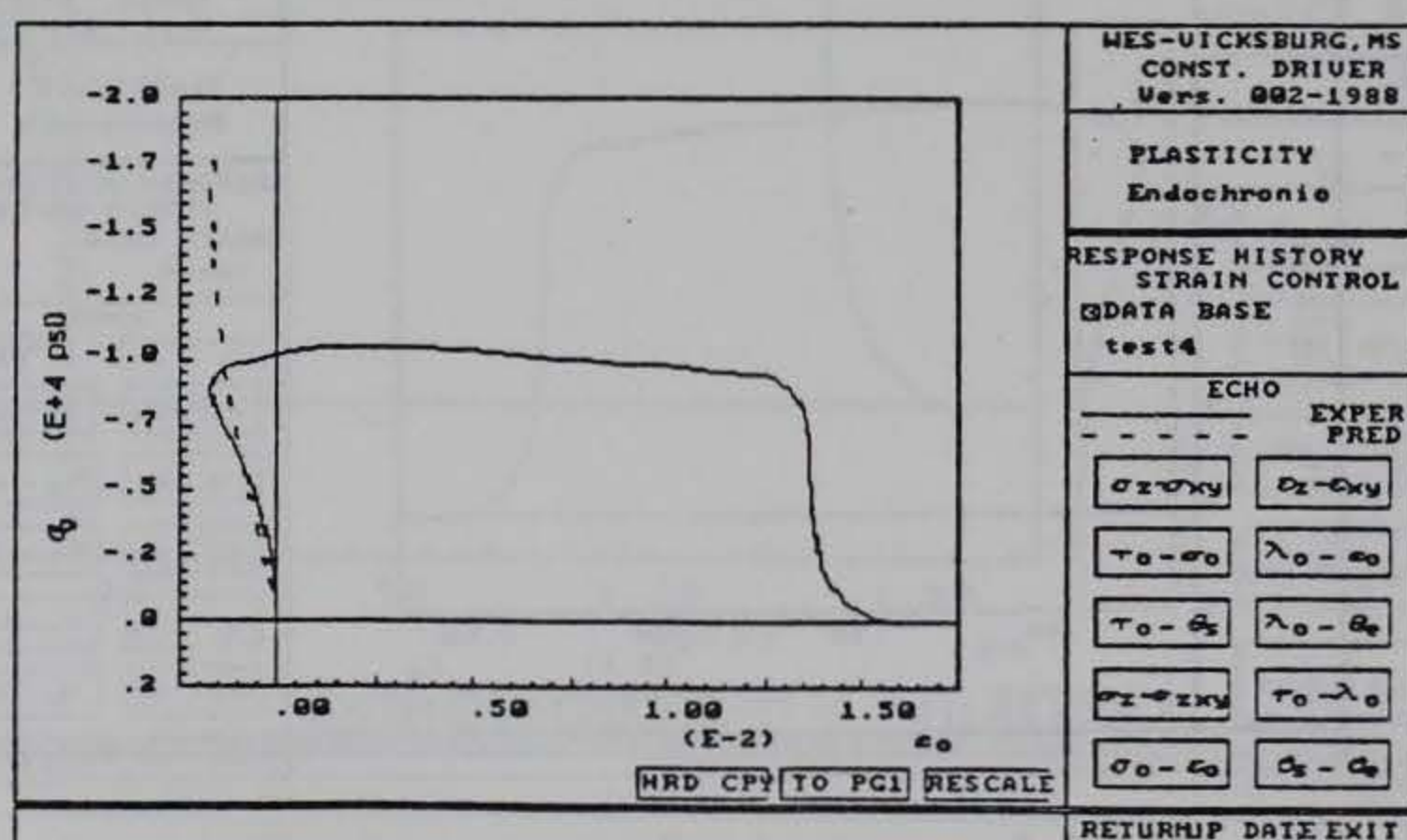




(a) stress path



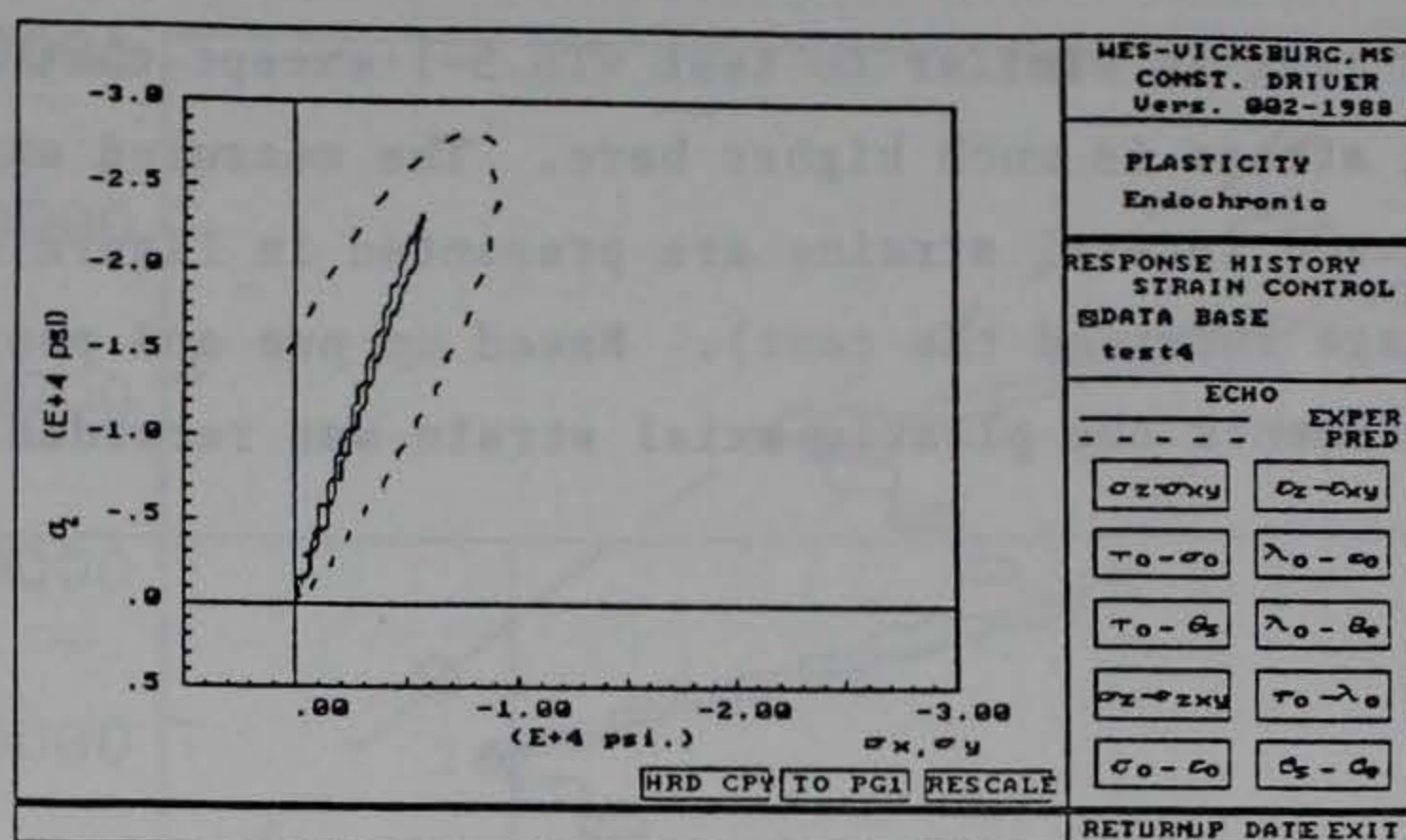
(b) normal stress strain



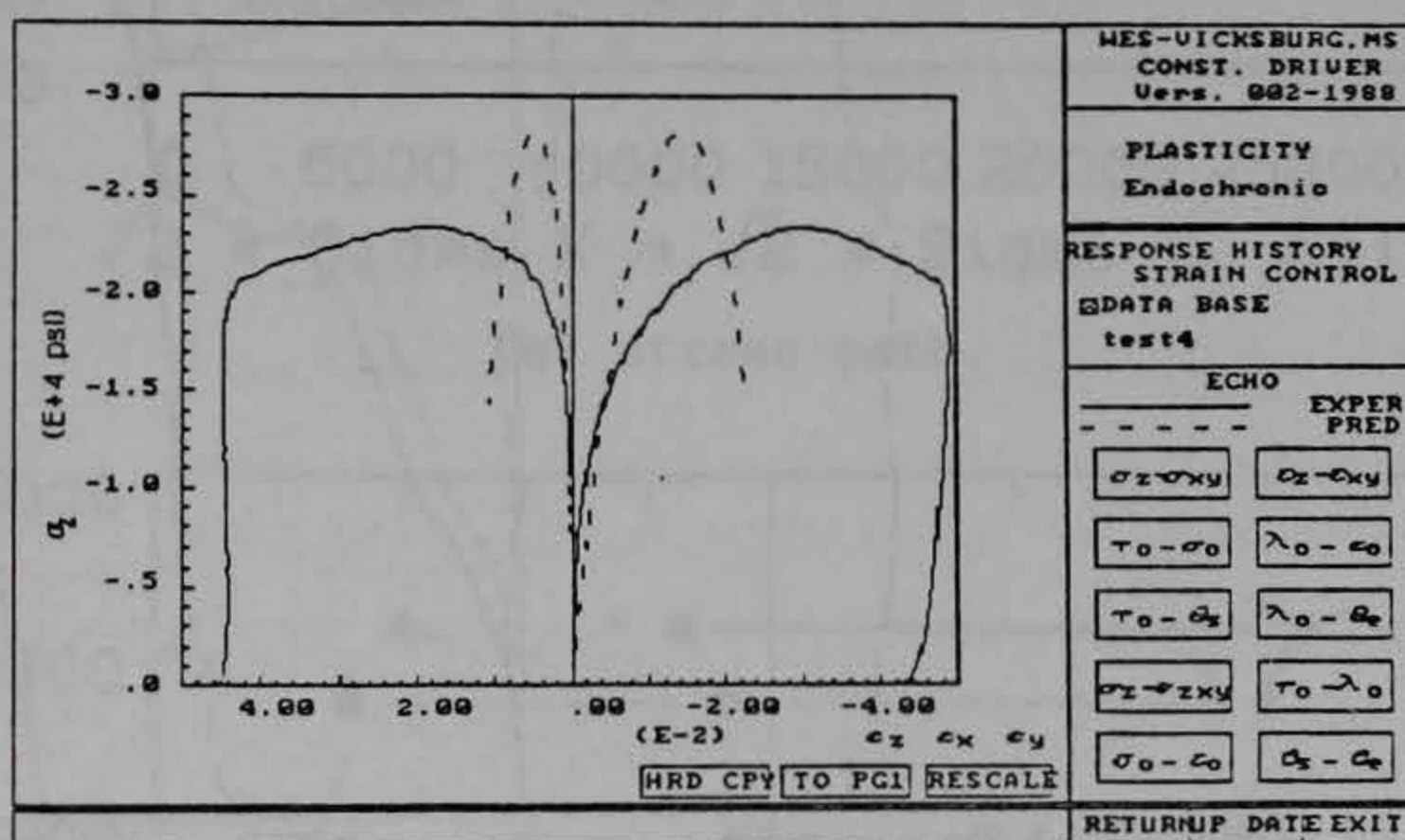
(c) octahedral stress strain

Figure 4.23 ECPM-VT6.5-2,  $\alpha_1 = 70$

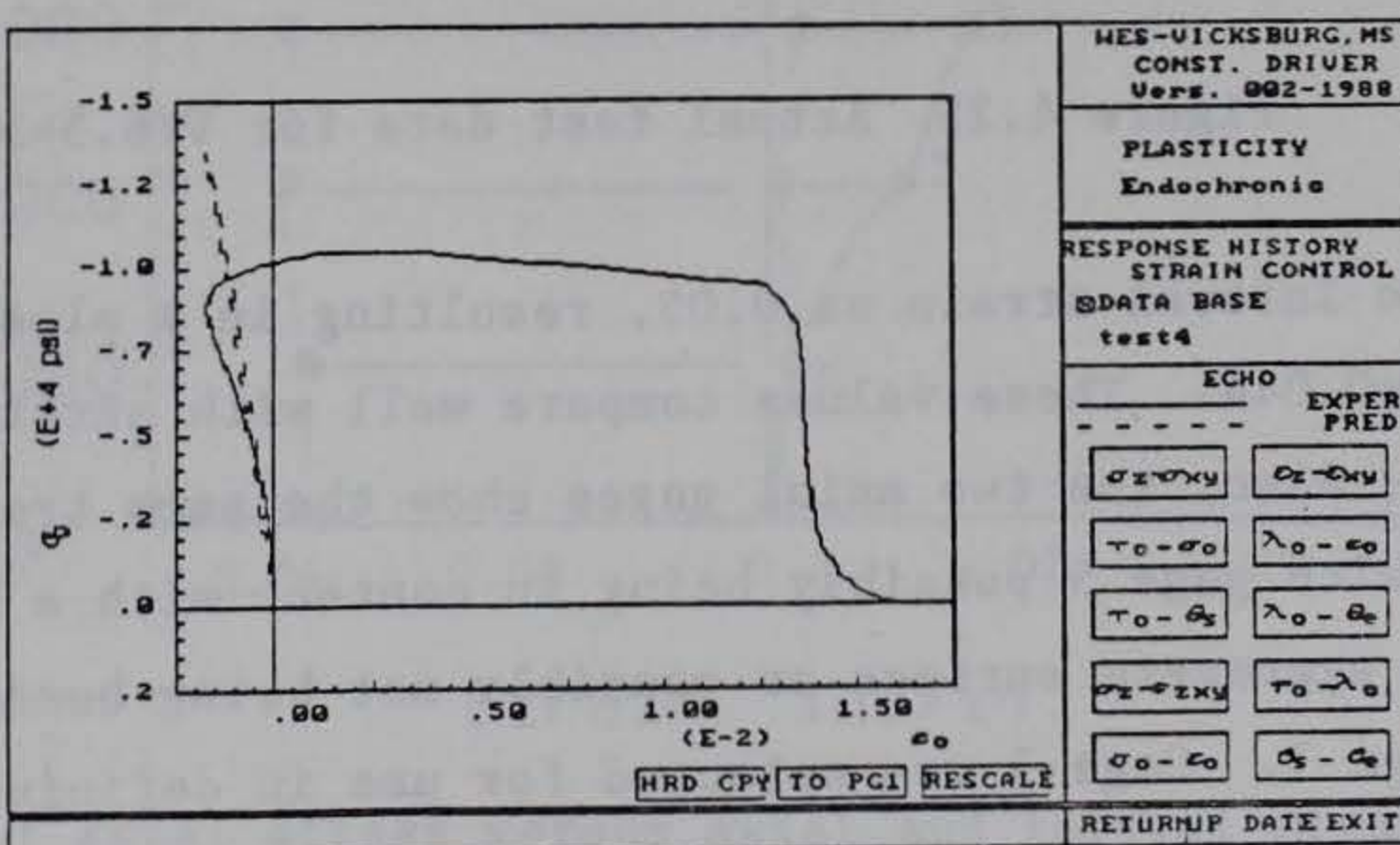




(a) stress path



(b) normal stress strain



(c) octahedral stress strain

Figure 4.24 ECPM-VT6.5-2,  $\alpha_1 = 250$



#### 4.3.6 FEBM - Test VT6.5-3

This test is similar to test VT6.5-1 except that the level of confining stress is much higher here. The measured axial stress versus axial and lateral strains are presented in Figure 4.25, (only one lateral gage survived the test). Based on pre and post test micrometer measurements the plastic axial strain was recorded as  $-0.058$  and

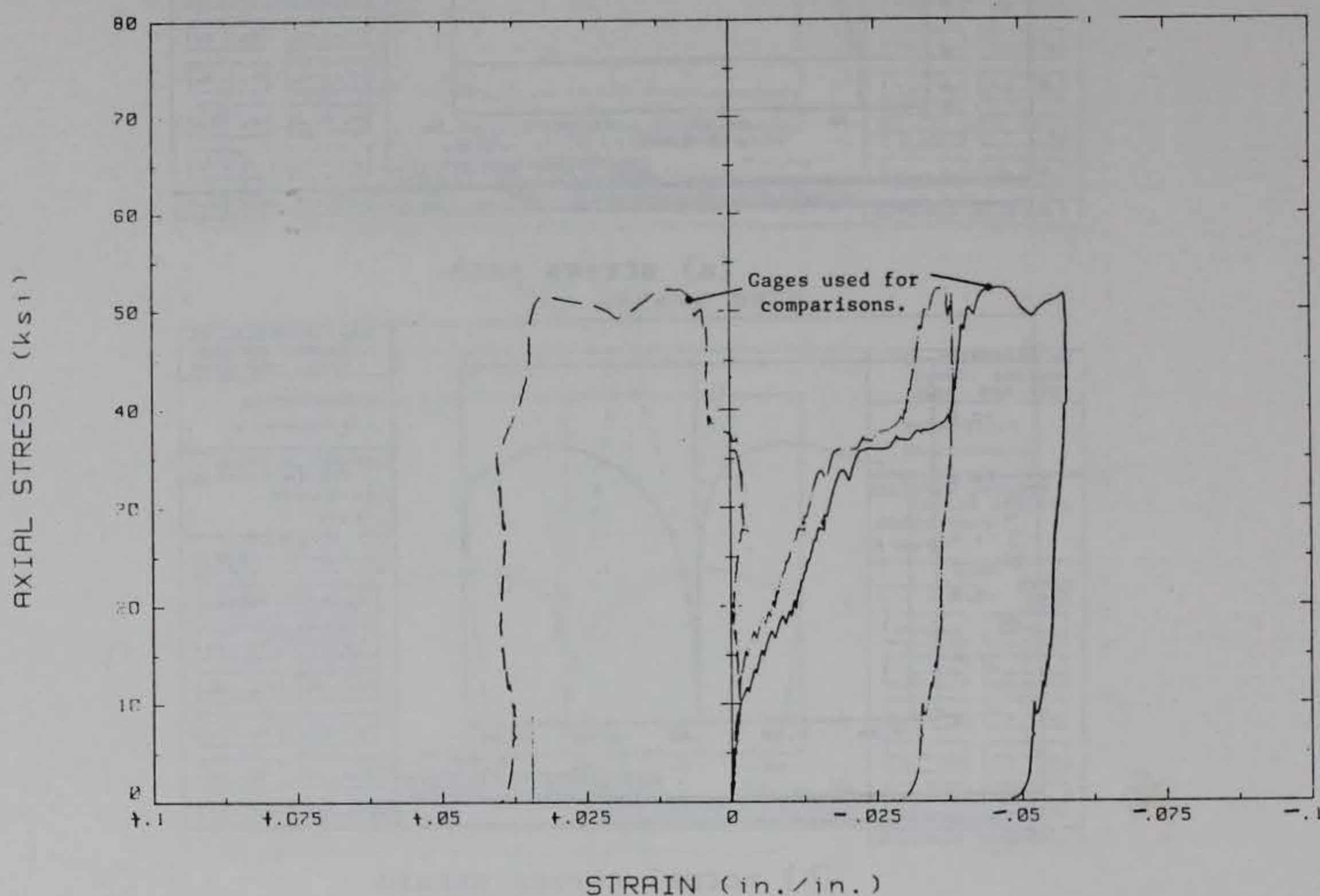
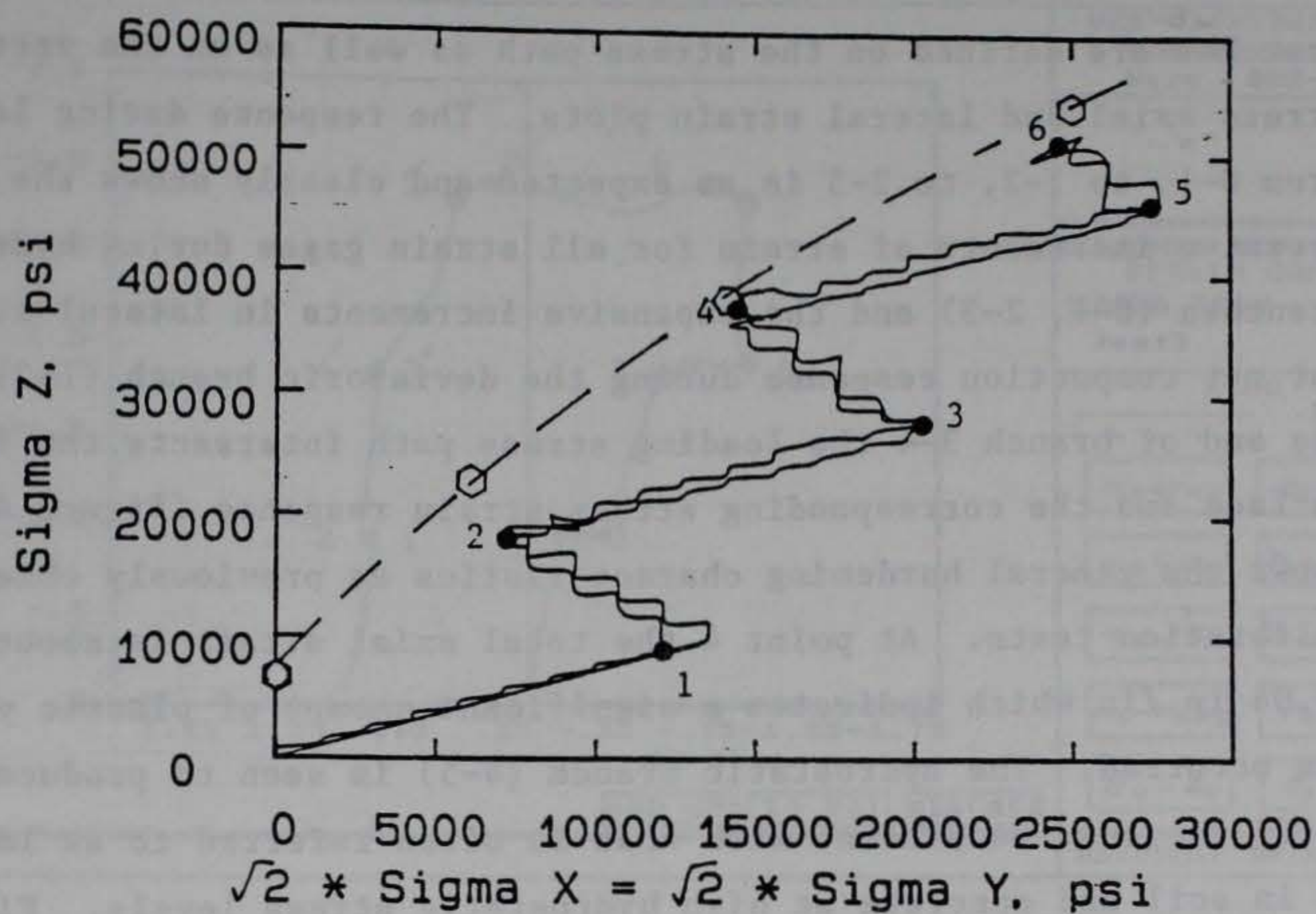


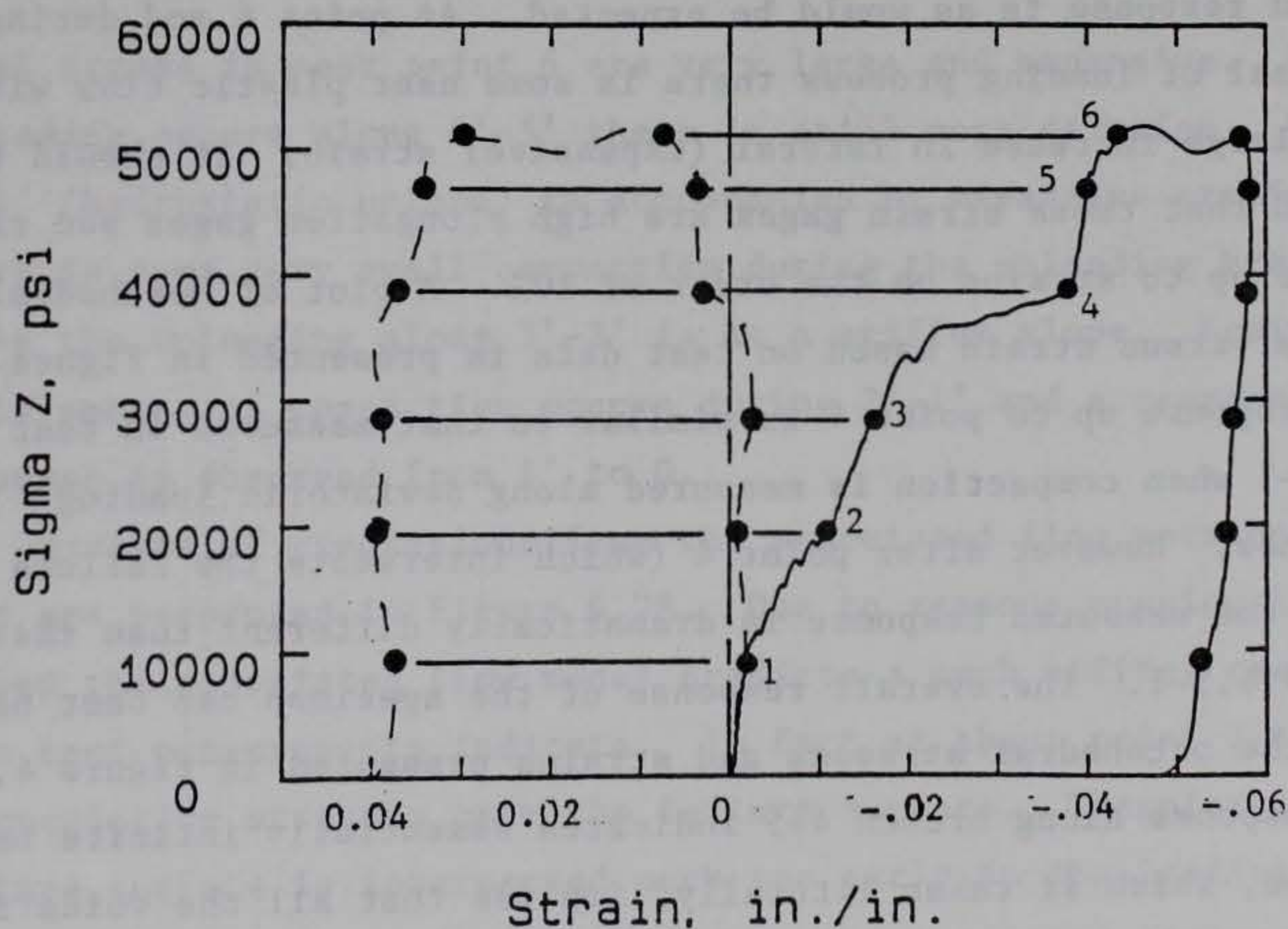
Figure 4.25 Actual test data for VT6.5-3

the plastic lateral strain as  $0.05$ , resulting in a plastic volume change of  $+0.044$ . These values compare well with strain gage measurements. Also, the two axial gages show the same trends in response, with gage 5 possibly being in contact with a higher percentage of aggregate surface or possibly not being bonded quite as good as gage 3. Gage 3 was selected for use in defining the axial response of the total specimen. Figure 4.26, presents the loading stress path for the test along with the failure surface predicted by





(a) stress path



(b) axial stress versus axial and lateral strains

Figure 4.26 WES test, VT6.5-3, hydrostatic deviatoric load path at high confining stress region, with stress strain response



the FEBM. The points of transition from hydrostatic to deviatoric branches are defined on the stress path as well as on the vertical stress axial and lateral strain plots. The response during loading from 0-1, to 1-2, to 2-3 is as expected and clearly shows the compressive increments of strain for all strain gages during hydrostatic branches (0-1, 2-3) and the expansive increments in lateral strains but net compaction response during the deviatoric branch (1-2). Near the end of branch 3-4 the loading stress path intersects the failure surface and the corresponding stress strain response (Figure 4.26b) shows the general hardening characteristics as previously observed in calibration tests. At point 4 the total axial strain is about -0.04 in./in which indicates a significant amount of plastic yielding has occurred. The hydrostatic branch (4-5) is seen to produce a very stiff response consistent with what is often referred to as locking up in soil and concrete at high hydrostatic stress levels. Finally the last branch of the deviatoric load path is (5-6) and the stress strain response is as would be expected. At point 6 and during the reversal of loading process there is some near plastic flow with a very large increase in lateral (expansive) strain. It should be mentioned that these strain gages are high elongation gages and rated linear up to strains on the order of 10%. A plot of octahedral stress versus strain based on test data is presented in Figure 4.27. The response up to point 4 is similar to that measured in test VT6.5-1 when compaction is measured along deviatoric loading branches. However after point 4 (which intersects the failure surface) the measured response is dramatically different than that of test VT6.5-1. The overall response of the specimen can best be seen from the octahedral stresses and strains presented in Figure 4.27. The response along branch 4-5 indicates essentially infinite bulk modulus, which if taken literally, implies that all the voids in the specimen have been closed. Along branch 5-6 the specimen begins to dilate unlike the compactive response seen along similar branches in test VT6.5-1. The plastic flow lateral strains occurring while the



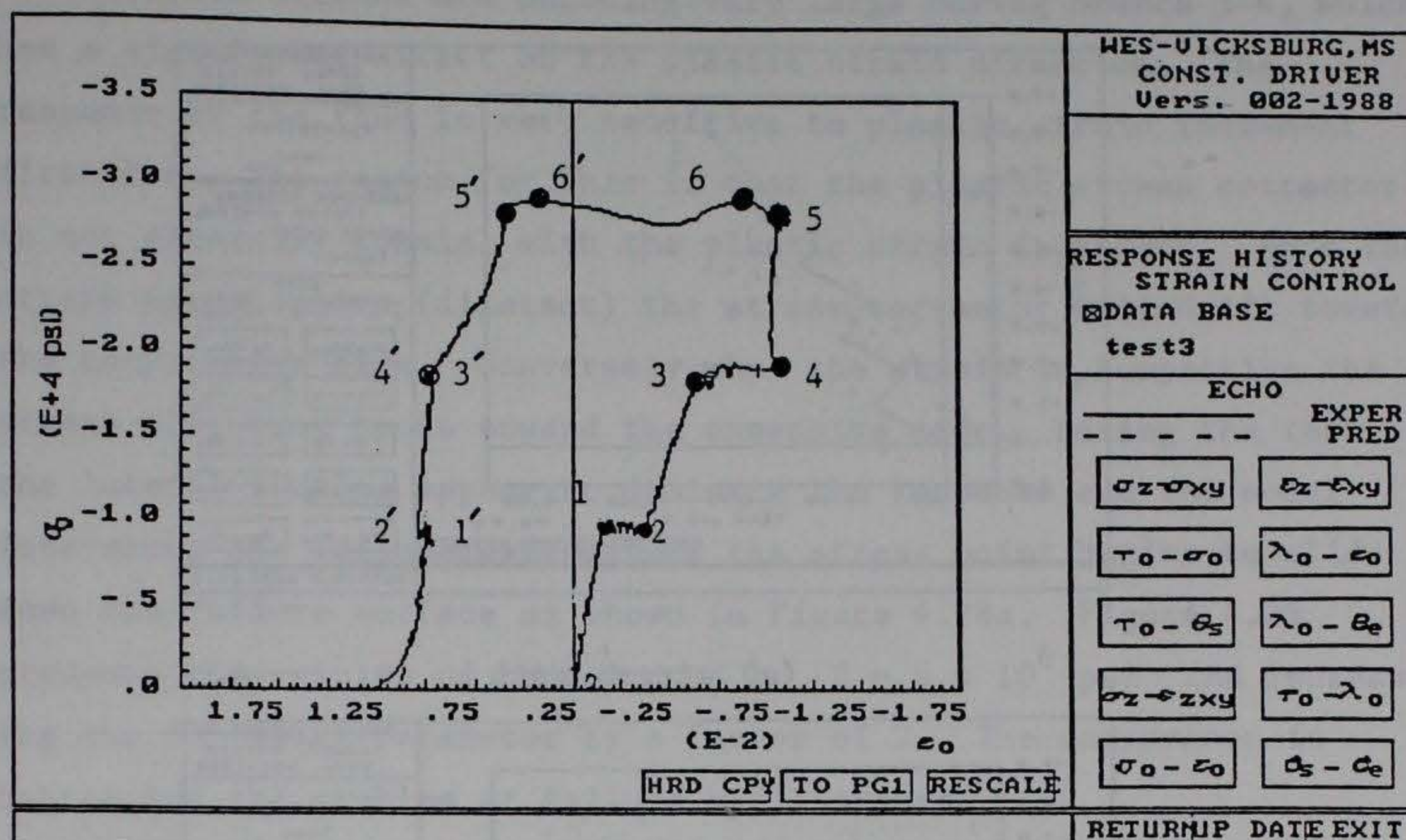
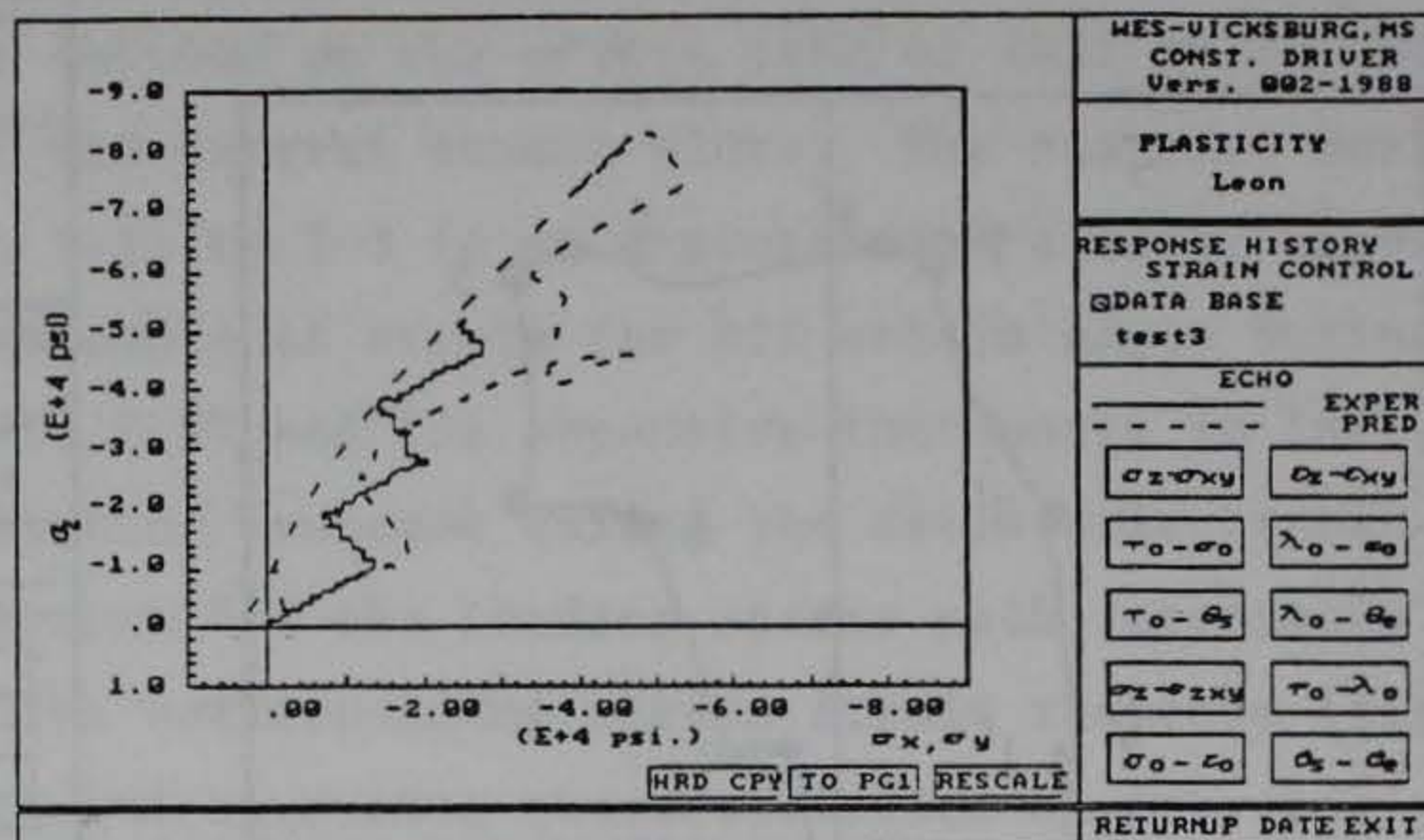


Figure 4.27 VT6.5-3, octahedral stress vs. strain

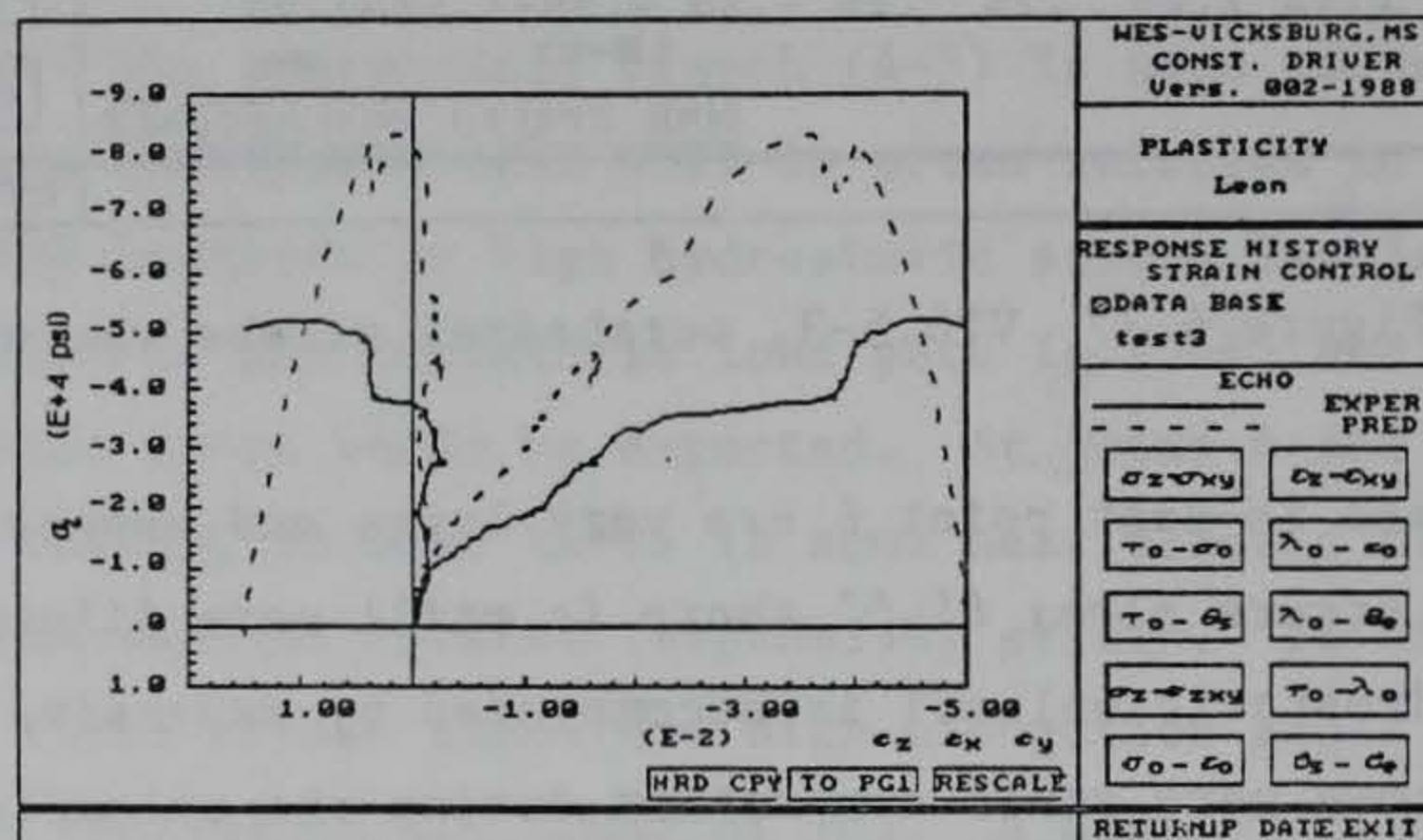
axial stress is near point 6 are very large and expansive. As unloading occurs along 6'-5' there is still more dilation. Branch 5'-4' (hydrostatic unload) is accompanied by expansive strains. There is some very small compaction during the unloading branch 4'-3' while the unloading along 3'-2' is at a stiffer slope. Again some small amount of compaction occurs during 2'-1' and a reasonable response is observed from 1' to 0.

Results of predictions from the associated flow version of the FEBM are presented in Figure 4.28. Due to reasons previously discussed the associated flow model predicts a much stiffer response than test measurements indicate. In fact at about point 3 the model is predicting stresses near the failure surface. Therefore, the failure surface is intersected much too early in the loading history and since strains continue to increase the predicted stress point moves up the failure surface to an extremely high axial stress of about 84 ksi. It is difficult to say exactly what is occurring in the model at this point.

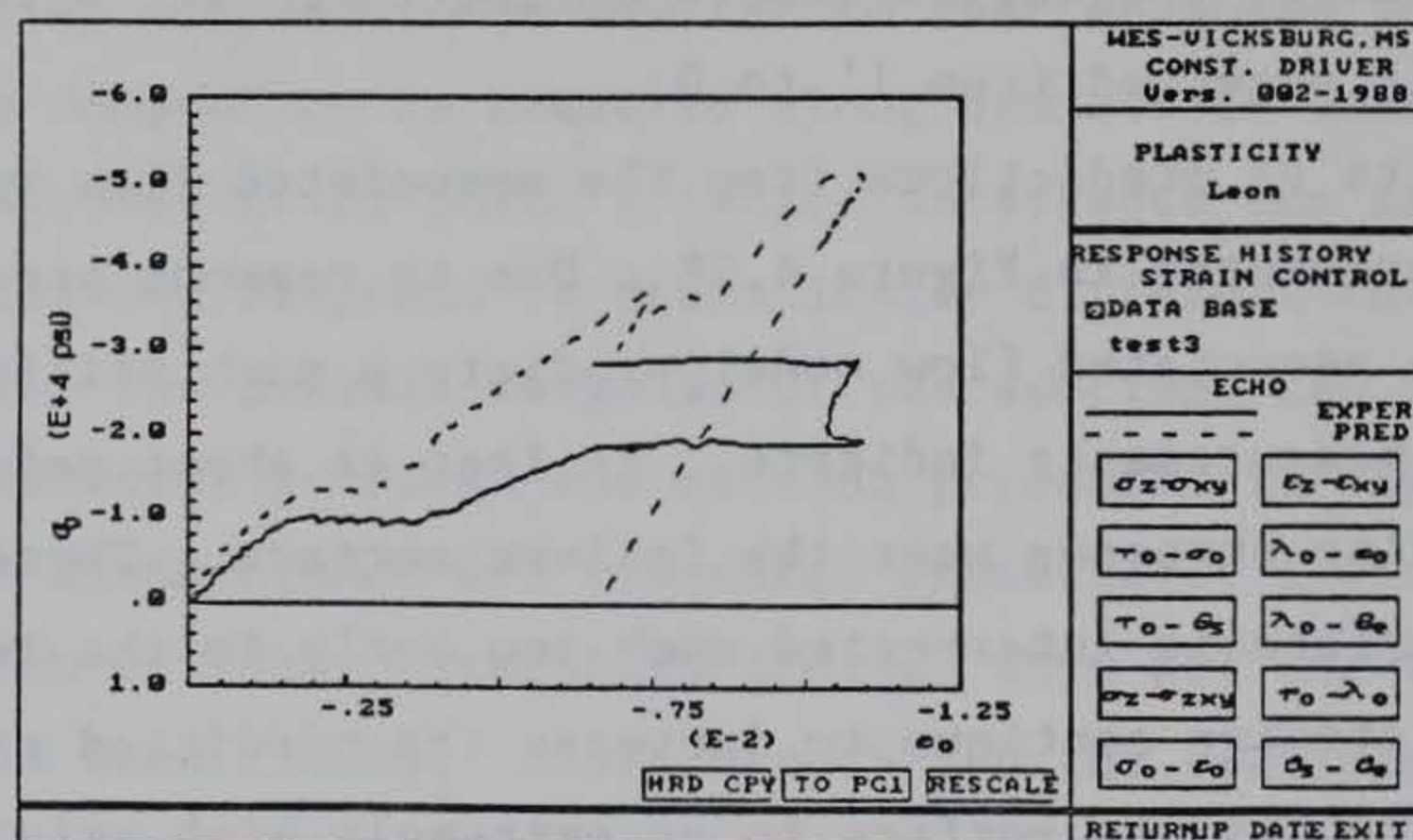




(a) stress path



(b) normal stress strain



(c) octahedral stress strain

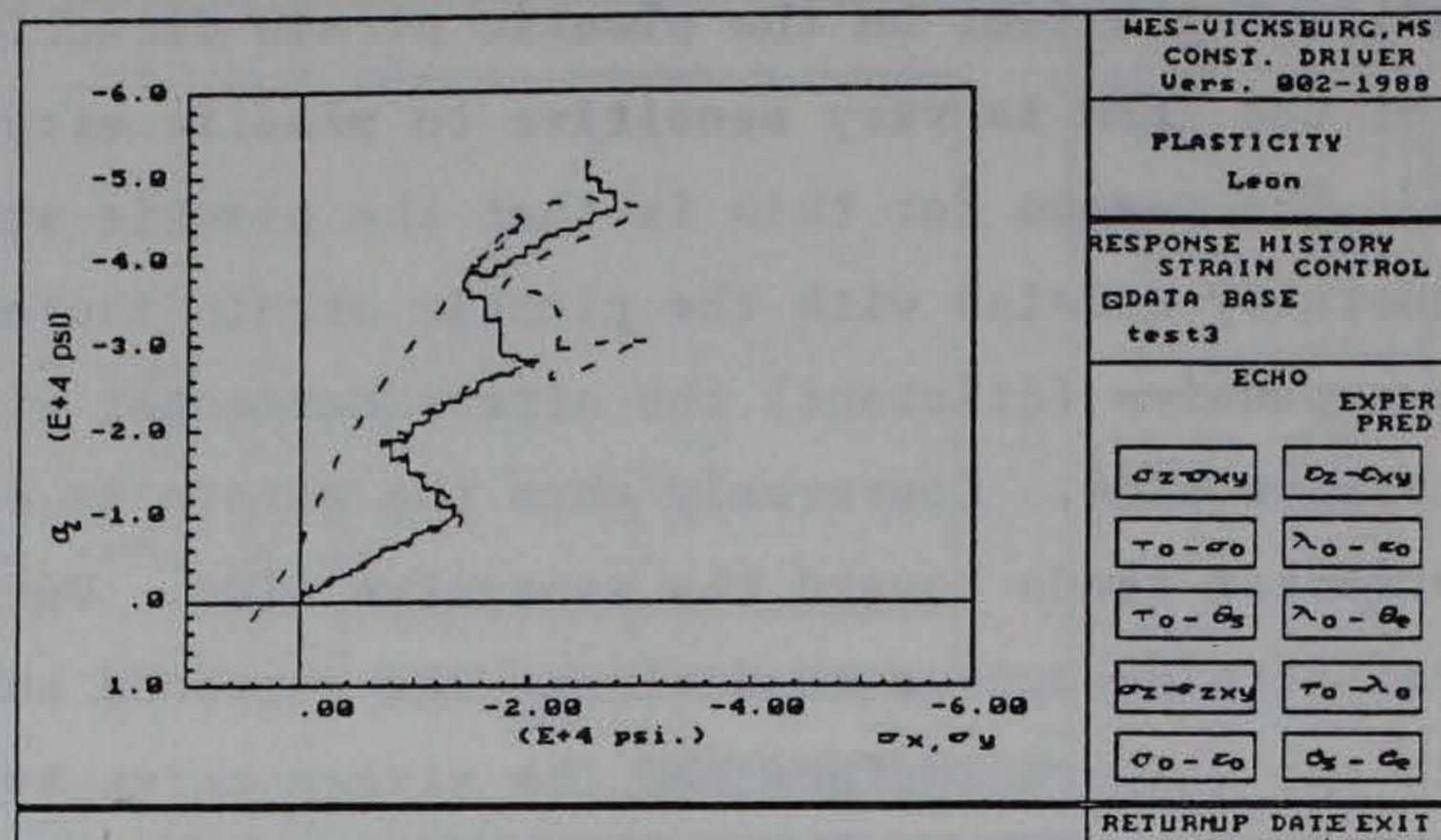
Figure 4.28 FEBM-VT6.5-3, associated flow, initial calibration



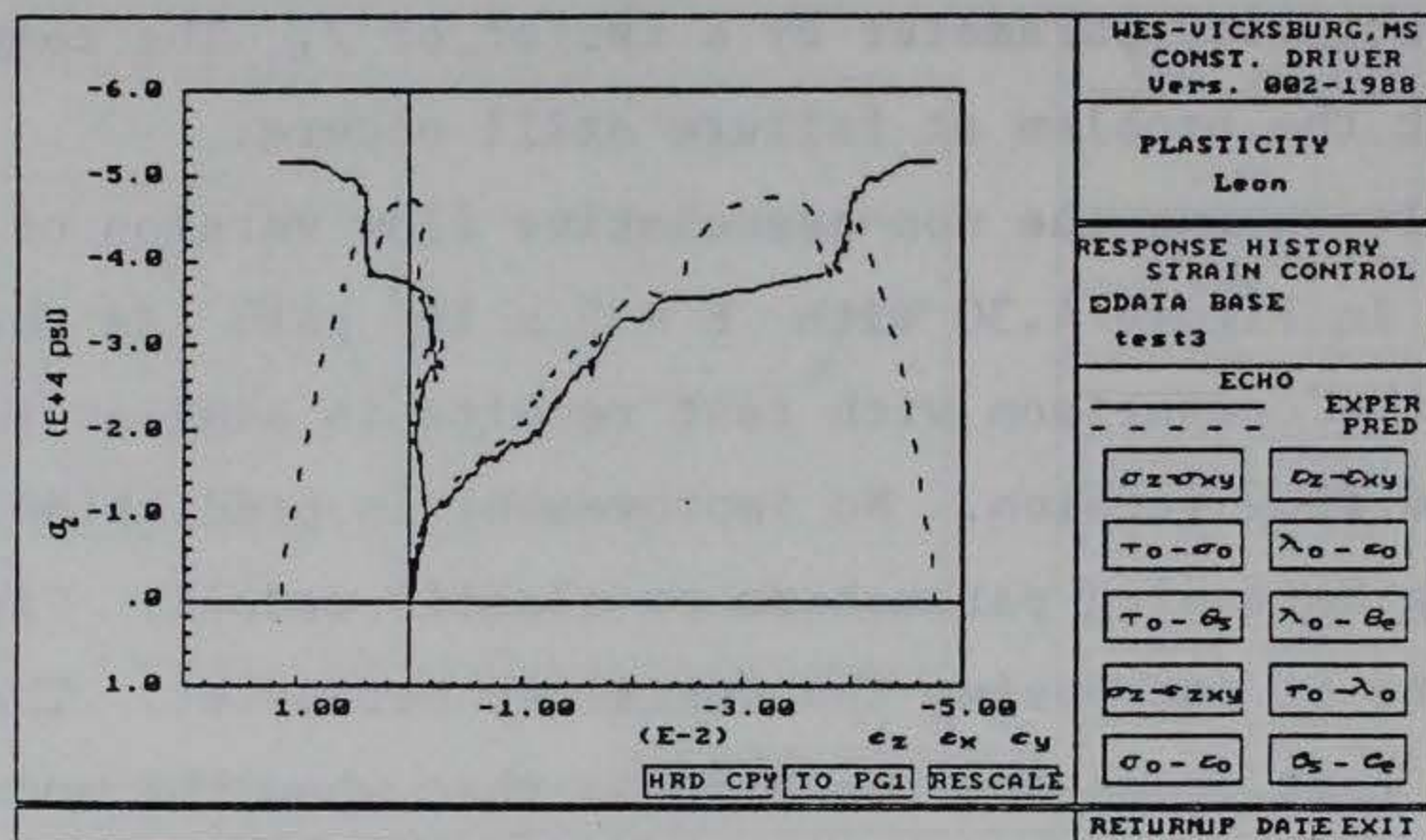
Lateral strains are becoming very large during branch 3-4, which has a significant affect on the plastic strain direction. The response of the FEBM is very sensitive to plastic strain increment direction. The reason for this is that the plastic stress corrector is not generally coaxial with the plastic strain increment. When the strain is expansive (dilatant) the stress corrector will drift toward the compressive side. Conversely when the strain is compactive the stress corrector tends toward the expansive side. During the test the lateral strains appear to dominate the response and the model intersects the failure surface and the stress point begins to slide down the failure surface as shown in Figure 4.28a. Figure 4.29 presents the results of reducing  $E$  to  $E = 5 \times 10^6$  psi and increasing the ductility parameter by a factor of 2. The comparison is better but the problem at failure still occurs.

Results using the non-associative flow version of the FEBM are presented in Figure 4.30 with  $E = 5 \times 10^6$  psi. As shown in Figure 4.30 the comparison with test results is similar to that with the associated flow version. No improvement in prediction were obtained by varying hardening parameters or elastic moduli. Figure 4.31 shows the effects of increasing the ductility parameter. The main problem that this test poses for the FEBM is that when the model predicts intersection of the stress path with the failure surface near point 4 (which actually occurs in the test) the hardening parameter has reached the maximum value of 1 and cannot decrease during the remainder of the test. Therefore, the model must either predict a purely elastic response if the stress point moves inside the failure surface or predict a response associated with a neutral type loading as the stress point slides along the failure surface. Another point to be made is that the model may have compared better if gage 5 (Figure 4.25) had been selected as the axial strain for comparison. However, this is doubtful since the relative magnitude of the lateral strains would be even larger for this case.

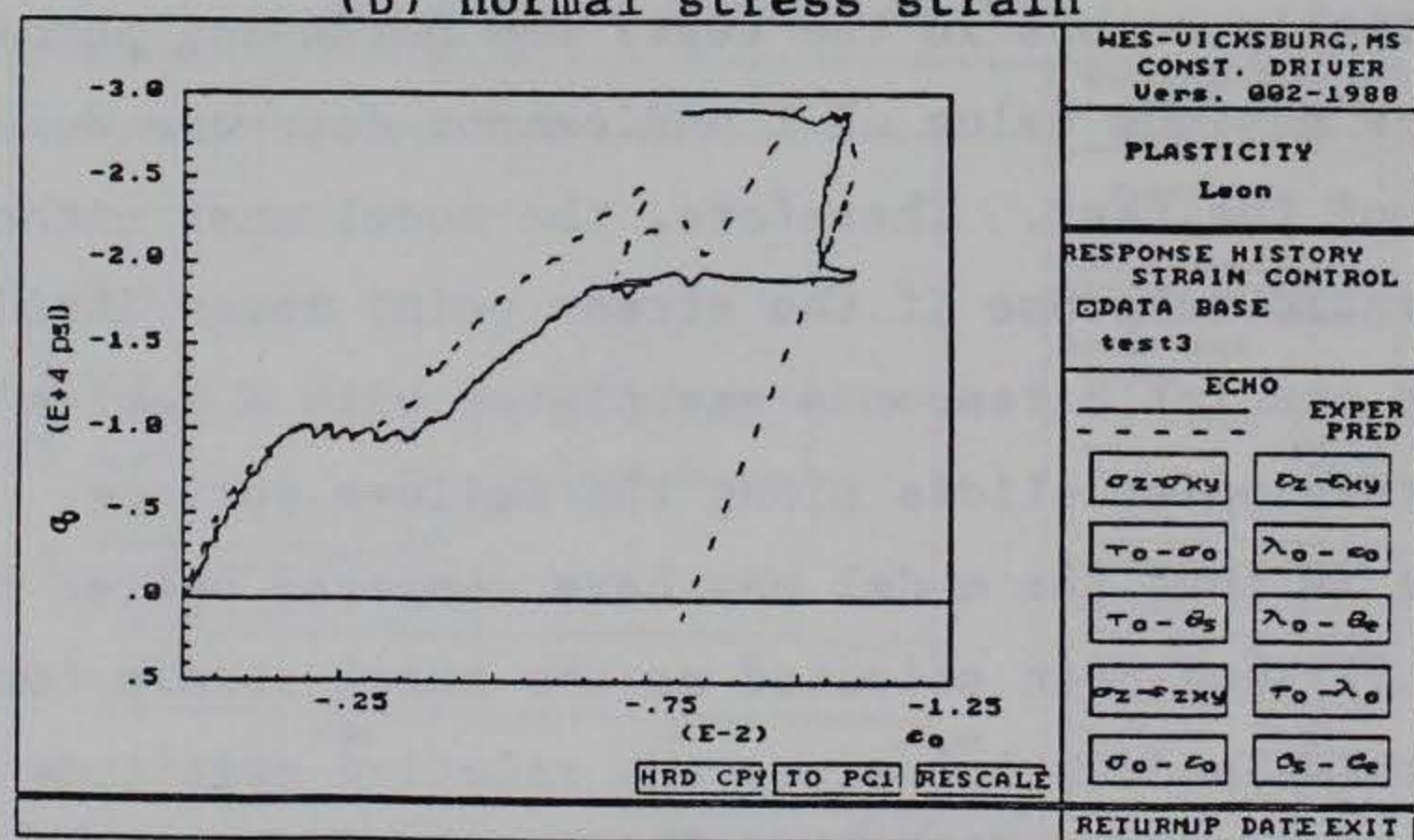




(a) stress path



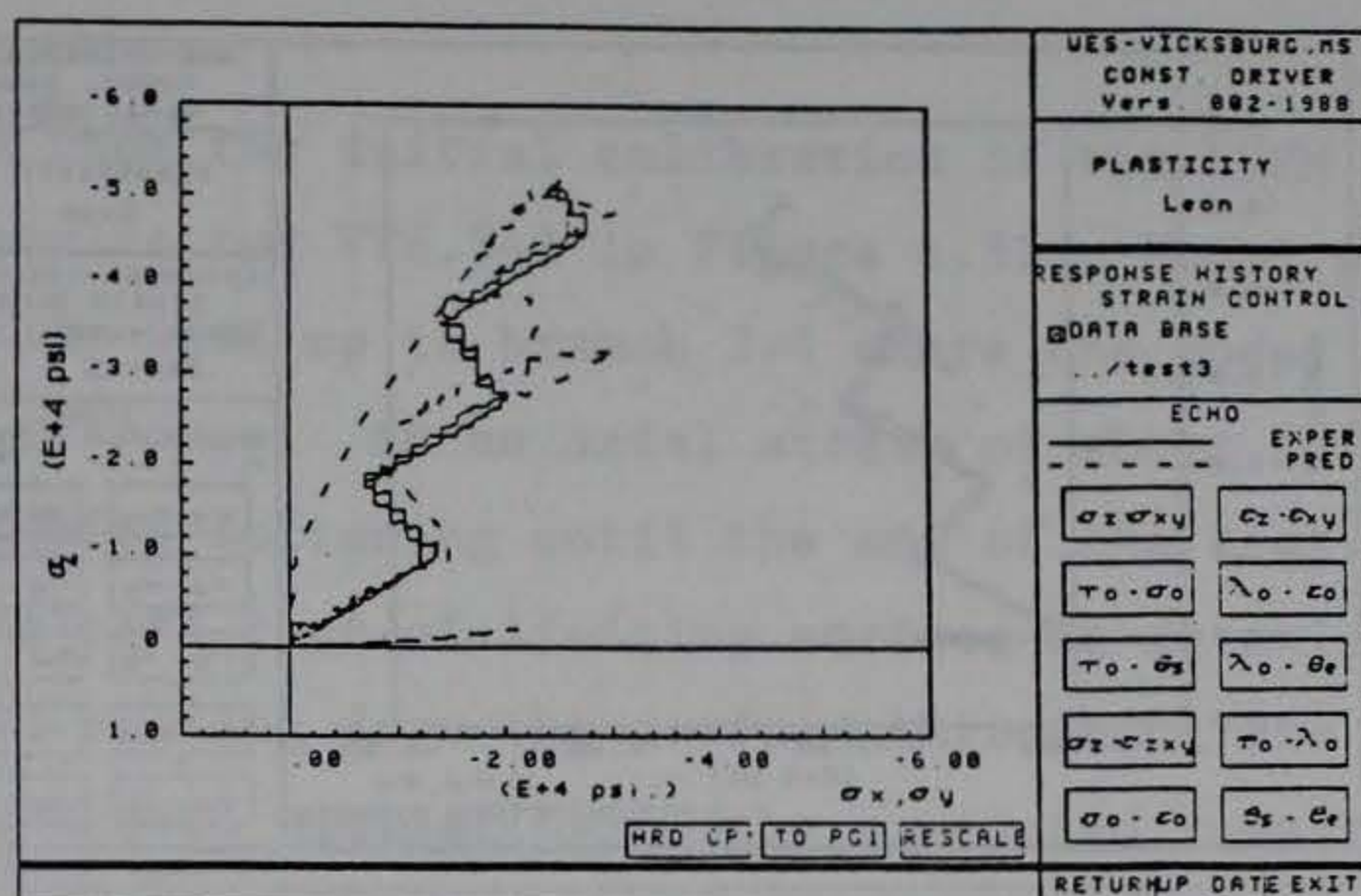
(b) normal stress strain



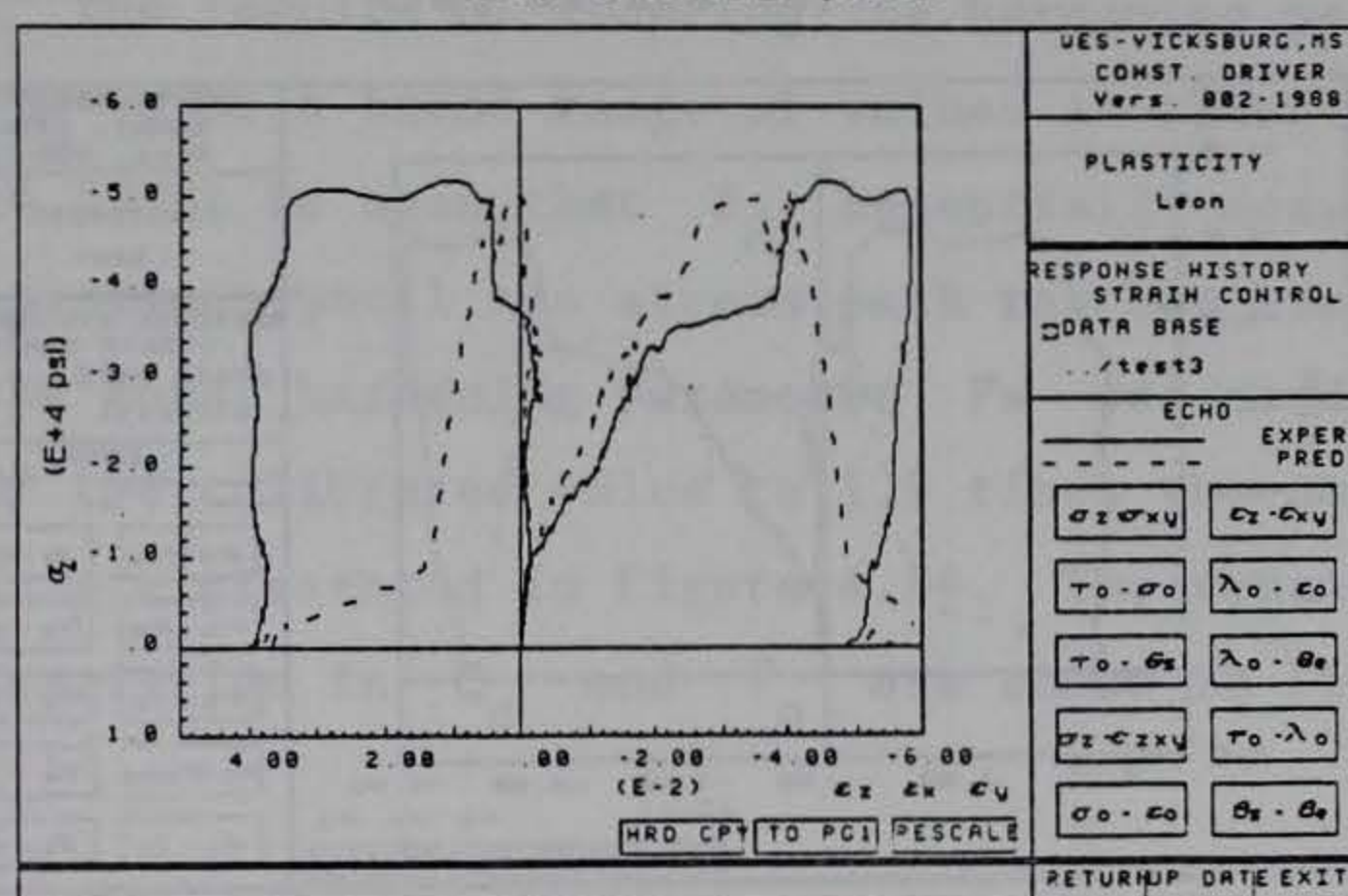
(c) octahedral stress strain

Figure 4.29 FEBM-VT6.5-3, associated flow,  $E=5.0E6$ ,  $X_p=2.0 \cdot X_p$  (initial)

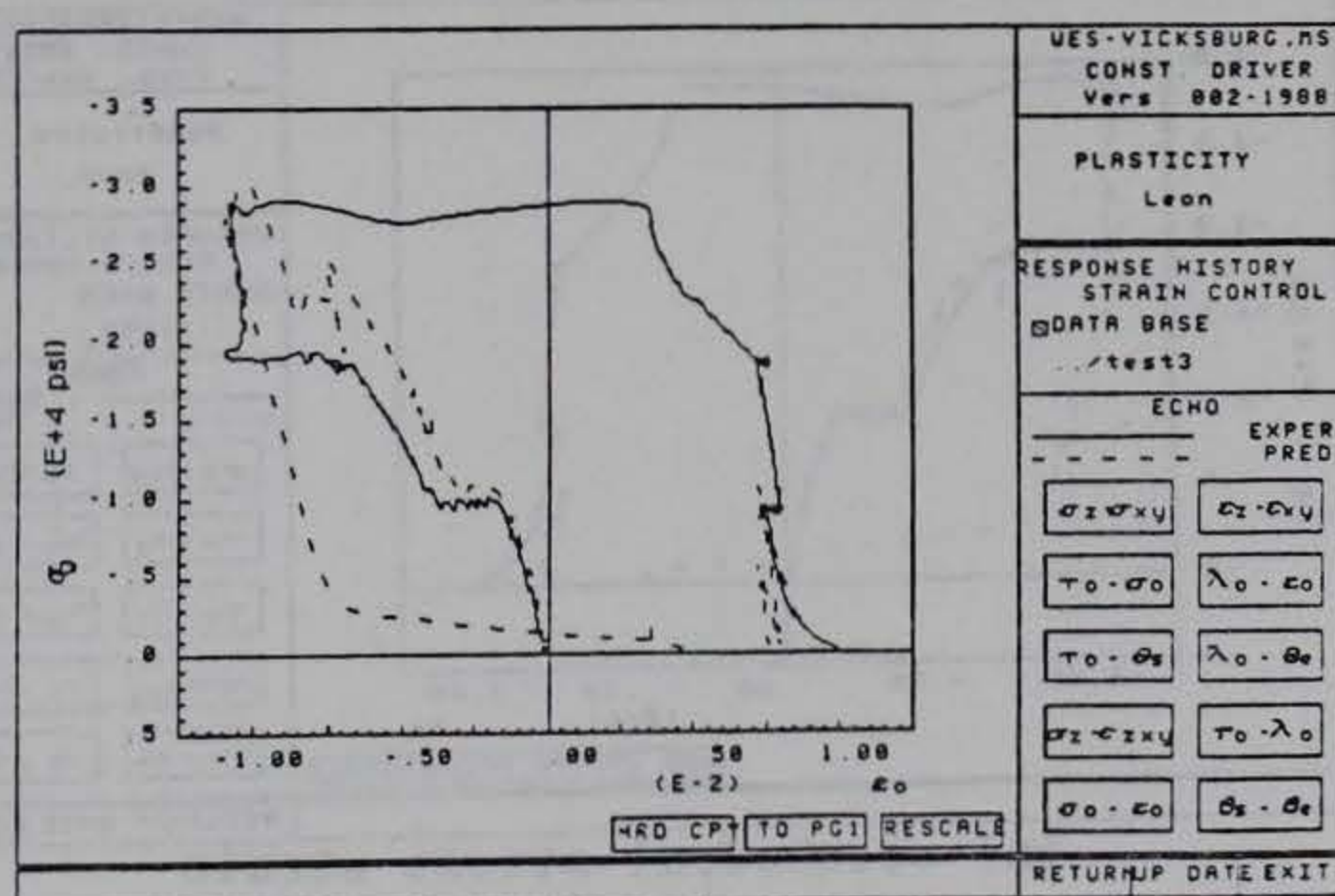




(a) stress path



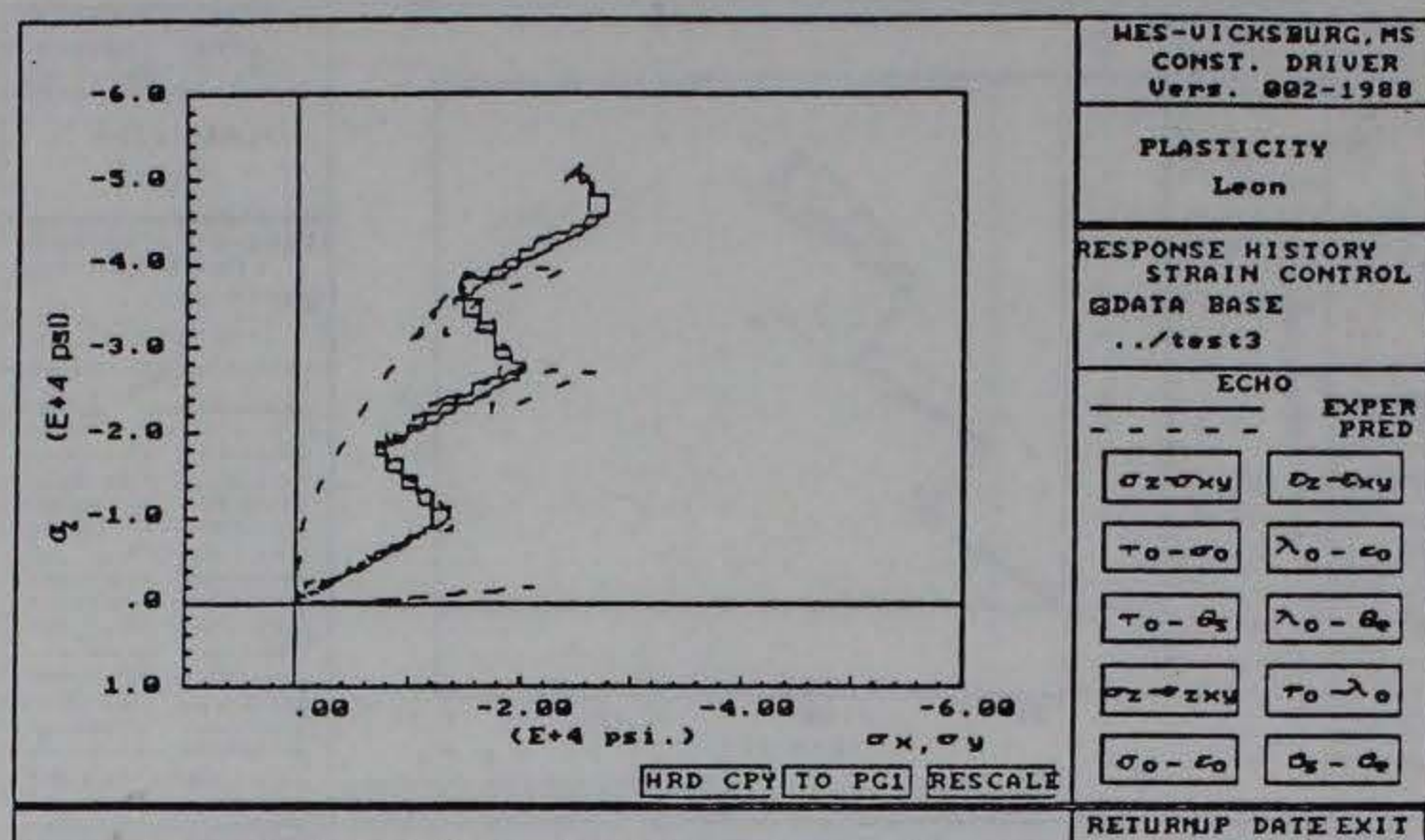
(b) normal stress strain



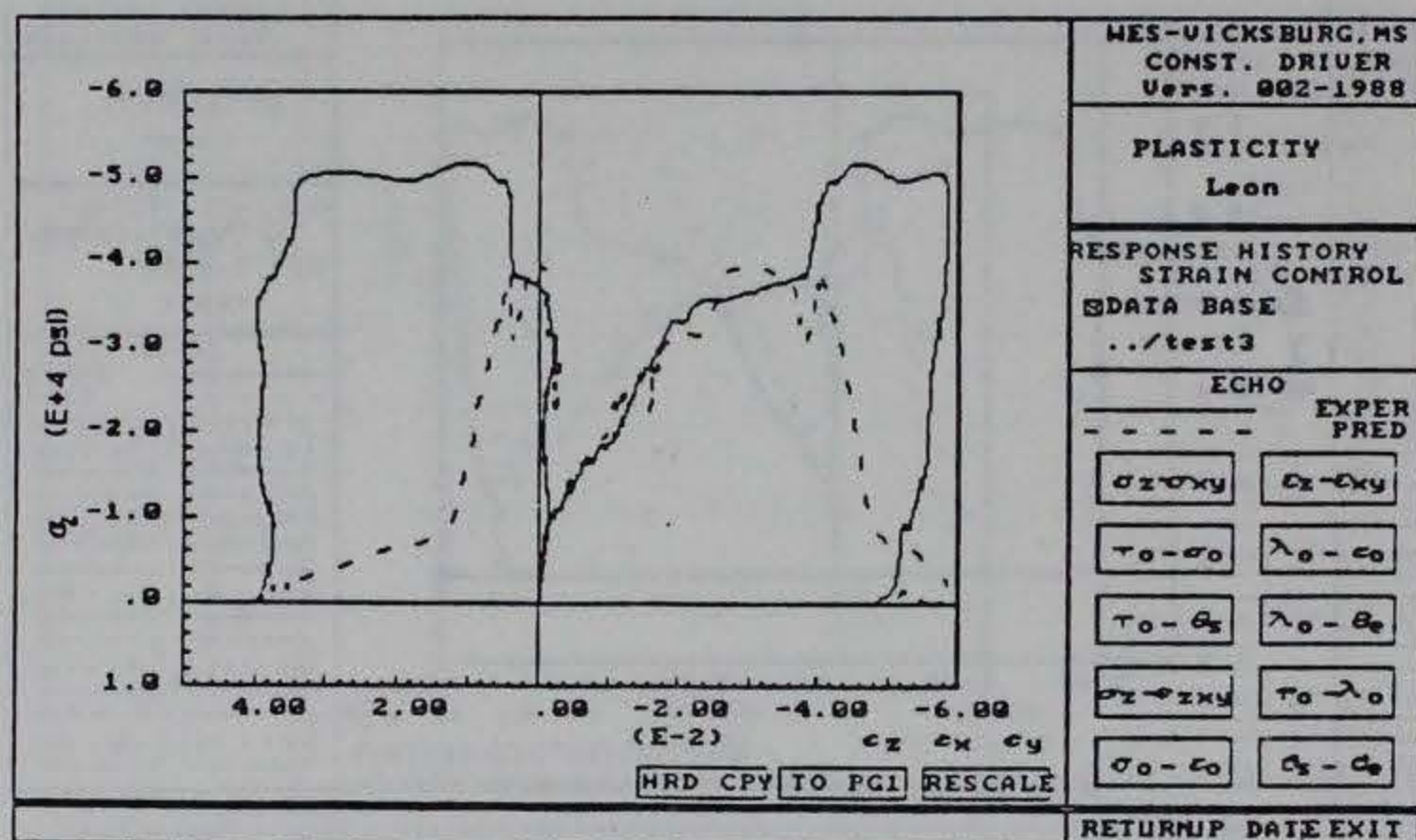
(c) octahedral stress strain

Figure 4.30 FEBM-VT6.5-3, non-associated flow,  $E=5.0E6$

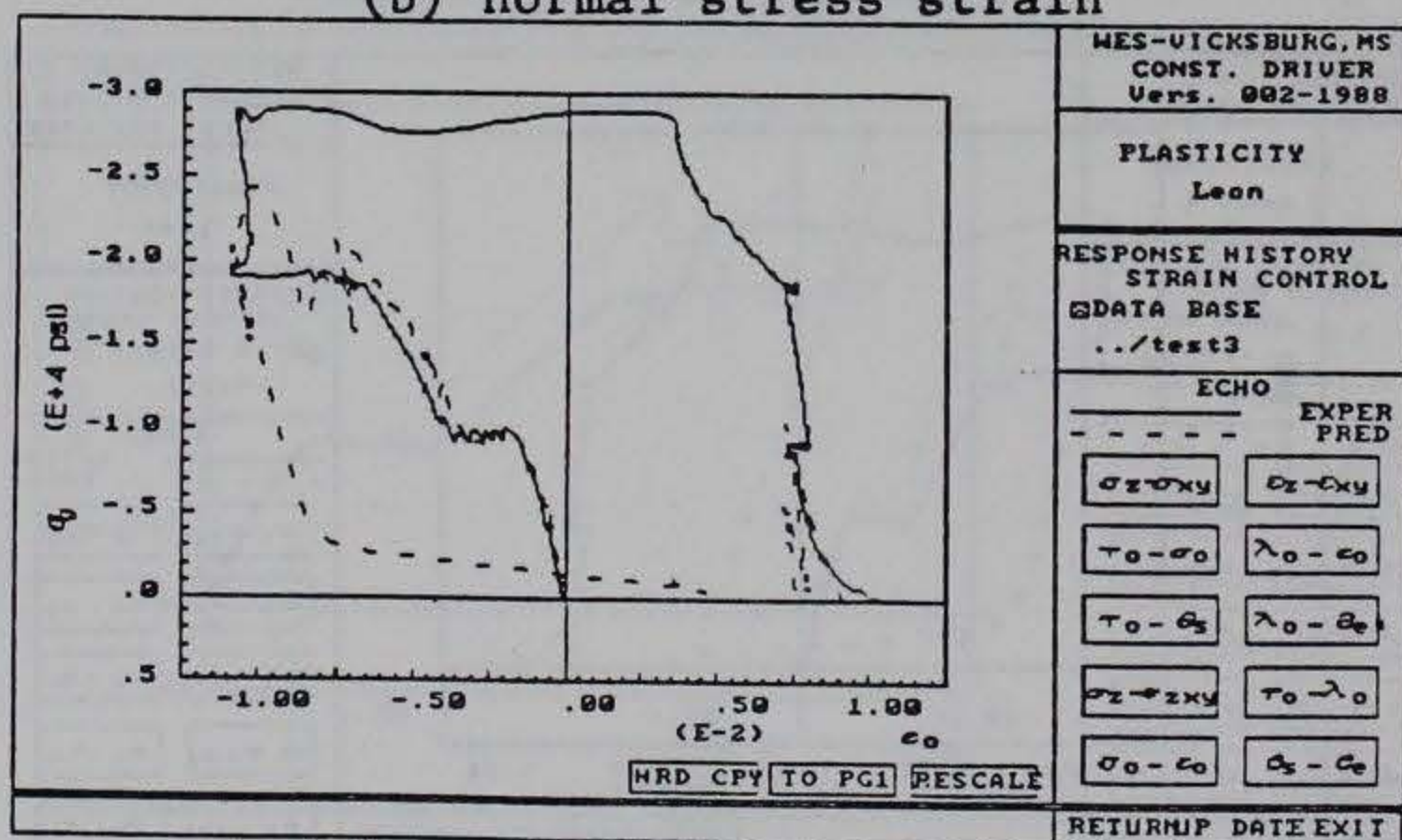




(a) stress path



(b) normal stress strain



(c) octahedral stress strain

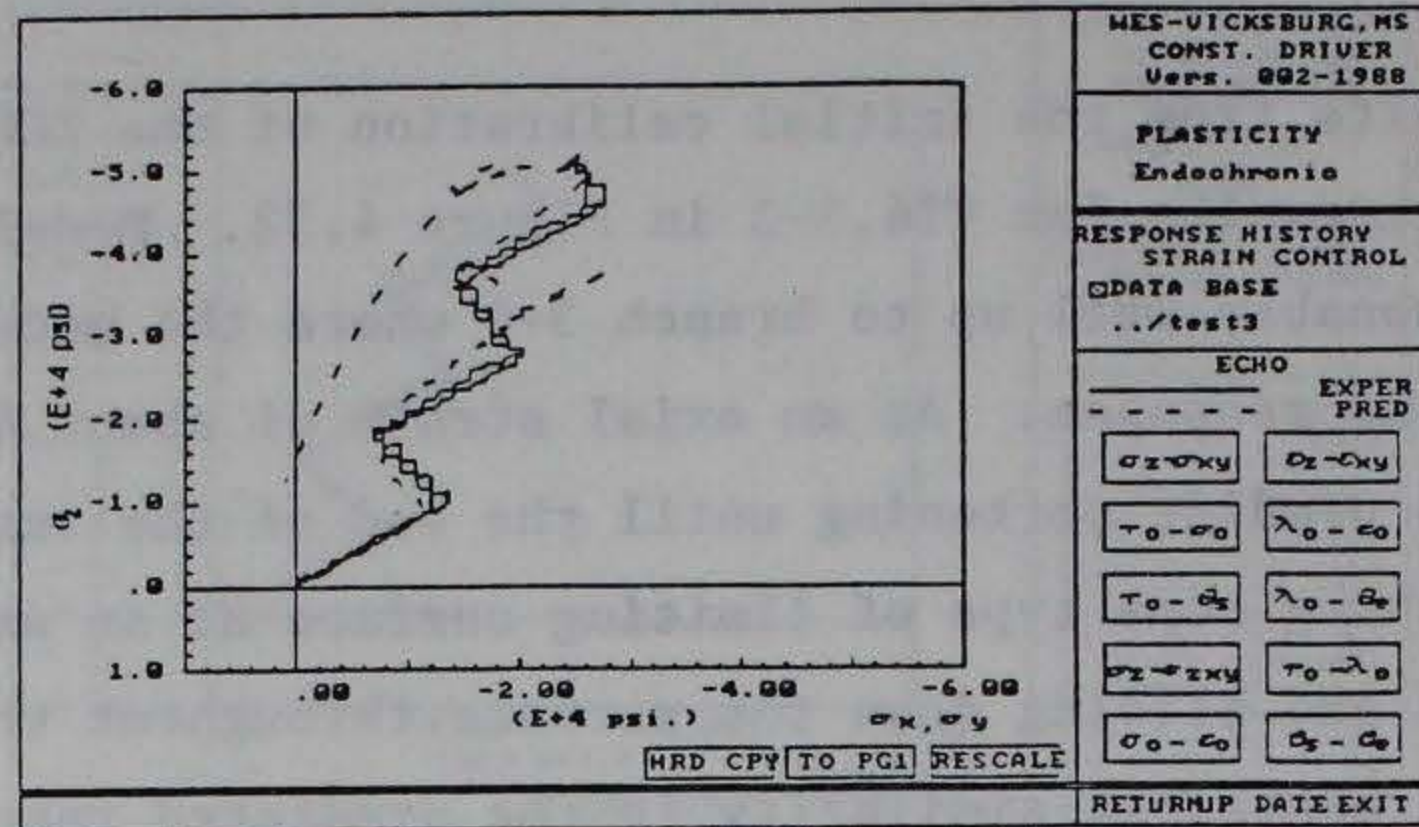
Figure 4.31 FEBM-VT6.5-3, non-associated flow,  $E=5.0E6$ ,  $X_p=1.5 \cdot X_p$   
(initial)



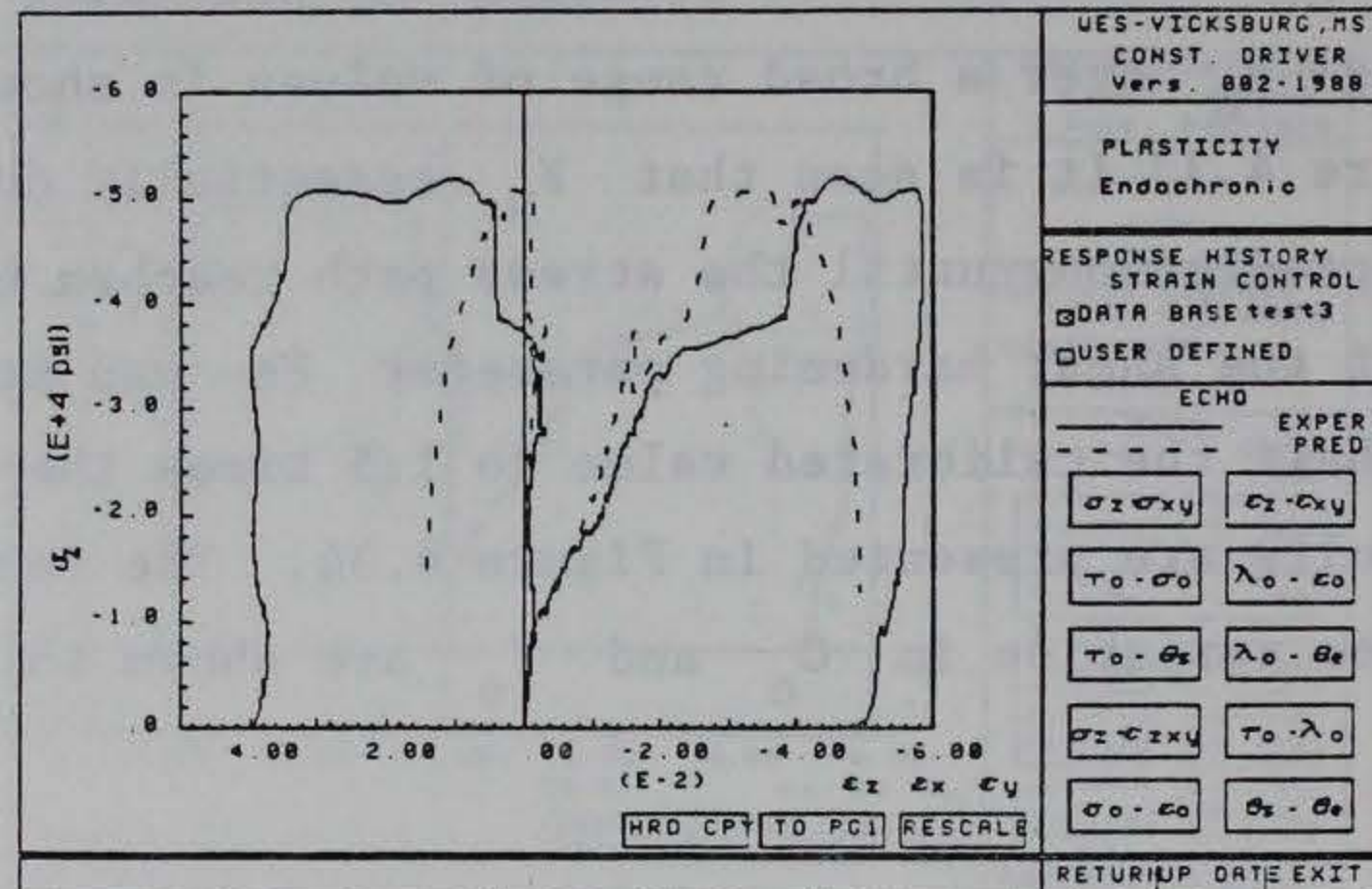
#### 4.3.7 ECPM Versus VT6.5-3

Results from the initial calibration of the ECPM are compared with test results for VT6.5-3 in Figure 4.32. Model predictions compare reasonably well up to branch 3-4 where the model tends to over-predict the response. At an axial strain of about 4% the model begins to predict softening until the end of the test. The ECPM is also reaching some type of limiting surface at an axial strain of about 41% and sliding down the surface throughout the rest of the test. A remarkable similarity in the predicted results of the two models for this test can be seen by comparing Figures 4.30 (FEBM) and 4.32 (ECPM). The results of reducing the hardening parameter  $F_H$  by varying  $\beta_H$  over a broad range of values is shown in Figure 4.33. From Figure 4.33 it is seen that  $F_H$  essentially does not impact response predictions until the stress path reaches branch 3-4. The effects of the shear hardening parameter  $F_s$  was studied by varying  $\beta_s$  from half the calibrated value to 1.5 times the calibrated value. These results are presented in Figure 4.34. The sensitivity of response to variation in  $C_o$  and  $\Gamma_o$  are shown in Figure 4.35.

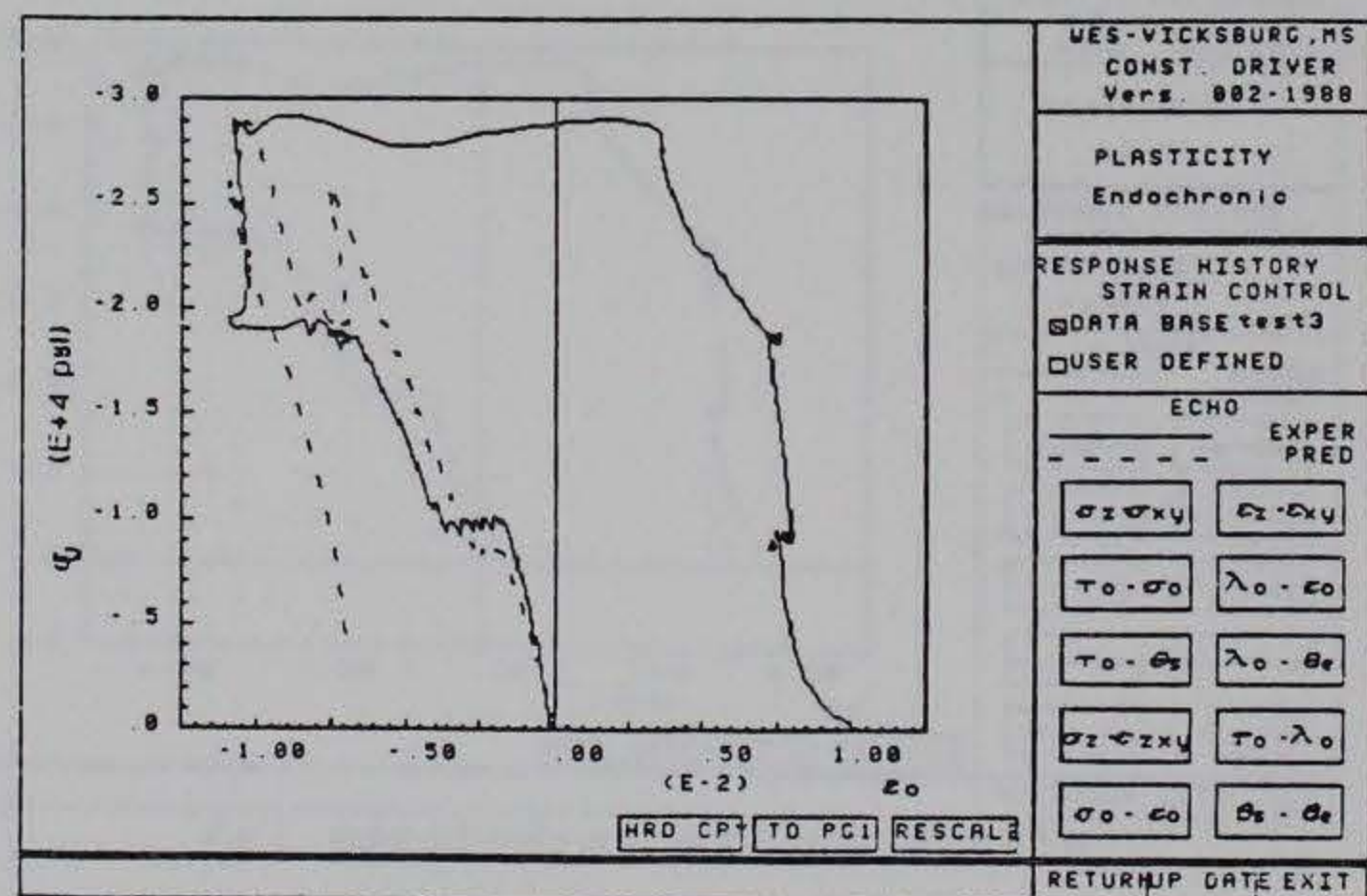




(a) stress path



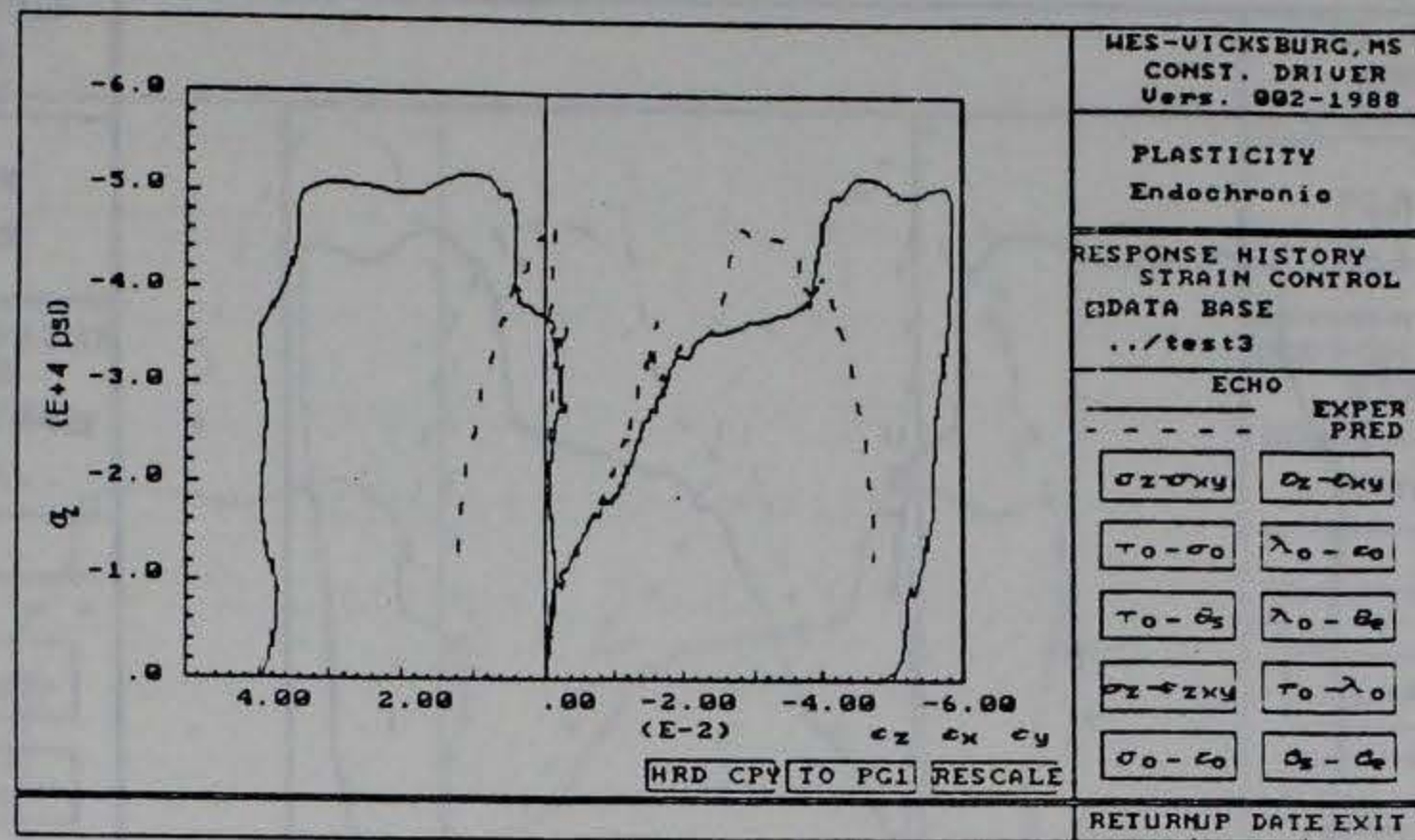
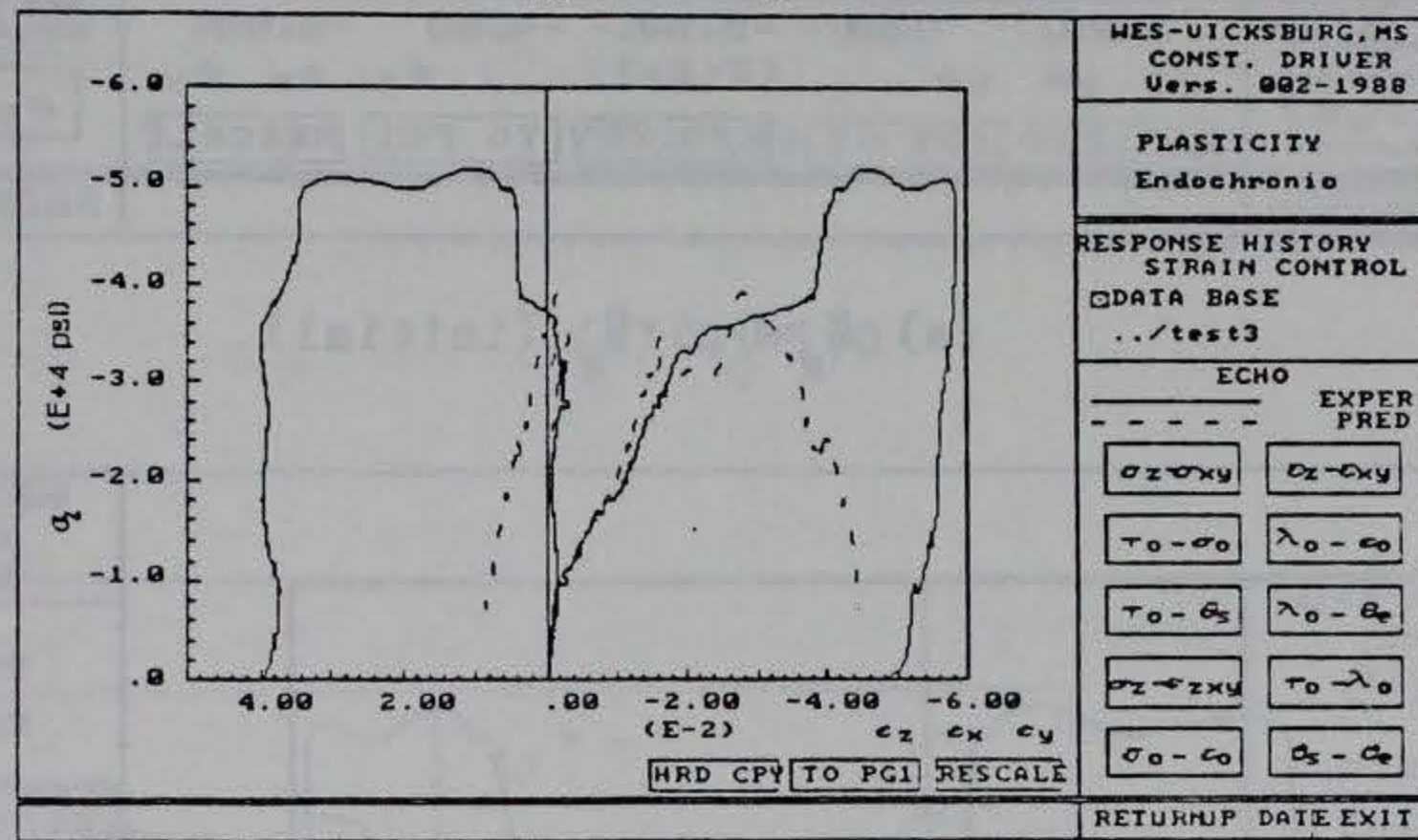
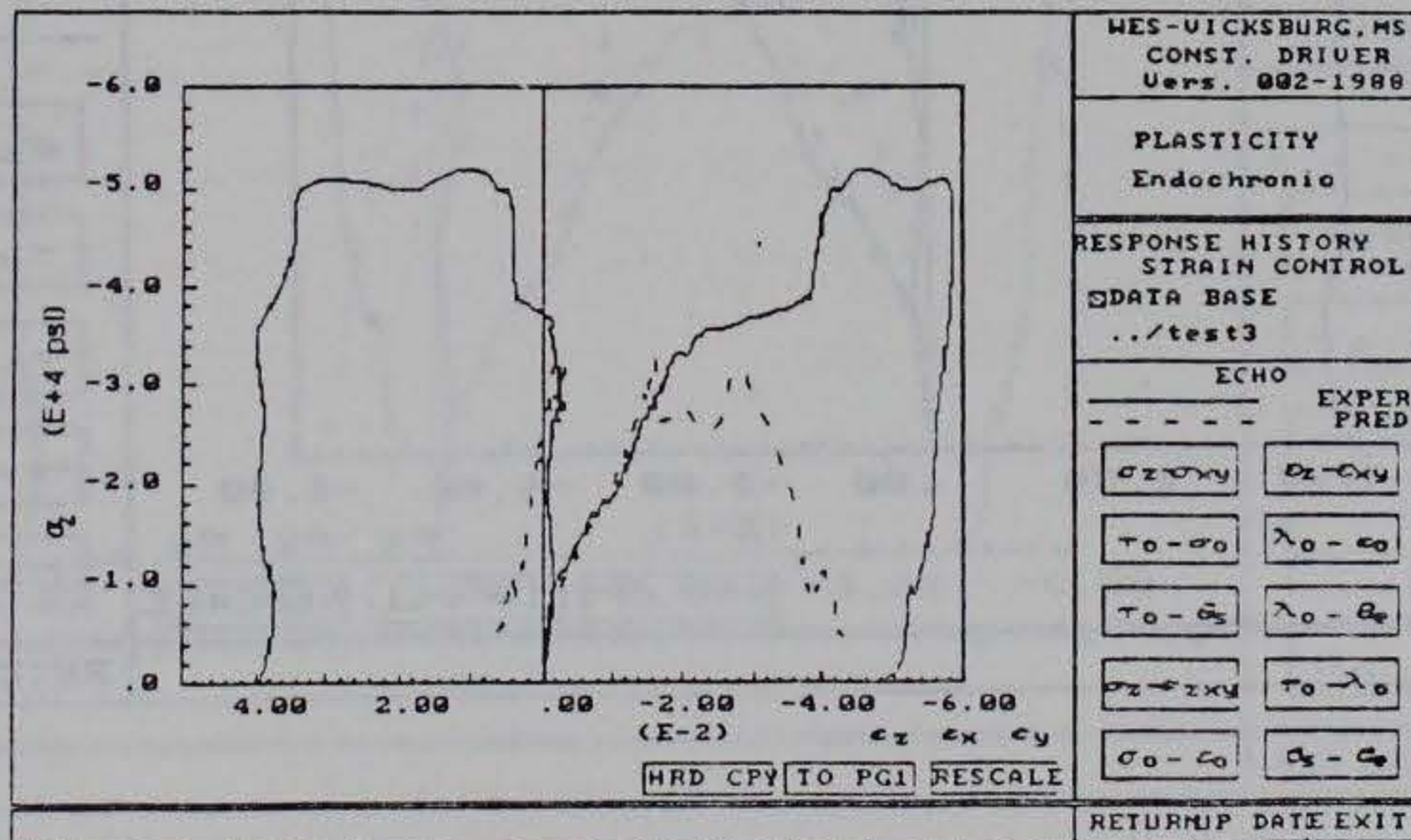
(b) normal stress strain



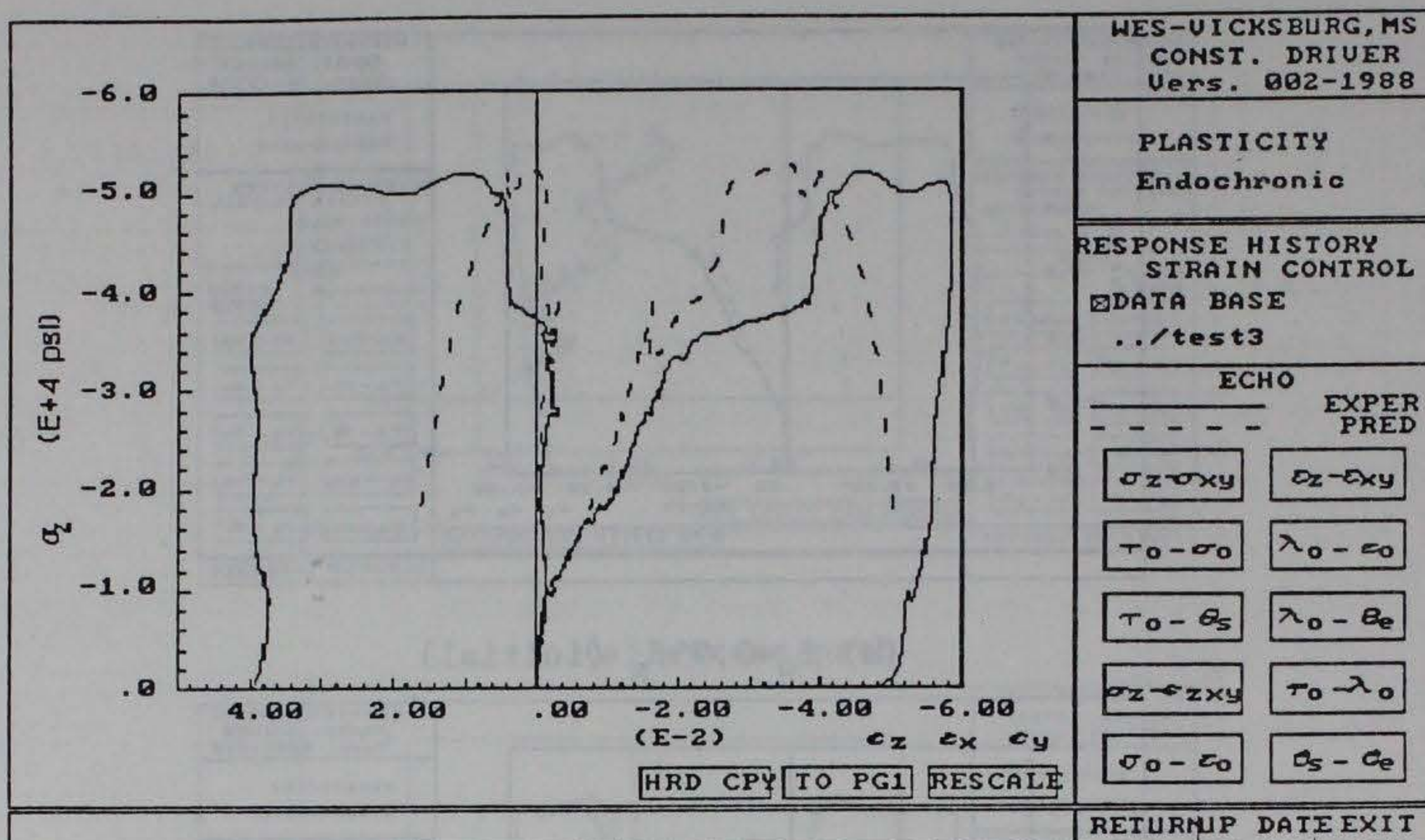
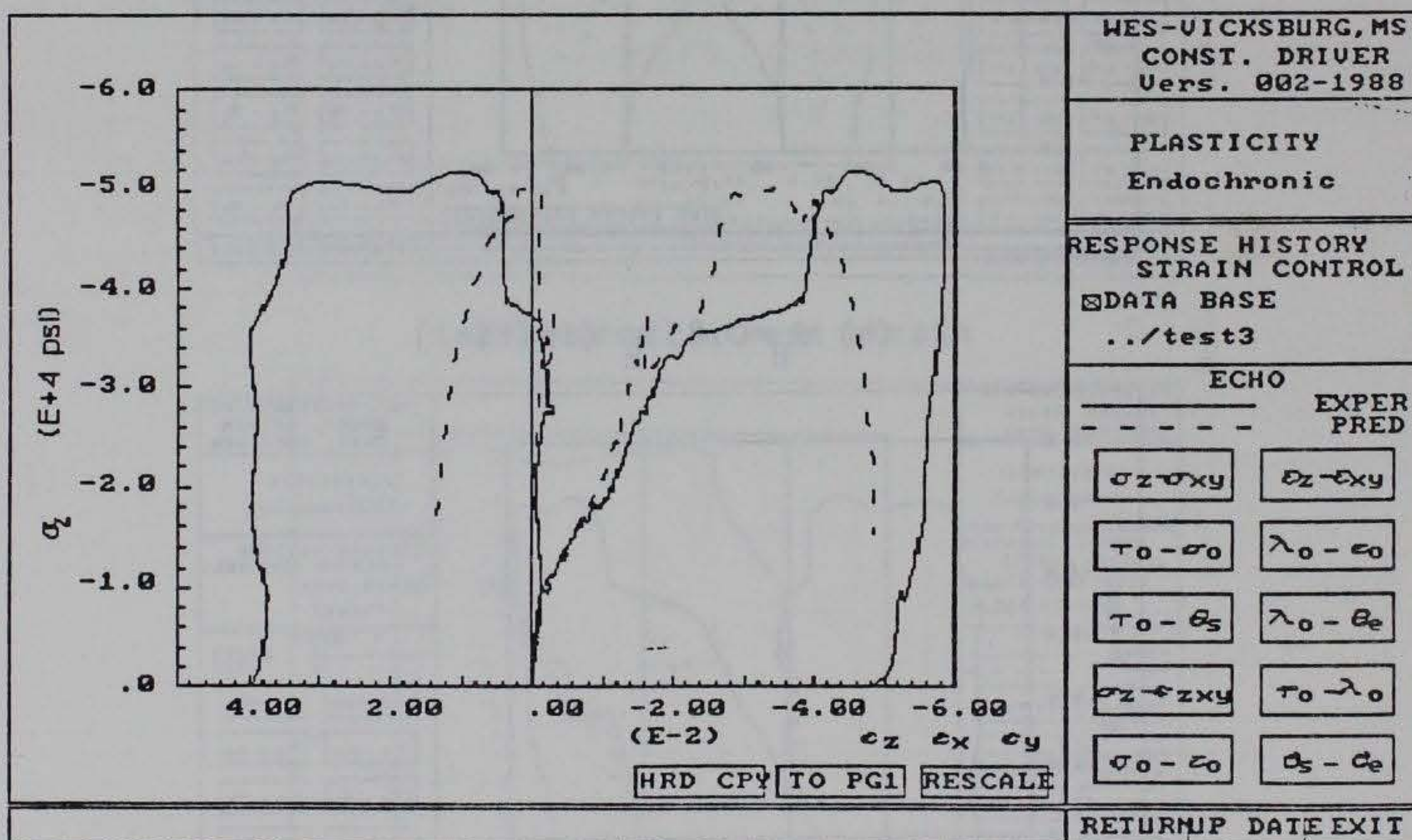
(c) octahedral stress strain

Figure 4.32 ECPM-VT6.5-3, initial calibration

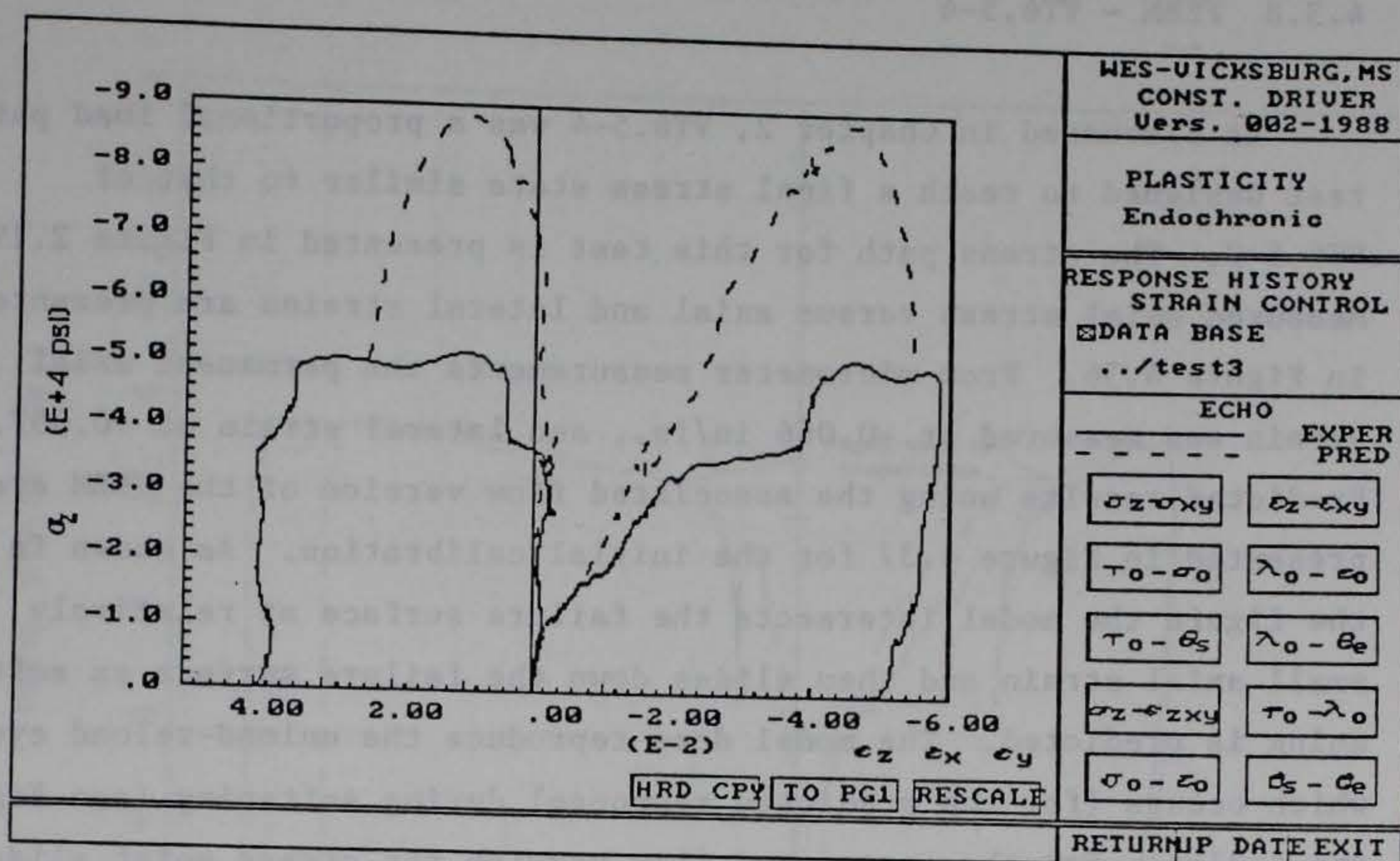
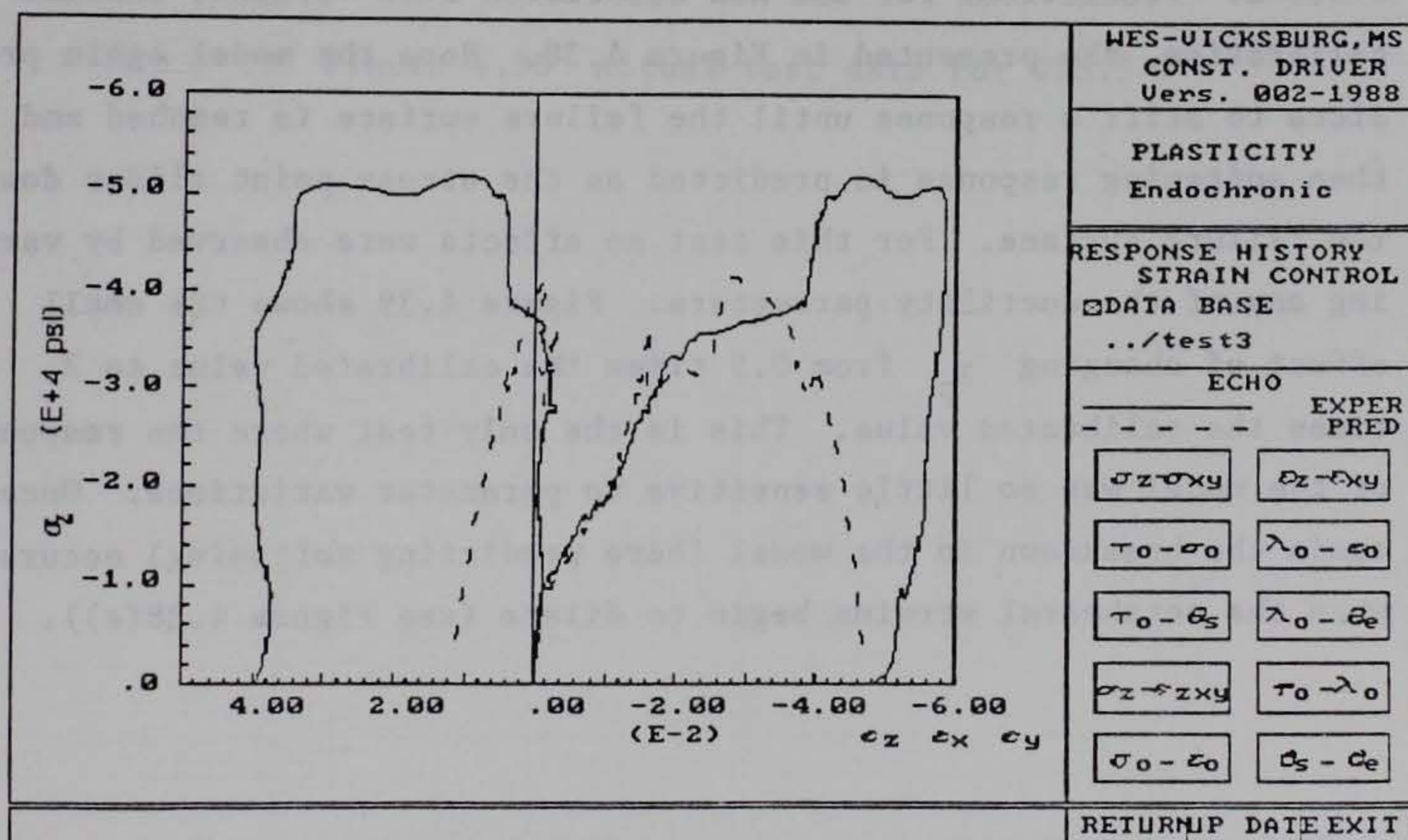


(a)  $\beta_H = 0.95\beta_H$  (initial)(b)  $\beta_H = 0.85\beta_H$  (initial)(c)  $\beta_H = 0.75\beta_H$  (initial)Figure 4.33 ECPM-VT6.5-3, affects of varying  $F_h$



(a)  $\beta_s = 0.5 \cdot \beta_s$  (initial)(b)  $\beta_s = 1.5 \cdot \beta_s$  (initial)Figure 4.34 ECPM-VT6.5-3, affects of varying  $F_s$



(a)  $C_0 = 1.0$ (b)  $\Gamma_0 = 1000.0$ Figure 4.35 ECPM-VT6.5-3, affects of varying  $C_0$  and  $\Gamma_0$



#### 4.3.8 FEBM - VT6.5-4

As discussed in Chapter 2, VT6.5-4 was a proportional load path test designed to reach a final stress state similar to that of VT6.5-3. The stress path for this test is presented in Figure 2.19. Measured axial stress versus axial and lateral strains are presented in Figure 4.36. From micrometer measurements the permanent axial strain was measured at  $-0.066$  in/in., and lateral strain at  $+0.057$ . Predicted results using the associated flow version of the FEBM are presented in Figure 4.37 for the initial calibration. As shown in the figure the model intersects the failure surface at relatively small axial strain and then slides down the failure surface as softening is predicted. The model does reproduce the unload-reload cycle which occurs (for the predicted response) during softening (see Figure 4.37b). For the associated flow version the stress point slides down the failure surface during softening so that no damage (or decohesion) is predicted as was predicted in the true softening test VT6.5-2. Predictions for the non associated flow version, initial calibration, are presented in Figure 4.38. Here the model again predicts to stiff a response until the failure surface is reached and then softening response is predicted as the stress point slides down the failure surface. For this test no affects were observed by varying any of the ductility parameters. Figure 4.39 shows the small effect of changing  $\chi_p$  from 0.5 times the calibrated value to 3 times the calibrated value. This is the only test where the response of the model was so little sensitive to parameter variations. Once again the breakdown in the model (here predicting softening) occurs when the octahedral strains begin to dilate (see Figure 4.38(c)).



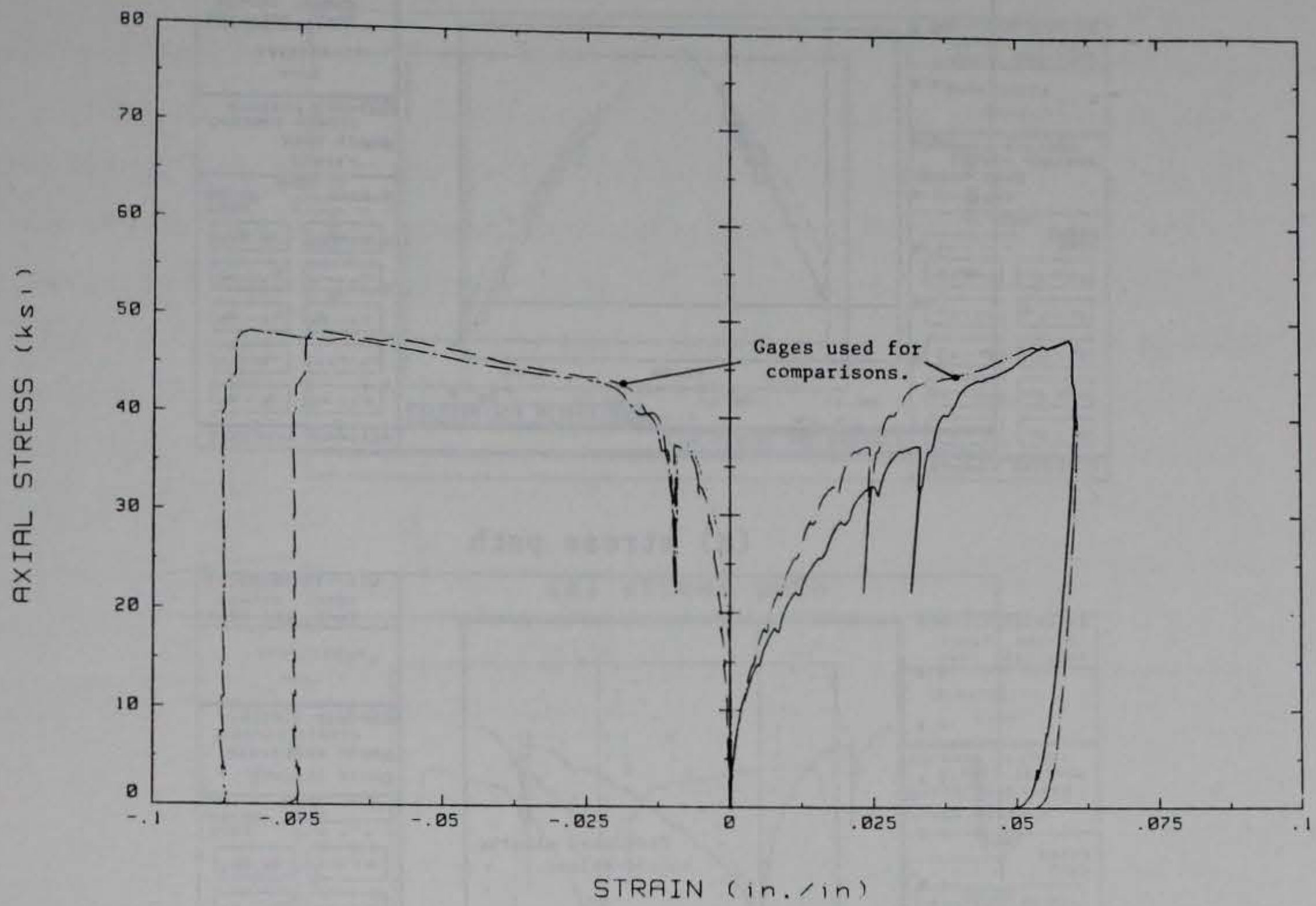
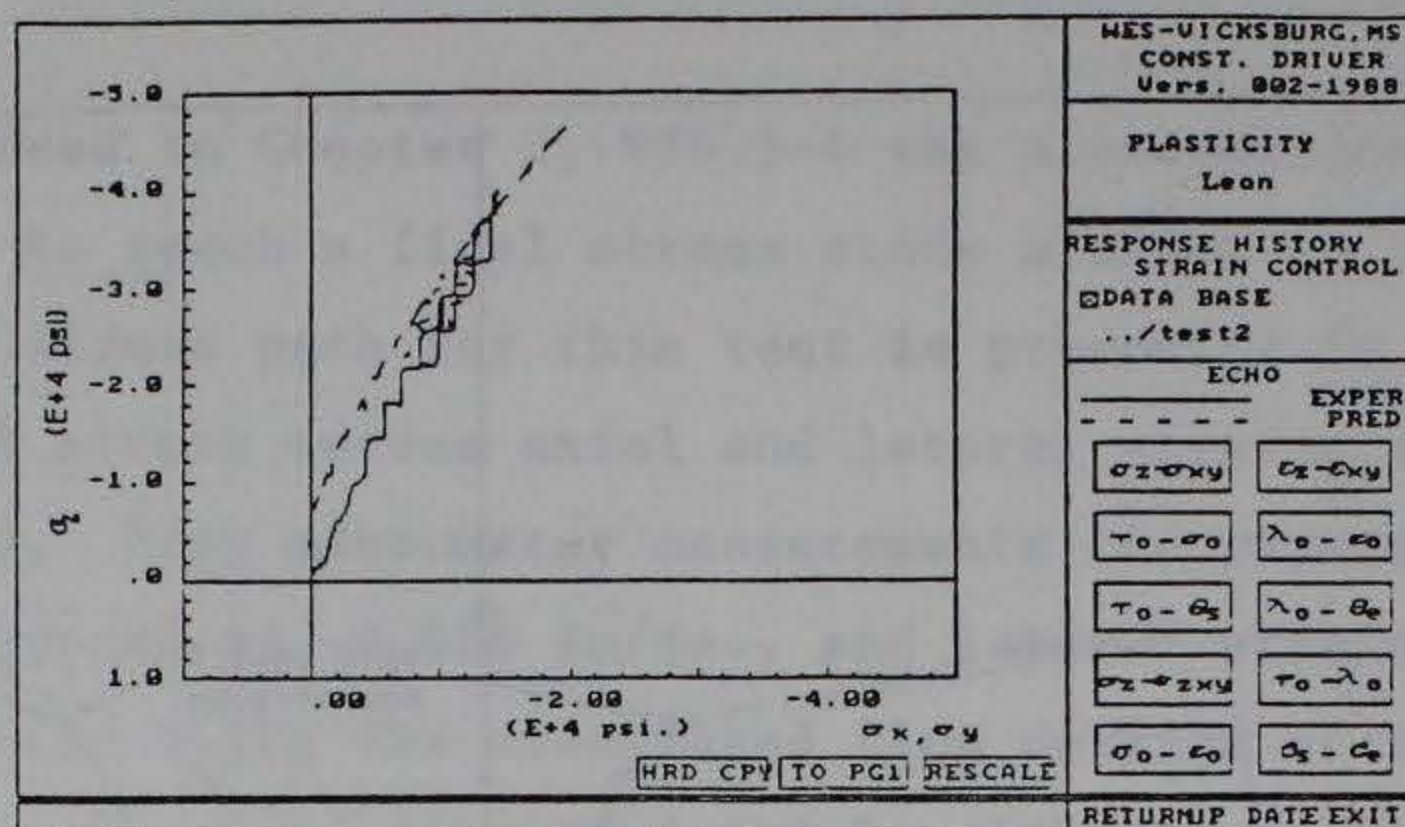
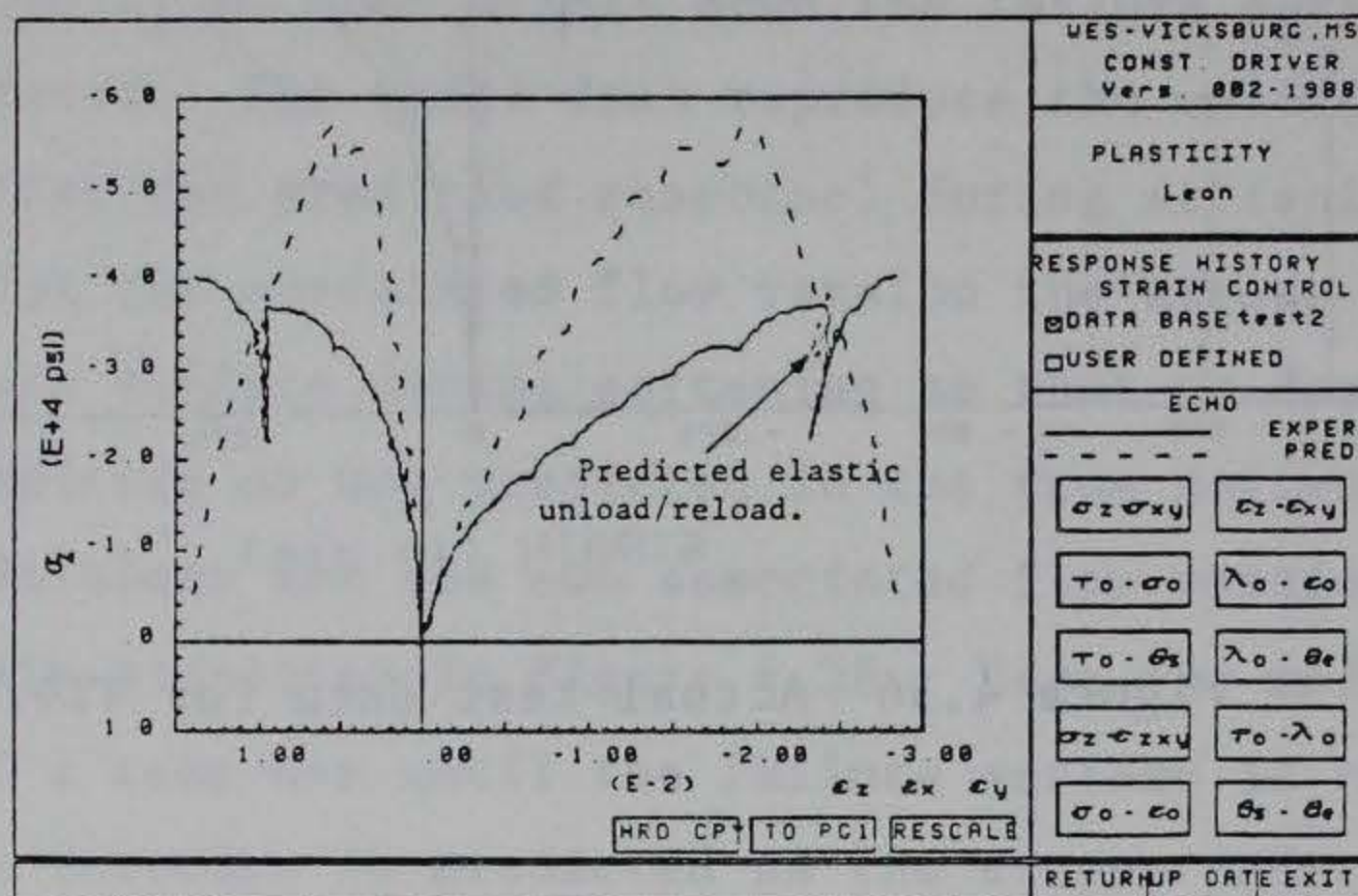


Figure 4.36 Actual test data for VT6.5-4

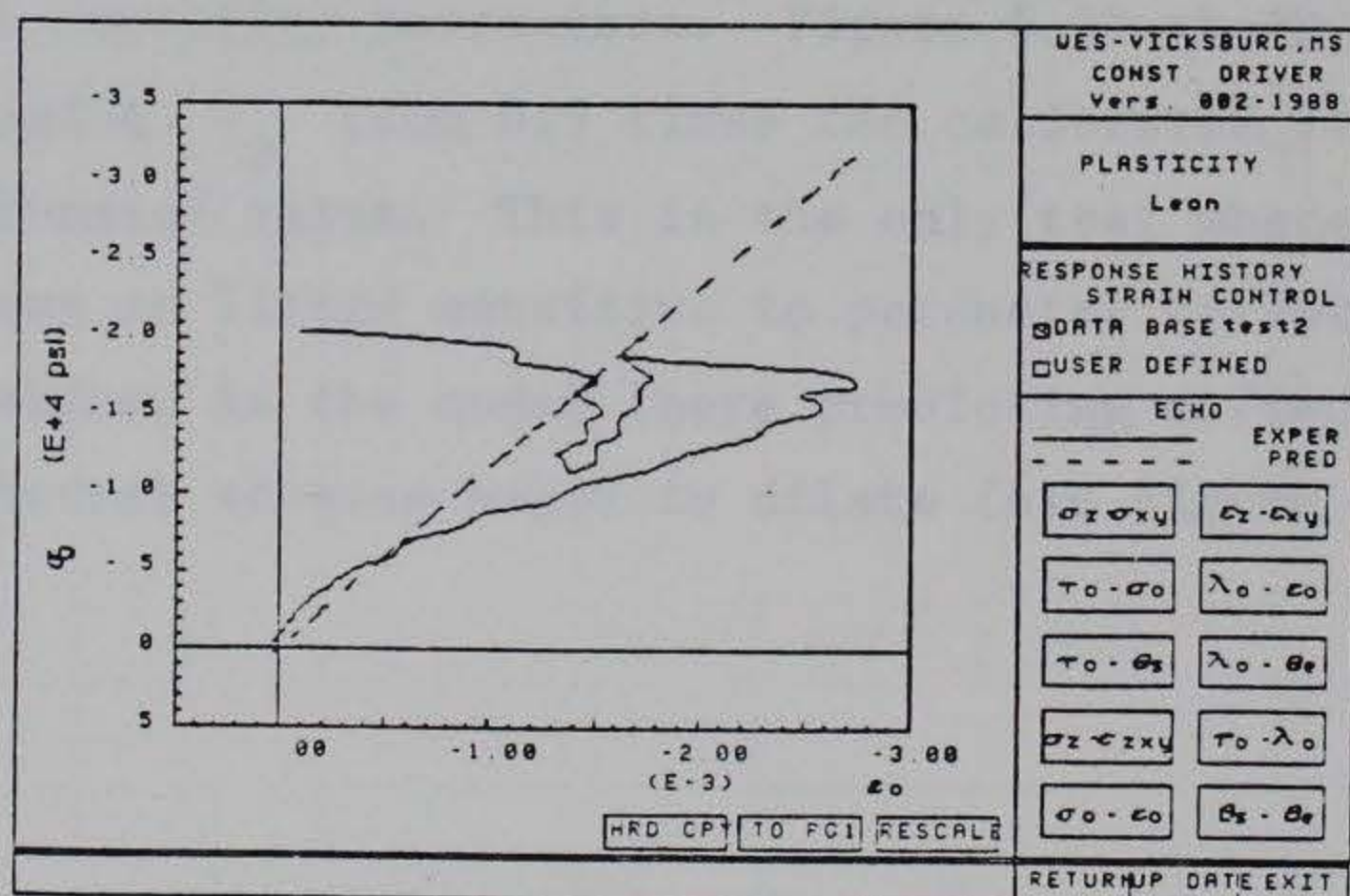




(a) stress path



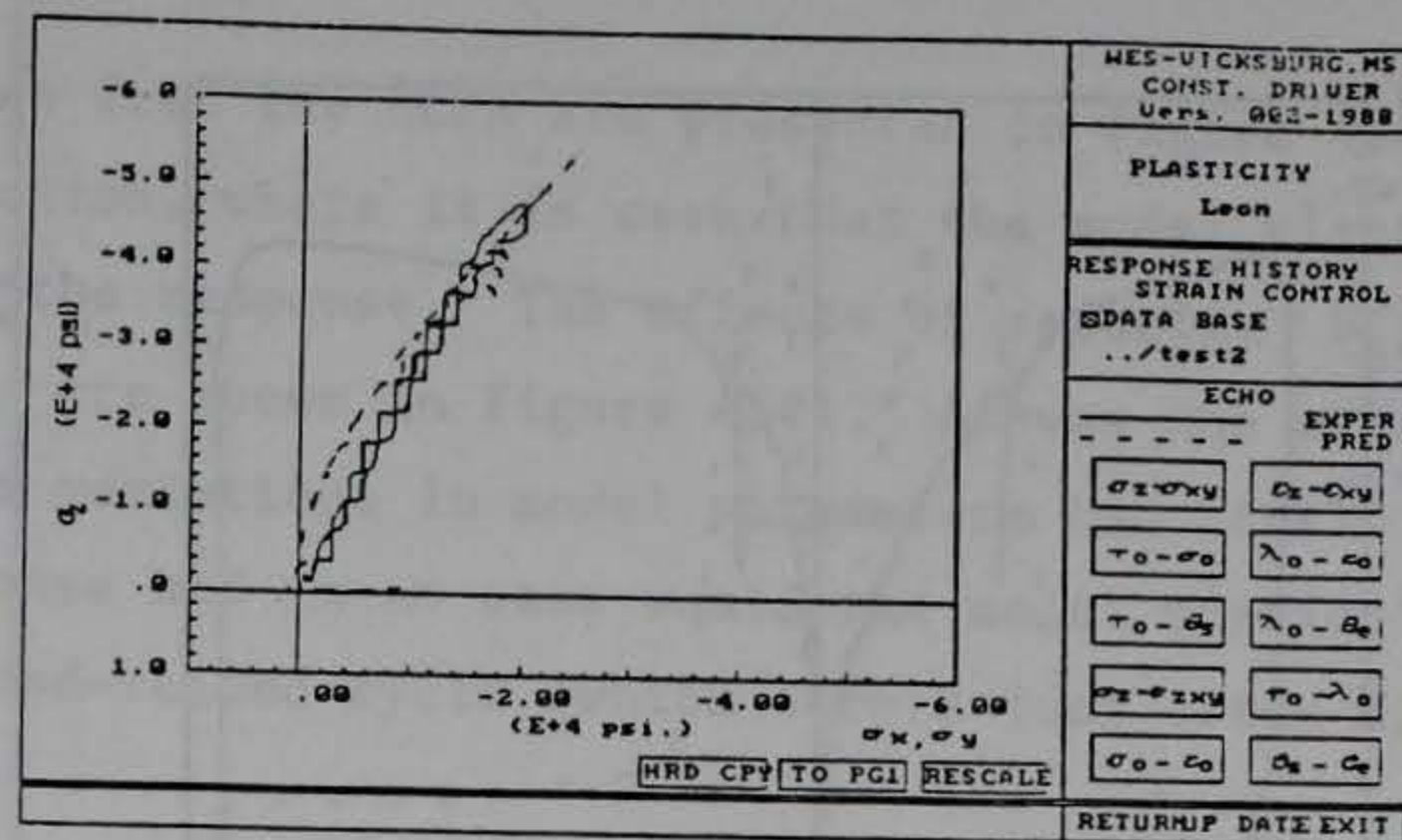
(b) normal stress strain



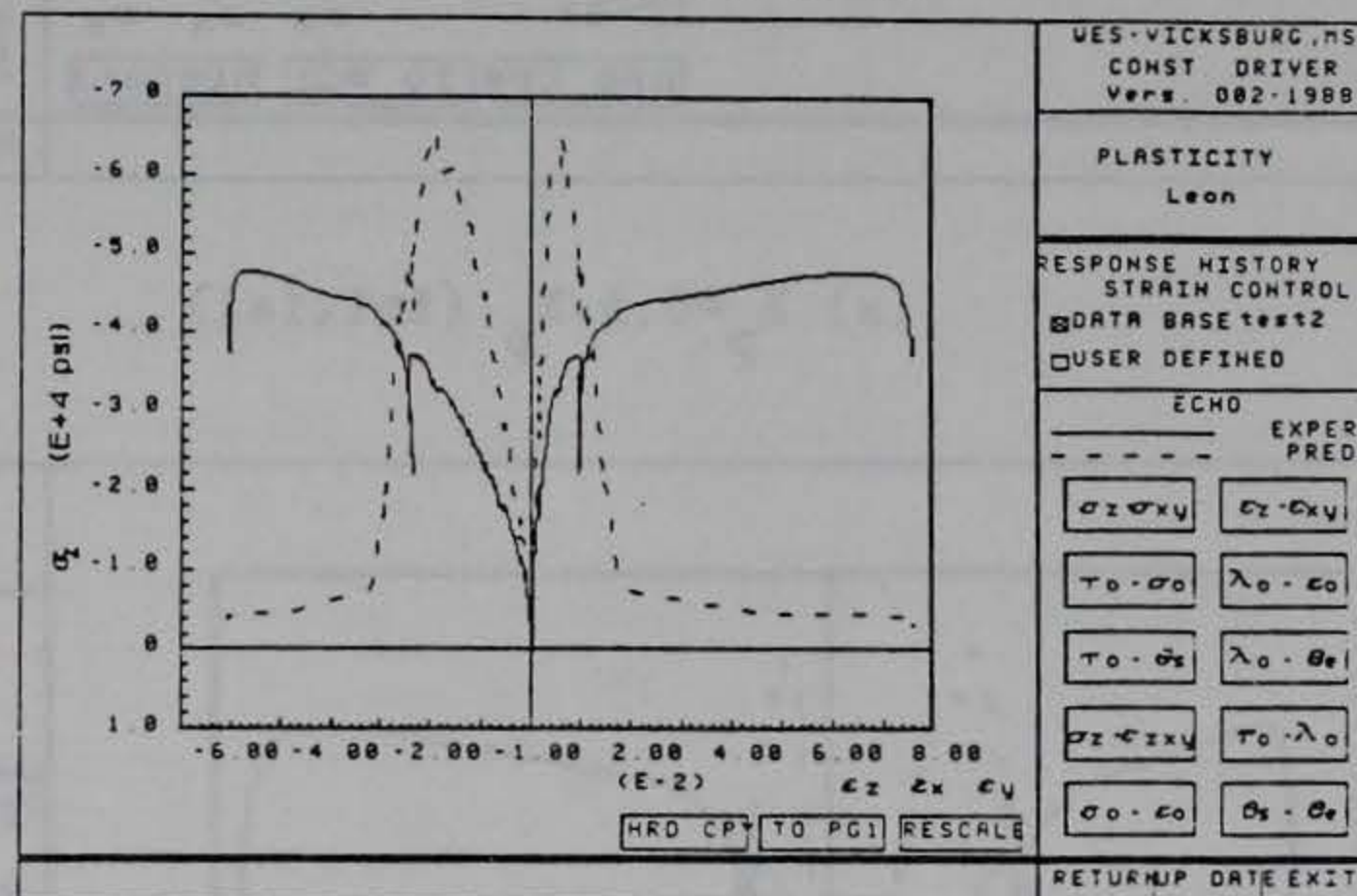
(c) octahedral stress strain

Figure 4.37 FEBM-VT6.5-4, associated flow, initial calibration

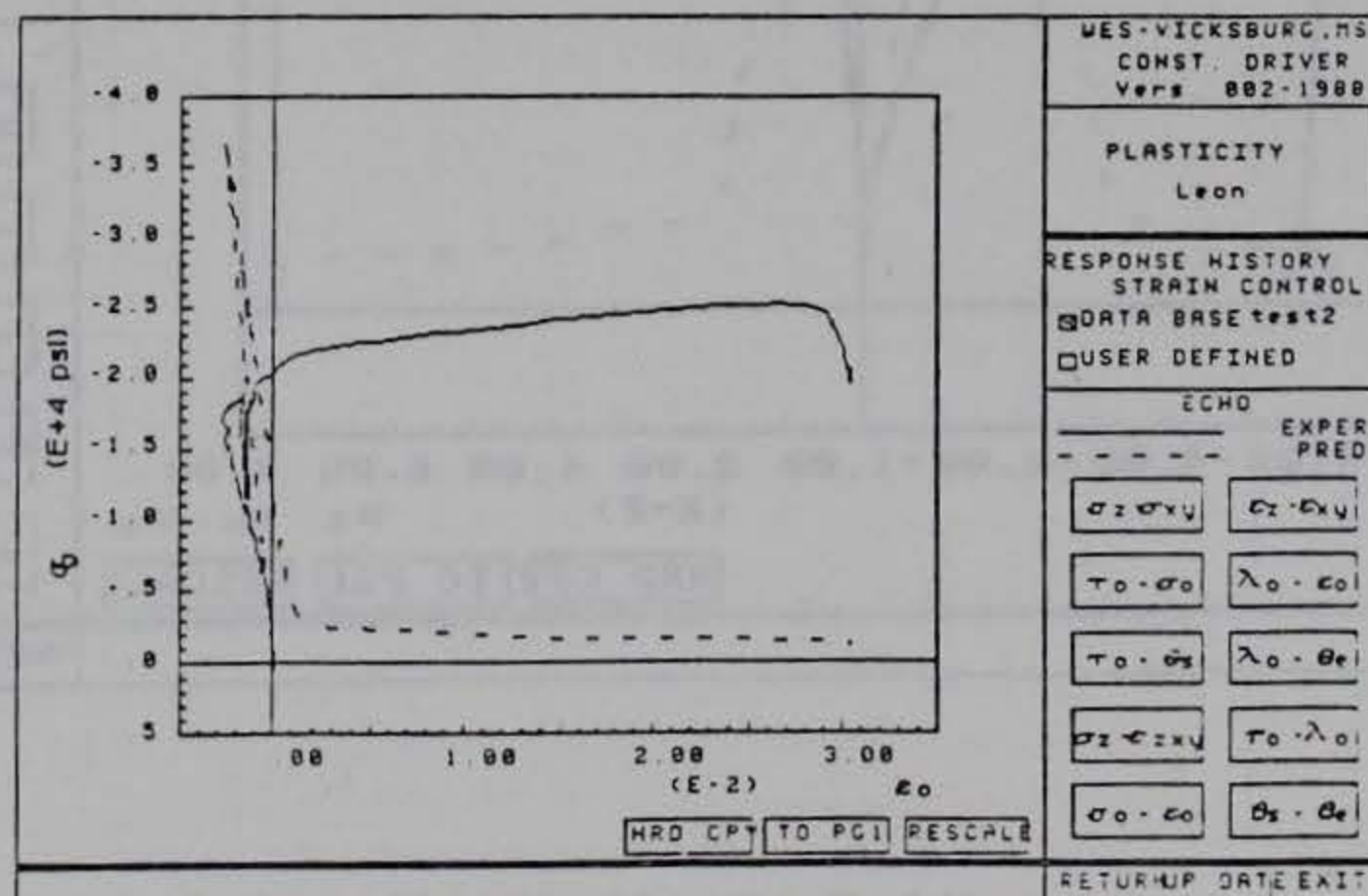




(a) stress path



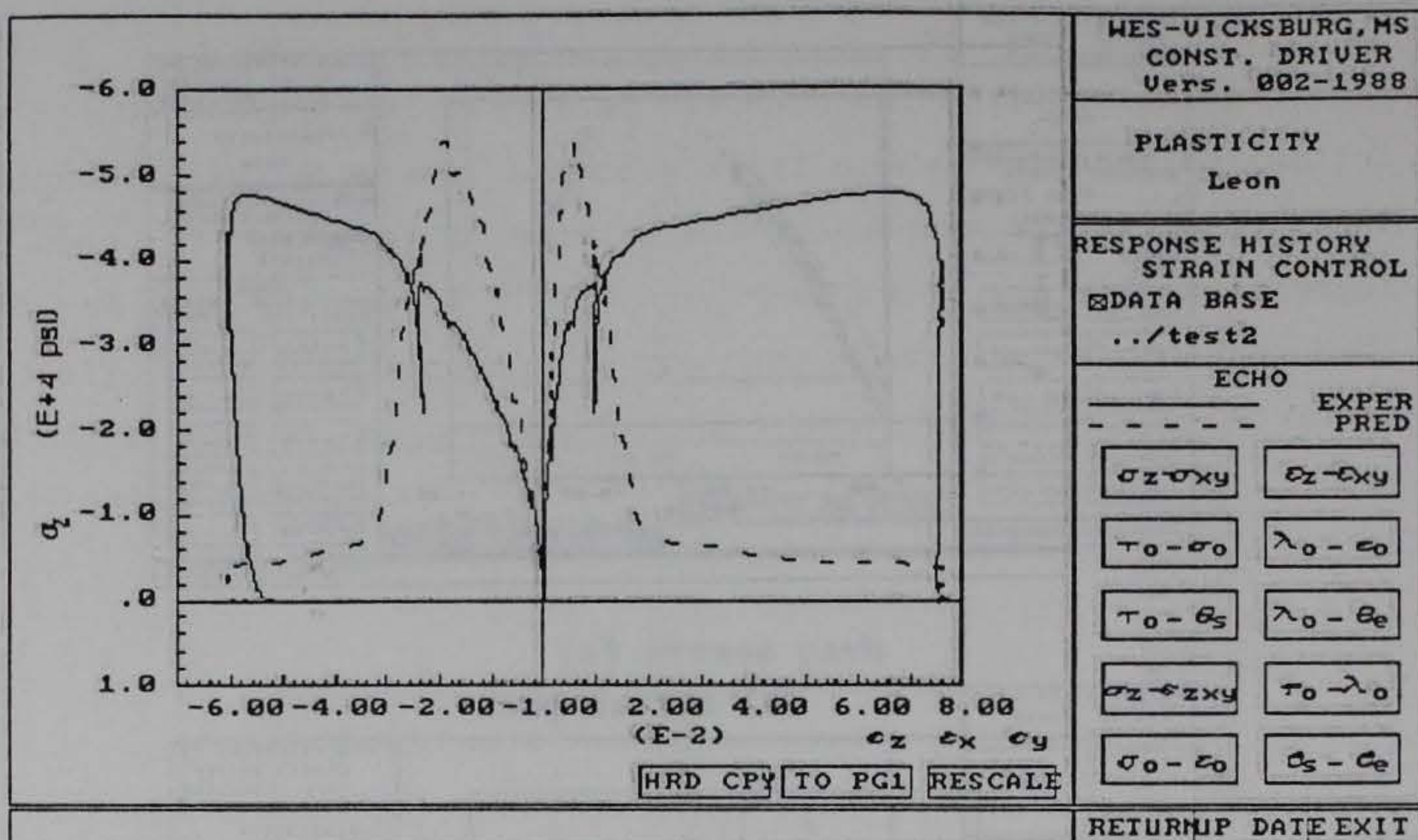
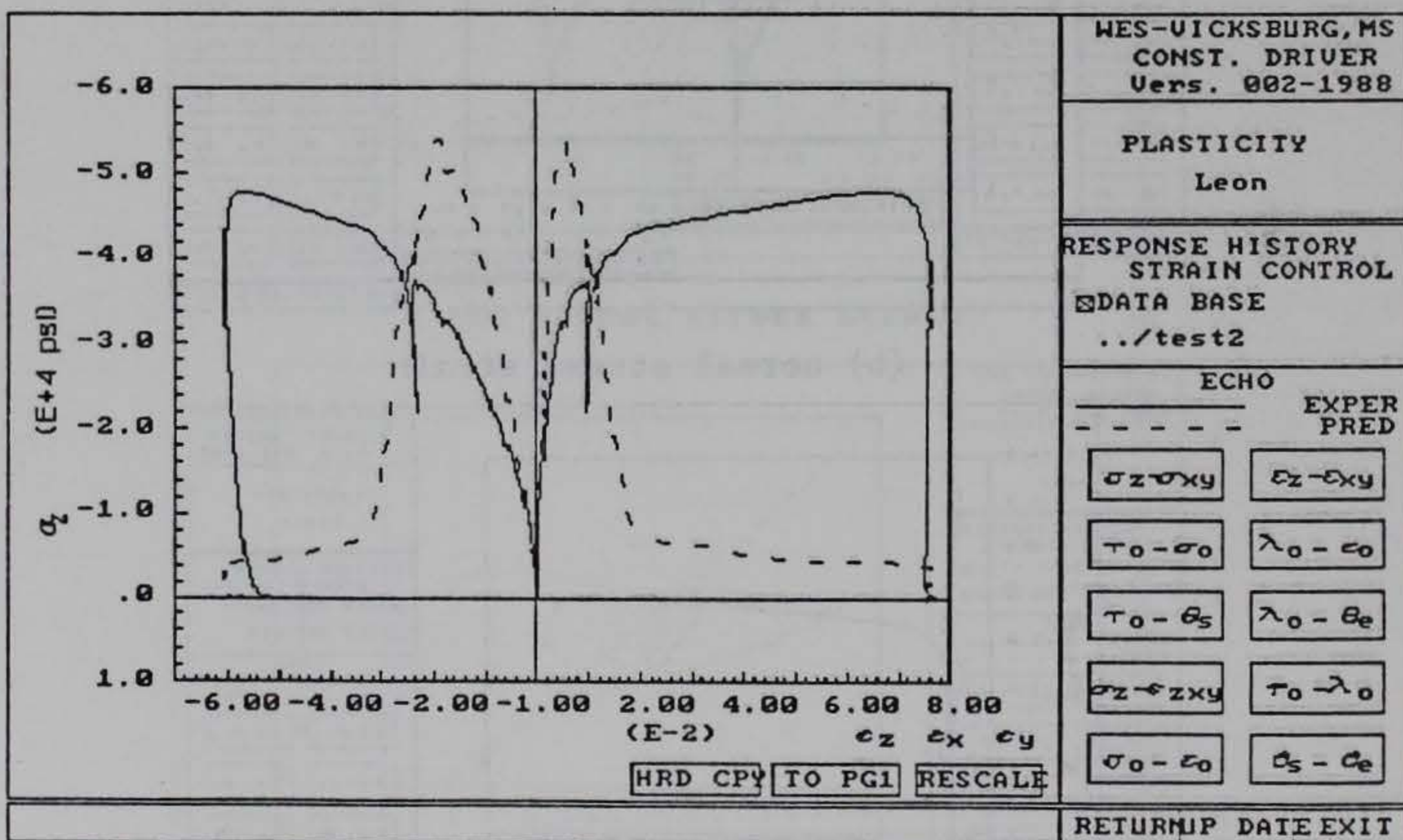
(b) normal stress strain



(c) octahedral stress strain

Figure 4.38 FEBM-VT6.5-4, non-associated flow, initial calibration



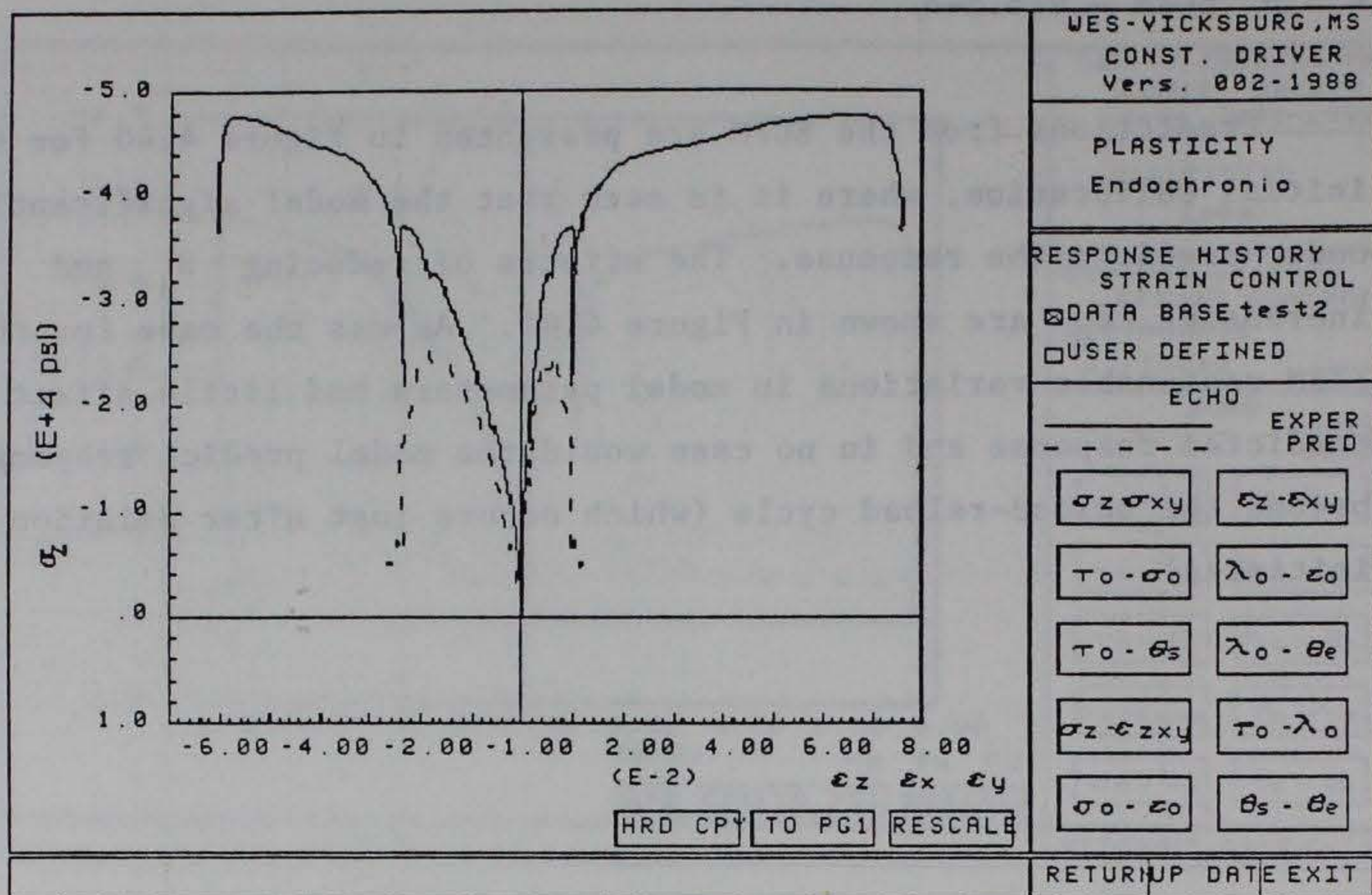
(a)  $X_p = 0.5 \cdot X_p(\text{initial})$ (b)  $X_p = X_p(\text{initial}) \cdot 3.0$ Figure 4.39 FEBM-VT6.5-4, affects of varying ductility parameter  $X_p$



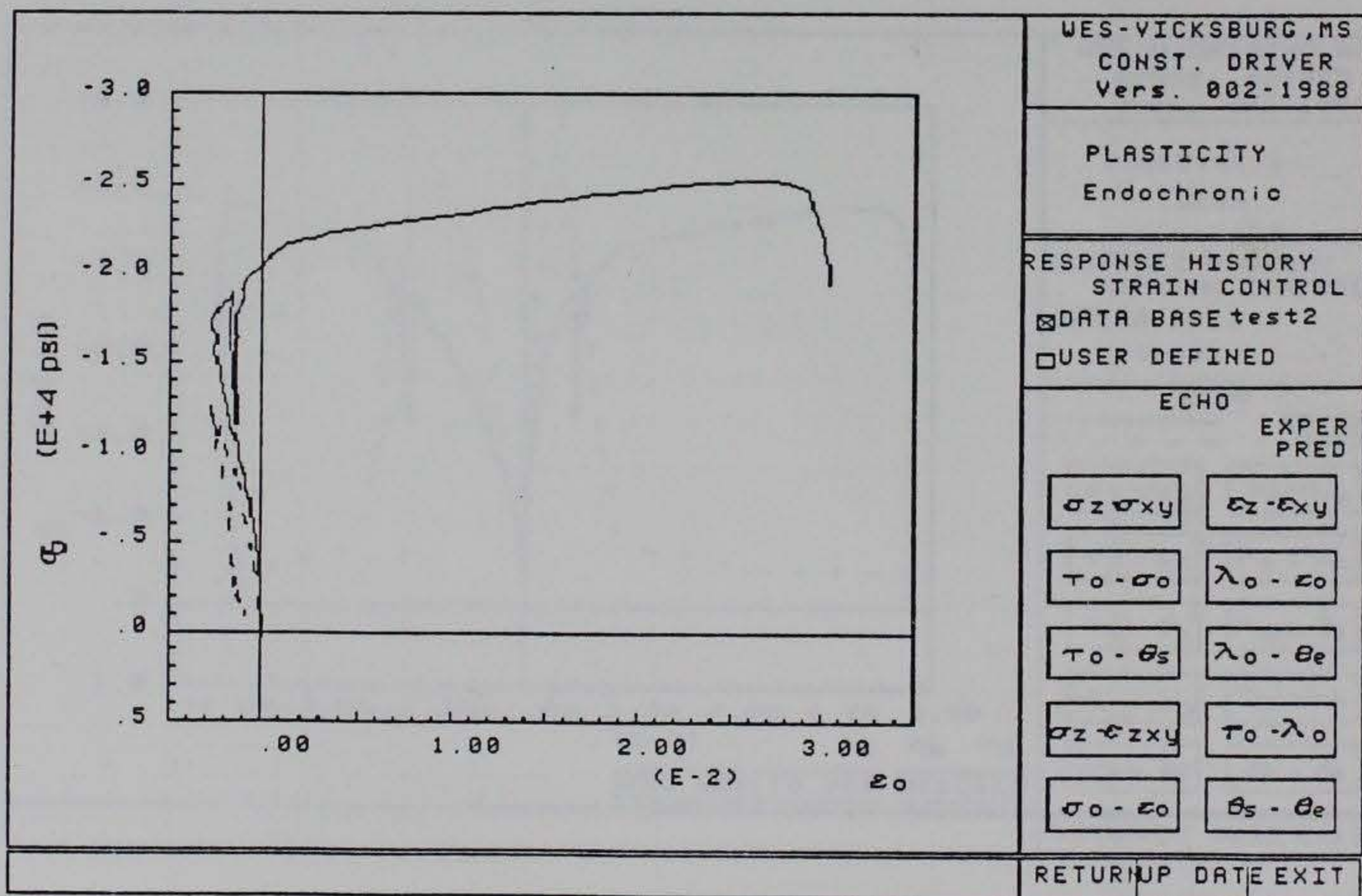
#### 4.3.9 ECPM - VT6.5-4

Predictions from the ECPM are presented in Figure 4.40 for the initial calibration, where it is seen that the model significantly under predicts the response. The effects of reducing  $\beta_s$  and increasing  $\beta_H$  are shown in Figure 4.41. As was the case for the FEBM reasonable variations in model parameters had little affect on predicted response and in no case would the model predict response beyond the unload-reload cycle (which occurs just after dilation initiates).





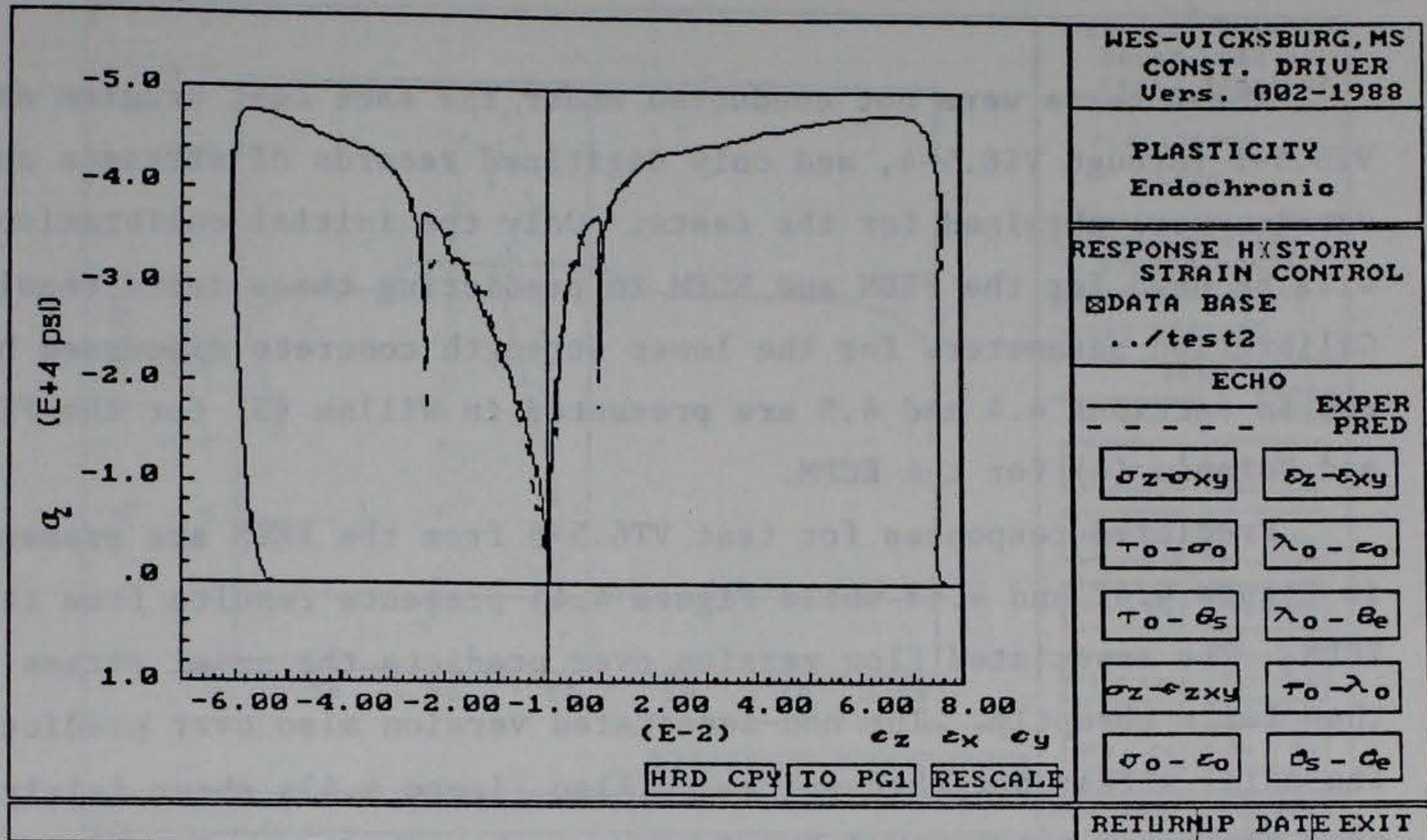
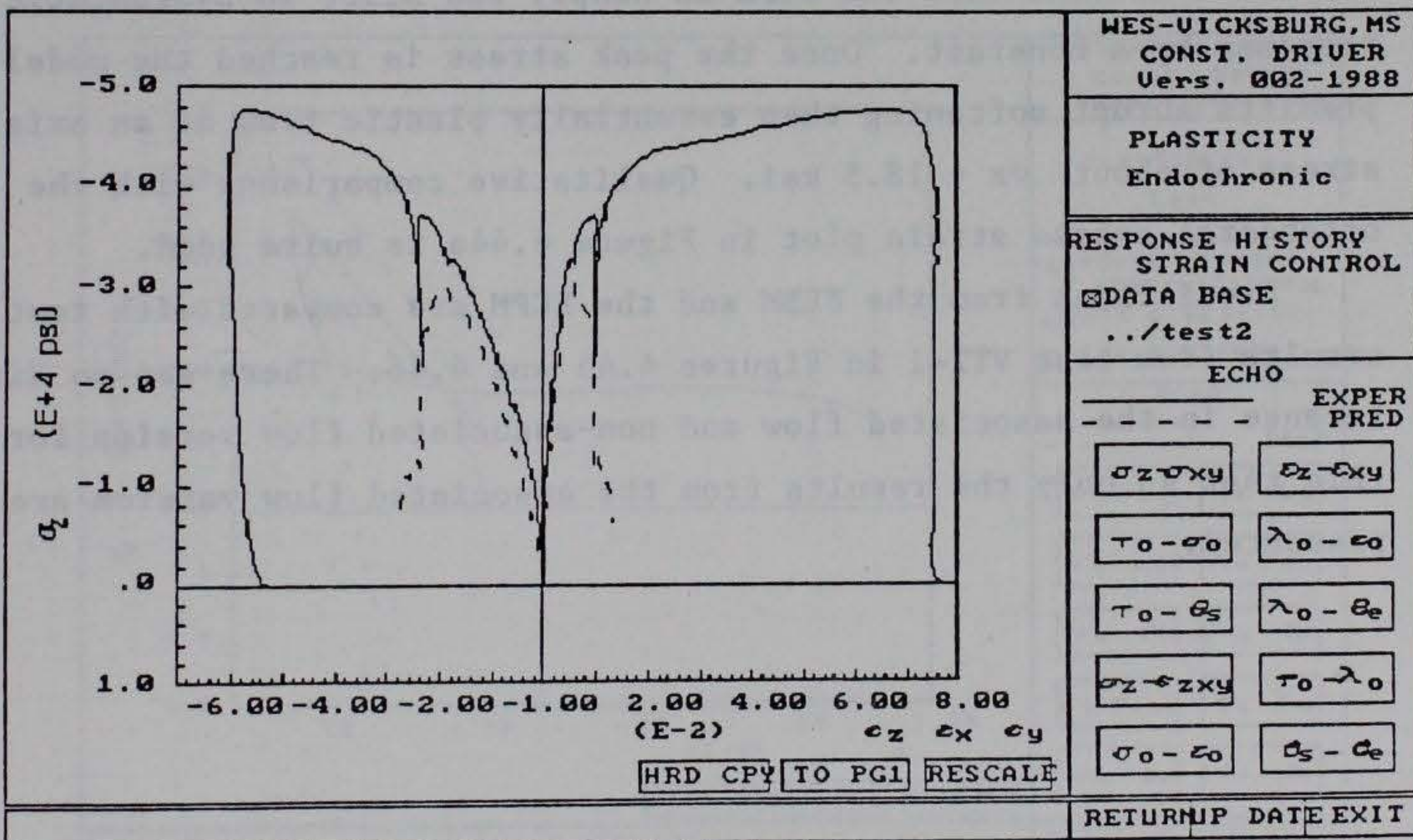
(a) normal stress strain



(b) octahedral stress strain

Figure 4.40 ECPM-VT6.5-4, initial calibration



(a)  $\beta_s = 0.25 \cdot \beta_s$  (initial)(b)  $\beta_H = 1.5 \cdot \beta_H$  (initial)Figure 4.41 ECPM-VT6.5-4, affects of varying  $\beta_s$  and  $\beta_H$



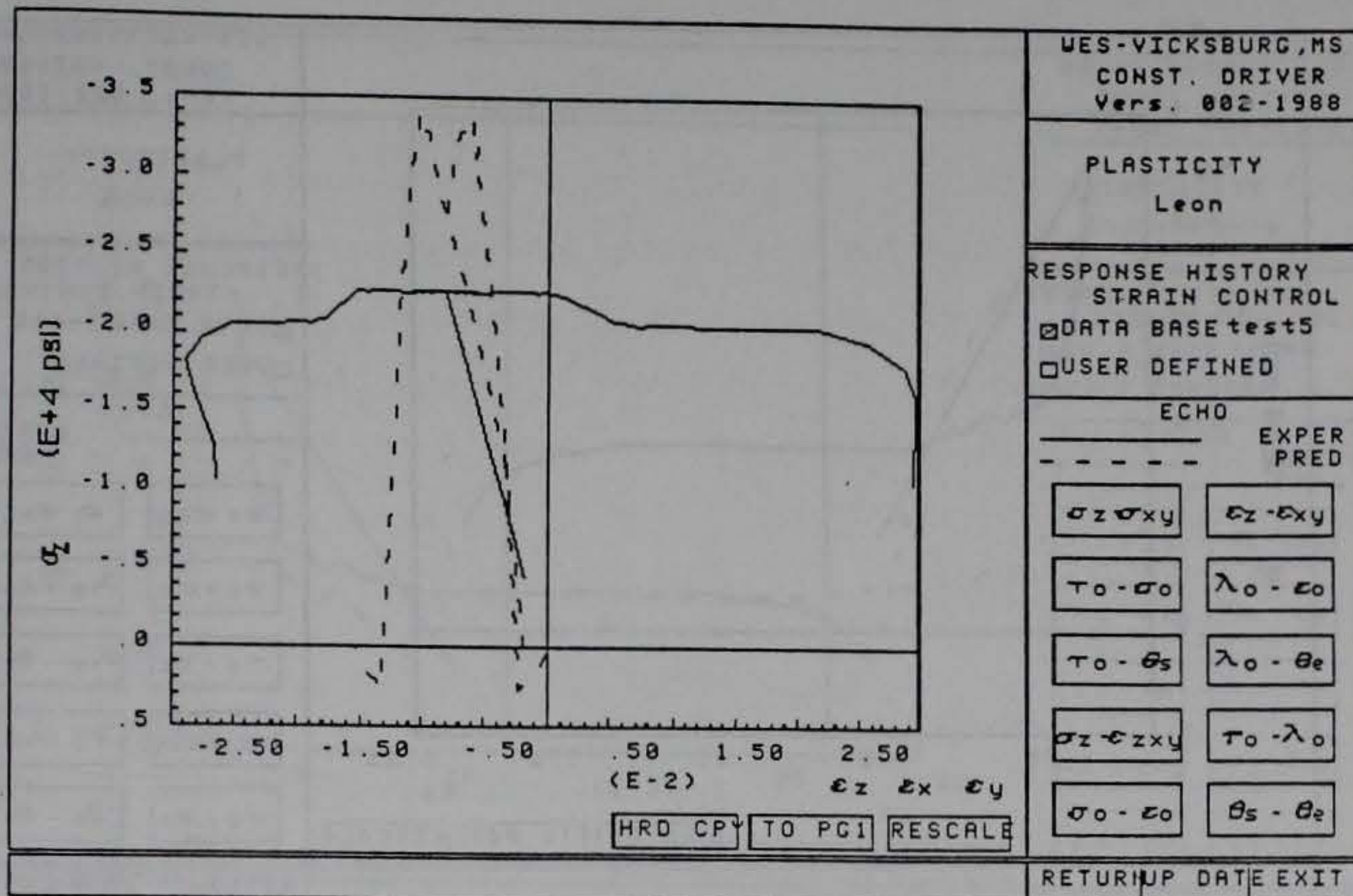
#### 4.3.10 FEBM and ECPM - VT6.5-5, VT2-1

These tests were not conducted under the same test program as VT6.5-1 through VT6.5-4, and only digitized records of stresses and strains were obtained for the tests. Only the initial calibration will be used for the FEBM and ECPM in predicting these tests results. Calibration parameters for the lower strength concrete discussed here and in sections 4.4 and 4.5 are presented in Willam (3) for the FEBM and Valanis (4) for the ECPM.

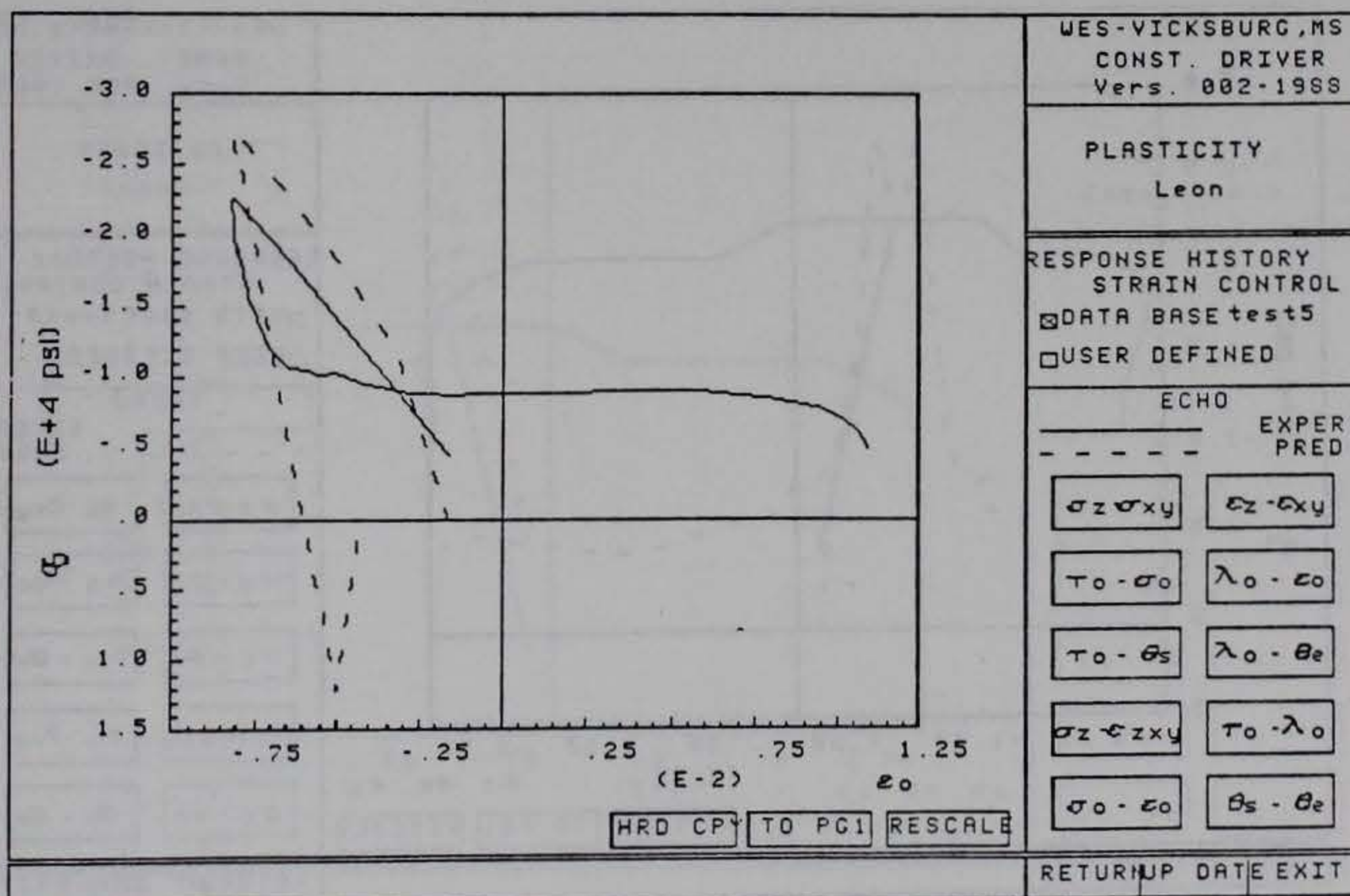
Predicted responses for test VT6.5-5 from the FEBM are presented in Figure 4.42 and 4.43 while Figure 4.44 presents results from the ECPM. The associated flow version over predicts the axial stress then fails abruptly. The non-associated version also over predicts the axial stress but then softens. Also Figure 4.43a shows fairly good agreement between model and test results in terms of  $\sigma_o$  vs  $\epsilon_o$  (at least qualitatively). The ECPM over predicts the axial stress but here it seems that the ECPM is simply too stiff in hydrostatic response by a constant. Once the peak stress is reached the model predicts abrupt softening then essentially plastic flow at an axial stress of about  $\sigma_z = 18.5$  ksi. Qualitative comparisons with the octahedral stress strain plot in Figure 4.44a is quite good.

Predictions from the FEBM and the ECPM are compared with test results from test VT2-1 in Figures 4.45 and 4.46. There was no difference in the associated flow and non-associated flow version for this test so only the results from the associated flow version are presented.





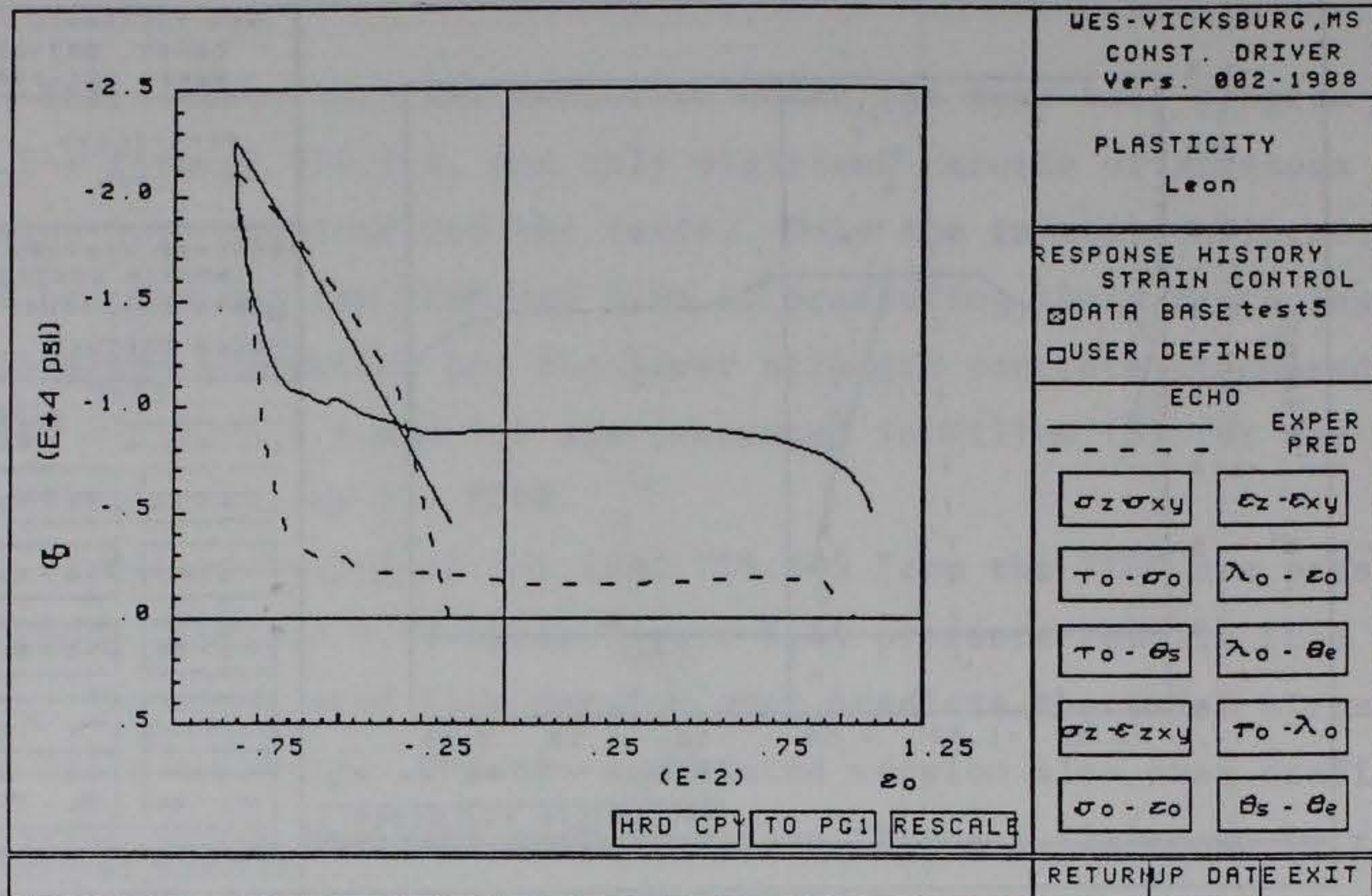
(a) normal stress strain



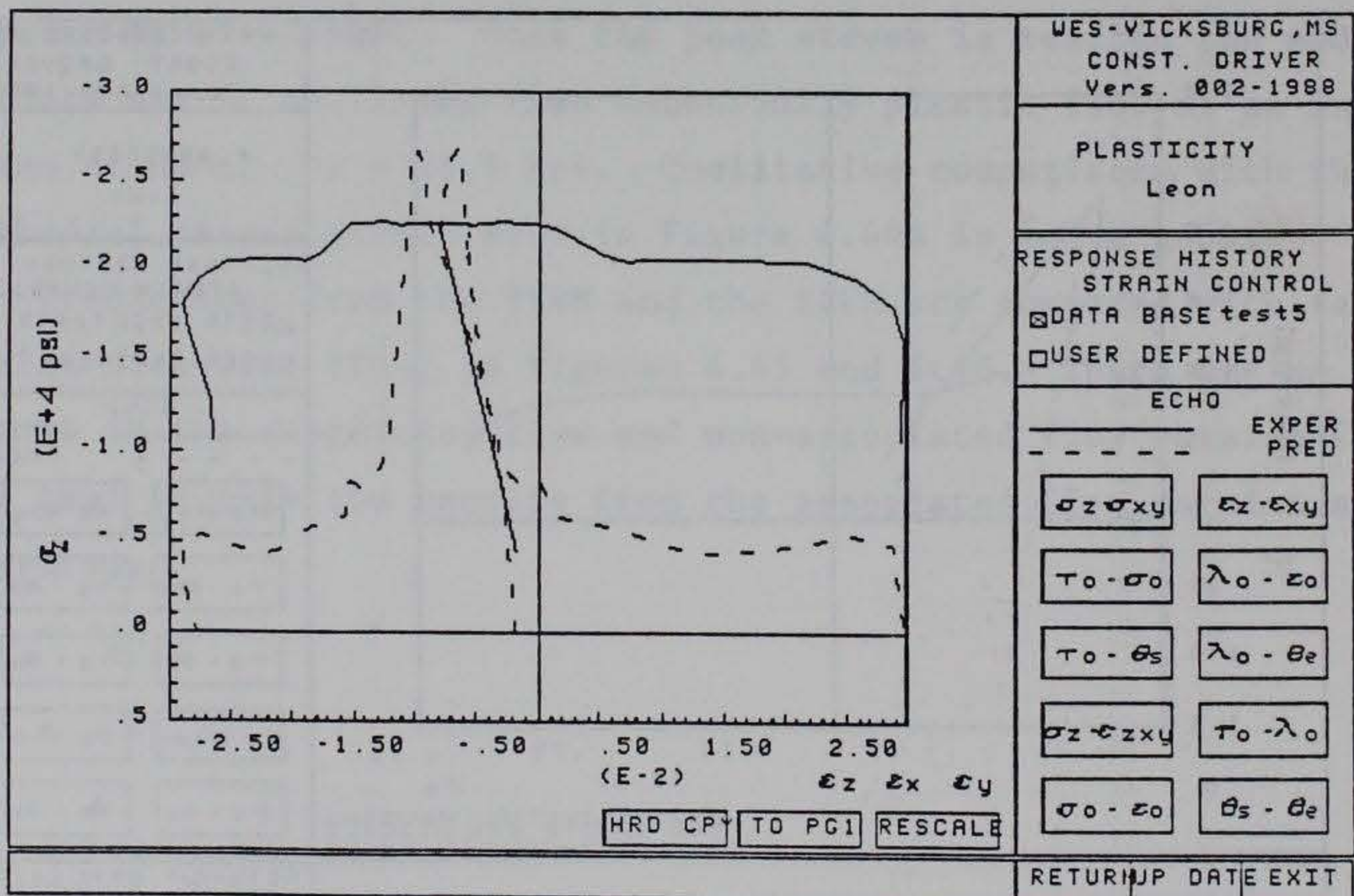
(b) octahedral stress strain

Figure 4.42 FEBM-VT6.5-5, associated flow





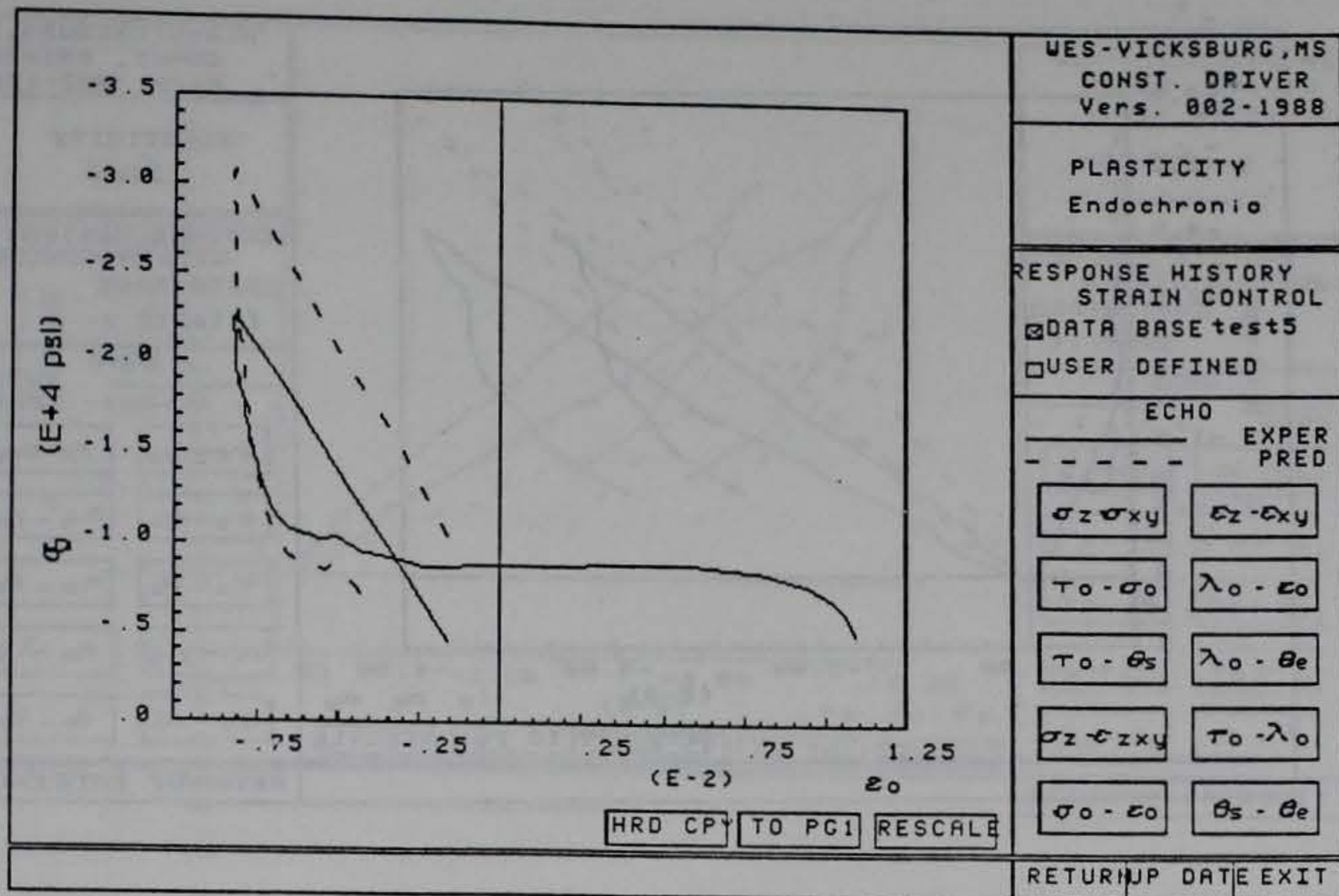
(a) octahedral stress strain



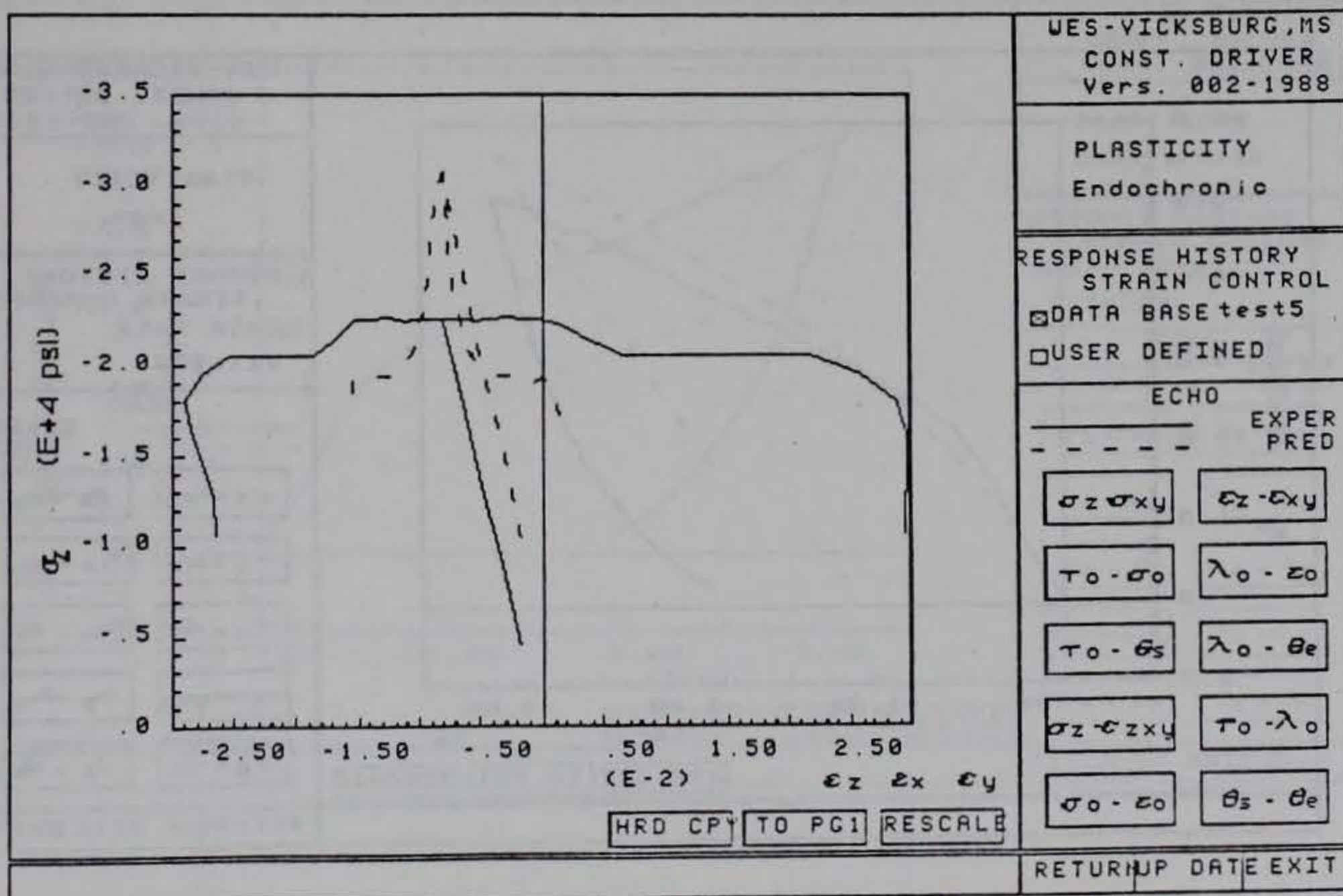
(b) normal stress strain

Figure 4.43 FEBM-VT6.5-5, non-associated flow





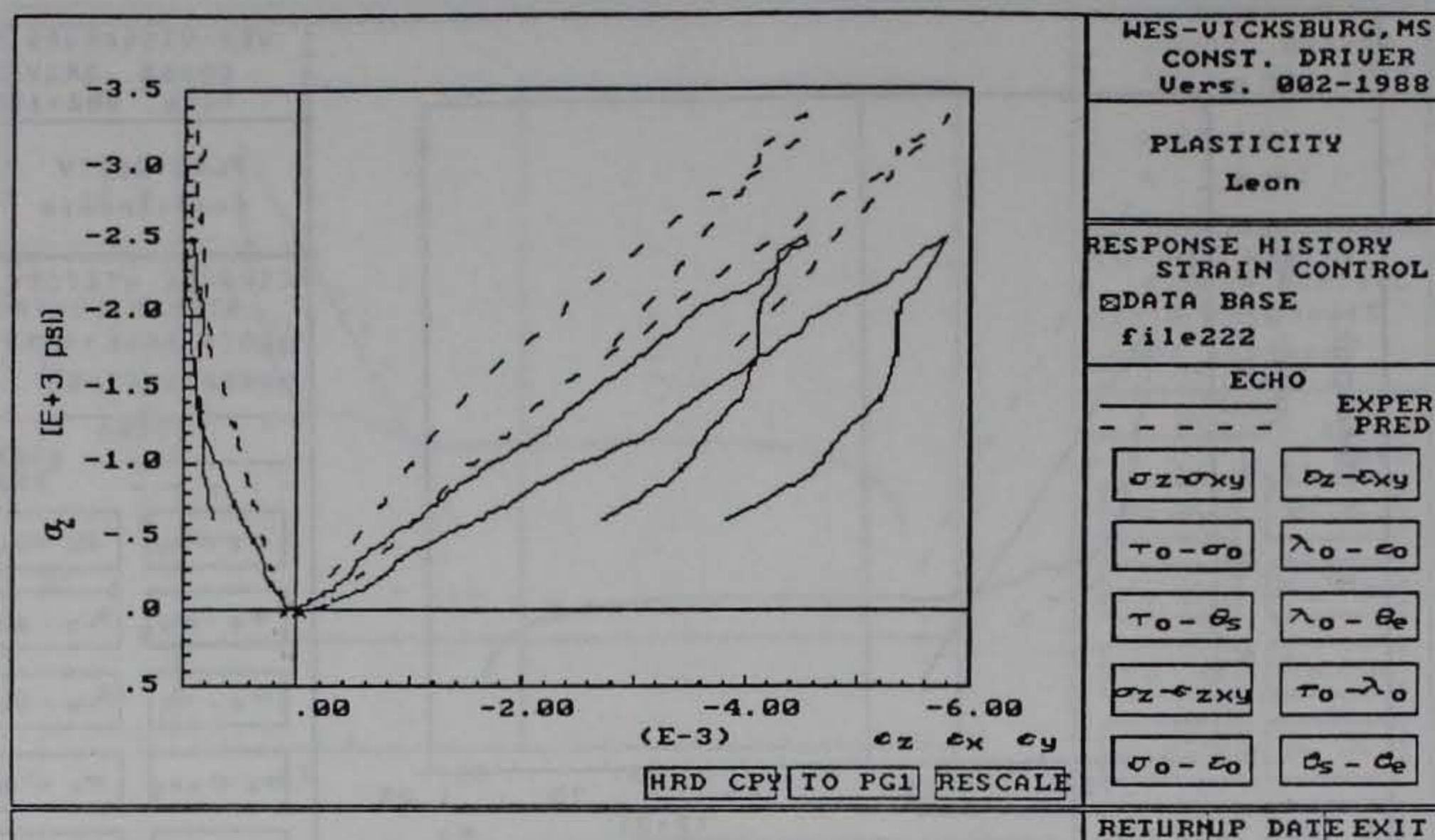
(a) octahedral stress strain



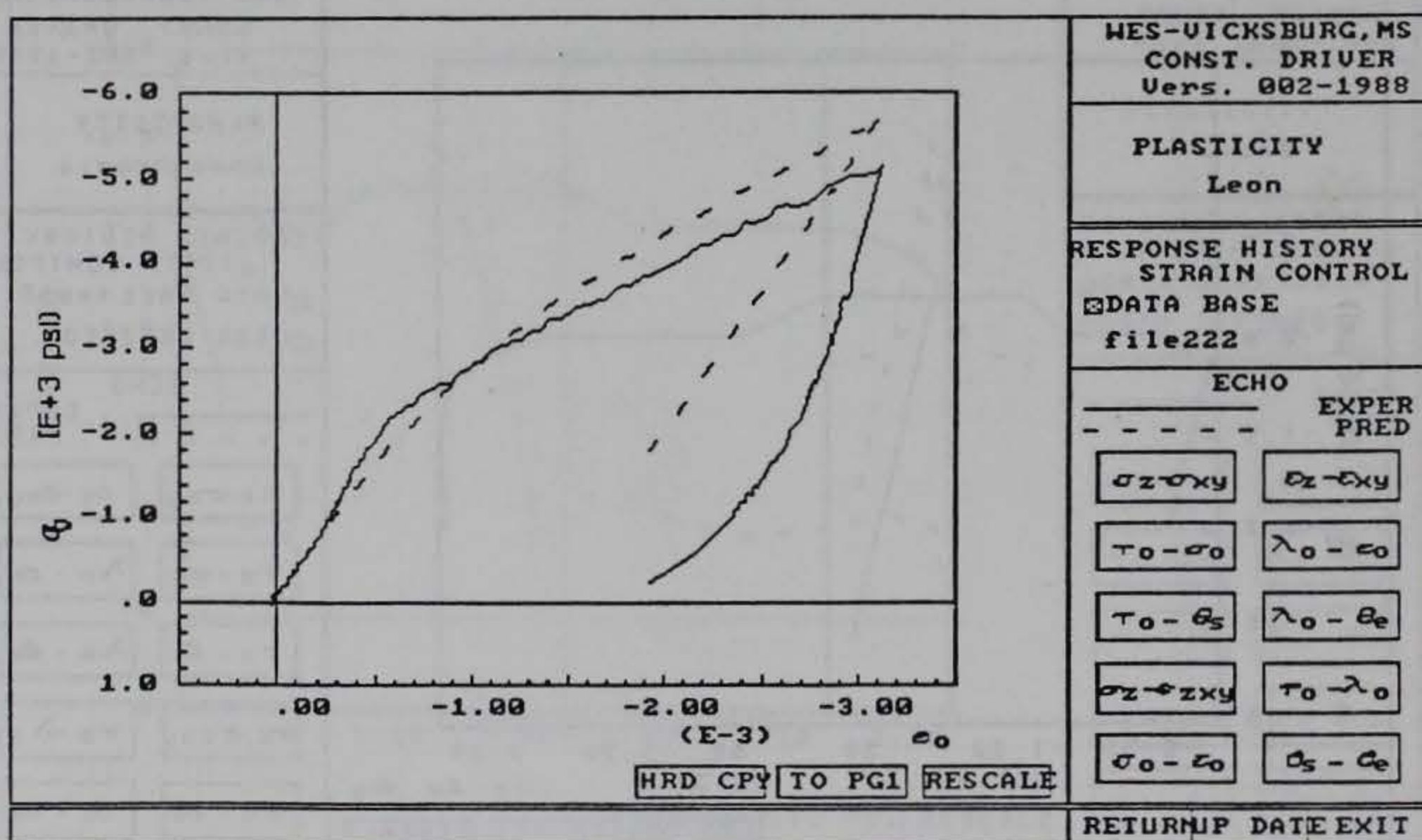
(b) normal stress strain

Figure 4.44 ECPM-VT6.5-5





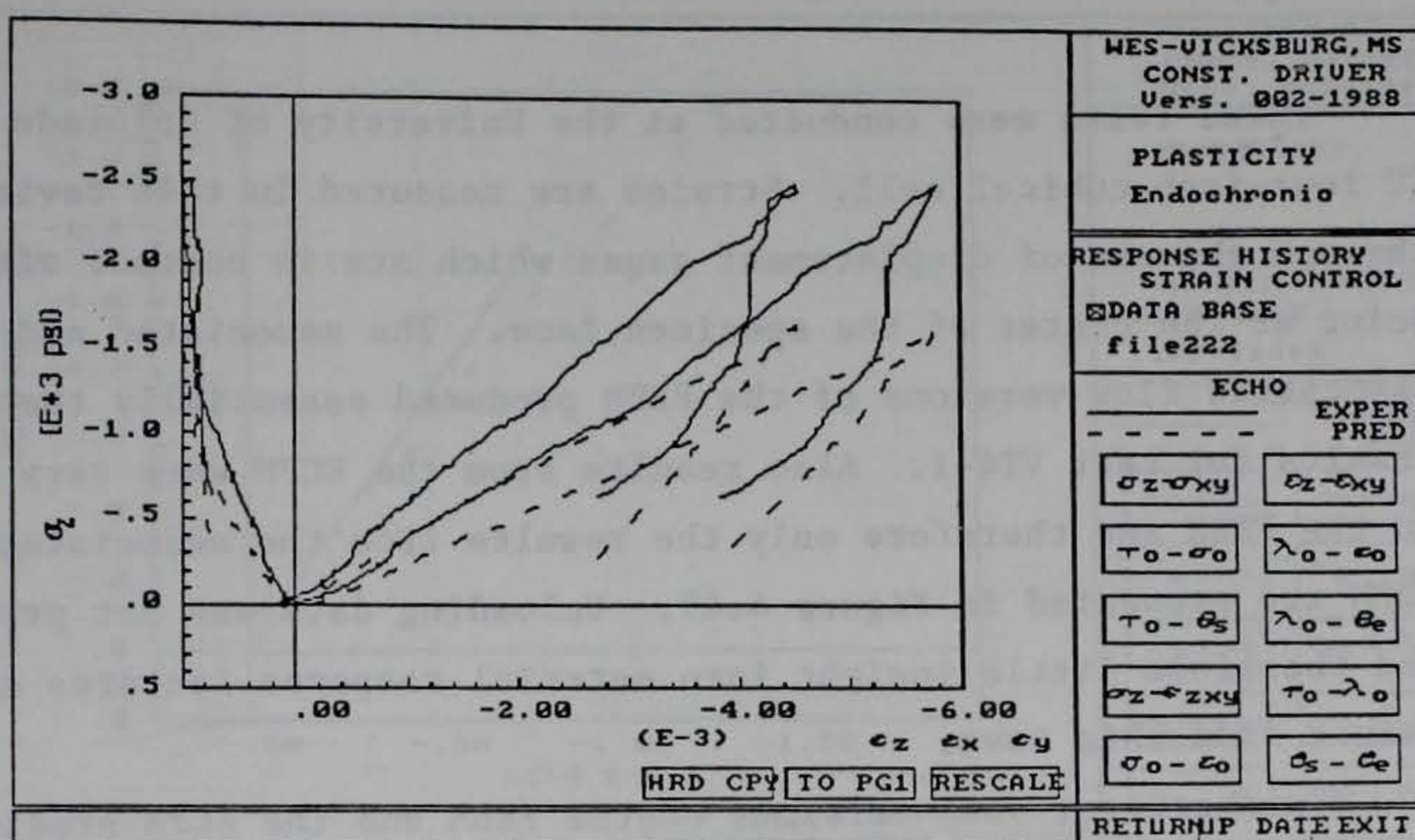
(a) normal stress strain



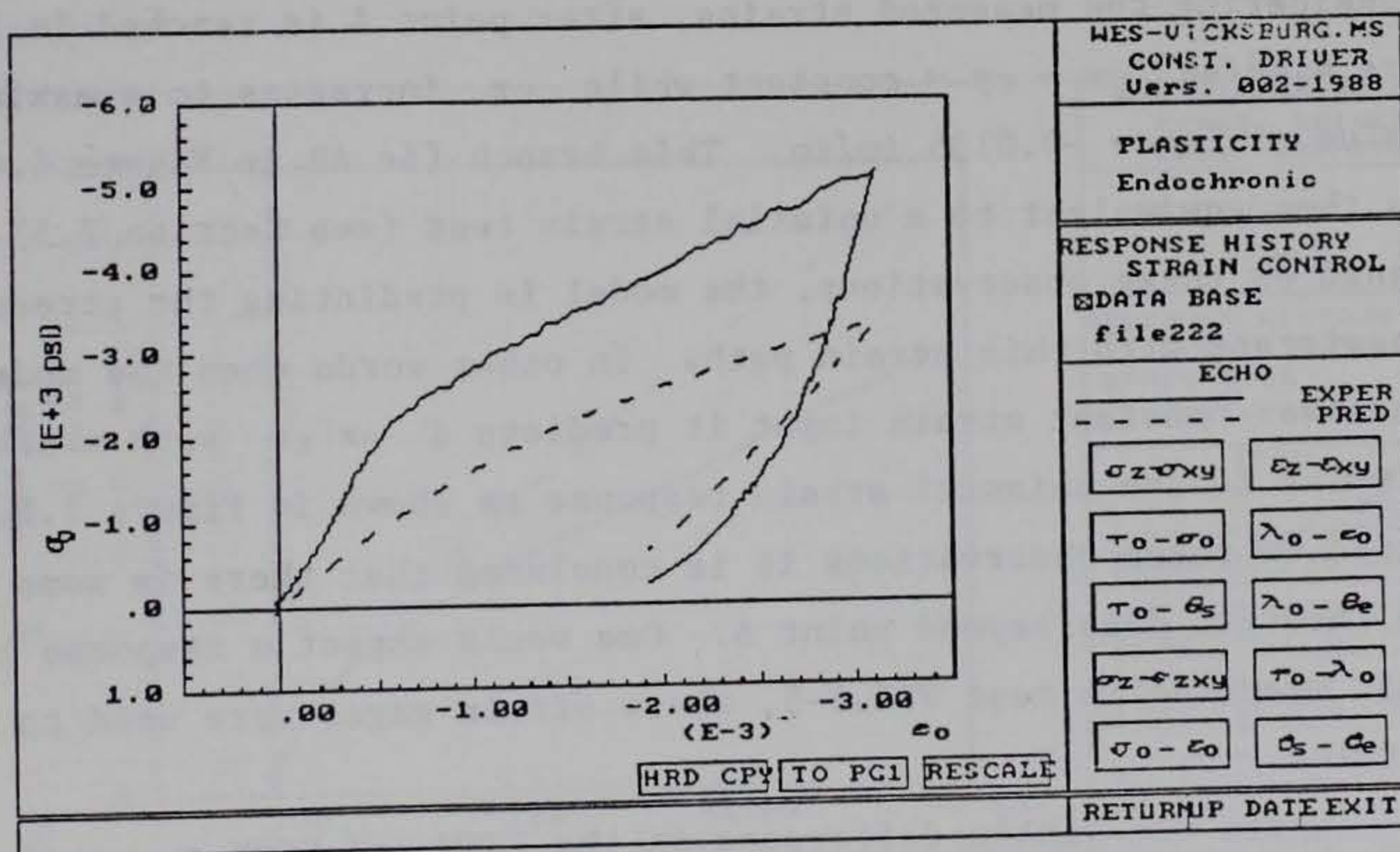
(b) octahedral stress strain

Figure 4.45 FEBM-VT2-1, associated flow





(a) normal stress strain



(b) octahedral stress strain

Figure 4.46 ECPM-VT2-1



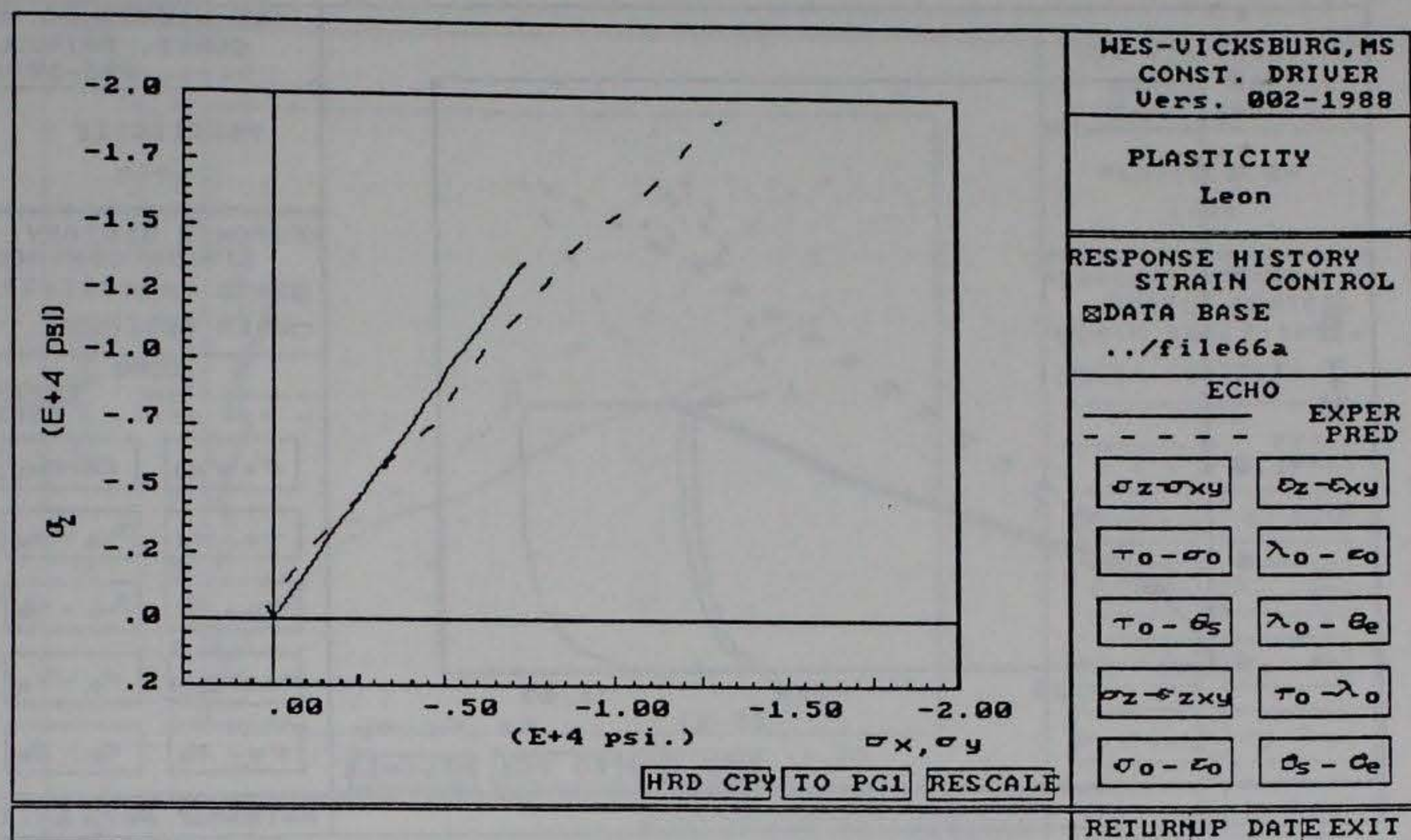
#### 4.4 FEBM and ECPM - VT4-1, VT4-2, VT4-3

These tests were conducted at the University of Colorado in the CU four-inch cubical cell. Strains are measured in this device through the use of displacement gages which are in contact with a point at the center of the specimen face. The associated and non-associated flow versions of the FEBM produced essentially the same results for test VT4-1. Also results from the ECPM were very similar to the FEBM and therefore only the results from the associated flow FEBM are presented in Figure 4.47. Unloading data was not provided and therefore little insight into material response features can be gained from this test.

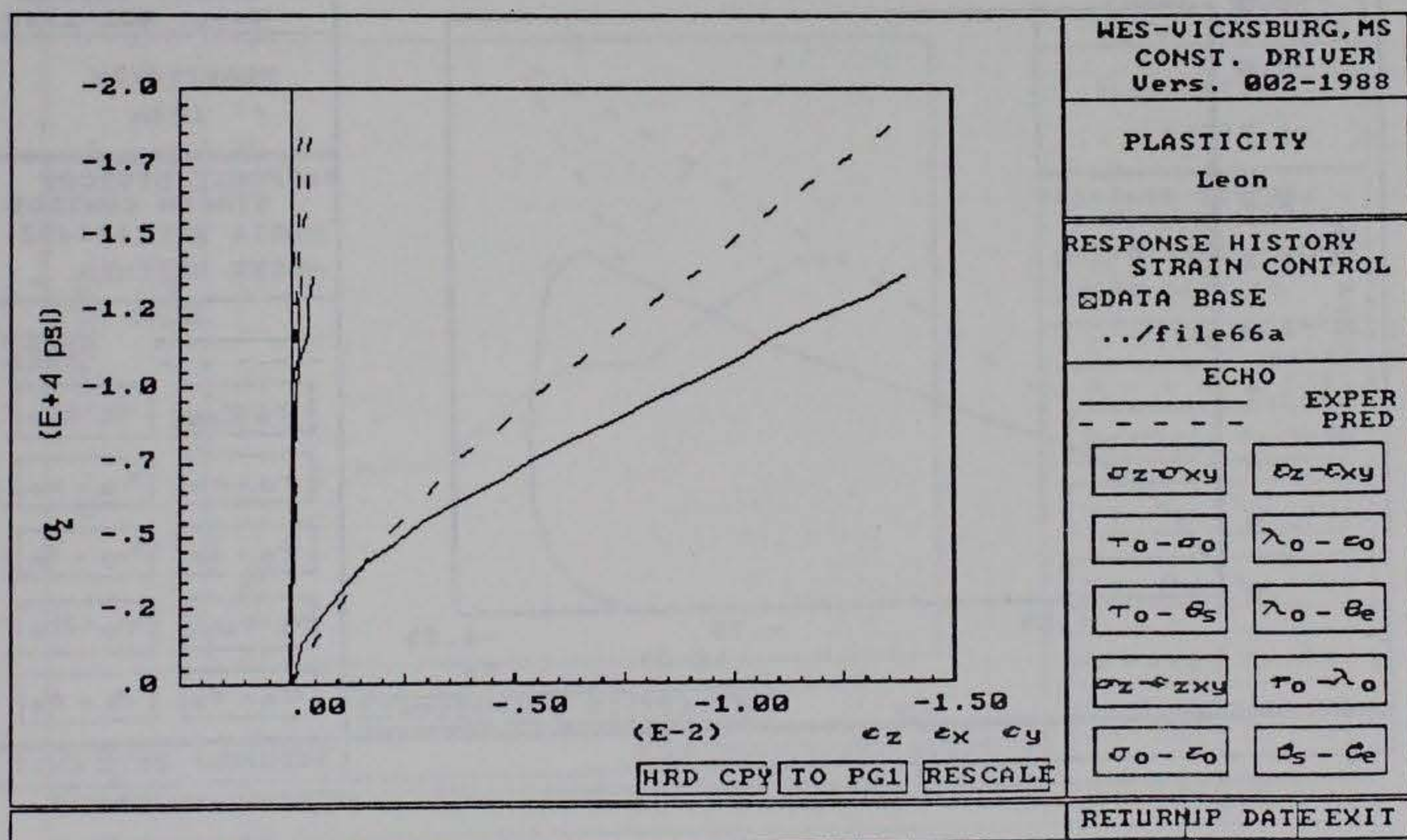
Furthermore, both versions of the FEBM and the ECPM predicted similar results for VT4-2 and therefore only, the FEBM results are presented in Figure 4.48. Studying the test data (VT4-2) and model predictions in more detail reveals some inconsistencies. First just considering the measured strains, after point A is reached in Figure 4.48(a)  $\epsilon_x = \epsilon_y = \text{constant}$  while  $\epsilon_z$  increases to a maximum value of  $\epsilon_z = -0.0135$  in/in. This branch (ie AB in Figure 4.48(a)) is then equivalent to a uniaxial strain test (see Section 2.5). Based on these observations, the model is predicting the stresses consistent with this strain path. In other words when the model receives constant strain input it predicts a  $\sigma_z$   $\epsilon_z$  path which is similar to the uniaxial strain response as shown in Figure 2.8. Based on these observations it is concluded that there is some error in the test data beyond point A. One would expect a response like that measured in test VT6.5-5, where strain gages were used to record strains.

There was little difference in the FEBM and ECPM in predicting the response for VT4-3 (Figure 4.49) which is a stair step hydrostatic-deviatoric test similar to VT6.5-1, and VT6.5-3, except that the unloading branches were not conducted. The improvement in model test comparisons using the mixed control option can be seen in





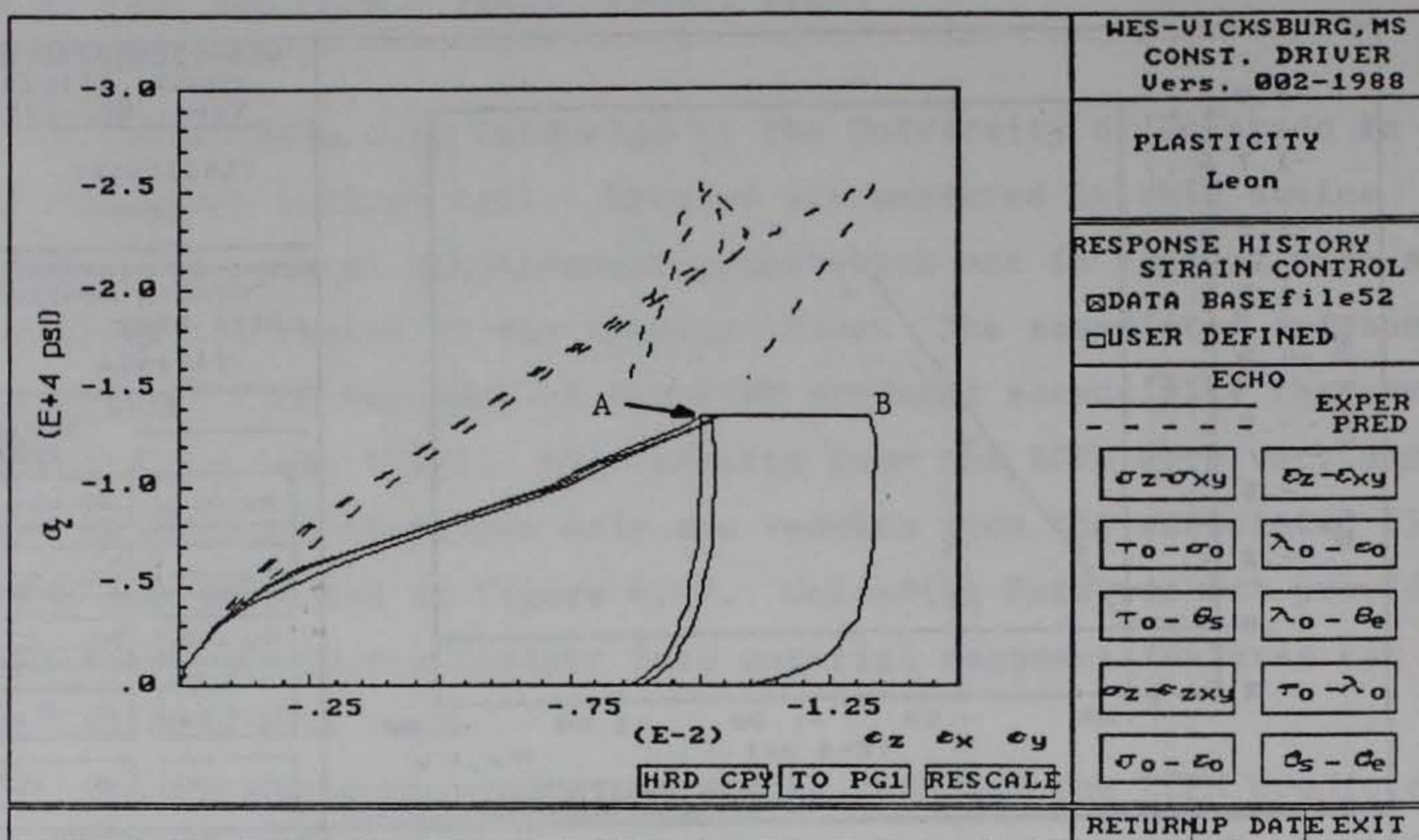
(a) stress path



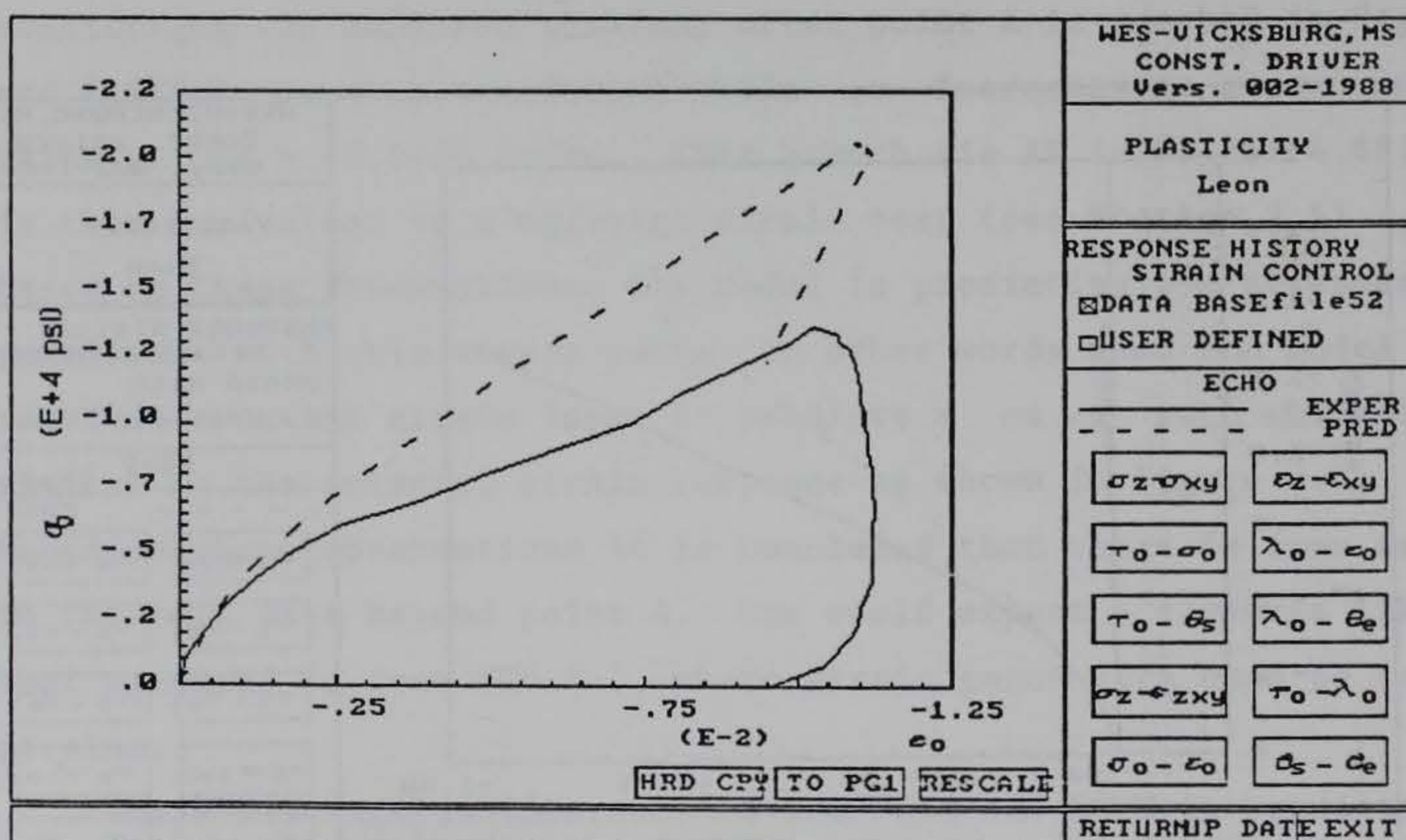
(b) normal stress strain

Figure 4.47 FEBM-VT4-1, associated flow





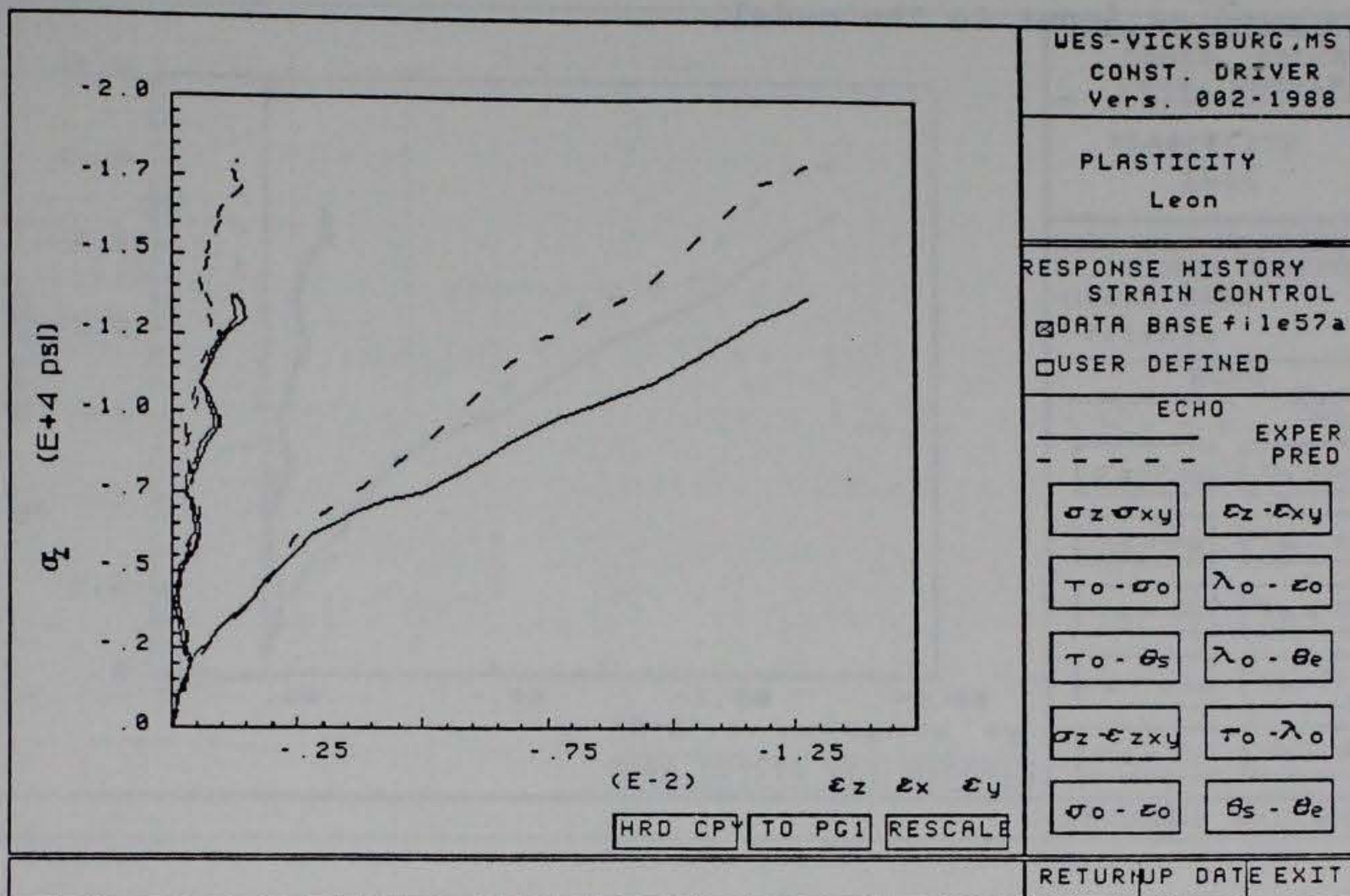
(a) normal stress strain



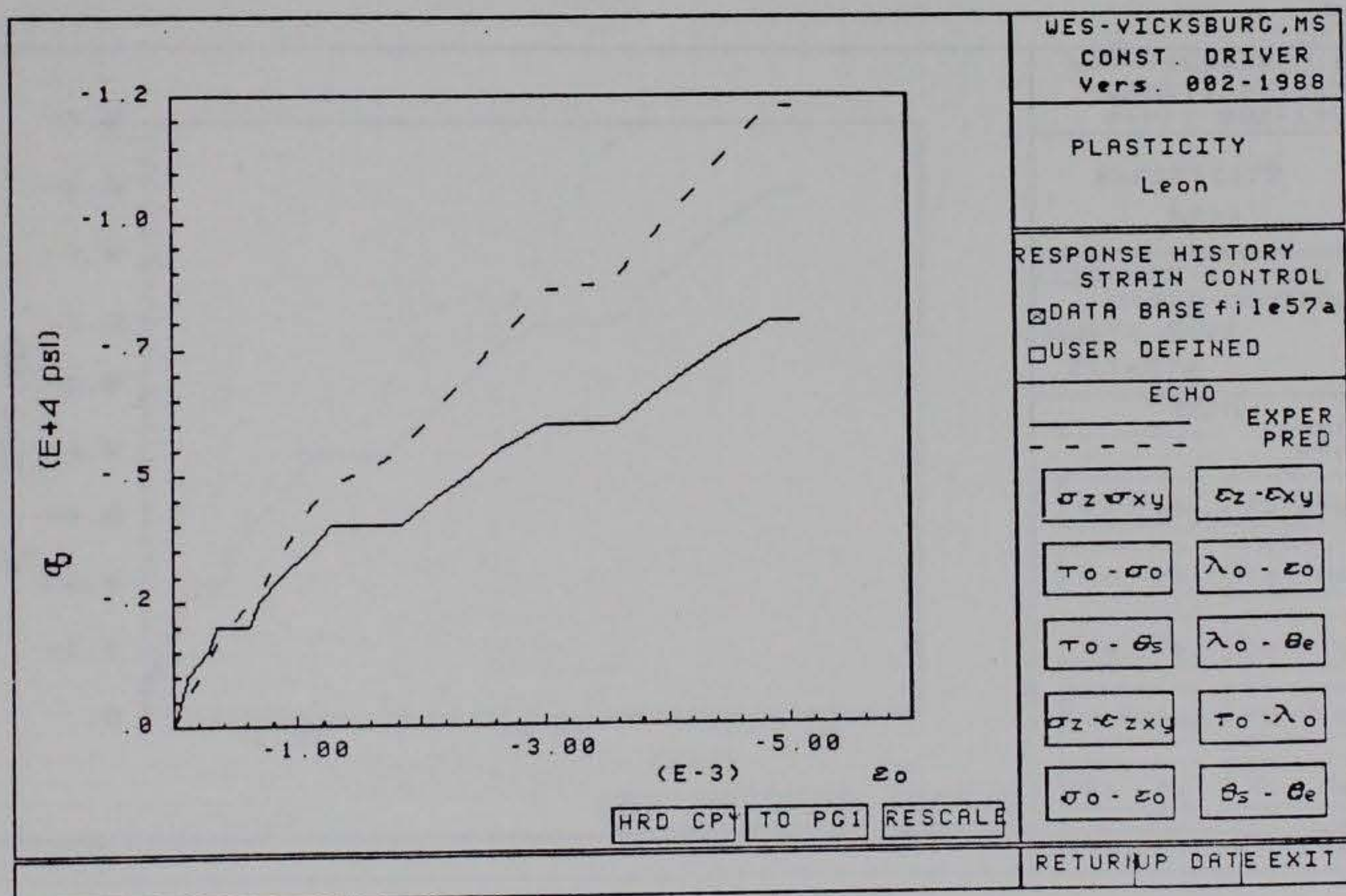
(b) octahedral stress strain

Figure 4.48 FEBM-VT4-2, associated flow





(a) normal stress strain

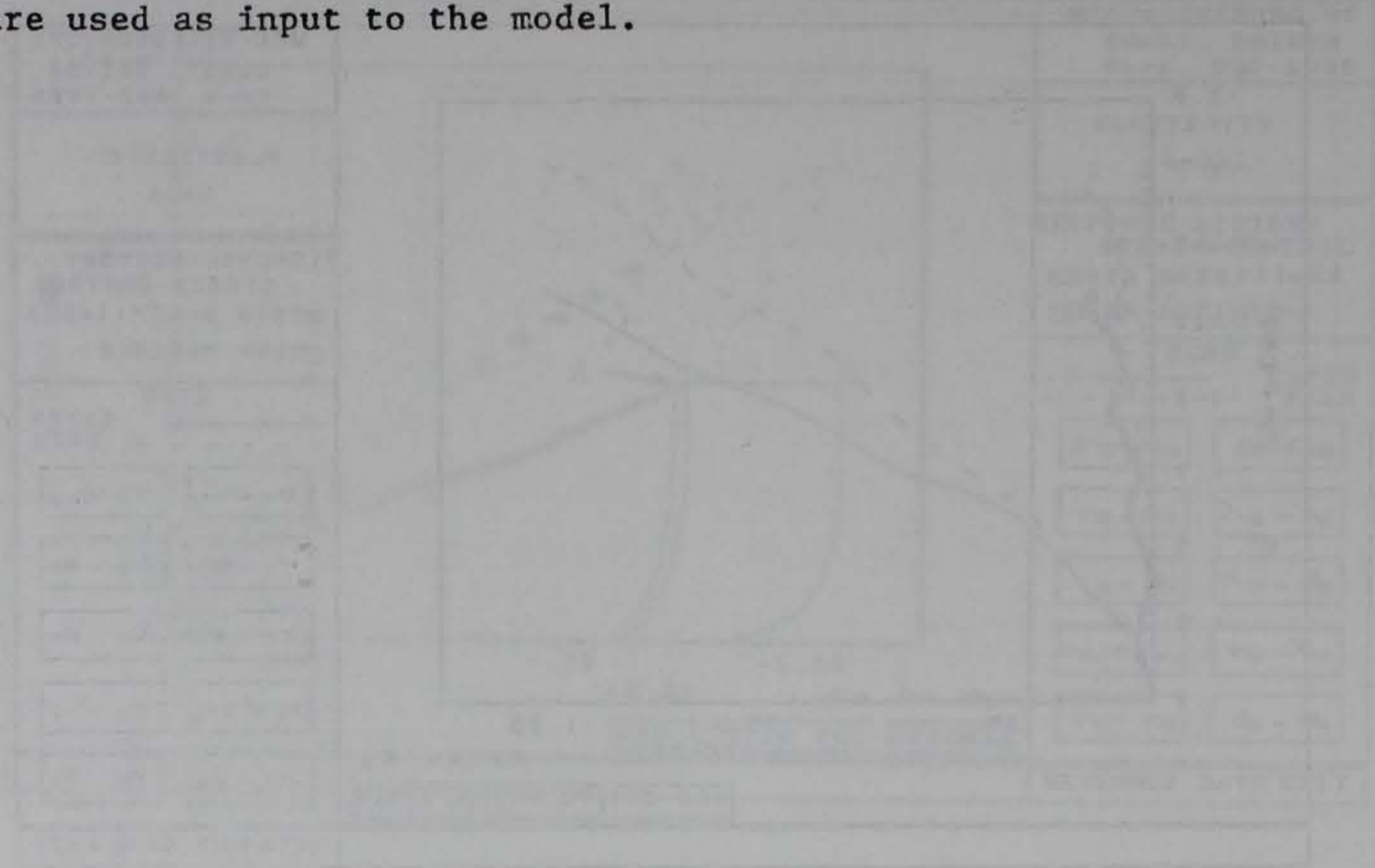


(b) octadedral stress strain

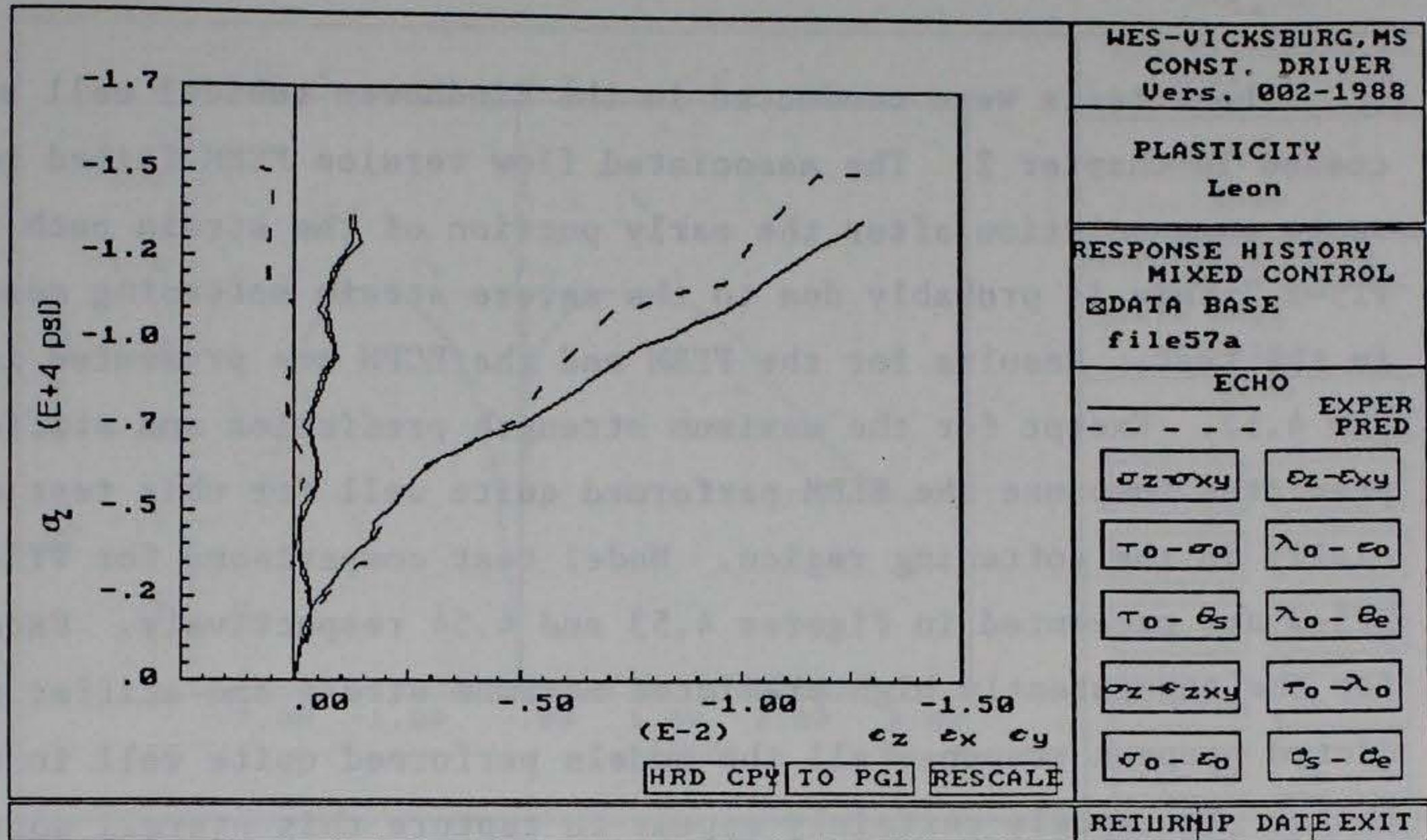
Figure 4.49 FEBM-VT4-3, associated flow



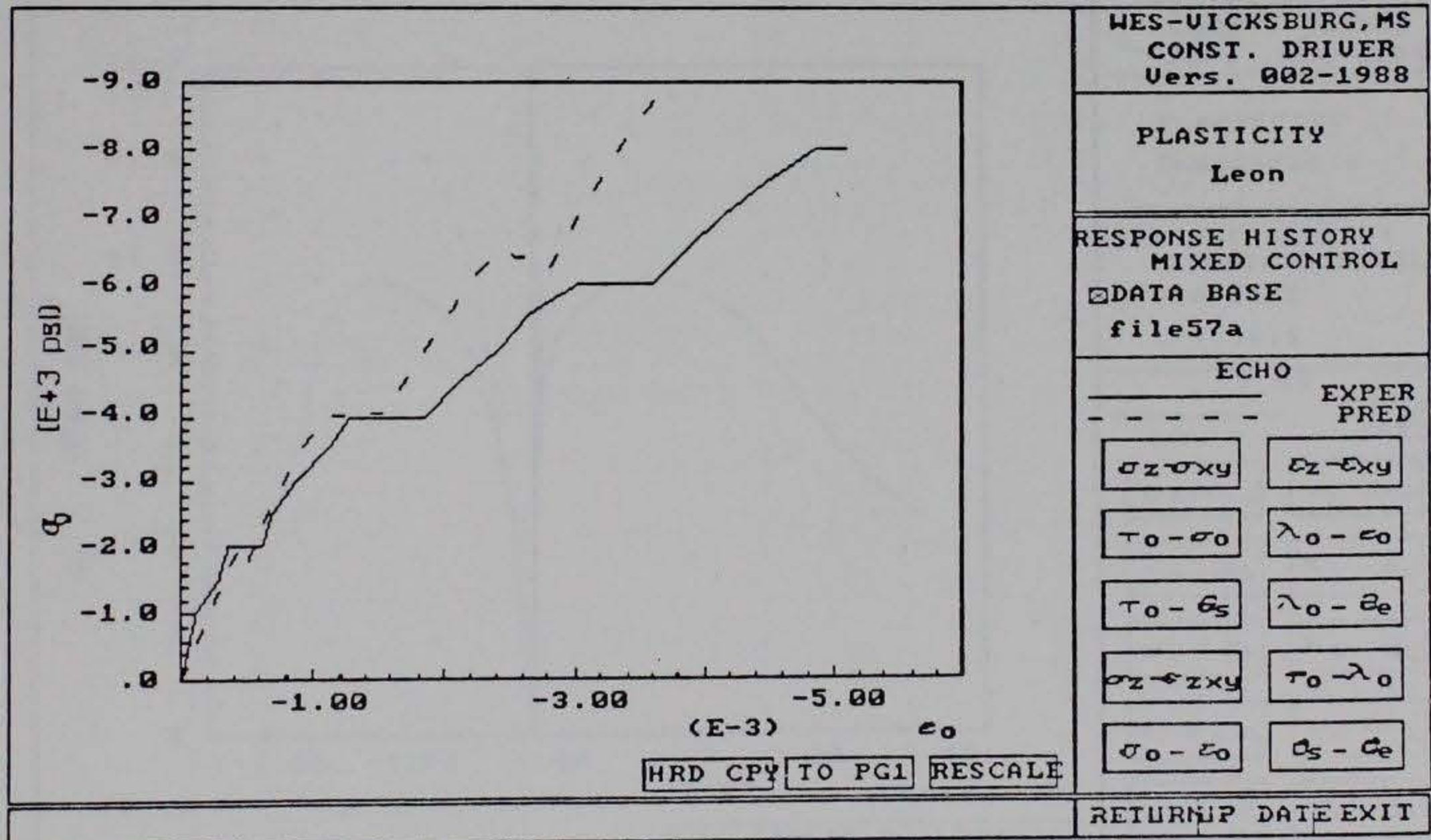
Figure 4.50. For mixed control axial strains and lateral stresses are used as input to the model.







(a) normal stress strain



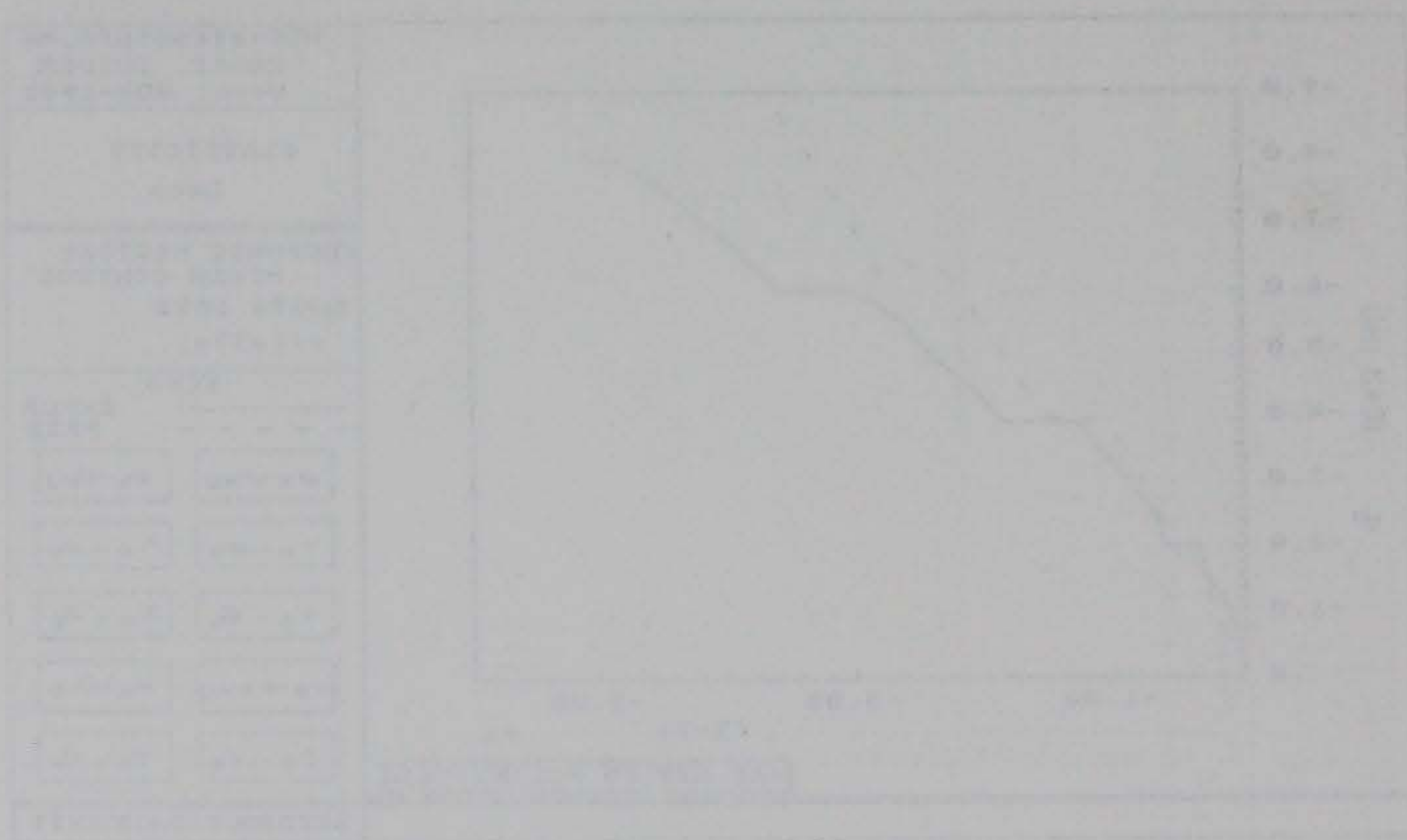
(b) octahedral stress strain

Figure 4.50 FEBM-VT4-3, associated flow, mixed control



#### 4.5 FEBM and ECPM - VT5-1, VT5-2, VT5-3

These tests were conducted in the Eindhoven cubical cell as discussed in Chapter 2. The associated flow version FEBM failed to converge on a solution after the early portion of the strain path for VT5-1. This is probably due to the severe strain softening measured in the test. Results for the FEBM and the ECPM are presented in Figure 4.52. Except for the maximum strength prediction and stiffer predicted response the FEBM performed quite well for this test especially in the softening region. Model test comparisons for VT5-2 and VT5-3 are presented in Figures 4.53 and 4.54 respectively. Except for the consistently high predicted maximum stress and stiffer predicted prepeak response all the models performed quite well in these tests. The models certainly appear to capture this overall softening response (ie Tests VT5-2 and VT5-3) much better than in test VT6.5-2.





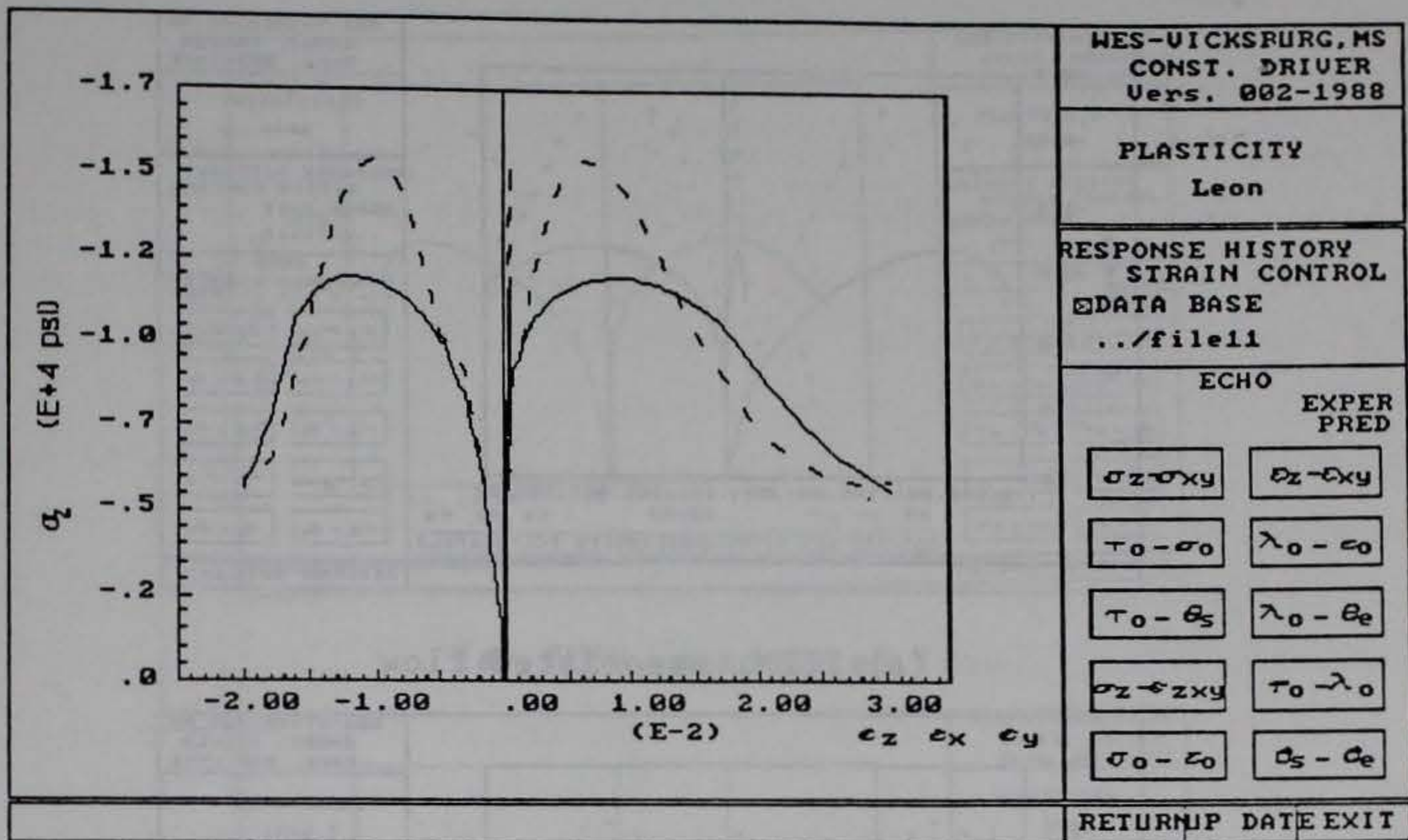


Figure 4.51 FEBM-VT5-1, non-associated flow, normal stress strain

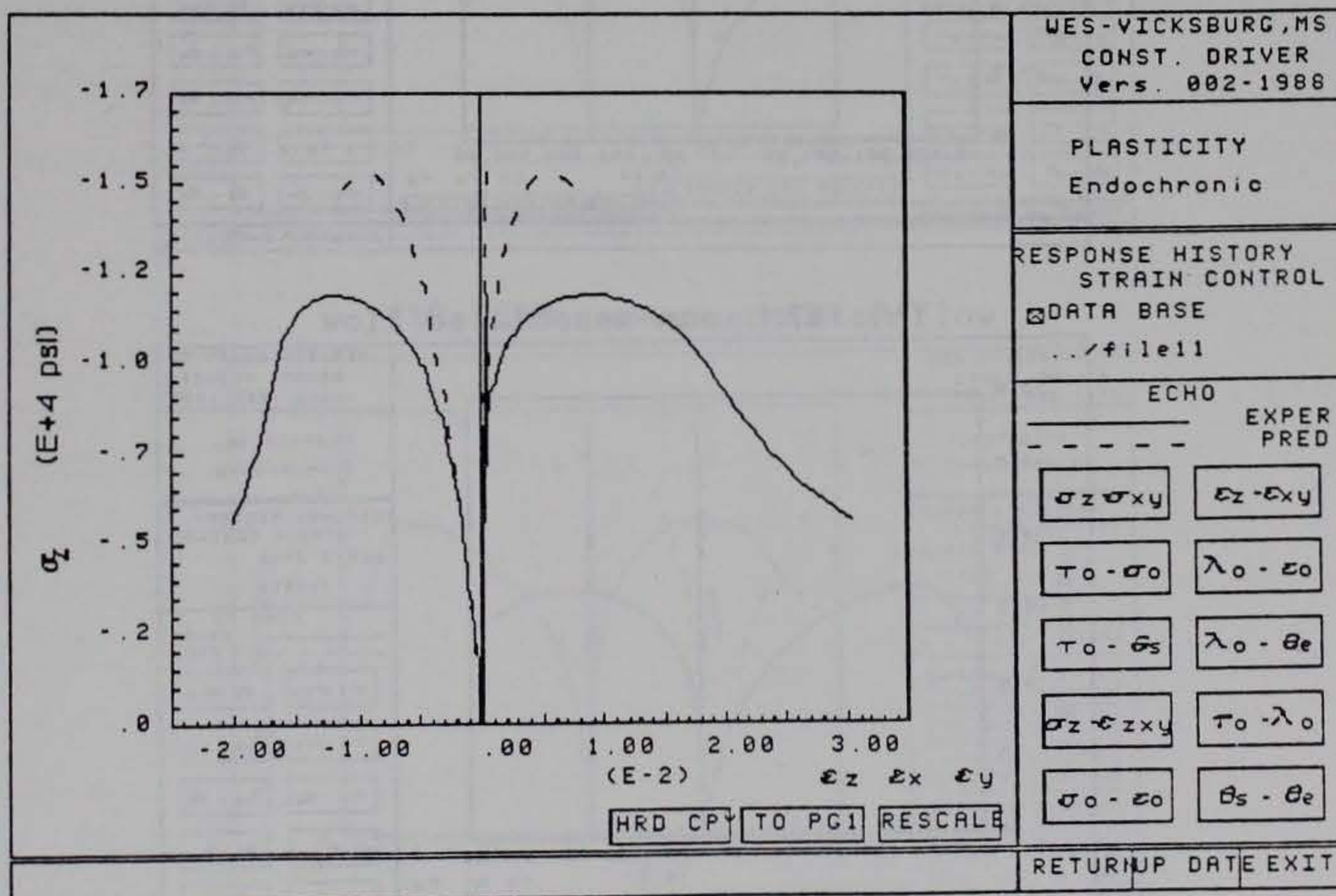
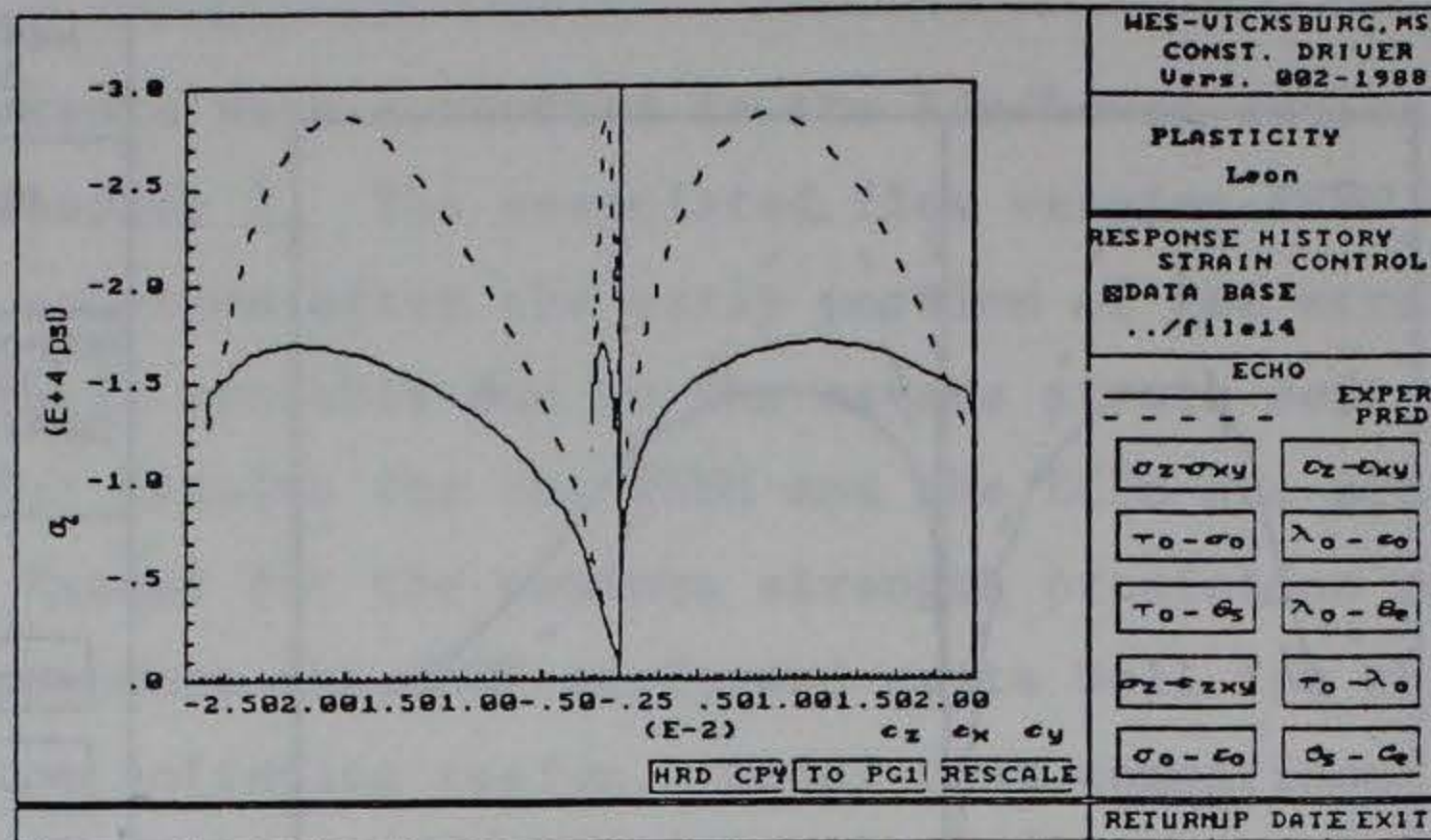
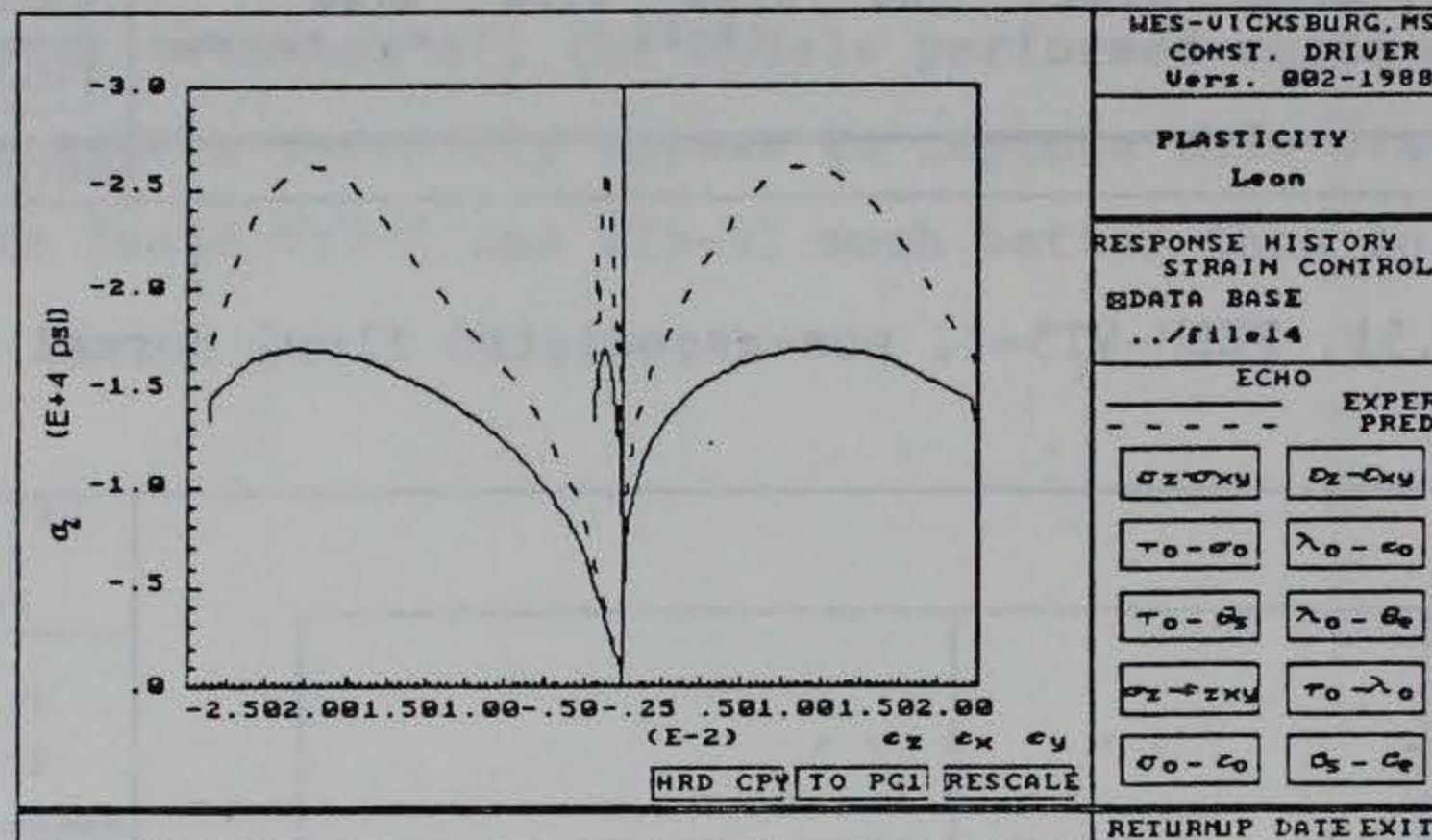


Figure 4.52 ECPM-VT5-1, normal stress strain

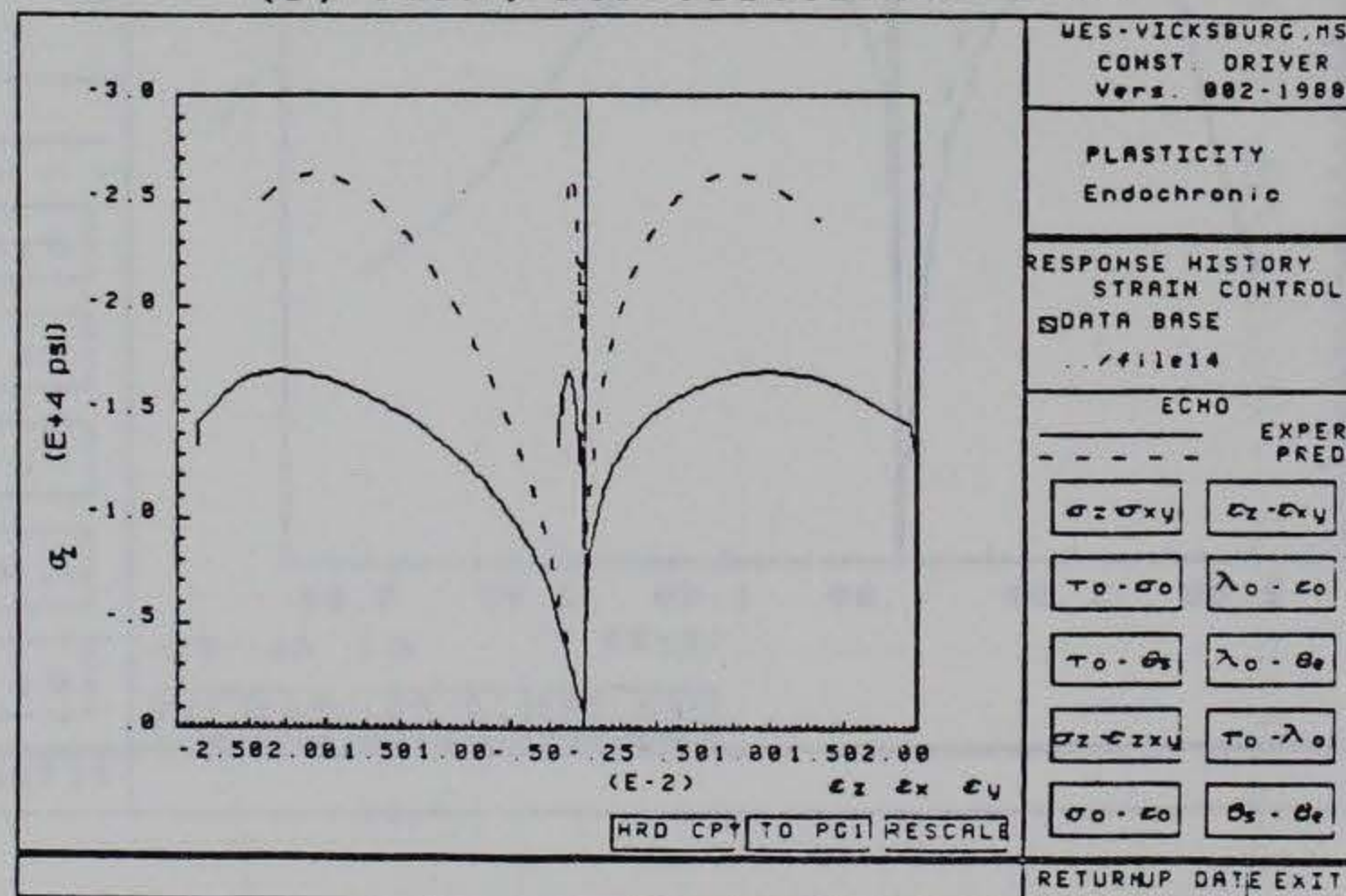




(a) FEBM, associated flow



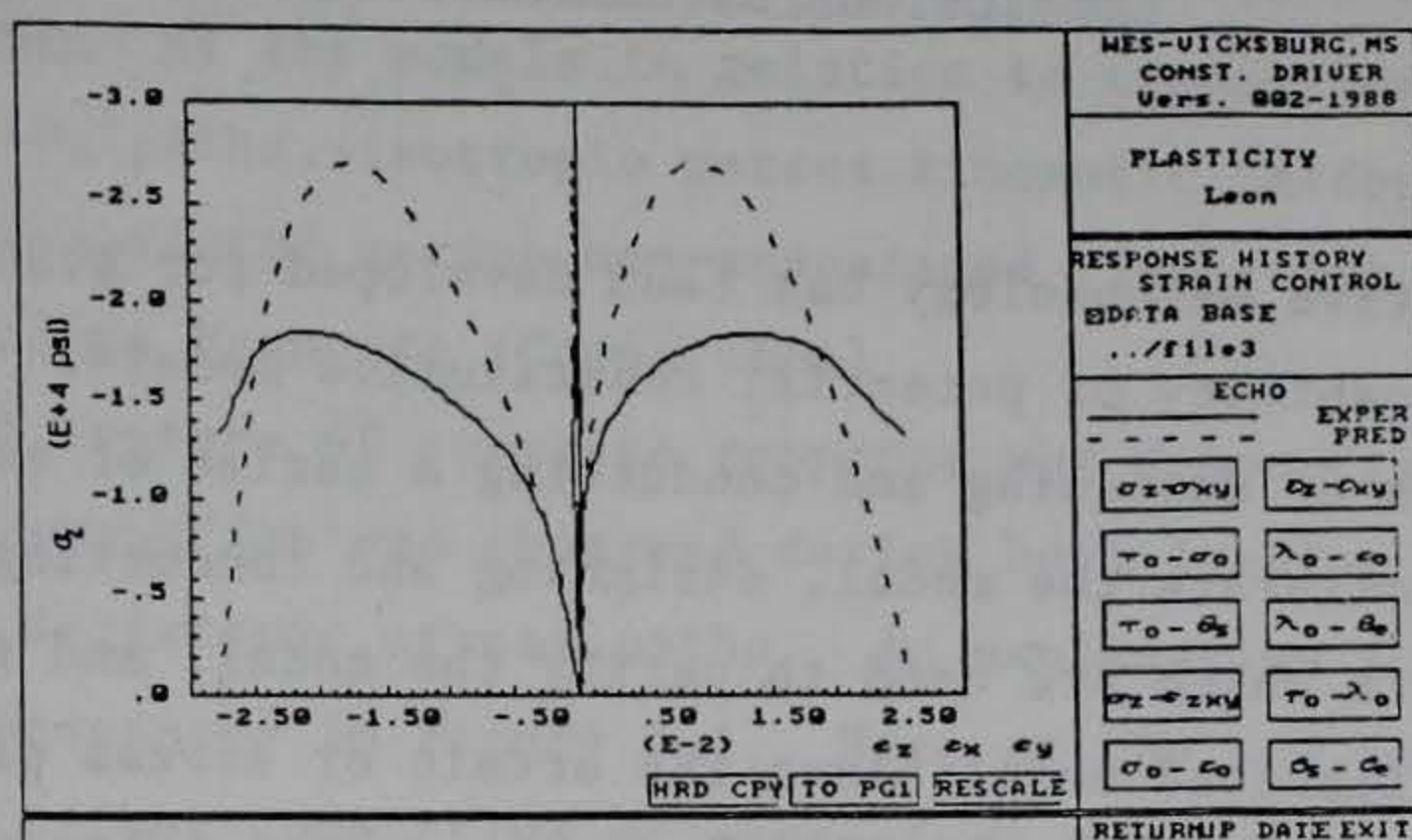
(b) FEBM, non-associated flow



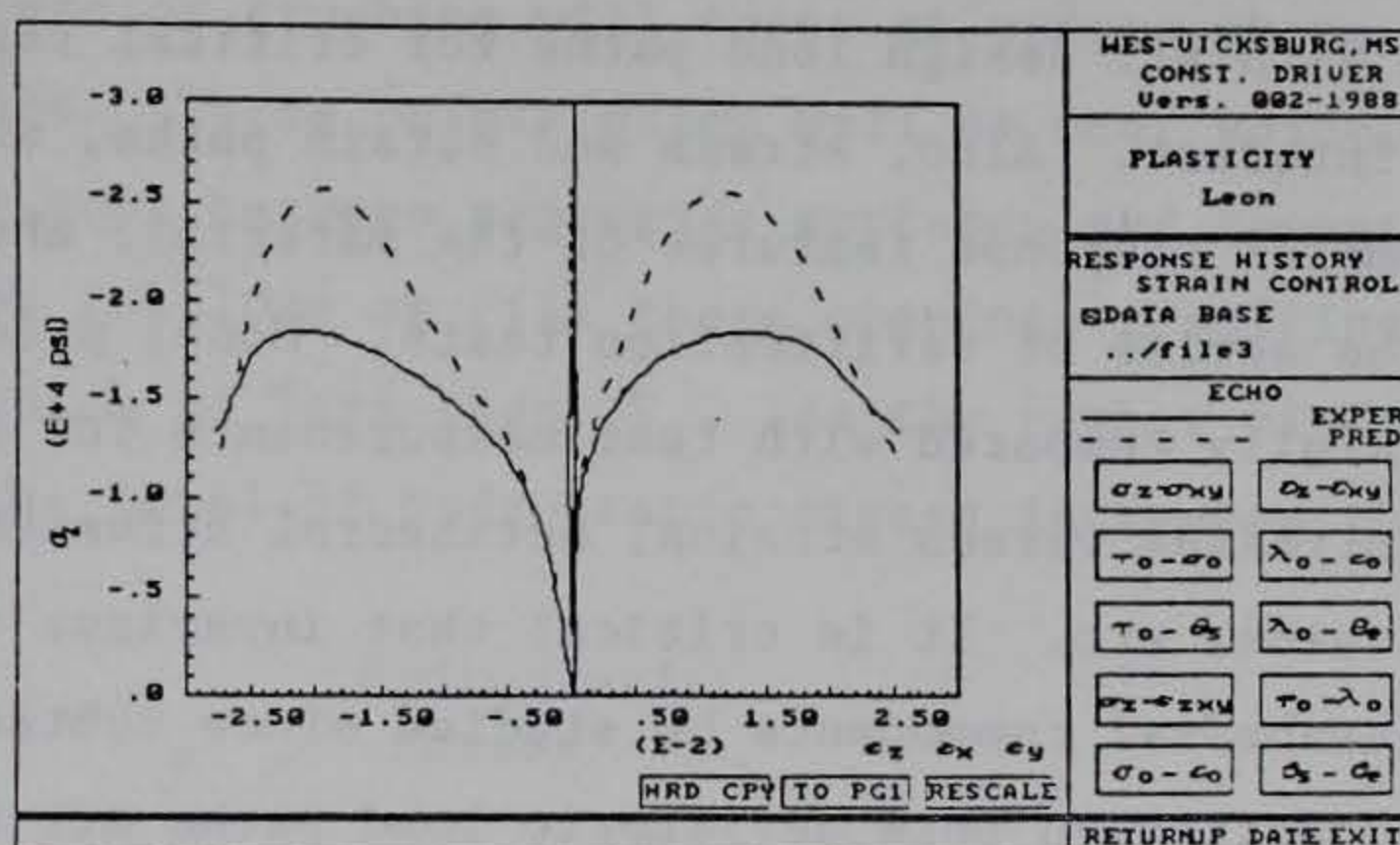
(c) ECPM

Figure 4.53 All models-VT-5-2, normal stress strain

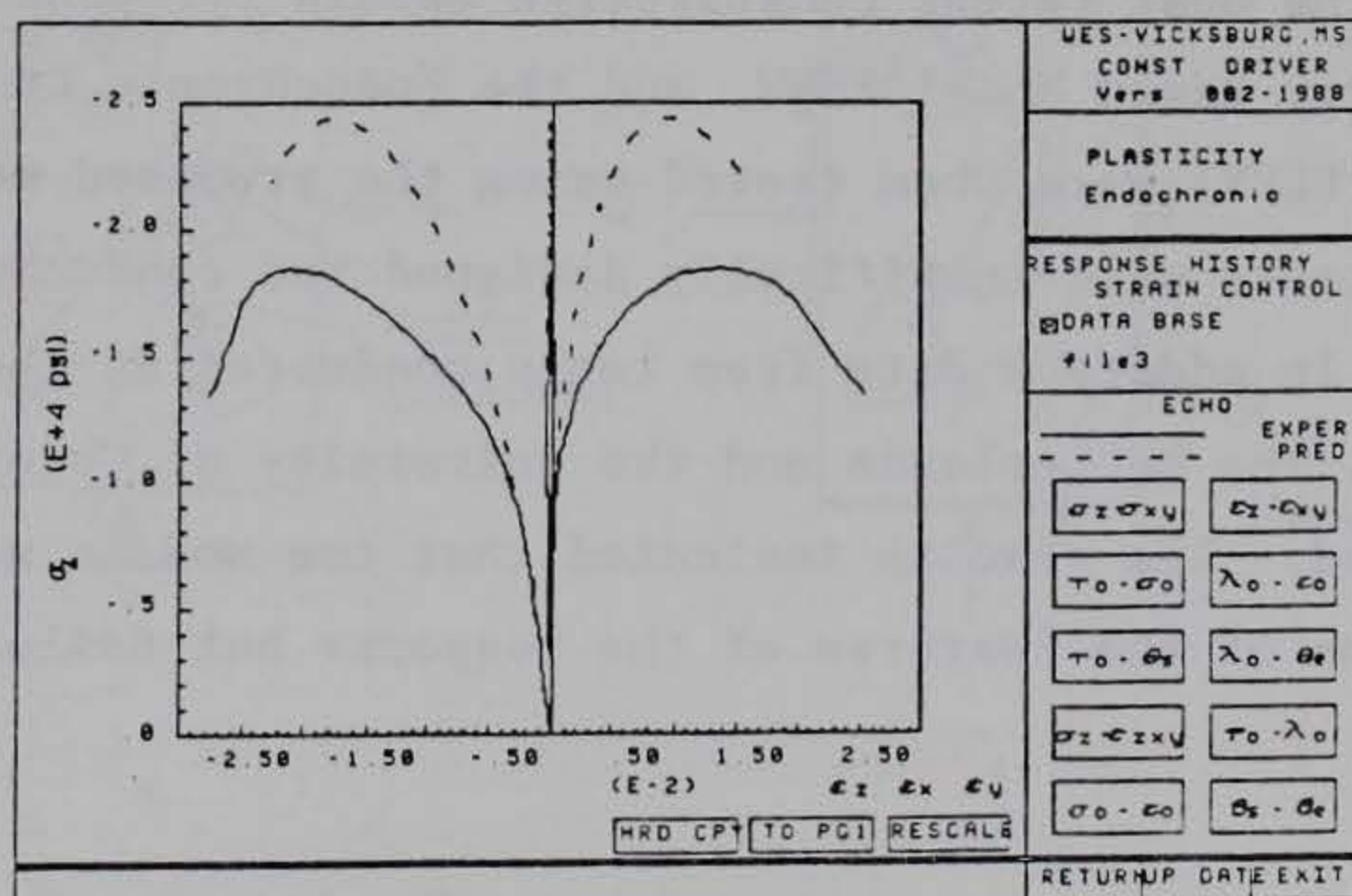




(a) FEM, associated flow



(b) FEM, non-associated flow



(c) ECPM

Figure 4.54 All models-VT5-3, normal stress strain



## Chapter 5

### Conclusions/Recommendations

#### 5.1 Summary

An effective methodology has been developed for evaluating the predictive capability of potential constitutive models. This methodology consists of designing and conducting a series of tests which are used to calibrate the model, designing and conducting a second series of tests which are used to verify the model, and finally exercising the calibrated model along the strain or stress paths of the verification tests so that predictions and test results can be compared. The stress and strain paths of the verification tests should be consistent with all design load paths for critical regions in the structure of interest. Also, stress and strain paths, which demonstrate key complex response features of the material, should be included in the series of verification tests. Model predictions should be carefully compared with test measurements for stress path, strain path, stresses versus strains, octahedral stresses versus octahedral strains, etc. It is critical that invariant quantities such as the octahedral components be studied since subtle features like shear compaction on pure deviatoric load paths are not so noticeable when looking at normal stress and strain plots.

Two of the most recent constitutive models for concrete (the Fracture Energy Based Model FEBM, and the Endochronic Concrete Plasticity Model ECPM) were then tested using the proposed methodology. A number of tests were specifically designed and conducted for the evaluation. In addition data from tests conducted at the University of Eindhoven, The Netherlands and the University of Colorado, Boulder were also used. The results indicated that the models would indeed reproduce some of the features of the response but failed in others.



## 5.2 Conclusions

A number of conclusions can be drawn from the tests conducted and the evaluation of the models in relation to compaction under pure deviatoric stress paths, isotropic versus kinematic hardening, strain softening and associated versus non-associated flow rules.

### 5.2.1 Shear Volume Response (Compaction)

A critical feature of concrete response was demonstrated in test VT6.5-1 where compaction was observed during both loading and unloading along pure deviatoric stress paths. An explanation for this phenomenon is presented in Figure 5.1. Here at the end of a hydrostatic branch (either compactive or expansive) the material is at some volume  $V_i$ . As shear is applied (with hydrostatic stress held constant) fracture or crushing will occur at points where stress concentrations exist. These points often will be near voids, small cracks or small gaps between aggregate surfaces and cement and the tendency will be to close or fill these openings resulting in a final volume ( $V_f$ ) which is less than  $V_i$ . As the number of deviatoric cycles and or the level of hydrostatic stress increases the volume

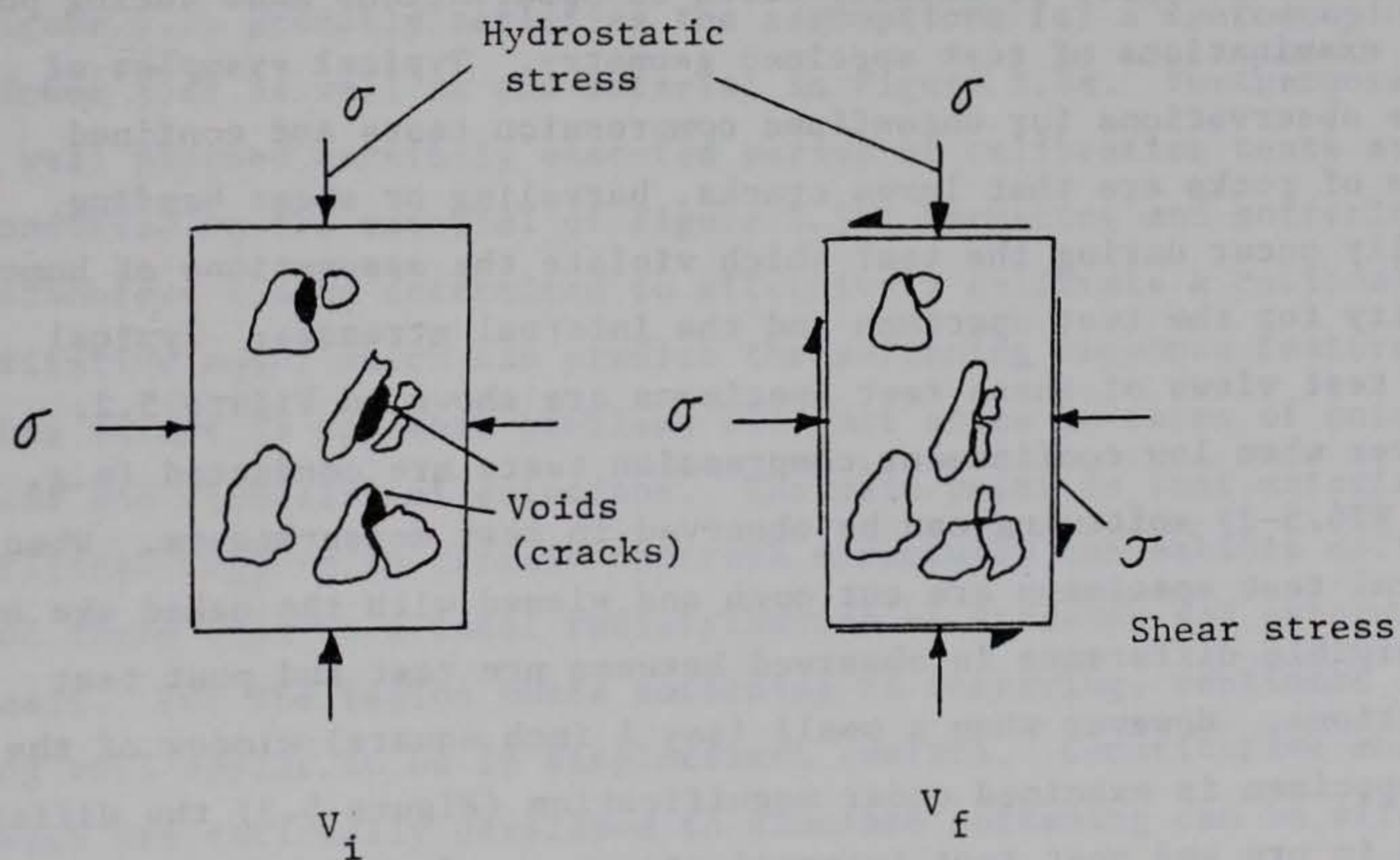


Figure 5.1 Shear compaction concept



change (ie  $V_f - V_i$ ) should approach zero. This was observed in test VT6.5-3 which was conducted at a much higher hydrostatic stress.

### 5.2.2 Conventional Isotropic Hardening Plasticity

It was pointed out in Chapter 4 that the "isotropic" hardening model used in the FEBM, results in failure of the model to predict important material response features (i.e. compaction along certain deviatoric paths). Also, since the loading surface does not contract the model only predicts elastic response, after the maximum strength surface is reached, and the stress point moves back into the assumed "elastic" region. In fact this is also the case for cap models which make use of isotropic hardening only. While this assumption is reasonable in many cases, for metal plasticity, it is inappropriate for concrete since significant plastic response can occur after the maximum strength surface is intersected and loading continues, in the direction toward the interior of the loading surface, which was precisely the case in test VT6.5-1 and VT6.5-3.

### 5.2.3 Strain Softening

The argument that strain softening is a structural as opposed to a material property is usually based on observations made during post test examinations of test specimen geometry. Typical examples of these observations for unconfined compression tests and confined tests of rocks are that large cracks, barreling or shear banding usually occur during the test which violate the assumptions of homogeneity for the test specimen and the internal stresses. Typical post test views of these test specimens are shown in Figure 5.2. However when low confinement compression tests are conducted (e.g. test VT6.5-2) softening can be observed in test measurements. When typical test specimens are cut open and viewed with the naked eye no discernible difference is observed between pre test and post test conditions. However when a small (say 1 inch square) window of the cut specimen is examined under magnification (Figure 5.3) the differences in pre and post test internal structure of the specimen can be clearly seen. In Figure 5.3(b) the fracture of aggregates, void



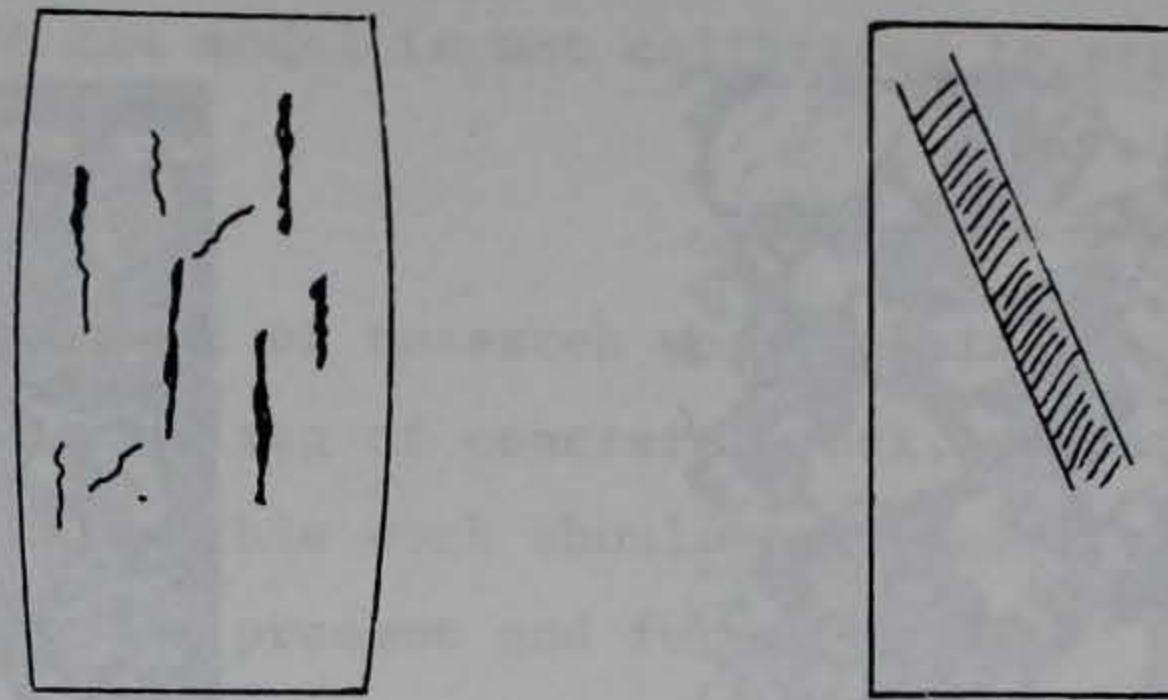
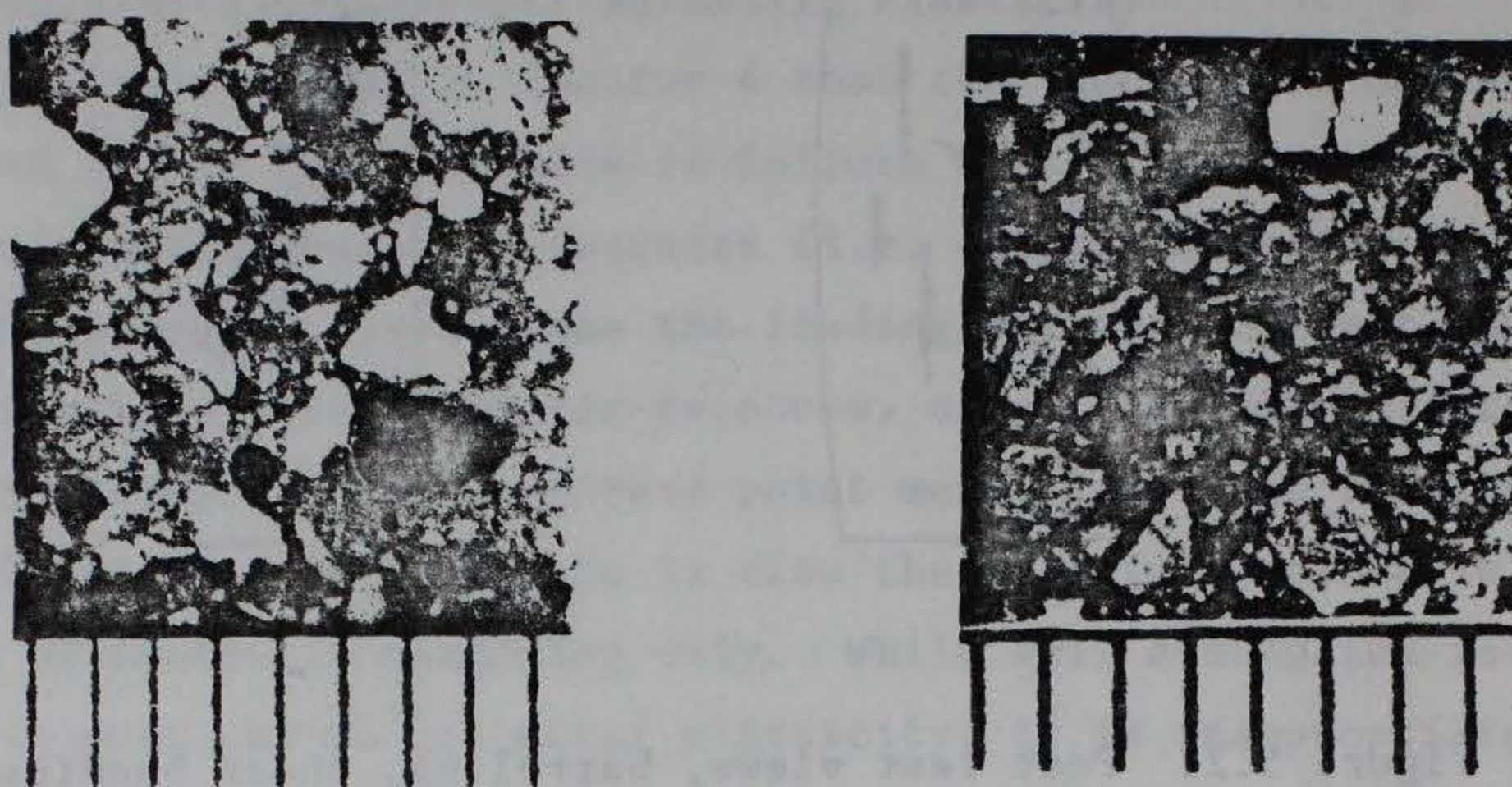


Figure 5.2. Post test views, barrelling, shear banding.

closure, and separation of aggregate from cement paste at some points can be seen. However, the post test specimen is still intact and similar specimens have been retested in unconfined compression and seen to still possess from 75% to 100% of their initial strength and elastic moduli. The conclusion drawn here is that the material of Figure 5.3b probably satisfies the assumptions for a macroscopic continuum just as well as the material in Figure 5.3a. Furthermore, if a well planned carefully executed series of calibration tests are conducted on the material of Figure 5.3b, hardening and softening parameters can be determined to effectively calibrate a rational constitutive model which can predict the softening response features. This is not to say that problems will not arise in terms of uniqueness and stability of solutions. The main point is that material at critical regions in certain concrete structures can exhibit softening and there will be a local redistribution of stresses and external loads. For the region where softening is occurring, continued loading will appear to be in displacement control. Constitutive models which are rationally developed to simulate softening can be effectively used to predict the stress redistribution in these structures.





(a) Pretest

(b) Post Test

Figure 5.3. 6X magnification, pre and post test.

#### 5.2.4 Non-Associated Flow

From an experimental standpoint results presented in this study (e.g. Figure 4.8) clearly indicate that concrete response does not necessarily satisfy conditions required for associated flow plasticity. The non-associated flow version of the FEBM generally improved the predictive capability of the model compared with the associated flow version.

#### 5.2.5 Endochronic Model

The main conclusion drawn for the ECPM is that the model seems to be based on just as sound and rational assumptions as plasticity models and is not based on a variety of curve fits. The capability of the model to predict compaction on all deviatoric branches in test VT6.5-1 is very impressive for such a simple model. The simple model presented here does not take advantage of the concept of adding together several endochronic elements in parallel so that a wide range of material responses can be modeled. This is one of the strong features of the endochronic theory. However, the ECPM did not



perform well in the softening region as shown in Figure 4.22. This is partly due to the use of only one endochronic element and partly due to the fact that the model is not calibrated to predict softening response.

### 5.3 Recommendations

A considerable amount of research work remains to be done in the area of constitutive modeling of concrete, rock, or soils. The methodology presented in this work should serve as a basis for calibration and evaluation of present and future models. Since the present study was limited to the evaluation of only two models it appears that some of the other models available or present should be subjected to the same process. Some recommendations on how to apply the proposed methodology and specific areas of behavior that need further examination are discussed next.

#### 5.3.1 Application of the Methodology

When the methodology developed in this study is used to evaluate constitutive models, calibration tests and verification tests should be repeated to demonstrate uniformity and consistency of measurements as well as variation in test results due to experimental error. Models should be driven under strain control, stress control, and mixed control for a full evaluation.

#### 5.3.2 Shear Volume Response

A series of hydrostatic-deviatoric tests should be conducted at different deviatoric sections to determine the effects of hydrostatic stress level on shear compaction. Also, similar tests where the deviatoric path is cycled several times should be conducted to determine this effect on limiting values for volume compaction.

#### 5.3.3 Hardening

It has been shown in this study that conventional isotropic hardening concepts alone cannot capture the nonlinear material response of concrete when the stress point reaches the maximum strength surface then moves back into the "elastic region." This is the case for both associated and non-associated flow. The simple



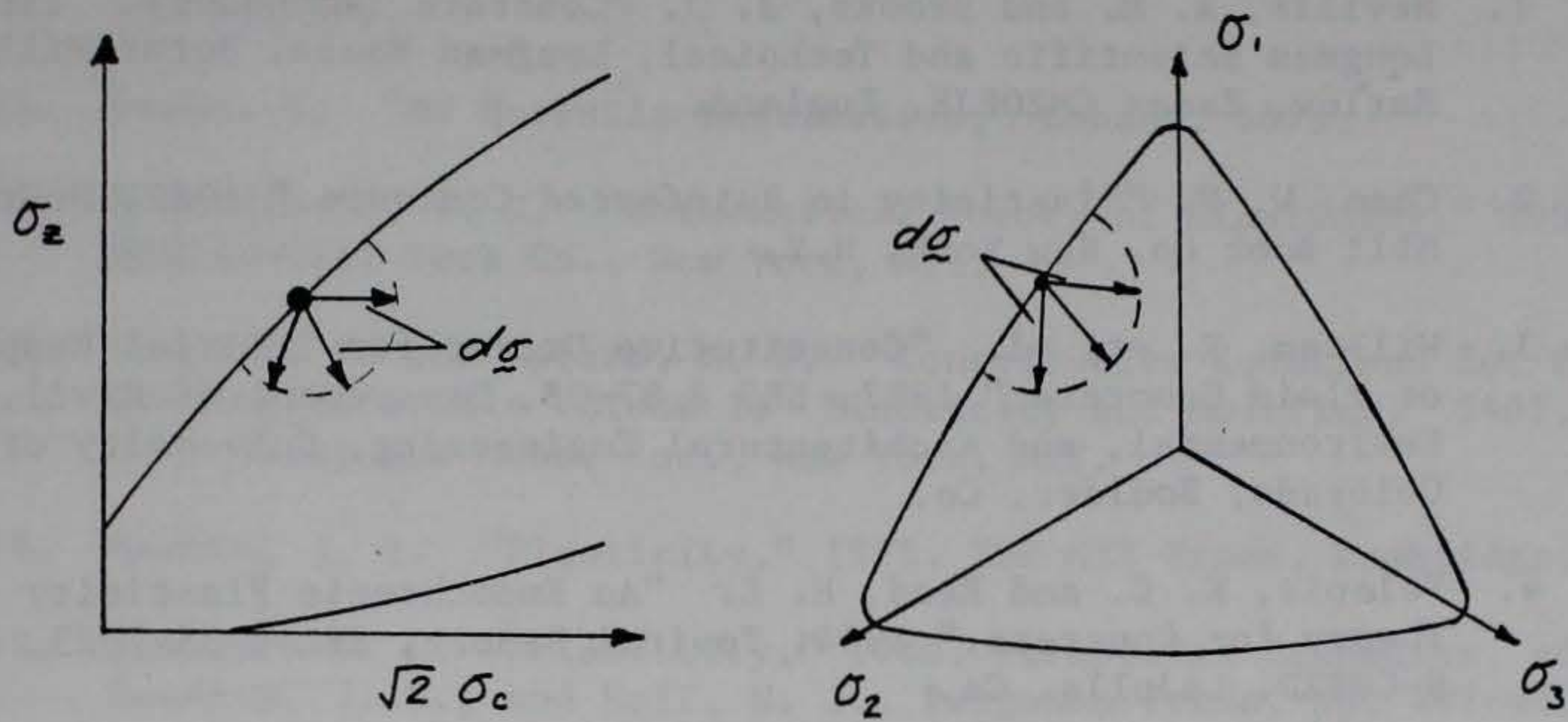
endochronic model did reasonably well in predicting this response and should be further studied and developed in this area. Also, kinematic hardening concepts should be further studied and developed in this context to determine their capabilities. Further testing should be conducted where the stress point moves out to the maximum strength surface (along different paths) then moves back into the elastic region (along different paths). Measured plastic strain increments should be plotted, along these paths, which will indicate the orientation and position of a kinematic surface (if one exists). These tests should be performed along load paths in the meridional plane (Figure 5.4a) as well as along fully three dimensional load paths (Figure 5.4b).

#### 5.3.4 Strain Softening

A carefully planned test program should be conducted to study the issue of strain softening. This test program should include the following considerations:

- (a) Careful preparation of test specimen to insure uniform consolidation.
- (b) Minimize friction on loaded surfaces of the specimen.
- (c) Repeated softening tests at different rates of loading.
- (d) Careful dissecting of specimen for internal microscopic examination.





(a) Rendulic Plane

(b) 3D Space

Figure 5.4 Loading into the elastic region along different load paths



## Chapter 6: Bibliography

1. Neville, A. M. and Brooks, J. J. "Concrete Technology," 1987, Longman Scientific and Technical, Longman House, Burnt Mill, Harlow, Essex CM202JE, England.
2. Chen, W. F. "Plasticity in Reinforced Concrete," 1982, McGraw-Hill Book Co. New York, N.Y.
3. William, K. et. al. "Constitutive Driver for Triaxial Response of Plain Concrete," 1987, SRS # 87-08, Department of Civil, Environmental, and Architectural Engineering, University of Colorado, Boulder, Co.
4. Valanis, K. C. and Read, H. E. "An Endochronic Plasticity Theory for Concrete," 1984, Topical Report, SSS-R-85-7023, S-CUBED, LaJolla, Ca.
5. Hegemies, G. A. et. al. "On the Development of Constitutive Relations for Plain and Reinforced Concrete," 1982, Final Report, SSS-R-82-5495, S-CUBED, LaJolla, Ca.
6. Green, S. J. and Swanson, S. R. "Static Constitutive Relations for Concrete," 1973, AFWL-TR-72-244, Air Force Weapons Laboratory, Kirtland Air Force Base, New Mexico.
7. Van Mies, J. G. M. "Strain Softening of Concrete under Multi-axial Loading Conditions," 1984, PhD. Dissertation, U. of Eindhoven, The Netherlands.
8. Gerstle, K. H., et. al. "Behavior of Concrete under Multiaxial Stress States," 1980, ASCE Journal of the Engineering Mechanics Division, Proceedings, Vol 106, No. EM6.
9. Pariseau, W. G. "A Finite Element Approach to Strain Softening and Size Effects in Rock Mechanics," 1979, Proceedings, Third International and Numerical Methods in Geomechanics, Aachen, Germany.
10. Bažant, Z. P. "Instability Ductility, and Size Effect in Strain-Softening Concrete," 1976, ASCE Journal of the Engineering Mechanics Division, Procedures, Vol 102, No. EM2.
11. Scavuzzo, R. et. al. "Stress-Strain Curves for Concrete Under Multiaxial Load Histories," 1983, Department of Civil, Environmental, and Architectural Engineering, University of Colorado, Boulder, Co.



12. Sandler, I. S. and Wright and J. P. "Strain-Softening Chapter 11, Theoretical Foundations for Large Scale Computations for Nonlinear Material Behavior," 1984, Martins Nighoff Publication, pp. 285-396.
13. Hooke, R. "De Potentia Restitutiva," London, 1678.
14. Sokolnikoff, I. S. "Mathematical Theory of Elasticity," 1956, McGraw-Hill Book Co., New York, N.Y.
15. Chen, W. F. and Saleeb, A. F. "Constitutive Equations for Engineering Materials Volume 1: Elasticity and Modeling," 1982, John Wiley and Sons, Inc., New York, N.Y.
16. Martin, J. B. "Plasticity," 1975, The MIT Press, Cambridge, Ma.
17. Drucker, D. C. "Plasticity," 1960, Structural Mechanics, ed., Goodies, J. N., and Hoff, N. J., Pergamon Press, pp. 407-455.
18. Romano, M. "On Leon's Criterion," 1969, Meccanica, pp. 48-66.
19. Valanis, K. C. "A Theory of Viscoplasticity Without a Yield Surface," 1971, Archiwerm Mechanike Stosowonej, Vol 23, No. 4, pp. 517-551.
20. Sandler, I. S. "On the Uniqueness and Stability of Endochronic Theories of Material Behavior," 1978, Journal of Applied Mechanics, Vol 45, No. 2.
21. Rivlin, R. S. "Some Comments on the Endochronic Theory of Plasticity," 1979, Technical Report No. CAM-100-33, Lehigh University, Bethlehem, Pa.
22. Valanis, K. C. "Endochronic Theory with Proper Hysteresis Loop Closure Properties," 1979, Topical Report, SSS-R-80-4182, Systems, Science, and Software, LaJolla, Ca.